TU
WIEN

TECHNISCHE
UNIVERSITÄT
WIEN
Vienna University of Technology

DISSERTATION

Modeling and Compensation of Direct Conversion Transmitters and Receivers

ausgeführt zum Zwecke der Erlangung des akademischen Grades eines

Doktors der technischen Wissenschaften unter der Leitung von

O.Univ.Prof. Dipl.-Ing. Dr.techn. Gottfried Magerl
E354
Institute of Electrodynamics, Microwave and Circuit Engineering

eingereicht an der Technischen Universität Wien
Fakultät für Elektrotechnick und Informationstechnik

von

Dipl.-Ing. Michael E. Gadringer
Matrikelnummer: 9627145
Autaler Straße 21a/4, 8042 Graz

Graz, 18. Oktober 2011   . . . .

Kurzfassung

Moderne Mobilfunksysteme sind einer ständigen Weiterentwicklung unterworfen, um den steigenden Datenraten Rechnung zu tragen. Hierzu werden Modulationsformate mit hoher spektraler Effizienz verwendet. Die resultierenden Sendesignale zeigen zusätzlich zu einer hohen Bandbreite auch eine zeitlich variable Hüllkurve. Die große Dynamik der Hüllkurve bei gleichzeitig steigendem Bandbreitebedarf der Informationssignale resultiert in einem stetigen Anstieg der Anforderungen an die einzelnen Komponenten des Übertragungssystems. Dem Design der entsprechenden Analoghardware kommt somit eine hohe Bedeutung zu. Im Sendezweig sind die generierten Datensignale auf die Sendefrequenz umzusetzen und mit dem gewünschten Pegel an der Antenne bereitzustellen. Hierbei hat eine geringe Leistungsaufnahme der Schaltung ebenso Priorität wie die Vermeidung von Störemissionen, die die Leistungsfähigkeit anderer Funksysteme negativ beeinflussen könnten. Diese konkurrierenden Eigenschaften gilt es zu erfüllen, und gleichzeitig den Kostenvorgaben gerecht zu werden. In der Empfängerschaltung wird das Signal von der Antenne empfangen und rauscharm verstärkt. Danach werden die Frequenzumsetzung und das Unterdrücken unerwünschter Signalkomponenten durchgeführt. Eine Vielzahl unterschiedlicher Sende- und Empfangsstrukturen wurde entwickelt, um eine möglichst effiziente Implementierung der genannten Aufgaben in Hardware zu ermöglichen.

Direkt umsetzenden Architekturen kommt hierbei eine große Bedeutung zu. Sie bieten zahlreiche Vorteile im Vergleich zu dem traditionellen superheterodynen Konzept. Unter anderem werden die Spiegelfrequenzfilterung, ZF-Verstärker und Bandpassfilter vermieden. Dadurch bieten direkt umsetzende Architekturen eine hohe Flexibilität in der Wahl der Mittenfrequenz ohne Einschränkung der Dynamik oder Bandbreite. Durch die Vermeidung bzw. Reduktion von Filtern im Hoch- und Zwischenfrequenzbereich ist die Realisierung dieser Architekturen als integrierte Schaltungen deutlich vereinfacht. Diese Vorteile stehen einer Reihe von Störmechanismen gegenüber, die sich begrenzend auf die Leistungsfähigkeit des Übertragungssystems auswirken. Zu den wichtigsten Störquellen gehören ungleiche Verstärkung der beiden Basisbandsignale, deterministische Störkomponenten und Phasenrauschen des lokalen Oszillators, sowie die Erzeugung von Intermodulationsstörungen und harmonischen Störprodukten der Hüllkurve. Üblicherweise wird ein I/Q-Mischer im Sende- und Empfangszweig zur Frequenzumsetzung verwendet. Die Eigenschaften dieser Mischer und der Frequenzgang der analogen Komponenten führen zu einem nichtlinear dynamischen Verhalten des Sende-und Empfangszweiges.

Im Rahmen dieser Dissertation wurden ein umfassendes Modell und ein Linearisierungskonzept für das Verhalten von direkt umsetzenden Architekturen für den Sender und den Empfänger entwickelt. Ein wichtiger Punkt hierfür war einerseits die Wiedergabe der Interaktionen der unterschiedlichen Störungsmechanismen als auch eine handhabbare Komplexität. Die entwickelten Modelle wurden in einem ersten Schritt mit dem simulierten Verhalten der betrachteten Architekturen verglichen. Anhand der gewonnenen Informationen konnte der Gültigkeitsbereich der Modelle als auch der Linearisierer

bestimmt werden.

Daraufhin wurden Algorithmen zur Extraktion der Modellparameter anhand von Messungen des Sende- und Empfangszweigs entwickelt. Eine wichtige Vorgabe dabei war, den Sende- und Empfangszweig unabhängig voneinander zu charakterisieren. Durch diese Vorgangsweise kann eine Überlagerung von Störungen generiert im Sendezweig mit jenen hervorgerufen im Empfangszweig vermieden werden. Aus diesem Grund wurden die Testsignale zur Charakterisierung des Empfangszweiges ausschließlich durch die Kombination von Sinusgeneratoren realisiert. Außerdem wurden die Testsignale so gewählt, dass jede Störquelle getrennt betrachtet werden konnte. Auf diese Weise war es möglich, die Störmechanismen unabhängig voneinander zu identifizieren. Die gewonnenen Koeffizienten müssen nicht direkt mit den Parametern des eigentlichen Modells übereinstimmen, da sie nur einen isolierten Teilbereich des Verhaltens beschreiben. In einem nächsten Schritt wurden dann die gewonnenen Parameter zu einem Blockmodell zusammengesetzt und von diesem das vollständige Modell parametrisiert. Eine analoge Vorgangsweise wurde auch für den Sendezweig angewendet.

Die Entwicklung der Linearisierungskonzepte wurde ausgehend von den Koeffizienten der Modelle des Sende- und Empfangszweiges durchgeführt. Daher können die Parameter der vollständigen Modelle direkt zur Reduktion der erzeugten Störung herangezogen werden.

Der linearisierte Sende- und Empfangszweig wurde einerseits als Referenzsystem für die Signalgenerierung und Signalanalyse herangezogen. Andererseits wurden sie zu einem breitbandigen Messsystem zusammengefügt, welches zur präzisen Vermessung von Hochfrequenzkomponenten in Funksystemen eingesetzt wird.

Abstract

Modern mobile communication systems are continuously evolved to account for the increasing data transmission rates. For this purpose complex modulation formats featuring high spectral efficiency are applied. The resulting communication signals need to have a wide bandwidth and show a non-constant envelope with a high crest factor. The analog components of these communication systems have to cope with these envelope fluctuations as well as the increasing bandwidth occupied by the information signals. These demands result in tight specifications of the corresponding hardware.

At the transmission branch the generated data signals have to be shifted to the output frequency and provided at the antenna amplified to the desired power level. For the design of this circuitry low power consumption together with the avoidance of distortion and spurious emissions are mandatory. These competing requirements have to be fulfilled while meeting the cost objective. At the receiver branch the signal received by the antenna is amplified using a low noise amplifier and shifted to the baseband. At the same time the desired signal must be separated from unwanted spectral components. A large variety of concepts was proposed to allow an efficient hardware implementation of all these tasks.

The direct conversion transmitter and receiver architectures are important concepts for mobile communication systems. They offer several advantages over the traditional superheterodyne topology. Among others, the filtering of the RF output to suppress the image signal, IF amplifiers, and bandpass filters are avoided. These properties allow a flexible RF frequency selection coupled with a high dynamic wide band operation. By reducing or avoiding filters at the RF or the IF band these architectures are well suited for integration. The advantages are, however, confronted by the presence of several distortion mechanisms limiting the achievable performance. The most important distortion sources are the gain imbalance between the two baseband branches, the spurious emissions and the phase noise of the local oscillator, as well as the generation of intermodulation and harmonic distortion of the envelope signal. Usually an I/Q-mixer is used within the transmit and receive branch to perform the frequency translation. Based on the properties of these mixers and the frequency response of the analog components both branches show a nonlinear dynamic behavior.

In this doctoral thesis a comprehensive model and a linearizer for direct conversion transmitter and receiver topologies were developed. An essential point for this task was to represent the interactions of the different distortion mechanisms while providing a description with reasonable complexity. The developed models were compared under different operating conditions to the simulated response of the architectures. Based on the extracted information the validity range for the models and the linearizers was verified.

Thereupon parameter extraction algorithms were developed on the basis of measurements of the transmit and receive branch. An important requirement was characterizing both branches independently. This approach avoids a superposition of the distortion generated in the transmit branch with the ones

created by the imperfections of the receiver. Therefore, the test signals for the receiver characterization were generated using single-tone sources. Furthermore, the test signals were designed to excite only one distortion source. By this approach an independent identification of the different distortion mechanisms was possible. The extracted coefficients needn't coincide with the parameters of the complete model as they only represent an isolated part of the behavior of the branches. In a next step the gathered information was used to compose a block model from which the complete model parameters were derived. The same methodology was also applied for the identification of the transmitter branch.

The development of the linearizers was based on the parameters of the complete model for the transmit and receive branch. Thus, the same set of coefficients is used to describe the system behavior as well as to reduce the generated distortion. On the one hand the linearized transmitter and receiver branch were used as reference systems for the generation and analysis of signals. On the other hand they were combined to compose the broadband measurement system allowing an accurate measurement of components located in the RF branch of communication systems.

Contents

Notation

f_0	...	Carrier frequency
ω_0	...	Angular carrier frequency
f_s	...	Sampling frequency of the baseband processing system
BW_m	...	Modulation bandwidth of the transmitter or receiver
BW_{BB}	...	Bandwidth of the baseband signal
$\tilde{s}$	...	Real-valued RF signal in the transmit branch
s	...	Complex baseband representation of $\tilde{s}$
s_I	...	Inphase component of the baseband signal
s_Q	...	Quadrature component of the baseband signal
$\tilde{r}$	...	Real-valued RF signal in the receive branch
r	...	Complex baseband representation of $\tilde{r}$
$\tilde{g}(\cdot)$	...	Real-valued RF amplifier gain function
$g(\cdot)$	...	Complex baseband amplifier gain function
		or real-valued baseband amplifier gain function
O	...	DC-offset
θ_e	...	Phase imbalance of a I/Q mixer
α_I, α_Q	...	Frequency independent gain of the inphase and the quadrature
		branch (without the baseband filters)
$\alpha_I(j\omega), \alpha_Q(j\omega)$	...	Frequency independent gain of the inphase and the quadrature
		branch including the baseband filters
γ	...	Ratio between the inphase and the quadrature branch
ϵ	...	Gain imbalance between the inphase and the quadrature branch
$\mathbf{a}$	...	Column vector (e.g., $\mathbf{a} = (a_1\, a_2\, \ldots\, a_n)^T$)
$\circ$	...	Hadamard product or entry-wise product
$\mathbf{a}^T$	...	Transpose of the vector $\mathbf{a}$
$\mathbf{a}^H$	...	Conjugate transpose of the vector $\mathbf{a}$
$\mathbf{1}$	...	One vector (e.g., $\mathbf{1} = (1\, 1\, \ldots\, 1)^T$)
$\bar{h}$	...	Memoryless approximation of the function $h(t)$ (e.g. $\bar{h} = h(0)$)
$\hat{g}_p$	...	Estimated p^{th}-order coefficient of a power series
$\delta(j\omega)$	...	Dirac's delta function
Re	...	Real-part operator
Im	...	Imaginary-part operator
$|\cdot|$	...	Magnitude of a complex number
$\angle$	...	Phase of a complex number
h^*	...	Conjugate of the complex number h
$\lfloor\cdot\rfloor$	...	Greatest integer less or equal to the enclosed value
$\mathrm{sign}(\cdot)$	...	Sign of the enclosed value
$(\cdot)_{2\pi}$	...	Modulo 2π of the enclosed value
$\mathscr{F}[\cdot]$	...	Fourier transform of the specified expression
$\mathscr{H}[\cdot]$	...	Hilbert transform of the specified expression
$*$	...	Convolution of two functions

Abbreviations

ADC	. . .	Analog-to-digital converter
AWG	. . .	Arbitrary waveform generator
BB	. . .	Baseband
CBTT	. . .	Channel based two-tone
CW	. . .	Continuous wave
DAC	. . .	Digital-to-analog converter
DSP	. . .	Digital signal processing
DSR	. . .	DC suppression ratio
DUT	. . .	Device under test
EER	. . .	Envelope Elimination and Restoration
FFT	. . .	Fast fourier transform
FIR	. . .	Finite impulse response
FPGA	. . .	Field-programmable gate array
FSTT	. . .	Frequency shifted two-tone
GSM	. . .	Global system for mobile communications
HD	. . .	Harmonic distortion
HP	. . .	Highpass
IBO	. . .	Input power back-off
IF	. . .	Intermediate frequency
IFFT	. . .	Inverse fast fourier transform
IMD	. . .	Intermodulation distortion
IP	. . .	Intercept point
LF	. . .	Low frequency
LO	. . .	Local oscillator
LP	. . .	Lowpass
LNA	. . .	Low noise amplifier
LS	. . .	Least-square
MIMO	. . .	Multiple-input / multiple-output
Msps	. . .	MSamples per second
MTA	. . .	Microwave transition analyzer
NCO	. . .	Numerically Controlled Oscillator
NL	. . .	Nonlinearity
NLS	. . .	Nonlinear least square
NMSE	. . .	Normalized mean square error
NOCEM	. . .	Non-constant envelope modulated
OFDM	. . .	Orthogonal frequency division multiplex
OpAmp	. . .	Operational amplifier
PA	. . .	Power amplifier
PAPR	. . .	Peak to average power ratio
PCWM	. . .	Parallel cascade Wiener model
PLL	. . .	Phase-locked loop

*PSD	. . .	Power spectral density
PWM	. . .	Pulse Width Modulation
QAM	. . .	Quadrature amplitude modulation
RF	. . .	Radio frequency
SA	. . .	Spectrum analyzer
SNR	. . .	Signal to noise ratio
SOLT	. . .	Short, open, line, through
SFDR	. . .	Spurious free dynamic range
SRAM	. . .	Static random access memory
VCO	. . .	Voltage controlled oscillator
VA	. . .	Vector attenuator
VNA	. . .	Vector network analyzer
VSA	. . .	Vector signal analyzer
VSG	. . .	Vector signal generator
WCDMA	. . .	Wideband code division multiple access
WiFi	. . .	Wireless Fidelity
WiMAX	. . .	Worldwide Interoperability for Microwave Access
ZBT	. . .	Zero Bus Turnaround

Chapter 1

Motivation

In wireless transmission systems, the trend has been implementing more and more functionality in the digital domain and, at the same time, increasing the bandwidth. Wireless digital communications have evolved from GSM to WCDMA towards 3.5G and 4G. [1]. With each new communications protocol, engineers are finding ways to use a given bandwidth more efficiently than ever before. WiFi, for example, has evolved to use better spectral efficiency with new methods such as OFDM and now MIMO. In addition, new communications standards like WiMAX have successfully improved channel throughput by using higher-order modulation schemes such as 256-QAM. However, while advances in spectral efficiency have enabled some technologies to achieve higher throughput, today's systems are often limited by various characteristics of the physical hardware. Thus, understanding the sources of error in these systems becomes paramount [2, 3].

Focusing on transmitters and receivers for non-constant envelope modulated (NOCEM) signals using in wireless communications still a large variety of structures were suggested as a wide range of applications must be supported. Common to all these frequency translation approaches is the requirement to cope with the constantly growing bandwidth and data rate demand.

1.1 Transmitter setups

The three primary functions of common transmitters are modulation, frequency conversion and power amplification. The modulation can be done using a digital or an analog implementation [4, 5]. Major issues in the design of wireless transmitters are the overall efficiency, wideband high dynamic range signal generation, and the suppression of noise and disturbances being added to the output signal [6].

For wireless communication transmitters most implementations can be put down to the following configurations:

- Superheterodyne transmitters

- Direct conversion transmitters

- Low IF transmitters

- Polar transmitters

- Direct digital RF transmitters

- Switched transmitters

Excluded from this list are transmitter configurations for pulsed applications (for example: [7]) as they are not able to cope with modulated signals. The mentioned structures are now summarized and their fundamental properties are discussed.

1.1.1 Superheterodyne transmitters

The superheterodyne concept, introduced by Armstrong in 1917, is the classical approach for implementing highly selective receiver and transmitter circuits [8]. For wireless communication applications the first IF signal is often generated using an I/Q modulator. This approach is also called "Two-Step Architecture" [4, 6, 9]. Based on the number of upconversion stages various variants of this structure exist. The principle structure of a superheterodyne transmitter is presented in Figure 1.1.
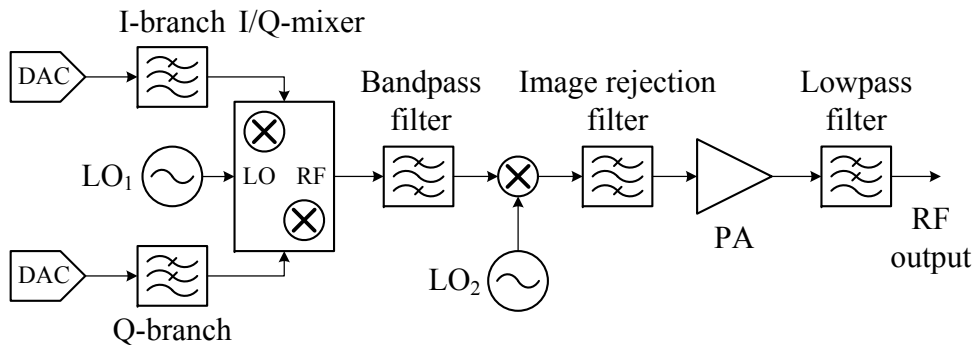
Figure 1.1: Superheterodyne transmitter structure [6].

Important advantages of superheterodyne transmitters are [6, 10]:

- Generation of wideband high dynamic RF signals

- High suppression of noise and spurious emissions

For the realization of this transmitter type key implementation challenges are summarized by:

- Complex structure for flexible RF frequency selection

- Careful filter design for high image sideband rejection required

- Structure is less suited for integration

The residual noise at the transmitter output is mainly influenced by the frequency synthesizer. The overall efficiency of a transmitter is dominantly influenced by the selected type of power amplifier. A comprehensive overview on power amplifiers (PAs) used in transmitter setups is given in [11].

1.1.2 Direct conversion transmitters

Direct conversion transmitters perform the frequency translation of the baseband (BB) signals directly to the desired RF output frequency. This concept is also known as "homodyne" and "zero IF" transmitters. By this approach the component count is significantly reduced compared to the superheterodyne structure. Direct conversion transmitters are often used at the signal generation branch of wireless communication chipsets [12, 13, 14, 15, 16]. The principle structure of a direct conversion transmitter is depicted in Figure 1.2.
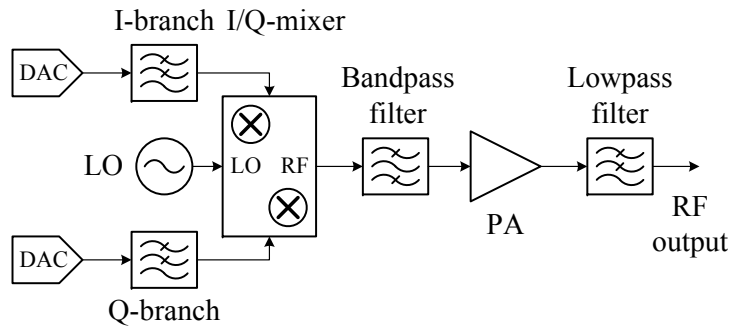
Figure 1.2: Principle structure of direct conversion transmitters [13].

Important advantages of direct conversion transmitters are [8, 9, 17]:

- Flexible RF frequency selection

- Generation of wideband high dynamic RF signals

- Less component count compared to superheterodyne transmitters

- Attractive for high level integration

The following implementation challenges for realizing this transmitter type have to be faced:

- Gain and phase imbalance between the two baseband channels

- DC offset / carrier leakage

- VCO injection pulling

- 1/f noise

The residual noise at the direct conversion transmitter output is mainly influenced by the BB amplifiers and filters, and the frequency synthesizer [10].

1.1.3 Low IF transmitters

Low IF transmitter structures are commonly used to circumvent the imbalance and DC-offset problems of direct conversion transmitters. To guarantee the generation of an imbalance free IF output this signal is

usually generated by a DA-converter directly [18]. Examples for low IF transmitter implementations are discussed in [19, 20, 21]. A major problem of the low IF transmitter setup is the image sideband generated close to the desired output signal after the upconversion to the RF frequency [9]. This sideband must be typically lowered by 50 to 60 dB. To sufficiently suppress this unwanted sideband several upconversion stages can be used [18]. Another possibility is to realize a weaver topology [22] by generating two IF signals and apply them to an I/Q-mixer. As in the direct conversion structure imbalances between the branches of this mixer set a limit for the achievable sideband suppression. The low IF transmitter concept is presented in Figure 1.3.
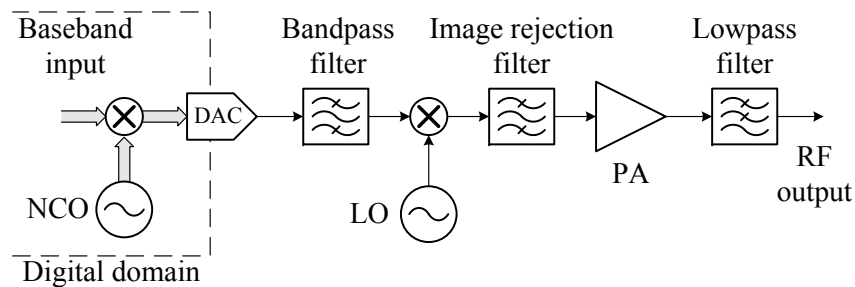
Figure 1.3: Low IF transmitter concept[18].

Important advantages of low IF transmitters are [8, 9, 10]:

- High dynamic imbalance free RF signal generation

- Less component count compared to superheterodyne transmitters

- Attractive for high level integration

As mentioned before the key challenge for the implementation of this topology is to achieve a sufficient suppression of the image sideband at the output signal. The residual noise of low IF transmitters is mainly influenced by the frequency synthesizer. The impact of the 1/f noise is less stringent depending on the selected IF frequency.

Compared to the direct conversion transmitters imbalance distortion, DC-offset and 1/f noise issues are lowered or avoided. Also the VCO pulling effect is circumvented as the LO frequency differs from the PA output frequency range. These advantages are confronted by a reduced flexibility in the RF frequency selection and a smaller signal bandwidth.

1.1.4 Polar transmitters

The concept of polar transmitters is based on efficiently amplifying a phase modulated constant envelope signal and introducing the corresponding amplitude variations by changing the supply voltage of the efficient amplifier [23]. This approach is closely related to the Envelope Elimination and Restoration (EER) efficiency enhancement concept [24]. A growing interest on polar transmitters in research and industry can be recognized over the last years explainable by the need of efficient and linear signal generation in mobile applications. Different implementations of polar transmitters are presented in [25, 26, 27, 28]. The principle structure of this concept is shown in Figure 1.4.
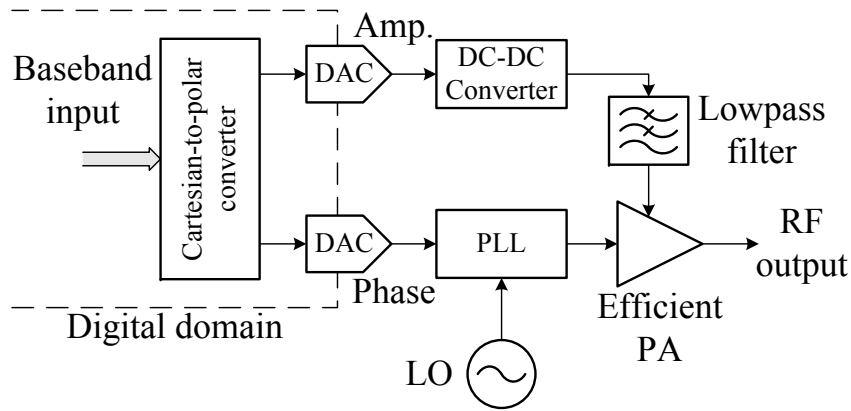
Figure 1.4: Polar transmitter structure [29].

Important advantages of polar transmitters are [24, 25, 17]:

- Highly efficient signal generation even at low output power levels

- Flexible RF frequency selection

- No VCO injection pulling

- Attractive for high level integration

For the realization of this transmitter type key implementation challenges are summarized by:

- Linear and efficient DC-DC converter required

- Delay matching between magnitude and phase signal mandatory

- High distortion generated by the efficient amplifier at low magnitude output signals

- Low output signal bandwidth

The residual noise at the transmitter output is mainly contributed by the PLL/frequency synthesizer and the DC-DC converter. Typically, this noise is limited to the narrow bandwidth of the output signal. The overall efficiency of this transmitter configuration is relatively high, mainly influenced by the efficiency of the PA and the DC-DC converter.

Compared to the direct conversion transmitter a high efficient operation even at the back-off regime of the PA can be established. Also no VCO injection pulling is observed. These advantages come at the cost of low signal bandwidth capabilities. Also the dynamic range is limited by the accuracy of the DC-DC converter.

1.1.5 Direct digital RF transmitters

The demand on highly flexibile transmitter chipsets pushes more and more functionality from the analog to the digital domain. Different approaches were suggested to perform the direct conversion of the digital BB signals to their RF correspondent. The most obvious implementation uses a digital quadrature upconverter and a numerically controlled oscillator (NCO) to calculate the signal provided to a RF-DAC [30]. Another concept called "digital polar PA" [17] implements both the PLL and the DC-DC converter of the polar transmitter in the digital domain. Instead of a PA a digital-to-RF-amplitude converter takes the digital magnitude information and activates a corresponding number of unit cells to provide the phase modulated RF signal [31]. The "mixing DAC" realization [17] is also based on separating magnitude and phase information of the BB signals. Using a PLL the phase modulated constant envelope signal is generated. This signal is utilized at the mixing DAC as carrier at which the magnitude signal is introduced [32]. The principle structure of a mixing DAC transmitter is depicted in Figure 1.5.
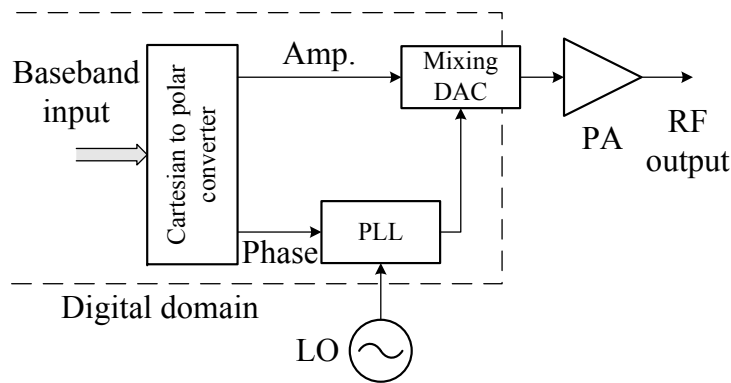
Figure 1.5: Mixing DAC implementation of a direct digital RF transmitter structure [32].

Further implementation examples of direct digital RF transmitters are discussed in [33, 34, 35]. Common to all variations of these transmitter concepts is the fact that they provide easy reconfigurability with digital functions. The clock based design generates spurious emissions and sampling noise in the out-of-band frequency range [17]. The support of wide BB bandwidth is limited for all concepts requiring the computationally complex Cartesian-to-polar conversion. The digital polar PA and mixing DAC approach introduce an additional bandwidth limitation by the bandwidth of the PLL.

1.1.6 Switched transmitters

The switched transmitters can be interpreted as another variant of direct digital RF transmitters. In contrast to the former concepts switched transmitters drive the PA with an input signal which is either a constant RF signal or zero. Correspondingly the PA input signal represents a carrier with pulse width modulation (PWM) envelope. This approach uses the PA as an integral part of a sigma-delta converter. The desired modulated RF signal is established by the bandpass filter located after the PA [36, 37, 38]. The advantage of this approach is the usability of an efficient switched-mode PA for the generation of NOCEM output signals. The principle structure of a switched transmitter is presented in Figure 1.6.

Important advantages of switched transmitters are [36, 10]:
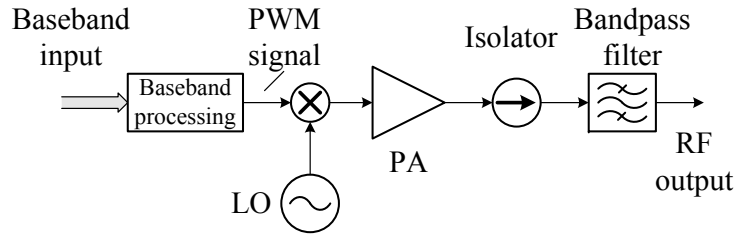
Figure 1.6: Basic concept of a switch transmitter [36].

- Highly efficient signal generation even at low output power levels

- Easy reconfigurability

- Attractive for high level integration

A major design challenge for the switched transmitter concept is the generated out-of-band noise. The sigma-delta modulator concept moves a significant part of the energy generated by the PA in the frequency range where it is suppressed by the isolator and bandpass filter. This effect results in a degradation of the achievable overall efficiency. Enhanced coding must be applied to lower the dissipated signal energy [39]. The bandwidth of the modulated output signal is limited by the applied PWM frequency which should be sufficiently above the maximum signal frequency to relax the design constraints of the bandpass filter.

Compared to the direct conversion transmitter the wide signal bandwidth and the flexible RF frequency selection is abandoned for an increased overall efficiency and a good suitability for high level integration.

1.2 Receiver setups

Receiver structures are intended to perform the inverse task of the transmitter. Despite of their similarities the design goals of receiver circuitries are significantly different from their transmitter correspondent. The main function of the receiver is to demodulate the desired signal in the presence of noise and interference. Due to the varying channels characteristics in a mobile communication scenario the received signal may change over a wide power range. Therefore, receiver structures must show a high selectivity and support a high input dynamic range. The nonlinear behavior must allow a proper treatment of weak signals despite of the presence of strong interferers. These prerequisites have to be fulfilled over the whole input frequency range while keeping the power consumption low [40, 41]. The demanding specifications resulted in a vast variety of different receiver implementations. The variety of receiver setups proposed up to now is also expressed in a significant amount of overview articles concerning this topic (for example: [4, 5, 6, 30, 40, 41, 42]). The following receiver structures provide the basis for many receivers used in wireless communication applications:

- Superheterodyne receivers

- Direct conversion receivers

- Low IF receivers

- Wideband IF receivers

- Six-port receivers

- Digital receivers

The fundamental properties of these setups are summarized in the following sections.

1.2.1 Superheterodyne receiver

As mentioned in Section 1.1.1 superheterodyne receivers were invented by Armstrong in 1917 [41]. For years most commercially available RF transceivers utilize some variants of the conventional heterodyne architecture. Especially superheterodyne receivers for wireless communication operating in multiple bands / standards may have different frequency plans and need different IF filters [10, 43]. The difficulties in integrating these filters drove superheterodyne receivers out of the low-cost mass market in recent years [6, 41]. This concept is still applied for high performance receivers and receivers for millimeter wave frequencies and above [44, 45].

The superheterodyne structure is composed of at least two mixing stages. The principle structure of these receivers is presented in Figure 1.7.
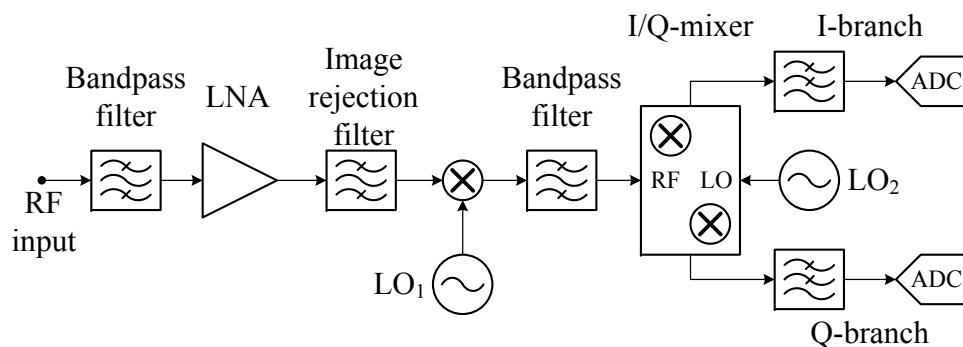
Figure 1.7: Principle structure of a superheterodyne receiver [40, 41].

The major advantage of the superheterodyne concept is the ability for high performance receiver implementations. This advantage is faced by several design challenges [5, 6]:

- Complex structure for flexible RF frequency selection

- Careful filter design / high-Q filter required for high selectivity

- Structure is less suited for integration

Assuming a proper filter design superheterodyne receivers with reasonable overall efficiency can be realized. To achieve this goal the input impedance of the image rejection filters have to assure a low current consumption of the preceding low noise amplifiers (LNAs) [5].

1.2.2 Direct conversion receiver

In contrast to the superheterodyne concept direct conversion receivers perform the frequency translation of the RF input signal to the baseband in one step. In this way the need for image rejection filtering is circumvented. Therefore, the component count for implementing directed conversion receivers is significantly lowered compared to the superheterodyne ones [10, 46]. Additionally, the reduced number of filters and amplifiers resulted in a good overall efficiency. These properties make the direct conversion receivers very suitable for integration [16, 47, 48, 49, 50]. The principle structure of a direct conversion receiver is shown in Figure 1.8.
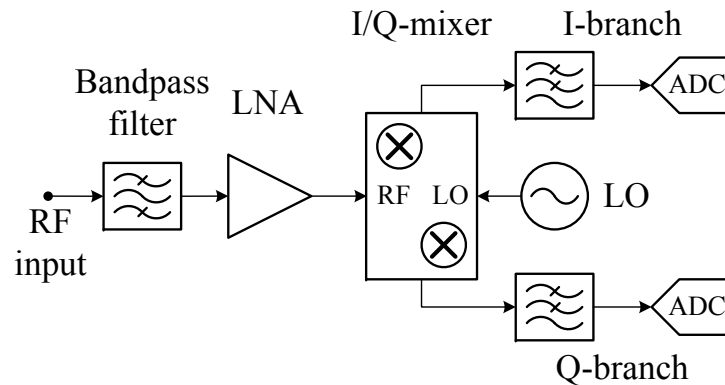
Figure 1.8: Direct conversion receiver structure [40, 41].

The simplicity of the direct conversion concept results also in a number of distortion effect which makes a high performance implementation challenging [6, 10, 46]:

- Gain and phase imbalance of the I/Q mixer

- DC offset, self mixing and LO leakage effects

- 1/f noise

- Even order distortion of the LNA

1.2.3 Low IF receiver

The low IF concept is a trade-off between the superheterodyne and the direct conversion receivers [46]. The idea behind this approach is to postpone the image-rejection filtering from the RF and performing it at a lower frequency. Therefore, low IF receivers use an IF frequency, usually ranging from half to several times the channel spacing [6]. Assuming a rather narrowband channel bandwidth the signal at the IF frequency range can be directly digitized by an AD converter. The structure of a low IF receiver is depicted in Figure 1.9. The RF input signal is downconverted to the IF using an I/Q-mixer. In this frequency range the signal is sampled. The channel selection and frequency translation to baseband is performed in the digital domain. The polyphase bandpass filter performs an initial image rejection filtering relaxing the AD converter requirements [6, 41]. Implementation examples of low IF receivers are presented in [14, 47, 51, 52].
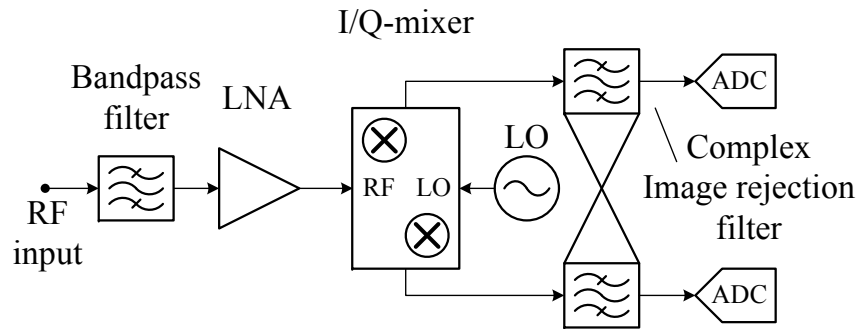
Figure 1.9: Concept of a low IF receiver [41].

The suitability for integrating and the overall efficiency of low IF receivers are comparable to direct conversion receivers. In a similar way this concept faces also performance degradation from the imperfections of the I/Q-mixer. Due to the low IF approach DC offset and 1/f noise problems are alleviated [40, 41]. These advantages come at the cost of a significantly reduced signal bandwidth when compared to a direct conversion receiver [47].

1.2.4 Wideband IF

Wideband IF receivers are closely related to the low IF concept. By introducing a second analog mixing stage the limitations on the frequency range of the first IF are relaxed and the ability to handle wideband input signals is kept. The concept of wideband IF receivers is presented in Figure 1.10. The second mixing stage together with the lowpass filters implements the frequency translation of the IF signal to the baseband and the suppression of the image sideband from the first IF. A discussion of several wideband IF receiver implementations is provided in [53, 54, 55]

As the first LO is different from the RF input frequency the LO leakage problem of direct conversion receivers is avoided. Due to the increased complexity and the usage of two frequency synthesizers the overall efficiency is lower than in the direct conversion or the low IF case. In contrast to low IF receivers 1/f noise may still reduce the sensitivity of the setup. To improve the limited image signal suppression caused by the I/Q-mixer imperfections four instead of two ADC's may be used. The summation of the mixer output signals of the second stage is then performed in the digital domain allowing improving the image signal cancelation by adaptive signal processing.

1.2.5 Six-port receiver

The six-port receiver concept was first used in vector network analyzers (VNAs) [30]. In 1994 the usage of this concept for communication receivers was proposed [56, 57]. Since then six-port structure was mainly utilized for wideband and millimeter wave receivers. The basic concept of a six-port receiver is shown in Figure 1.11. The six-port setup together with the associated AD converters replaces the I/Q modulator in a direct conversion receiver [58]. Six-port receiver implementations are, for example, discussed in [58, 59, 60].

A major drawback of six-port receivers is that a calibration is required to accurately derive the complex-valued received signal from the four detector outputs. Additionally, the quadrature hybrids
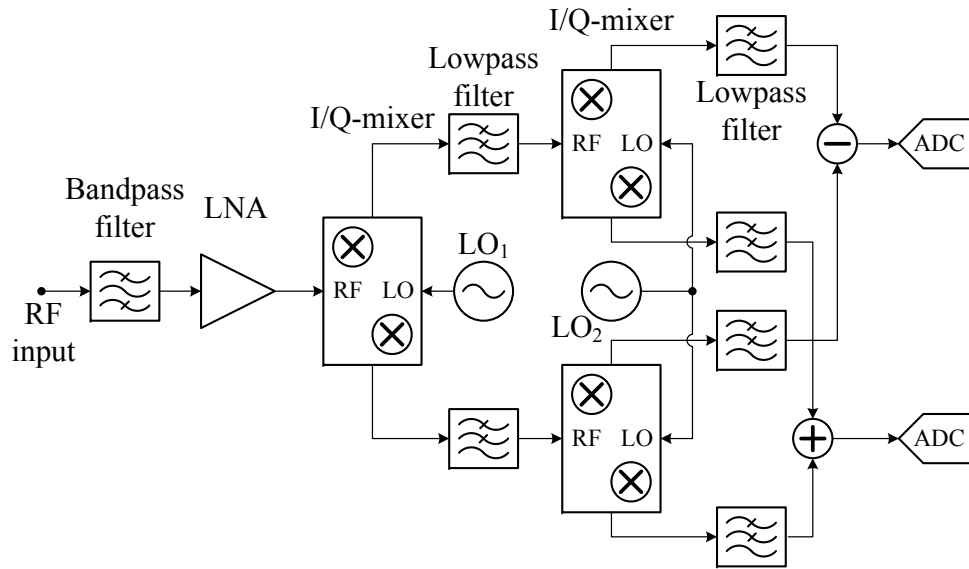
Figure 1.10: Wideband IF receiver structure [41].
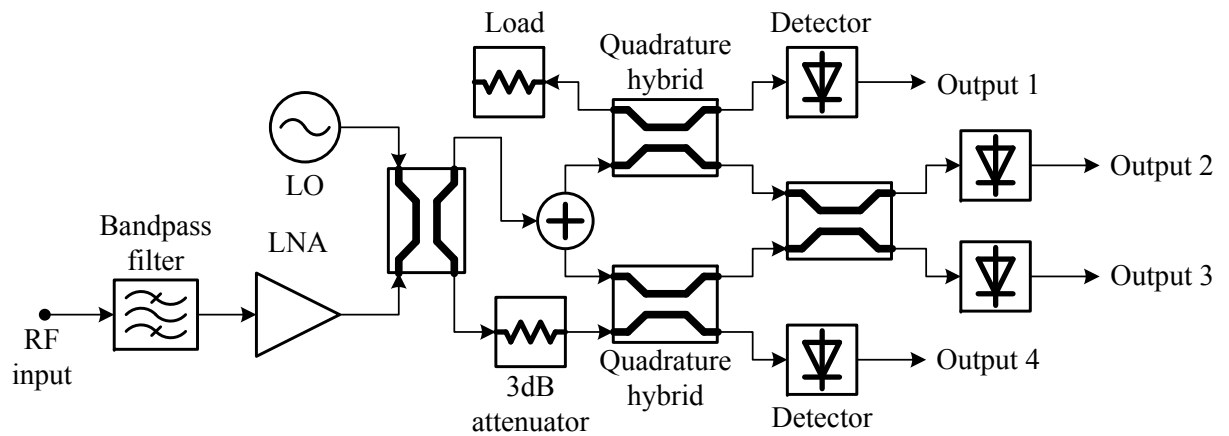
Figure 1.11: Basic six-port receiver concept [30].

are only suitable for integration at very high frequencies. As mentioned before the six-port operating principle is similar to the direct conversion receiver. Due to the power detectors, the six-port receiver is vulnerable to 1/f noise. The dynamic range is limited by the sensitivity of the detectors and the accuracy of the calibration. Also self-mixing effects are observed in six-port receivers. An advantage of six-port compared to conventional receivers is the reduced LO power requirement [61]. Using this technique receivers showing good overall efficiency can be realized depending on the current consumption of the four AD converters.

1.2.6 Digital receiver

The vision of an optimal digital receiver structure consists of a bandpass filter followed by a LNA and an AD converter. All further tasks are accomplished in the digital domain. For this purpose the AD converter must be ultra-broadband and show a very high resolution [5]. Assuming a sufficiently narrowband bandpass filter an AD converter equipped with a fast sample-and-hold gate could operate at lower clock rate using the subsampling technique [62]. Up to now the optimal digital receiver structure was only realized in demonstration setups. But the trend of moving more and more tasks to the digital domain is clearly present [30]. The term "digital receiver" is also used for architectures employing a single mixer stage and then performing the signal quantification at the IF [62]. Some examples for digital receiver circuits are discussed in [63, 64, 65].

Practical implementations of digital receivers sampling at high IF frequencies are rather rare due to the considerable power consumption of fast AD converters. Additionally, high speed AD converters are susceptible to aperture jitter and aperture distortion. These effects introduce a reduction of the receiver sensitivity. Clearly, in a long term these concepts will find their usage even in mobile communication applications [5].

1.3 Summary and thesis outline

An overview on important transmitter and receiver configurations was presented in Section 1.1 and Section 1.2. Clearly, neither in the transmitter nor in the receiver case a concept with dominating importance can be identified. Too different are the design goals in wireless communication applications so that a single frequency translation approach would be able to cope with it.

In the transmitter case, focusing on wideband high dynamic signal generation, the direct conversion concept is used in numerous applications. If a methodology is found to reduce the impact of its distortion mechanisms, the performance of this structure would prevail over the others as long as the efficiency is acceptable. Here the linearity and dynamic range achieved by using two DA converters with half the RF bandwidth outperforms the approaches using a single one requiring at least the RF bandwidth. All concepts using magnitude and phase instead of the Cartesian BB signals for the output generation have already a significant drawback in wideband applications as the Cartesian-to-polar conversion produces signals showing about five to ten times the BB bandwidth. A significant change of this situation is not expected in the short to medium term range.

In the receiver case, the situation is not as clear as in the transmitter case. Still direct conversion receivers play an important role for handling wideband RF signals. But the implementation challenges introduced by self mixing, LO leakage effects and 1/f noise are not easy to fulfill for receivers showing a
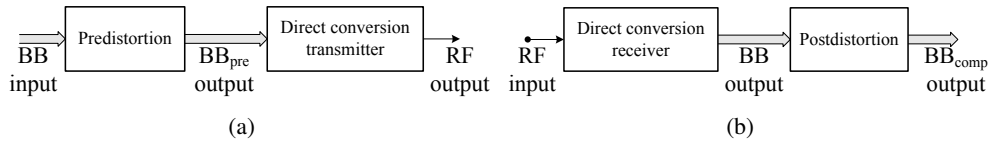
Figure 1.12: Structure of (a) the transmitter and (b) the receiver compensation approach.

wide input power range. Still, if the generated distortion is kept low or can be reduced by postprocessing wideband high dynamic signal reception at a high performance level is possible.

Due to these reasons this thesis aims at developing algorithms able to enhance the performance of direct conversion transmitters and receivers. As shown in Figure 1.12(a), in the transmitter case, the BB input signals are processed by the predistortion algorithm. The modified signals are then applied to the upconverter. Correspondingly, the signals available at the direct conversion receiver output are treated by the postdistortion algorithm to get a better estimate of the original RF input signal (Figure 1.12(b)). As direct conversion transmitters and receivers are used in various applications the developed compensation approach should not be tailored to a specific implementation or input signal. Also an independent treatment of either the transmitter or the receiver must be supported. On the basis of the application independency the developed algorithms focus on maximum distortion reduction instead of certain implementation issues. For the predistortion of the direct conversion transmitters the impact of the PA is excluded. RF power amplifiers show a nonlinear dynamic behavior dependent on the input signal magnitude. Some of the distortion mechanisms in direct conversion transmitters show further dependencies which cannot be removed by typical PA linearizer [66]. To assure high performance PA predistortion the corresponding transmitter must show a linear behavior.

The general structure of the pre- and postdistorter should allow an independent treatment of each considered distortion mechanism. This approach enables an adaptation of the developed compensators to certain hardware or implementations if required. It is important to note that based on the underlying distortion mechanisms the suggested pre- and postdistorters can also be used in combination with superheterodyne transmitters and receivers as long as they apply I/Q mixers in the first or last mixing stage, respectively, and where the image sideband is sufficiently suppressed.

To exemplify the performance of the developed direct conversion transmitter and receiver compensators a custom hardware was built. The measured response of both transmitter and receiver were then used to describe its behavior and to reduce the impact of the different distortion mechanisms. A discussion of the custom hardware design and the corresponding measurement setups are presented in Chapter 2. For the implementation of the transmitter and receiver a flexible hardware structure was mandatory. The setups were realized using mainly off-the-shelf components. Additionally, a measurement system was composed to accurately evaluate the transmitter response as well as at the receiver input signal.

The measurement of all distortion components at the transmitter output provide the basis for the identification of the corresponding distortion mechanisms. The link between the transmitter response and the distortion generation mechanisms was established using a model of the direct conversion transmitter imperfections. In Chapter 3 the linear and nonlinear transmitter models are derived and their behavior is analyzed. After a partitioning of the model into separable blocks each of them is characterized and parameterized using the transmitter measurements. The extracted coefficients are then used to compose a full model of the transmitter behavior. The same information is also used for the predistorter

development.

In a similar manner the direct conversion receiver model and postdistorter are developed. The corresponding design approach is presented in Chapter 4. Thereafter the measurement results of the transmitter and receiver are discussed in Chapter 5. Here, the differences of each of the distortion mechanisms at the transmitter and receiver are worked out. The distortion reduction achieved by the pre- and postdistorter are highlighted for each structure separately. Then the performance of the combined operation of compensated transmitter and receiver are investigated.

Chapter 2

Measurement system design

In this chapter the design and implementation of a direct conversion transmitter and receiver is discussed. Based on measurements of the response of this transmitter and receiver the corresponding models are parameterized using the approaches discussed in Chapter 3 and Chapter 4. The design of the transmitter and receiver is not tailored to a specific application. In contrast, the resulting setups should support a wide RF frequency range as well as a wide BB bandwidth. High dynamic signal generation and signal acquisition should allow an operation as measurement system. The same properties are also required when operating as a reference transmitter or receiver. Additionally to these requirements, the possibility should be provided changing the linear and NL characteristics. In this way a highly linear operation and reasonable large distortion generation should be possible using the same setup. This behavior allows evaluating the mentioned modeling approaches under different conditions.

Despite of the flexibility the transmitter and receiver should provide, the performance of these systems will be evaluated at generating and capturing WiMax / HiperMAN signals located in the frequency range between 3.4 and 3.8 GHz [67]. As RF center frequency for all measurements 3.5 GHz was selected. At the transmitter side an output power of about 20 dBm is desired.

In Section 2.1 the design of the transmitter and receiver setup is presented. Additionally, important devices employed in these setups are discussed. Thereafter, the custom built BB amplifiers and the interface hardware for the sampler board is introduced in Section 2.2. The measurement setups used for characterizing the transmitter output and the receiver input signals are treated in Section 2.3. Here, also the achievable dynamic range and measurement accuracy is investigated.

2.1   System design

Both the transmitter and the receiver should be realized using mainly off-the-shelf components. The IQ-mixers and a sampler card were initially selected for the system design. All other devices were then chosen correspondingly based on the limitations imposed by the two devices and the mentioned prerequisites.

The structure of the direct conversion transmitter is presented in Figure 2.1. The two BB signals are generated at the host PC and downloaded into the field programmable gate array (FPGA) at the sampler card. A summary on the features of this card is provided in Section 2.1.1. The output signals of the two DA converters are boosted by the adjustable amplifiers on the interface board. More information

on these devices is presented in Section 2.2. After the reconstruction filtering the signals are provided to the I/Q-mixer. These components are discussed in Section 2.1.2 and 2.1.3. The attenuator placed in front of the mixer inputs guarantees a proper matching of the corresponding ports. The local oscillator (LO) generated by a single-tone source is amplified and lowpass filtered before applying it to the corresponding mixer input. By the lowpass filter the second-order harmonic content at the amplifier output is suppressed. The I/Q-mixer output is passed through the diplexer before providing it to the attenuator and preamplifier cascade. The diplexer allows separating the second- and third-order harmonic signal components and terminating them in a load. Using a filter in this case the harmonic content would be reflected back to the mixer and could cause additional nonlinear (NL) distortion.
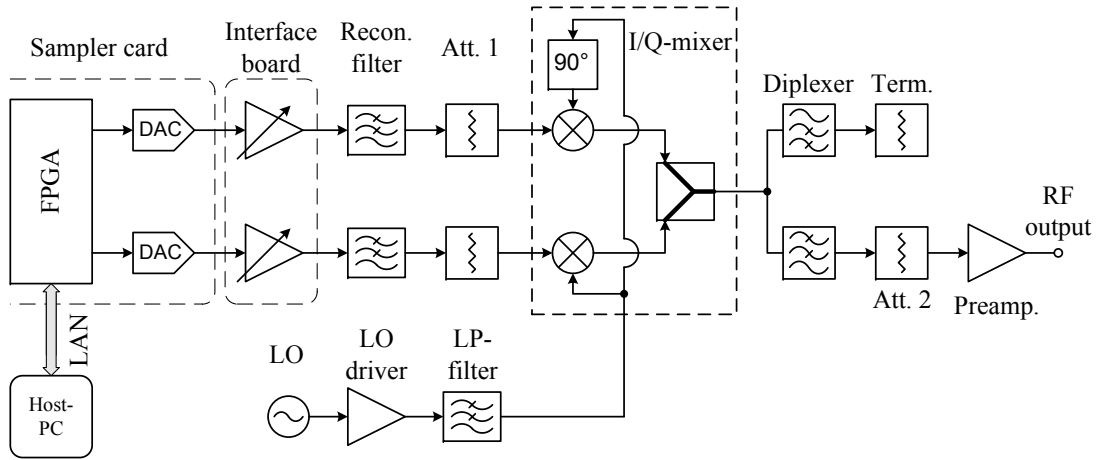
Figure 2.1: Structure of the realized direct conversion transmitter.

The gains and intercept points of the devices located in this setup are summarized in Table 2.1. These characteristics will be used to evaluate the link budget of the desired signal and the IMD components. As mentioned in the beginning of this chapter a RF carrier frequency of $3.5\,\text{GHz}$ was applied. The IP_3 of the devices correspond to the NL performance caused by a two-tone input signal at about $40\,\text{MHz}$ offset to the carrier. The input power to the transmitter is set to the maximum output power of the amplifiers located at the custom built interface board. Hence, the different gain settings selectable by these amplifiers are represented by the corresponding attenuation compared to the maximum output level.

	Gain (dB)	Input IP$_3$ (dBm)	Output IP$_3$ (dBm)
BB-preamp	$0/-6/-12/-18$		42
LP-Filter	-1.2		
Attenuator 1	-6		
IQ-mixer	-5.7	19	
Diplexer	-0.8		
Attenuator 2	-6		
RF-preamp	35		40

Table 2.1: Characteristics of the devices used at the direct conversion transmitter setup.

At this transmitter a low and high distortion operation mode is developed. In the low distortion case a reduced BB output power is used. The transmitter performance in both cases is shown in Figure 2.2. The corresponding output power levels are summarized in Table 2.2. The maximum two-tone output power of the BB amplifiers, indicated in Table 2.2 at "Input", is 8 dBm. At the low and high distortion configuration this level is attenuated by 18 and 6 dB, respectively. Only in the high distortion configuration the output power is close to the desired 20 dBm.

Figure 2.2: Link budget of the direct conversion transmitter. The black traces show the high distortion configuration while the grey ones represent the low distortion version.

	Low dist.			High dist.		
	P (dBm)	**P_{IM} (dBm)**	**IMD (dB)**	**P (dBm)**	**P_{IM} (dBm)**	**IMD (dB)**
Input	8.0			8.0		
BB-Preamp	-10.3	-88.3	-78.0	1.7	-78.3	-80.0
LP-Filter	-11.6	-89.6	-78.0	0.4	-69.6	-80.0
Attenuator 1	-17.8	-95.8	-78.0	-5.8	-85.8	-80.0
IQ-Mixer	-23.7	-93.2	-69.5	-11.7	-61.0	-49.3
Diplexer	-24.7	-94.2	-69.5	-12.7	-62.0	-49.3
Attenuator 2	-30.9	-100.4	-69.5	-18.9	-68.2	-49.3
RF-Preamp	4.0	-60.6	-64.5	16.0	-26.5	-42.5

Table 2.2: Power of the desired signal and the IM distortion at the different stages of the direct conversion transmitter setup.

The structure of the direct conversion receiver, presented in Figure 2.3, shows a design equivalent to the one of the transmitter. The RF input signal is filtered by the diplexer to terminate any harmonic components and is then downconverted by the I/Q-mixer. Thereafter, the BB signals are provided to the attenuator preamplifier cascade. These custom built amplifiers were optimized for performing a low noise amplification of the BB signals without introducing significant DC-offsets. Their performance is discussed in Section 2.2. After accomplishing the anti-aliasing filtering the BB signals are boosted by the second amplifier stage before they are quantized by the AD converters. This information is stored in the memory of the sampler card and can be downloaded to the host-PC.

The characteristics of the different devices in the setup are taken together in Table 2.3. It should be
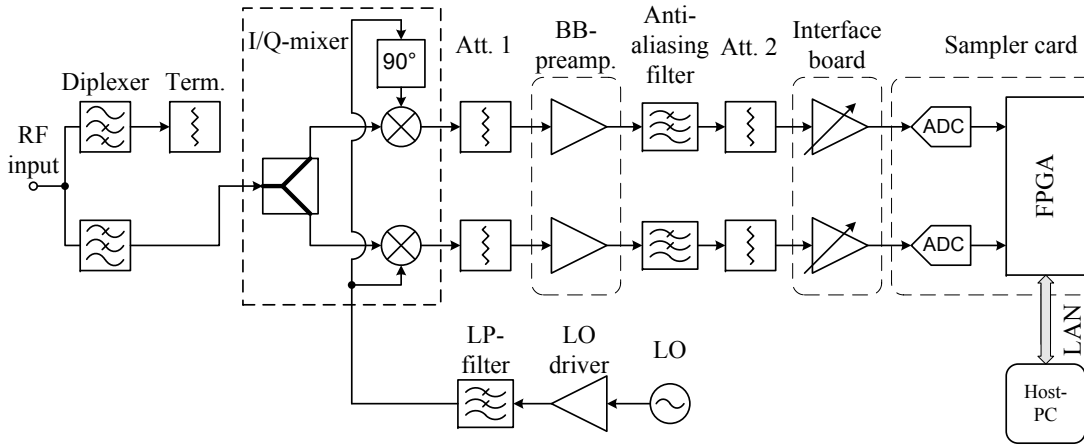
Figure 2.3: Structure of the realized direct conversion receiver.

noted, that the conversion loss of the I/Q-mixer in the receiver case is 3 dB higher compared to the one shown in Table 2.1. At the transmitter the gain represents the conversion of the two BB to the RF output signal. In the receiver case the mean power of only one BB channel is considered after the I/Q-mixer. In this way half of the RF power is neglected. The step-attenuators used in the second BB amplifier stage allow changing the gain by 31 dB in 1 dB steps (compare Section 2.2). Only two of the possible amplifications, corresponding to 0 and 6 dB attenuation, are mentioned in the table. The ADCs require a differential input signal. The last row of the table presents the gain of this single-ended to differential conversion together with the associated impedance change.

	Gain (dB)	Input IP$_3$ (dBm)	Output IP$_3$ (dBm)
Diplexer	-0.8		
IQ-mixer	-8.7	19	
Attenuator 1	$-1/-3$		
BB-preamp. Stage1	25		39
LP-Filter	-4.3		
Attenuator 2	$0/-10$		
BB-preamp. Stage2	18.3/12.5		41
Single-to-diff.	-13		34

Table 2.3: Characteristics of the devices used at the direct conversion receiver setup.

The link budget of the receiver is displayed in Figure 2.4. The corresponding power levels are summarized in Table 2.4. Again a low and a high distortion configuration were realized. The ADC input requires a differential signal of 2.2 V$_{pp}$ into a 1 kΩ load for full excitation. These prerequisites correspond to -2.1 dBm input power. In both cases the ADCs were operated at 3 dB back-off. A distortion level of -100 dBm was assumed at the receiver input. This level is sufficiently low to avoid implications on the resulting overall performance. Figure 2.4 visualizes the impact of the high input power requirement to the single-ended to differential conversion. This requirement exacerbates a highly linear behavior of the receivers.
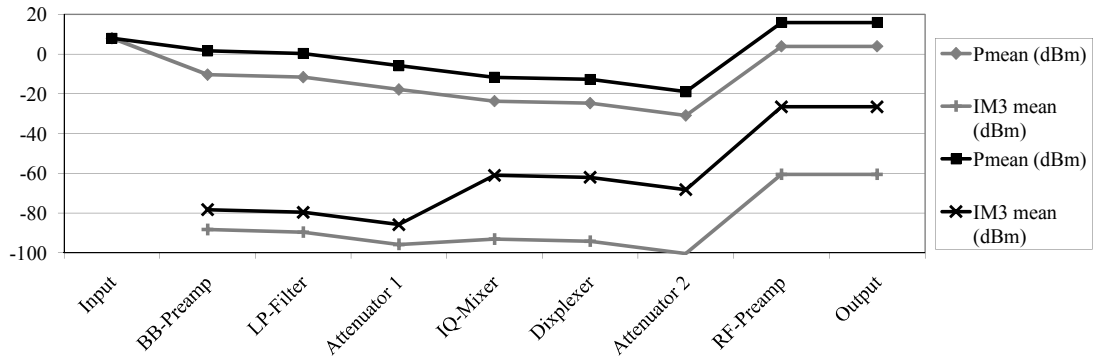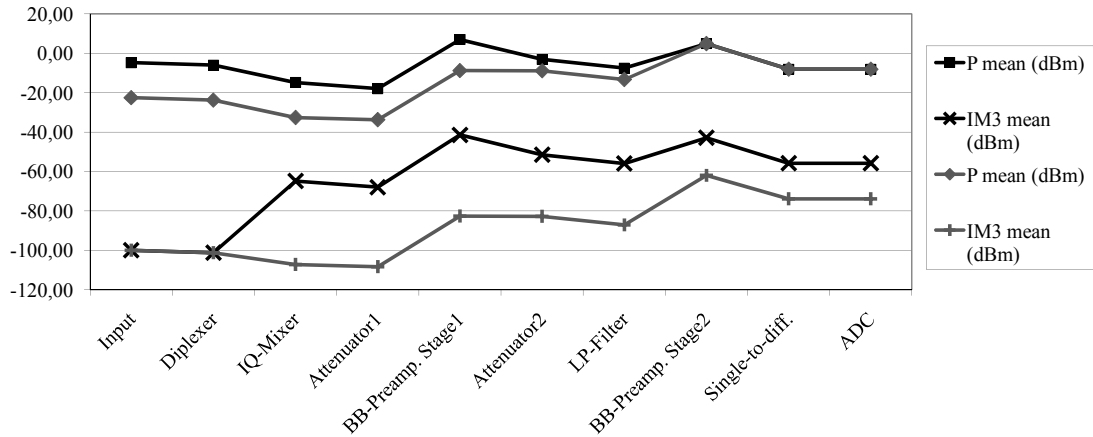
Figure 2.4: Link budget of the direct conversion receiver. The black traces show the high distortion configuration while the grey ones represent the low distortion version.

	Low dist.			High dist.		
	P (dBm)	**P_{IM} (dBm)**	**IMD (dB)**	**P (dBm)**	**P_{IM} (dBm)**	**IMD (dB)**
Input	−22.6	−100.0	−77.4	−4.8	−100.0	−95.2
Diplexer	−23.8	−101.3	−77.4	−6.0	−101.3	−95.2
IQ-mixer	−32.6	−107.2	−74.6	−14.8	−64.8	−50.0
Attenuator 1	−33.7	−108.3	−74.6	−17.9	−67.9	−50.0
BB-Preamp. Stage1	−8.8	−82.7	−73.8	7.0	−41.4	−48.4
LP-Filter	−8.9	−82.8	−73.8	−3.1	−51.5	−48.4
Attenuator 2	−13.3	−87.2	−73.8	−7.5	−55.9	−48.4
BB-Preamp. Stage2	4.9	−62.0	−66.9	4.9	−42.9	−47.8
Single-to-diff.	−8.1	−73.9	−65.8	−8.1	−55.8	−47.7
ADC	−8.1	−73.9	−65.8	−8.1	−55.8	−47.7

Table 2.4: Power of the desired signal and the IM distortion at the different stages of the direct conversion receiver.

2.1.1 Sampler card

The generation and acquisition of the BB signals is accomplished by the Nallatech BenADDA board. This module is placed on the BenONE motherboard providing access to a PCI and a LAN interface. In this way a high speed data link can be established if the motherboard is mounted within a PC. For a stand-alone operation access is provided by the LAN interface. In this case a reduced data rate must be accepted. The advantages of the stand-alone operation are a simplified integration into a measurement setup due to the reduced mechanical dimensions and the avoidance of interferences from the noisy PC environment.

The BenADDA board provides two DA- and two AD-converter interfaces. All converters show 14 bit resolution and support up to 105 Msps clock rate. The analog interfaces are accessed by a XC2V6000 Xilinx$^{®}$ field programmable gate array (FPGA), also called User-FPGA. The 4 MB Zero Bus Turnaround (ZBT)-SRAM are used for storing the captured signals and provide the information for the DACs. An own clock FPGA allows handling different clock sources. For the custom built transmitter and receiver setups the clock signal was always generated by a single-tone generator and provided to the external clock input. The onboard 105 MHz quartz oscillator was only used for testing purpose. A custom written firmware running at the User-FPGA configured all devices on the board, initiated the measurements, and handled the communication to the host-PC. The principle structure of this firmware is depicted in Figure 2.5 [68].

Central building block of this software is the arbiter responsible for the flow control of the system. It handles the two memory blocks at full speed and passes this information on to the corresponding units. Each memory address corresponds to a 36 bit word. Hence, at one read access the output samples of the two DA converters are fetched. Equivalently, at one write access the samples generated by the AD converters in one cycle are stored. The two ZBT-SRAM blocks will be treated as one continuous memory. It is possible using one part of the memory for storing the analog input samples while the other one is used for the signal generation. At the analog input up to 16 times averaging is supported. Four marker signals are outputted synchronously to the DA samples. The generation or acquisition of the analog signals is initiated by the trigger unit. An external hardware and software triggering is supported. The communication to the host system is performed via the Nallatech PCI interface FPGA. Here, the information is either routed to the LAN or to the PCI interface. Also the controlling of external hardware by the use of general purpose IO signals is supported. These signals are taken together by a 34-pin connectorized interface at the BenONE board.

The two analog inputs of the BenADDA are accessed by single-ended 50 Ω interfaces. The bipolar input signals are converted to the differential drive signal for the ADCs by the Analog Device AD8138 operational amplifier (OpAmp). In this operation mode an input IP$_3$ of better 34 dBm up to 40 MHz BB bandwidth is supported by this differential driver (compare Table 2.3). The Analog Device AD6645 AD-converters are used in the frequency range DC to f$_s$/2. An IF sampling operation is not supported by the single-ended to differential converter.

The analog output signals are generated by Analog Devices AD9772A DA-converters. They support a clock rate up to 160 Msps and provide a 2× interpolation filter and clock multiplier. By the upsampling and lowpass filtering process a 0.005 dB passband ripple is achieved. The arbiter at the firmware takes care that, despite of the interpolation filter implemented in the DACs, a synchronous start of the signal generation and signal acquisition is possible. The DACs provide a differential current interface able to handle up to 20 mA. For a high linear operation the corresponding output voltages should not
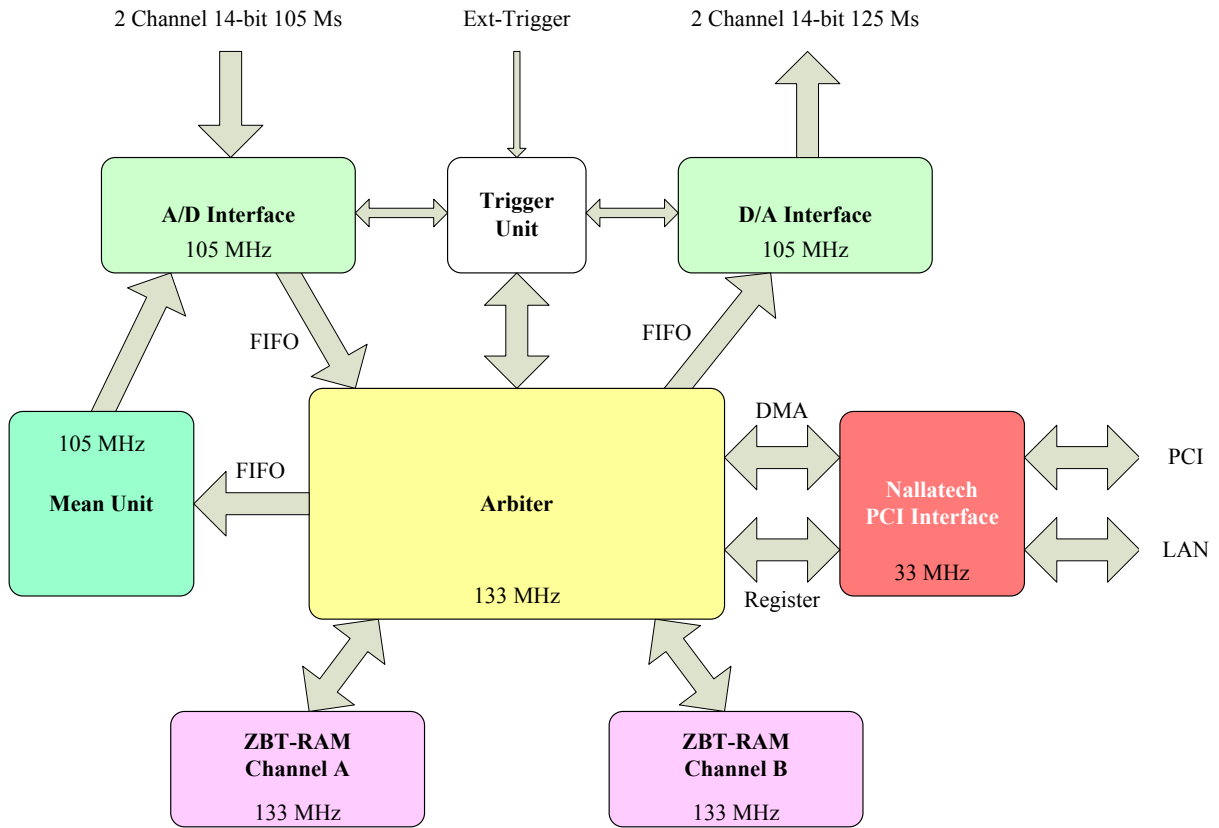
Figure 2.5: Structure of the firmware located in the User-FPGA of the BenADDA board [68].

exceed $\pm 500\,\mathrm{mV_{pp}}$. The differential to single-ended conversion was realized at a custom built hardware described in Section 2.2. This circuitry translated the 20 mA into a 1.2 V output signal magnitude at a 50 Ω interface.

The external clock input of the BenADDA board required a DC symmetrical input signal between 10 and 100 mV amplitude into 50 Ω. An input frequency range between 15 MHz$\leq f_s \leq$105 MHz is supported.

2.1.2 Baseband filters

The anti-aliasing and reconstruction filtering is accomplished by the K&R filters KR2455 and KR2515, respectively. The former is a 45 MHz lowpass filter providing a group delay equalized response and $\sin(x)/x$ compensation. Although the $\sin(x)/x$ compensation is not required for the anti-aliasing filtering the sharp transition to 60 dB attenuation was the reason for acquiring this filter type. Hence, a usable passband bandwidth of 40 MHz is achieved when operating the AD converters at 100 Msps clock rate. The reconstruction filter provides a passband bandwidth of 50 MHz and a stopband attenuation of better 60 dB starting from 73 MHz. These relaxed filter specifications are sufficient due to the rise of the sampling rate by the DA converters. The measured gain and group delay variation of the two anti-aliasing and reconstruction filters are presented in Figure 2.6. The group delay was derived from the slope of the

phase-frequency response [69].
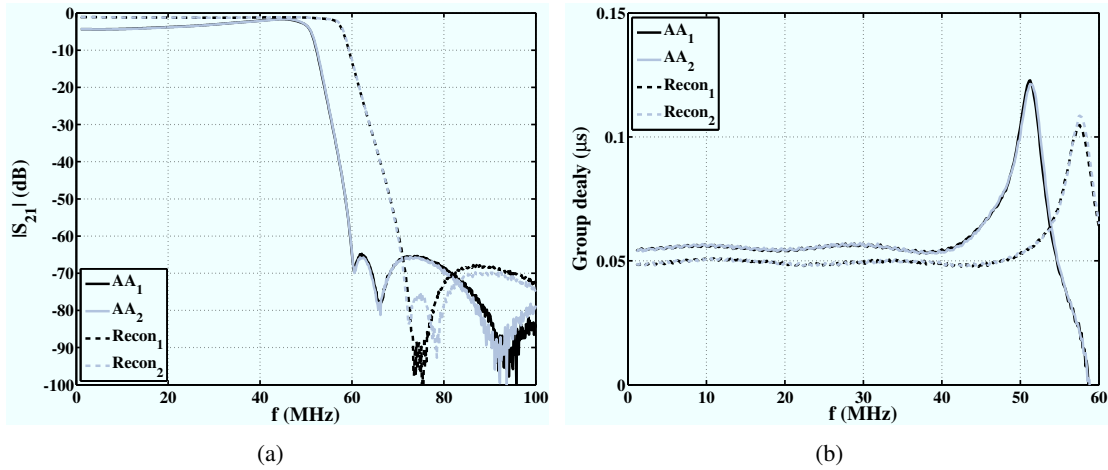
Figure 2.6: (a) Gain and (b) group delay measurements of the anti-aliasing (AA) and the reconstruction (Recon) lowpass filters.

2.1.3 IQ-mixers

The Marki microwave mixers IQ-1545 and IQ-0307 was used for the up- and downconversion of the corresponding signals. They support an RF frequency range of 1.5 to 4.5 GHz and of 3 to 7 GHz, respectively. Providing 500 MHz bandwidth at the inphase and quadrature channel, wideband signal handling capabilities are supported. The specifications achieved by both mixer types are:

- IF bandwidth: DC - 500 MHz

- Conversion loss: 5.5 dB

- Image rejection: >18 dB

- 1 dB compression point: 4 dBm

- Input IP_3: 14 dBm

The linearity specification requires an LO input level of 16 dBm. Performing two-tone measurements at 3.5 GHz showed a conversion loss of 5.7 dB and and input IP_3 of 19 dBm for the IQ-1545 mixers. The same IP_3 was evaluated in up- and downconversion operation. This performance exceeds the ones of the IQ-0307 (IP_3 of 15.5 dBm) at the same frequency.

2.2 Amplifier boards

In this section the custom built amplifier boards used for signal conditioning and providing access to the sampler card are discussed. The interface board was introduced in Figures 2.1 and 2.3. Its main
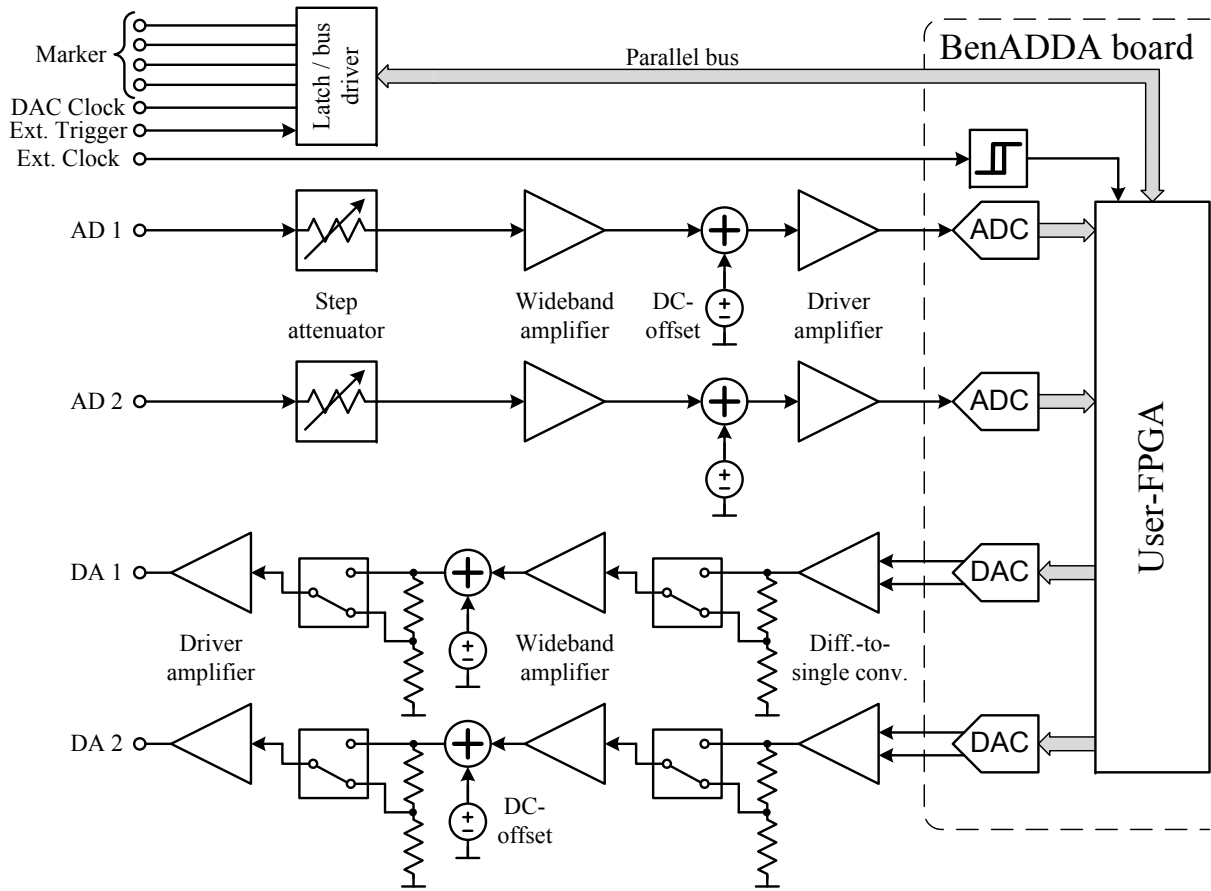
Figure 2.7: Structure of the interface board for the BenADDA sampler card.

application is integrating the sampler card functionality into the transmitter and receiver setup. The second board acts as a wideband low noise preamplifier generating only small DC-offset. This general purpose amplifier is characterized by a high gain and a reasonable linear performance. In the following both circuitries are presented and their behavior is analyzed.

2.2.1 Interface board

The structure of the interface board is shown in Figure 2.7. At the analog input branch the signals are amplified and DC-offsets are added. The value of all DC-offsets is set by the User-FPGA. The step-attenuators provide a 31 dB tuning range of the input power level in 1 dB steps. At the DA-branch first the differential output signals are converted to single-ended ones. Thereafter, the signals are amplified and the DC-offsets are added. The gain is altered by the use of reed-contacts selecting either the center tap of a resistive divider or bypassing it. In this way a 18 dB attenuation range was achieved selectable in steps of 6 dB. Additionally, the interface board provides access to the four markers as well as to the DAC clock signal. Minimizing the spurious emissions at the analog signals the generation of the DAC clock output must be enabled in the firmware. The TTL-level external trigger signal is transferred by
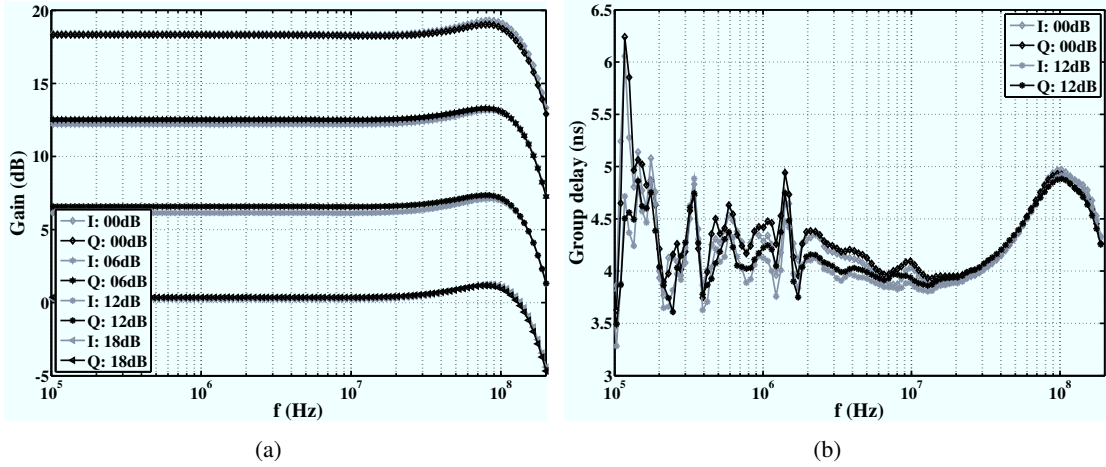
Figure 2.8: (a) Gain and (b) group delay measurements [69] of the two AD branches at different step-attenuator settings.

the same parallel bus to the User-FPGA. The external clock signal is passed on to the corresponding Schmitt-trigger on the sampler board.

Based on the receiver link budget the design requirements for the AD channels of the interface board are given by [70]:

- Gain: 18 dB

- Bandwidth: >40 MHz

- SFDR: >70 dBc at P_{out} = 7 dBm

A DC-offset of up to ± 350 mV can be generated at the sampler board input. At the DA branch a peak output power of 11 dBm should be generated while fulfilling the same linearity performance as in the AD case. Achieving these spurious free dynamic range (SFDR) requirements also a low noise power supply for the OpAmps is mandatory. Based on these requirements the amplifiers were designed. The schematic of the circuitry and a picture of the board is presented in Appendix A.

At the AD-channel input the M/A-COM 5-bit digital attenuator AT65-0263 was used to adjust the input power level. It is controlled by a TTL-compatible interface. The 14 dB gain wideband amplifier was implemented using a Texas Instrument OPA843. To generate the DC-offset the Texas Instrument 10-bit DA converter TLV5617 in combination with an Analog Device AD8045 OpAmp was used. Care must be taken to suppress the noise from the DA-converter from being added to the wanted signal. As last part of this amplifier stage, the driver must be able to provide the high input power required by the ADC interface without adding significant nonlinear distortion. The Texas Instruments OPA653 wideband voltage-feedback OpAmp was selected for this task. This device achieved 70 dBc IMD for a 7 dBm two-tone output signal at 45 MHz in stand-alone operation.

The magnitude response of the two AD branches is shown in Figure 2.8(a) exemplified for four different input attenuator settings. The amplifiers' gain was optimized for attenuations between 0 and 4 dB to have minimum deviation. In this range the maximum difference between the gain of the two amplifiers

(a) (b)

Figure 2.9: (a) 3rd-order IMD contour plot of the inphase branch at $0\,dB$ attenuation. (b) IP$_3$ frequency response at different step-attenuator settings.

is below $0.2\,dB$. At higher attenuation values these deviations increase due to differences in the digital attenuators. The absolute magnitude of the frequency response shows an overshoot of about $1\,dB$ (at $80\,MHz$) at the transition into the stopband. This behavior caused $0.3\,dB$ passband ripple. Figure 2.8(b) visualizes the group delay variation of the two amplifiers at two different attenuator settings. The mean group delay varies about $0.4\,ns$ over all attenuator settings. The maximum deviation between the group delays of the two amplifiers is below $1.5\,ns$. At the input a return loss of $-14\,dB$ at $0\,dB$ attenuation up to $100\,MHz$ was achieved. At all other step-attenuator settings at least $-18\,dB$ are provided. At the output a S$_{22}$ of better $-25\,dB$ was measured in the same frequency range.

The frequency and input power dependency of the 3rd-order IMD of the inphase branch amplifier is presented in Figure 2.9(a). These measurements were performed at $0\,dB$ attenuation. The line in the plot indicates $7\,dBm$ mean output power of the two-tone signal. Under these conditions the amplifier is able to achieve $70\,dBc$ IMD up to a frequency of $28\,MHz$. If the input power is reduced to $5\,dB$ the requested performance can be achieved over the full bandwidth of the ADC. A comparison of the frequency dependent NL behavior at different step-attenuator settings is visualized in Figure 2.9(b). Independent of the actual attenuation the quadrature branch showed slightly better performance than the inphase one. It can be recognized that the magnitude of the IP$_3$ drops at higher attenuations. As the maximum power delivered by the driver stays constant this behavior can only be ascribed to the step-attenuator. At an increased attenuation this electrical attenuator has to cope with higher input power to achieve the same AD converter power level. In this way the performance loss at higher attenuations can be explained.

At the DA-channels the Analog Device AD8045 is used in a differential configuration to perform the conversion of the DAC output signal to a single-ended one. Thereafter, using reed contacts a switchable $6\,dB$ divider stage is added. As in the AD-branches the second amplifier implements a $6\,dB$ gain stage and the addition of the DC-offset. The output signal of this OpAmp is passed through a switchable $18\,dB$ divider before it is provided to the Texas Instruments OPA653 driver OpAmp.

The single-tone response of the two DA branches is shown in Figure 2.10. The input signal to
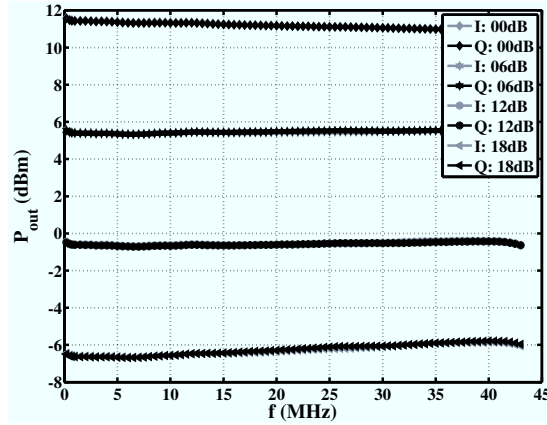
Figure 2.10: Output power measurements of the two DA branches at different attenuations.

the channels was generated by the BenADDA board. Therefore, the amplifiers were only tested up to 43 MHz. In this range the maximum difference between the output power of the two amplifiers is below 0.11 dB. Due to the combined characterization of BB amplifiers and DA-converters the group delay evaluation was omitted.

The 3rd-order IMD contour plot of the inphase branch amplifier at 0 dB attenuation is presented in Figure 2.11(a). The two-tone output signal was measured by a spectrum analyzer (SA) configured to 75 dB dynamic. As can be recognized, the distortion generated by the DA driver amplifier is only at 5 dBm output power and frequencies above 35 MHz above this limit. Compared to the same measurement at the AD-branch, presented in Figure 2.9(a), a significantly increased performance can be recognized. As both branches use the same second stage and driver amplifier the higher IMD level at the AD-channel can only be caused by the step-attenuator or the first amplifier stage. It is assumed using the switchable divider approach to change the gain of the AD-branches, an equivalent linear performance would be achieved. The reason for using the step-attenuators was the increased flexibility in the input level adjustment.

A comparison of the intercept points as a function of the input frequency at both DA-branches is shown in Figure 2.11(b). These results were calculated from the measurements at 4 dBm output power and not from the IMD slope at a power sweep as it was applied at the AD-branches. As mentioned before the SA measurement dynamic was the limiting factor at the distortion evaluation. Hence, no input power dependent increase of the IMD was observed. As a result it seems that the inphase channel outperforms the quadrature one over a wide part of the bandwidth. The different distortion magnitudes are mainly caused by the interactions with the measurement noise. A comparable NL behavior can be assumed for both channels. In a similar way the difference of the intercept points at two attenuations are approximately equal to the gain difference, indicating the limited measurement dynamic as the cause for the IP_3 reduction. Only at input frequencies above 30 MHz an increased distortion level can be recognized.
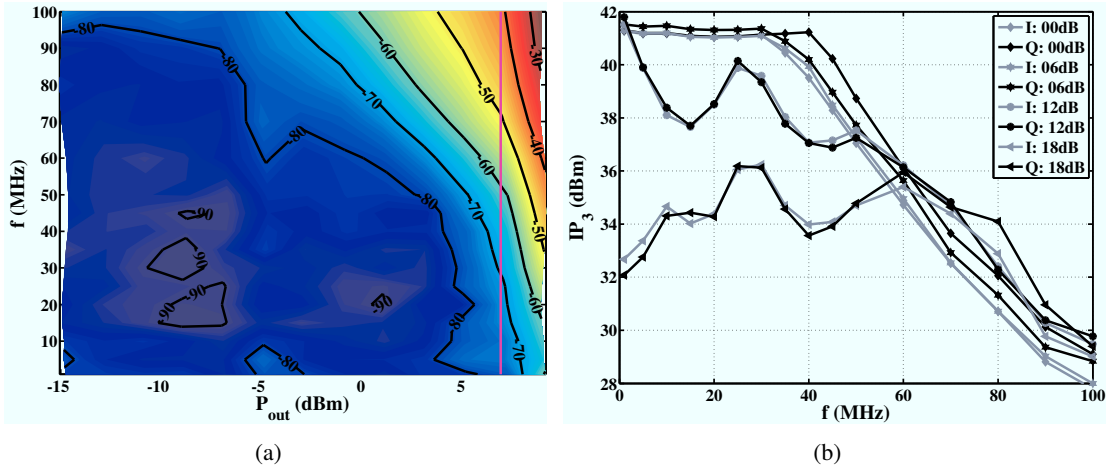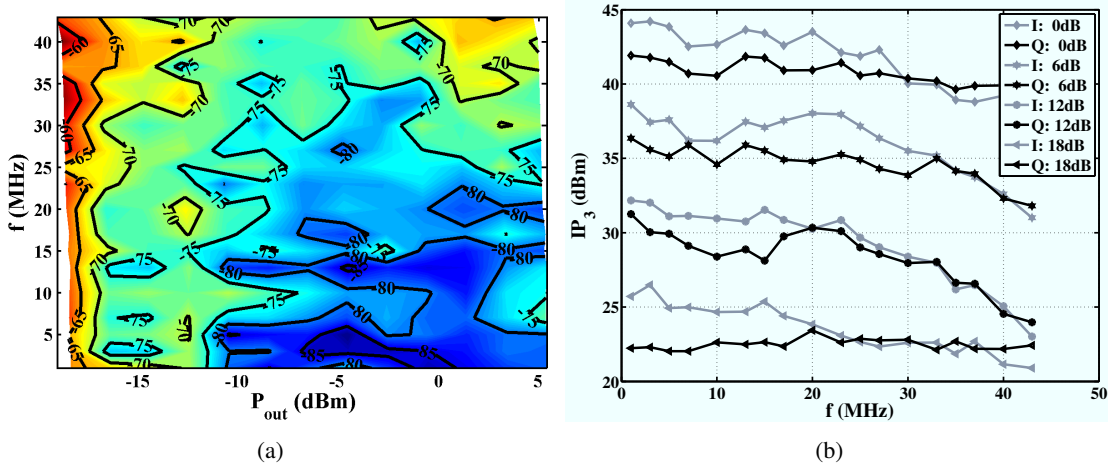
Figure 2.11: (a) 3rd-order IMD contour plot of the inphase branch at 0 dB attenuation. (b) IP_3 frequency response at different attenuator settings.

2.2.2 Preamplifier board

Based on requirements imposed by the link budget of the direct conversion receiver shown in Figure 2.4 the specifications for the preamplifier are summarized by [70]:

- Gain: 25 dB

- Bandwidth: >40 MHz

- $IP_{3,output}$: >35 dBm

- Low DC-offset

- Low noise figure

The intercept point was selected assuring a negligible distortion contribution at the ADC input. To simultaneously fulfill the wide band and low DC-offset requirement a split-band amplifier design, as presented in Figure 2.12, was used [71]. This concept applies a broadband amplifier treating the high frequency components of the input signal. The low frequency (LF) part is handled by a slow amplifier showing high DC precision. Using the highpass (HP) filter composed of C_{HP} / R_{HP} the high frequency content is passed via the summation point to the input of the broadband amplifier. The low frequency input signal part is separated by R_{LP1} / C_{LP1} and scaled by a narrowband amplifier. The resulting output signal is added to the broadband signal. By comparing the driver output to the input signal any drift introduced by the two wideband amplifiers is compensated.

For the actual implementation of the splitband structure the Texas Instruments OpAmps OPA847 and OPA277 were used as wideband and DC precision amplifier, respectively. As driver a Texas Instrument THS3201 current feedback OpAmp was selected. The OPA847 combines a high gain bandwidth product of 3.9 GHz with low input voltage noise (approx. $0.85 \, nV/\sqrt{Hz}$). These characteristics make the OPA847 well suited for the low noise preamplifier application. This OpAmp is stable for gains ≥ 12.
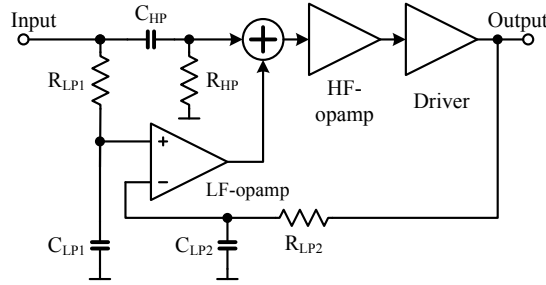
Figure 2.12: Splitband amplifier concept applied at the preamplifier.

(a)

(b)
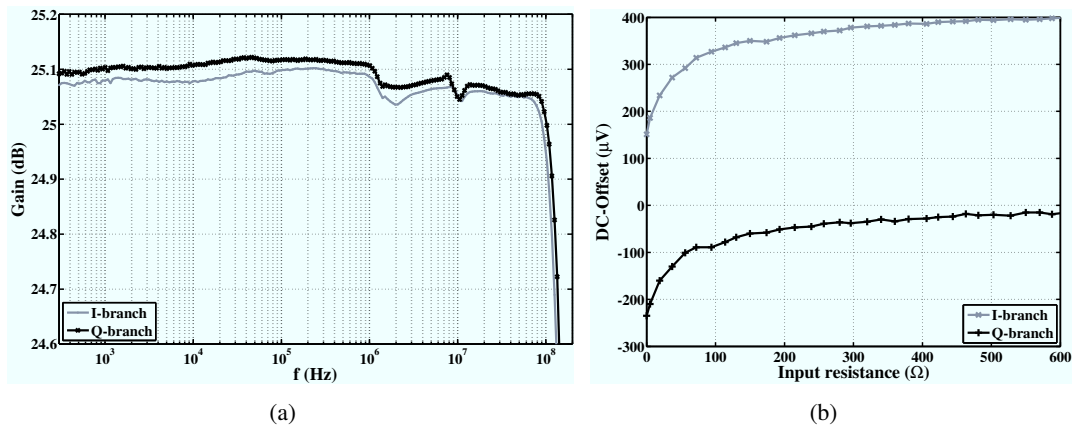
Figure 2.13: (a) Frequency response and (b) DC-offset sensitivity to input impedance variations of the preamplifier.

By providing $10\,\mu$V DC-offset and $\pm0.1\,\mu$V/$^\circ$C temperature dependency the OPA277 fulfils the requirements of the DC-precision narrowband amplifier. The THS3201 is characterized by an IP_3 of $45\,$dBm and a unity gain bandwidth of $1.8\,$GHz.

A gain of 25 dB was selected for the first BB amplifier stage. This high gain is required for assuring a stable operation of the OPA847 and for achieving a flat frequency response of the amplifier up to the cutoff frequency. The handover frequency between the low and high frequency part of the circuitry was set to $f_g = 720\,$Hz. The lowpass (LP) R_{LP2} / C_{LP2} is used to remove the high frequency components from the LF-OpAmp input. This LP-filter in the feedback path is transferred into a HP characteristic at the frequency response of the LF-OpAmp. A cutoff frequency of $50\,$kHz was selected at this lowpass to avoid interference with the handover range of the splitband amplifier set by C_{HP} / R_{HP} and R_{LP1} / C_{LP1}. The schematic of the circuitry and a picture of the board is presented in Appendix A.

The small signal frequency response of the two branches is depicted in Figure 2.13(a). Up to $50\,$MHz the gain variations are below $0.1\,$dB. The mean group delays of the amplifiers are approx. $2.8\,$ns. The maximum deviation between the two group delays is below $1\,$ns. It was evaluated for frequencies above $200\,$kHz to limit the noise enhancement due to the numerical differentiation. The influence of different input impedances on the DC-offset generation is presented in Figure 2.13. At $50\,\Omega$ the DC-offset mag-

nitude is below $300\,\mu$V for both channels. Up to $100\,$MHz a S_{11} magnitude of better $-15\,$dB and a S_{22} of better $-40\,$dB was evaluated. The reduced input matching is causes by the LP R_{LP1} / C_{LP1} which introduces the deviation from $50\,\Omega$ at higher frequencies.
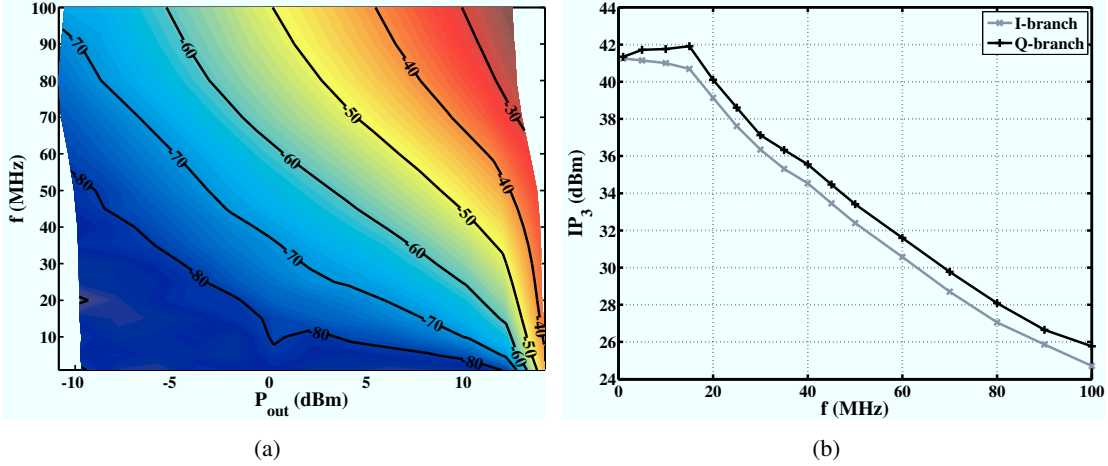
Figure 2.14: 3rd-order (a) IMD contour plot of the inphase branch and (b) intercept point frequency response.

The progression of the third-order IMD of the inphase branch amplifier for a two-tone input signal is visualized in Figure 2.14(a). The plot reveals an increase of the generated distortion with increasing frequency and increasing input power as it is the case for voltage feedback OpAmps [72]. A comparison of the intercept point frequency response for both channels is shown in Figure 2.14(b). An similar NL performance as the interface board AD-channels can be recognized up to $20\,$MHz. At higher frequencies a rapid drop of the IP_3 magnitude is observed. Measurements of the driver OpAmp in a stand-alone operation showed that this behavior was introduced by the wideband amplifier.

2.3 Measurement setups

In Figure 2.1 and 2.3 the structure of the direct conversion transmitter and receiver was introduced. The properties and performance of the devices used in these setups were discussed in Section 2.1 and 2.2. A measurement setup for characterizing the transmitter response in the RF and providing this signal to the receiver is presented in Figure 2.15. A picture of this measurement setup is shown in Figure 2.16. The BB output signals are generated by the BenADDA, interface board cascade and upconverted by the IQ-mixer. After the RF output signal is boosted by the driver amplifier it is characterized by the SA, the power meter (P) and a random sampling scope. The transmitter output signal is then scaled to the desired receiver input signal magnitude before it is downconverted to BB and recorded.

A measurement application and the parameter extraction algorithms were implemented using a MATLAB® environment running on the host PC. The complex baseband signals are generated by the measurement application and loaded into the BenADDA memory. The same program is also used for remotely accessing scope, SA, PM, and step-attenuator. After the measurement is completed the traces
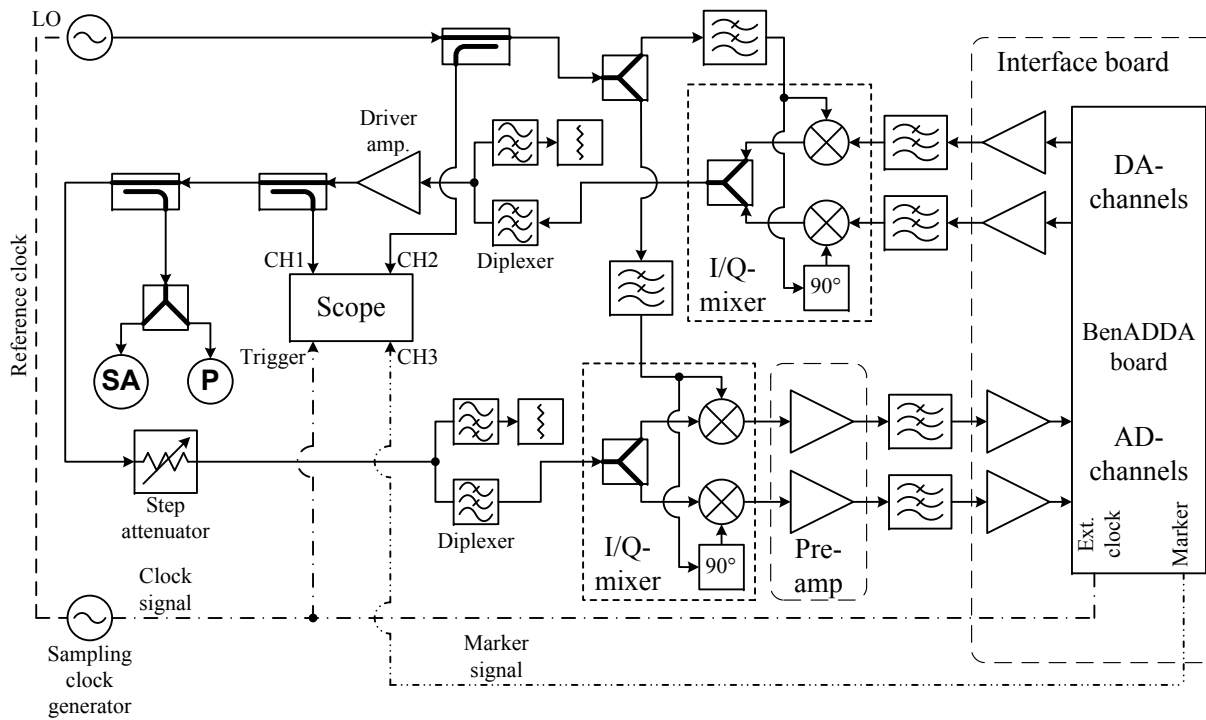
Figure 2.15: Measurement setup for a combined operation of the transmitter and receiver.
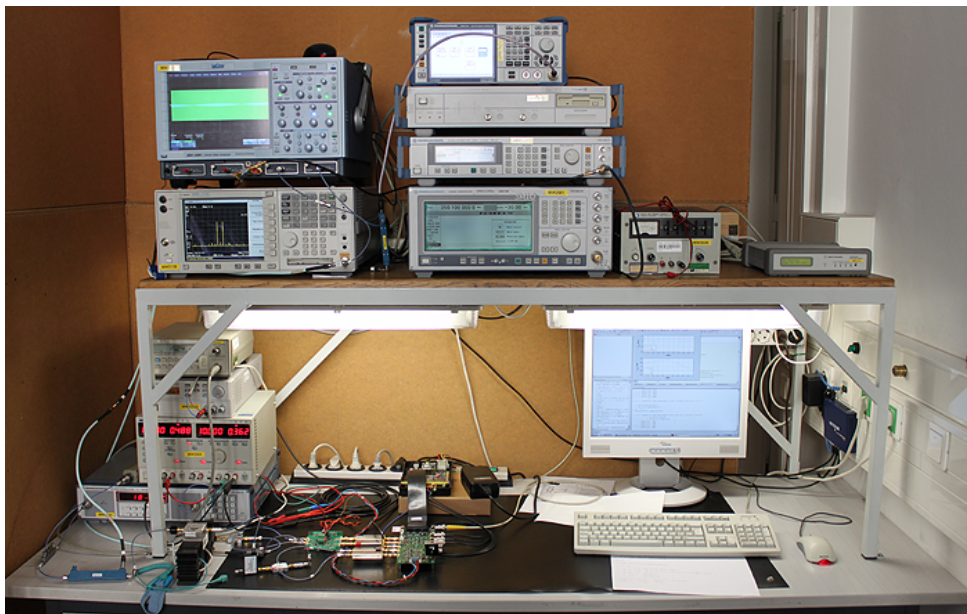
Figure 2.16: Photograph of the measurement setup for the direct conversion transmitter and receiver.

stored by the ADCs are transferred to the measurement application and are postprocessed. It is assumed, that the LO and the sampling clock generators are set once during the startup of the system and don't change their parameters during a measurement.

The critical part of this measurement setup is to guarantee stable phase measurements even if the transmitter output signal is modulated. For this task the LeCroy SDA 100H scope was triggered by the sampling clock of the BenADDA board. Using a fractional-N phase-locked loop (PLL) of the scope a trigger frequency is selected which is a least common multiple of all considered envelope spectral components. In this way a stable measurement at the scope is established. This benefit is confronted by the change in the phase relationship to the LO and the transmitter output signal each time the PLL has to lock again onto the clock signal initiated by a change of an important parameter. Without any additional actions it is impossible to relate the phases of two consecutive measurements, for example, during a power sweep. To overcome this behavior a marker signal was generated by the BenADDA board at the minimum envelope frequency ($1/T_{\text{signal}}$). This marker signal is also measured by the scope. The rising edge of the marker establishes the time reference to which the spectral components of the transmitter output signal are compared to. It should be noted, that the marker signal cannot be provided at the trigger input of the scope as it is too noisy. Even the combined usage of the sampling clock as trigger signal and the marker as time reference turned out to show phase variations of $10°$ when measuring a single-tone output signal. To further lower the phase uncertainties of the measurement setup a two stage phase alignment was applied. Assuming a multi-tone transmitter output signal, measured by the scope, given by:

$$
\begin{aligned}
\tilde{s}_{\text{RF,scope}}(t) &= \frac{A}{N} \sum_{k=1}^{N} \cos(2\pi \text{f}_k t + \phi_k) \\
&= \frac{A}{N} \sum_{k=1}^{N} \cos\left(2\pi(\text{f}_{\text{RF}} + k\text{f}_{sp})t + \phi_{\text{RF}} + \phi_{sp,k}\right)
\end{aligned}
\tag{2.1}
$$

where f_k identifies the RF tone frequencies which are composed of $\text{f}_{\text{RF}}, \text{f}_{sp}$, the carrier frequency and the tone spacing. At the same time f_{sp} represents the frequency of the marker output signal. Each of the tones shows a magnitude A/N and phase shifts ϕ_k. The tilde at $\tilde{s}_{\text{RF,scope}}(t)$ indicates a real-valued RF output signal in contrast to its complex envelope representation $s_{\text{RF,scope}}(t)$. At the same time also the marker signal and the LO is captured:

$$
\begin{aligned}
\tilde{s}_{\text{LO,scope}}(t) &= A_{\text{LO}} \cos(2\pi \text{f}_{\text{LO}}t + \phi_{\text{LO}}) \\
\tilde{s}_{\text{Marker,scope}}(t) &= A_{\text{Marker}} \cos(2\pi \text{f}_{sp}t + \phi_{\text{Marker}})
\end{aligned}
\tag{2.2}
$$

For simplicity a sinusoidal marker signal was used instead of a rectangular one. Using the time delay equivalent to the phase of the marker signal:

$$
T_{\text{Marker}} = \frac{\phi_{\text{Marker}}}{2\pi \text{f}_{sp}}
\tag{2.3}
$$

the phase aligned transmitter output signal is given by:

$$
\tilde{s}_{\text{RF,aligned}}(t) = \frac{A}{N} \sum_{k=1}^{N} \cos\left(2\pi \text{f}_k t + \phi_k - \phi_{\text{LO}} - 2\pi k\text{f}_{sp}T_{\text{Marker}}\right)
\tag{2.4}
$$

In this way the remaining RF phase expresses the phase difference to the LO. The time reference introduced by the noisy marker signal is only used to shift the spectral components in the envelope domain. The stability of the LO phase measurement at $f_{LO} = 3.5\,\text{GHz}$ is analyzed in Figure 2.17(a). At this measurement 16 realizations of the LO were used to estimate the initial phase $\phi_{LO,ini.}$. In the next half hour the LO phase was continuously measured and $\phi_{LO,ini.}$ was subtracted. The overall drift of the LO phase is below $10°$ over this period. A warmup time of 12 hours was applied before these measurements were performed. Additionally, the phase variation at 16 consecutive measurements was evaluated. These results are summarized in Figure 2.17(b). A peak short term phase variation of approx. $2°$ can be recognized. In average a phase variation of $1.2°$ over 16 measurements was achieved.

(a)   (b)
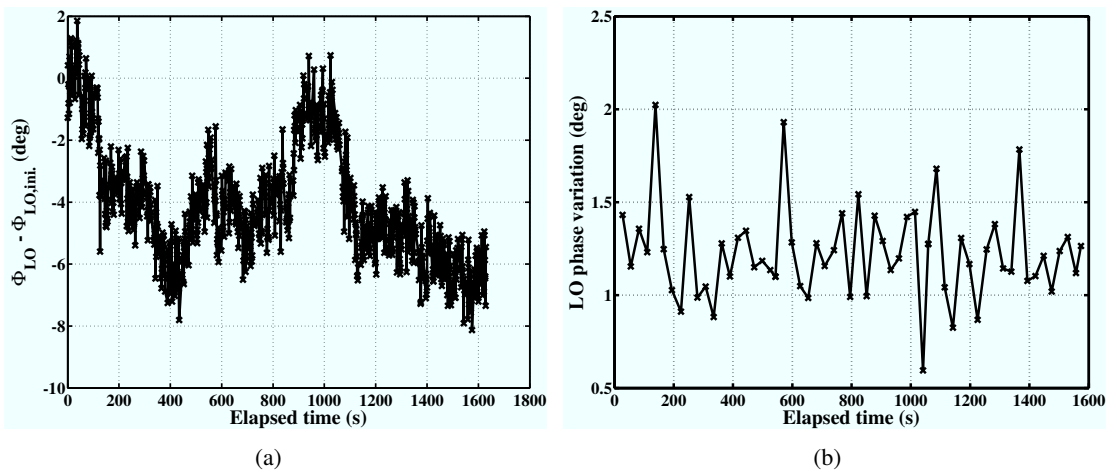
Figure 2.17: Measurement of the (a) drift and (b) variation of the LO phase.

Similar measurements were performed for a two-tone signal generated by the transmitter. The long term stability of both tones of the two-tone signal evaluated at different tone spacings is shown in Figure 2.18(a). At these measurements the drift of the LO and of the sampling clock add up. From these measurements no statement on a systematical dependency of the tone spacing on the corresponding phase drift can be made. The short term stability over 16 measurements of the corrected tone phases, is visualized in Figure 2.18(b). As the LO and marker signal phase changes are compensated from these results a significantly lower phase variation compared to the LO stand-alone measurements can be observed. A mean phase variation of $0.18°$ is, therefore, feasible. Also the receiver measurement results of the two-tone signal generated by the transmitter were analyzed. Over 16 measurements the standard deviation of the tone phases extracted from the receiver traces were below $0.09°$.

Achieving correct magnitude measurements the transmitter output spectrum is measured using the power meter and the SA. Over a large bandwidth the SA can be configured for measuring multi-sine signals with high dynamic range by properly choosing its resolution bandwidth and mixer input level [73]. Typically, the mixer input level is responsible for the distortion generated by the SA while the resolution bandwidth filter determines the measurement noise. Both distortion sources must be low enough for achieving the desired measurement dynamic. Lowering the mixer level and reducing the resolution filter bandwidth increases the dynamic range and also the duration for a measurement (due to a longer filter settling time). Hence, a highly dynamic SA measurement can be achieved at the cost
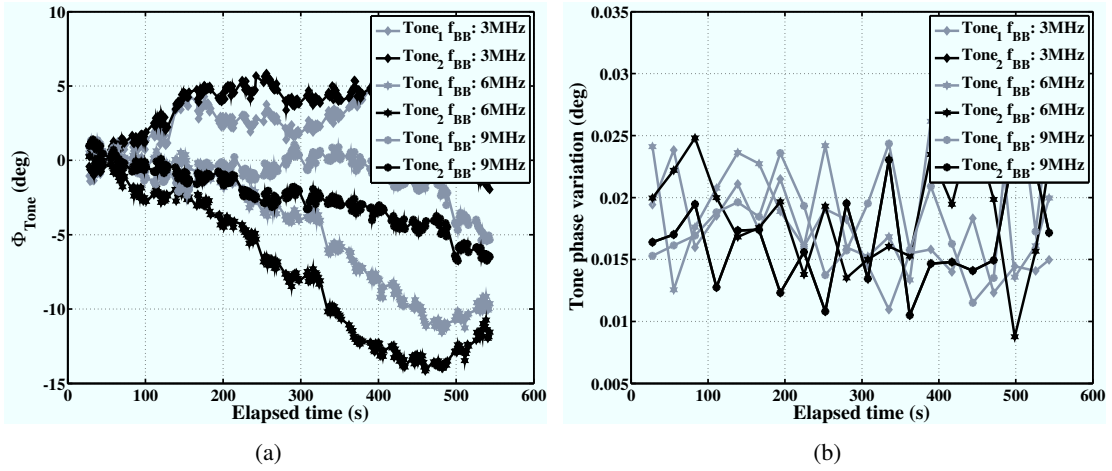
Figure 2.18: Measurement of the (a) drift and (b) variation of the phases of a two-tone signal generated by the transmitter.

of an increased measurement time duration. The accuracy of absolute power measurements using a SA is significantly lower than the power meter ones. Therefore, the tone magnitudes measured by the SA are modified showing the same absolute power level as evaluated by the power meter. In this way long term tone magnitude drift below 0.1 dB was accomplished. In case the two-tone signal generated by the transmitter is measured by the receiver a tone magnitude standard deviation over 16 measurements of 0.003 dB was extracted from the receiver traces. At the same measurements a short term drift of 0.1 dB was observed.

The measurement setup for an independent characterization of the receiver is presented in Figure 2.19. A photo of this measurement setup is depicted in Figure 2.20. The receiver input signal is composed for one or two tones generated by single carrier sources. Hence, low distortion imbalance free excitation signals are produced. At a power sweep the sources are always operated at the maximum required output power. The change of the input power at the receiver is then obtained through the step-attenuator. By this approach a constant phase relationship is assured. Assuming that the frequency response of the step-attenuator was characterized at the applied attenuations all tone phases at the receiver input are known while sweeping the power.

For a stable phase measurement the same approach is used as before. The tone spacing of the two-tone signal is again used for generating a marker signal acting as time reference for the spectral components of the envelope. By locking all frequency generators to the same reference signal the drift between the sources is minimized.

Additionally to the discussed measurement setups, the characteristics of a direct conversion transmitter composed of an arbitrary waveform generator (AWG) and a vector signal generator (VSG) was evaluated. Only the magnitude response of this transmitter was measured. The setup applied in this case is presented in Figure 2.21. As AWG and VSG a Rohde & Schwarz AMIQ and SMIQ, respectively, was used. Similar to the BenADDA board the AMIQ is equipped with two 14-bit DAC's which are able of providing 70 dB SFDR and a signal to noise ratio (SNR) of 11-bit effective for a 5 MHz single-tone output signal sampled at 50 Msps. It was operated at a sampling frequency $f_s = 100$ Msps. The SMIQ
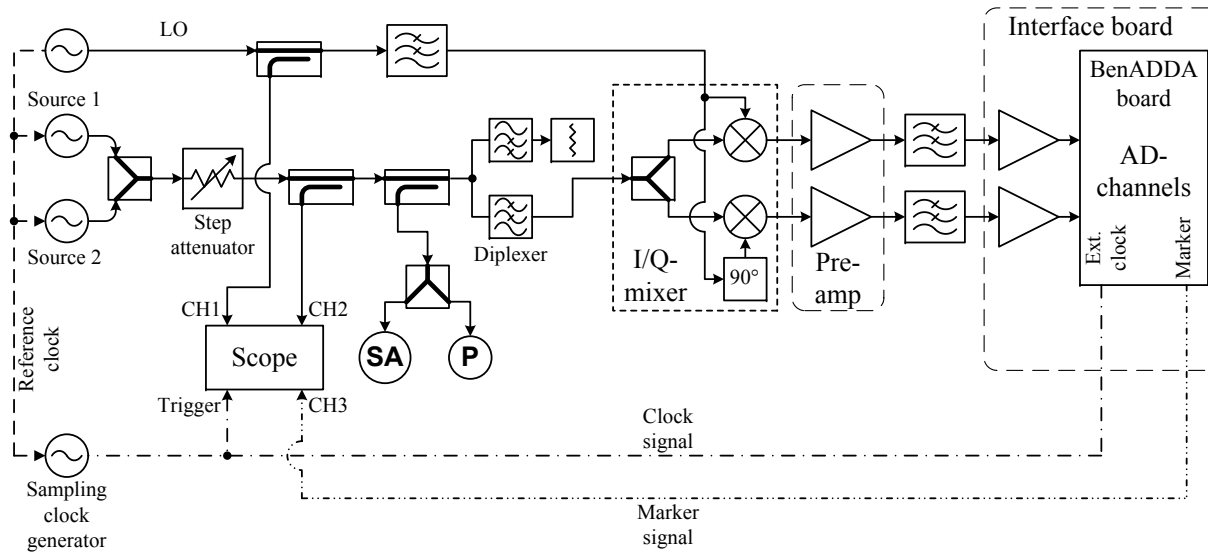
Figure 2.19: Measurement setup for single- and two-tone power sweeps at the receiver.
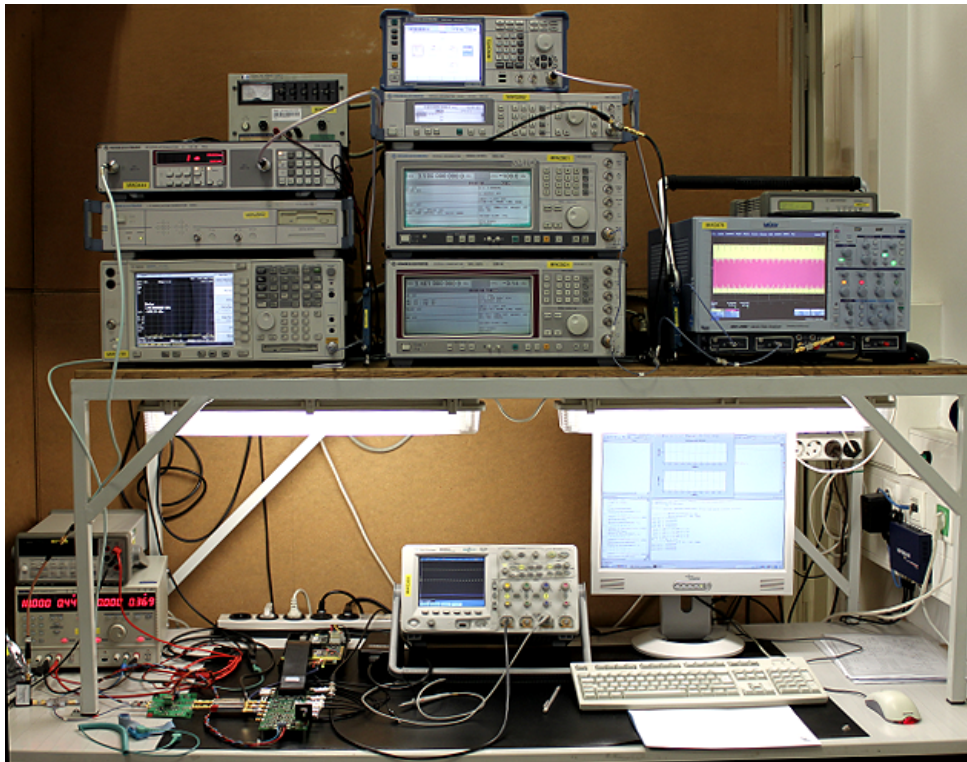
Figure 2.20: Photograph of the measurement setup performing single- and two-tone power sweeps at the receiver.
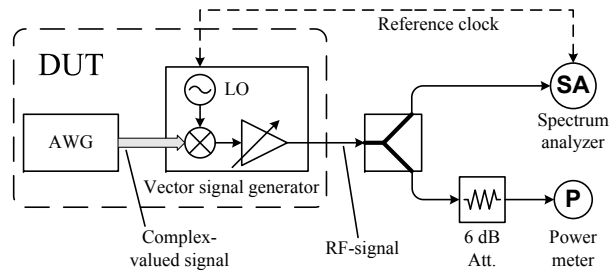
Figure 2.21: Measurement setup used to characterize a transmitter composed of an AWG and a VSG.

was set to 0 dBm RF output power. The direct conversion transmitter implemented in this way showed LO spurious emissions. Their characterization and compensation is discussed in Section 3.7.

Chapter 3

Transmitter modeling and compensation

In contrast to the classical power amplifier model which is described by its AM-AM and AM-PM conversion characteristics the behavior of a transmitter is more complex. Especially, the imbalances of the I/Q modulator may cause PM-AM and PM-PM distortion effects. Phase noise reduces the purity of the transmit signal. The BB amplifiers generate distortion located at the harmonics of the input signal. In the following the various disturbances are treated based on the structure of the transmitter system.

The model of the imperfections of an I/Q modulator is presented in Figure 3.1 which is based on the description suggested in [74]. In this model the ideal mixers perform the frequency conversion. The inphase $s_{\mathrm{BB},I}$ and the quadrature $s_{\mathrm{BB},Q}$ part of the complex baseband signal s_{BB} are provided at the inputs of the modulator after the lowpass filtering by $h_{\mathrm{LP},I}$ and $h_{\mathrm{LP},Q}$. These signals are passed through the amplifiers $g_I(\cdot)$ and $g_Q(\cdot)$. The amplifiers show a nonlinear behavior and add DC-offsets to the two baseband channels. The local oscillator provides the carrier signal which is degraded by phase noise and spurious emissions. The LO output signal is divided in two equal parts. The carrier signal for the quadrature channel is then phase-shifted by an angle $90° + \theta_e$ (asymmetrical phase-error model). Each of the carrier signal copies is boosted by the corresponding amplifiers g_{CI} and g_{CQ} and altered by a DC-offset (O_{CI} and O_{CQ}). The two LO amplifiers are modeled as distortion free.

After adding the DC-offsets the carrier signals are fed into the corresponding mixers. The mixer output signal is filtered by an ideal bandpass for suppressing the DC-offset and the baseband signal feed-through. This filtered signal $\tilde{s}_{\mathrm{BP}}(t) = \mathrm{Re}\left\{ s_{\mathrm{BP}}(t)e^{j\omega_0 t} \right\}$ is then passed through the output nonlinearity $\tilde{g}_{\mathrm{M}}(\cdot)$ of the mixer. This mixer output signal s_{mod} is afterwards applied to the (nonlinear dynamic) power amplifier $\tilde{g}_{\mathrm{RF}}(\cdot)$.

In case an I/Q modulator implements the first mixing stage of a superheterodyne transmitter (compare Figure 1.1) the impact of the additional mixing stages are represented by $\tilde{g}_{\mathrm{M}}(\cdot)$. The structure shown in Figure 3.1 can be used to model the behavior of such transmitters as long as the effect of the residual image sideband is negligible.

To evaluate the characteristics of the modulator the RF output signal $\tilde{s}_{\mathrm{RF}}(t)$ is calculated. The complex baseband modulator input signal shows a frequency dependent gain imbalance introduced by the two lowpass filters. The baseband signal components are, thereafter, boosted by the two nonlinear
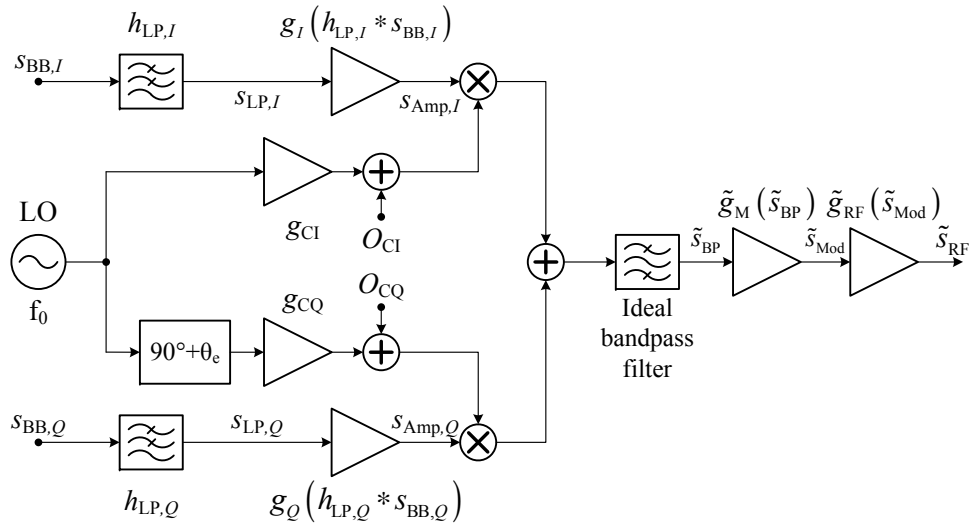
Figure 3.1: Model of the imperfections within the transmit branch.

amplifiers:

$$
\begin{aligned}
s_{\mathrm{Amp},I}(t) &= g_I\big(h_{\mathrm{LP},I}(t) * s_{\mathrm{BB},I}(t)\big) \\
s_{\mathrm{Amp},Q}(t) &= g_Q\big(h_{\mathrm{LP},Q}(t) * s_{\mathrm{BB},Q}(t)\big) \\
|s_{\mathrm{Amp}}(t)| &= \sqrt{s_{\mathrm{Amp},I}^2(t) + s_{\mathrm{Amp},Q}^2(t)} \\
\angle s_{\mathrm{Amp}}(t) &= \arctan\left(\frac{s_{\mathrm{Amp},Q}(t)}{s_{\mathrm{Amp},I}(t)}\right)
\end{aligned}
\tag{3.1}
$$

As these two amplifiers are normally implemented as Class-A small signal amplifiers operating far below their 1 dB-compression point a weakly nonlinear model can be justified. The inphase and quadrature output signal components of the following mixers are given by:

$$
\begin{aligned}
s_{\mathrm{Amp},I}(t)\cdot\Big[O_{\mathrm{CI}} + \sum_{k=0}^{N_{\mathrm{spur}}} g_{\mathrm{CI},k}\cos(\omega_0 t + \Delta\omega_k + \varphi_{\mathrm{PH},k}(t) + \varphi_{\mathrm{LO},k})\Big] = \\
O_{\mathrm{CI}}s_{\mathrm{Amp},I}(t) + \sum_{k=0}^{N_{\mathrm{spur}}} g_{\mathrm{CI},k}s_{\mathrm{Amp},I}(t)\cos(\omega_0 t + \Delta\omega_k + \varphi_{\mathrm{PH},k}(t) + \varphi_{\mathrm{LO},k}) \\
-s_{\mathrm{Amp},Q}(t)\cdot\Big[O_{\mathrm{CQ}} + \sum_{k=0}^{N_{\mathrm{spur}}} g_{\mathrm{CQ},k}\sin(\omega_0 t + \Delta\omega_k + \varphi_{\mathrm{PH},k}(t) + \varphi_{\mathrm{LO},k} + \theta_e)\Big] = \\
-O_{\mathrm{CQ}}s_{\mathrm{Amp},Q}(t) - \sum_{k=0}^{N_{\mathrm{spur}}} g_{\mathrm{CQ},k}s_{\mathrm{Amp},Q}(t)\sin(\omega_0 t + \Delta\omega_k + \varphi_{\mathrm{PH},k}(t) + \varphi_{\mathrm{LO},k} + \theta_e)
\end{aligned}
\tag{3.2}
$$

At these equations N_{spur} spurious emissions are present at the output of the local oscillator. These spurs are at an offset $\Delta\omega_k$ from the center frequency and show a phase shift $\varphi_{\mathrm{LO},k}$. The carrier is identified by the index $k = 0$ (i.e., $\Delta\omega_0 = 0$). For simplifying the notation the inphase and quadrature magnitudes of the LO output products are represented by $g_{\mathrm{CI},k}$, $g_{\mathrm{CQ},k}$. The time-varying phases $\varphi_{\mathrm{PH},k}(t)$ describe the phase noise impact on the carrier and the spurs. In contrast to the other parameters used for the model $\varphi_{\mathrm{PH},k}(t)$ represent random processes of the jitter in the phase-locked oscillator.

Clearly, the two carrier DC-offsets cause the feed-through of the baseband output signal. Even if these feed-through signals are removed by the bandpass filter they can also induce a reduction of the mixer dynamic range as they add up with the desired mixer output signal. The DC-part of $s_{\text{Amp}}(t)$ is responsible for the carrier leakage.

The ideal bandpass filter located after the mixers suppresses all signal components outside the fundamental signal band. Therefore, the complex envelope of the mixer output nonlinearity $g_{\text{M}}(\ \cdot\ )$ input signal results to [75]:

$$
\begin{aligned}
s_{\text{BP}}(t) &= \sum_{k=0}^{N_{\text{spur}}} \left[g_{\text{CI},k} s_{\text{Amp},I}(t) + j g_{\text{CQ},k} s_{\text{Amp},Q}(t) e^{j\theta_e} \right] \ e^{j(\Delta\omega_k t + \varphi_{\text{PH},k}(t) + \varphi_{\text{LO},k})} \\
&= \sum_{k=0}^{N_{\text{spur}}} \left[\tfrac{1}{2} s_{\text{Amp}}(t) \left(g_{\text{CI},k} + g_{\text{CQ},k} e^{j\theta_e} \right) \right. \\
&\qquad \left. + \tfrac{1}{2} s_{\text{Amp}}^*(t) \left(g_{\text{CI},k} - g_{\text{CQ},k} e^{j\theta_e} \right) \right] \ e^{j(\Delta\omega_k t + \varphi_{\text{PH},k}(t) + \varphi_{\text{LO},k})}
\end{aligned} \tag{3.3}
$$

After the amplification by the PA the transmitter output signal is given by:

$$
\begin{aligned}
s_{\text{RF}}(t) &= g_{\text{RF}}(s_{\text{mod}}(t)) \\
&= g_{\text{RF}}\left(g_{\text{M}} \left[\sum_{k=0}^{N_{\text{spur}}} \left[g_{\text{CI},k} s_{\text{Amp},I}(t) + j g_{\text{CQ},k} s_{\text{Amp},Q}(t) e^{j\theta_e} \right] \ e^{j(\Delta\omega_k t + \varphi_{\text{PH},k}(t) + \varphi_{\text{LO},k})} \right] \right) \\
&= g_{\text{RF}}\left(g_{\text{M}} \left[\sum_{k=0}^{N_{\text{spur}}} \left[g_{\text{CI},k} g_I \left(h_{\text{LP},I}(t) * s_{\text{BB},I}(t) \right) + j g_{\text{CQ},k} g_Q \left(h_{\text{LP},Q}(t) * s_{\text{BB},Q}(t) \right) e^{j\theta_e} \right] \right. \right. \\
&\qquad \left. \left. \cdot e^{j(\Delta\omega_k t + \varphi_{\text{PH},k}(t) + \varphi_{\text{LO},k})} \right] \right)
\end{aligned}
$$

$$\tag{3.4}$$

3.1 Linear transmitter model

The complexity of the relationship presented in (3.4) reduces significantly if all amplifiers are assumed to be linear and if the LO spurs are neglected. The DC-offset of the two baseband amplifiers are identified by $g_{I,0}$ and $g_{Q,0}$. In this case, the frequency domain representation of the transmitter branch output signal is given by:

$$
\begin{aligned}
S_{\text{RF}}(j\omega) &= g_{\text{RF}} g_{\text{M}} e^{j\varphi_{\text{LO},0}} S_{\text{PH},0}(j\omega) * \left[2\pi\delta(j\omega) O_{\alpha_d,0} \right. \\
&\qquad \left. + \alpha_d(j\omega) S_{\text{BB}}(j\omega) + \alpha_v(j\omega) S_{\text{BB}}^*(-j\omega) \right]
\end{aligned} \tag{3.5}
$$

In this equation the Fourier transform of the signal $s(t)$ was identified as $S(j\omega)$. The linear gain of the PA and the mixer output NL were represented by g_{RF} and g_{M}. The power spectral density (PSD) of the carrier phase noise is identified by $S_{\text{PH},0}(j\omega)$. The impact of the modulator imbalance was expressed by

the parameters $\alpha_d(j\omega)$ and $\alpha_v(j\omega)$ and the carrier leakage was incorporated by O_{α_d}:

$$
\begin{aligned}
\alpha_I(j\omega) &= g_{\text{CI},0}g_I H_{\text{LP},I}(j\omega) \\
\alpha_Q(j\omega) &= g_{\text{CQ},0}g_Q H_{\text{LP},Q}(j\omega) \\
\alpha_d(j\omega) &= \tfrac{1}{2}\left[\alpha_I(j\omega) + \alpha_Q(j\omega)\,e^{j\theta_e}\right] \\
\alpha_v(j\omega) &= \tfrac{1}{2}\left[\alpha_I(j\omega) - \alpha_Q(j\omega)\,e^{j\theta_e}\right] \\
O_{\alpha_d,k} &= g_{\text{CI},k}g_{I,0} + jg_{\text{CQ},k}g_{Q,0}\,e^{j\theta_e}
\end{aligned}
\tag{3.6}
$$

where the frequency dependent inphase and quadrature branch gain were identified by $\alpha_I(j\omega)$ and $\alpha_Q(j\omega)$. Another possibility for expressing the linear dependencies is based on the inphase and quadrature input signal components:

$$
\begin{aligned}
S_{\text{RF}}(j\omega) &= g_{\text{RF}}g_{\text{M}}e^{j\varphi_{\text{LO},0}}S_{\text{PH},0}(j\omega) * \Big(2\pi\delta(j\omega)O_{\alpha_d,0} + \alpha_I(j\omega)\big[S_{\text{BB},I}(j\omega) \\
&\quad -\gamma(j\omega)\sin(\theta_e)S_{\text{BB},Q}(j\omega) + j\gamma(j\omega)\cos(\theta_e)S_{\text{BB},Q}(j\omega)\big]\Big) \\
&= g_{\text{RF}}g_{\text{M}}e^{j\varphi_{\text{LO},0}}S_{\text{PH},0}(j\omega) * \Big(2\pi\delta(j\omega)O_{\alpha_d,0} + \alpha_I(j\omega)\big[S_{\text{BB},I}(j\omega) \\
&\quad -|\gamma(j\omega)|\sin(\theta_e + \phi_\gamma(j\omega))S_{\text{BB},Q}(j\omega) + j|\gamma(j\omega)|\cos(\theta_e + \phi_\gamma(j\omega))S_{\text{BB},Q}(j\omega)\big]\Big)
\end{aligned}
\tag{3.7}
$$

Here the inphase channel of the modulator was selected as reference. The gain ratio between the inphase and the quadrature channel is expressed by $\gamma(j\omega)$. The parameter $\epsilon(j\omega)$ is used for identifying the magnitude imbalance. These parameters are defined as [76]:

$$
\begin{aligned}
\gamma(j\omega) &= \frac{g_{\text{CQ},0}g_Q H_{\text{LP},Q}(j\omega)}{g_{\text{CI},0}g_I H_{\text{LP},I}(j\omega)} = \frac{\alpha_Q(j\omega)}{\alpha_I(j\omega)} \\
\gamma(j\omega) &= |\gamma(j\omega)|e^{j\phi_\gamma(j\omega)} \\
\epsilon(j\omega) &= 1 - |\gamma(j\omega)|
\end{aligned}
\tag{3.8}
$$

In equation (3.7) it was shown, that the frequency dependent phase imbalance $\phi_\gamma(j\omega)$ introduced by the low-pass filters and the mixer phase imbalance θ_e cause the same imbalance distortion mechanism [77, 78]. Only the impact of the sum of these two parameters can be recognized.

This linear transmitter model is based on the assumption that the imbalance function $\gamma(j\omega)$ is derived from the ratio of the quadrature channel frequency response to the inphase channel one (3.8). Hence, $\gamma(j\omega)$ behaves like a real-valued system showing an even symmetry at the magnitude and an odd at the phase response. Due to a non-negligible RF-transfer characteristic $\gamma(j\omega)$ may violate these symmetries. In such cases equation (3.5) should be used instead of (3.7) to correctly describe the imbalance of the transmitter.

It is important to note that for the linear transmitter mode described in equations (3.5) to (3.8) a frequency depending I/Q mixer phase error can be introduced by exchanging θ_e by $\theta_e(j\omega)$ [79].

3.1.1 Quantification of the imbalance and the DC-offset

The nonlinear effects of the different amplifiers or the mixers can be easily compared to each other using the third-order intercept point. For quantifying and comparing the gain and phase imbalance at a certain

frequency and the carrier feed-through two measures were suggested in [80]. The image suppression ratio (ISR), which evaluates the magnitude and phase imbalance, is based on the power ratio between the desired and the image frequency component for a single-tone input signal. This ratio is derived from the phase noise free linear transmitter model [76]. To measure the ISR a single-tone signal is generated at a frequency ω_m occupying the full-scale output of the DACs. In this case, the output power of the transmit branch for this signal is given by:

$$
\begin{aligned}
|s_{\text{RF}}(j\omega)|^2 &= \pi^2 |\alpha_I(j\omega)|^2 \delta(j\omega - j\omega_m) \left[1 + |\gamma(j\omega)|^2 + 2|\gamma(j\omega)|\cos(\theta_e + \phi_\gamma(j\omega))\right] \\
&\quad + \pi^2 |\alpha_I(j\omega)|^2 \delta(-j\omega - j\omega_m) \left[1 + |\gamma(j\omega)|^2 - 2|\gamma(j\omega)|\cos(\theta_e - \phi_\gamma(j\omega))\right]
\end{aligned}
\tag{3.9}
$$

where $\phi_\gamma(j\omega)$ was defined in (3.8). The power ratio of the undesired tone at $-\omega_m$ to the desired one at ω_m (which corresponds to the image signal suppression at low-IF receiver structures) results to [75, 81]:

$$
\text{ISR}(j\omega) = \frac{\text{P}_s(-j\omega_m)}{\text{P}_s(j\omega_m)} = \frac{1 + |\gamma(j\omega)|^2 - 2|\gamma(j\omega)|\cos(\theta_e - \phi_\gamma(j\omega))}{1 + |\gamma(j\omega)|^2 + 2|\gamma(j\omega)|\cos(\theta_e + \phi_\gamma(j\omega))}
\tag{3.10}
$$

In this equation $\text{P}_s(j\omega)$ identifies the power of the signal component at ω. By using the approximation $\cos(x) \approx 1 - x^2/2$ and assuming that both angles θ_e and $\phi_\gamma(j\omega)$ are small the relationship presented in (3.10) can be approximated by:

$$
\text{ISR}(j\omega) \approx \frac{1}{4}\left[\epsilon(j\omega)^2 + (\phi_\gamma(j\omega) - \theta_e)^2\right]
\tag{3.11}
$$

For extending the frequency dependent $\text{ISR}(j\omega)$ to a version describing the whole transmitter the $\text{ISR}(j\omega)$ performance must be averaged over the whole BB bandwidth:

$$
\text{ISR} = \frac{1}{\text{BW}_{\text{BB}}} \int \text{ISR}(j\omega) d\omega
\tag{3.12}
$$

For quantifying the impact of the carrier feed-through, the power of this distortion is compared to the power of the full-scale single-tone calculated in (3.9). This ratio is called DC suppression ratio (DSR):

$$
\text{DSR} = \frac{\text{P}_s(0)}{\text{P}_s(j\omega_m)} = \frac{|O_{\alpha_d,0}|^2}{\pi^2 |\alpha_I(j\omega)|^2 \left[1 + |\gamma(j\omega)|^2 + 2|\gamma(j\omega)|\cos(\theta_e + \phi_\gamma(j\omega))\right]}
\tag{3.13}
$$

It should be noted, that, for correctly evaluating the DSR, $s_{\text{BB}}(t)$ must be set to zero during the measurement of $\text{P}_s(0)$. Otherwise, the second-order distortion of the baseband amplifiers will create additional DC-offsets which are dependent on the power and frequency of $\text{P}_s(j\omega_m)$.

The ISR and DSR could also be evaluated from the nonlinear transmitter description by neglecting the generated harmonics but, in this case, equations (3.10) to (3.13) are significantly more complicated.

3.2 Impact of modulator behavior

After introducing the model of the modulator the impact of the different distortion sources should be visualized. For this purpose three different test signals are used:

- Single-tone

- Two-tone with incommensurable tone frequencies [82]

- Two-tone with commensurable tone frequencies

- Two-tone with tone frequencies symmetrical to DC

The two-tone input signal is represented by:

$$
\begin{aligned}
s_{\mathrm{BB}}(t) &= A_{\mathrm{TT}} \left(e^{j(\omega_1 t + \varphi_1)} + e^{j(\omega_2 t + \varphi_2)} \right) \\
&= 2 A_{\mathrm{TT}} e^{\frac{j}{2}\left[(\omega_1 + \omega_2)t + \varphi_1 + \varphi_2 \right]} \cos \left(\tfrac{1}{2}\left[(\omega_1 - \omega_2)t + \varphi_1 - \varphi_2 \right] \right)
\end{aligned}
\tag{3.14}
$$

where f_1, f_2 are the two tone frequencies and φ_1, φ_2 the tone phases. The impact of the test signals on the different transmitter distortion sources is analytically derived and visualized using simulations in the next section. These simulations were performed based on the following parameters (assuming an input signal magnitude of $s_{\mathrm{BB,mag}}$):

DC offsets: $O_I = 0.05\, s_{\mathrm{BB,mag}}$, $O_Q = 0.07\, s_{\mathrm{BB,mag}}$

Baseband amplifier: The amplifiers were modeled by a 3rd-order polynomial. At the input signal magnitude the amplifiers showed 1.5 dB gain compression. The linear gain of the inphase channel amplifier was set to unity, the gain of the quadrature one to 0.9.

Phase imbalance: θ_e was set to $-12°$.

Power amplifier: The PA is assumed to be ideal.

All spurious emissions and the phase noise impact were neglected.

3.2.1   DC-offset

The above mentioned test signals are now applied to a transmitter showing only a DC-offset. Under this assumption the transmitter output signal (3.4) simplifies to:

$$
s_{\mathrm{RF,DC}}(t) = g_{\mathrm{RF}} g_{\mathrm{M}} e^{j\varphi_{\mathrm{LO},0}} \left[s_{\mathrm{BB}}(t) + (g_{I,0} + j g_{Q,0}) \right]
\tag{3.15}
$$

The corresponding transmitter gain is given by:

$$
\begin{aligned}
G_{\mathrm{RF,DC}}(t) &= s_{\mathrm{RF}}(t) s_{\mathrm{BB}}^{-1}(t) \\
&= g_{\mathrm{RF}} g_{\mathrm{M}} e^{j\varphi_{\mathrm{LO},0}} \left[1 + (g_{I,0} + j g_{Q,0}) s_{\mathrm{BB}}^{-1}(t) \right] \\
&= g_{\mathrm{Lin}} \left[1 + g_{\mathrm{Amp},0} s_{\mathrm{BB}}^{-1}(t) \right]
\end{aligned}
\tag{3.16}
$$

where g_{Lin} and $g_{\mathrm{Amp},0}$ represent the linear transmitter gain and the BB amplifier DC-offset, respectively. A PM-AM and PM-PM conversion is found if the mean gain shows a dependency on the input phase.

For a single-tone input signal the mean transmitter gain results to:

$$
s_{\mathrm{BB}}(t) = A_{\mathrm{ST}} e^{j(\omega_1 t + \varphi_1)}
$$

$$
\bar{G}_{\mathrm{RF,DC}} = \frac{2\pi g_{\mathrm{Lin}}}{\omega_1} \int\limits_{0}^{2\pi/\omega_1} \left[1 + g_{\mathrm{Amp},0} A_{\mathrm{ST}}^{-1} e^{-j(\omega_1 t + \varphi_1)} \right] dt = g_{\mathrm{Lin}}
\tag{3.17}
$$

This expression highlights the missing of any PM-AM and PM-PM effects due to a DC-offset for the single-tone input. In case of a two-tone signal $\bar{G}_{\text{RF,DC}}$ is given by:

$$\bar{G}_{\text{RF,DC}} = \frac{1}{T} \int\limits_{0}^{T} g_{\text{Lin}} \left[1 + \frac{1}{2} g_{\text{Amp},0} A_{\text{TT}}^{-1} e^{-\frac{j}{2}[(\omega_1+\omega_2)t+\varphi_1+\varphi_2]} \cos^{-1}\left(\frac{1}{2}\left[(\omega_1-\omega_2)t + \varphi_1 - \varphi_2 \right] \right) \right] dt$$

(3.18)

Clearly, as in the single-tone case, the constant term within the squared brackets provides a phase independent contribution to the mean gain. To evaluate the remaining integral assumptions on the relation of the two frequencies are required. In case of incommensurable frequencies the period time of the two-tone signal is infinite. By this assumption the integration results to:

$$\bar{G}_{\text{RF,DC}} = g_{\text{Lin}} + \lim_{T\to\infty} \frac{g_{\text{Lin}} g_{\text{Amp},0} e^{-\frac{j}{2}(\varphi_1+\varphi_2)}}{4T A_{\text{TT}}} \int\limits_{-T}^{T} e^{-\frac{j}{2}(\omega_1+\omega_2)t} \cos^{-1}\left(\frac{1}{2}\left[(\omega_1-\omega_2)t + \varphi_1 - \varphi_2 \right] \right) dt$$

(3.19)

Additionally, the integration range was extended to $(-\infty, \infty)$. This expression can be solved using Cauchy's residue theorem [83] after converting the cosine into a rational function. For this task the integration range is divided into segments of 2π length based on the argument of the cosine function:

$$\bar{G}_{\text{RF,DC}} = g_{\text{Lin}} + \lim_{T\to\infty} \frac{g_{\text{Lin}} g_{\text{Amp},0}}{8\pi T A_{\text{TT}}(\omega_1-\omega_2)} e^{-j\frac{\omega_1\varphi_2-\omega_2\varphi_1}{\omega_1-\omega_2}} \sum_{n=-T}^{T} \int\limits_{2\pi n}^{2\pi(n+1)} e^{-j\frac{\omega_1+\omega_2}{\omega_1-\omega_2}\tau} \cos^{-1}(\tau) d\tau \quad (3.20)$$

By substituting $z = \exp(j\tau)$ the inverse cosine function is converted into a rational:

$$\bar{G}_{\text{RF,DC}} = g_{\text{Lin}} + \lim_{T\to\infty} \frac{-j g_{\text{Lin}} g_{\text{Amp},0}}{4\pi T A_{\text{TT}}(\omega_1-\omega_2)} e^{-j\frac{\omega_1\varphi_2-\omega_2\varphi_1}{\omega_1-\omega_2}} \sum_{n=-T}^{T} \oint\limits_{|z|=1} \frac{z^{-\frac{\omega_1+\omega_2}{\omega_1-\omega_2}}}{z^2+1} dz$$

(3.21)

The path of the contour for the integration is taken to be the unit circle passed through in counterclockwise orientation for $n > 0$. This integration is performed infinite times in both directions. The denominator of the rational function has two roots located at j and $-j$. The sum of the corresponding residue results to:

$$\frac{j}{2}\left[(-j)^{-\frac{\omega_1+\omega_2}{\omega_1-\omega_2}} + j^{-\frac{\omega_1+\omega_2}{\omega_1-\omega_2}} \right] = -\sin\left(\frac{\pi}{2}\frac{\omega_1+\omega_2}{\omega_1-\omega_2} \right) \tag{3.22}$$

Substituting (3.22) into (3.21) the mean transmitter gain is given by:

$$\bar{G}_{\text{RF,DC}} = g_{\text{Lin}} + \lim_{T\to\infty} \frac{-g_{\text{Lin}} g_{\text{Amp},0}}{2T A_{\text{TT}}(\omega_1-\omega_2)} e^{-j\frac{\omega_1\varphi_2-\omega_2\varphi_1}{\omega_1-\omega_2}} \left(\sum_{n=0}^{T} 1 - \sum_{n=-1}^{-T} 1 \right) \sin\left(\frac{\pi}{2}\frac{\omega_1+\omega_2}{\omega_1-\omega_2} \right) = g_{\text{Lin}}$$

(3.23)

For $T \to \infty$ both summations result in the same limit value and mean transmitter gain cancels out. It is interesting to note, that averaging the gain in the range $[0, \infty)$ would result in an input phase dependent behavior. For a two-tone input signal with commensurable frequencies the tone frequencies are related

by $\omega_2 = p\,\omega_1/q$, $p, q \in \mathbb{N}$. Applying this prerequisite to (3.19) to (3.23) shows the same result for the mean transmitter gain.

In case of a DC-symmetrical two-tone signal the evaluation of the mean transmitter gain is similar. As in the single-tone case the averaging over one period is sufficient. Substituting $\omega_2 = -\omega_1$ in (3.18) provides the desired expression:

$$
\bar{G}_{\mathrm{RF,DC}} = \frac{\omega_1}{2\pi} \int\limits_0^{2\pi/\omega_1} g_{\mathrm{Lin}} \left[1 + \frac{1}{2} g_{\mathrm{Amp,0}} A_{\mathrm{TT}}^{-1} e^{-\frac{j}{2}(\varphi_1+\varphi_2)} \cos^{-1}\left(\omega_1 t + \frac{1}{2}[\varphi_1 - \varphi_2] \right) \right] dt
$$

$$
= g_{\mathrm{Lin}} + \frac{\omega_1 g_{\mathrm{Lin}} g_{\mathrm{Amp,0}}}{4\pi A_{\mathrm{TT}}} e^{-\frac{j}{2}(\varphi_1+\varphi_2)} \int\limits_0^{2\pi} \cos^{-1}(\tau)\,d\tau
$$

(3.24)

As for the incommensurable frequency two-tone the constant factor g_{Lin} can be separated. The remaining integration is again evaluated using Cauchy's residue theorem:

$$
\bar{G}_{\mathrm{RF,DC}} = g_{\mathrm{Lin}} + \frac{-j\omega_1 g_{\mathrm{Lin}} g_{\mathrm{Amp,0}}}{2\pi A_{\mathrm{TT}}} e^{-\frac{j}{2}(\varphi_1+\varphi_2)} \oint\limits_{|z|=1} \frac{1}{z^2+1}\,dz = g_{\mathrm{Lin}}
$$

(3.25)

The residue of this contour integral are 1 and -1. The sum of these two cancels the second term in (3.25). Equation (3.23) and (3.25) proved that a DC-offset does not introduce phase dependent gain variation at all considered input signals.

A simulation of the DC-offset based origin shift for a single-tone input signal is presented in Figure 3.2. For this simulation a DSR of approx. 21 dB was selected. The magnitude of the input signals was set to unity.
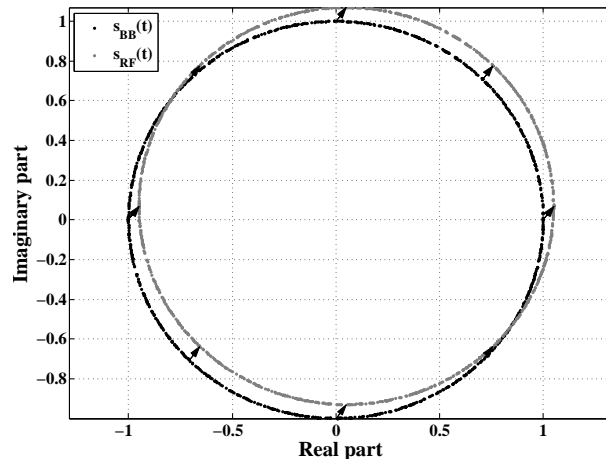
Figure 3.2: Origin shift in the I/Q plot caused by the carrier leakage for a single-tone input signal.

3.2.2 Magnitude and phase imbalance

A linear transmitter showing only static magnitude and phase imbalance is represented by (3.5):

$$s_{\text{RF,Imb}}(t) = g_{\text{Lin}}\big[\alpha_d s_{\text{BB}}(t) + \alpha_v s_{\text{BB}}^*(t)\big] \tag{3.26}$$

where α_d and α_v are introduced in (3.6). The corresponding transmitter gain results to:

$$\begin{aligned} G_{\text{RF,Imb}}(t) &= s_{\text{RF}}(t) s_{\text{BB}}^{-1}(t) \\ &= g_{\text{Lin}}\big[\alpha_d + \alpha_v s_{\text{BB}}^*(t) s_{\text{BB}}^{-1}(t)\big] \end{aligned} \tag{3.27}$$

This expression visualizes the input signal dependent gain variations introduced by imbalance. For a single-tone input signal the mean transmitter gain is given by:

$$\bar{G}_{\text{RF,Imb}} = \frac{\omega_1}{2\pi} \int\limits_0^{2\pi/\omega_1} g_{\text{Lin}}\big[\alpha_d + \alpha_v e^{-2j(\omega_1 t + \varphi_1)}\big]\,dt = g_{\text{Lin}}\alpha_d \tag{3.28}$$

This term highlights the missing of any PM-AM and PM-PM effect due to imbalance effects for a single-tone input. In case of a two-tone signal $\bar{G}_{\text{RF,Imb}}$ is represented by:

$$\bar{G}_{\text{RF,Imb}} = \frac{1}{T} \int\limits_0^T g_{\text{Lin}}\left[\alpha_d + \alpha_v e^{-j\big[(\omega_1+\omega_2)t + \varphi_1 + \varphi_2\big]}\right]dt \tag{3.29}$$

To evaluate (3.29) in case of an incommensurable frequency two-tone the gain is averaged over the range $[0, \infty)$. In this case the integration leads to the same result as for the single-tone signal. Also in case of commensurable tone frequencies the impact of the input tone phases averages out. Only in case $\omega_2 = -\omega_1$ the mean gain is given by:

$$\bar{G}_{\text{RF,Imb}} = g_{\text{Lin}}\left[\alpha_d + \alpha_v e^{-j(\varphi_1+\varphi_2)}\right] \tag{3.30}$$

For this two-tone signal the time dependent complex exponential function in (3.29) simplifies to a phase shift. The sum of the two input phases controls the magnitude of the cosine term applied to the inphase and quadrature channel. In this way PM-AM and PM-PM distortion is generated. The magnitude of the gain variation generated by this effect is defined by $|\alpha_v/\alpha_d|$ (i.e.: the ISR).

The phase dependent gain variation caused by magnitude imbalance is visualized in Figure 3.3(a). The input phase φ_{in} is applied to both input tones. In this presentation the mean gain evaluated over all input phases was subtracted. Therefore, the two graphs depict only the magnitude and phase of the gain error. As in the DC-offset case a polar plot of the transmitter input and output signals for a single-tone excitation are presented in Figure 3.3(b). A γ of 0.9 was used for these simulations resulting in an ISR of $-25\,\text{dB}$.

A phase error causes a rotation of the I/Q plot. Due to the asymmetric error model only the quadrature axis is rotated which deforms the initial circle into an ellipse as shown in Figure 3.4(b). In this figure the two black arrows identify the original ordinate and abscissa. The rotated quadrature axis is shown in grey color. This phase imbalance causes -18 dB ISR. The input phase dependent gain variations introduced by the phase imbalance are depicted in Figure 3.4(a)
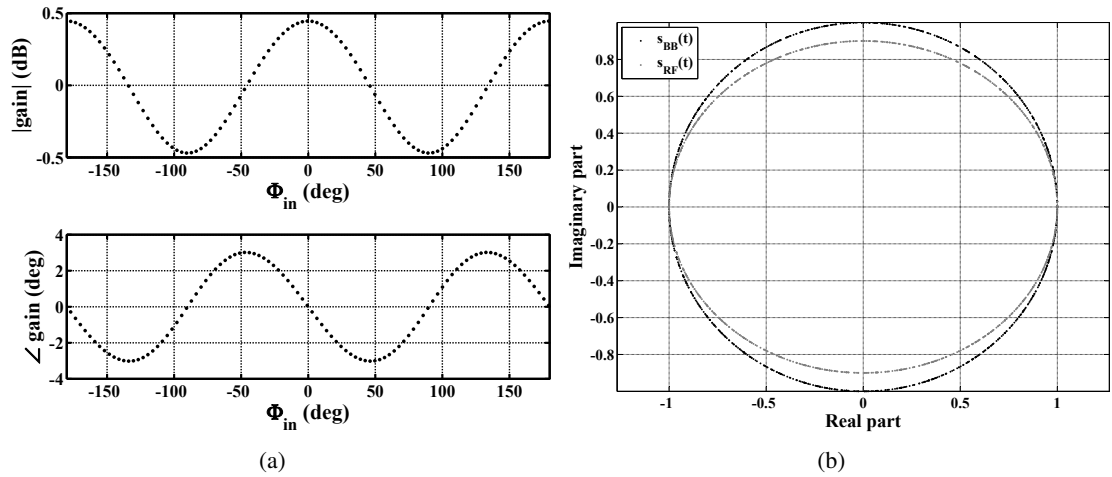
Figure 3.3: (a) PM-AM and PM-PM conversion caused by a two-tone with tone frequencies symmetrical to DC. (b) I/Q plot due to gain imbalance between the baseband channels for a single-tone excitation.
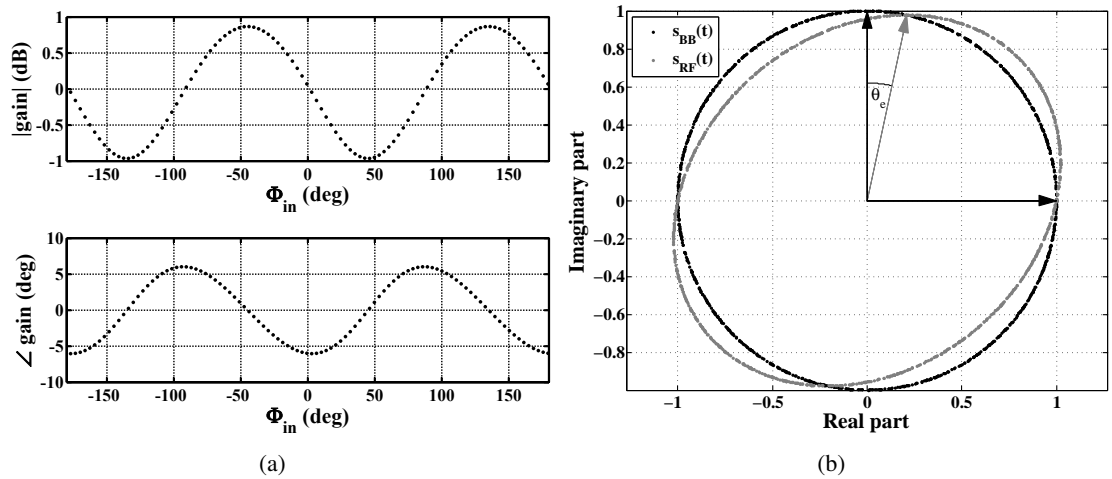
Figure 3.4: (a) PM-AM and PM-PM conversion for a two-tone with tone frequencies symmetrical to DC and (b) I/Q plot deformation caused by a static phase imbalance (single-tone excitation).

The presentation above covers only frequency independent imbalance effects. In case of a single-tone input signals no difference to the frequency dependent version exists. In this case the single-tone excitation samples the dynamic behavior at the actual tone frequency.

For a two-tone signal the above results are also directly applicable if the tone spacing is sufficiently small and the dynamic effects introduced by the lowpass filters $h_{\mathrm{LP},I}$ and $h_{\mathrm{LP},Q}$ can be approximated by their static correspondent. If this simplification cannot be applied two different constants $\alpha_d(\omega_1), \alpha_d(\omega_2)$ and $\alpha_v(\omega_1), \alpha_v(\omega_2)$ have to be used. Despite the increased complexity of the mean gain calculation the beforehand derived conclusions on the input phase dependency still apply.

3.2.3 Nonlinear static gain

For the evaluation of the input phase impact on the mean gain for a static nonlinear transmitter only the two baseband nonlinearities $g_I(\,\cdot\,), g_Q(\,\cdot\,)$ are considered. The passband nonlinearities $\tilde{g}_{\mathrm{M}}$ and $\tilde{g}_{\mathrm{RF}}$ introduce only AM-AM and AM-PM conversion and are, therefore, treated as linear. In the following both nonlinearities are approximated by $\mathrm{n^{th}}$-order polynomials. Therefore, the response of the two frequency independent nonlinearities is given by:

$$s_{\mathrm{RF,NL}}(t) = g_{\mathrm{RF}}g_{\mathrm{M}}e^{j\varphi_{\mathrm{LO},0}}\left(\sum_{k=0}^{N} g_{I,k}\mathrm{Re}\{s_{\mathrm{BB}}(t)\}^k + je^{j\theta_e}\sum_{k=0}^{N} g_{Q,k}\mathrm{Im}\{s_{\mathrm{BB}}(t)\}^k\right) \quad (3.31)$$

This expression includes the DC-offset and the linear part which are already treated in the sections above. In a next step the expressions for $\mathrm{Re}\{s_{\mathrm{BB}}(t)\}^k$ and $\mathrm{Im}\{s_{\mathrm{BB}}(t)\}^k$ are expanded and rearranged:

$$s_{\mathrm{RF,NL}}(t) = g_{\mathrm{Lin}}\left(g_{I,0} + jg_{Q,0}e^{j\theta_e} + \sum_{k=1}^{N}\sum_{l=0}^{k}\frac{1}{2^k}\left(g_{I,k} + (-1)^{k+l-1}j^{k-1}g_{Q,k}e^{j\theta_e}\right)\binom{k}{l}s_{\mathrm{BB}}^{k-l}(t)s_{\mathrm{BB}}^{*l}(t)\right)$$
$$(3.32)$$

where g_{Lin} summarizes $g_{\mathrm{RF}}g_{\mathrm{M}}e^{j\varphi_{\mathrm{LO},0}}$. The even- and odd-order distortion products, starting at $k = 2$ and $k = 3$, respectively, are given by:

$$s_{\mathrm{RF,NL,even}}(t) = g_{\mathrm{Lin}}\sum_{k=1}^{N_{\mathrm{E}}}\sum_{l=0}^{2k}\frac{1}{4^k}\left(g_{I,2k} + j(-1)^{k+l}g_{Q,2k}e^{j\theta_e}\right)\binom{2k}{l}s_{\mathrm{BB}}^{2k-l}(t)s_{\mathrm{BB}}^{*l}(t)$$

$$s_{\mathrm{RF,NL,odd}}(t) = g_{\mathrm{Lin}}\sum_{k=1}^{N_{\mathrm{O}}}\sum_{l=0}^{2k+1}\frac{1}{2^{2k+1}}\left(g_{I,2k+1} + (-1)^{k+l}g_{Q,2k+1}e^{j\theta_e}\right)\binom{2k+1}{l}s_{\mathrm{BB}}^{2k+1-l}(t)s_{\mathrm{BB}}^{*l}(t)$$
$$(3.33)$$

The upper summation limits N_{O} and N_{E} are derived for N as:

$$N_{\mathrm{O}} = \left\lfloor\frac{N+1}{2}\right\rfloor \qquad N_{\mathrm{E}} = \left\lfloor\frac{N}{2}\right\rfloor \quad (3.34)$$

where $\lfloor\,\cdot\,\rfloor$ provides the greatest integer less or equal to the enclosed value.

In (3.33) the even order distortion is composed of a summation of products, each one showing the structure $s_{\mathrm{BB}}^{n_1}(t)s_{\mathrm{BB}}^{*n_2}(t)$, $n_1, n_2 \in \mathbb{N}_0$, $n_1 + n_2 = 2k$. To highlight the input phase dependency of the even-order distortion it is sufficient to analyze the contribution due to $s_{\mathrm{BB}}^{n_1}(t)s_{\mathrm{BB}}^{*n_2}(t)$ for n_1, n_2 fulfilling

the above requirements. In a similar way also the input phase dependency of the odd-order distortion is demonstrated by evaluating the contributions structured as $s_{\text{BB}}^{n_1+1}(t)s_{\text{BB}}^{*n_2}(t)$ and $s_{\text{BB}}^{n_1}(t)s_{\text{BB}}^{*(n_2+1)}(t)$ under the same requirements for n_1, n_2. This task will be performed in the following two sections.

3.2.3.1 Even-order distortion products

The contribution to the transmitter gain based on the even-order distortion results to (neglecting the associated scaling factors):

$$G_{\text{part},2k} = s_{\text{BB}}^{n_1}(t)s_{\text{BB}}^{*n_2}(t)s_{\text{BB}}^{-1}(t) \tag{3.35}$$

provided that $n_1, n_2 \in \mathbb{N}_0$, $n_1 + n_2 = 2k$. For a single-tone input signal the mean gain is given by:

$$\bar{G}_{\text{part},2k} = \frac{2\pi}{\omega_1} \int\limits_0^{2\pi/\omega_1} A_{\text{ST}}^{(n_1-n_2-1)} e^{j(n_1-n_2-1)(\omega_1 t+\varphi_1)} dt = 0 \tag{3.36}$$

Clearly, for all valid combinations of n_1, n_2 the result of the integration diminishes. In case of a two-tone signal the gain contribution is given by:

$$\bar{G}_{\text{part},2k} = \frac{1}{T} 2^{(n_1-n_2-1)} A_{\text{TT}}^{(n_1-n_2-1)}$$
$$\cdot \int\limits_0^T e^{j\frac{n_1-n_2-1}{2}[(\omega_1+\omega_2)t+\varphi_1+\varphi_2]} \cos^{(n_1-n_2-1)}\left(\frac{1}{2}[(\omega_1+\omega_2)t+\varphi_1+\varphi_2]\right) dt \tag{3.37}$$

In case of an incommensurable two-tone excitation the integration can only lead to a nonzero result if $n_2 = n_1 - 1$ and, therefore, the complex exponential function disappears. As this condition violates the prerequisite $n_1 + n_2 = 2k$ no input phase dependency can be recognized. The same argumentation is also valid for the commensurable two-tone case.

For a DC-symmetrical two-tone input signal (3.37) simplifies to:

$$\bar{G}_{\text{part},2k} = \frac{\omega_1}{2\pi} 2^{(n_1-n_2-1)} A_{\text{TT}}^{(n_1-n_2-1)} e^{j\frac{n_1-n_2-1}{2}(\varphi_1+\varphi_2)}$$
$$\cdot \int\limits_0^{2\pi/\omega_1} \cos^{(n_1-n_2-1)}\left(\omega_1 t+\frac{1}{2}[\varphi_1+\varphi_2]\right) dt \tag{3.38}$$

Here, based on the defaults for the indices, the powers of the cosine function $n_1 - n_2 - 1$ can only be of odd order and greater or equal to zero. Therefore, the integration will lead to a zero result for all valid combinations of n_1, n_2.

This evaluation showed that the even-order distortion products do not generate PM-AM or PM-PM conversion effects for all considered input signal types.

3.2.3.2 Odd-order distortion products

The two types of products contributing to the transmitter gain based on the odd-order distortion are:

$$G_{\text{part},2k-1,1} = s_{\text{BB}}^{n_1+1}(t)s_{\text{BB}}^{*n_2}(t)s_{\text{BB}}^{-1}(t)$$
$$G_{\text{part},2k-1,2} = s_{\text{BB}}^{n_1}(t)\left(s_{\text{BB}}^*(t)\right)^{(n_2+1)} s_{\text{BB}}^{-1}(t) \tag{3.39}$$

In case of a single-tone input signal the mean gain results to:

$$\bar{G}_{\text{part},2k-1,r} = \frac{2\pi}{\omega_1} A_{\text{ST}}^{(n_1+n_2)} \int\limits_0^{2\pi/\omega_1} e^{j[n_1-n_2-2(r-1)](\omega_1 t+\varphi_1)} dt \tag{3.40}$$

where $r = 1$ at type 1 and $r = 2$ at type 2. Considering $\bar{G}_{\text{part},2k-1,1}$ a nonzero integration result is derived in case $n_2 = n_1$. For all other valid combinations of n_1, n_2 the mean gain is zero. In case of $\bar{G}_{\text{part},2k-1,2}$ a nonzero integration result is found for $n_2 = n_1 - 2$. For both types of odd-order distortion products no phase dependent effects were recognizable for a single-tone input signal.

Providing a two-tone excitation at the input of the transmitter the corresponding mean gains are given by:

$$\bar{G}_{\text{part},2k-1,r} = \frac{(2A_{\text{TT}})^{(n_1+n_2)}}{T} \int\limits_0^T e^{j\frac{n_1-n_2-2(r-1)[(\omega_1+\omega_2)t+\varphi_1+\varphi_2]}{2}} \cos^{n_1+n_2}\left(\frac{1}{2}[(\omega_1-\omega_2)t+\varphi_1-\varphi_2]\right) dt \tag{3.41}$$

For an incommensurable or a commensurable two-tone excitation the two integrations will show a nonzero result if the complex exponential function cancels. The corresponding combination of the indices is the same as for the single-tone input signal. In these cases the mean gain results to:

$$\bar{G}_{\text{part},2k-1} = \binom{n_1+n_2}{(n_1+n_2)/2} A_{\text{TT}}^{(n_1+n_2)} \begin{cases} \text{type1} : n_2 = n_1 \\ \text{type2} : n_2 = n_1 - 2 \end{cases} \tag{3.42}$$

This evaluation proves the independency of the mean gain from the tone phases for the incommensurable and the commensurable two-tone. Applying a DC-symmetrical two-tone at the transmitter input the mean gain expressions change to:

$$\bar{G}_{\text{part},2k-1,r} = \frac{2\pi\,(2A_{\text{TT}})^{(n_1+n_2)}\,e^{j\frac{n_1-n_2-2(r-1)}{2}(\varphi_1+\varphi_2)}}{\omega_1} \int\limits_0^{2\pi/\omega_1} \cos^{n_1+n_2}\left(\omega_1 t + \frac{1}{2}[\varphi_1-\varphi_2]\right) dt \tag{3.43}$$

These integrations result in an input phase independent factor for the indices combinations summarized in (3.42). For all other combinations of n_1, n_2 PM-AM and PM-PM distortion effects are generated:

$$\bar{G}_{\text{part},2k-1,r} = \binom{n_1+n_2}{(n_1+n_2)/2} A_{\text{TT}}^{(n_1+n_2)} e^{j\frac{n_1-n_2-2(r-1)}{2}(\varphi_1+\varphi_2)} \tag{3.44}$$

If the parameter n_1 and n_2 are traced back to the indices k, l used in (3.34) the powers of the tone magnitude A_{TT} and the complex exponential function simplify to:

$$\begin{aligned} \text{type1} &: n_1 + n_2 = 2k, \quad n_1 - n_2 = 2(k-l) \\ \text{type2} &: n_1 + n_2 = 2k, \quad n_1 - n_2 - 2 = 2(l+1) \end{aligned} \tag{3.45}$$

By combining these results with (3.25), (3.30) and (3.32) the mean transmitter gain for a DC-symmetrical two-tone input is given by:

$$
\begin{aligned}
\bar{G}_{\text{RF}} = g_{\text{Lin}} \Big(&\tfrac{1}{2} \left(g_{I,1} + g_{Q,1} e^{j\theta_e} \right) + \tfrac{1}{2} \left(g_{I,1} - g_{Q,1} e^{j\theta_e} \right) e^{-j(\varphi_1 + \varphi_2)} \\
&+ \sum_{k=1}^{N_{\text{O}}} \sum_{l=0}^{k-1} \tfrac{1}{2^{2k+1}} \left(g_{I,2k+1} + (-1)^{k+l} g_{Q,2k+1} e^{j\theta_e} \right) \binom{2k+1}{l} \binom{2k}{k} A_{\text{TT}}^{2k} e^{j(k-l)(\varphi_1 + \varphi_2)} \\
&+ \sum_{k=1}^{N_{\text{O}}} \sum_{l=0}^{k} \tfrac{1}{2^{2k+1}} \left(g_{I,2k+1} - (-1)^{l} g_{Q,2k+1} e^{j\theta_e} \right) \binom{2k+1}{l} \binom{2k}{k} A_{\text{TT}}^{2k} e^{-j(l+1)(\varphi_1 + \varphi_2)} \Big)
\end{aligned}
\tag{3.46}
$$

The first line of this expression summarizes the impact of the DC-offset and the static imbalance. The other two lines represent the odd-order distortion impact. It should be noted that a perfectly balanced transmitter would cancel the input phase dependency of the magnitude and phase imbalance but not of the odd-order distortion. As soon as odd-order harmonic components are present PM-AM and PM-PM distortion effects are generated. As mentioned before in the linear case the ISR controls the impact of the input phase dependency. At the nonlinear distortion the corresponding coefficients and the input signal magnitude determine the effect.

The combined impact of imbalance and nonlinear effects is visualized in Figure 3.5. By the imbalance of the two branches an ISR of $-25\,\text{dB}$ is generated. The BB amplifiers introduce $0.6\,\text{dB}$ gain compression. Due to the presence of nonlinear distortion the magnitude of the gain variation increased by 12% compared to the magnitude imbalance presented in Figure 3.3.
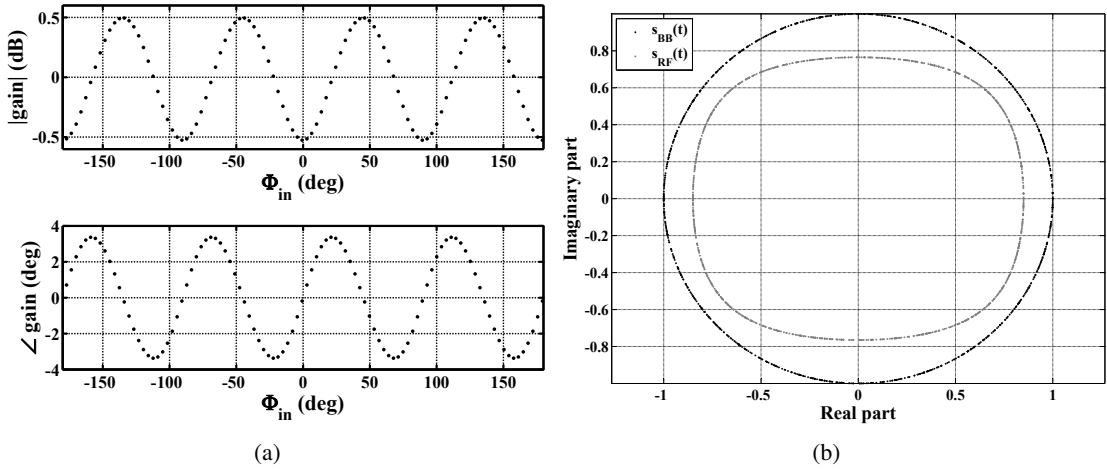
Figure 3.5: (a) PM-AM and PM-PM conversion excited by a DC symmetrical two-tone and (b) distortion for a single-tone input shown in the I/Q plot caused by the nonlinear baseband amplifiers.

3.3 Nonlinear I/Q modulator model

The modeling of the transmitter system presented up to now covered a general description of the transmitter without introducing specific models for the amplifiers. In this section the nonlinear characteristics of the baseband amplifiers are introduced. In a simple approximation the behavior of these amplifiers

could be described by truncated Taylor series. Such frequency independent models fail of expressing the rise of the generated distortion with increasing frequency as it is typically recognized at operational amplifiers (OpAmps). For properly describing this effect a frequency dependent "coefficient" has to be provided for each nonlinear order. The resulting model, able of generating intermodulation and harmonic distortion, is composed of several branches. Each branch consists of a linear filter followed by a nonlinear element (exemplified for the inphase branch):

$$g_I\big(s_{\text{LP},I}(t)\big) = g_{I,0} + \sum_{p=1}^{P} \big(g_{I,p}(t) * h_{\text{LP},I}(t) * s_{\text{BB},I}(t)\big)^p \tag{3.47}$$

where $g_{I,0}$ specifies the DC-offset of the amplifier and $g_{I,p}(t)$ represents the pth-order frequency dependent nonlinear coefficient. This model presents a simplified version of a parallel cascade Wiener model (PCWM) [84, 85].

As each function $g_{I,p}(t)$ is convolved with the transfer characteristic of the lowpass filter (3.47) this series connection can be abbreviated as:

$$\begin{aligned} h_{I,p}(t) &= g_{I,p}(t) * h_{\text{LP},I}(t) \\ s_{I,p}(t) &= h_{I,p}(t) * s_{\text{BB},I}(t) \\ g_I\big(s_{\text{LP},I}(t)\big) &= g_{I,0} + \sum_{p=1}^{P} s_{I,p}(t)^p \end{aligned} \tag{3.48}$$

The same type of model applies for the quadrature amplifier by changing the index I to Q.

The behavior of the mixer output nonlinearity will be represented by a complex-valued polynomial. This description is justifiable as long as the output matching network of the device is broadband compared to the modulator output signal bandwidth. The impact of the mixers' input matching network and its nonlinear effect are not explicitly added to the model. Their influence on the system performance will be incorporated into the PCWM of the baseband amplifiers.

The resulting I/Q-modulator model shows a parallel Wiener structure. Even if this type of structure could represent nonlinear dynamic effects, it depends on the applied parameter fitting procedure if nonlinear dynamic effects are describable. Considering that the baseband amplifiers together with the mixer nonlinearities are typically operated in the linear regime, justifies a weakly nonlinear description.

By truncating the PCWM after the 3rd-order, the complex baseband mixer input signal results to:

$$s_{\text{Amp}}(t) = g_{I,0} + jg_{Q,0} + s_{I,1}(t) + js_{Q,1}(t) + s_{I,2}^2(t) + js_{Q,2}^2(t) + s_{I,3}^3(t) + js_{Q,3}^3(t) \tag{3.49}$$

For highlighting the nonlinear distortion generated by the baseband amplifiers (3.49) is analyzed for the memoryless case. In the following all frequency independent results will be indicated by a "$\bar{}$" placed above the corresponding symbol. Hence, the frequency independent coefficient of the pth-order branch is noted as $\bar{h}_{I,p} = h_{I,p}(\omega_m)$. Using this simplification, the mixer input signal is given by:

$$\begin{aligned} \bar{s}_{\text{Amp}}(t) &= g_{I,0} + jg_{Q,0} + \tfrac{1}{2}(\bar{h}_{I,1} + \bar{h}_{Q,1})s_{\text{BB}}(t) + \tfrac{1}{2}(\bar{h}_{I,1} - \bar{h}_{Q,1})s_{\text{BB}}^*(t) \\ &\quad + \tfrac{1}{2}(\bar{h}_{I,2}^2 + j\bar{h}_{Q,2}^2)\big|s_{\text{BB}}(t)\big|^2 + \tfrac{1}{2}(\bar{h}_{I,2}^2 - j\bar{h}_{Q,2}^2)\,\text{Re}\big\{s_{\text{BB}}^2(t)\big\} \\ &\quad + \tfrac{1}{8}(\bar{h}_{I,3}^3 + \bar{h}_{Q,3}^3)\Big(s_{\text{BB}}^{*3}(t) + 3\big|s_{\text{BB}}(t)\big|^2 s_{\text{BB}}(t)\Big) \\ &\quad + \tfrac{1}{8}(\bar{h}_{I,3}^3 - \bar{h}_{Q,3}^3)\Big(s_{\text{BB}}^3(t) + 3\big|s_{\text{BB}}(t)\big|^2 s_{\text{BB}}^*(t)\Big) \end{aligned} \tag{3.50}$$

 The DC-offset and the linear response are given in a way similar to (3.5) and (3.6). The factor $\bar{h}_{I,1} + \bar{h}_{Q,1}$ specifies the scaling of the desired signal while $\bar{h}_{I,1} - \bar{h}_{Q,1}$ represents the coefficient for the spectrally mirrored signal. At the 3rd-order distortion the scaling coefficients $\bar{h}_{I,3}^3 + \bar{h}_{Q,3}^3$ identify the contribution present in the imbalance free case. This distortion product is composed of a complex baseband equivalent third-order distortion term $|s_{\text{BB}}(t)|^2 s_{\text{BB}}(t)$ [86] and a product $s_{\text{BB}}^{*3}(t)$ which introduces the harmonics generated by the BB amplifiers. The 3rd-order distortion components introduced by the imbalance of the BB branches is associated with the factor $\bar{h}_{I,3}^3 - \bar{h}_{Q,3}^3$.

At the second order distortion product two complex-valued scaling factors, $\bar{h}_{I,2}^2 + j\bar{h}_{Q,2}^2$ and its complex conjugate, can be recognized. Assuming that both amplifiers have a similar magnitude for the 2nd-order distortion, these two coefficients show an angle of approximately $\pm 45°$.

For visualizing the impact of the nonlinear baseband amplifiers in the frequency domain the following definitions are useful:

$$
\begin{aligned}
S_1(j\omega) &= \tfrac{1}{2}(\bar{h}_{I,1} + \bar{h}_{Q,1})S_{\text{BB}}(j\omega) + \tfrac{1}{2}(\bar{h}_{I,1} - \bar{h}_{Q,1})S_{\text{BB}}^*(-j\omega) \\
S_{2,1}(j\omega) &= \tfrac{1}{2\pi}S_{\text{BB}}(j\omega) * S_{\text{BB}}^*(-j\omega) \\
S_{2,2}(j\omega) &= \tfrac{1}{2\pi}\left[S_{\text{BB}}(j\omega) * S_{\text{BB}}(j\omega) + S_{\text{BB}}^*(-j\omega) * S_{\text{BB}}^*(-j\omega)\right] \\
S_{3,1}(j\omega) &= \tfrac{1}{4\pi^2}S_{\text{BB}}^*(-j\omega) * S_{\text{BB}}^*(-j\omega) * S_{\text{BB}}^*(-j\omega) \\
S_{3,2}(j\omega) &= \tfrac{1}{4\pi^2}S_{\text{BB}}(j\omega) * S_{\text{BB}}(j\omega) * S_{\text{BB}}^*(-j\omega)
\end{aligned}
\tag{3.51}
$$

 A simulation of the behavior of the baseband amplifiers was performed, for a single-tone input signal, based on the following parameters:

Input signal: Single-tone at $\text{f}_m/\text{f}_s = 0.1$ with a magnitude corresponding to $0\,\text{dBm}$ input power.

Lowpass filter: $\epsilon = 2\%$

Baseband amplifiers: $g_{I,0} = 0.005$; $\bar{g}_{I,1} = 1.0$; $\bar{g}_{I,2} = 0.04$; $\bar{g}_{I,3} = -0.16$. Both amplifiers were simulated using the same parameters.

These parameters correspond to a typical transmitter performance providing $30\,\text{dB}$ suppression of the residual carrier and a second and third-order distortion approx. $45\,\text{dB}$ below the carrier. The intermodulation and harmonic distortion levels are equivalent to an $\text{IP}_{2,\text{output}}$ of $44\,\text{dBm}$ and an $\text{IP}_{3,\text{output}}$ of $24\,\text{dBm}$.

The linear amplifier response $S_1(j\omega)$ and the complete output signal $S_{\text{Amp}}(j\omega)$ are presented in Figure 3.6. By setting $\bar{g}_{I,1} = \bar{g}_{Q,1} = 1.0$ the signal $S_1(j\omega)$ corresponds also to the baseband amplifier input signal. The second input tone located at $-\text{f}_m$ was caused by the imbalance of the lowpass filters. As the same parameter set was used for simulating both amplifiers the spectrally mirrored signal components at the linear and third-order product vanish.

The second- and third-order distortions contributing to the output signal are shown in Figure 3.7. Here the coefficients k_1 to k_4 identify the scaling factors introduced in front of the corresponding distortion terms in (3.50). The two second order distortion spectra are visible in Figure 3.7(a). The output of $k_1|s_{\text{BB}}(t)|^2$ (circular markers) has a dominating DC-component while the spectra generated by $k_2\text{Re}\{s_{\text{BB}}^2(t)\}$ (squared markers) mainly contribute to the distortion at $\pm 2\text{f}_m$. The sum of these two terms results again in an even distortion spectrum.

The harmonic distortion generated by the third-order nonlinearity is identified by the circular markers in Figure 3.7(b). The strongest harmonic distortion caused by the input signal at f_m is found at $-3f_m$ at the amplifiers' output. The harmonic contribution generated by the input tone at $-f_m$ has a power of approx. $-135\,\text{dBm}$ and is not displayed in this plot. Due to the second input tone also intermodulation distortion is generated.
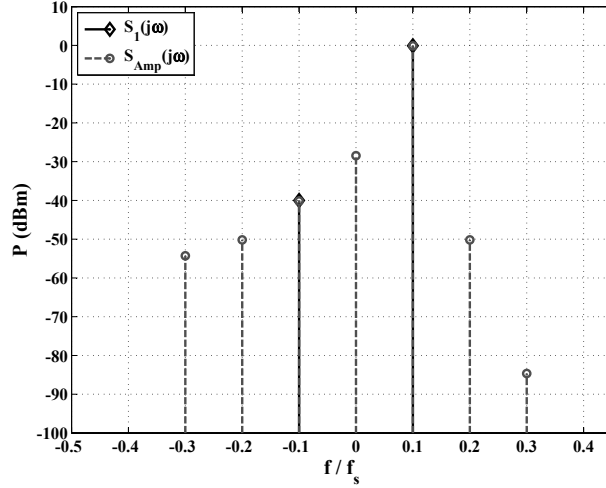
Figure 3.6: Input signal to and output signal from the baseband amplifier as modeled by (3.50).

(a)	(b)
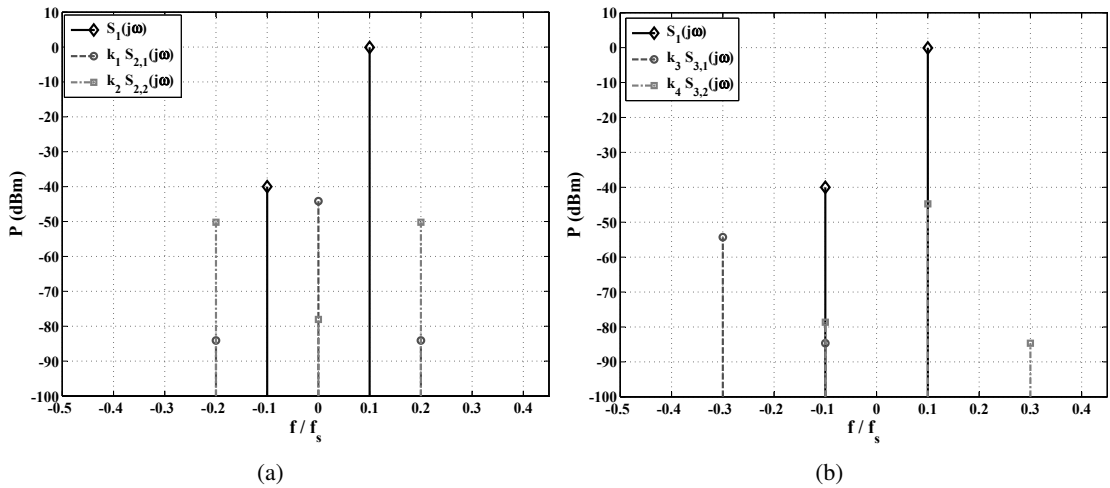
Figure 3.7: (a) Second-order and (b) third-order distortion product contributing to the baseband amplifier output signal as presented in Figure 3.6.

The extension of the result presented in (3.50) for the frequency dependent case is straightforward. The only problem is that the compactness of the notation is lost for the second- and third-order distortion products. For expressing the powers of the filtered input signal in closed form connoted of specifying

the corresponding parts of a Volterra series [87, 84]:

$$
\begin{aligned}
s_{\mathrm{Amp}}(t) =\ & g_{I,0} + j g_{Q,0} \\
& + \tfrac{1}{2} \int_{-\infty}^{\infty} \big[h_{I,1}(\tau_1) + h_{Q,1}(\tau_1) \big] s_{\mathrm{BB}}(t - \tau_1) d\tau_1 \\
& + \tfrac{1}{2} \int_{-\infty}^{\infty} \big[h_{I,1}(\tau_1) - h_{Q,1}(\tau_1) \big] s_{\mathrm{BB}}^*(t - \tau_1) d\tau_1 \\
& + \tfrac{1}{2} \int_{-\infty}^{\infty} \int_{-\infty}^{\infty} \big[h_{I,2}(\tau_1) h_{I,2}(\tau_2) - j h_{Q,2}(\tau_1) h_{Q,2}(\tau_2) \big] \mathrm{Re}\big\{ s_{\mathrm{BB}}(t-\tau_1) s_{\mathrm{BB}}(t-\tau_2) \big\} d\tau_1 d\tau_2 \\
& + \tfrac{1}{2} \int_{-\infty}^{\infty} \int_{-\infty}^{\infty} \big[h_{I,2}(\tau_1) h_{I,2}(\tau_2) + j h_{Q,2}(\tau_1) h_{Q,2}(\tau_2) \big] s_{\mathrm{BB}}(t-\tau_1) s_{\mathrm{BB}}^*(t-\tau_2) d\tau_1 d\tau_2 \\
& + \tfrac{1}{8} \int_{-\infty}^{\infty} \int_{-\infty}^{\infty} \int_{-\infty}^{\infty} \big[h_{I,3}(\tau_1) h_{I,3}(\tau_2) h_{I,3}(\tau_3) + h_{Q,3}(\tau_1) h_{Q,3}(\tau_2) h_{Q,3}(\tau_3) \big] \\
& \qquad \cdot s_{\mathrm{BB}}^*(t-\tau_1) s_{\mathrm{BB}}^*(t-\tau_2) s_{\mathrm{BB}}^*(t-\tau_3) d\tau_1 d\tau_2 d\tau_3 \\
& + \tfrac{3}{8} \int_{-\infty}^{\infty} \int_{-\infty}^{\infty} \int_{-\infty}^{\infty} \big[h_{I,3}(\tau_1) h_{I,3}(\tau_2) h_{I,3}(\tau_3) + h_{Q,3}(\tau_1) h_{Q,3}(\tau_2) h_{Q,3}(\tau_3) \big] \\
& \qquad \cdot s_{\mathrm{BB}}(t-\tau_1) s_{\mathrm{BB}}(t-\tau_2) s_{\mathrm{BB}}^*(t-\tau_3) d\tau_1 d\tau_2 d\tau_3 \\
& + \tfrac{1}{8} \int_{-\infty}^{\infty} \int_{-\infty}^{\infty} \int_{-\infty}^{\infty} \big[h_{I,3}(\tau_1) h_{I,3}(\tau_2) h_{I,3}(\tau_3) - h_{Q,3}(\tau_1) h_{Q,3}(\tau_2) h_{Q,3}(\tau_3) \big] \\
& \qquad \cdot s_{\mathrm{BB}}(t-\tau_1) s_{\mathrm{BB}}(t-\tau_2) s_{\mathrm{BB}}(t-\tau_3) d\tau_1 d\tau_2 d\tau_3 \\
& + \tfrac{3}{8} \int_{-\infty}^{\infty} \int_{-\infty}^{\infty} \int_{-\infty}^{\infty} \big[h_{I,3}(\tau_1) h_{I,3}(\tau_2) h_{I,3}(\tau_3) - h_{Q,3}(\tau_1) h_{Q,3}(\tau_2) h_{Q,3}(\tau_3) \big] \\
& \qquad \cdot s_{\mathrm{BB}}(t-\tau_1) s_{\mathrm{BB}}^*(t-\tau_2) s_{\mathrm{BB}}^*(t-\tau_3) d\tau_1 d\tau_2 d\tau_3
\end{aligned}
\tag{3.52}
$$

Clearly, the 4. and 5. line of this equation present the two second-order distortion components (NL terms $\mathrm{Re}\big\{ s_{\mathrm{BB}}(t - \tau_1) s_{\mathrm{BB}}(t - \tau_2) \big\}$, $s_{\mathrm{BB}}(t - \tau_1) s_{\mathrm{BB}}^*(t - \tau_2)$). The corresponding Volterra kernels $\tfrac{1}{2}(h_{I,2}(\tau_1) h_{I,2}(\tau_2) + j h_{Q,2}(\tau_1) h_{Q,2}(\tau_2))$ and $\tfrac{1}{2}(h_{I,2}(\tau_1) h_{I,2}(\tau_2) - j h_{Q,2}(\tau_1) h_{Q,2}(\tau_2))$ are symmetric [87]. This is also true for the third-order distortion presented in the last four lines of (3.52). For a complete suppression of the effects introduced by imbalance the filters $h_{I,1}(\tau)$, $h_{Q,1}(\tau)$ and $h_{I,3}(\tau)$, $h_{Q,3}(\tau)$ must be equal over the full time duration.

During the upconversion the mixer input signal is spread by the carrier phase noise. Additional copies of the BB amplifier output signal are generated by the spurious emissions. For limiting the complexity of the resulting transmitter model the impact of the spurs on the nonlinear BB amplifier distortion is neglected. For simplifying the notation the carrier phase noise $\varphi_{\mathrm{PH},0}(t)$ and phase shift $\varphi_{\mathrm{LO},0}$ will be abbreviated by $\varphi_{\mathrm{PH}}(t)$, φ_{LO}. Based on these simplifications, the linear and second-order parts of the input signal to the mixer output nonlinearity $s_{\mathrm{BP}}(t)$ results to:

$$
\begin{aligned}
s_{\mathrm{BP}}(t) \approx\ & s_{\mathrm{BP},0}(t) + s_{\mathrm{BP},1}(t) + s_{\mathrm{BP},2}(t) + s_{\mathrm{BP},3}(t) \\
s_{\mathrm{BP},0}(t) =\ & \sum_{k=0}^{N_{\mathrm{spur}}} e^{j(\Delta\omega_k t + \varphi_{\mathrm{PH},k}(t) + \varphi_{\mathrm{LO},k})} O_{\alpha_d,k} \\
s_{\mathrm{BP},1}(t) =\ & e^{j(\varphi_{\mathrm{PH}}(t) + \varphi_{\mathrm{LO}})} \big[\alpha_{d,1}(t) * s_{\mathrm{BB}}(t) + \alpha_{v,1}(t) * s_{\mathrm{BB}}^*(t) \big] \\
& + \sum_{k=1}^{N_{\mathrm{spur}}} e^{j(\Delta\omega_k t + \varphi_{\mathrm{PH},k}(t) + \varphi_{\mathrm{LO},k})} \big[\tfrac{1}{2} \big(g_{\mathrm{CI},k} h_{I,1}(t) + g_{\mathrm{CQ},k} h_{Q,1}(t) e^{j\theta_e} \big) * s_{\mathrm{BB}}(t) \\
& + \tfrac{1}{2} \big(g_{\mathrm{CI},k} h_{I,1}(t) - g_{\mathrm{CQ},k} h_{Q,1}(t) e^{j\theta_e} \big) * s_{\mathrm{BB}}^*(t) \big] \\
s_{\mathrm{BP},2}(t) =\ & e^{j(\varphi_{\mathrm{PH}}(t) + \varphi_{\mathrm{LO}})} \Big[\int_{-\infty}^{\infty} \int_{-\infty}^{\infty} 2\alpha_{d,2}(\tau_1, \tau_2) s_{\mathrm{BB}}(t-\tau_1) s_{\mathrm{BB}}^*(t-\tau_2) d\tau_1 d\tau_2 \\
& + \int_{-\infty}^{\infty} \int_{-\infty}^{\infty} 2\alpha_{v,2}(\tau_1, \tau_2) \mathrm{Re}\big\{ s_{\mathrm{BB}}(t-\tau_1) s_{\mathrm{BB}}(t-\tau_2) \big\} d\tau_1 d\tau_2 \Big]
\end{aligned}
\tag{3.53}
$$

In this equation the DC-offset $O_{\alpha_d,k}$ was defined in (3.6). For the linear response $s_{\mathrm{BP},1}(t)$ a distinction between the output signal generated by the carrier and those of the spurious emissions was made. The third-order nonlinear distortion product of $s_{\mathrm{BP}}(t)$ can be written as:

$$
\begin{aligned}
s_{\mathrm{BP},3}(t) \;=\; & e^{j(\varphi_{\mathrm{PH}}(t)+\varphi_{\mathrm{LO}})}\Big(\textstyle\int_{-\infty}^{\infty}\cdots\int_{-\infty}^{\infty} \alpha_{d,3}(\tau_1,\tau_2,\tau_3)\big[s_{\mathrm{BB}}^*(t-\tau_1)s_{\mathrm{BB}}^*(t-\tau_2)s_{\mathrm{BB}}^*(t-\tau_3) \\
& +3s_{\mathrm{BB}}(t-\tau_1)s_{\mathrm{BB}}(t-\tau_2)s_{\mathrm{BB}}^*(t-\tau_3)\big]d\tau_1 d\tau_2 d\tau_3 \\
& + \textstyle\int_{-\infty}^{\infty}\cdots\int_{-\infty}^{\infty} \alpha_{v,3}(\tau_1,\tau_2,\tau_3)\big[s_{\mathrm{BB}}(t-\tau_1)s_{\mathrm{BB}}(t-\tau_2)s_{\mathrm{BB}}(t-\tau_3) \\
& +3s_{\mathrm{BB}}(t-\tau_1)s_{\mathrm{BB}}^*(t-\tau_2)s_{\mathrm{BB}}^*(t-\tau_3)\big]d\tau_1 d\tau_2 d\tau_3 \Big)
\end{aligned}
$$

$$(3.54)$$

The filtering functions for the other output signal components are summarized in (3.55). This signal is then fed into the output nonlinearity of the mixer. The static nonlinear function of $g_{\mathrm{M}}(\cdot)$ is modeled as the first zone output of a third-order polynomial $g_{\mathrm{M}}(s_{\mathrm{BP}}(t)) = g_{\mathrm{M},1}s_{\mathrm{BP}}(t) + g_{\mathrm{M},3}s_{\mathrm{BP}}(t)|s_{\mathrm{BP}}(t)|^2$. The distortion products generated by passing the bandpass signal through the mixer output nonlinearity are summarized in (3.56). In this expression the distortion terms up to the 3rd power of the BB signal magnitude are included.

In this equation the different output signal components were sorted based on their nonlinear order. Most of the nonlinear output signal components resulting from $g_{\mathrm{M},3}s_{\mathrm{BP}}(t)|s_{\mathrm{BP}}(t)|^2$ are negligible assuming the I/Q modulator is operated in back-off. The evaluation of the important distortion contributors is influenced by the considered input signal as well as the parameters of the nonlinearities. To get a better insight in the interrelationships between the modulator parameters, the input signal type and the dominating distortion products, simulations were performed. The goal for these simulations was to find an approximation for (3.56) with reasonable accuracy using a low number of nonlinear terms.

$$
\begin{aligned}
\alpha_{d,1}(t) \;=\;& \tfrac{1}{2}\big(g_{\mathrm{CI},0}h_{I,1}(t) + g_{\mathrm{CQ},0}h_{Q,1}(t)e^{j\theta_e}\big) \\
\alpha_{v,1}(t) \;=\;& \tfrac{1}{2}\big(g_{\mathrm{CI},0}h_{I,1}(t) - g_{\mathrm{CQ},0}h_{Q,1}(t)e^{j\theta_e}\big) \\
\alpha_{d,2}(t_1,t_2) \;=\;& \tfrac{1}{4}\big(g_{\mathrm{CI},0}h_{I,2}(t_1)h_{I,2}(t_2) + jg_{\mathrm{CQ},0}h_{Q,2}(t_1)h_{Q,2}(t_2)e^{j\theta_e}\big) \\
\alpha_{v,2}(t_1,t_2) \;=\;& \tfrac{1}{4}\big(g_{\mathrm{CI},0}h_{I,2}(t_1)h_{I,2}(t_2) - jg_{\mathrm{CQ},0}h_{Q,2}(t_1)h_{Q,2}(t_2)e^{j\theta_e}\big) \\
\alpha_{d,3}(t_1,t_2,t_3) \;=\;& \tfrac{1}{8}\big(g_{\mathrm{CI},0}h_{I,3}(t_1)h_{I,3}(t_2)h_{I,3}(t_3) + g_{\mathrm{CQ},0}h_{Q,3}(t_1)h_{Q,3}(t_2)h_{Q,3}(t_3)e^{j\theta_e}\big) \\
\alpha_{v,3}(t_1,t_2,t_3) \;=\;& \tfrac{1}{8}\big(g_{\mathrm{CI},0}h_{I,3}(t_1)h_{I,3}(t_2)h_{I,3}(t_3) - g_{\mathrm{CQ},0}h_{Q,3}(t_1)h_{Q,3}(t_2)h_{Q,3}(t_3)e^{j\theta_e}\big)
\end{aligned}
$$

$$(3.55)$$

$$
\begin{aligned}
s_{\mathrm{mod}}(t) \;=\;& g_{\mathrm{M},1}s_{\mathrm{BP}}(t) + g_{\mathrm{M},3}s_{\mathrm{BP}}(t)|s_{\mathrm{BP}}(t)|^2 \\
=\;& g_{\mathrm{M},1}\big[s_{\mathrm{BP},0}(t) + s_{\mathrm{BP},1}(t) + s_{\mathrm{BP},2}(t) + s_{\mathrm{BP},3}(t)\big] \\
& +g_{\mathrm{M},3}\big[s_{\mathrm{BP},0}(t)|s_{\mathrm{BP},0}(t)|^2 + s_{\mathrm{BP},0}^2(t)s_{\mathrm{BP},1}^*(t) + 2|s_{\mathrm{BP},0}(t)|^2 s_{\mathrm{BP},1}(t) \\
& +2s_{\mathrm{BP},0}(t)|s_{\mathrm{BP},1}(t)|^2 + 2|s_{\mathrm{BP},0}(t)|^2 s_{\mathrm{BP},2}(t) + s_{\mathrm{BP},0}^2(t)s_{\mathrm{BP},2}^{*2}(t) \\
& +s_{\mathrm{BP},0}^*(t)s_{\mathrm{BP},1}^2(t) + s_{\mathrm{BP},1}(t)|s_{\mathrm{BP},1}(t)|^2 + s_{\mathrm{BP},0}^2(t)s_{\mathrm{BP},3}^*(t) \\
& +2s_{\mathrm{BP},0}(t)s_{\mathrm{BP},1}(t)s_{\mathrm{BP},2}^*(t) + 2s_{\mathrm{BP},0}(t)s_{\mathrm{BP},1}^*(t)s_{\mathrm{BP},2}(t) \\
& +2|s_{\mathrm{BP},0}(t)|^2 s_{\mathrm{BP},3}(t) + 2s_{\mathrm{BP},0}^*(t)s_{\mathrm{BP},1}(t)s_{\mathrm{BP},2}(t) + O\big(|s_{\mathrm{BB}}(t)|^4\big)\big]
\end{aligned}
$$

$$(3.56)$$

These tasks were performed using the same settings as applied for the results shown in Figures 3.6 and 3.7. Additionally to these parameters, a $3°$ phase error was assumed for the I/Q mixer. The coefficients of the mixer output nonlinearity were set to a gain of $0\,\mathrm{dB}$ and to the same IP_3 as used for the baseband amplifiers. Two different types of input signals, a single carrier and a two-tone signal with incommensurable frequencies were considered. These two test signal avoid any input phase dependent gain variations as presented in Section 3.2.

It turned out that for input signal power levels between -30 and $-20\,\mathrm{dB}$ below IP_3 the third-order distortion product $g_{\mathrm{M},3}s_{\mathrm{BP},1}(t)\big|s_{\mathrm{BP},1}(t)\big|^2$ is dominating the distortion term generated by the mixer output nonlinearity. Substituting (3.53) into this term results in ten different distortion terms:

$$
\begin{aligned}
s_{\mathrm{BP},1}(t)\big|s_{\mathrm{BP},1}(t)\big|^2 = {} & e^{j(\varphi_{\mathrm{PH}}(t)+\varphi_{\mathrm{LO}})}\Big[\\
& + \int_{-\infty}^{\infty}\int_{-\infty}^{\infty}\int_{-\infty}^{\infty}\big[\alpha_{d,1}(\tau_1)\alpha_{d,1}(\tau_2)\alpha_{d,1}^*(\tau_3) + 2\alpha_{d,1}(\tau_1)\alpha_{v,1}(\tau_2)\alpha_{v,1}^*(\tau_3)\big] \\
& \cdot s_{\mathrm{BB}}(t-\tau_1)s_{\mathrm{BB}}(t-\tau_2)s_{\mathrm{BB}}^*(t-\tau_3)d\tau_1 d\tau_2 d\tau_3 \\
& + \int_{-\infty}^{\infty}\int_{-\infty}^{\infty}\int_{-\infty}^{\infty}\big[\alpha_{v,1}(\tau_1)\alpha_{v,1}(\tau_2)\alpha_{v,1}^*(\tau_3) + 2\alpha_{d,1}(\tau_1)\alpha_{d,1}^*(\tau_2)\alpha_{v,1}(\tau_3)\big] \\
& \cdot s_{\mathrm{BB}}(t-\tau_1)s_{\mathrm{BB}}^*(t-\tau_2)s_{\mathrm{BB}}^*(t-\tau_3)d\tau_1 d\tau_2 d\tau_3 \\
& + \int_{-\infty}^{\infty}\int_{-\infty}^{\infty}\int_{-\infty}^{\infty}\alpha_{d,1}(\tau_1)\alpha_{d,1}(\tau_2)\alpha_{v,1}^*(\tau_3)s_{\mathrm{BB}}(t-\tau_1)s_{\mathrm{BB}}(t-\tau_2)s_{\mathrm{BB}}(t-\tau_3)d\tau_1 d\tau_2 d\tau_3 \\
& + \int_{-\infty}^{\infty}\int_{-\infty}^{\infty}\int_{-\infty}^{\infty}\alpha_{d,1}^*(\tau_1)\alpha_{v,1}(\tau_2)\alpha_{v,1}(\tau_3)s_{\mathrm{BB}}^*(t-\tau_1)s_{\mathrm{BB}}^*(t-\tau_2)s_{\mathrm{BB}}^*(t-\tau_3)d\tau_1 d\tau_2 d\tau_3 \Big]
\end{aligned}
\tag{3.57}
$$

From these components the term $\alpha_{d,1}(\tau_1)\alpha_{d,1}(\tau_2)\alpha_{d,1}^*(\tau_2)s_{\mathrm{BB}}(t-\tau_1)s_{\mathrm{BB}}(t-\tau_2)s_{\mathrm{BB}}^*(t-\tau_3)$ is the dominating one at $\mathrm{P}_{\mathrm{BB}} = 0\,\mathrm{dBm}$. This result is evident, as the desired signal is the dominating signal part throughout the whole transmitter structure. All components created by the linear and nonlinear distortion sources are significantly lower. Therefore, the distortion product caused by the interaction of this desired signal $\alpha_{d,1}(t)*s_{\mathrm{BB}}(t)$ is dominating the distortion spectrum of the mixer output nonlinearity. Using this approximation the resulting I/Q modulator output description is presented in (3.58).

Beside of the phase noise and the spurious emission, several differences between this expression and the baseband amplifier output signal (3.52) can be found. At the modulator output the first and third order scaling functions are now complex-valued, due to the phase imbalance of the I/Q mixer. An additional Volterra kernel was introduced by the mixer output nonlinearity. In contrast to the other kernels this one is not symmetric [87].

The error of this approximation for a two-tone power sweep is presented in Figure 3.8(a). At this simulation all parameters were selected as described above, only the magnitude imbalance was varied between 0.78 and 0.94. In this plot the ISR is used to quantify the resulting imbalance. A similar simulation was also performed for the phase imbalance. As only slight differences in the impact of both effects were recognizable only the magnitude imbalance dependent simulation is presented. This plot highlights the low dependency of the modeling accuracy on the imbalance. Even at high input power level the imbalance is correctly predicted. In Figure 3.8(b) the impact of odd and even order distortion is visualized. When operating in the modulator in the back-off, $10\,\mathrm{dB}$ below the $1\,\mathrm{dB}$ compression point, changing the IP_2 causes only slight impact on the performance of the model. At this input power level the approximation error varies between $-55\,\mathrm{dB}$ and $-52\,\mathrm{dB}$. At around $\mathrm{P}_{\mathrm{BB}} = 5\,\mathrm{dBm}$ the slope of the

error is increasing. This effect can be explained by the gain compression of the BB amplifiers. This gain compression causes a reduction of the mixer input signal magnitude.

$$
\begin{aligned}
s_{\mathrm{mod}}(t) \ \approx \ & g_{\mathrm{M},1}\Bigg(\sum_{k=0}^{N_{\mathrm{spur}}} e^{j(\Delta\omega_k t + \varphi_{\mathrm{PH},k}(t) + \varphi_{\mathrm{LO},k})} O_{\alpha_d,k} \\
& + e^{j(\varphi_{\mathrm{PH}}(t) + \varphi_{\mathrm{LO}})} \left[\alpha_{d,1}(t) * s_{\mathrm{BB}}(t) + \alpha_{v,1}(t) * s_{\mathrm{BB}}^*(t) \right] \\
& + \sum_{k=1}^{N_{\mathrm{spur}}} e^{j(\Delta\omega_k t + \varphi_{\mathrm{PH},k}(t) + \varphi_{\mathrm{LO},k})} \left[\tfrac{1}{2} \left(g_{\mathrm{CI},k} h_{I,1}(t) + g_{\mathrm{CQ},k} h_{Q,1}(t) e^{j\theta_e} \right) * s_{\mathrm{BB}}(t) \right. \\
& \left. + \tfrac{1}{2} \left(g_{\mathrm{CI},k} h_{I,1}(t) - g_{\mathrm{CQ},k} h_{Q,1}(t) e^{j\theta_e} \right) * s_{\mathrm{BB}}^*(t) \right] \Bigg) \\
& + g_{\mathrm{M},1} e^{j(\varphi_{\mathrm{PH}}(t) + \varphi_{\mathrm{LO}})} \Bigg(\\
& \int_{-\infty}^{\infty} \int_{-\infty}^{\infty} 2\alpha_{d,2}(\tau_1,\tau_2) s_{\mathrm{BB}}(t-\tau_1) s_{\mathrm{BB}}^*(t-\tau_2) d\tau_1 d\tau_2 \\
& + \int_{-\infty}^{\infty} \int_{-\infty}^{\infty} 2\alpha_{v,2}(\tau_1,\tau_2) \mathrm{Re}\left\{ s_{\mathrm{BB}}(t-\tau_1) s_{\mathrm{BB}}(t-\tau_2) \right\} d\tau_1 d\tau_2 \\
& + \int_{-\infty}^{\infty} \int_{-\infty}^{\infty} \int_{-\infty}^{\infty} \alpha_{d,3}(\tau_1,\tau_2,\tau_3) s_{\mathrm{BB}}^*(t-\tau_1) s_{\mathrm{BB}}^*(t-\tau_2) s_{\mathrm{BB}}^*(t-\tau_3) d\tau_1 d\tau_2 d\tau_3 \\
& + \int_{-\infty}^{\infty} \int_{-\infty}^{\infty} \int_{-\infty}^{\infty} \left[3\alpha_{d,3}(\tau_1,\tau_2,\tau_3) + \tfrac{g_{\mathrm{M},3}}{g_{\mathrm{M},1}} \alpha_{d,1}(\tau_1) \alpha_{d,1}(\tau_2) \alpha_{d,1}^*(\tau_3) \right] \\
& \cdot s_{\mathrm{BB}}(t-\tau_1) s_{\mathrm{BB}}(t-\tau_2) s_{\mathrm{BB}}^*(t-\tau_3) d\tau_1 d\tau_2 d\tau_3 \\
& + \int_{-\infty}^{\infty} \int_{-\infty}^{\infty} \int_{-\infty}^{\infty} \alpha_{v,3}(\tau_1,\tau_2,\tau_3) \big[s_{\mathrm{BB}}(t-\tau_1) s_{\mathrm{BB}}(t-\tau_2) s_{\mathrm{BB}}(t-\tau_3) \\
& + 3 s_{\mathrm{BB}}(t-\tau_1) s_{\mathrm{BB}}^*(t-\tau_2) s_{\mathrm{BB}}^*(t-\tau_3) \big] d\tau_1 d\tau_2 d\tau_3 \Bigg)
\end{aligned}
\tag{3.58}
$$
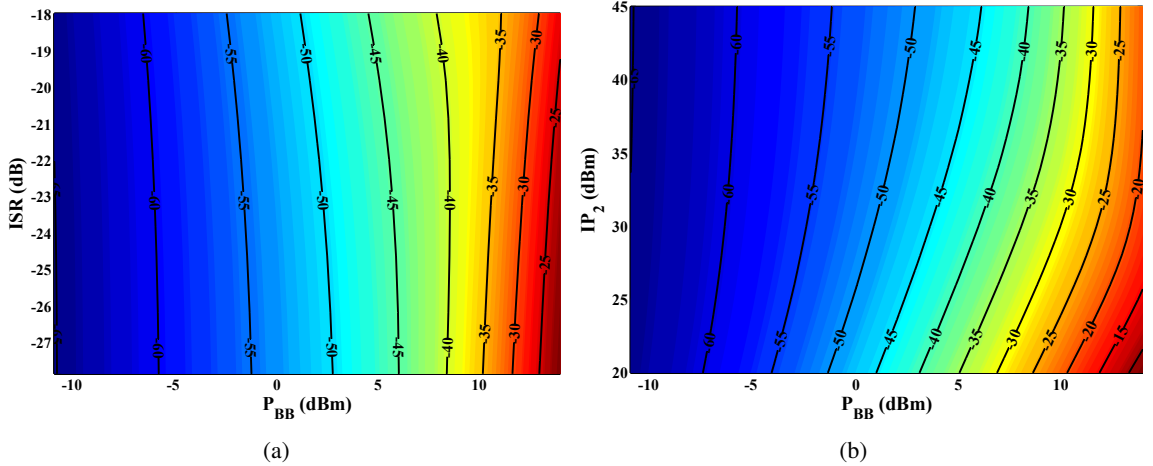
Figure 3.8: Mean square error surface plot of the full and the approximated modulator description. (a) Input power and magnitude imbalance sweep. In this plot the impact of the magnitude imbalance is quantified using the ISR (b) Input power and IP_2 sweep.

In this way, the rate of the distortion generation at the mixer output NL is lowered. By using the signal $\alpha_{d,1}(t) * s_{\mathrm{BB}}(t)$ as basis for the mixer output NL distortion calculation, this effect is not reflected by the approximation (3.58). By including further terms from (3.56) or (3.57) into (3.58) the average approximation error can be lowered. In this way the accuracy of the actual approximation can be improved for achieving the required performance.

The selected approximations neglect distortion products of fourth and higher orders. With increasing input power these distortion products gain importance. The accuracy of the approximation improves if the nonlinearities in the baseband are dominating the modulator performance. Based on the same simulation results important contributors to the fourth and fifth-order distortion generated by the $g_{\mathrm{M},3}s_{\mathrm{BP}}(t)|s_{\mathrm{BP}}(t)|^2$ nonlinearity are:

$$
\begin{aligned}
&\int_{-\infty}^{\infty} \cdots \int_{-\infty}^{\infty} 4g_{\mathrm{M},3}\Big[\alpha_{d,2}(\tau_1,\tau_2)\alpha_{d,1}(\tau_3)\alpha_{d,1}^*(\tau_4) + \alpha_{v,2}(\tau_1,\tau_2)\mathrm{Re}\left\{\alpha_{d,1}(\tau_3)\alpha_{v,1}^*(\tau_4)\right\}\Big] \\
&\cdot s_{\mathrm{BB}}(t-\tau_1)s_{\mathrm{BB}}(t-\tau_2)s_{\mathrm{BB}}^*(t-\tau_3)s_{\mathrm{BB}}^*(t-\tau_4)d\tau_1 d\tau_2 d\tau_3 d\tau_4 \\
&\int_{-\infty}^{\infty} \cdots \int_{-\infty}^{\infty} 4g_{\mathrm{M},3}\alpha_{d,1}(\tau_1)\alpha_{d,1}(\tau_2)\alpha_{v,2}(\tau_3,\tau_4)\mathrm{Re}\left\{s_{\mathrm{BB}}(t-\tau_1)s_{\mathrm{BB}}(t-\tau_2)\right\} \\
&\cdot s_{\mathrm{BB}}(t-\tau_3)s_{\mathrm{BB}}^*(t-\tau_4)d\tau_1 d\tau_2 d\tau_3 d\tau_4 \\
&\int_{-\infty}^{\infty} \cdots \int_{-\infty}^{\infty} 2g_{\mathrm{M},3}\alpha_{d,1}(\tau_1)\alpha_{d,1}^*(\tau_2)\alpha_{d,3}(\tau_3,\tau_4,\tau_5) \\
&\cdot\big[s_{\mathrm{BB}}(t-\tau_1)s_{\mathrm{BB}}^*(t-\tau_2)s_{\mathrm{BB}}^*(t-\tau_3)s_{\mathrm{BB}}^*(t-\tau_4)s_{\mathrm{BB}}^*(t-\tau_5) \\
&+3s_{\mathrm{BB}}(t-\tau_1)s_{\mathrm{BB}}(t-\tau_2)s_{\mathrm{BB}}(t-\tau_3)s_{\mathrm{BB}}^*(t-\tau_4)s_{\mathrm{BB}}^*(t-\tau_5)\big]d\tau_1 d\tau_2 d\tau_3 d\tau_4 d\tau_5
\end{aligned}
\tag{3.59}
$$

If the I/Q modulator is operated at very high back-off levels ($\mathrm{P}_{\mathrm{BB}} = -10\,\mathrm{dBm}$ the DC-offset is getting an important distortion product. Due to this fact, the following second order distortion factor cannot be neglected any more:

$$
\int_{-\infty}^{\infty}\int_{-\infty}^{\infty} g_{\mathrm{M},3}\big[2O_{\alpha_d}\alpha_{d,1}(\tau1)\alpha_{v,1}^*(\tau_2) + O_{\alpha_d}*\alpha_{d,1}(\tau_1)\alpha_{d,1}(\tau_2)\big]s_{\mathrm{BB}}(t-\tau_1)s_{\mathrm{BB}}(t-\tau_2)d\tau_1 d\tau_2 \tag{3.60}
$$

3.4 Characterization and compensation of the transmitter distortion

In the previous section models describing the imperfections of a transmitter were developed. These imperfections can have a significant impact on the performance of a communication system as analyzed in [88]. Based on the developed models the distortion effects are now characterized and this information is also used for compensating the undesired transmitter behavior. Several approaches for characterizing and compensating a direct conversion transmitter can be found in the literature. The compensation of the magnitude and phase imbalance by measuring the power of a single-tone signal at the transmitter output signals was suggested in [89]. Based on this idea a linear model of the transmitter and an adaptive compensation algorithm was published by Cavers *et al.* [76]. In this work the authors treated also the receiver branch by providing an adaptive algorithm for the compensation and an estimation of the impact of the imbalance errors on the transmission symbol error rate. The discussion of the combined compensation of the transmitter imbalance and the linearization of the following power amplifier is presented in [66]. Using a broadband input signal the authors suggested an adaptive algorithm which optimizes the imbalance compensator and the predistorter coefficients simultaneously.

The measurement of a direct conversion transmitter by a low-IF receiver was discussed in [90]. The downconverted transmitter output signal was used for characterizing and compensating the phase

response and the frequency dependent imbalance of the transmitter. Unfortunately, the authors did not mention if they considered a phase response characterization of the receiver system.

The time domain measurement system presented in [91] provided a full calibration of the linear effects of the transmitter and the receiver. The complete calibration procedure consisted of several steps and is not presented here in detail. One very interesting implementation of an I/Q demodulation should be sketched: The transmitter output signal was provided to a mixer for shifting this signal into a lower frequency range where it was captured by a microwave transition analyzer (MTA). A local oscillator (LO), phase-locked to the LO of the transmitter, was connected to the mixer via a phase-shifter. In a first step the inphase signal was recorded by the MTA, then the phase shifter was set to $90°$ phase shift and the quadrature signal was digitized. As this phase shift can be generated with very high accuracy, the consecutively performed I/Q demodulation is free of imbalances.

A time domain measurement setup able of capturing the complex envelopes of the incident and reflected power waves of a device under test (DUT) was discussed in [92]. Initially, the error coefficient matrix of the four-channel broadband receiver was identified using a SOLT calibration. By this approach the linear distortion effects of the receivers were characterized. The only information not provided by this calibration is the absolute phase of the incident power waves over the considered baseband bandwidth. For this characterization task a RF multi-sine generator with known phase relationship would be required. As such a phase calibration standard was not available a Rhode & Schwarz generator was used for providing a phase aligned multi-sine signal which was measured by the receivers. The small deviation from the linear slope of the phase was used as indication for the linear phase response of the four-channel receiver. After the calibration of the receiver branch a multi-sine signal was generated by the transmitter and was measured. These measurement results were used for compensating the imbalance of the transmitter.

Most approaches presented up to now focused on the characterization and compensation of the linear transmitter effects. A frequency independent nonlinear transmitter description was provided in [93, 94]. In this case the baseband amplifiers were modeled by two 5th-order polynomials. Their output is fed into an I/Q-mixer with phase imbalance. The mixer is connected to an amplifier with static nonlinear characteristic. The parameters of this model were extracted from measurement results of a two-tone signal generated by a direct conversion transmitter using optimizing algorithms. The output measurements of the transmitter were performed capturing the complex-envelope of this signal. Unfortunately, it was not mentioned which type of receiver was used for this purpose nor in which way it was calibrated.

A full nonlinear dynamic compensator used to linearize power amplifiers driven by an IQ-modulator with imbalance is discussed in [95]. The suggested compensator places a real-valued Volterra-series model in the inphase and quadrature branch. These models use the real and imaginary input signals to the transmitter to derive the signals fed into the modulator. The models are parameterized by measuring the transmitter response onto broadband excitation signals.

In contrast to the characterization and compensation procedures presented up to now in [96, 97] an iterative optimization of the output signal as used. In [96] the output of a transmitter is measured by a SA and additional frequency components are added to the input signal at the distortion frequencies for canceling their effects. Then the magnitudes and phases of these additional tones are altered until all distortion components are below a desired limit. Hence, it is possible to accomplish the desired magnitude response without any assumption on the transmitter structure. This advantage is achieved at the cost of an iterative algorithm which must be re-executed each time the signal, the carrier frequency, or the output power of the transmitter is changed.

The extension of this idea to the phase response of the transmitter was discussed in [97]. Again, using an iterative algorithm similar to the harmonic balance (HB) the authors were able of compensating deviations from the desired transmitter output signal by measuring it with a MTA. In this way the magnitude and phase response of the transmitter were corrected.

A full nonlinear dynamic compensator used to linearize power amplifiers driven by an IQ-modulator with imbalance is discussed in [95]. The suggested compensator places a real-valued Volterra-series model in the inphase and quadrature branch. These models use the real and imaginary input signals to the transmitter to derive the signals fed into the modulator. The models are parameterized by measuring the transmitter response onto broadband excitation signals. The disadvantage of this approach is introduced by the real-valued Volterra models. At these models the generated intermodulation distortion (IMD) and the corresponding odd order harmonics are directly related. As the IMD of the PA is the dominating source of distortion an overestimation of the odd order harmonic will occur. This harmonic distortion is usually generated in the baseband of the transmitter only. Its magnitude is significantly below the level of the PAs' IMD.

A novel concept for nonlinear dynamic direct conversion transmitter linearization is derived in [98]. The authors develop a parallel structure consisting of two memory polynomial models allowing identifying the imbalance distortion and the PA nonlinear dynamic behavior at once. A fully adaptive signal processing approach for the parameterization of the predistorter is presented.

Additionally to the I/Q imbalance and nonlinear distortion effects, carrier phase noise and spurious emissions cause performance degradation in transmitter systems [88, 99, 100]. Different noise sources, like flicker-of-phase (l/f), flicker-of-frequency (l/f^3), white phase (l/f^0), etc., are contributing to the phase noise of a carrier [101, 102]. The power spectral density of the phase noise and the generated spurious emissions depend on the selected oscillator or synthesizer design, respectively [103, 104, 105]. While the adverse effects of nonlinearities, imbalance or DC-offsets can be mitigated, those from poor spectral purity cannot be compensated directly [101]. Phase noise compensation schemes apply, for example, an additional downconversion branch for sampling the time varying carrier phase [106]. By the use of this signal the phase noise is estimated and is utilized for improving the receiver SNR. Other phase noise compensation approaches apply a feedback from the symbol decision for tracking and reducing the phase variations [107], or advantageously arrange the transmit symbols at a specific modulation technique to lower the phase noise impact [108]. These compensation schemes require either additional hardware, a specific modulation format, or information from the symbol decision. The goal of the transmitter compensator, derived in the next sections, is to improve the performance based on the provided input signal without additional hardware and without modulation format constraints. Therefore, the characterization and compensation of the phase noise was omitted.

Unlike the phase noise, static inband spurious emissions can be compensated without introducing constraints on the hardware or modulation format, as mentioned before. The reduction of spurs starts at the oscillator or synthesizer design [109, 110]. The impact of the spurious emissions located in within the BB bandwidth of the transmitter can the canceled, if their phase noise is negligible.

3.4.1 Transmitter model partitioning

The model presented in (3.58) was derived from the structure introduced in Figure 3.1. This task was accomplished without focusing on the independency of the model parameters. For example, the magnitude imbalance is influenced by the gain of the BB amplifiers, by differences in the LO magnitude at the two

I/Q mixer inputs, or by deviations in the frequency response of the lowpass-filters. A possibility of overcoming this problem is the usage of optimizing algorithms for finding the best fit between the measured and modeled transmitter response. This approach suffers from the great number of local minima in the cost function used for the parameter extraction. Without a proper starting point, the performance of the optimum search seems questionable.

In case the LO spurious emissions are negligible, the model parameterization can be performed by measuring the modulator response onto a persistent excitation signal using a vector signal analyzer (VSA). The Volterra series kernels are then derived using least square estimation methods [95]. This approach is only practicable if the distortion generated by the VSA is significantly below the one of the considered modulator. Additionally, it would be desirable if the considered VSA uses a different frequency translation method.

If these requirements are not fulfilled the model coefficients cannot be evaluated at once. Instead, the model is extracted by dividing the modulator behavior in groups, where each one is related to a single distortion mechanism. During the measurement of a distortion mechanism, interactions with other distortion effects must be avoided (or at least, kept low).

The partitioning of the transmitter behavior is performed based on the following distinguishable distortion effects:

- Carrier leakage

- Magnitude and phase imbalance for a single-tone input signal

- Spurious emissions present in the single-tone response

- Intermodulation and harmonic distortion from a two-tone input

- Intermodulation and harmonic distortion from a frequency shifted complex-valued two-tone signal

The carrier phase noise $\varphi_{PH}(t)$ is excluded from the characterization process due to the problems mentioned before. The carrier leakage is related to the factor O_{α_d} (3.58). A further itemization into the baseband amplifiers' DC-offsets $g_{I,0}$, $g_{Q,0}$ and the LO inphase and quadrature branch gain g_{CI}, g_{CQ} will not be performed. The magnitude and phase imbalance is caused by the lowpass-filters, the linear baseband amplifier response, and by the I/Q-mixer phase imbalance (3.58). From single-tone measurements the terms $g_{M,1}g_{CI}h_{I,1}(t)$, $g_{M,1}g_{CQ}h_{Q,1}(t)$ and θ_e can be extracted. If spurious emissions are found in the transmitter output spectrum, their frequency offset $\Delta\omega_k$, phase-shift $\varphi_{LO,k}$ and magnitude $(g_{CI,k} + g_{CQ,k})/2$ will be characterized. As for the carrier, also the spurious emissions phase noise $\varphi_{PH,k}(t)$ is not considered.

Finally, the nonlinear behavior of the transmitter is characterized by the two-tone response. Obviously, the magnitude imbalance of $g_{M,1}g_{CI}h_{I,1}(t)$ and $g_{M,1}g_{CQ}h_{Q,1}(t)$ are characterized by the imbalance and by the two-tone measurements. An interference of the linear magnitude and phase imbalance on the two-tone characterization is impossible, as the two-tone input signal is applied for each channel separately. A deterioration of the linear imbalance measurement by nonlinear effects can be kept low by properly selecting the single-tones' magnitude.

Only the frequency shifted complex valued two-tone signal measurement requires a compensation of the linear imbalance distortion. In this case a two-tone signal is generated at a given frequency offset

from the carrier. For using these measurement results for the estimation of the mixer output nonlinearity impact, the image signal component must be suppressed.

Practical measurements showed that some influence between the measurements can be recognized. For maximizing the accuracy of the transmitter characterization process the measurements have to be performed twice. After performing all measurements a first time, the transmitter coefficients were extracted. Based on these coefficients a compensator was parameterized and used for suppressing the generated distortion. Then the measurements are performed again minimizing all distortion effects except the one actually considered. From these second set of measurements the final transmitter parameters are extracted. These considerations showed the need for developing algorithms for the parameterization and compensation of the distortion generated by the transmitter for accurately identifying the transmitter behavior.

A default for the measurement of the transmitter response was the independence of the receivers' behavior. Otherwise, assuming that the receiver shows the same behavior as the transmitter, the signal components measured by the receiver could be significantly altered by its distortion. As the distortion is caused by the same mechanisms as in the transmitter, these errors could not be detected.

Furthermore, the measurement equipment used for characterizing the transmitter has to be sufficiently broadband for covering the full output spectra and must also be able of providing a dynamic range high enough for capturing all generated distortion products. For capturing the full transmitter behavior, the output signal components have to be measured in magnitude and phase.

A possibility to fulfill these requirements is the usage of a low-IF receiver for the characterization [90]. The linear phase response of this device would be taken as reference with which the transmitter is compared. The phase response measurement using a reference transmitter was suggested in [111]. In this case the reference transmitter generates an output signal which is fed into a vector attenuator (VA) before it is combined with the output signal of the transmitter to be measured. By changing the magnitude and phase of the VA the considered output signal component is canceled. After this task is performed, the VA is measured by a vector network analyzer. In this way the magnitude and phase difference to the reference transmitter signal component is evaluated. This process has to be repeated for each output signal product. It is important to note that the reference transmitter and the one to be measured must be phase-locked for guaranteeing a fixed phase relationship during the whole measurement process. The same phase measurement approach using a different setup was discussed in [112].

At the direct conversion transmitter measurement setup presented in Figure 2.15 the phase measurements will be performed by a random sampling scope. Based on the applied synchronization approach accurate phase measurements are achieved. The frequency response of this scope will be taken as reference the transmitter is compared to.

3.5 DC-offset characterization

The characterization and compensation of the DC-offset could also be treated as part of the transmitter nonlinearity extraction as this type of distortion was incorporated into the baseband amplifier description in the nonlinear amplifier model (3.47) - (3.58). The reason for discussing it in a separate section is the different characterization procedure used for the identification of the DC-offset and the nonlinear transmitter distortion. Additionally, for the separation of the nonlinear transmitter effects in the ones caused by the baseband and the ones caused by the mixer output nonlinearity, measurement must be

performed with compensated DC-offset.

The quantification of the DC-offset is achieved by measuring the transmitter output power at the carrier frequency using a spectrum analyzer and comparing this measurement result to the power of a full-scale single-tone output signal. This type of DC-offset quantification was introduced in connection with the definition of the DSR (3.13). It is important to note that no baseband signal may be present during the power measurement at the carrier frequency as otherwise second-order distortion components generated by the baseband amplifiers may add to the desired measurement result. Without compensation a DSR of 56 dB was measured compared to a full-scale single-tone output signal located 1 MHz above the RF center frequency.

For compensating the DC-offset two different approaches were tested:

- LS minimization as suggested by [76]

- Pattern search algorithm as provided by the *Genetic Algorithm and Direct Search Toolbox* from MATLAB®

The LS minimization approach assumes that the power of the DC-offset is measured with a detector showing a square-law characteristic:

$$\mathrm{P}_{DC}\left(\mathbf{S}_{\mathrm{BB}}\right) = G_e \left\|\mathbf{S}_{\mathrm{BB}} + \mathbf{O}\right\|^2 + B_e \tag{3.61}$$

where the transmitter DC-offset is represented by the vector $\mathbf{O} = [g_{I,0} g_{Q,0}]^T$ and a (DC) input signal to the transmitter by $\mathbf{S}_{\mathrm{BB}}$. The gain and the minimum output value of the detector are summarized by G_e and B_e, respectively. In this equation all nonlinear and imbalance effects introduced by the transmitter were neglected. The calculation of the DC output power can be also expressed as the inner product of two vectors:

$$\begin{aligned} \mathrm{P}_{DC}\left(\mathbf{S}_{\mathrm{BB}}\right) &= \mathbf{h}(\mathbf{S}_{\mathrm{BB}})^T \mathbf{p} \\ \mathbf{h}(\mathbf{S}_{\mathrm{BB}}) &= \left[S_{\mathrm{BB},I}^2 + S_{\mathrm{BB},Q}^2, S_{\mathrm{BB},I}, S_{\mathrm{BB},Q}, 1\right]^T \\ \mathbf{p} &= \left[G_e, 2G_2 g_{I,0}, 2G_e g_{Q,0}, G_e(g_{I,0}^2 + g_{Q,0}^2) + B_e\right]^T \end{aligned} \tag{3.62}$$

Based on the DC-offset measurement for N different DC input signals to the transmitter the vector $\mathbf{p}$ will be estimated:

$$\begin{aligned} \hat{\mathbf{p}} &= \mathbf{R}^{-1}\mathbf{w} \\ \mathbf{R} &= \frac{1}{N}\sum_{k=1}^{N} \mathbf{h}\left(\mathbf{S}_{\mathrm{BB}}(k)\right)\mathbf{h}\left(\mathbf{S}_{\mathrm{BB}}(k)\right)^T \\ \mathbf{w} &= \frac{1}{N}\sum_{k=1}^{N} \mathrm{P}_{DC}\left(\mathbf{S}_{\mathrm{BB}}(k)\right)\mathbf{h}\left(\mathbf{S}_{\mathrm{BB}}(k)\right) \end{aligned} \tag{3.63}$$

where "ˆ" is used for identifying the estimated vector $\mathbf{p}$. Using this result the desired DC-offsets are found by [76]:

$$\begin{aligned} \hat{g}_{I,0} &= -\frac{1}{2}\frac{\mathbf{p}_{\mathrm{est.}}(2)}{\mathbf{p}_{\mathrm{est.}}(1)} \\ \hat{g}_{Q,0} &= -\frac{1}{2}\frac{\mathbf{p}_{\mathrm{est.}}(3)}{\mathbf{p}_{\mathrm{est.}}(1)} \end{aligned} \tag{3.64}$$

 For the evaluation of the correction coefficients 20 measurements were performed. From these measurements one was performed without input signals and 8 were taken at an input of magnitude one each time rotated by $\pi/4$. The rest of the values were randomly selected. By this approach it was possible to improve the DSR to approx. 70 dBc. Due to the achieved carrier reduction the residual magnitude and phase error of the evaluated coefficient can be estimated to be less than 20% and $\pm 6°$, respectively.

 The pattern search algorithm used the carrier power measurement as objective function to be minimized. In simulations the pattern search algorithm showed an excellent performance even in the presence of significant imbalance and nonlinear distortion in the transmitter behavior. Applying this algorithm to the real transmitter, it was not possible to achieve the same level of DSR as compared with the LS approach even at 100 carrier power evaluations using four times averaging. Due to the good performance and low complexity of the LS minimization it was not tried optimizing the parameters of the pattern search algorithm for enhancing its performance.

3.6 Transmitter imbalance characterization

Starting point for the magnitude and phase imbalance evaluation was the work of Faulkner *et al.* [89] and Cavers *et al.* [76]. The evaluation of the frequency-dependent imbalance effect was achieved by minimizing the distortion product at the image frequency for a single-tone input signal, separately for each considered frequency point. The frequency-dependent imbalance compensators can be divided into real-valued and complex-valued gamma compensators. The real-valued version is able of compensating a transmitter characteristic as presented in the linear transmitter model (3.5) to (3.7). A default for this transmitter model was the assumption, that the mixer output nonlinearity shows a flat response over the considered baseband bandwidth. If this condition is not fulfilled, the function $|\gamma(j\omega)|$ (3.8) departs from its even characteristic and $\phi_\gamma(j\omega)$ from its odd characteristic. This property can only be achieved if the two functions $h_{\mathrm{LP},I}(t)$ and $h_{\mathrm{LP},Q}(t)$ are complex-valued, as these two must represent the corresponding lowpass filter function convolved with the transmitter output nonlinearity frequency characteristic. Even if such a behavior is not covered in the scope of applications of the presented transmitter model, compensators will be presented able of handling such general imbalance cases. In the following the real-valued gamma imbalance compensator is derived and the evaluation of the magnitude and phase imbalance coefficients is explained. Then the complex-valued gamma imbalance compensators are introduced.

3.6.1 Real-valued gamma imbalance compensation

Neglecting the DC-offset-term the compensated (linear) transmitter input signal is given by:

$$
\begin{aligned}
S_{\mathrm{BB}}(j\omega) =\ & \frac{1}{\alpha_I(j\omega)}\Big(S_{in,I}(j\omega) + S_{in,Q}(j\omega)\tan(\theta_e) \\
& + j S_{in,Q}(j\omega)\big[\gamma(j\omega)\cos(\theta_e)\big]^{-1}\Big) \\
=\ & \frac{1}{\alpha_I(j\omega)}\Big(S_{in,I}(j\omega) + S_{in,Q}(j\omega)\tan(\theta_e + \phi_\gamma(j\omega)) \\
& + j S_{in,Q}(j\omega)\big[|\gamma(j\omega)|\cos(\theta_e + \phi_\gamma(j\omega))\big]^{-1}\Big)
\end{aligned}
\tag{3.65}
$$

 The signal $S_{in}(j\omega) = S_{in,I}(j\omega) + j S_{in,Q}(j\omega)$ in this equation identifies the input signal to the compensator which, at the same time, is the desired transmitter output signal. By dividing by the factor $\alpha_I(j\omega)$

the gain of the transmitter is equalized. If this factor is only applied within a certain frequency range and outside substituted by unity, a frequency dependent gain equalization is implemented. This feature can be advantageous as the minimum gain found over the baseband bandwidth defines the level to which the others are reduced to.

3.6.2   Imbalance coefficients evaluation

The approaches presented in [76, 89] are both based on measuring the transmitter output using a broadband power detector. Like in [89], the magnitude imbalance is characterized by consecutively measuring the output power level of a sine-function applied to the inphase and the quadrature branch. The ratio between these two power measurements is an estimate for $|\gamma(j\omega)|$. Using a geometrical relationship the phase imbalance can be derived by measuring the transmitter output for two single-tone signals with magnitude $(A + jA)$ and $(-A + jA)$. The disadvantage of this approach, especially for transmitters with a low imbalance, is that the difference between the power measurements are small and measurement noise can deteriorate the characterization result significantly. For example, for a gain imbalance $\epsilon = 2\%$ the difference in the output power levels of the two branches will be only 0.18 dB. Therefore, a frequency selective measurement of the transmitter output signal and the distortion component located at the image frequency is performed. In the following an algorithm will be developed based on the cancelation of the image frequency distortion product for a single-tone input. The advantages of the usage of (3.65) for the evaluation of the coefficients $|\gamma(j\omega)|$ and $\theta_e + \phi_\gamma(j\omega)$ is that knowing these two quantities is sufficient for canceling the actual imbalance. If the image frequency product is fully suppressed using (3.65) the magnitude and phase imbalance are correctly evaluated. Assuming the transmitter input $S_{\mathrm{BB}}(j\omega)$ is derived using (3.65) for a single-tone input signal the two parameters $K \neq 1/|\gamma(j\omega)|$ and $\phi_K \neq -\phi_\gamma(j\omega) - \theta_e$ can be used to influence the image signal suppression. If these two quantities would be zero the ratio between the desired and the image signal component is approximated by (3.11). Based on a similar approach as used for deriving (3.11) the dependency of the image distortion product power on the parameters K and ϕ_K results in:

$$\mathrm{P}_s(-j\omega) \approx \frac{A^2}{8Z_0} g_{\mathrm{RF}} g_{\mathrm{M}} g_{\mathrm{CI}} g_I |H_{\mathrm{LP},I}(j\omega)|^2 \Big[(1 - K|\gamma(j\omega)|)^2 + (\phi_K + \phi_\gamma(j\omega) + \theta_e)^2 \Big] \tag{3.66}$$

where Z_0 is the reference impedance and A is the magnitude of the single-tone. This approximation reveals that the power level depends on the square of the parameters K and ϕ_K and that no cross products between these parameters exist. Hence, magnitude and phase imbalance can be optimized separately. In Figure 3.9 measurement results of the image distortion product power level for a sweep of the magnitude and phase parameter are shown. At each sweep the other quantity was kept constant. In both cases the sweep range was chosen for covering ISR ratios of better than 20 dB.

In the case of the phase imbalance the additive relationship between ϕ_K and $\phi_\gamma(j\omega) + \theta_e$ allows the estimation of the optimum phase compensator setting using least-square (LS) techniques. But simulations using the transmitter model (3.58) showed that the least-square phase estimation result could not provide the same accuracy compared to the evaluation method of [89] for the desired level of ISR. Hence, the approximation of the cosine function by a quadratic polynomial is insufficient for the required accuracy in which ϕ_K must be specified.

An improvement of the phase estimation was achieved by performing a spline interpolation [113] of the phase parameter sweep, as plotted in Figure 3.9(b), and selecting the phase value corresponding to
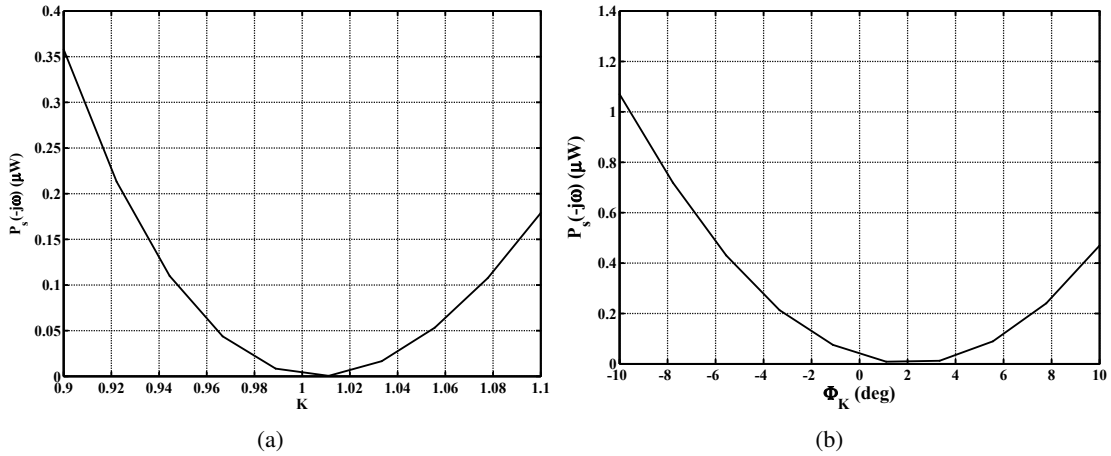
Figure 3.9: Measurement of the image distortion product power level for a sweep of (a) the magnitude and (b) the phase parameter.

the minimum interpolated power level. This approach was successfully used for the evaluation of ϕ_K and K both in simulation and measurement.

Even if the spline interpolation approach resulted in a reasonable image signal suppression it is still based on the assumption that the magnitude and phase imbalance can be separately compensated. A further enhancement can be achieved if the vicinity of the actual parameter set $\phi_{K,0}$ and K_0, evaluated by the spline interpolation, is investigated. By performing a combined sweep of ϕ_K and K around $\phi_{K,0}$ and K_0 and measuring the power of the image signal product the location of the global minimum can be evaluated. For limiting the number of required measurements for this two-dimensional sweep the measurement results were interpolated using a 2D-spline interpolation. Finally, the parameter set corresponding to the minimum of the interpolated power values was used as result of the imbalance coefficients evaluation process (i.e., $|\hat{\gamma}(j\omega_m)| = K_{\min}$, $\hat{\phi}_\gamma(j\omega_m) = \phi_{K,\min}$).

Also the pattern search algorithm provided by MATLAB$^{\circledR}$ was also evaluated for the minimization of the magnitude and phase imbalance. In this case the optimization was performed separately for each frequency by varying ϕ_K and K simultaneously. The objective function for the minimization task was the minimization of $P_s(-j\omega)$. Despite the maximum number of function evaluations were set to 100 (i.e. 100-times $P_s(-j\omega)$ was measured) and the starting point for the optimization was provided by the spline interpolation this algorithm was not able of improving the ISR. This may be due to selected parameters and constraints used to run the algorithm. Due to the time consuming procedure of finding the correct parameters for the pattern search and the efficiency of the approach described above it was not used for the ISR enhancement.

It is important to note that in case of a single-tone input signal generated at a frequency offset f_m from the carrier, the power of the image distortion at $-f_m$ was measured. By minimizing the amplitude of this distortion product, the magnitude and phase imbalance at $-f_m$ was characterized. Therefore, using a single-tone frequency sweep over the baseband bandwidth from $-f_s/2$ to $f_s/2$ the imbalance is evaluated over the frequency range $f_s/2$ to $-f_s/2$. These measurement results must be frequency mirrored to get the desired frequency response of $\hat{\gamma}(j\omega)$. After this step the mixer phase error $\hat{\theta}_e(j\omega)$ can be extracted

from the phase imbalance by evaluating the even response of the $\hat{\phi}_\gamma(j\omega)$ function. The mean of $\hat{\theta}_e(j\omega)$ determines the estimate for $\hat{\theta}_e$. This approach provided a complex-valued $\hat{\gamma}(j\omega)$ vector which was used for modeling the imbalance in the transmitter model as well as for the compensation of this distortion effect.

3.6.3 Complex-valued gamma imbalance compensation

After the evaluation of $\hat{\gamma}(j\omega)$ for the custom direct conversion transmitter it turned out that this function cannot be realized by real-valued functions (see (3.8)) as mentioned before. This fact led to the requirement of developing an imbalance compensator which is not based on the inphase / quadrature branch model (3.7). Instead, (3.5) and (3.6) have to be the starting point for the compensator development as in this case the complex-valued signals $S_{\mathrm{BB}}(j\omega)$ and $S_{\mathrm{BB}}^*(-j\omega)$ are combined for achieving the linear transmitter response:

$$S_{\mathrm{RF}}(j\omega) = g_{\mathrm{RF}} g_{\mathrm{M}} e^{j\varphi_{\mathrm{LO}}} \alpha_I(j\omega) \left[\frac{1}{2}\left(1 + \gamma(j\omega)e^{j\theta_e}\right) S_{\mathrm{BB}}(j\omega) + \frac{1}{2}\left(1 - \gamma(j\omega)e^{j\theta_e}\right) S_{\mathrm{BB}}^*(-j\omega) \right]$$
(3.67)

Two different approaches were found for deriving the complex-valued gamma imbalance compensator:

- After representing $\gamma(j\omega)$ and the complex baseband input signal by their real and imaginary parts in (3.67) the imbalance compensator equation can be extracted from this expression.

- Based on (3.67) an iterative approach can be found for compensating the transmitter imbalance.

3.6.3.1 Component based imbalance compensator

By substituting $\gamma(j\omega)$ by $\gamma_I(j\omega) = \mathscr{F}[\mathrm{Re}\{\gamma(t)\}]$ and $\gamma_Q(j\omega) = \mathscr{F}[\mathrm{Im}\{\gamma(t)\}]$ equation (3.67) converts to:

$$\begin{aligned}
S_{\mathrm{RF}}(j\omega) =& g_{\mathrm{RF}} g_{\mathrm{M}} e^{j\varphi_{\mathrm{LO}}} \alpha_I(j\omega) \Big[S_{\mathrm{BB},I}(j\omega) + S_{\mathrm{BB},Q}(j\omega)\Big(-\sin(\theta_e)\big[\gamma_I(j\omega) + j\gamma_Q(j\omega)\big] \\
&+ \cos(\theta_e)\big[j\gamma_I(j\omega) - \gamma_Q(j\omega)\big]\Big)\Big]
\end{aligned}$$
(3.68)

The part of this equation located within the outer squared brackets is responsible for the imbalance generation. The real and imaginary components of this part of (3.68) are given by:

$$\begin{aligned}
S_{in,I}(j\omega) =& S_{\mathrm{BB},I}(j\omega) + S_{\mathrm{BB},Q}(j\omega)\big[\sin(\theta_e)\gamma_I(j\omega) - \cos(\theta_e)\gamma_Q(j\omega)\big] \\
S_{in,Q}(j\omega) =& S_{\mathrm{BB},Q}(j\omega)\big[\sin(\theta_e)\gamma_Q(j\omega) + \cos(\theta_e)\gamma_I(j\omega)\big]
\end{aligned}$$
(3.69)

Here $S_{in,I}(j\omega)$ and $S_{in,Q}(j\omega)$ represents the signals provided at the input of the compensator (as introduced in conjunction with (3.65)). By extracting $S_{\mathrm{BB},I}(j\omega)$ and $S_{\mathrm{BB},Q}(j\omega)$ these equations lead to the desired imbalance compensator equations:

$$\begin{aligned}
S_{\mathrm{BB},I}(j\omega) =& S_{in,I}(j\omega) + S_{in,Q}(j\omega)\frac{\sin(\theta_e)\gamma_I(j\omega) + \cos(\theta_e)\gamma_Q(j\omega)}{\cos(\theta_e)\gamma_I(j\omega) - \sin(\theta_e)\gamma_Q(j\omega)} \\
S_{\mathrm{BB},Q}(j\omega) =& \frac{S_{in,Q}(j\omega)}{\cos(\theta_e)\gamma_I(j\omega) - \sin(\theta_e)\gamma_Q(j\omega)}
\end{aligned}$$
(3.70)

If $\gamma_Q(j\omega)$ is set to zero, this imbalance compensator equals the one presented in (3.65).

3.6.3.2 Iterative imbalance compensator

For compensating the linear distortion of $S_{\mathrm{BB}}(j\omega)$ in (3.67) the transmitter input signal is (neglecting the impact of $g_{\mathrm{RF}}g_{\mathrm{M}}\alpha_I(j\omega)e^{j\varphi_{\mathrm{LO}}}$):

$$S_{\mathrm{BB},0}(j\omega) = \frac{2}{1+\gamma(j\omega)e^{j\theta_e}}S_{in}(j\omega) \tag{3.71}$$

The corresponding transmitter output signal results to:

$$S_{\mathrm{RF},0}(j\omega) = g_{\mathrm{RF}}g_{\mathrm{M}}\alpha_I(j\omega)\left[S_{in}(j\omega) + \frac{1-\gamma(j\omega)e^{j\theta_e}}{1+\gamma^*(-j\omega)e^{-j\theta_e}}S_{in}^*(-j\omega)\right] \tag{3.72}$$

For removing the imbalance distortion from $S_{\mathrm{RF},0}(j\omega)$ the transmitter input signal has to be extended to:

$$S_{\mathrm{BB},1}(j\omega) = \frac{2}{1+\gamma(j\omega)e^{j\theta_e}}\left(S_{in}(j\omega) - \frac{1-\gamma(j\omega)e^{j\theta_e}}{1+\gamma^*(-j\omega)e^{-j\theta_e}}S_{in}^*(-j\omega)\right) \tag{3.73}$$

The imbalance distortion of this transmitter output signal is now completely removed, but an additional function is modifying $S_{\mathrm{BB}}(j\omega)$:

$$S_{\mathrm{RF},1}(j\omega) = g_{\mathrm{RF}}g_{\mathrm{M}}\alpha_I(j\omega)\left[S_{in}(j\omega)\left(1 - \frac{1-\gamma(j\omega)e^{j\theta_e}}{1+\gamma^*(-j\omega)e^{-j\theta_e}}\frac{1-\gamma^*(-j\omega)e^{-j\theta_e}}{1+\gamma(j\omega)e^{j\theta_e}}\right)\right] \tag{3.74}$$

The impact on $S_{\mathrm{BB}}(j\omega)$ by this factor is on the order of $\epsilon(j\omega)^2$. Clearly, the sketched process of compensation can be repeated as desired. At each iteration the residual imbalance distortion at the transmitter output is evaluated and added with opposite sign to the input signal. In continuation of the notation used in (3.71) to (3.74) an even sub index corresponds to the desired signal perturbance compensation while an odd one represents perfect imbalance suppression. For specifying the nth-order compensator output signal the following definitions will be used:

$$
\begin{aligned}
k_0 &= \frac{2}{1+\gamma(j\omega)e^{j\theta_e}} \\
k_1 &= \frac{1-\gamma(j\omega)e^{j\theta_e}}{1+\gamma^*(-j\omega)e^{-j\theta_e}} \\
k_2 &= \frac{1-\gamma^*(-j\omega)e^{-j\theta_e}}{1+\gamma(j\omega)e^{j\theta_e}}
\end{aligned} \tag{3.75}
$$

The compensator output signals are now given by the recursions:

$$
\begin{aligned}
S_{\mathrm{BB},n\,\mathrm{even}}(j\omega) &= S_{\mathrm{BB},n-1}(j\omega) + k_0 k_1^{\frac{n}{2}} k_2^{\frac{n}{2}} S_{in}(j\omega) \\
S_{\mathrm{BB},n\,\mathrm{odd}}(j\omega) &= S_{\mathrm{BB},n-1}(j\omega) + k_0 k_1^{\frac{n+1}{2}} k_2^{\frac{n-1}{2}} S_{in}^*(-j\omega) \\
S_{\mathrm{BB},0}(j\omega) &= k_0 S_{in}(j\omega)
\end{aligned} \tag{3.76}
$$

Compared to the imbalance compensator presented in (3.70) this one does not provide a perfect imbalance compensation. The order of magnitude in which the recursion reduces the residual distortion is quite high. If a transmitter shows an ISR of only $-20\,\mathrm{dB}$ the error on $S_{\mathrm{BB}}(j\omega)$ at $n=3$ is just 0.1 dB. It is interesting to note, that it is not possible to find an imbalance compensator similar to (3.70) based on $S_{\mathrm{BB}}(j\omega)$ and $S_{\mathrm{BB}}^*(-j\omega)$ instead of their real and imaginary components.

3.7 Spurious emissions

To introduce the characterization approach for the spurious emissions, the transmitter response is evaluated assuming DC-offset compensation and a negligible impact of the BB amplifiers and the RF output NL:

$$
\begin{aligned}
s_{\text{mod}}(t) = \ & g_{\text{M}}e^{j(\varphi_{\text{PH}}(t)+\varphi_{\text{LO}})}\big[\alpha_I(t)*s_{\text{BB},I}(t)+j\alpha_Q(t)e^{j\theta_e}*s_{\text{BB}_Q}(t)\big] \\
& +g_{\text{M}}\sum_{k=1}^{N_{\text{spur}}}e^{j(\Delta\omega_k t+\varphi_{\text{PH},k}(t)+\varphi_{\text{LO},k})}\big[g_{\text{CI},k}g_I h_{\text{LP},I}(t)*s_{\text{BB},I}(t) \\
& +jg_{\text{CQ},k}g_Q h_{\text{LP},Q}(t)e^{j\theta_e}*s_{\text{BB},Q}(t)\big]
\end{aligned}
\tag{3.77}
$$

In the following the impact of the phase noise on the desired signal and the spurious emission is neglected. Based on these simplifications the frequency domain representation of the output signal is given by:

$$
\begin{aligned}
S_{\text{mod}}(j\omega) = \ & g_{\text{M}}e^{j\varphi_{\text{LO}}}\big[\alpha_I(j\omega)S_{\text{BB},I}(j\omega)+j\alpha_Q(j\omega)e^{j\theta_e}S_{\text{BB},Q}(j\omega)\big] \\
& +g_{\text{M}}\sum_{k=1}^{N_{\text{spur}}}e^{j(\varphi_{\text{LO}}+\Delta\varphi_{\text{LO},k})}\Big[\tfrac{g_{\text{CI},k}}{g_{\text{CI},0}}\alpha_I(j\omega-j\Delta\omega_k)S_{\text{BB},I}(j\omega-j\Delta\omega_k) \\
& +\tfrac{g_{\text{CQ},k}}{g_{\text{CQ},0}}\alpha_Q(j\omega-j\Delta\omega_k)e^{j\theta_e}S_{\text{BB},Q}(j\omega-j\Delta\omega_k)\Big]
\end{aligned}
\tag{3.78}
$$

In this expression the phase of the spurious emissions $\varphi_{\text{LO},k}$ is given relative to the carrier phase $\varphi_{\text{LO}}+\Delta\varphi_{\text{LO},k}$. After some manipulations it can be shown that the above expression is equivalent to:

$$
\begin{aligned}
S_{\text{mod}}(j\omega) = \ & g_{\text{M}}e^{j\varphi_{\text{LO}}}\big[\alpha_d(j\omega)S_{\text{BB}}(j\omega)+\alpha_v(j\omega)S_{\text{BB}}^*(-j\omega)\big] \\
& +g_{\text{M}}\sum_{k=1}^{N_{\text{spur}}}e^{j(\varphi_{\text{LO}}+\Delta\varphi_{\text{LO},k})}\Big[\tfrac{g_{\text{CI},k}+g_{\text{CQ},k}}{g_{\text{CI},0}+g_{\text{CQ},0}}\alpha_d(j\omega-j\Delta\omega_k)S_{\text{BB}}(j\omega-j\Delta\omega_k) \\
& +\tfrac{g_{\text{CI},k}-g_{\text{CQ},k}}{g_{\text{CI},0}-g_{\text{CQ},k}}\alpha_v(j\omega-j\Delta\omega_k)S_{\text{BB}}^*(-j\omega-j\Delta\omega_k)\Big]
\end{aligned}
\tag{3.79}
$$

The functions $\alpha_I(j\omega)$, $\alpha_Q(j\omega)$, $\alpha_d(j\omega)$ and $\alpha_v(j\omega)$ were defined in (3.6). This result highlights that the imbalance present at the spurious emissions is a scaled version of the imbalance at the desired signal. The factor $(g_{\text{CI},k}+g_{\text{CQ},k})/(g_{\text{CI},0}+g_{\text{CQ},0})$ represents the scaling of the kth spurious emission relative to the desired signal. As discussed in the last section no distinction between the different imbalance contributions was made. It is therefore advantageous to substitute the ratios $(g_{\text{CI},k}+g_{\text{CQ},k})/(g_{\text{CI},0}+g_{\text{CQ},0})$, $(g_{\text{CI},k}-g_{\text{CQ},k})/(g_{\text{CI},0}-g_{\text{CQ},0})$ and the phase shift $\exp(j\Delta\varphi_{\text{LO},k})$ by the complex-valued scaling factors $\alpha_{\text{spur},d,k}$ and $\alpha_{\text{spur},v,k}$. Additionally, the imbalance was expressed by the parameters $\alpha_I(j\omega)$, $\gamma(j\omega)$ instead of $\alpha_d(j\omega)$ and $\alpha_v(j\omega)$. Incorporating these modifications in (3.79) results to:

$$
\begin{aligned}
S_{\text{mod}}(j\omega) = \ & \tfrac{g_{\text{M}}}{2}e^{j\varphi_{\text{LO}}}\alpha_I(j\omega)\Big[\big(1+\gamma(j\omega)e^{j\theta_e}\big)S_{\text{BB}}(j\omega)+\big(1-\gamma(j\omega)e^{j\theta_e}\big)S_{\text{BB}}^*(-j\omega)\Big] \\
& +\tfrac{g_{\text{M}}}{2}e^{j\varphi_{\text{LO}}}\sum_{k=1}^{N_{\text{spur}}}\alpha_I(j\omega-j\Delta\omega_k)\Big[\alpha_{\text{spur},d,k}\big(1+\gamma(j\omega-j\Delta\omega_k)e^{j\theta_e}\big)S_{\text{BB}}(j\omega-j\Delta\omega_k) \\
& +\alpha_{\text{spur},v,k}\big(1-\gamma(j\omega-j\Delta\omega_k)e^{j\theta_e}\big)S_{\text{BB}}^*(-j\omega-j\Delta\omega_k)\Big]
\end{aligned}
\tag{3.80}
$$

Due to the linear relationship between the baseband input signal and the spurious emissions, a cancelation approach similar to the imbalance compensation can be used. This approach only makes sense, if a deterministic connection between the carrier and the spurious emissions' phase exists. Otherwise,

$\alpha_{\mathrm{spur},d,k}$ and $\alpha_{\mathrm{spur},v,k}$ would represent random variables and could not be extracted in the way discussed below.

A single-tone input signal will be used for generating the spurs. As mentioned before, the DC-offset should be compensated for these measurements. The single-tone will be swept over the BB bandwidth and the magnitude of the corresponding distortion products will be recorded. In contrast to imbalance, harmonic, and intermodulation distortion, spurious emissions are always in a constant frequency offset from the input signal. In this way the response onto the frequency swept single-tone allows distinguishing between spurs and other distortion products.

After the spurs are identified the coefficients $\alpha_{\mathrm{spur},d,k}$ and $\alpha_{\mathrm{spur},v,k}$ can be extracted. By changing magnitude and phase of two coefficients the power of the spurious emissions at $\Delta\omega_k$ are reduced. The transmitter input signal for this task is given by:

$$
\begin{aligned}
S_{\mathrm{BB}}(j\omega) = \quad & 2\pi\big[A_{ST}\delta(j\omega - j\omega_m) \\
& + K_d e^{j\phi_{K_d}} A_{ST}\delta(j\omega - j\omega_m - j\Delta\omega_k) \\
& + K_v e^{j\phi_{K_v}} A_{ST}^*\delta(j\omega + j\omega_m - j\Delta\omega_k)\big]
\end{aligned}
\tag{3.81}
$$

where $K_d e^{j\phi_{K_d}}$ and $K_v e^{j\phi_{K_v}}$ are the tuning coefficients used for minimizing the power of the corresponding spurious emissions. The parameter A_{ST} represents the amplitude of the signal exciting the spurs. Based on (3.80) the associate transmitter output results to:

$$
\begin{aligned}
S_{\mathrm{mod}}(j\omega) \approx & \ \pi g_{\mathrm{M}} e^{j\varphi_{\mathrm{LO}}} \alpha_I(j\omega)\Big[\big(1 + \gamma(j\omega)e^{j\theta_e}\big) A_{ST}\delta(j\omega - j\omega_m) \\
& + \big(1 - \gamma(j\omega)e^{j\theta_e}\big) A_{ST}^*\delta(j\omega + j\omega_m)\Big] \\
& + \pi g_{\mathrm{M}} e^{j\varphi_{\mathrm{LO}}} \sum_{l=1}^{N_{\mathrm{spur}}} \alpha_I(j\omega - j\Delta\omega_l)\Big[\alpha_{\mathrm{spur},d,l}\big(1 + \gamma(j\omega - j\Delta\omega_l)e^{j\theta_e}\big) A_{ST}\delta(j\omega - j\omega_m - j\Delta\omega_l) \\
& + \alpha_{\mathrm{spur},v,l}\big(1 - \gamma(j\omega - j\Delta\omega_l)e^{j\theta_e}\big) A_{ST}^*\delta(j\omega + j\omega_m - j\Delta\omega_l)\Big] \\
& + \pi g_{\mathrm{M}} e^{j\varphi_{\mathrm{LO}}} \alpha_I(j\omega)\big(1 + \gamma(j\omega)e^{j\theta_e}\big) K_d e^{j\phi_{K_d}} A_{ST}\delta(j\omega - j\omega_m - j\Delta\omega_k) \\
& + \pi g_{\mathrm{M}} e^{j\varphi_{\mathrm{LO}}} \alpha_I(j\omega)\big(1 + \gamma(j\omega)e^{j\theta_e}\big) K_v e^{j\phi_{K_v}} A_{ST}\delta(j\omega + j\omega_m - j\Delta\omega_k)
\end{aligned}
\tag{3.82}
$$

Here the imbalance distortion and the spurs of the two compensation tones were neglected. From this expression the cancelation condition for the spurious emissions at $\Delta\omega_k$ is found by comparing the amplitude of the corresponding tones:

$$
\begin{aligned}
& \alpha_I(j\omega_m)\alpha_{\mathrm{spur},d,k}\big(1 + \gamma(j\omega_m)e^{j\theta_e}\big) \\
& \qquad = -\alpha_I(j\omega_m + j\Delta\omega_k)\big(1 + \gamma(j\omega_m + j\Delta\omega_k)e^{j\theta_e}\big) K_d e^{j\phi_{K_d}} \\
& \alpha_I(-j\omega_m)\alpha_{\mathrm{spur},v,k}\big(1 - \gamma(-j\omega_m)e^{j\theta_e}\big) \\
& \qquad = -\alpha_I(-j\omega_m + j\Delta\omega_k)\big(1 + \gamma(-j\omega_m + j\Delta\omega_k)e^{j\theta_e}\big) K_v e^{j\phi_{K_v}}
\end{aligned}
\tag{3.83}
$$

Using the coefficients $K_d e^{j\phi_{K_d}}$ and $K_v e^{j\phi_{K_v}}$ the scaling parameters of the spurious emissions $\hat{\alpha}_{\mathrm{spur},d,k}(j\omega_m)$ and $\hat{\alpha}_{\mathrm{spur},v,k}(j\omega_m)$ are derived by:

$$
\begin{aligned}
\hat{\alpha}_{\mathrm{spur},d,k}(j\omega_m) = & \ \frac{-K_d e^{j\phi_{K_d}} \alpha_I(j\omega_m + j\Delta\omega_k)\big(1 + \gamma(j\omega_m + j\Delta\omega_k)e^{j\theta_e}\big)}{\alpha_I(j\omega_m)\big(1 + \gamma(j\omega_m)e^{j\theta_e}\big)} \\
\hat{\alpha}_{\mathrm{spur},v,k}(-j\omega_m) = & \ \frac{-K_v e^{j\phi_{K_v}} \alpha_I(-j\omega_m + j\Delta\omega_k)\big(1 + \gamma(-j\omega_m + j\Delta\omega_k)e^{j\theta_e}\big)}{\alpha_I(-j\omega_m)\big(1 - \gamma(-j\omega_m)e^{j\theta_e}\big)}
\end{aligned}
\tag{3.84}
$$

Here, the dependency on desired tone frequency is highlighted at the parameters $\hat{\alpha}_{\mathrm{spur},d,k}(j\omega_m)$ and $\hat{\alpha}_{\mathrm{spur},v,k}(j\omega_m)$. The factors at the denominator compensate the scaling introduced by the imbalance distortion and the reference channel gain on the desired tone at f_m. The two corresponding factors at the nominator equalize the impact onto the compensation signal.

At the beginning of the cancelation process the parameters K_d and K_v were set to the magnitude ratio between the distortion product and the desired signal power measured without compensation. Then the phase parameters ϕ_{K_P} and ϕ_{K_N} were tested at 4 angles spaced $\pi/2$ for finding the quadrant in which the phase parameter minimizes the distortion power level. In the resulting quadrant the power of the distortion product was measured at 20 angles equally spaced over the full $\pi/2$ range. These power measurement results were interpolated using splines for finding the phase parameter associated with the minimum interpolated distortion power.

In a next step the magnitude coefficient was varied in 20 steps between 0.7 and 1.3 times its initial value. Also in this case the power of the distortion product was measured at these magnitude steps and the resulting resolution was improved using spline interpolation. The interpolation results are used to select the scaling factor related to the highest distortion suppression. If required, further evaluations at an increased magnitude and phase resolution can be performed. This process has to be repeated for all considered frequency offsets $\Delta\omega_k$.

It should be noted, that the two scaling factors in (3.84) incorporate the phase difference between the spurious emissions at $\Delta\omega_k$ and the carrier. For a correct modeling of these spurs the absolute phase of the carrier φ_{LO} is required additionally. This parameter is not provided by the suggested cancelation approach.

Based on the evaluated $\hat{\alpha}_{\mathrm{spur},d,k}(j\omega_m)$ and $\hat{\alpha}_{\mathrm{spur},v,k}(j\omega_m)$ at one frequency, no decision on the validity of the selected model can be made. Therefore, the extraction of $\hat{\alpha}_{\mathrm{spur},d,k}(j\omega_m)$, $\hat{\alpha}_{\mathrm{spur},v,k}(j\omega_m)$ has to be repeated at several frequencies f_m covering the BB bandwidth. Based on the frequency response of these parameters the following cases can be distinguished:

- $\hat{\alpha}_{\mathrm{spur},d,k}(j\omega_m)$ and $\hat{\alpha}_{\mathrm{spur},v,k}(j\omega_m)$ are approximately constant:
  Both spurious emissions are properly described by the model. $\hat{\alpha}_{\mathrm{spur},d,k}$ and $\hat{\alpha}_{\mathrm{spur},v,k}$ are calculated by averaging $\hat{\alpha}_{\mathrm{spur},d,k}(j\omega_m)$ and $\hat{\alpha}_{\mathrm{spur},v,k}(j\omega_m)$.

- Only one of the two functions $\hat{\alpha}_{\mathrm{spur},d,k}(j\omega_m)$, $\hat{\alpha}_{\mathrm{spur},v,k}(j\omega_m)$ is approximately constant:
  The spurious emissions at $+\Delta\omega_k$ and $-\Delta\omega_k$ have to be treated separately. The approximately constant function is averaged for achieving the corresponding parameter. The other parameter is set to zero.

- The considered function doesn't show an approximately constant characteristic:
  This distortion product cannot be modeled using constant scaling factors $\hat{\alpha}_{\mathrm{spur},d,k}$, $\hat{\alpha}_{\mathrm{spur},v,k}$. The frequency depending function must be used instead.

3.7.1 Spurious emissions compensation

The calculation of the spurious emissions compensator response, based on $\hat{\alpha}_{\mathrm{spur},d,k}$ and $\hat{\alpha}_{\mathrm{spur},v,k}$, is directly related to (3.84):

$$
\begin{aligned}
S_{\mathrm{BB}}(j\omega) = \ & -\sum_{k=1}^{N_{\mathrm{spur}}} \hat{\alpha}_{\mathrm{spur},d,k} \frac{\left[\alpha_I(j\omega)\left(1+\gamma(j\omega)e^{j\theta_e}\right)S_{in}(j\omega)\right]*\delta(j\omega-j\omega_k)}{\alpha_I(j\omega)\left(1+\gamma(j\omega)e^{j\theta_e}\right)} \\
& -\sum_{k=1}^{N_{\mathrm{spur}}} \hat{\alpha}_{\mathrm{spur},v,k} \frac{\left[\alpha_I(j\omega)\left(1-\gamma(j\omega)e^{j\theta_e}\right)S_{in}^*(-j\omega)\right]*\delta(j\omega-j\omega_k)}{\alpha_I(j\omega)\left(1+\gamma(j\omega)e^{j\theta_e}\right)}
\end{aligned}
\tag{3.85}
$$

In this expression $S_{in}(j\omega)$ identifies the input signal. Using this compensator the spurs generated by the desired input signal are canceled, but also additional imbalance distortion and spurious emissions are generated. Usually, the spurs of the compensation signal components are neglected, as they move rapidly out of the bandwidth of the BB signal generator. The imbalance introduced by the cancelation signals can be decreased by the use of the component based imbalance compensator (3.67):

$$
\begin{aligned}
S_{\mathrm{BB}}(j\omega) = \ & -\sum_{k=1}^{N_{\mathrm{spur}}} \hat{\alpha}_{\mathrm{spur},d,k} \frac{\mathrm{Comp}_{\mathrm{Imb.}}\left\{\left[\alpha_I(j\omega)\left(1+\gamma(j\omega)e^{j\theta_e}\right)S_{in}(j\omega)\right]*\delta(j\omega-j\omega_k)\right\}}{\alpha_I(j\omega)} \\
& -\sum_{k=1}^{N_{\mathrm{spur}}} \hat{\alpha}_{\mathrm{spur},v,k} \frac{\mathrm{Comp}_{\mathrm{Imb.}}\left\{\left[\alpha_I(j\omega)\left(1-\gamma(j\omega)e^{j\theta_e}\right)S_{in}^*(-j\omega)\right]*\delta(j\omega-j\omega_k)\right\}}{\alpha_I(j\omega)}
\end{aligned}
\tag{3.86}
$$

where $\mathrm{Comp}_{\mathrm{Imb.}}\{\,\cdot\,\}$ represents the imbalance compensator.

3.8 Characterization of the nonlinear behavior

In this section the characterization of the nonlinear transmitter behavior is presented. As the DAC's, the baseband amplifier and the mixer input nonlinearities generate IMD and harmonic distortion (HD) the resulting polynomials will be composed of even- and odd-order coefficients. The output signals of the two baseband branches are then combined, frequency shifted and passed through the mixer output nonlinearity. The harmonic distortion of the mixer output nonlinearity is not considered. In contrast to the imbalance and spurious emissions evaluation, no possibility was found for capturing the transmitter phase response and the AM-PM conversion using optimization techniques. This inability forces the measurement of the transmitter output signal in magnitude and phase for fully characterizing the nonlinear behavior.

The suggested parameter extraction approach assumes the absence of nonlinear dynamic effects. This means that a two-tone power sweep does not create IMD asymmetries. Additionally, spurious emissions and phase noise effect were neglected for the nonlinear behavior characterization.

In the following the procedure of separating the impact of the baseband and the mixer output nonlinearity will be explained. The starting point for this discussion is a (quasi) frequency independent transmitter model as shown in Figure 3.10. The notation used in this diagram was introduced in connection with (3.50). For a narrowband input signal this structure is equivalent to the one presented in Figure 3.1. The only frequency dependent effect covered by this model is the time delay introduced by the transmitter.

The basic idea for the separation is that the odd-order distortion generated by the baseband nonlinearities consists of intermodulation and harmonic distortion. After the baseband signals are frequency shifted and passed through the mixer output nonlinearity additional intermodulation distortion will be generated, but the harmonic distortion will stay mostly unchanged. For recognizing the difference in the intermodulation and harmonic distortion, the test signal may not be symmetric with reference to the RF center frequency. A two-tone signal shifted from the carrier frequency was selected for this purpose:

$$s_{\mathrm{BB}}(t) = A_{\mathrm{FSTT}} \cos(2\pi \mathrm{f}_{sp} t + \phi_{sp}) e^{j2\pi \mathrm{f}_m t + j\phi_m} \tag{3.87}$$

where f_{sp} identifies the tone-spacing and f_m the frequency offset from the RF center frequency and A_{FSTT} the input signal magnitude. ϕ_{sp} and ϕ_m represent the phase shifts associated to f_{sp} and f_m. In the following this type of signal will be called frequency-shifted two-tone (FSTT). Using this input signal it is possible to estimate the odd-order baseband and the mixer output nonlinear contribution.
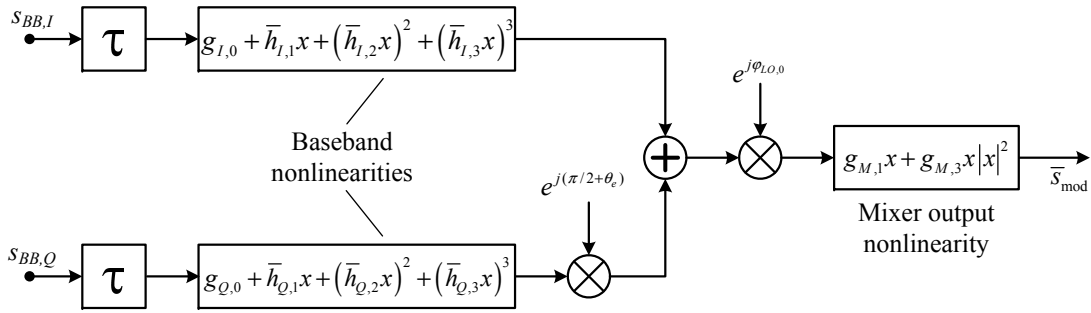
Figure 3.10: Memoryless nonlinear transmitter model used for the parameter extraction.

The result of the mixer output nonlinearity identification can then be used for deembedding the impact of this nonlinearity for generating the measurement results corresponding to the signals present at the output of the baseband nonlinearities. For this deembedding task frequency-shifted two-tone signals are applied separately for each channel. These channel-based two-tone (CBTT) signals are given by:

$$\begin{aligned}
s_{\mathrm{BB},I}(t) &= A_{\mathrm{CBTT}} \cos(2\pi \mathrm{f}_{sp} t + \phi_{sp}) \cos(2\pi \mathrm{f}_m t + \phi_m) \\
s_{\mathrm{BB},Q}(t) &= j A_{\mathrm{CBTT}} \cos(2\pi \mathrm{f}_{sp} t + \phi_{sp}) \cos(2\pi \mathrm{f}_m t + \phi_m)
\end{aligned} \tag{3.88}$$

For the validity of the suggested transmitter identification the following assumptions must be fulfilled:

- The mixer output nonlinearity is frequency independent. This assumption includes that the measurement of the odd-order IMD and HD relate only to the nonlinear effects and is not deteriorated by additional linear filtering.

- The PCWM is applicable for describing the considered transmitter.

- During a power sweep of the transmitter the LO phase must be constant.

The first assumption is required for a valid mixer output NL extraction. In case of a frequency dependent mixer output NL the separation of the dynamic transmitter behavior in the BB and the RF part is not unique.

For parameterizing the transmitter response in magnitude and phase a fixed phase relationship between the measured distortion products is required. At the FSTT input the LO phase may not change during a power sweep measurement (at a selected frequency offset f_m). A deterministic relationship between the phases of the IMD and HD distortion products must exist. In a similar way a constant LO phase is also assumed for the CBTT power sweeps. At a selected f_m the phases of the even- and odd-order distortion products at both channels are deterministically related to each other. Between power sweeps at different f_m or between the FSTT and the CBTT measurements a constant LO phase is not required.

For using this quasi memoryless model for describing the FSTT transmitter response a further assumption on the tone spacing is required. After this signal is applied at the transmitter input the BB amplifier output results to:

$$s_{\text{Amp}}(t) = \sum_{k=1}^{N_{\text{BB}}} (h_{I,k}(t) * \text{Re}\{s_{\text{BB}}(t-\tau)\})^k + j \sum_{k=1}^{N_{\text{BB}}} (h_{Q,k}(t) * \text{Im}\{s_{\text{BB}}(t-\tau)\})^k \qquad (3.89)$$

Here, the DC-component of the two nonlinearities was neglected. The two baseband nonlinearities are of order N_{BB}. The tone spacing f_{sp} of the FSTT input signal has to be set sufficiently small for guaranteeing:

$$H_{I,k}(j\omega_m) \simeq H_{I,k}(j\omega_m \pm j\omega_{sp}) \qquad (3.90)$$

The filter functions $H_{I,k}(j\omega_m)$ implement the delay compensated response of the dynamic devices within the transmitter. This condition legitimates the representation of the filter magnitude response by a constant factor $\bar{h}_{I,k} = |H_{I,k}(j\omega_m)|$. Additionally, the same phase rotation is applied for all PCWM filtering functions $\angle H_{I,k}(j\omega_m)$. This fact is expressed by dropping the nonlinear index from the phase parameter $\bar{\phi}_I = \angle H_{I,1}(j\omega_m)$. In case of phase difference to $\bar{\phi}_I$ the corresponding coefficient will be complex-valued. Note that these parameters are frequency-independent for the considered input signal but still show a dependency on f_m. Without a loss of generality, the parameters $g_{\text{CI},0}$ and $g_{\text{CQ},0}$ were assumed to be unity.

Under these assumptions an equivalent memoryless model can be applied to the measured transmitter response onto a FSTT signal for extracting the impact of the mixer output nonlinearity.

In summary, the transmitter identification process includes the following tasks:

- Transmitter delay and phase extraction

- Transmitter output nonlinearity parameterization

- Deembedding of the output nonlinearity impact

- Identification of the BB NL coefficients

- Evaluation of the corresponding PCWM filtering functions

- Optionally, the estimation of the mixer output NL parameterization can be improved using the extracted BB coefficients

Based on the frequency independent mixer output NL assumption these coefficients are extracted from FSTT power sweeps at least at one frequency f_m. Once this NL is identified, the parameters will be used for the calculation of the BB amplifier identification over the whole BB bandwidth.

After the complete transmitter was parameterized, a compensator will be presented for reducing the generated nonlinear distortion.

3.8.1 Transmitter response onto a FSTT input signal

The BB amplifier response onto a FSTT input signal was summarized in (3.89). Assuming a sufficiently narrowband tone spacing this equation can be expanded to:

$$
\begin{aligned}
s_{\text{Amp}}(t) &= \sum_{k=1}^{N_{\text{O,BB}}} (\bar{h}_{I,2k-1} A_{\text{FSTT}})^{2k-1} \cos^{2k-1}(\omega_{sp}(t-\tau) + \phi_{sp}) \cos^{2k-1}(\omega_m(t-\tau) + \phi_m + \bar{\phi}_I) \\
&+ \sum_{k=1}^{N_{\text{E,BB}}} (\bar{h}_{I,2k} A_{\text{FSTT}})^{2k} \cos^{2k}(\omega_{sp}(t-\tau) + \phi_{sp}) \cos^{2k}(\omega_m(t-\tau) + \phi_m + \bar{\phi}_I) \\
&+ j \sum_{k=1}^{N_{\text{O,BB}}} (\bar{h}_{Q,2k-1} A_{\text{FSTT}})^{2k-1} \cos^{2k-1}(\omega_{sp}(t-\tau) + \phi_{sp}) \sin^{2k-1}(\omega_m(t-\tau) + \phi_m + \bar{\phi}_Q) \\
&+ j \sum_{k=1}^{N_{\text{E,BB}}} (\bar{h}_{Q,2k} A_{\text{FSTT}})^{2k} \cos^{2k}(\omega_{sp}(t-\tau) + \phi_{sp}) \sin^{2k}(\omega_m(t-\tau) + \phi_m + \bar{\phi}_Q)
\end{aligned}
$$

$$(3.91)$$

The summation parameters $N_{\text{O,BB}}$ and $N_{\text{E,BB}}$ used in this equation are given by:

$$
N_{\text{O,BB}} = \left\lfloor \frac{N_{\text{BB}}+1}{2} \right\rfloor \qquad N_{\text{E,BB}} = \left\lfloor \frac{N_{\text{BB}}}{2} \right\rfloor
$$

$$(3.92)$$

where $\lfloor \cdot \rfloor$ provides the greatest integer less or equal to the enclosed value. After combining the same powers of the input signal magnitude from the inphase and the quadrature branch $s_{\text{Amp}}(t)$ results to:

$$
\begin{aligned}
s_{\text{Amp}}(t) &= \sum_{k=1}^{N_{\text{O,BB}}} \Big[\bar{h}_{I,2k-1}^{2k-1} \cos^{2k-1}(\omega_m(t-\tau) + \phi_m + \bar{\phi}_I) + j\bar{h}_{Q,2k-1}^{2k-1} \\
&\quad \sin^{2k-1}(\omega_m(t-\tau) + \phi_m + \bar{\phi}_Q) \Big] \cdot A_{\text{FSTT}}^{2k-1} \cos^{2k-1}(\omega_{sp}(t-\tau) + \phi_{sp}) \\
&+ \sum_{k=1}^{N_{\text{E,BB}}} \Big[\bar{h}_{I,2k}^{2k} \cos^{2k}(\omega_m(t-\tau) + \phi_m + \bar{\phi}_I) + j\bar{h}_{Q,2k}^{2k} \sin^{2k}(\omega_m(t-\tau) + \phi_m + \bar{\phi}_Q) \Big] \\
&\quad \cdot A_{\text{FSTT}}^{2k} \cos^{2k}(\omega_{sp}(t-\tau) + \phi_{sp})
\end{aligned}
$$

$$(3.93)$$

Here, the expression $\cos^{2k-1}(\omega_m(t-\tau) + \phi_m + \bar{\phi}_I) + j \sin^{2k-1}(\omega_m(t-\tau) + \phi_m + \bar{\phi}_Q)$ can be expanded in a series using trigonometric identities [114]:

$$
\begin{aligned}
&\cos^{2k-1}(\omega_m(t-\tau) + \phi_m + \bar{\phi}_I) + j \sin^{2k-1}(\omega_m(t-\tau) + \phi_m + \bar{\phi}_Q) = \frac{2}{4^k} \sum_{m=0}^{k-1} \binom{2k-1}{m} \Bigg[\\
&\left(e^{j(-1)^{k-1-m}(2k-1-2m)\bar{\phi}_I} + e^{j(-1)^{k-1-m}(2k-1-2m)\bar{\phi}_Q} \right) e^{j(-1)^{k-1-m}(2k-1-2m)(\omega_m(t-\tau)+\phi_m)} \\
&+ \left(e^{-j(-1)^{k-1-m}(2k-1-2m)\bar{\phi}_I} - e^{-j(-1)^{k-1-m}(2k-1-2m)\bar{\phi}_Q} \right) e^{-j(-1)^{k-1-m}(2k-1-2m)(\omega_m(t-\tau)+\phi_m)} \Bigg]
\end{aligned}
$$

$$(3.94)$$

This result can be simplified by expressing $\bar{\phi}_Q = \bar{\phi}_I + \bar{\phi}_\gamma$. It should be noted, that $\bar{\phi}_\gamma$ represents the

imbalance of the lowpass filters evaluated at f_m. Based on this substitution (3.94) can be written as:

$$
\cos^{2k-1}(\omega_m(t-\tau)+\phi_m+\bar{\phi}_I) + j\sin^{2k-1}(\omega_m(t-\tau)+\phi_m+\bar{\phi}_I+\bar{\phi}_\gamma) = \frac{2}{4^k}\sum_{m=0}^{k-1}\binom{2k-1}{m}\Bigg[
$$
$$
\left(1+e^{j(-1)^{k-1-m}(2k-1-2m)\bar{\phi}_\gamma}\right)e^{j(-1)^{k-1-m}(2k-1-2m)(\omega_m(t-\tau)+\phi_m+\bar{\phi}_I)}
$$
$$
+\left(1-e^{-j(-1)^{k-1-m}(2k-1-2m)\bar{\phi}_\gamma}\right)e^{-j(-1)^{k-1-m}(2k-1-2m)(\omega_m(t-\tau)+\phi_m+\bar{\phi}_I)}\Bigg]
$$
(3.95)

In the same way as before $\cos^{2k}(\omega_m(t-\tau)+\phi_m+\bar{\phi}_I)+j\sin^{2k}(\omega_m(t-\tau)+\phi_m+\bar{\phi}_Q)$ is also expanded in a series [114]:

$$
\cos^{2k}(\omega_m(t-\tau)+\phi_m+\bar{\phi}_I) + j\sin^{2k}(\omega_m(t-\tau)+\phi_m+\bar{\phi}_I+\bar{\phi}_\gamma) = \frac{1+j}{4^k}\binom{2k}{k} + \frac{1}{4^k}\sum_{m=0}^{k-1}\binom{2k}{m}\Bigg[
$$
$$
\left(1+j(-1)^{k-m}e^{j(-1)^{k-m}2(k-m)\bar{\phi}_\gamma}\right)e^{j(-1)^{k-m}2(k-m)(\omega_m(t-\tau)+\phi_m+\bar{\phi}_I)}
$$
$$
+\left(1+j(-1)^{k-m}e^{-j(-1)^{k-m}2(k-m)\bar{\phi}_\gamma}\right)e^{-j(-1)^{k-m}2(k-m)(\omega_m(t-\tau)+\phi_m+\bar{\phi}_I)}\Bigg]
$$
(3.96)

Substituting (3.95) into (3.93) and considering only the odd part of the BB amplifier response leads to:

$$
s_{\text{Amp,odd}}(t) = \sum_{k=1}^{N_{\text{O,BB}}}\Bigg[\frac{2}{4^k}\sum_{m=0}^{k-1}\left(\bar{h}_{I,2k-1}^{2k-1}+\bar{h}_{Q,2k-1}^{2k-1}e^{j(-1)^{k-1-m}(2k-1-2m)\bar{\phi}_\gamma}\right)\binom{2k-1}{m}
$$
$$
\cdot e^{j(-1)^{k-1-m}(2k-1-2m)(\omega_m(t-\tau)+\phi_m+\bar{\phi}_I)}
$$
$$
+\frac{2}{4^k}\sum_{m=0}^{k-1}\left(\bar{h}_{I,2k-1}^{2k-1}-\bar{h}_{Q,2k-1}^{2k-1}e^{-j(-1)^{k-1-m}(2k-1-2m)\bar{\phi}_\gamma}\right)\binom{2k-1}{m}
$$
$$
\cdot e^{-j(-1)^{k-1-m}(2k-1-2m)(\omega_m(t-\tau)+\phi_m+\bar{\phi}_I)}\Bigg]A_{\text{FSTT}}^{2k-1}\cos^{2k-1}(\omega_{sp}(t-\tau)+\phi_{sp})
$$
(3.97)

At this result the expression $\cos^{2k-1}(\omega_{sp}t+\phi_{sp})$ is now also expanded in a series:

$$
s_{\text{Amp,odd}}(t) = \sum_{k=1}^{N_{\text{O,BB}}}\Bigg[\frac{2}{4^k}\sum_{m=0}^{k-1}\left(\bar{h}_{I,2k-1}^{2k-1}+\bar{h}_{Q,2k-1}^{2k-1}e^{j(-1)^{k-1-m}(2k-1-2m)\bar{\phi}_\gamma}\right)\binom{2k-1}{m}
$$
$$
\cdot e^{j(-1)^{k-1-m}(2k-1-2m)(\omega_m(t-\tau)+\phi_m+\bar{\phi}_I)}
$$
$$
+\frac{2}{4^k}\sum_{m=0}^{k-1}\left(\bar{h}_{I,2k-1}^{2k-1}-\bar{h}_{Q,2k-1}^{2k-1}e^{-j(-1)^{k-1-m}(2k-1-2m)\bar{\phi}_\gamma}\right)\binom{2k-1}{m}
$$
$$
\cdot e^{-j(-1)^{k-1-m}(2k-1-2m)(\omega_m(t-\tau)+\phi_m+\bar{\phi}_I)}\Bigg]
$$
$$
\cdot\frac{1}{4^{k-1}}\sum_{l=0}^{k-1}\binom{2k-1}{l}A_{\text{FSTT}}^{2k-1}\cos([2k-1-2l][\omega_{sp}(t-\tau)+\phi_{sp}])
$$
(3.98)

Equation (3.98) is sorted based on the powers of the input signal magnitude A_{FSTT}. It is advanta-

geous of rearranging this equation based on the frequency of the different signal components:

$$
s_{\text{Amp,odd}}(t) = \sum_{k=1}^{N_{\text{O,BB}}} \sum_{l=1}^{N_{\text{O,BB}}} \sum_{m=\max(k,l)}^{N_{\text{O,BB}}} \frac{8}{16^m} \binom{2m-1}{m-k}\binom{2m-1}{m-l} A_{\text{FSTT}}^{2m-1} \cos([2l-1][\omega_{sp}(t-\tau)+\phi_{sp}])
$$

$$
\cdot \left[\left(\bar{h}_{I,2m-1}^{2m-1} + \bar{h}_{Q,2m-1}^{2m-1}\, e^{j(-1)^{k-1}(2k-1)\bar{\phi}_\gamma} \right) e^{j(-1)^{k-1}(2k-1)(\omega_m(t-\tau)+\phi_m+\bar{\phi}_I)} \right.
$$

$$
\left. + \left(\bar{h}_{I,2m-1}^{2m-1} - \bar{h}_{Q,2m-1}^{2m-1}\, e^{-j(-1)^{k-1}(2k-1)\bar{\phi}_\gamma} \right) e^{-j(-1)^{k-1}(2k-1)(\omega_m(t-\tau)+\phi_m+\bar{\phi}_I)} \right]
$$

(3.99)

Substituting (3.96) into (3.93) and expanding $\cos^{2k}(\omega_{sp}t+\phi_{sp})$ provides the even-order BB amplifier response:

$$
s_{\text{Amp,even}}(t) = \sum_{k=1}^{N_{\text{E,BB}}} A_{\text{FSTT}}^{2k} \left(\frac{\bar{h}_{I,2k}^{2k}+j\bar{h}_{Q,2k}^{2k}}{4^k}\binom{2k}{k} + \frac{1}{4^k}\sum_{m=0}^{k-1}\binom{2k}{m} \right[
$$

$$
\left(\bar{h}_{I,2k}^{2k} + j(-1)^{k-m}\bar{h}_{Q,2k}^{2k}\, e^{j(-1)^{k-m}2(k-m)\bar{\phi}_\gamma} \right) e^{j(-1)^{k-m}2(k-m)(\omega_m(t-\tau)+\phi_m+\bar{\phi}_I)}
$$

$$
\left. + \left(\bar{h}_{I,2k}^{2k} + j(-1)^{k-m}\bar{h}_{Q,2k}^{2k}\, e^{-j(-1)^{k-m}2(k-m)\bar{\phi}_\gamma} \right) e^{-j(-1)^{k-m}2(k-m)(\omega_m(t-\tau)+\phi_m+\bar{\phi}_I)} \right] \right)
$$

$$
\cdot \left[\frac{1}{4^k}\binom{2k}{k} + \frac{2}{4^k}\sum_{l=0}^{k-1}\binom{2k}{l}\cos(2[k-l][\omega_{sp}(t-\tau)+\phi_{sp}]) \right]
$$

(3.100)

Also this result is now sorted based on the frequency of the signal components:

$$
s_{\text{Amp,even}}(t) = \sum_{k=1}^{N_{\text{E,BB}}} \frac{1}{16^k}\binom{2k}{k}^2 A_{\text{FSTT}}^{2k}\left(\bar{h}_{I,2k}^{2k} + j\bar{h}_{Q,2k}^{2k} \right)
$$

$$
+ \sum_{k=1}^{N_{\text{E,BB}}} \sum_{l=k}^{N_{\text{E,BB}}} \frac{1}{16^l}\binom{2l}{l}\binom{2l}{l-k} A_{\text{FSTT}}^{2l}\left[2\left(\bar{h}_{I,2l}^{2l} + j\bar{h}_{Q,2l}^{2l} \right)\cos(2k[\omega_{sp}(t-\tau)+\phi_{sp}]) \right.
$$

$$
+ \left(\bar{h}_{I,2l}^{2l} + j(-1)^k\bar{h}_{Q,2l}^{2l}\, e^{j(-1)^k 2k\bar{\phi}_\gamma} \right) e^{j(-1)^k 2k(\omega_m(t-\tau)+\phi_m+\bar{\phi}_I)}
$$

$$
\left. + \left(\bar{h}_{I,2l}^{2l} + j(-1)^k\bar{h}_{Q,2l}^{2l}\, e^{-j(-1)^k 2k\bar{\phi}_\gamma} \right) e^{-j(-1)^k 2k(\omega_m(t-\tau)+\phi_m+\bar{\phi}_I)} \right]
$$

$$
+ \sum_{k=1}^{N_{\text{E,BB}}} \sum_{l=1}^{N_{\text{E,BB}}} \sum_{m=\max(k,l)}^{N_{\text{E,BB}}} \frac{2}{16^m}\binom{2m}{m-k}\binom{2m}{m-l} A_{\text{FSTT}}^{2m}\cos(2l[\omega_{sp}(t-\tau)+\phi_{sp}])
$$

$$
\cdot \left[\left(\bar{h}_{I,2m}^{2m} + j(-1)^k\bar{h}_{Q,2m}^{2m}\, e^{j(-1)^k 2k\bar{\phi}_\gamma} \right) e^{j(-1)^k 2k(\omega_m(t-\tau)+\phi_m+\bar{\phi}_I)} \right.
$$

$$
\left. + \left(\bar{h}_{I,2m}^{2m} + j(-1)^k\bar{h}_{Q,2m}^{2m}\, e^{-j(-1)^k 2k\bar{\phi}_\gamma} \right) e^{-j(-1)^k 2k(\omega_m(t-\tau)+\phi_m+\bar{\phi}_I)} \right]
$$

(3.101)

Equations (3.99) and (3.101) analytically describe the magnitudes of all distortion products present at the output of the baseband amplifiers for a FSTT input signal. One important result of this derivation is, that intermodulation and harmonic distortions of equal magnitude are present. This fact is expressed by the summation indices used in (3.99). Here, the index k selects the different carrier frequency offsets of the FSTT and l the tone-spacing of the actual considered signal component. Exchanging the values of

the index k and l will switch between intermodulation and harmonic distortion but results in the same magnitude of the signal component. For example, the output of the third-order intermodulation distortion (selected by $k = 1$ and $l = 2$):

$$
\begin{aligned}
s_{\text{Amp,IMD}_3}(t) = {} & \sum_{m=2}^{N_{\text{O,BB}}} \frac{8}{16^m} \binom{2m-1}{m-1} \binom{2m-1}{m-2} \left(\bar{h}_{I,2m-1}^{2m-1} + \bar{h}_{Q,2m-1}^{2m-1} e^{j\bar{\phi}_\gamma} \right) e^{j(\omega_m(t-\tau)+\phi_m+\bar{\phi}_I)} \\
& \cdot A_{\text{FSTT}}^{2m-1} \cos(3\omega_{sp}(t-\tau)+3\phi_{sp})
\end{aligned}
\tag{3.102}
$$

and the center tone and the third order harmonics (selected by $k = 2$ and $l = 1$):

$$
\begin{aligned}
s_{\text{Amp,HD}_3}(t) = {} & \sum_{m=2}^{N_{\text{O,BB}}} \frac{8}{16^m} \binom{2m-1}{m-2} \binom{2m-1}{m-1} \left(\bar{h}_{I,2m-1}^{2m-1} + \bar{h}_{Q,2m-1}^{2m-1} e^{-j3\bar{\phi}_\gamma} \right) e^{-j3(\omega_m(t-\tau)+\phi_m+\bar{\phi}_I)} \\
& \cdot A_{\text{FSTT}}^{2m-1} \cos(\omega_{sp}(t-\tau)+\phi_{sp})
\end{aligned}
\tag{3.103}
$$

show the same magnitude assuming a negligible impact of the lowpass filter phase imbalance $\bar{\phi}_\gamma$.

After the upconversion by the I/Q-mixers an additional phase imbalance is introduced to (3.99) and (3.101). Therefore, the input signal to the mixer output nonlinearity is given by:

$$
\begin{aligned}
s_{\text{BP}}(t) = {} & e^{j\varphi_{\text{LO}}} \left(\sum_{k=1}^{N_{\text{O,BB}}} \sum_{l=1}^{N_{\text{O,BB}}} \sum_{m=\max(k,l)}^{N_{\text{O,BB}}} \frac{8}{16^m} \binom{2m-1}{m-k} \binom{2m-1}{m-l} A_{\text{FSTT}}^{2m-1} \cos([2l-1][\omega_{sp}(t-\tau)+\phi_{sp}]) \right. \\
& \cdot \left[\left(\bar{h}_{I,2m-1}^{2m-1} + \bar{h}_{Q,2m-1}^{2m-1} e^{j(\theta_e+(-1)^{k-1}(2k-1)\bar{\phi}_\gamma)} \right) e^{j(-1)^{k-1}(2k-1)(\omega_m(t-\tau)+\phi_m+\bar{\phi}_I)} \right. \\
& \left. + \left(\bar{h}_{I,2m-1}^{2m-1} - \bar{h}_{Q,2m-1}^{2m-1} e^{j(\theta_e-(-1)^{k-1}(2k-1)\bar{\phi}_\gamma)} \right) e^{-j(-1)^{k-1}(2k-1)(\omega_m(t-\tau)+\phi_m+\bar{\phi}_I)} \right] \\
& + \sum_{k=1}^{N_{\text{E,BB}}} \frac{1}{16^k} \binom{2k}{k}^2 A_{\text{FSTT}}^{2k} \left(\bar{h}_{I,2k}^{2k} + j\bar{h}_{Q,2k}^{2k} e^{j\theta_e} \right) \\
& + \sum_{k=1}^{N_{\text{E,BB}}} \sum_{l=k}^{N_{\text{E,BB}}} \frac{1}{16^l} \binom{2l}{l} \binom{2l}{l-k} A_{\text{FSTT}}^{2l} \left[2 \left(\bar{h}_{I,2l}^{2l} + j\bar{h}_{Q,2l}^{2l} e^{j\theta_e} \right) \cos(2k[\omega_{sp}(t-\tau)+\phi_{sp}]) \right. \\
& + \left(\bar{h}_{I,2l}^{2l} + j(-1)^k \bar{h}_{Q,2l}^{2l} e^{j(\theta_e+(-1)^k 2k\bar{\phi}_\gamma)} \right) e^{j(-1)^k 2k(\omega_m(t-\tau)+\phi_m+\bar{\phi}_I)} \\
& \left. + \left(\bar{h}_{I,2l}^{2l} + j(-1)^k \bar{h}_{Q,2l}^{2l} e^{j(\theta_e-(-1)^k 2k\bar{\phi}_\gamma)} \right) e^{-j(-1)^k 2k(\omega_m(t-\tau)+\phi_m+\bar{\phi}_I)} \right] \\
& + \sum_{k=1}^{N_{\text{E,BB}}} \sum_{l=1}^{N_{\text{E,BB}}} \sum_{m=\max(k,l)}^{N_{\text{E,BB}}} \frac{2}{16^m} \binom{2m}{m-k} \binom{2m}{m-l} A_{\text{FSTT}}^{2m} \cos(2l[\omega_{sp}(t-\tau)+\phi_{sp}]) \\
& \cdot \left[\left(\bar{h}_{I,2m}^{2m} + j(-1)^k \bar{h}_{Q,2m}^{2m} e^{j(\theta_e+(-1)^k 2k\bar{\phi}_\gamma)} \right) e^{j(-1)^k 2k(\omega_m(t-\tau)+\phi_m+\bar{\phi}_I)} \right. \\
& \left. \left. + \left(\bar{h}_{I,2m}^{2m} + j(-1)^k \bar{h}_{Q,2m}^{2m} e^{j(\theta_e-(-1)^k 2k\bar{\phi}_\gamma)} \right) e^{-j(-1)^k 2k(\omega_m(t-\tau)+\phi_m+\bar{\phi}_I)} \right] \right)
\end{aligned}
\tag{3.104}
$$

Assuming a mixer output nonlinearity of order N_{RF} the output of the transmitter results to:

$$
s_{\text{mod}}(t) = \sum_{n=1}^{(N_{\text{RF}}+1)/2} g_{\text{M},2n-1} s_{\text{BP}}(t) \left| s_{\text{BP}}(t) \right|^{2(n-1)}
\tag{3.105}
$$

Clearly, by passing the distorted spectrum from the baseband nonlinearities through the mixer output NL leads to a huge number of intermodulation distortion products. For keeping the complexity of the analytical transmitter output signal description manageable only distortion products of the output nonlinearity

are calculated which are caused by the desired FSTT signal. The nonlinear interactions between the desired signal and distortion products caused by the baseband nonlinearities or between combinations of these distortion products are neglected. The desired signal at the input of the mixer output nonlinearity is already compressed by the baseband amplifiers. This desired input signal is given by:

$$
\begin{aligned}
s_{\mathrm{Amp,des.}}(t) =\ & A_{\mathrm{des.}}\cos(\omega_{sp}(t-\tau)+\phi_{sp})e^{j(\omega_m(t-\tau)+\phi_m+\bar{\phi}_I+\phi_{\mathrm{des.}}+\varphi_{\mathrm{LO}})} \\
A_{\mathrm{des.}}e^{j\phi_{\mathrm{des.}}} =\ & \sum_{m=1}^{N_{\mathrm{O,BB}}} \tfrac{8}{16^m}\binom{2m-1}{m-1}^2 \left(\bar{h}_{I,2m-1}^{2m-1}+\bar{h}_{Q,2m-1}^{2m-1}\,e^{j(\theta_e+\bar{\phi}_\gamma)}\right)A_{\mathrm{FSTT}}^{2m-1}
\end{aligned} \tag{3.106}
$$

Under the assumption that the inphase and quadrature BB amplifiers' odd-order coefficients are approximately equal (i.e., $\bar{h}_{I,2m-1} \approx \bar{h}_{Q,2m-1}$) the phase shift due to the phase imbalance results to $\phi_{\mathrm{des.}} = (\theta_e + \bar{\phi}_\gamma)/2$. This phase shift is independent of the input signal magnitude A_{FSTT}^{2m-1}. If the BB amplifiers' coefficients magnitude ratio $\bar{h}_{Q,2m-1}/\bar{h}_{I,2m-1}$ differs for each order, AM-PM conversion will be generated, even if the BB amplifiers do not generate this type of distortion by themselves! This AM-PM conversion is a result of the simultaneous presence of magnitude and phase imbalance (i.e., by the presence of two linear distortion effects).

By the use of $A_{\mathrm{des.}}$ and $\phi_{\mathrm{des.}}$ the transmitter output signal can be approximated by:

$$
\begin{aligned}
s_{\mathrm{mod}}(t) \approx\ & g_{\mathrm{M,1}}s_{\mathrm{BP}}(t) + \sum_{l=1}^{(N_{\mathrm{RF}}+1)/2}\ \sum_{m=\max(l,2)}^{(N_{\mathrm{RF}}+1)/2} \tfrac{1}{4^{m-1}}g_{\mathrm{M},2m-1}\binom{2m-1}{m-l}A_{\mathrm{des.}}^{2m-1} \\
& \cdot \cos([2l-1][\omega_{sp}(t-\tau)+\phi_{sp}])\,e^{j(\omega_m(t-\tau)+\phi_m+\bar{\phi}_I+\phi_{\mathrm{des.}}+\varphi_{\mathrm{LO}})}
\end{aligned} \tag{3.107}
$$

Substituting (3.104) into (3.107) provides the complete analytical description of the output signal approximation:

$$
\begin{aligned}
s_{\mathrm{mod}}(t) \approx\ & \sum_{k=1}^{N_{\mathrm{O,BB}}}\ \sum_{l=1}^{N_{\mathrm{O,BB}}}\ \sum_{m=\max(k,l)}^{N_{\mathrm{O,BB}}} \tfrac{8}{16^m}g_{\mathrm{M,1}}\binom{2m-1}{m-k}\binom{2m-1}{m-l}A_{\mathrm{FSTT}}^{2m-1}\cos([2l-1][\omega_{sp}(t-\tau)+\phi_{sp}]) \\
& \cdot\left[\left(\bar{h}_{I,2m-1}^{2m-1}+\bar{h}_{Q,2m-1}^{2m-1}\,e^{j(\theta_e+(-1)^{k-1}(2k-1)\bar{\phi}_\gamma)}\right)e^{j(\varphi_{\mathrm{LO}}+(-1)^{k-1}(2k-1)[\omega_m(t-\tau)+\phi_m+\bar{\phi}_I])} \right. \\
& \left. +\left(\bar{h}_{I,2m-1}^{2m-1}-\bar{h}_{Q,2m-1}^{2m-1}\,e^{j(\theta_e-(-1)^{k-1}(2k-1)\bar{\phi}_\gamma)}\right)e^{j(\varphi_{\mathrm{LO}}-(-1)^{k-1}(2k-1)[\omega_m(t-\tau)+\phi_m+\bar{\phi}_I])}\right] \\
& + \sum_{l=1}^{(N_{\mathrm{RF}}+1)/2}\ \sum_{m=\max(l,2)}^{(N_{\mathrm{RF}}+1)/2} \tfrac{1}{4^{m-1}}g_{\mathrm{M},2m-1}\binom{2m-1}{m-l}A_{\mathrm{des.}}^{2m-1}\cos([2l-1][\omega_{sp}(t-\tau)+\phi_{sp}]) \\
& \cdot e^{j(\omega_m(t-\tau)+\phi_m+\bar{\phi}_I+\phi_{\mathrm{des.}}+\varphi_{\mathrm{LO}})} \\
& + \ldots \ (\text{continued on the next page})
\end{aligned}
$$

$$
\begin{aligned}
+&\sum_{k=1}^{N_{\mathrm{E,BB}}} \frac{1}{16^k} g_{\mathrm{M},1} \binom{2k}{k}^2 A_{\mathrm{FSTT}}^{2k} \left(\bar{h}_{I,2k}^{2k} + j\bar{h}_{Q,2k}^{2k} e^{j\theta_e} \right) e^{j\varphi_{\mathrm{LO}}} \\
+&\sum_{k=1}^{N_{\mathrm{E,BB}}} \sum_{l=k}^{N_{\mathrm{E,BB}}} \frac{g_{\mathrm{M},1}}{16^l} \binom{2l}{l}\binom{2l}{l-k} A_{\mathrm{FSTT}}^{2l} \Big[2\left(\bar{h}_{I,2l}^{2l} + j\bar{h}_{Q,2l}^{2l} e^{j\theta_e} \right) \cos(2k[\omega_{sp}(t-\tau)+\phi_{sp}]) e^{j\varphi_{\mathrm{LO}}} \\
&+ \left(\bar{h}_{I,2l}^{2l} + j(-1)^k \bar{h}_{Q,2l}^{2l} e^{j(\theta_e+(-1)^k 2k\bar{\phi}_\gamma)} \right) e^{j(\varphi_{\mathrm{LO}}+(-1)^k 2k[\omega_m(t-\tau)+\phi_m+\bar{\phi}_I])} \\
&+ \left(\bar{h}_{I,2l}^{2l} + j(-1)^k \bar{h}_{Q,2l}^{2l} e^{j(\theta_e-(-1)^k 2k\bar{\phi}_\gamma)} \right) e^{j(\varphi_{\mathrm{LO}}-(-1)^k 2k[\omega_m(t-\tau)+\phi_m+\bar{\phi}_I])} \Big] \\
+&\sum_{k=1}^{N_{\mathrm{E,BB}}} \sum_{l=1}^{N_{\mathrm{E,BB}}} \sum_{m=\max(k,l)}^{N_{\mathrm{E,BB}}} \frac{2}{16^m} g_{\mathrm{M},1} \binom{2m}{m-k}\binom{2m}{m-l} A_{\mathrm{FSTT}}^{2m} \cos(2l[\omega_{sp}(t-\tau)+\phi_{sp}]) \\
&\cdot \Big[\left(\bar{h}_{I,2m}^{2m} + j(-1)^k \bar{h}_{Q,2m}^{2m} e^{j(\theta_e+(-1)^k 2k\bar{\phi}_\gamma)} \right) e^{j(\varphi_{\mathrm{LO}}+(-1)^k 2k[\omega_m(t-\tau)+\phi_m+\bar{\phi}_I])} \\
&+ \left(\bar{h}_{I,2m}^{2m} + j(-1)^k \bar{h}_{Q,2m}^{2m} e^{j(\theta_e-(-1)^k 2k\bar{\phi}_\gamma)} \right) e^{j(\varphi_{\mathrm{LO}}-(-1)^k 2k[\omega_m(t-\tau)+\phi_m+\bar{\phi}_I])} \Big]
\end{aligned}
$$

(3.108)

The first term of this result presents the baseband contribution to the FSTT output signal, the IMD, and the odd-order harmonic distortion at the desired and the image frequencies. The second term specifies the IMD generated by the RF nonlinearity. Then the distortion products located at the even-order harmonics of the FSTT center frequency f_m are given.

For validating the accuracy of this approximation the response of a transmitter onto a FSTT input signal was simulated. For this simulation the same parameters were used as for the nonlinear model accuracy evaluation in Section 3.3 (i.e., $\gamma = 0.95$, $\theta_e = 3°$, $\mathrm{IP}_{2,\mathrm{output}} = 44\,\mathrm{dBm}$ and an $\mathrm{IP}_{3,\mathrm{output}} = 24\,\mathrm{dBm}$, $\mathrm{IP}_{3,\mathrm{RF},\mathrm{output}} = 24\,\mathrm{dBm}$). Additionally, a lowpass filter phase imbalance $\bar{\phi}_\gamma = 4°$ and $\tau = 0$ were assumed.

The transmitter response for a 5 dBm input signal and the gain compression for an input signal power sweep are depicted in Figure 3.11.

(a)   (b)
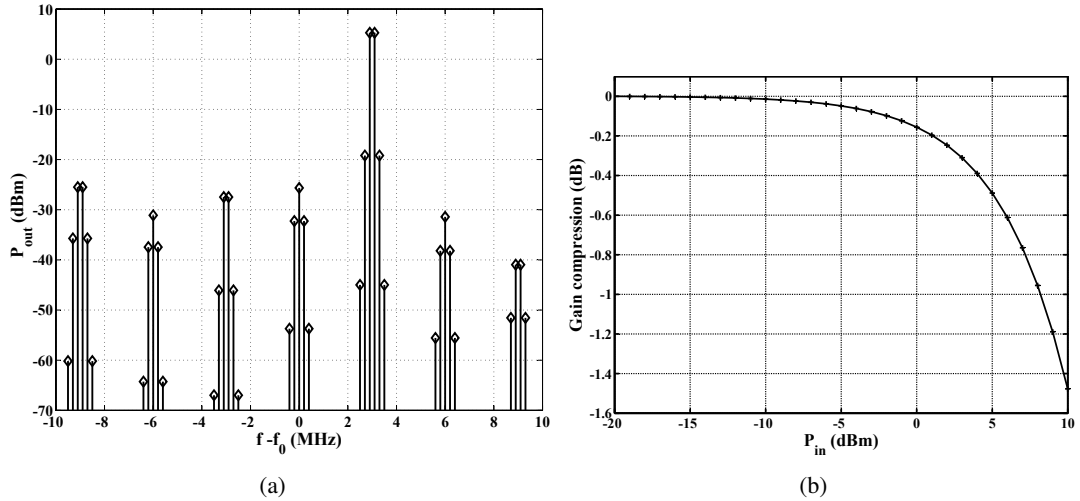
Figure 3.11: Simulation of a transmitter response on a FSTT input signal. (a) Output spectrum for an input signal at $\mathrm{P}_{\mathrm{in}} = 10\,\mathrm{dBm}$, (b) gain compression of the transmitter.

The simulated transmitter response was then compared with the approximation presented in (3.108). The differences between the predicted and simulated magnitudes and phases of the output signal components are summarized in Figure 3.12. In these plots the transmitter output signal components are identified using $A_{n,m}$. The corresponding output signal product is located at a frequency offset nf_{sp} and mf_m from the carrier.

For the desired tones (i.e., $A_{1,1}$, $\phi_{1,1}$) the maximum magnitude and phase errors are 0.02 dB and 0.08°. The prediction of the 3rd-order IMD (i.e., $A_{3,1}$, $\phi_{3,1}$) results in an error of 0.8 dB and $-1.7°$ at the maximum input power. These prediction errors correspond to a gain compression of about 1.5 dB.

Clearly, the effect of the neglected BB amplifier distortion interactions is much more severe at the distortion components than at the desired output tones. Considering higher orders of distortion will result in a further increase of the approximation error. Especially, the even- and odd-order harmonic distortion is modeled without the gain compression caused by desired signal, acting as a kind of interferer in this case. Neglecting this distortion mechanism results in a significant prediction error.

(a)   (b)
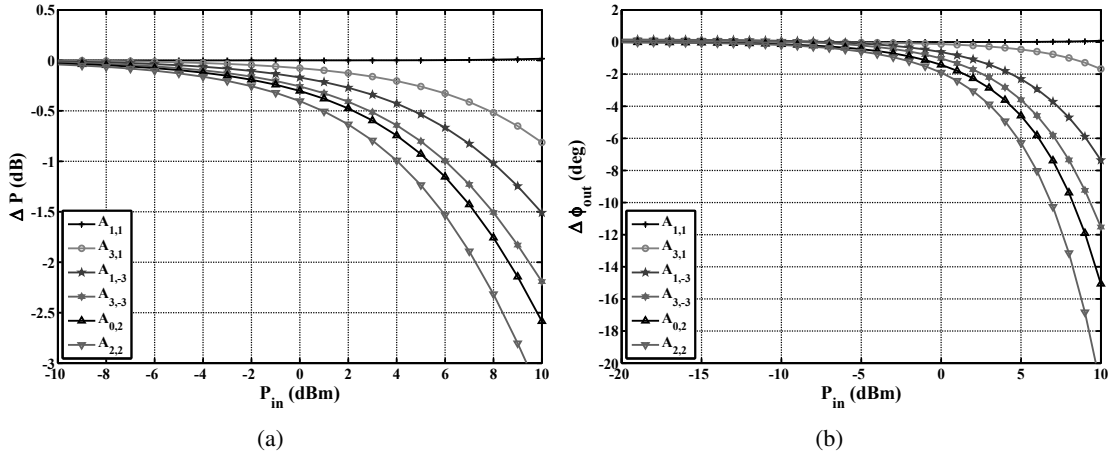
Figure 3.12: Accuracy of the transmitter FSTT response calculation. (a) Magnitude error, (b) phase error.

3.8.2 Transmitter response onto a CBTT input signal

The CBTT input signal for testing the inphase and the quadrature channel is given by:

$$
\begin{aligned}
s_{\mathrm{BB},I}(t) &= A_{\mathrm{CBTT}} \cos(2\pi f_{sp}t + \phi_{sp}) \cos(2\pi f_m t + \phi_m) \\
s_{\mathrm{BB},Q}(t) &= j A_{\mathrm{CBTT}} \cos(2\pi f_{sp}t + \phi_{sp}) \cos(2\pi f_m t + \phi_m)
\end{aligned}
\tag{3.109}
$$

In both cases the signal corresponds to the real part of the FSTT input. Therefore, the transmitter response is closely related to the results derived in the last section and will be only briefly summarized here. Additionally, the derivation is only performed for the quadrature channel. The inphase channel description is found by changing the index Q to I, setting the phase imbalance factors $\bar{\phi}_\gamma$ and θ_e to zero and multiplying the right hand side of the equations by $-j$.

Based on the CBTT input signal defined in (3.109) the BB amplifier output signal results to:

$$
\begin{aligned}
s_{\text{Amp,Q}}(t) = \ & j\Bigg[\sum_{k=1}^{N_{\text{O,BB}}}\sum_{l=1}^{N_{\text{O,BB}}}\sum_{m=\max(k,l)}^{N_{\text{O,BB}}}\frac{1}{16^{m-1}}\binom{2m-1}{m-k}\binom{2m-1}{m-l}\bar{h}_{Q,2m-1}^{2m-1}A_{\text{CBTT}}^{2m-1} \\
& \cdot\cos([2l-1][\omega_{sp}(t-\tau)+\phi_{sp}])\cos([2k-1][\omega_m(t-\tau)+\phi_m+\bar{\phi}_I+\bar{\phi}_\gamma]) \\
& +\sum_{k=1}^{N_{\text{E,BB}}}\frac{1}{16^k}\binom{2k}{k}^2\bar{h}_{Q,2k}^{2k}A_{\text{CBTT}}^{2k} \\
& +\sum_{k=1}^{N_{\text{E,BB}}}\sum_{l=k}^{N_{\text{E,BB}}}\frac{2}{16^l}\binom{2l}{l}\binom{2l}{l-k}\bar{h}_{Q,2l}^{2l}A_{\text{CBTT}}^{2l}\Big[\cos(2k[\omega_{sp}(t-\tau)+\phi_{sp}]) \\
& \qquad +\cos(2k[\omega_m(t-\tau)+\phi_m+\bar{\phi}_I+\bar{\phi}_\gamma])\Big] \\
& +\sum_{k=1}^{N_{\text{E,BB}}}\sum_{l=1}^{N_{\text{E,BB}}}\sum_{m=\max(k,l)}^{N_{\text{E,BB}}}\frac{4}{16^m}\binom{2m}{m-k}\binom{2m}{m-l}\bar{h}_{Q,2m}^{2m}A_{\text{CBTT}}^{2m} \\
& \cdot\cos(2l[\omega_{sp}(t-\tau)+\phi_{sp}])\cos(2k[\omega_m(t-\tau)+\phi_m+\bar{\phi}_I+\bar{\phi}_\gamma])\Bigg]
\end{aligned}
$$

(3.110)

By feeding this signal into the I/Q modulator it is shifted into the RF frequency range and an additional phase imbalance is added. Additionally, the signal is rotated by the LO phase. At the input of the mixer output NL the magnitude and phase of the four desired tones are calculated similar to (3.105) and (3.106):

$$
\begin{aligned}
s_{\text{Amp,Q,des.}}(t) = \ & jA_{\text{Q,des.}}\cos(\omega_{sp}(t-\tau)+\phi_{sp})\cos(\omega_m(t-\tau)+\phi_m+\bar{\phi}_I+\bar{\phi}_\gamma)e^{j(\theta_e+\varphi_{\text{LO}})} \\
A_{\text{Q,des.}} = \ & \sum_{m=1}^{N_{\text{O,BB}}}\frac{1}{16^{m-1}}\binom{2m-1}{m-1}^2\bar{h}_{Q,2m-1}^{2m-1}A_{\text{CBTT}}^{2m-1}
\end{aligned}
$$

(3.111)

It should be noted, that the AM-PM conversion introduced by the imbalance $\phi_{\text{des.}}$ at the FSTT excitation reduces to a constant phase shift in the CBTT case. By the use of $A_{\text{des.}}$ the transmitter output signal can be approximated by:

$$
\begin{aligned}
s_{\text{mod,Q}}(t) \approx \ & je^{j(\theta_e+\varphi_{\text{LO}})}g_{\text{M,1}}\Bigg[\sum_{k=1}^{N_{\text{O,BB}}}\sum_{l=1}^{N_{\text{O,BB}}}\sum_{m=\max(k,l)}^{N_{\text{O,BB}}}\frac{1}{16^{m-1}}\binom{2m-1}{m-k}\binom{2m-1}{m-l}\bar{h}_{Q,2m-1}^{2m-1} \\
& \cdot A_{\text{CBTT}}^{2m-1}\cos([2l-1][\omega_{sp}(t-\tau)+\phi_{sp}])\cos([2k-1][\omega_m(t-\tau)+\phi_m+\bar{\phi}_I+\bar{\phi}_\gamma]) \\
& +\sum_{k=1}^{(N_{\text{RF}}+1)/2}\sum_{l=1}^{(N_{\text{RF}}+1)/2}\sum_{m=\max(k,l,2)}^{(N_{\text{RF}}+1)/2}\frac{1}{16^{m-1}}\binom{2m-1}{m-k}\binom{2m-1}{m-l}\frac{g_{\text{M,2m-1}}}{g_{\text{M,1}}}A_{\text{Q,des.}}^{2m-1} \\
& \cdot\cos([2l-1][\omega_{sp}(t-\tau)+\phi_{sp}])\cos([2k-1][\omega_m(t-\tau)+\phi_m+\bar{\phi}_I+\bar{\phi}_\gamma]) \\
& +\dots\text{ (continued on the next page)}
\end{aligned}
$$

$$+ \sum_{k=1}^{N_{\mathrm{E,BB}}} \frac{1}{16^k} \binom{2k}{k}^2 \bar{h}_{Q,2k}^{2k} A_{\mathrm{CBTT}}^{2k}$$

$$+ \sum_{k=1}^{N_{\mathrm{E,BB}}} \sum_{l=k}^{N_{\mathrm{E,BB}}} \frac{2}{16^l} \binom{2l}{l} \binom{2l}{l-k} \bar{h}_{Q,2l}^{2l} A_{\mathrm{CBTT}}^{2l} \Big[\cos(2k[\omega_{sp}(t-\tau) + \phi_{sp}])$$

$$+ \cos(2k[\omega_m(t-\tau) + \phi_m + \bar{\phi}_I + \bar{\phi}_\gamma]) \Big] \tag{3.112}$$

$$+ \sum_{k=1}^{N_{\mathrm{E,BB}}} \sum_{l=1}^{N_{\mathrm{E,BB}}} \sum_{m=\max(k,l)}^{N_{\mathrm{E,BB}}} \frac{4}{16^m} \binom{2m}{m-k} \binom{2m}{m-l} \bar{h}_{Q,2m}^{2m} A_{\mathrm{CBTT}}^{2m}$$

$$\cdot \cos(2l[\omega_{sp}(t-\tau) + \phi_{sp}]) \cos(2k[\omega_m(t-\tau) + \phi_m + \bar{\phi}_I + \bar{\phi}_\gamma]) \Big]$$

3.8.3 Power normalization

As sketched at the beginning of Section 3.8 the transmitter nonlinearity identification process is based on FSTT and CBTT power sweep measurements. Depending on the application of the extracted parameter set a normalization of the measurement results is required. If the evaluated coefficients are used for modeling the transmitter behavior the tone magnitudes can be directly derived from the measured traces. In case the identified parameters are used for compensating the distortion of the transmitter a normalization of the measurement results is required. This requirement leads to a loss of the linkage between the magnitudes used for extracting the parameters and the absolute level of the corresponding power measurement results. Hence, all measurements are interpreted as results captured at the output of the memoryless nonlinear transmitter model presented in Figure 3.10. The overall gain of this structure is usually set to 0 dB. For evaluating the correct scaling factor FSTT and CBTT power sweeps close to the carrier are used. Usually the same measurements are also applied for the mixer output NL parameterization. The power of the two desired tones in back-off operation are then scaled to match the power of the corresponding transmitter model output in the distortion-free case. This scaling includes two assumptions: the response of the transmitter close to the carrier is selected as the reference one; the gain-compression of the transmitter in the back-off is negligible. These assumptions are important as the scaling of the measurements is the first task in the parameterization procedure and may not be based on previous extraction results. The evaluated scaling factors are then applied to all measurement results required for the nonlinear transmitter characterization. Thus, it is of great importance that all transmitter output measurements show the correct absolute power!

The calculation of the magnitudes from the scaled power measurements is based on the distortion-free memoryless transmitter model. Considering output signal components $A_{n,m}$, $m, n > 0$ the desired relationship for the FSTT and the CBTT results to:

$$\begin{aligned} s_{n,m}(t) &= A_{\mathrm{FSTT},n,m} \cos(n\,\omega_{sp}(t-\tau)) e^{jm\,\omega_m(t-\tau)} e^{j\omega_0 t} \\ \mathrm{P}_{\mathrm{FSTT},n,m} &= \frac{A_{n,m}^2}{2Z_0} \end{aligned} \tag{3.113}$$

$$\begin{aligned} s_{n,m}(t) &= A_{\mathrm{CBTT}n,m} \cos(n\,\omega_{sp}(t-\tau)) \cos(m\,\omega_m(t-\tau)) e^{j\omega_0 t} \\ \mathrm{P}_{\mathrm{CBTT},n,m} &= \frac{A_{n,m}^2}{8Z_0} \end{aligned} \tag{3.114}$$

where Z_0 is the characteristic impedance present at the power measurements. If $n = 0$, as for example at the center HD_2 distortion component, the relationship in (3.114) results to $P_{0,m} = A^2_{CBTT,0,m}/(2Z_0)$.

In a next step the target output magnitude has to be defined and the imbalance impact has to be estimated. For the general case the maximum input and the maximum linear transmitter output magnitude are represented by $A_{in,max}$ and $A_{out,max}$, respectively. The ratio $A_{out,max}/A_{in,max}$ sets the desired transmitter gain for the parameter extraction. Therefore, the maximum output power is given by:

$$
\begin{aligned}
P_{FSTT,max} &= \frac{A_{out,max}\cdot^2}{2Z_0} \\
P_{CBTT,max} &= \frac{A_{out,max}\cdot^2}{8Z_0}
\end{aligned}
\tag{3.115}
$$

At the linear transmitter the imbalance distortion may reduce the transmitter gain. Based on the beforehand characterized imbalance parameters (compare Section 3.6) this impact is estimated as:

$$
\gamma_{eff} = \frac{1}{2}\left|1 + \hat{\gamma}(j2\pi f_m)\right|
\tag{3.116}
$$

During the power sweep the input signal is applied to the transmitter scaled to $P_1, P_2, \ldots, P_K$ power values. It is assumed that these power levels are sorted in ascending order. In the FSTT case the corresponding output magnitudes are identified by $A_{FSTT,n,m,P_1}, A_{FSTT,n,m,P_2}, \ldots, A_{FSTT,n,m,P_K}$. The same notation is also applied for the CBTT measurements. Combining these results the power scaling factor for the FSTT measurements is given by:

$$
\Delta P_{FSTT} = \frac{P_1}{P_K}\frac{P_{FSTT,max}}{P_{FSTT,1,1,P_1}}\left|\gamma_{eff}\right|^2
\tag{3.117}
$$

where $P_{FSTT,1,1,P_1}$ represents the power of $A_{FSTT,1,1,P_1}$. In the CBTT case the power scaling factors results to:

$$
\Delta P_{CBTT} = \frac{P_1}{P_K}\frac{2P_{CBTT,max}}{P_{CBTT,I,1,1,P_1} + |\hat{\gamma}(j2\pi f_m)|^{-2}P_{CBTT,Q,1,1,P_1}}
\tag{3.118}
$$

The square root of these factors are used for the normalization of the magnitude measurements.

3.8.4 CBTT delay and phase extraction

Even if the main information for the mixer output NL extraction is taken from the FSTT measurements the phase information from the CBTT power sweeps is also required for this task. Therefore, the extraction of the phases from the CBTT measurements is discussed as initial step of the nonlinear parameter identification.

For efficiently explaining the parameter extraction process the measurement results are combined in vectors. The vector $\mathbf{A}_{CBTT,Q,n,m}$ summarizes the K normalized magnitudes and phases of the quadrature branch CBTT power sweep output signal component located at nf_{sp} and mf_m:

$$
\mathbf{A}_{CBTT,Q,n,m} = \begin{pmatrix} A_{CBTT,Q,n,m,P_1}e^{j\phi_{CBTT,Q,n,m,P_1}} \\ A_{CBTT,Q,n,m,P_2}e^{j\phi_{CBTT,Q,n,m,P_2}} \\ \vdots \\ A_{CBTT,Q,n,m,P_K}e^{j\phi_{CBTT,Q,n,m,P_K}} \end{pmatrix}
\tag{3.119}
$$

Here, the phase factor $\phi_{\text{CBTT},Q,n,m,\text{P}_k}$ combines all phase shifts of the corresponding output signal component at the kth power level (exemplified for $N_{\text{RF}} = 1$; m, n odd):

$$\phi_{\text{CBTT},Q,n,m,\text{P}_k} = (\pi/2) + n\phi_{sp} + m(\phi_m + \bar{\phi}_I + \bar{\phi}_\gamma) - (n\omega_{sp} + m\omega_m)\tau + \varphi_{\text{LO}} + \theta_e + \angle g_{\text{M},1} \quad (3.120)$$

At this notation the indices n and m can be positive or negative integers for covering all tones of the output signal spectrum. The kth element of the vector $\mathbf{A}_{\text{CBTT},Q,n,m}$ is accessed by $\mathbf{A}_{\text{CBTT},Q,n,m}(k)$.

The response of the transmitter onto a CBTT input signal at the quadrature branch was developed in Section 3.8.2. Using (3.120) the linear approximation of the four desired tone phases are found by choosing $m = \pm 1$ and $n = \pm 1$. Using these four cases it is clear that not all contributing phase components can be distinguished. Three equivalent phases are used for representing the phase response:

$$\begin{aligned}
\phi_{\text{CBTT},Q,n,m,\text{P}_k} &= n\phi_{\text{BB},sp,Q} + m\phi_{\text{BB},m,Q} + \phi_{\text{RF},Q} \\
\phi_{\text{BB},sp,Q} &= \phi_{sp} - \omega_{sp}\tau \\
\phi_{\text{BB},m,Q} &= \phi_m - \omega_m\tau + \bar{\phi}_I + \bar{\phi}_\gamma \\
\phi_{\text{RF},Q} &= (\pi/2) + \varphi_{\text{LO}} + \theta_e + \angle g_{\text{M},1}
\end{aligned} \quad (3.121)$$

Here, $\phi_{\text{BB},m,Q}$ summarized all components added by the analog signal processing in the baseband. This phase factor changes its sign with the sign of the parameter m but independent of n. In a similar way $\phi_{\text{BB},sp,Q}$ combines the phase parameters independent of the index m. $\phi_{\text{RF},Q}$ incorporates all RF phase contributions. This factor stays constant while changing the sign of m or n. These considerations are used for extracting the phase components from the measurement results. For a valid approximation of the linear transmitter response $\phi_{\text{BB},m,Q}$ and $\phi_{\text{RF},Q}$ are taken from measurements in back-off operation. Due to this reason only the four desired tones are used for the phase extraction. The IMD and HD components of the transmitter in back-off are significantly deteriorated by measurement noise and, therefore, omitted.

In a first step the transmitter delay is extracted. In Figure 3.10 the time delay was placed at the input of the structure. It is important to note that the location of the time delay within the structure does not influence the model behavior. Just the delay introduced at the two baseband branches must be the same. This behavior is explainable as only time invariant devices are used for the transmitter description. Another way to argue this behavior is by using the shifting property of distributions [115]. Therefore, the transmitter delay can be directly extracted from the measured response independent of the location of the delay within the underlying structure. The delay introduces a dependent change of the tone phases. To evaluate the delay the phases of the four desired tones are recorded over a frequency sweep. In case the transmitter shows a long time delay the frequency spacing may not be too large. Otherwise, the slope of the tone phases may show positive jumps or even a positive sign. In case of a negative slope exhibiting some positive phase jumps a negative extension of the phase slope has to be performed. After accomplishing this task the delay can be evaluated by the slope of the regression line described by the tone phases. Performing this process for all four desired tones and averaging the results provides a further increase of the identification accuracy. The impact of the delay is then removed from all measured results. At all further steps in the parameter extraction process only the delay compensated measurements are used.

Thereafter, the phase factors $\phi_{\text{BB},sp,Q}$ are extracted from the measured tone phases. Based on the CBTT signal definition (3.88) they are derived from the difference of the corresponding tone phases. This calculation only provides the desired result if both phases $\phi_{\text{CBTT},\pm1,1}(k) = \angle\mathbf{A}_{\text{CBTT},Q,\pm1,1}(k)$

show the same sign. If this is not the case one of the tone phases must be shifted by 2π.

$$\forall \, \mathrm{sign}(\phi_{\mathrm{CBTT},+1,1}(k)) \neq \mathrm{sign}(\phi_{\mathrm{CBTT},-1,1}(k)) \rightarrow$$
$$\begin{cases} \phi_{\mathrm{CBTT},+1,1}(k) = \phi_{\mathrm{CBTT},+1,1}(k) + 2\pi, & \text{if } \mathrm{sign}(\phi_{\mathrm{CBTT},+1,1}(k)) < 0 \\ \phi_{\mathrm{CBTT},-1,1}(k) = \phi_{\mathrm{CBTT},-1,1}(k) + 2\pi, & \text{if } \mathrm{sign}(\phi_{\mathrm{CBTT},-1,1}(k)) < 0 \end{cases} \quad (3.122)$$

All elements of the vectors $\phi_{\mathrm{CBTT},\pm1,\pm1}$ are considered for the estimation of $\phi_{\mathrm{BB},sp,Q}$, as this parameter is not altered by the transmitters' AM-PM conversion:

$$\begin{aligned} \hat{\phi}^{(+)}_{\mathrm{BB},sp,Q} &= \tfrac{1}{2K} \mathbf{1}^T \cdot \left(\phi_{\mathrm{CBTT},+1,1} - \phi_{\mathrm{CBTT},-1,1} \right) \\ \hat{\phi}^{(-)}_{\mathrm{BB},sp,Q} &= \tfrac{1}{2K} \mathbf{1}^T \cdot \left(\phi_{\mathrm{CBTT},+1,-1} - \phi_{\mathrm{CBTT},-1,-1} \right) \end{aligned} \quad (3.123)$$

Here $\hat{\phi}^{(+)}_{\mathrm{BB},sp,Q}$ represents the identification result from the two tones located above the carrier. The vector $\mathbf{1}$ incorporates a column vector with all elements set to one. Using (3.123) for the calculation of $\hat{\phi}^{(\pm)}_{\mathrm{BB},sp,Q}$ the resulting parameters are periodic with π. For a non-ambiguous evaluation of ϕ_{sp} from (3.88) the validity range of this phase factor is limited to, for example, $-\pi/2 \leq \hat{\phi}^{(\pm)}_{\mathrm{BB},sp,Q} < \pi/2$. In cases $\hat{\phi}^{(\pm)}_{\mathrm{BB},sp,Q}$ lies outside the validity range it has to be shifted by π. After this correction $\hat{\phi}_{\mathrm{BB},sp,Q}$ is taken as the mean of the two identification results. The identified $\hat{\phi}_{\mathrm{BB},sp,Q}$ has to be equal to ϕ_{sp} used during the signal generation up to a residual phase measurement error. As highlighted in (3.121) an incorrectly compensated time delay may cause a deviation between the specified and the estimated $\phi_{\mathrm{BB},sp,Q}$. In case of differences between the two phase factors the overall delay is underestimated by a multiple of the delay given by the frequency spacing during the frequency sweep. By iteratively increasing the overall time delay and evaluating $\hat{\phi}_{\mathrm{BB},sp,Q}$ for the updated phase measurements the correct delay is found.

For extracting $\phi_{\mathrm{BB},Q}$ and $\phi_{\mathrm{RF},Q}$ initially the common phase components, independent of the sign of n, are determined:

$$\begin{aligned} \hat{\phi}^{(+)}_{C,Q} &= \left(\tfrac{1}{2} \phi_{\mathrm{CBTT},+1,1}(1) + \tfrac{1}{2} \phi_{\mathrm{CBTT},-1,1}(1) \right)_{2\pi} \\ \hat{\phi}^{(-)}_{C,Q} &= \left(\tfrac{1}{2} \phi_{\mathrm{CBTT},+1,-1}(1) + \tfrac{1}{2} \phi_{\mathrm{CBTT},-1,-1}(1) \right)_{2\pi} \end{aligned} \quad (3.124)$$

In this equation $(\,\cdot\,)_{2\pi}$ performs the modulo 2π operation on the enclosed value. As the AM-PM conversion adds to this phase factor only the back-off measurement results are used. In contrast to $\hat{\phi}_{\mathrm{BB},sp,Q}$ no limitation of the area of validity is applied for $\phi^{(+)}_{C,Q}, \phi^{(-)}_{C,Q}$. But still the derived phases are periodic with π. Hence, a cross-check is required to guarantee that the extracted phase factors represent the corresponding tone phases. Due to the validity range constraint on $\hat{\phi}_{\mathrm{BB},sp,Q}$ a phase shift by π may be required. To cope with the noisy measurement data this cross-check is implemented by the comparison of two error functions:

$$\begin{aligned} \varepsilon^{(+)}_{C,Q,1} &= \left| \phi_{\mathrm{CBTT},-1,1}(1) - (-\hat{\phi}_{\mathrm{BB},sp,Q} + \hat{\phi}^{(+)}_{C,Q})_{2\pi} \right| + \left| \phi_{\mathrm{CBTT},+1,1}(1) - (\hat{\phi}_{\mathrm{BB},sp,Q} + \hat{\phi}^{(+)}_{C,Q})_{2\pi} \right| \\ \varepsilon^{(+)}_{C,Q,2} &= \left| \phi_{\mathrm{CBTT},-1,1}(1) - (-\hat{\phi}_{\mathrm{BB},sp,Q} + \hat{\phi}^{(+)}_{C,Q} + \pi)_{2\pi} \right| \\ &\quad + \left| \phi_{\mathrm{CBTT},+1,1}(1) - (\hat{\phi}_{\mathrm{BB},sp,Q} + \hat{\phi}^{(+)}_{C,Q} + \pi)_{2\pi} \right| \end{aligned}$$

$$(3.125)$$

If $\varepsilon_{C,Q,2}^{(+)} < \varepsilon_{C,Q,1}^{(+)}$ the identification results must be shifted: $\hat{\phi}_{C,Q}^{(+)} = (\hat{\phi}_{C,Q}^{(+)} + \pi)_{2\pi}$. The same steps are also performed for $\hat{\phi}_{C,Q}^{(-)}$. The phase factors $\phi_{\mathrm{BB},Q}$ and $\phi_{\mathrm{RF},Q}$ are now extracted from these results:

$$
\begin{aligned}
\hat{\phi}_{\mathrm{BB},Q} &= \left(\tfrac{1}{2}\hat{\phi}_{C,Q}^{(+)} - \tfrac{1}{2}\hat{\phi}_{C,Q}^{(-)} \right)_{2\pi} \\
\hat{\phi}_{\mathrm{RF},Q} &= \left(\tfrac{1}{2}\hat{\phi}_{C,Q}^{(+)} + \tfrac{1}{2}\hat{\phi}_{C,Q}^{(-)} \right)_{2\pi}
\end{aligned}
\tag{3.126}
$$

Also these phase components are periodic in π. Additionally, the measurements of the four desired tones cannot be used for the cross-check as both, $\hat{\phi}_{\mathrm{BB},Q}$ and $\hat{\phi}_{\mathrm{RF},Q}$, are extracted from the common phase part $\hat{\phi}_{C,Q}^{(+)}, \hat{\phi}_{C,Q}^{(-)}$. There are phase combinations of $\hat{\phi}_{\mathrm{BB},Q}$ and $\hat{\phi}_{\mathrm{RF},Q}$ at which a test equivalent to (3.125) shows no difference in the error functions. In such cases the measurement noise may turn the balance between the two solutions. For that reason the phase of a strong even-order distortion component should be used instead. When considering the middle, 2nd-order HD product (e.g., $A_{0,\pm2}$) the error terms result to:

$$
\begin{aligned}
\varepsilon_{\mathrm{BB},Q,1} &= \left| \phi_{\mathrm{CBTT},Q,0,2,\mathrm{P}_K} - (2\hat{\phi}_{\mathrm{BB},Q} + \hat{\phi}_{\mathrm{RF},Q})_{2\pi} \right| \\
&\quad + \left| \phi_{\mathrm{CBTT},Q,0,-2,\mathrm{P}_K} - (-2\hat{\phi}_{\mathrm{BB},Q} + \hat{\phi}_{\mathrm{RF},Q})_{2\pi} \right| \\
\varepsilon_{\mathrm{BB},Q,2} &= \left| \phi_{\mathrm{CBTT},Q,0,2,\mathrm{P}_K} - (2\hat{\phi}_{\mathrm{BB},Q} + \hat{\phi}_{\mathrm{RF},Q} + \pi)_{2\pi} \right| \\
&\quad + \left| \phi_{\mathrm{CBTT},Q,0,-2,\mathrm{P}_K} - (-2\hat{\phi}_{\mathrm{BB},Q} + \hat{\phi}_{\mathrm{RF},Q} + \pi)_{2\pi} \right|
\end{aligned}
\tag{3.127}
$$

It should be noted, that the HD component corresponding to the highest input power was used for the cross-check. This approach is advantageous if the measurement noise impact is dominant compared to the AM-PM conversion. In case $\varepsilon_{\mathrm{BB},Q,2} < \varepsilon_{\mathrm{BB},Q,1}$ the phase factors have to be shifted by π:

$$
\begin{aligned}
\hat{\phi}_{\mathrm{BB},Q} &= \left(\hat{\phi}_{\mathrm{BB},Q} + \pi \right)_{2\pi} \\
\hat{\phi}_{\mathrm{RF},Q} &= \left(\hat{\phi}_{\mathrm{RF},Q} + \pi \right)_{2\pi}
\end{aligned}
\tag{3.128}
$$

At the quadrature branch the impact of the $\pi/2$ I/Q mixer phase shift is still present. For a $\hat{\phi}_{\mathrm{RF},Q}$ equivalent to the definition in (3.121) this phase shift must be subtracted.

The same steps are also applied for extracting $\hat{\phi}_{sp,I}$, $\hat{\phi}_{\mathrm{BB},I}$ and $\hat{\phi}_{\mathrm{RF},I}$ from the inphase branch measurements. Combining the phase factors of the two channels allows the evaluation of the phase imbalance and the lowpass filter phase shift:

$$
\begin{aligned}
\hat{\bar{\phi}}_{\gamma} &= \left(\hat{\phi}_{\mathrm{BB},Q} - \hat{\phi}_{\mathrm{BB},I} \right)_{2\pi} \\
\hat{\theta}_e &= \left(\hat{\phi}_{\mathrm{RF},Q} - \hat{\phi}_{\mathrm{RF},I} \right)_{2\pi} \\
\hat{\bar{\phi}}_I &= \left(\hat{\phi}_{\mathrm{BB},I} - \phi_m \right)_{2\pi}
\end{aligned}
\tag{3.129}
$$

The phase imbalance coefficients evaluated in this way can be compared to the one extracted by canceling the single-tone input signal (compare Section 3.6). Significant differences highlight the presence of errors in one of the two identification processes. Slight difference may exist between $\hat{\bar{\phi}}_{\gamma}$ identified in (3.129) and according to Section 3.6.2 as the above expression provides only the odd symmetric phase

imbalance. The optimization based approach for identifying the phase imbalance covers also the even symmetric contribution.

It is interesting to note, that in the transmitter case it is possible to calculate the phase shift of the two BB lowpass filters. On the other hand the LO phase rotation cannot be separated from the phase shift introduced by $g_{\mathrm{M},1}$.

3.8.5 Mixer output nonlinearity identification

The analytical approximation of the transmitter output signal presented in Section 3.8.1 is the basis for the extraction of the output nonlinearity. The whole identification process of this part can be divided in the following tasks:

- Evaluation of the transmitter gain

- Estimation of the BB amplifier contribution to the output IMD

- Identification of the mixer output nonlinearity

These tasks are performed based on the transmitter response onto a FSTT excitation signal. One default for this identification process is the assumption of a mixer output NL gain of $0\,\mathrm{dB}$. This assumption is required as the linear gain of the whole structure can be arbitrarily allocated between the BB and the RF block. By setting $\tilde{g}_{\mathrm{M},1} = 1$ the complete linear gain is represented by the BB nonlinearities. The mixer output NL models only AM-AM and AM-PM conversion. Hence, the NL identification process will not provide the "true" mixer output coefficients $g_{\mathrm{M},1}, g_{\mathrm{M},3}, ...$ but normalized ones $1, g_{\mathrm{M},3}/g_{\mathrm{M},1}, ...$ This approach coincides also with the fact mentioned in the last section, that the LO phase rotation and the $g_{\mathrm{M},1}$ phase shift cannot be separated.

For the evaluation of the (linear) transmitter gain a polynomial covering the odd order coefficients is identified. This strategy improves the gain identification accuracy at the presence of AM-AM conversion. The IMD components up to $N_{\mathrm{ID,RF}}$ order are considered for this task. The $(2K(N_{\mathrm{ID,RF}} + 1)/2) \times 1$ vector, representing the measured transmitter response, is defined as:

$$\mathbf{Y} = \begin{pmatrix} \mathbf{A}_{\mathrm{FSTT},(-N_{\mathrm{ID,RF}}),1} \\ \mathbf{A}_{\mathrm{FSTT},(-N_{\mathrm{ID,RF}}+2),1} \\ \vdots \\ \mathbf{A}_{\mathrm{FSTT},-1,1} \\ \mathbf{A}_{\mathrm{FSTT},1,1} \\ \vdots \\ \mathbf{A}_{\mathrm{FSTT},(N_{\mathrm{ID,RF}}),1} \end{pmatrix} \tag{3.130}$$

Here, the FSTT output signal components are arranged in vectors in the same way as exemplified for the CBTT case in (3.119). The powers of the gain compressed input signal are summarized by the vectors:

$$\begin{aligned} \mathbf{H}^{(+)}_{\mathrm{RF},l,m} &= \tfrac{8}{16^m} \binom{2m-1}{m-1}\binom{2m-1}{m-l} \mathbf{A}^{2m-1}_{\mathrm{FSTT}} e^{j(\phi_m+(2l-1)\phi_{sp})} \\ \mathbf{H}^{(-)}_{\mathrm{RF},l,m} &= \tfrac{8}{16^m} \binom{2m-1}{m-1}\binom{2m-1}{m-l} \mathbf{A}^{2m-1}_{\mathrm{FSTT}} e^{j(\phi_m-(2l-1)\phi_{sp})} \end{aligned} \tag{3.131}$$

where $\mathbf{A}_{\text{FSTT}}$ summarizes the input signal magnitudes applied during the power sweep. The mth power of this vector is derived by performing m^{th} times the Hadamard product $\mathbf{A}_{\text{FSTT}} \circ \mathbf{A}_{\text{FSTT}} \circ \cdots \circ \mathbf{A}_{\text{FSTT}}$.

The vectors defined in (3.131) are now used for composing the $(2K N_{\text{O,ID,RF}}) \times N_{\text{O,ID,RF}}$ matrix $\mathbf{H}_{\text{RF}}$:

$$\mathbf{H}_{\text{RF}} = \begin{pmatrix} & & & & \mathbf{H}^{(-)}_{\text{RF},N_{\text{O,ID,RF}},N_{\text{O,ID,RF}}} \\ & & \iddots & & \vdots \\ & \mathbf{H}^{(-)}_{\text{RF},2,2} & \cdots & & \mathbf{H}^{(-)}_{\text{RF},2,N_{\text{O,ID,RF}}} \\ \mathbf{H}^{(-)}_{\text{RF},1,1} & \mathbf{H}^{(-)}_{\text{RF},1,2} & \cdots & & \mathbf{H}^{(-)}_{\text{RF},1,N_{\text{O,ID,RF}}} \\ \mathbf{H}^{(+)}_{\text{RF},1,1} & \mathbf{H}^{(+)}_{\text{RF},1,2} & \cdots & & \mathbf{H}^{(+)}_{\text{RF},1,N_{\text{O,ID,RF}}} \\ & \mathbf{H}^{(+)}_{\text{RF},2,2} & \cdots & & \mathbf{H}^{(+)}_{\text{RF},2,N_{\text{O,ID,RF}}} \\ & & \ddots & & \vdots \\ & & & & \mathbf{H}^{(+)}_{\text{RF},N_{\text{O,ID,RF}},N_{\text{O,ID,RF}}} \end{pmatrix} \tag{3.132}$$

Here, the abbreviation $N_{\text{O,ID,RF}} = (N_{\text{ID,RF}} + 1)/2$ was used. The coefficients to be estimated are combined by the vector $\hat{\boldsymbol{\lambda}}_{lin} = (\hat{g}_1 \, \hat{g}_3 \, \ldots \, \hat{g}_{N_{\text{O,ID,RF}}})^T$. These coefficients can be now evaluated by solving the following equation:

$$\mathbf{H}^H_{\text{RF}} \mathbf{H}_{\text{RF}} \hat{\boldsymbol{\lambda}}_{lin} = \mathbf{H}^H_{\text{RF}} \mathbf{Y} \tag{3.133}$$

where $\mathbf{H}^H_{\text{RF}}$ denotes the conjugate transpose of $\mathbf{H}_{\text{RF}}$. The linear transmitter gain is found by selecting the first element of the coefficient vector $\hat{\alpha}_{d,\text{RF},1} = \hat{\boldsymbol{\lambda}}_{lin}(1)$.

The nonlinear response of the BB amplifiers and the mixer input NL is now derived from the 3rd-order harmonic distortion centered at -3f_m. Even if this signal shows a gain compression and AM-PM conversion introduced by the presence of the two desired tones, it allows an estimation of the performance of the BB devices. Following the FSTT response derivation in Section 3.8.1 the number of odd-order coefficients used for modeling the BB response is represented by $N_{\text{O,BB}}$. It is advantageous to increase this number $N_{O,ID,\text{BB}} \geq N_{\text{O,BB}}$ to cope with the gain compression due to the desired tones' interactions.

Similar to the evaluation of the linear transmitter gain the measured output amplitudes are summarized by the $(2K(N_{\text{O,ID,BB}} + 1)/2) \times 1$ vector:

$$\mathbf{Y} = \begin{pmatrix} \mathbf{A}_{\text{FSTT},(-2N_{\text{O,ID,BB}}+1),-3} \\ \mathbf{A}_{\text{FSTT},(-2N_{\text{O,ID,BB}}+3),-3} \\ \vdots \\ \mathbf{A}_{\text{FSTT},-1,-3} \\ \mathbf{A}_{\text{FSTT},1,-3} \\ \vdots \\ \mathbf{A}_{\text{FSTT},(2N_{\text{O,ID,BB}}-1),-3} \end{pmatrix} \tag{3.134}$$

The modeled BB response is incorporated in the $(2KN_{\mathrm{O,ID,BB}}) \times (N_{\mathrm{O,ID,BB}} - 1)$ matrix:

$$
\mathbf{H}_{\mathrm{HD}} = \begin{pmatrix}
 & & & & \mathbf{H}^{(-)}_{\mathrm{HD},N_{\mathrm{O,ID,BB}},N_{\mathrm{O,ID,BB}}} \\
 & \iddots & & & \vdots \\
\mathbf{H}^{(-)}_{\mathrm{HD},2,2} & \cdots & & & \mathbf{H}^{(-)}_{\mathrm{HD},2,N_{\mathrm{O,ID,BB}}} \\
\mathbf{H}^{(-)}_{\mathrm{HD},1,2} & \cdots & & & \mathbf{H}^{(-)}_{\mathrm{HD},1,N_{\mathrm{O,ID,BB}}} \\
\mathbf{H}^{(+)}_{\mathrm{HD},1,2} & \cdots & & & \mathbf{H}^{(+)}_{\mathrm{HD},1,N_{\mathrm{O,ID,BB}}} \\
\mathbf{H}^{(+)}_{\mathrm{HD},2,2} & \cdots & & & \mathbf{H}^{(+)}_{\mathrm{HD},2,N_{\mathrm{O,ID,BB}}} \\
 & \ddots & & & \vdots \\
 & & & & \mathbf{H}^{(+)}_{\mathrm{HD},N_{\mathrm{O,ID,BB}},N_{\mathrm{O,ID,BB}}}
\end{pmatrix}
\tag{3.135}
$$

where the vectors $\mathbf{H}^{(\pm)}_{\mathrm{HD},l,m}$ are composed as follows:

$$
\begin{aligned}
\mathbf{H}^{(+)}_{\mathrm{HD},l,m} &= \tfrac{8}{16^m} \binom{2m-1}{m-2}\binom{2m-1}{m-l} \mathbf{A}^{2m-1}_{\mathrm{FSTT}} e^{j(-3\phi_m + (2l-1)\hat{\phi}_{sp})} \\
\mathbf{H}^{(-)}_{\mathrm{HD},l,m} &= \tfrac{8}{16^m} \binom{2m-1}{m-2}\binom{2m-1}{m-l} \mathbf{A}^{2m-1}_{\mathrm{FSTT}} e^{j(-3\phi_m - (2l-1)\hat{\phi}_{sp})}
\end{aligned}
\tag{3.136}
$$

Based on these definitions the coefficient vector $\hat{\boldsymbol{\lambda}}_{\mathrm{HD}}$ is extracted by solving the equation:

$$
\mathbf{H}^H_{\mathrm{HD}}\mathbf{H}_{\mathrm{HD}}\hat{\boldsymbol{\lambda}}_{\mathrm{HD}} = \mathbf{H}^H_{\mathrm{HD}}\mathbf{Y}
\tag{3.137}
$$

The estimated NL BB coefficient located at the first $N_{\mathrm{O,BB}}$ elements of the vector $\hat{\boldsymbol{\lambda}}_{\mathrm{HD}}$:

$$
\hat{\alpha}_{d,\mathrm{HD},2p-1} = \hat{\boldsymbol{\lambda}}_{\mathrm{HD}}(p-1) \qquad p = 2 \ldots N_{\mathrm{O,BB}}
\tag{3.138}
$$

The identification results of (3.133) and (3.137) must now be combined for representing the BB amplifier response. This step is not straightforward, as the different phase shifts at these coefficients must be compensated first. The phase of the parameters $\alpha_{d,\mathrm{RF},1}$ and $\alpha_{d,\mathrm{HD},2p-1}$ are grouped in the same way as applied for the CBTT phase extraction in Section 3.8.4:

$$
\begin{aligned}
\angle\alpha_{d,\mathrm{RF},1} &= \phi_{\mathrm{BB,FSTT}} + \phi_{\mathrm{RF,FSTT}} \\
\angle\alpha_{d,\mathrm{HD},2p-1} &= (-1)^{p-1}(2p-1)\phi_{\mathrm{BB,FSTT}} + \phi_{\mathrm{RF,FSTT}} \pm \pi
\end{aligned}
\tag{3.139}
$$

At the $\alpha_{d,HD,2p-1}$ phase the factor $\pm\pi$ represents the impact of negative coefficients $\bar{h}^{2p-1}_{I,2p-1}$. The parameters $\phi_{\mathrm{BB,FSTT}}$ and $\phi_{\mathrm{RF,FSTT}}$ are on their parts composed of the following phase shifts:

$$
\begin{aligned}
\phi_{\mathrm{BB,FSTT}} &= \bar{\phi}_I + \angle(1 + |\bar{\gamma}|e^{j\bar{\phi}_\gamma}) \\
\phi_{\mathrm{RF,FSTT}} &= \varphi_{\mathrm{LO}} + \angle g_{\mathrm{M},1} + \angle(1 + |\bar{\gamma}|e^{j\theta_e})
\end{aligned}
\tag{3.140}
$$

It is important to note that the factor ϕ_m was not considered at $\phi_{\mathrm{BB,FSTT}}$ as the presented identification approach removes this contribution.

Based on (3.139) the phases of the estimated coefficients can be used for extracting $\phi_{\mathrm{BB,FSTT}}$ and $\phi_{\mathrm{RF,FSTT}}$:

$$
\begin{aligned}
\hat{\phi}_{\mathrm{BB,FSTT},2p-1} &= \tfrac{1}{(-1)^{p-1}(2p-1)-1}\left(\angle\hat{\alpha}_{d,\mathrm{HD},2p-1} - \angle\hat{\alpha}_{d,\mathrm{RF},1}\right) + (0\,1\,-1)^T\pi \\
\hat{\phi}_{\mathrm{RF,FSTT},2p-1} &= \tfrac{1}{(-1)^p(2p-1)+1}\left(\angle\hat{\alpha}_{d,\mathrm{HD},2p-1} + (-1)^p(2p-1)\angle\hat{\alpha}_{d,\mathrm{RF},1}\right) + (0\,1\,-1)^T\pi
\end{aligned}
\tag{3.141}
$$

These vectors provide three results corresponding to a positive or a negative coefficient $\bar{h}_{I,2p-1}^{2p-1}$. For finding the correct solution the proper representation of $\angle \hat{\alpha}_{d,\mathrm{RF},1}$ and $\hat{\phi}_{\mathrm{BB,FSTT}}$ is evaluated. The (estimated) BB phase shift $\hat{\phi}_{\mathrm{BB,est.}}$ is calculated using the CBTT phase extraction and imbalance characterization results obtained beforehand:

$$\hat{\phi}_{\mathrm{BB,est.}} = \left(\hat{\phi}_{\mathrm{BB},I} - \phi_m + \angle \left[1 + |\hat{\bar{\gamma}}| e^{j\hat{\bar{\phi}}_\gamma} \right] \right)_{2\pi} \tag{3.142}$$

Using this phase factor the following error vector is composed:

$$\begin{aligned} \varepsilon_{\mathrm{BB,FSTT},2p-1} &= \left| \frac{1}{\hat{\phi}_{\mathrm{BB,est.}}} (\hat{\boldsymbol{\phi}}_{\mathrm{BB,FSTT},2p-1} - \hat{\phi}_{\mathrm{BB,est.}})_{2\pi} \right| \\ &+ \left| \frac{1}{\angle \hat{\alpha}_{d,\mathrm{RF},1}} (\hat{\boldsymbol{\phi}}_{\mathrm{BB,FSTT},2p-1} + \hat{\boldsymbol{\phi}}_{\mathrm{RF,FSTT},2p-1} - \angle \hat{\alpha}_{d,\mathrm{RF},1})_{2\pi} \right| \end{aligned} \tag{3.143}$$

The smallest element of this vector corresponds to the correct result in (3.141). This evaluation is performed for all coefficients $\hat{\alpha}_{d,\mathrm{HD},2p-1}$. The process provides $N_{\mathrm{O,BB}} - 1$ parameters $\hat{\phi}_{\mathrm{BB,FSTT},2p-1}$, $\hat{\phi}_{\mathrm{RF,FSTT},2p-1}$. As highlighted in (3.140) $\hat{\phi}_{\mathrm{BB,FSTT},2p-1}$ consists of the inphase channel lowpass filter phase shift and the effective lowpass filter phase imbalance $\angle(1 + |\bar{\gamma}| e^{j\bar{\phi}_\gamma})$. It should be noted that this phase imbalance changes at different NL orders $2p - 1$ based on the magnitude ratio $\bar{h}_{Q,2p-1}^{2p-1}/\bar{h}_{I,2p-1}^{2p-1}$ while the filter phase shift stays constant. These effective phase imbalance factors must be integrated into the BB amplifier coefficients. For this task the constant part of $\phi_{\mathrm{RF,FSTT}}$ must be evaluated using the beforehand extracted magnitude and phase imbalance coefficients:

$$\hat{\phi}_{\mathrm{RF,FSTT,est.}} = \left(\angle \hat{\alpha}_{d,\mathrm{RF},1} - \hat{\phi}_{\mathrm{BB,FSTT},3} - \angle \left[1 + |\hat{\bar{\gamma}}| e^{j\hat{\theta}_e} \right] \right)_{2\pi} \tag{3.144}$$

In this expression the magnitude imbalance was taken from the imbalance characterization process while the I/Q-mixer phase error was extracted from the CBTT measurements. $\hat{\phi}_{\mathrm{RF,FSTT,est.}}$ cannot be directly taken from the CBTT phase extraction process as the LO phase may change between the FSTT and the CBTT measurements. Based on the former results the coefficients modeling the BB amplifier behavior are given by:

$$\begin{aligned} \hat{\alpha}_{d,1} &= |\hat{\alpha}_{d,\mathrm{RF},1}| e^{j(\angle \hat{\alpha}_{d,\mathrm{RF},1} - \hat{\bar{\phi}}_I - \hat{\phi}_{\mathrm{RF,FSTT,est.}})} \\ \hat{\alpha}_{d,2p-1} &= |\hat{\alpha}_{d,\mathrm{HD},2p-1}| e^{j(\angle \hat{\alpha}_{d,\mathrm{HD},2p-1} + [(-1)^p (2p-1)+1]\hat{\phi}_{\mathrm{BB,FSTT},2p-1} - \hat{\phi}_{\mathrm{RF,FSTT,est.}} - \hat{\bar{\phi}}_I)} \\ & \quad p = 2 \ldots N_{\mathrm{O,BB}} \end{aligned} \tag{3.145}$$

These coefficients can now be used for evaluating the compressed signal magnitude at the input of the mixer output NL (compare (3.106)):

$$\mathbf{A}_{\mathrm{des.}} \circ e^{j\boldsymbol{\phi}_{\mathrm{des.}}} = \sum_{m=1}^{N_{\mathrm{O,BB}}} \frac{8}{16^m} \binom{2m-1}{m-1}^2 \hat{\alpha}_{d,2m-1} \mathbf{A}_{\mathrm{FSTT}}^{2m-1} \tag{3.146}$$

Here the complex exponential function is element-wise applied to the entries of the vector $\boldsymbol{\phi}_{\mathrm{des.}}$. Based on the two vectors the mixer output NL coefficients are identified from the transmitter FSTT response at f_m. The output signal amplitudes are arranged in a vector as presented in (3.130). For the generation of

the input signal based matrix the powers of the BB amplifier output magnitudes at the two desired tones are required:

$$
\begin{aligned}
\mathbf{H}_{\mathrm{BB},l,m}^{(+)} &= \tfrac{1}{4^{m-1}}\binom{2m-1}{m-l}\mathbf{A}_{\mathrm{des.}}^{2m-1} \circ e^{j(\phi_m+\hat{\bar{\phi}}_I+\phi_{\mathrm{des.}}+\hat{\phi}_{\mathrm{RF,FSTT,est.}}+(2l-1)\phi_{sp})} \\
\mathbf{H}_{\mathrm{BB},l,m}^{(-)} &= \tfrac{1}{4^{m-1}}\binom{2m-1}{m-l}\mathbf{A}_{\mathrm{des.}}^{2m-1} \circ e^{j(\phi_m+\hat{\bar{\phi}}_I+\phi_{\mathrm{des.}}+\hat{\phi}_{\mathrm{RF,FSTT,est.}}-(2l-1)\phi_{sp})}
\end{aligned}
\tag{3.147}
$$

Additionally, the BB amplifier IMD is evaluated:

$$
\begin{aligned}
\mathbf{H}_{\mathrm{BB,out},l}^{(+)} &= \sum_{m=l}^{N_{\mathrm{O,BB}}} \tfrac{8}{16^m}\hat{\alpha}_{d,2m-1}\binom{2m-1}{m-1}\binom{2m-1}{m-l}\mathbf{A}_{\mathrm{FSTT}}^{2m-1}e^{j(\phi_m+\hat{\bar{\phi}}_I+\hat{\phi}_{\mathrm{RF,FSTT,est.}}+(2l-1)\phi_{sp})} \\
\mathbf{H}_{\mathrm{BB,out},l}^{(-)} &= \sum_{m=l}^{N_{\mathrm{O,BB}}} \tfrac{8}{16^m}\hat{\alpha}_{d,2m-1}\binom{2m-1}{m-1}\binom{2m-1}{m-l}\mathbf{A}_{\mathrm{FSTT}}^{2m-1}e^{j(\phi_m+\hat{\bar{\phi}}_I+\hat{\phi}_{\mathrm{RF,FSTT,est.}}-(2l-1)\phi_{sp})}
\end{aligned}
\tag{3.148}
$$

The $(2KN_{\mathrm{O,ID,RF}}) \times N_{\mathrm{O,RF}}$ combines the four vectors describing the BB amplifier behavior:

$$
\mathbf{H}_{\mathrm{RF}} =
\begin{pmatrix}
\mathbf{H}_{\mathrm{BB,out},N_{\mathrm{O,ID,RF}}}^{(-)} & & & & \mathbf{H}_{\mathrm{BB},N_{\mathrm{O,ID,RF}},N_{\mathrm{O,RF}}}^{(-)} \\
\vdots & & & \iddots & \vdots \\
\mathbf{H}_{\mathrm{BB,out},3}^{(-)} & & \mathbf{H}_{\mathrm{BB},3,3}^{(-)} & \cdots & \mathbf{H}_{\mathrm{BB},3,N_{\mathrm{O,RF}}}^{(-)} \\
\mathbf{H}_{\mathrm{BB,out},2}^{(-)} & \mathbf{H}_{\mathrm{BB},2,2}^{(-)} & \mathbf{H}_{\mathrm{BB},2,3}^{(-)} & \cdots & \mathbf{H}_{\mathrm{BB},2,N_{\mathrm{O,RF}}}^{(-)} \\
\mathbf{H}_{\mathrm{BB},1,1}^{(-)} & \mathbf{H}_{\mathrm{BB},1,2}^{(-)} & \mathbf{H}_{\mathrm{BB},1,3}^{(-)} & \cdots & \mathbf{H}_{\mathrm{BB},1,N_{\mathrm{O,RF}}}^{(-)} \\
\mathbf{H}_{\mathrm{BB},1,1}^{(+)} & \mathbf{H}_{\mathrm{BB},1,2}^{(+)} & \mathbf{H}_{\mathrm{BB},1,3}^{(+)} & \cdots & \mathbf{H}_{\mathrm{BB},1,N_{\mathrm{O,RF}}}^{(+)} \\
\mathbf{H}_{\mathrm{BB,out},2}^{(+)} & \mathbf{H}_{\mathrm{BB},2,2}^{(+)} & \mathbf{H}_{\mathrm{BB},2,3}^{(+)} & \cdots & \mathbf{H}_{\mathrm{BB},2,N_{\mathrm{O,RF}}}^{(+)} \\
\mathbf{H}_{\mathrm{BB,out},3}^{(+)} & & \mathbf{H}_{\mathrm{BB},3,3}^{(+)} & \cdots & \mathbf{H}_{\mathrm{BB},3,N_{\mathrm{O,RF}}}^{(+)} \\
\vdots & & & \ddots & \vdots \\
\mathbf{H}_{\mathrm{BB,out},N_{\mathrm{O,ID,RF}}}^{(+)} & & & & \mathbf{H}_{\mathrm{BB},N_{\mathrm{O,ID,RF}},N_{\mathrm{O,RF}}}^{(+)}
\end{pmatrix}
\tag{3.149}
$$

where $N_{\mathrm{O,RF}}$ identifies the number of coefficients considered for the identification:

$$
N_{\mathrm{O,RF}} = \left\lfloor \frac{N_{\mathrm{RF}} + 1}{2} \right\rfloor
\tag{3.150}
$$

The mixer output NL coefficients are arranged in the vector $\hat{\boldsymbol{\lambda}}_{g_{\mathrm{M}}} = (\hat{g}_{\mathrm{M},1}\,\hat{g}_{\mathrm{M},3}\,\ldots\,\hat{g}_{\mathrm{M},N_{\mathrm{RF}}})^T$ and evaluated by solving the equation:

$$
\mathbf{H}_{\mathrm{RF}}^H \mathbf{H}_{\mathrm{RF}} \hat{\boldsymbol{\lambda}}_{g_{\mathrm{M}}} = \mathbf{H}_{\mathrm{RF}}^H \mathbf{Y}
\tag{3.151}
$$

Typically, after calculating $\hat{\boldsymbol{\lambda}}_{g_{\mathrm{M}}}$ the coefficient $g_{\mathrm{M},1}$ is not exactly one. This fact can be compensated by setting:

$$
\begin{aligned}
\hat{\alpha}_{d,2m-1} &= \hat{\alpha}_{d,2m-1}|g_{\mathrm{M},1}| \\
\hat{\phi}_{\mathrm{RF,FSTT,est.}} &= \hat{\phi}_{\mathrm{RF,FSTT,est.}} + \angle g_{\mathrm{M},1}
\end{aligned}
\tag{3.152}
$$

With the updated parameters the vectors (3.146) to (3.149) are recomposed and (3.151) is solved again. Simulations showed that this computationally intensive approach provides an increased identification accuracy of the mixer coefficients $g_{\mathrm{M},2m-1}$ $m \geq 2$ and a $g_{\mathrm{M},1}$ which is exactly unity.

3.8.5.1 Least square algorithm optimized for high linearity systems

Solving (3.151) in case of a low distortion magnitude can result in erroneous parameter estimations due to the following problem. The data vector $\mathbf{Y}$ used at (3.151) is composed of the measured amplitudes of the desired tones and the intermodulation distortion. The least square solution minimizes the overall error and selects the optimum coefficients for the provided data. Usually, the measurement error of the desired tone magnitude is negligible compared to the other distortion sources (like the uncertainties of the IMDs amplitudes). As long as the magnitude of the distortion is sufficiently high a clear gain compression or expansion is observed and the LS algorithm will provide desired parameters. In high linearity systems a negligible gain compression takes place. Even more, the overall gain compression can be below the measurement error of the desired tones. Hence, the slight variations in the desired tone magnitudes may result in an incorrect estimation of the nonlinear system response due to the minimization of the overall errors. In this way not only the gain compression but also the corresponding IMD will be modeled much too large. From this explanation it is clear that the limits for observing this problem depend on the nonlinear response of the characterized system and the accuracy of the measurement setup. To circumvent this behavior the identification of the linear and the nonlinear contributions to the LS solution must be derived separately . In the following the implementation of a LS algorithm for highly linear systems is presented. This algorithm is exemplified for the extraction of the RF NL coefficients but will be used several times at the transmitter or receiver NL behavior identification if appropriate. The usage of either the classical or the optimized LS version depending of the properties of the considered system is indicated by $\hat{\boldsymbol{\lambda}} = \mathrm{LS_{opt}}(\mathbf{H}, \mathbf{Y})$. The system response matrix for the LS algorithm is represented by $\mathbf{H}$ and the measurement data vector by $\mathbf{Y}$ in this expression. The evaluated coefficients are summarized using the vector $\hat{\boldsymbol{\lambda}}$. It is important to note, that the principle structure of the equations stays the same independent of the application of the optimized LS. If applied to a different problem the calculation of the linear an NL response must be updated accordingly. In a similar way changes to the presented equations are required if additional distortion terms are included.

At the beginning the nonlinear system response is extracted without the carrier tones. Hence, implicitly a unity linear gain is assumed. The modified system response matrix for this task is given by:

$$\mathbf{H}_{\mathrm{RF,P_2}} = \begin{pmatrix} & & & & \mathbf{H}^{(-)}_{\mathrm{BB},N_{\mathrm{O,ID,RF}},N_{\mathrm{O,RF}}} \\ & & & \iddots & \vdots \\ & & \mathbf{H}^{(-)}_{\mathrm{BB},3,3} & \cdots & \mathbf{H}^{(-)}_{\mathrm{BB},3,N_{\mathrm{O,RF}}} \\ & \mathbf{H}^{(-)}_{\mathrm{BB},2,2} & \mathbf{H}^{(-)}_{\mathrm{BB},2,3} & \cdots & \mathbf{H}^{(-)}_{\mathrm{BB},2,N_{\mathrm{O,RF}}} \\ & \mathbf{H}^{(+)}_{\mathrm{BB},2,2} & \mathbf{H}^{(+)}_{\mathrm{BB},2,3} & \cdots & \mathbf{H}^{(+)}_{\mathrm{BB},2,N_{\mathrm{O,RF}}} \\ & & \mathbf{H}^{(+)}_{\mathrm{BB},3,3} & \cdots & \mathbf{H}^{(+)}_{\mathrm{BB},3,N_{\mathrm{O,RF}}} \\ & & & \ddots & \vdots \\ & & & \mathbf{H}^{(+)}_{\mathrm{BB},N_{\mathrm{O,ID,RF}},N_{\mathrm{O,RF}}} \end{pmatrix} \qquad (3.153)$$

In a similar way the corresponding measurement results are composed:

$$
\mathbf{Y} = \begin{pmatrix} \mathbf{A}_{\mathrm{FSTT},(-2N_{\mathrm{O,ID,BB}}+1),1} \\ \vdots \\ \mathbf{A}_{\mathrm{FSTT},(-3),1} \\ \mathbf{A}_{\mathrm{FSTT},(+3),1} \\ \vdots \\ \mathbf{A}_{\mathrm{FSTT},(2N_{\mathrm{O,ID,BB}}-1),1} \end{pmatrix}
\tag{3.154}
$$

The mixer output NL coefficients are arranged in the vector $\hat{\boldsymbol{\lambda}}_{g_{\mathrm{M,P}_2}} = (\hat{g}_{\mathrm{M,3}} \ \ldots \ \hat{g}_{\mathrm{M},N_{\mathrm{RF}}})^T$ and evaluated by solving the equation:

$$
\mathbf{H}_{\mathrm{RF,P}_2}^H \mathbf{H}_{\mathrm{RF,P}_2} \hat{\boldsymbol{\lambda}}_{g_{\mathrm{M,P}_2}} = \mathbf{H}_{\mathrm{RF,P}_2}^H \mathbf{Y}
\tag{3.155}
$$

The gain compression or expansion introduced by the NL system response is now removed from the desired tone amplitude:

$$
\mathbf{Y}_{\mathrm{corr}} = \sum_{m=2}^{N_{\mathrm{O,RF}}} \frac{1}{4^{m-1}} \hat{\boldsymbol{\lambda}}_{g_{\mathrm{M,P}_2},2m-3} \binom{2m-1}{m-1} \mathbf{A}_{\mathrm{des.}}^{2m-1} \circ e^{j(\phi_m + \hat{\bar{\phi}}_I + \phi_{\mathrm{des.}} + \hat{\phi}_{\mathrm{RF,FSTT,est.}})}
\tag{3.156}
$$

$$
\mathbf{Y} = \begin{pmatrix} \mathbf{A}_{\mathrm{FSTT},(-1),1} - \mathbf{Y}_{\mathrm{corr}} e^{-j\phi_{sp}} \\ \mathbf{A}_{\mathrm{FSTT},(+1),1} - \mathbf{Y}_{\mathrm{corr}} e^{j\phi_{sp}} \end{pmatrix}
\tag{3.157}
$$

Using a system response matrix composed of the two middle lines of (3.149) identified by $\mathbf{H}_{\mathrm{RF,P}_1}$ and a coefficient vector composed of a single element $\hat{\boldsymbol{\lambda}}_{g_{\mathrm{M,P}_1}} = \hat{g}_{\mathrm{M,1}}$ the least square solution for the linear gain is derived as indicated in (3.155). Finally, the NL coefficients are extracted a second time taking into account $\hat{g}_{\mathrm{M,1}}$ and the IMD distortion generated by the BB amplifiers. For this task the measurement data vector will be updated:

$$
\mathbf{Y} = \begin{pmatrix} \mathbf{A}_{\mathrm{FSTT},(-2N_{\mathrm{O,ID,BB}}+1),1} - \hat{g}_{\mathrm{M,1}} \mathbf{H}_{\mathrm{BB,out},N_{\mathrm{O,ID,BB}}}^{(-)} \\ \vdots \\ \mathbf{A}_{\mathrm{FSTT},(-3),1} - \hat{g}_{\mathrm{M,1}} \mathbf{H}_{\mathrm{BB,out},2}^{(-)} \\ \mathbf{A}_{\mathrm{FSTT},(+3),1} - \hat{g}_{\mathrm{M,1}} \mathbf{H}_{\mathrm{BB,out},2}^{(+)} \\ \vdots \\ \mathbf{A}_{\mathrm{FSTT},(2N_{\mathrm{O,ID,BB}}-1),1} - \hat{g}_{\mathrm{M,1}} \mathbf{H}_{\mathrm{BB,out},N_{\mathrm{O,ID,BB}}}^{(+)} \end{pmatrix}
\tag{3.158}
$$

Using this vector and $\mathbf{H}_{\mathrm{RF,P}_2}$ (3.155) is solved. The overall coefficients vector is composed of both identification results:

$$
\hat{\boldsymbol{\lambda}}_{g_{\mathrm{M}}} = (\hat{g}_{\mathrm{M,1}} \ \hat{\boldsymbol{\lambda}}_{g_{\mathrm{M,P}_2}}^T)^T
\tag{3.159}
$$

3.8.5.2 Mixer output nonlinearity parameterization accuracy

For analyzing the impact of the neglected distortion products in (3.149) the transmitter output spectrum was calculated for a 3rd-order baseband and a 3rd-order mixer output nonlinearity. The calculation was

limited to distortion products up to 5th-order. For the presentation the BB amplifier coefficients were arranged in the following expressions (grouped by the NL order):

$$
\begin{aligned}
\bar{\alpha}_{d,1} &= \tfrac{1}{2}\left(\bar{h}_{I,1} + \bar{h}_{Q,1}e^{j(\theta_e + \bar{\phi}_\gamma)}\right) \\
\bar{\alpha}_{v,1} &= \tfrac{1}{2}\left(\bar{h}_{I,1} - \bar{h}_{Q,1}e^{j(\theta_e - \bar{\phi}_\gamma)}\right)
\end{aligned}
\tag{3.160}
$$

$$
\begin{aligned}
\bar{\alpha}_{d,2} &= \tfrac{1}{4}\left(\bar{h}_{I,2}^2 + j\bar{h}_{Q,2}^2 e^{j\theta_e}\right) \\
\bar{\alpha}_{v,2,n} &= \tfrac{1}{4}\left(\bar{h}_{I,2}^2 - j\bar{h}_{Q,2}^2 e^{j(\theta_e - 2\bar{\phi}_\gamma)}\right) \\
\bar{\alpha}_{v,2,p} &= \tfrac{1}{4}\left(\bar{h}_{I,2}^2 - j\bar{h}_{Q,2}^2 e^{j(\theta_e + 2\bar{\phi}_\gamma)}\right)
\end{aligned}
\tag{3.161}
$$

$$
\begin{aligned}
\bar{\alpha}_{d,3} &= \tfrac{1}{8}\left(\bar{h}_{I,3}^3 + \bar{h}_{Q,3}^3 e^{j(\theta_e + \bar{\phi}_\gamma)}\right) \\
\bar{\alpha}_{d,3,n} &= \tfrac{1}{8}\left(\bar{h}_{I,3}^3 + \bar{h}_{Q,3}^3 e^{j(\theta_e - 3\bar{\phi}_\gamma)}\right) \\
\bar{\alpha}_{v,3} &= \tfrac{1}{8}\left(\bar{h}_{I,3}^3 - \bar{h}_{Q,3}^3 e^{j(\theta_e - \bar{\phi}_\gamma)}\right) \\
\bar{\alpha}_{v,3,p} &= \tfrac{1}{8}\left(\bar{h}_{I,3}^3 - \bar{h}_{Q,3}^3 e^{j(\theta_e + 3\bar{\phi}_\gamma)}\right)
\end{aligned}
\tag{3.162}
$$

These equations are in agreement with the equivalent memoryless BB amplifier coefficient as defined at the beginning of Section 3.8. The transmitter response at the desired tones, the IMD$_3$, the IMD$_5$ and the HD$_3$ is now derived using the former definitions:

$$
\begin{aligned}
A_{\text{FSTT,M,1,1}} &\approx e^{j(\phi_m + \bar{\phi}_I + \phi_{sp})}\Big(g_{\text{M,1}}\left(\bar{\alpha}_{d,1}A_{\text{FSTT}} + \tfrac{9}{4}\bar{\alpha}_{d,3}A_{\text{FSTT}}^3\right) \\
&\quad + g_{\text{M,3}}\left(\tfrac{3}{2}\bar{\alpha}_{d,1}|\bar{\alpha}_{v,1}|^2 + \tfrac{3}{4}\bar{\alpha}_{d,1}|\bar{\alpha}_{d,1}|^2\right)A_{\text{FSTT}}^3 \\
&\quad + g_{\text{M,3}}\Big[5\bar{\alpha}_{d,1}|\bar{\alpha}_{d,2}|^2 + \tfrac{15}{4}|\bar{\alpha}_{d,1}|^2\bar{\alpha}_{d,3} + \tfrac{15}{8}\bar{\alpha}_{d,1}^2\bar{\alpha}_{d,3}^* + \tfrac{5}{2}\bar{\alpha}_{d,1}^*\bar{\alpha}_{d,2}\bar{\alpha}_{v,2,p} + \tfrac{5}{4}\bar{\alpha}_{d,1}|\bar{\alpha}_{v,2,n}|^2 \\
&\quad + \tfrac{5}{4}\bar{\alpha}_{d,1}|\bar{\alpha}_{v,2,p}|^2 + \bar{\alpha}_{v,1}\left(\tfrac{15}{4}\bar{\alpha}_{d,1}\bar{\alpha}_{v,3}^* + \tfrac{5}{4}\bar{\alpha}_{d,1}^*\bar{\alpha}_{v,3,p} + \tfrac{5}{2}\bar{\alpha}_{d,2}\bar{\alpha}_{v,2,n}^* + \tfrac{5}{2}\bar{\alpha}_{d,2}^*\bar{\alpha}_{v,2,p}\right) \\
&\quad + \bar{\alpha}_{v,1}^*\left(\tfrac{15}{4}\bar{\alpha}_{d,1}\bar{\alpha}_{v,3} + \tfrac{5}{2}\bar{\alpha}_{d,2}^2 + \tfrac{5}{4}\bar{\alpha}_{v,2,p}\bar{\alpha}_{v,2,n}\right) + \tfrac{5}{8}\bar{\alpha}_{v,1}^2\bar{\alpha}_{d,3,n}^* + \tfrac{15}{4}|\bar{\alpha}_{v,1}|^2\bar{\alpha}_{d,3}\Big]A_{\text{FSTT}}^5\Big)
\end{aligned}
\tag{3.163}
$$

$$
\begin{aligned}
A_{\text{FSTT,M,3,1}} &\approx e^{j(\phi_m + \bar{\phi}_I + 3\phi_{sp})}\Big(\tfrac{3}{4}g_{\text{M,1}}\bar{\alpha}_{d,3}A_{\text{FSTT}}^3 + g_{\text{M,3}}\left(\tfrac{1}{4}\bar{\alpha}_{d,1}|\bar{\alpha}_{d,1}|^2 + \tfrac{1}{2}\bar{\alpha}_{d,1}|\bar{\alpha}_{v,1}|^2\right)A_{\text{FSTT}}^3 \\
&\quad + g_{\text{M,3}}\Big[\tfrac{5}{8}\bar{\alpha}_{d,1}|\bar{\alpha}_{v,2,n}|^2 + \tfrac{5}{8}\bar{\alpha}_{d,1}|\bar{\alpha}_{v,2,p}|^2 + \tfrac{5}{2}\bar{\alpha}_{d,1}|\bar{\alpha}_{d,2}|^2 + \tfrac{5}{4}\bar{\alpha}_{d,1}^*\bar{\alpha}_{d,2}\bar{\alpha}_{v,2,p} \\
&\quad + \tfrac{15}{16}\bar{\alpha}_{d,1}^2\bar{\alpha}_{d,3}^* + \tfrac{15}{8}|\bar{\alpha}_{d,1}|^2\bar{\alpha}_{d,3} + \bar{\alpha}_{v,1}^*\left(\tfrac{15}{8}\bar{\alpha}_{d,1}\bar{\alpha}_{v,3} + \tfrac{5}{4}\bar{\alpha}_{d,2}^2 + \tfrac{5}{8}\bar{\alpha}_{v,2,p}\bar{\alpha}_{v,2,n}\right) \\
&\quad + \bar{\alpha}_{v,1}\left(\tfrac{15}{8}\bar{\alpha}_{d,1}\bar{\alpha}_{v,3}^* + \tfrac{5}{8}\bar{\alpha}_{d,1}^*\bar{\alpha}_{v,3,p} + \tfrac{5}{4}\bar{\alpha}_{d,2}^*\bar{\alpha}_{v,2,p} + \tfrac{5}{4}\bar{\alpha}_{d,2}\bar{\alpha}_{v,2,n}^*\right) \\
&\quad + \tfrac{15}{8}|\bar{\alpha}_{v,1}|^2\bar{\alpha}_{d,3} + \tfrac{15}{16}\bar{\alpha}_{v,1}^2\bar{\alpha}_{d,3,n}^*\Big]A_{\text{FSTT}}^5\Big)
\end{aligned}
\tag{3.164}
$$

$$
\begin{aligned}
A_{\text{FSTT,M},5,1} \approx{}& e^{j(\phi_m + \bar{\phi}_I + 5\phi_{sp})} g_{\text{M},3} \left[\tfrac{1}{2}\bar{\alpha}_{d,1}|\bar{\alpha}_{d,2}|^2 + \tfrac{1}{4}\bar{\alpha}_{d,1}^*\bar{\alpha}_{d,2}\bar{\alpha}_{v,2,p} + \tfrac{1}{8}\bar{\alpha}_{d,1}|\bar{\alpha}_{v,2,n}|^2 \right. \\
&+ \tfrac{1}{8}\bar{\alpha}_{d,1}|\bar{\alpha}_{v,2,p}|^2 + \tfrac{3}{16}\bar{\alpha}_{d,1}^2\bar{\alpha}_{d,3}^* + \tfrac{3}{8}|\bar{\alpha}_{d,1}|^2\bar{\alpha}_{d,3} \\
&+ \bar{\alpha}_{v,1}\left(\tfrac{1}{8}\bar{\alpha}_{d,1}^*\bar{\alpha}_{v,3,p} + \tfrac{1}{4}\bar{\alpha}_{d,2}\bar{\alpha}_{v,2,n}^* + \tfrac{1}{4}\bar{\alpha}_{d,2}^*\bar{\alpha}_{v,2,p} + \tfrac{3}{8}\bar{\alpha}_{v,3}^* \right) \\
&+ \bar{\alpha}_{v,1}^*\left(\tfrac{3}{8}\bar{\alpha}_{d,1}\bar{\alpha}_{v,3} + \tfrac{1}{4}\bar{\alpha}_{d,2}^2 + \tfrac{1}{8}\bar{\alpha}_{v,2,p}\bar{\alpha}_{v,2,n} \right) \\
&\left. + \tfrac{1}{16}\bar{\alpha}_{v,1}^2\bar{\alpha}_{d,3,n}^* + \tfrac{3}{8}|\bar{\alpha}_{v,1}|^2\bar{\alpha}_{d,3} \right] A_{\text{FSTT}}^5
\end{aligned}
\tag{3.165}
$$

$$
\begin{aligned}
A_{\text{FSTT,M},1,-3} \approx{}& e^{j(-3\phi_m - 3\bar{\phi}_I + \phi_{sp})} \left(\tfrac{3}{4}g_{\text{M},1}\bar{\alpha}_{d,3,n}A_{\text{FSTT}}^3 + \tfrac{3}{4}g_{\text{M},3}\bar{\alpha}_{d,1}^*\bar{\alpha}_{v,1}^2 A_{\text{FSTT}}^3 \right. \\
&+ g_{\text{M},3}\left[\tfrac{5}{4}|\bar{\alpha}_{d,1}|^2\bar{\alpha}_{d,3,n} + \tfrac{5}{4}\bar{\alpha}_{d,1}\bar{\alpha}_{v,2,n}\bar{\alpha}_{v,2,p}^* + \tfrac{5}{2}\bar{\alpha}_{d,1}^*\bar{\alpha}_{d,2}\bar{\alpha}_{v,2,n} \right. \\
&+ \bar{\alpha}_{v,1}\left(\tfrac{5}{4}\bar{\alpha}_{d,1}\bar{\alpha}_{v,3,p}^* + \tfrac{15}{4}\bar{\alpha}_{d,1}^*\bar{\alpha}_{v,3} + \tfrac{5}{2}\bar{\alpha}_{d,2}^*\bar{\alpha}_{v,2,n} + \tfrac{5}{2}\bar{\alpha}_{d,2}\bar{\alpha}_{v,2,p}^* \right) \\
&\left.\left. + \tfrac{5}{8}\bar{\alpha}_{v,1}^*\bar{\alpha}_{v,2,n}^2 + \tfrac{15}{8}\bar{\alpha}_{v,1}^2\bar{\alpha}_{d,3}^* + \tfrac{5}{4}|\bar{\alpha}_{v,1}|^2\bar{\alpha}_{d,3,n} \right] A_{\text{FSTT}}^5 \right)
\end{aligned}
\tag{3.166}
$$

Here, the index M was added for distinguishing these results from the measurements $A_{\text{FSTT},n,m}$. At all presented output magnitudes the signal components were sorted in ascending order of the input amplitude. Additionally, all factors containing $\bar{\alpha}_{v,1}$ are grouped together. Assuming a proper image suppression these terms are quite small.

Based on a transmitter modeled by a third-order baseband and a third-order mixer output nonlinearity the harmonic distortion magnitude $A_{\text{FSTT,M},1,-3}$ will be used for identifying $\bar{\alpha}_{d,3,n}$. The 3$^{\text{rd}}$-order intermodulation distortion will then be used for extracting $g_{\text{M},3}$. The IMD$_5$ expression is added as this result will be required in Section 3.8.8.

In the case of the HD$_3$ the expression $\tfrac{3}{4}g_{\text{M},1}\bar{\alpha}_{d,3,n}A_{\text{FSTT}}^3$ provides the desired information on the odd-order baseband nonlinearity. The compression introduced by interactions of the two desired tones at the mixer output NL is expressed by the coefficient $\tfrac{5}{4}g_{\text{M},3}|\bar{\alpha}_{d,1}|^2\bar{\alpha}_{d,3,n}A_{\text{FSTT}}^5$. The factors $\tfrac{5}{4}g_{\text{M},3}\bar{\alpha}_{d,1}\bar{\alpha}_{v,2,n}$ $\bar{\alpha}_{v,2,p}^*A_{\text{FSTT}}^5$, $\tfrac{5}{2}g_{\text{M},3}\bar{\alpha}_{d,1}^*\bar{\alpha}_{d,2}\bar{\alpha}_{v,2,n}A_{\text{FSTT}}^5$ describe the impact of the second order distortion onto the output signal magnitude. Both effects are not covered by the approximation (3.108).

A similar situation is found for the extraction of $g_{\text{M},3}$ from the measurement of $A_{\text{FSTT},3,1}$. Here the term $\tfrac{3}{4}g_{\text{M},1}\bar{\alpha}_{d,3}A_{\text{FSTT}}^3$ should be canceled out by the beforehand identified $\bar{\alpha}_{d,3,n}$ parameter. During the extraction of this coefficient care was taken for compensating the phase difference between $\bar{\alpha}_{d,3}$ and $\bar{\alpha}_{d,3,n}$. The factor $g_{\text{M},3}\tfrac{1}{4}\bar{\alpha}_{d,1}|\bar{\alpha}_{d,1}|^2A_{\text{FSTT}}^3$ is then used for calculating $g_{\text{M},3}$. The causes for a degradation of the parameter identification are provided by four second order distortion products which are combined with the desired signal by the output nonlinearity. Driven close to compression the mixer output NL IMD modeled by $\tfrac{15}{16}g_{\text{M},3}\bar{\alpha}_{d,1}^2\bar{\alpha}_{d,3}^*A_{\text{FSTT}}^5$ and $\tfrac{15}{8}g_{\text{M},3}|\bar{\alpha}_{d,1}|^2\bar{\alpha}_{d,3}A_{\text{FSTT}}^5$ will gain importance.

For validating the accuracy of the suggested parameter extraction process simulations were performed. The response of the transmitter onto a FSTT input signal was calculated under different operation conditions. The basis for these simulations was a memoryless transmitter model as presented in Figure 3.10 without DC-offsets. The mixer output nonlinearity was extracted for these data and compared to the desired value. The magnitude of the input signal was swept up to $P_{in} = 10\,\text{dBm}$ (i.e., $A_{\text{FSTT}} = 1$). The intercept point for the two baseband amplifiers was set to IP$_2 = 38\,\text{dBm}$ and IP$_3 = 23\,\text{dBm}$. Both amplifiers were simulated using the same parameters. The mixer output nonlinearity IP$_3$ was the same

as the one of the baseband amplifiers. The transmitter was modeled imbalance free. Based on these specifications the transmitter exhibits strong nonlinear effects causing the output to compress by $2\,\mathrm{dB}$ at the maximum input power. The chosen baseband amplifier intercept results in an IMD_3 and HD_2 distortion both $30\,\mathrm{dB}$ below the desired signal. Under these unfavorable operating conditions the $g_{\mathrm{M},3}$ coefficient of the mixer output nonlinearity is evaluated with an accuracy better than $-25.9\,\mathrm{dB}$. In a next step a lowpass-filter and an I/Q-mixer phase imbalance of $6°$ and $4°$, respectively, was introduced to the transmitter. The magnitude imbalance γ was set to 0.95. Due to the imbalance distortion the evaluation accuracy dropped to $-25.7\,\mathrm{dB}$. Using the same parameters as for the discussion of the baseband amplifier output spectrum Figure 3.11 an evaluation accuracy of $-26.2\,\mathrm{dB}$ was achieved. Further consideration on the mixer output nonlinearity parameterization accuracy will be presented in Section 3.8.9.

3.8.6 Deembedding of the mixer output nonlinearity impact

After the mixer output nonlinearity is extracted this information is used for evaluating the signal components present at the output of the BB NL. By that step a virtual interface is generated which is located within the I/Q-mixer hardware. Due to this reason it is not possible to measure these signal components directly. They represent the impact of the baseband amplifier and the mixer input nonlinearity.

Based on the polynomial model of the mixer output nonlinearity a postdistorter will be used for removing the distortion added by this device as shown in Figure 3.13. This polynomial postdistorter is parameterized based on the coefficients of the mixer output nonlinearity. At the beginning of the
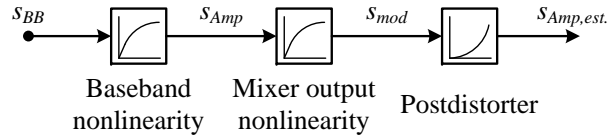
Figure 3.13: Concept of the mixer output nonlinearity deembedding by postdistortion.

deembedding task CBTT power sweeps which are performed at both channels resulting in output signals symmetrical to the carrier frequency. The signals are free of imbalance effects. These measurements have to cover the bandwidth of the baseband channels in order to allow the extraction of the PCWM. The transmitter response measurements include the desired signal, the IMD and the HD generated in the baseband. As for the mixer output nonlinearity extraction the measured signal components are represented by $A_{\mathrm{CBTT},Q,n,m}$, $\phi_{\mathrm{CBTT},Q,n,m}$ (i.e., the signal component located at nf_{sp} and mf_m from the carrier frequency). In the following all required steps are presented for the quadrature channel. The inphase branch results are derived in the same way.

Due to the memoryless assumption no difference between the upper and lower distortion products may exist at the positive and negative frequency offset $\pm f_m$ from the carrier. If differences in the magnitudes of the corresponding output signal components are recognized the mean of the corresponding measurement values will be used for the nonlinearity characterization. For this averaging task the impact of ϕ_{sp} and $\phi_{\mathrm{BB},Q} = \phi_m + \bar{\phi}_I + \bar{\phi}_\gamma$ is removed from the measured phases $\phi_{\mathrm{CBTT},Q,n,m}$. The evaluation of $\hat{\phi}_{\mathrm{BB},Q}$ from the CBTT power sweep measurements was presented in Section 3.8.2. The resulting tone phase represents only $\phi_{\mathrm{RF},Q} = \varphi_{\mathrm{LO}} + \theta_e + \angle g_{\mathrm{M},1}$ which is independent of the parameters n, m. In this way the corresponding magnitudes and phases can be averaged. The outcome of this preprocessing

step are complex-valued data sets $A_{\text{CBTT},Q,n,m;\text{P}_K} = A_{\text{CBTT},Q,n,m;\text{P}_K} \exp(j\phi_{\text{CBTT},RF,Q,n,m;\text{P}_K})$. For simplifying the notation in this section no new symbol was introduced for these data sets.

Assuming a 3rd-order mixer output and a 5th-order postdistorter nonlinearity the cascade of the two blocks results to:

$$
\begin{aligned}
s_{\text{mod}}(t) &= g_{\text{M},1}s_{\text{Amp}}(t) + g_{\text{M},3}s_{\text{Amp}}(t)\left|s_{\text{Amp}}(t)\right|^2 \\
s_{\text{Amp,est.}}(t) &= \sum_{k=1}^{3} g_{PD,2k-1}s_{\text{mod}}(t)\left|s_{\text{mod}}(t)\right|^{2(k-1)}
\end{aligned}
\tag{3.167}
$$

where $g_{PD,2k-1}$ represents the coefficients of the postdistorter. As a cascade of the mixer output NL and the postdistorter should result in a system characterized by a linear gain k_{lin} the first-order postdistorter coefficient results to:

$$
g_{PD,1} = \frac{k_{lin}}{g_{\text{M},1}}
\tag{3.168}
$$

By substituting (3.168) into (3.167) and truncating the equation after the 3rd-order of $s_{\text{Amp}}(t)$ leads to:

$$
s_{\text{Amp,est.}}(t) = k_{lin}s_{\text{Amp}}(t) + \left(\frac{k_{lin}g_{\text{M},3}}{g_{\text{M},1}} + g_{PD,3}\,g_{\text{M},1}|g_{\text{M},1}|^2\right)s_{\text{Amp}}(t)\left|s_{\text{Amp}}(t)\right|^2 + \ldots
\tag{3.169}
$$

For canceling the 3rd-order distortion the expression enclosed in the brackets must be zero. Hence, the third-order postdistorter coefficient is given by:

$$
g_{PD,3} = -\frac{k_{lin}g_{\text{M},3}}{g_{\text{M},1}^2|g_{\text{M},1}|^2}
\tag{3.170}
$$

Repeating the same steps by substituting (3.168) and (3.170) into (3.167) and forcing the 5th-order coefficient to be zero results in:

$$
g_{PD,5} = \frac{k_{lin}\left(g_{\text{M},1}|g_{\text{M},3}|^2 + 2g_{\text{M},1}^*g_{\text{M},3}\right)}{g_{\text{M},1}|g_{\text{M},1}|^6}
\tag{3.171}
$$

These postdistorter coefficients suppress the impact of the mixer output nonlinearity up to the fifth order. The evaluation of higher order coefficients can easily be achieved by substituting all former extracted parameters into (3.167) and calculating the factors contributing to the highest nonzero order of $s_{\text{Amp}}(t)$.

The derived postdistortion result can only be applied to signals but not to the measured CBTT signal components. Cherishing the concept of signal components instead of the complete transmitter output signal provides the following advantages:

- The signal component description fulfills all symmetry properties used for the derivation of the transmitter response description (compare Section 3.8.2). This approach is advantageous compared to the procedure of performing the data fusion by the polynomial postdistorter itself

- Undesired distortion effects, like spurious emissions, can easily be masked out.

- The measurement bandwidth can be reduced by utilizing relationships between the signal components.

Due to these reasons the presented postdistorter is adopted for coping with the signal component approach. By passing the analytical representation of the transmitter output signal through the postdistorter and selecting the desired signal magnitudes at its output the desired interrelationship is established. The problem of the sketched approach is that a huge number of signal components are generated by the different nonlinearities which result in lengthy expressions. Therefore, all results presented in the following were truncated after the fifth order. The signal present at the transmitter output for a 3rd-order baseband and 3rd-order RF nonlinearity is given by:

$$
\begin{aligned}
s_{\text{mod}}(t) \quad = \quad & \Big[A_{\text{CBTT},Q,1,1} \cos(\omega_{sp}t)\cos(\omega_m t) + A_{\text{CBTT},Q,2,0}\cos(2\omega_{sp}t) + A_{\text{CBTT},Q,0,2}\cos(2\omega_m t) \\
& + A_{\text{CBTT},Q,0,0} + A_{\text{CBTT},Q,2,2}\cos(2\omega_{sp}t)\cos(2\omega_m t) + A_{\text{CBTT},Q,3,1}\cos(3\omega_{sp}t)\cos(\omega_m t) \\
& + A_{\text{CBTT},Q,1,3}\cos(\omega_{sp}t)\cos(3\omega_m t) + A_{\text{CBTT},Q,3,3}\cos(3\omega_{sp}t)\cos(3\omega_m t) \\
& + A_{\text{CBTT},Q,4,0}\cos(4\omega_{sp}t) + A_{\text{CBTT},Q,4,2}\cos(4\omega_{sp}t)\cos(2\omega_m t) + A_{\text{CBTT},Q,0,4}\cos(4\omega_m t) \\
& + A_{\text{CBTT},Q,2,4}\cos(2\omega_{sp}t)\cos(4\omega_m t) + A_{\text{CBTT},Q,4,4}\cos(4\omega_{sp}t)\cos(4\omega_m t) \\
& + A_{\text{CBTT},Q,5,1}\cos(5\omega_{sp}t)\cos(\omega_m t) + A_{\text{CBTT},Q,5,3}\cos(5\omega_{sp}t)\cos(3\omega_m t) \\
& + A_{\text{CBTT},Q,1,5}\cos(\omega_{sp}t)\cos(5\omega_m t) + A_{\text{CBTT},Q,3,5}\cos(3\omega_{sp}t)\cos(5\omega_m t) \\
& + A_{\text{CBTT},Q,5,5}\cos(5\omega_{sp}t)\cos(5\omega_m t) \Big] \cos(\omega_0 t)
\end{aligned}
$$

$$(3.172)$$

In this expression the tone phases ϕ_{sp}, ϕ_m were neglected to abridge the equation. For the following calculations these phases were of course included. The magnitudes $A_{\text{CBTT},Q,n,m}$ represent the preprocessed measurement results as described at the beginning of this section.

In (3.172) are several signal components showing the same magnitude, like for example, $A_{\text{CBTT},Q,3,1}$ and $A_{\text{CBTT},Q,1,3}$. These distinctions are kept for generality, even if it is desirable to perform the data fusion step before the postdistortion is performed. The advantages of preprocessing the input data in the predistortion case were analyzed in [116].

A further reduction of the considered magnitudes can be achieved by substituting magnitudes which are approximately equal. For visualizing the selected approximation the dependency on the magnitude of the CBTT input is presented:

$$
\begin{aligned}
A_{\text{CBTT},Q,0,0} \quad &= \quad \tfrac{1}{4}g_{\text{M},1}h_{Q,2}^2 e^{j\phi_{\text{RF}}}A_{\text{CBTT}}^2 + \tfrac{27}{64}g_{\text{M},3}h_{Q,1}^2 h_{Q,2}^2 e^{j\phi_{\text{RF}}}A_{\text{CBTT}}^4 \\
A_{\text{CBTT},Q,2,0} \quad &= \quad \tfrac{1}{4}g_{\text{M},1}h_{Q,2}^2 e^{j\phi_{\text{RF}}}A_{\text{CBTT}}^2 + \tfrac{9}{16}g_{\text{M},3}h_{Q,1}^2 h_{Q,2}^2 e^{j\phi_{\text{RF}}}A_{\text{CBTT}}^4 \\
A_{\text{CBTT},Q,2,2} \quad &= \quad \tfrac{1}{4}g_{\text{M},1}h_{Q,2}^2 e^{j\phi_{\text{RF}}}A_{\text{CBTT}}^2 + \tfrac{12}{16}g_{\text{M},3}h_{Q,1}^2 h_{Q,2}^2 e^{j\phi_{\text{RF}}}A_{\text{CBTT}}^4 \\
A_{\text{CBTT},Q,0,0} \quad &\approx \quad A_{\text{CBTT},Q,2,0} \\
A_{\text{CBTT},Q,2,2} \quad &\approx \quad A_{\text{CBTT},Q,2,0}
\end{aligned}
$$

$$(3.173)$$

$$
\begin{aligned}
A_{\mathrm{CBTT},Q,3,1} &= \left(\tfrac{3}{16}g_{\mathrm{M},1}h_{Q,3}^3 + \tfrac{3}{16}g_{\mathrm{M},3}h_{Q,1}^3\right)e^{j\phi_{\mathrm{RF}}}A_{\mathrm{CBTT}}^3 \\
&\quad + \left(\tfrac{75}{128}g_{\mathrm{M},3}h_{Q,1}h_{Q,2}^4 + \tfrac{75}{128}g_{\mathrm{M},3}h_{Q,1}^2h_{Q,3}^3\right)e^{j\phi_{\mathrm{RF}}}A_{\mathrm{CBTT}}^5 \\
A_{\mathrm{CBTT},Q,3,3} &= \left(\tfrac{1}{16}g_{\mathrm{M},1}h_{Q,3}^3 + \tfrac{1}{16}g_{\mathrm{M},3}h_{Q,1}^3\right)e^{j\phi_{\mathrm{RF}}}A_{\mathrm{CBTT}}^3 \\
&\quad + \left(\tfrac{75}{256}g_{\mathrm{M},3}h_{Q,1}h_{Q,2}^4 + \tfrac{75}{256}g_{\mathrm{M},3}h_{Q,1}^2h_{Q,3}^3\right)e^{j\phi_{\mathrm{RF}}}A_{\mathrm{CBTT}}^5 \\
A_{\mathrm{CBTT},Q,3,3} &\approx \tfrac{1}{3}A_{\mathrm{CBTT},Q,3,1}
\end{aligned}
\tag{3.174}
$$

$$
\begin{aligned}
A_{\mathrm{CBTT},Q,4,0} &= \tfrac{9}{64}g_{\mathrm{M},1}h_{Q,1}^2h_{Q,2}^2 e^{j\phi_{\mathrm{RF}}}A_{\mathrm{CBTT}}^4 \\
A_{\mathrm{CBTT},Q,4,2} &= \tfrac{3}{16}g_{\mathrm{M},1}h_{Q,1}^2h_{Q,2}^2 e^{j\phi_{\mathrm{RF}}}A_{\mathrm{CBTT}}^4 \\
A_{\mathrm{CBTT},Q,4,4} &= \tfrac{3}{64}g_{\mathrm{M},1}h_{Q,1}^2h_{Q,2}^2 e^{j\phi_{\mathrm{RF}}}A_{\mathrm{CBTT}}^4 \\
A_{\mathrm{CBTT},Q,4,2} &\approx \tfrac{4}{3}A_{\mathrm{CBTT},Q,4,0} \\
A_{\mathrm{CBTT},Q,4,4} &\approx \tfrac{1}{3}A_{\mathrm{CBTT},Q,4,0}
\end{aligned}
\tag{3.175}
$$

$$
\begin{aligned}
A_{\mathrm{CBTT},Q,5,1} &= \left(\tfrac{15}{128}g_{\mathrm{M},3}h_{Q,1}h_{Q,2}^4 + \tfrac{15}{128}g_{\mathrm{M},3}h_{Q,1}^2h_{Q,3}^3\right)e^{j\phi_{\mathrm{RF}}}A_{\mathrm{CBTT}}^5 \\
A_{\mathrm{CBTT},Q,5,1} &= \left(\tfrac{15}{256}g_{\mathrm{M},3}h_{Q,1}h_{Q,2}^4 + \tfrac{15}{256}g_{\mathrm{M},3}h_{Q,1}^2h_{Q,3}^3\right)e^{j\phi_{\mathrm{RF}}}A_{\mathrm{CBTT}}^5 \\
A_{\mathrm{CBTT},5,3} &\approx \tfrac{1}{2}A_{\mathrm{CBTT},5,1}
\end{aligned}
\tag{3.176}
$$

These approximations can be used for raising the identification accuracy of the desired coefficients as signal components showing a large measurement error can be replaced. For example, (3.173) may be applied for substituting the "DC"-component by the tone magnitude located at the second harmonic as $A_{\mathrm{CBTT},Q,2,0}$ and $A_{\mathrm{CBTT},Q,0,2}$ are equal.

In the following the signal component based postdistortion equations for a 5th-order postdistorter and CBTT input signals are presented. Despite of this limitation components up to the 35th power of the input signal magnitude are created. These products were truncated after the 5th-order:

$$
\begin{aligned}
A_{\mathrm{comp},Q,0,2} \approx k_{lin}e^{-j\hat{\phi}_{\mathrm{RF},Q}}\Big(&\tfrac{1}{g_{\hat{\mathrm{M}},1}}A_{\mathrm{CBTT},Q,0,2} - \tfrac{1}{4}\tfrac{g_{\hat{\mathrm{M}},3}}{g_{\hat{\mathrm{M}},1}^4}A_{\mathrm{CBTT},Q,0,2}|A_{\mathrm{CBTT},Q,1,1}|^2 \\
&-\tfrac{1}{8}\tfrac{g_{\hat{\mathrm{M}},3}}{g_{\hat{\mathrm{M}},1}^4}A_{\mathrm{CBTT},Q,2,2}|A_{\mathrm{CBTT},Q,1,1}|^2 - \tfrac{1}{8}\tfrac{g_{\hat{\mathrm{M}},3}}{g_{\hat{\mathrm{M}},1}^4}A_{\mathrm{CBTT},Q,2,0}|A_{\mathrm{CBTT},Q,1,1}|^2 \\
&-\tfrac{1}{4}\tfrac{g_{\hat{\mathrm{M}},3}}{g_{\hat{\mathrm{M}},1}^4}A_{\mathrm{CBTT},Q,0,0}|A_{\mathrm{CBTT},Q,1,1}|^2\Big)
\end{aligned}
\tag{3.177}
$$

$$
\begin{aligned}
A_{\mathrm{comp},Q,2,2} \approx k_{lin}e^{-j\hat{\phi}_{\mathrm{RF},Q}}\Big(&\tfrac{1}{g_{\hat{\mathrm{M}},1}}A_{\mathrm{CBTT},Q,2,2} - \tfrac{1}{4}\tfrac{g_{\hat{\mathrm{M}},3}}{g_{\hat{\mathrm{M}},1}^4}A_{\mathrm{CBTT},Q,2,0}|A_{\mathrm{CBTT},Q,1,1}|^2 \\
&-\tfrac{1}{4}\tfrac{g_{\hat{\mathrm{M}},3}}{g_{\hat{\mathrm{M}},1}^4}A_{\mathrm{CBTT},Q,0,0}|A_{\mathrm{CBTT},Q,1,1}|^2 - \tfrac{1}{4}\tfrac{g_{\hat{\mathrm{M}},3}}{g_{\hat{\mathrm{M}},1}^4}A_{\mathrm{CBTT},Q,2,2}|A_{\mathrm{CBTT},Q,1,1}|^2 \\
&-\tfrac{1}{4}\tfrac{g_{\hat{\mathrm{M}},3}}{g_{\hat{\mathrm{M}},1}^4}A_{\mathrm{CBTT},Q,0,2}|A_{\mathrm{CBTT},Q,1,1}|^2\Big)
\end{aligned}
\tag{3.178}
$$

$$
\begin{aligned}
A_{\mathrm{comp},Q,1,1} \approx{}& k_{lin} e^{-j\hat{\phi}_{\mathrm{RF},Q}} \Big(\frac{1}{g_{\hat{\mathrm{M}},1}} A_{\mathrm{CBTT},Q,1,1} - \frac{9}{16}\frac{g_{\hat{\mathrm{M}},3}}{g_{\hat{\mathrm{M}},1}^4} A_{\mathrm{CBTT},Q,1,1} |A_{\mathrm{CBTT},Q,1,1}|^2 \\
& - \frac{3}{16}\frac{g_{\hat{\mathrm{M}},3}}{g_{\hat{\mathrm{M}},1}^4} A_{\mathrm{CBTT},Q,3,1} |A_{\mathrm{CBTT},Q,1,1}|^2 - \frac{3}{16}\frac{g_{\hat{\mathrm{M}},3}}{g_{\hat{\mathrm{M}},1}^4} A_{\mathrm{CBTT},Q,1,3} |A_{\mathrm{CBTT},Q,1,1}|^2 \\
& - \frac{1}{16}\frac{g_{\hat{\mathrm{M}},3}}{g_{\hat{\mathrm{M}},1}^4} A_{\mathrm{CBTT},Q,3,3} |A_{\mathrm{CBTT},Q,1,1}|^2 + \frac{25}{32}\frac{g_{\hat{\mathrm{M}},3}^2}{g_{\hat{\mathrm{M}},1}^7} A_{\mathrm{CBTT},Q,1,1} |A_{\mathrm{CBTT},Q,1,1}|^4 \\
& + \frac{25}{64}\frac{|g_{\hat{\mathrm{M}},3}|^2}{g_{\hat{\mathrm{M}},1}^7} A_{\mathrm{CBTT},Q,1,1} |A_{\mathrm{CBTT},Q,1,1}|^4 \Big)
\end{aligned}
\tag{3.179}
$$

$$
\begin{aligned}
A_{\mathrm{comp},Q,3,1} \approx{}& k_{lin} e^{-j\hat{\phi}_{\mathrm{RF},Q}} \Big(\frac{1}{g_{\hat{\mathrm{M}},1}} A_{\mathrm{CBTT},Q,3,1} - \frac{3}{16}\frac{g_{\hat{\mathrm{M}},3}}{g_{\hat{\mathrm{M}},1}^4} A_{\mathrm{CBTT},Q,1,1} |A_{\mathrm{CBTT},Q,1,1}|^2 \\
& - \frac{3}{8}\frac{g_{\hat{\mathrm{M}},3}}{g_{\hat{\mathrm{M}},1}^4} A_{\mathrm{CBTT},Q,3,1} |A_{\mathrm{CBTT},Q,1,1}|^2 + \frac{25}{128}\frac{|g_{\hat{\mathrm{M}},3}|^2}{g_{\hat{\mathrm{M}},1}^7} A_{\mathrm{CBTT},Q,1,1} |A_{\mathrm{CBTT},Q,1,1}|^4 \\
& + \frac{25}{64}\frac{g_{\hat{\mathrm{M}},3}^2}{g_{\hat{\mathrm{M}},1}^7} A_{\mathrm{CBTT},Q,1,1} |A_{\mathrm{CBTT},Q,1,1}|^4 - \frac{1}{8}\frac{g_{\hat{\mathrm{M}},3}}{g_{\hat{\mathrm{M}},1}^4} A_{\mathrm{CBTT},Q,3,3} |A_{\mathrm{CBTT},Q,1,1}|^2 \\
& - \frac{1}{16}\frac{g_{\hat{\mathrm{M}},3}}{g_{\hat{\mathrm{M}},1}^4} A_{\mathrm{CBTT},Q,1,3} |A_{\mathrm{CBTT},Q,1,1}|^2 \Big)
\end{aligned}
\tag{3.180}
$$

The simplifications presented in (3.173) to (3.176) were not included in these equations. In this way measurement results can be used instead if desired.

Equations (3.177) - (3.180) convert the tone amplitudes measured at the transmitter output to the ones present at the output of the baseband nonlinearity. As mentioned at the beginning of this section the complex-valued amplitudes $A_{\mathrm{CBTT},Q,n,m}$ include only the RF phase contributions. By the multiplication with the factor $\exp(-j\hat{\phi}_{\mathrm{RF},Q})$ in (3.177) - (3.180) this part of the phase response should be removed. Assuming a correct identification of the coefficient $\hat{g}_{\mathrm{M},1}$ and $\hat{g}_{\mathrm{M},3}$ also the AM-PM conversion introduced by the mixer output NL should be compensated.

3.8.7 Baseband nonlinearity parameter extraction

After the deembedding of the tone magnitudes was performed the baseband nonlinearities can be parameterized. Examples for the extraction of power series coefficients from the measurement of a TT power sweep were presented in [117, 85]. In these two cases the magnitudes of the desired TT signal and the intermodulation products were measured at the output of a microwave amplifier. Based on these measurement results an odd-order power series was parameterized. In [85] this task was performed at different tone spacings of the TT signal (but at a fixed center frequency) and the resulting set of polynomial coefficients was then used for fitting a nonlinear dynamic model. Instead of characterizing the baseband nonlinearity at a constant frequency offset from the carrier and vary the tone spacing the nonlinearity was measured over the baseband bandwidth at a constant tone spacing. This approach is justified by the assumption that the baseband nonlinearities do show linear memory effects but no nonlinear dynamic behavior. The second important difference to the two former approaches is that in the actual case the nonlinearity is located in the baseband. Hence, the calculation of the TT magnitudes is similar for the baseband and the RF case but the CBTT results in a four-tone signal at the transmitter output.

In the following the extraction of the BB PCWM coefficient will be exemplified for the quadrature channel. The inphase channel results are achieved in the same way. The BB amplifier response to a CBTT input signal was derived in (3.110). This expression summarizes all signal components present at the BB NL output. The analytical description of the magnitudes of these signal components is now used

for extracting the corresponding nonlinear coefficients. As at this point of the transmitter no interactions between the even- and odd-order distortion components exist the identification of the corresponding polynomial coefficients will be discussed separately.

The odd-order distortion components presented in (3.110) include the intermodulation and harmonic distortion. Due to the preceding deembedding step only the IMD distortion is used for the extraction of the odd order coefficients.

Assuming K measurements are covered by the power sweep the $2K \times 1$ vector summarizing the deembedded odd-order amplitudes is given by:

$$\mathbf{Y} = \begin{pmatrix} A_{\mathrm{comp},Q,1,1,\mathrm{f}_m,\mathrm{P}_1} \\ \vdots \\ A_{\mathrm{comp},Q,1,1,\mathrm{f}_m,\mathrm{P}_K} \\ A_{\mathrm{comp},Q,3,1,\mathrm{f}_m,\mathrm{P}_1} \\ \vdots \\ A_{\mathrm{comp},Q,3,1,\mathrm{f}_m,\mathrm{P}_K} \end{pmatrix} \tag{3.181}$$

Here, the deembedding results are indexed by f_m to highlight their dependency on the different center frequencies. The modeled BB response is incorporated in the $2K \times 2$ matrix:

$$\mathbf{H}_{\mathrm{BB,O}} = \begin{pmatrix} \mathbf{H}_{\mathrm{BB,O},1,1} & \mathbf{H}_{\mathrm{BB,O},1,2} \\ & \mathbf{H}_{\mathrm{BB,O},2,2} \end{pmatrix} \tag{3.182}$$

where the vectors $\mathbf{H}_{\mathrm{BB,O},l,m}$ are composed as follows:

$$\mathbf{H}_{\mathrm{BB,O},l,m} = \frac{1}{16^{m-1}} \binom{2m-1}{m-1} \binom{2m-1}{m-l} \mathbf{A}_{\mathrm{CBTT}}^{2m-1} \tag{3.183}$$

The vector $\mathbf{A}_{\mathrm{CBTT}}$ summarizes the input signal magnitudes applied during the power sweep. Based on these definitions the coefficient vector $\hat{\boldsymbol{\lambda}}_{\mathrm{BB,O,f}_m}$ is extracted by:

$$\hat{\boldsymbol{\lambda}}_{\mathrm{BB,O,f}_m} = \mathrm{LS}_{\mathrm{opt}}(\mathbf{H}_{\mathrm{BB,O}}, \mathbf{Y}) \tag{3.184}$$

In a similar way the even-order coefficient is extracted. The even-order deembedding results are arranged in the $2K \times 1$ vector:

$$\mathbf{Y} = \begin{pmatrix} A_{\mathrm{comp},Q,0,2,\mathrm{f}_m,\mathrm{P}_1} \\ \vdots \\ A_{\mathrm{comp},Q,0,2,\mathrm{f}_m,\mathrm{P}_K} \\ A_{\mathrm{comp},Q,2,2,\mathrm{f}_m,\mathrm{P}_1} \\ \vdots \\ A_{\mathrm{comp},Q,2,2,\mathrm{f}_m,\mathrm{P}_K} \end{pmatrix} \tag{3.185}$$

The corresponding $2K \times 1$ vector providing the modeled BB response given by:

$$\mathbf{H}_{\mathrm{BB},E} = \begin{pmatrix} \mathbf{H}_{\mathrm{BB},E,1,1} \\ \mathbf{H}_{\mathrm{BB},E,1,1,1} \end{pmatrix} \tag{3.186}$$

where the two vectors are composed as follows:

$$\begin{aligned}
\mathbf{H}_{\text{BB},E,k,l} &= \tfrac{2}{16^l}\binom{2l}{l}\binom{2l}{l-k}\mathbf{A}_{\text{CBTT}}^{2l} \\
\mathbf{H}_{\text{BB},E,k,l,m} &= \tfrac{4}{16^m}\binom{2m}{m-k}\binom{2m}{m-l}\mathbf{A}_{\text{CBTT}}^{2m}
\end{aligned} \tag{3.187}$$

The indices k, l and m in these expressions correspond to the last two terms of (3.110). Using these results the even-order coefficient vector $\hat{\boldsymbol{\lambda}}_{\text{BB},E,\text{f}_m}$ is derived by solving the equation:

$$\mathbf{H}_{\text{BB},E}^{H}\mathbf{H}_{\text{BB},E}\hat{\boldsymbol{\lambda}}_{\text{BB},E,\text{f}_m} = \mathbf{H}_{\text{BB},E}^{H}\mathbf{Y} \tag{3.188}$$

The even- and odd-order polynomial parameters derived in (3.184) and (3.188) are merged into one set of coefficients:

$$\begin{aligned}
\hat{g}_{\text{BB},Q,2k-1} &= \hat{\boldsymbol{\lambda}}_{\text{BB},O}(k) \\
\hat{g}_{\text{BB},Q,2k} &= \hat{\boldsymbol{\lambda}}_{\text{BB},E}(k)
\end{aligned} \tag{3.189}$$

After identifying the polynomial coefficients from the inphase and quadrature channel the corresponding input related "Wiener" parameters can be calculated by taking the pth-root of the identified coefficients. Additionally, the lowpass filter phase shift must be reintroduced. This information is taken from the CBTT phase extraction process described in Section 3.8.4:

$$\begin{aligned}
\hat{h}_{Q,2k-1,\text{f}_m} &= \text{sign}(\text{Re}\{\hat{g}_{\text{BB},Q,2k-1,\text{f}_m}\})\,|\hat{g}_{\text{BB},Q,2k-1,\text{f}_m}|^{\frac{1}{2k-1}} \\
&\quad \cdot \exp\left(j\frac{\hat{\tilde{\phi}}_{I,\text{f}_m}}{2k-1} + j\frac{\angle\left\{\text{sign}(\text{Re}\{\hat{g}_{\text{BB},Q,2k-1,\text{f}_m}\})\hat{g}_{\text{BB},Q,2k-1,\text{f}_m}\right\}}{2k-1}\right) \\
\hat{h}_{Q,2k,\text{f}_m} &= \hat{g}_{\text{BB},Q,2k,\text{f}_m}^{\frac{1}{2k}}e^{j\frac{\hat{\tilde{\phi}}_{I,\text{f}_m}}{2k}}
\end{aligned} \tag{3.190}$$

In this equation the index f_m was added to the polynomial coefficients for highlighting their dependency on the center frequency of the CBTT signal. This dependency was neglected at the derivation of the coefficients (3.173) - (3.188) to simplify the notation.

At this point of the parameter extraction process the connection to the imbalance extraction must be established. Due to this reason at (3.190) the phase shift $\hat{\tilde{\phi}}_{\gamma,\text{f}_m}$ is not included. In Section 3.6 the parameters $|\hat{\gamma}(j\omega_m)|$, $\hat{\phi}_{\gamma}(j\omega_m)$ and $\hat{\theta}_e$ were extracted from single-tone measurements. As mentioned in Section 3.8.4 the phases derived in (3.129) should agree with the ones extracted from the image signal suppression. In a similar way $|\hat{h}_{Q,1,\text{f}_m}/\hat{h}_{I,1,\text{f}_m}|$ should agree with $|\hat{\gamma}(j\omega_m)|$ up to an error due to measurement noise. For a complete transmitter model, as discussed in Section 3.9, the impact of $|\hat{\gamma}(j\omega_m)|$ and $\hat{\phi}_{\gamma}(j\omega_m)$ can be represented by the BB amplifier models or by an additional imbalance block. This decision influences the conversion of the parameters $\hat{h}_{I,k,\text{f}_m}$, $\hat{h}_{Q,k,\text{f}_m}$ to the corresponding PCWM filtering functions. In both cases the imbalance parameters extracted in Section 3.6 and the ones from the NL coefficient identification can be combined to:

$$\begin{aligned}
|\hat{\gamma}_{\text{fin.}}(j2\pi\text{f}_m)| &= \tfrac{1}{2}\left(|\hat{\gamma}(j2\pi\text{f}_m)| + \frac{\hat{h}_{Q,1,\text{f}_m}}{\hat{h}_{I,1,\text{f}_m}}\right) \\
\hat{\phi}_{\gamma,\text{fin.}}(j2\pi\text{f}_m) &= \tfrac{1}{2}\left(\hat{\phi}_{\gamma}(j2\pi\text{f}_m) + \hat{\tilde{\phi}}_{\gamma,\text{f}_m}\right)
\end{aligned} \tag{3.191}$$

In case of using an imbalance block no additional magnitude or phase imbalance may be introduced by the BB amplifier models. This restriction applies only to the linear model response. The ratio between

linear output and predicted nonlinear distortion may not be changed. As the inphase branch is taken as reference, these coefficients stay the same. Therefore, the other parameters convert to:

$$
\begin{aligned}
\hat{h}_{I,k,\mathrm{f}_m,\mathrm{fin.}} &= \hat{h}_{I,k,\mathrm{f}_m} \\
\hat{h}_{Q,1,\mathrm{f}_m,\mathrm{fin.}} &= \hat{h}_{I,1,\mathrm{f}_m} \\
\hat{h}_{Q,k,\mathrm{f}_m,\mathrm{fin.}} &= \hat{h}_{Q,k,\mathrm{f}_m} \left(\frac{\hat{h}_{I,1,\mathrm{f}_m}}{\hat{h}_{Q,1,\mathrm{f}_m} |\hat{\gamma}_{\mathrm{fin.}}(j2\pi\mathrm{f}_m)|^{k-1}} \right)^{1/k} \approx \frac{\hat{h}_{Q,k,\mathrm{f}_m}}{|\hat{\gamma}_{\mathrm{fin.}}(j2\pi\mathrm{f}_m)|} \quad k > 1
\end{aligned}
\tag{3.192}
$$

In case the imbalance block models only the I/Q mixer phase error, the magnitude of the extracted nonlinear coefficient stays unchanged. For the quadrature branch the phase difference to the inphase channel $\hat{\phi}_{\gamma,\mathrm{fin.}}(j\omega_m)$ is introduced to the parameters:

$$
\hat{h}_{Q,k,\mathrm{f}_m,\mathrm{fin.}} = \hat{h}_{Q,k,\mathrm{f}_m}\, e^{j\hat{\phi}_{\gamma,\mathrm{fin.}}(j2\pi\mathrm{f}_m)}
\tag{3.193}
$$

These input related parameters can now be arranged in N_{BB} filters each one representing the frequency response of the corresponding nonlinear order. Depending on the implementation of the transmitter model / compensator the filters can be realized in the time or in the frequency domain. An approach for implementing the filters in the time domain, using linear phase FIR filter synthesis, can be found in the literature (for example [118]). For this work the frequency domain implementation of the filters was used. Further issues on the evaluation of the PCWM filtering functions from the extracted polynomials are discussed in Section 3.8.10.

This filter synthesis step provides the transition of the set of memoryless polynomial coefficients $\hat{\boldsymbol{\lambda}}_{\mathrm{BB},O,\mathrm{f}_m}$, $\hat{\boldsymbol{\lambda}}_{\mathrm{BB},E,\mathrm{f}_m}$ to their PCWM dynamic correspondent $\hat{H}_{I,p}(j\omega)$, $\hat{H}_{Q,p}(j\omega)$. These filters implement the transmitter frequency response up to a phase rotation introduced by the LO and the linear phase shift of the mixer output nonlinearity. The accuracy of the evaluated phase response is directly related to the behavior of the measurement receiver. The PCWM filters together with the RF input nonlinearity coefficients and the imbalance description compose a model of the nonlinear dynamic transmitter behavior.

3.8.8 Mixer output nonlinearity postidentification

After the BB coefficients have been extracted the response of these NLs can be predicted. In turn, this information can be used for calculating all distortion products present at the input of the mixer output NL. Furthermore, it can be applied for improving the estimation of the parameters $g_{\mathrm{M},k}$. The basis of this postidentification of the mixer output NL are the BB coefficients (3.189) and the transmitter response equations provided in Section 3.8.5.2 . The BB parameters are taken from the measurements performed at the same center frequency f_m as the FSTT results.

Similar to the postdistorter case the cascade of the BB and the mixer output NLs result in a significant number of distortion products. In contrast to the analytical response derivation in Section 3.8.1 the transmitter behavior evaluation is not provided for arbitrary NL orders of the BB and the mixer output NLs, N_{BB} and N_{RF}, respectively. Instead third-order polynomials were assumed in both cases. Additionally, the transmitter response prediction is limited to the 5th-power of the input signal magnitude and to the 5th-order distortion products. These specifications are in agreement with the defaults used for deriving the postdistorter expressions. Compared to Section 3.8.1 the interaction of the different distortion products at the mixer output NL were included, but the degree of the polynomials and the maximum power of the input signal magnitude were limited.

For applying the results presented in Section 3.8.5.2 the coefficients $\bar{h}_{I,k}^{k}$, $\bar{h}_{Q,k}^{k}$ are substituted by $\hat{g}_{\mathrm{BB},I,k}$, $\hat{g}_{\mathrm{BB},Q,k}$. The parameters $\hat{\bar{\phi}}_I$, $\hat{\bar{\phi}}_\gamma$ and $\hat{\theta}_e$ were derived in (3.129). The equations (3.163) - (3.165) are evaluated using the vector $\mathbf{A}_{\mathrm{FSTT}}$ summarizing the K power sweep input signal magnitudes instead of the scalar correspondent. The resulting vectors are now used for composing the $6K \times 2$ matrix $\mathbf{H}_{\mathrm{RF}}$:

$$
\mathbf{H}_{\mathrm{RF}} = \begin{pmatrix}
& \mathbf{A}_{\mathrm{FSTT,M},-5,1}\big|_{g_{\mathrm{M},3}=1} \\
\mathbf{A}_{\mathrm{FSTT,M},-3,1}\big|_{\substack{g_{\mathrm{M},1}=1 \\ g_{\mathrm{M},3}=0}} & \mathbf{A}_{\mathrm{FSTT,M},-3,1}\big|_{\substack{g_{\mathrm{M},1}=0 \\ g_{\mathrm{M},3}=1}} \\
\mathbf{A}_{\mathrm{FSTT,M},-1,1}\big|_{\substack{g_{\mathrm{M},1}=1 \\ g_{\mathrm{M},3}=0}} & \mathbf{A}_{\mathrm{FSTT,M},-1,1}\big|_{\substack{g_{\mathrm{M},1}=0 \\ g_{\mathrm{M},3}=1}} \\
\mathbf{A}_{\mathrm{FSTT,M},1,1}\big|_{\substack{g_{\mathrm{M},1}=1 \\ g_{\mathrm{M},3}=0}} & \mathbf{A}_{\mathrm{FSTT,M},1,1}\big|_{\substack{g_{\mathrm{M},1}=0 \\ g_{\mathrm{M},3}=1}} \\
\mathbf{A}_{\mathrm{FSTT,M},3,1}\big|_{\substack{g_{\mathrm{M},1}=1 \\ g_{\mathrm{M},3}=0}} & \mathbf{A}_{\mathrm{FSTT,M},3,1}\big|_{\substack{g_{\mathrm{M},1}=0 \\ g_{\mathrm{M},3}=1}} \\
& \mathbf{A}_{\mathrm{FSTT,M},5,1}\big|_{g_{\mathrm{M},3}=1}
\end{pmatrix}
\tag{3.194}
$$

It is interesting to note, that the structure of this matrix is different from the former ones (c.f., (3.132)). Here, the IMD$_3$ distortion products are considered for the linear coefficient estimation $g_{\mathrm{M},1}$. As 3rd-order IMD components generated by the BB amplifiers contribute linearly to the IMD$_3$ distortion at the transmitter output, explains this arrangement.

The transmitter model (3.163) - (3.165) presented in Section 3.8.5 doesn't describe the phase shift introduced by the LO and the linear mixer output NL response. This phase rotation, provided by (3.144), has to be removed from the FSTT measurements. The $6K \times 1$ vector arranging the measured transmitter response is therefore given by:

$$
\mathbf{Y} = e^{-j\hat{\phi}_{\mathrm{RF,FSTT,est.}}} \begin{pmatrix}
\mathbf{A}_{\mathrm{FSTT},-5,1} \\
\mathbf{A}_{\mathrm{FSTT},-3,1} \\
\mathbf{A}_{\mathrm{FSTT},-1,1} \\
\mathbf{A}_{\mathrm{FSTT},1,1} \\
\mathbf{A}_{\mathrm{FSTT},3,1} \\
\mathbf{A}_{\mathrm{FSTT},5,1}
\end{pmatrix}
\tag{3.195}
$$

The coefficients to be estimated are combined by the vector $\hat{\boldsymbol{\lambda}}_{\mathrm{RF}} = (\hat{g}_{\mathrm{M},1}\, \hat{g}_{\mathrm{M},3})^T$. These coefficients are evaluated by:

$$
\hat{\boldsymbol{\lambda}}_{\mathrm{RF}} = \mathrm{LS}_{\mathrm{opt}}(\mathbf{H}_{\mathrm{RF}}, \mathbf{Y})
\tag{3.196}
$$

Also at this identification the parameter $\hat{g}_{\mathrm{M},1}$ is typically not exactly one. By updating the coefficients as shown in (3.197), recomposing (3.194) and performing the evaluation of the parameters $\hat{g}_{\mathrm{M},1}$, $\hat{g}_{\mathrm{M},3}$ again overcomes this drawback.

$$
\begin{aligned}
\hat{g}_{\mathrm{BB},I,k} &= \hat{g}_{\mathrm{BB},I,k}|\hat{\boldsymbol{\lambda}}_{\mathrm{RF}}(1)| \\
\hat{g}_{\mathrm{BB},Q,k} &= \hat{g}_{\mathrm{BB},Q,k}|\hat{\boldsymbol{\lambda}}_{\mathrm{RF}}(1)| \\
\hat{\bar{\phi}}_I &= \hat{\bar{\phi}}_I + \angle\hat{\boldsymbol{\lambda}}_{\mathrm{RF}}(1)
\end{aligned}
\tag{3.197}
$$

It is important to note that the changes to the parameters $\hat{g}_{\mathrm{BB},I,k}$, $\hat{g}_{\mathrm{BB},Q,k}$ and $\hat{\bar{\phi}}_I$ in (3.197) were only used to force $\hat{g}_{\mathrm{M},1} = 1$. These changes are not taken over into the final model.

Simulation showed that by the use of the mixer output NL postidentification the identification accuracy of the evaluated model is improved. An analysis of the performance improvement achieved by this task is given in the next section.

3.8.9 Nonlinear parameter extraction algorithm performance

The accuracy of the mixer output NL coefficients extraction depends on the validity of the response approximation for a FSTT input signal as well as the proper deembedding of the BB NLs output signals. Simulations using the frequency independent transmitter model have been performed for visualizing the accuracy of the extracted model as well as the sensitivity to measurement noise.

The simulations were based on the same parameters as used for the validation of the FSTT receiver response approximation in Section 3.8.1 (i.e., $\gamma = 0.95$, $\theta_e = 3°$, $\phi_\gamma = 4°$, $IP_{2,\text{output}} = 44\,\text{dBm}$ and an $IP_{3,\text{output}} = 24\,\text{dBm}$, $IP_{3,\text{RF,output}} = 24\,\text{dBm}$). Additionally, a linear phase shift of the RF input NL $\angle g_{\text{M},1} = 10°$ and a lowpass filter phase shift $\bar{\phi}_I = 13°$ were considered. For extracting the transmitter parameters, FSTT power sweeps between $P_{\text{in}} = -20\ldots10\,\text{dBm}$ were used. The power levels in the CBTT case were 3 dB lower. For both types of power sweep the LO phase was randomly chosen. The BB amplifiers and the mixer output NL were described by 3rd-order polynomials. The identified coefficients were incorporated into a transmitter model. The response of the model onto a FSTT and a CBTT power sweep was evaluated. Then the normalized mean square error (NMSE) between the original and modeled transmitter response was evaluated for each power level by comparing the transmitter output signals. Assuming that these two signals are represented by time-discrete sequences the NMSE is given by [119]:

$$\text{NMSE} = \frac{\sum_n |y_{\text{ref}}(n) - y_{\text{Model}}(n)|^2}{\sum_n |y_{\text{ref}}(n)|^2} \tag{3.198}$$

Here, the reference sequence $y_{\text{ref}}(n)$ identifies the transmitter response using the original parameters. The sequence $y_{\text{Model}}(n)$ represents the output derived from the extracted coefficients. As mentioned in Section 3.8.5 the extracted transmitter model does not predict the phase shift introduced by the LO and the parameter $g_{\text{M},1}$. For a correct comparison of the two signals according to (3.198) the modeled transmitter output must be first phase shifted to be aligned to $y_{\text{ref}}(n)$. At the FSTT signal the parameter $\hat{\phi}_{\text{RF,FSTT,est.}}$, introduced in (3.144), is used for this task. In case of the CBTT signals the parameters $\hat{\phi}_{\text{RF},I}$ and $\hat{\phi}_{\text{RF},Q} - \hat{\theta}_e$ defined in Section 3.8.4 are applied.

The mean over all power levels and all three input signals was used as modeling error. This error was named $\text{NMSE}_{\text{Model}}$. Also the identification error of $\hat{g}_{\text{M},3}$ was evaluated by calculating $|\Delta g_{\text{M},3}|^2/|g_{\text{M},3,\text{Ref}}|^2 = |\hat{g}_{\text{M},3} - g_{\text{M},3,\text{Ref}}|^2/|g_{\text{M},3,\text{Ref}}|^2$. The parameter $g_{\text{M},3,\text{Ref}}$ represents the scaled 3rd-order RF input NL coefficient $g_{\text{M},3}/g_{\text{M},1}$.

At the beginning, the transmitter parameterization process without the mixer output NL postidentification is analyzed. The ratio between $IP_{3,\text{BB}}$ and $IP_{3,\text{RF}}$ has a major influence on the performance of the resulting model. Figure 3.14(a) shows the impact of the two parameters on $\text{NMSE}_{\text{Model}}$. As expected, at a low $IP_{3,\text{BB}}$ and a large $IP_{3,\text{RF}}$ the extracted model performs best. Under these operation conditions the postdistorter introduces only slight corrections to the measured CBTT amplitudes. In most cases a reduction of $IP_{3,\text{RF}}$ results in an improved modeling accuracy. Within the 20 dB variation range of

$IP_{3,RF}$ the modeling error drops by about 37 dB. Sweeping $IP_{3,BB}$ over the same range causes up to 19 dB variation in the $NMSE_{Model}$.

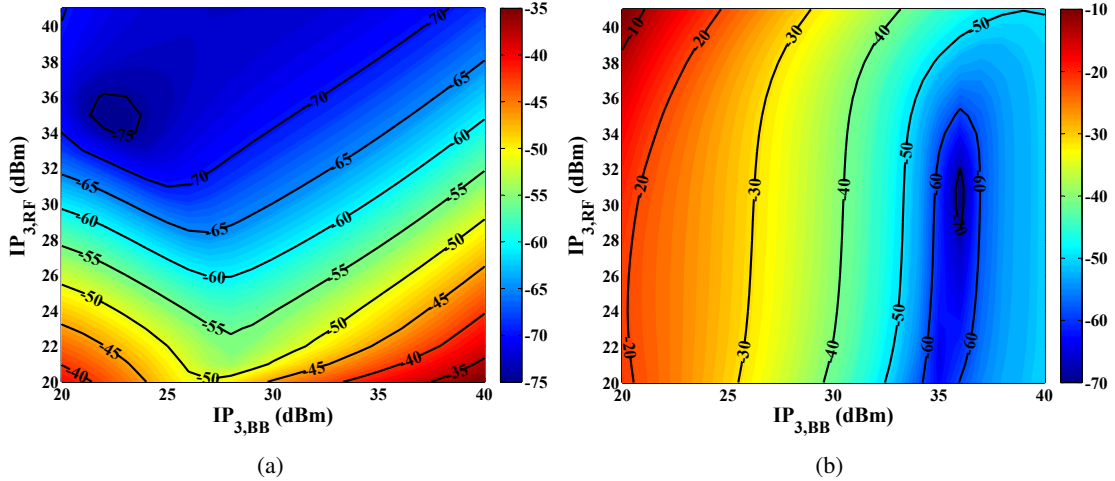(a)   (b)

Figure 3.14: Simulation of the influence of the $IP_{3,BB}$, $IP_{3,RF}$ on (a) the modeling error $NMSE_{Model}$ and (b) the identification error of $\hat{g}_{M,3}$.

In contrast to the transmitter modeling error the identification accuracy of $\hat{g}_{M,3}$ depends mainly on the $IP_{3,BB}$. At a large $IP_{3,BB}$ the IMD_3 of the FSTT signal at the transmitter output is dominated by the contribution of the mixer output nonlinearity. Hence, only minor changes are introduced to the measured amplitudes by the BB contribution. In both cases, the error of the overall model and of $\hat{g}_{M,3}$, the best performance is achieved if the distortion cancelation process has only little impact on the measurements. This explains the opposite behavior of the prediction accuracy in the two cases.

For the mixer output nonlinearity extraction the validity of the analytical FSTT response approximation is essential. As mentioned in Section 3.8.5.2 the second-order distortion interactions and the impact of the two desired tones are the main effects not predicted by the approximation (3.108). The influence of these two factors on the accuracy of $\hat{g}_{M,3}$ is analyzed in Figure 3.15(a). From this plot a destructive interference of the two distortion mechanisms can be recognized at $IP_{2,BB} = 32.5$ dBm and $IP_{3,RF} < 30$ dBm for a $IP_{3,BB} = 24$ dBm.

The impact of noisy measurements on the evaluation of $\hat{g}_{M,3}$ and the resulting model is considered in Figure 3.15(b). Here, the noise power level was evaluated relative to the highest input power level during the power sweep (i.e., $P_{in,max} = 10$ dBm). This noise level was used for the corresponding power sweep. In this way, the measurements at low input signal power are more affected by the measurement noise. This fact complicates the evaluation of the tone magnitudes and phases to which the other measurements are compared to. For coping with this problem five times averaging of the measurement results was used. For each SNR level the model coefficient extraction was repeated 30 times. The continuous lines in Figure 3.15(b) represent the mean over all realizations. The upper and lower triangles identify the 3σ variation range of the corresponding error function. It is interesting to note, that the $\hat{g}_{M,3}$ evaluation accuracy is nearly independent of the SNR level. The transmitter modeling error is more sensitive to measurement noise showing a 8 dB drop in the prediction accuracy by a 20 dB SNR reduction.

In Figure 3.16 the performance of the transmitter identification algorithm including the mixer out-
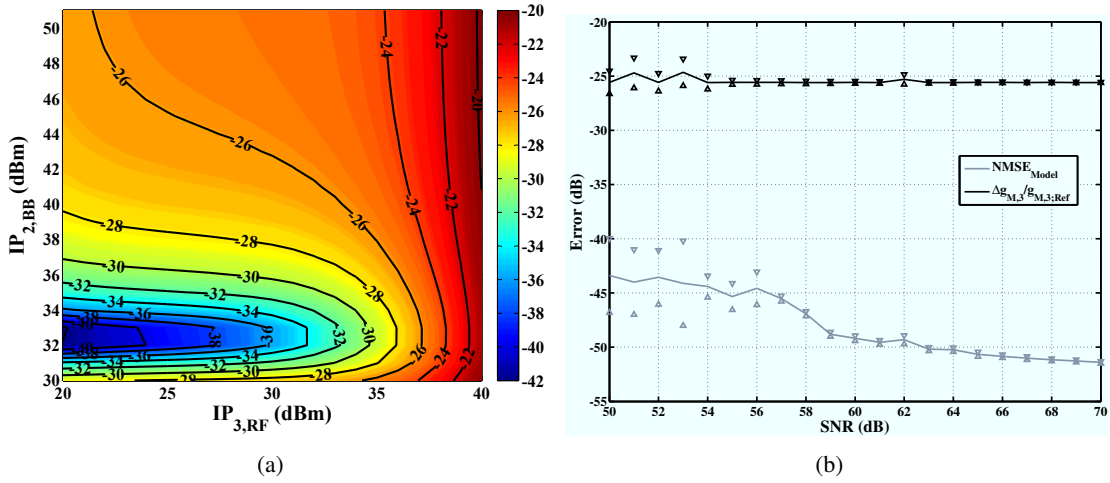
Figure 3.15: Simulation of (a) the $\hat{g}_{M,3}$ identification accuracy as a function of the $IP_{3,RF}$, $IP_{2,BB}$ and (b) the $NMSE_{Model}$ and the $\hat{g}_{M,3}$ modeling error at the presence of measurement noise.

put NL postidentification is presented. The prediction accuracy of $\hat{g}_{M,3}$ is significantly improved at $IP_{3,BB} < 30\,\mathrm{dBm}$ as shown in Figure 3.16(b). Above this limit a degradation of the achievable performance can be recognized. This improvement results only in a slight rise of the overall modeling error $NMSE_{Model}$ of approx. $0.3\,\mathrm{dB}$ in the lower range of $IP_{3,BB}$. It is interesting to note that if $NMSE_{Model}$ is calculated from the tone magnitudes required from the transmitter parameterization an improvement of up to $4\,\mathrm{dB}$ is achieved.

3.8.10 Model implementation issues

Up to now the main part of the parameter extraction focused on the CBTT measurements. As soon as the model coefficients are derived and the model is composed as described in Section 3.9 the modeled and simulated FSTT measurement can be compared. Especially, if the FSTT transmitter response was captured over a certain bandwidth $\pm f_m$ issues on the implementation of the PCWM filtering functions can be derived.

During the discussion of the BB parameter extraction in Section 3.8.7 the polynomial coefficients were evaluated at certain measurement frequencies covering the positive BB frequency range. Then the transition from the polynomial to the corresponding PCWM coefficients was explained. In the next step the function represented by the PCWM coefficients was implemented as a filter. With implicit understanding the usage of real-valued filters was assumed at this task. Depending on the frequency response of the PCWM coefficients an undesired model behavior may be initiated.

The fundamental idea of the BB polynomial extraction approach was representing the complete phase information by the parameters $\hat{\phi}_{RF}$, $\hat{\phi}_I$, by the imbalance coefficients $\hat{\phi}_\gamma$, $\hat{\theta}_e$, and the cancelation of the AM-PM conversion of the mixer output nonlinearity during the deembedding process. Therefore, if the BB amplifiers show no AM-PM conversion real-valued coefficients should be derived by (3.184) and (3.188). Clearly, the real-valued condition is guaranteed for the linear parameter. Examples for the phase of extracted second and third-order polynomial coefficients are presented in Figure 3.17(a). In case of
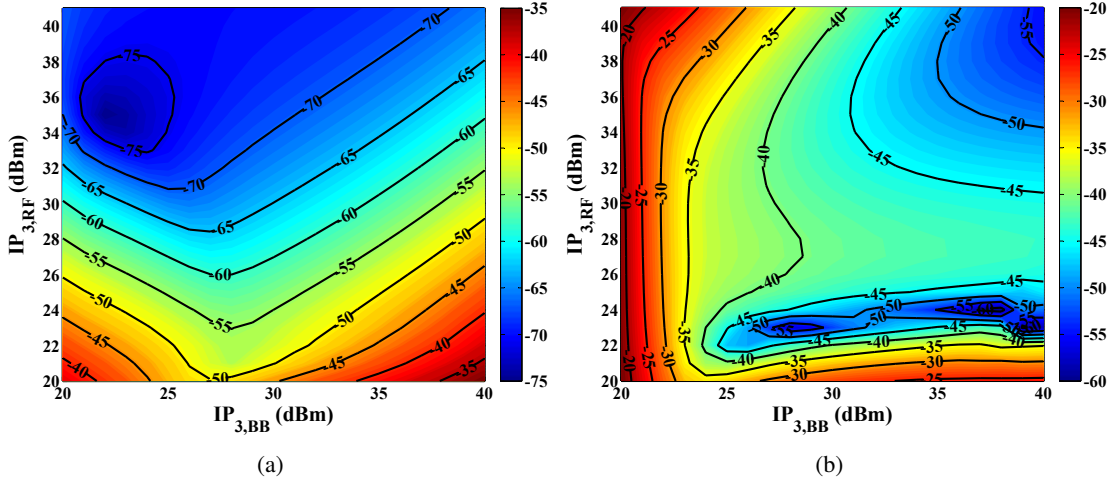
(a)

(b)

Figure 3.16: Simulation of influence of the $IP_{3,BB}$, $IP_{3,RF}$ on the (a) modeling error $NMSE_{Model}$ and (b) on the identification error of $\hat{g}_{M,3}$ using the transmitter identification algorithm including the mixer output NL postidentification.

the 3rd-order coefficient a slight deviation from $180°$ can be recognized. A phase shift of about 7 to $9°$ was identified. In contrast to this behavior the 2nd-order parameter shows a phase deviation varying between 60 and $74°$. The impact of a real- and a complex-valued implementation of the second order PCWM filtering function are compared in Figure 3.17(b). Additionally, the measured HD_2 phase is plotted, which was extracted from the FSTT measurements. Clearly, in case of a real-valued extension of the evaluated frequency response the non-vanishing imaginary part causes a jump of the simulated tone phase around DC. This jump is not observed in the transmitter measurements. Therefore, a real-valued implementation of the PCWM filtering functions is only appropriate if the imaginary part of the extracted coefficients tends to zero when approaching DC. This condition is approximately fulfilled at the third order coefficient but not for the second order one.

The real- or complex-valued implementation of the PCWM filtering functions impact the behavior of the transmitter system. For a polynomial describing the behavior of RF amplifiers complex-valued normalized coefficients are associated with AM-PM conversion effects (i.e.: a_{2n-1}/a_1, $a_{2n-1} \in \mathbb{C}$ ... polynomial coefficients). As mentioned before complex-valued PCWM coefficients can be implemented using real-valued time domain filtering functions. Calculating the gain of this model using a real-valued single-tone input signal only AM-AM conversion can be observed, if the time domain average of the output to input signal ratio is evaluated (compare Section 3.2). If, on the other hand, the gain is derived by dividing the complex-valued amplitude of the output by the corresponding input tone AM-PM conversion will be recognized. This example highlights the difficulties in detecting AM-PM conversion for broadband real-valued systems and the dependency on the applied gain definition.

The complex-valued implementation of the PCWM filtering functions is not only introducing AM-PM conversion according to the definition above. If applying an input signal to such a PCWM the distortion at the RF output acts like being created in both baseband branches. This crosstalk of the corresponding distortion can be significantly above the level introduced by imbalance effect for the NL signal components. The complex-valued time domain filtering functions can be directly inserted in (3.58) for
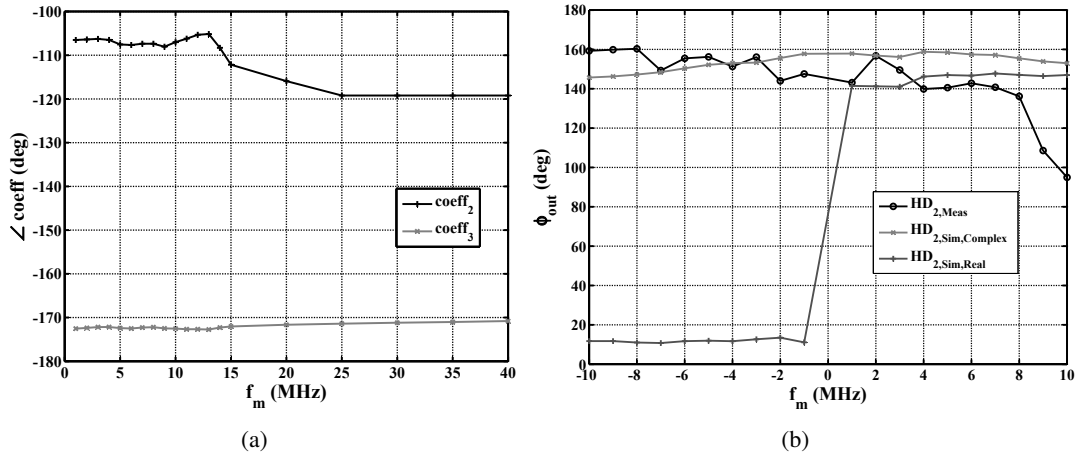
Figure 3.17: (a) Examples for the extracted phases of the second and third order polynomial coefficients. (b) Comparison of the real- and complex-valued implementation of the 2nd-order PCWM filtering function.

representing this distortion generation mechanism. It should be noted, that despite the simplicity of the implementation of the distortion crosstalk at the transmitter model it significantly raises the complexity of the corresponding predistorter.

3.8.11 Predistorter design

After discussing the nonlinear transmitter model parameterization a compensator should be developed for reducing the generated distortion. The basis for the design of the predistorter will be the nonlinear transmitter model composed of a 3rd-order PCWM followed by a 3rd-order complex power series (i.e., $N_{\text{BB}} = 3$, $N_{\text{RF}} = 3$). The time domain response of the nonlinear transmitter on an input signal $s_{\text{BB}}(t)$ is given by:

$$s_{\text{Amp}}(t) = \sum_{k=1}^{N_{\text{BB}}} [h_{I,k}(t) * \text{Re}\{s_{\text{BB}}(t)\}])^k + j \sum_{k=1}^{N_{\text{BB}}} [h_{Q,k}(t) * \text{Im}\{s_{\text{BB}}(t)\}]^k$$

$$s_{\text{mod}}(t) = \sum_{k=1}^{(N_{\text{RF}}+1)/2} g_{\text{M},k} s_{\text{Amp}}(t) |s_{\text{Amp}}(t)|^{2(k-1)}$$

$$(3.199)$$

For this model, again, the DC-offset was excluded. The DC-offset compensation will not be part of the predistorter design.

3.8.11.1 Baseband amplifier predistorter

As the filters of the PCWM were implemented in the frequency domain it proved advantageous of designing also the BB predistorter in the frequency domain. For calculating the amplifier output spectrum

the frequency domain representation of the real and the imaginary parts of the input signal are required:

$$S_{\text{BB,Re}}(j\omega) = \mathscr{F}\left[\text{Re}\{s_{\text{BB}}(t)\}\right]$$
$$S_{\text{BB,Im}}(j\omega) = \mathscr{F}\left[\text{Im}\{s_{\text{BB}}(t)\}\right]$$

(3.200)

where $\mathscr{F}[\cdot]$ performs the Fourier transform of the enclosed expression. To represent the crosstalk between the two baseband channels all PCWM filtering functions are divided in their real and imaginary part (exemplified for the linear response):

$$H_{II,1}(j\omega) = \mathscr{F}\left[\text{Re}\{h_{I,1}(t)\}\right]$$
$$H_{IQ,1}(j\omega) = \mathscr{F}\left[\text{Im}\{h_{I,1}(t)\}\right]$$
$$H_{QQ,1}(j\omega) = \mathscr{F}\left[\text{Re}\{h_{Q,1}(t)\}\right]$$
$$H_{QI,1}(j\omega) = \mathscr{F}\left[\text{Im}\{h_{Q,1}(t)\}\right]$$

(3.201)

Using these definitions the output spectrum of the BB amplifiers results to:

$$
\begin{aligned}
S_{\text{Amp}}(j\omega) = \\
&\left[H_{II,1}(j\omega) + H_{IQ,1}(j\omega)\right]S_{\text{BB,Re}}(j\omega) + \left[H_{QQ,1}(j\omega) + H_{QI,1}(j\omega)\right]S_{\text{BB,Im}}(j\omega) \\
&+\left[H_{II,2}(j\omega) * H_{II,2}(j\omega) + 2jH_{II,2}(j\omega) * H_{IQ,2}(j\omega)\right. \\
&\left.-H_{IQ,2}(j\omega) * H_{IQ,2}(j\omega)\right]S_{\text{BB,Re}}(j\omega) * S_{\text{BB,Re}}(j\omega) \\
&+j\left[H_{QQ,2}(j\omega) * H_{QQ,2}(j\omega) + 2jH_{QQ,2}(j\omega) * H_{QI,2}(j\omega)\right. \\
&\left.-H_{QI,2}(j\omega) * H_{QI,2}(j\omega)\right]S_{\text{BB,Im}}(j\omega) * S_{\text{BB,Im}}(j\omega) \\
&+[H_{II,3}(j\omega)H_{II,3}(j\omega) * H_{II,3}(j\omega) + 3jH_{II,3}(j\omega) * H_{II,3}(j\omega) * H_{IQ,3}(j\omega) \\
&\left.-jH_{IQ,3}(j\omega) * H_{IQ,3}(j\omega) * H_{IQ,3}(j\omega) - 3H_{II,3}(j\omega) * H_{IQ,3}(j\omega) * H_{IQ,3}(j\omega)\right]) \\
&\cdot S_{\text{BB,Re}}(j\omega) * S_{\text{BB,Re}}(j\omega) * S_{\text{BB,Re}}(j\omega) \\
&+j\left[H_{QQ,3}(j\omega)H_{QQ,3}(j\omega) * H_{QQ,3}(j\omega) + 3jH_{QQ,3}(j\omega) * H_{QQ,3}(j\omega) * H_{QI,3}(j\omega)\right. \\
&\left.-jH_{QI,3}(j\omega) * H_{QI,3}(j\omega) * H_{QI,3}(j\omega) - 3H_{QQ,3}(j\omega) * H_{QI,3}(j\omega) * H_{QI,3}(j\omega)\right] \\
&\cdot S_{\text{BB,Im}}(j\omega) * S_{\text{BB,Im}}(j\omega) * S_{\text{BB,Im}}(j\omega)
\end{aligned}
$$

(3.202)

The design of the predistorter was based on the approaches suggested in [87, 120]. Using the amplifier response (3.202) the distortion introduced by the different orders of nonlinearity will be successively compensated starting with the linear one. Assuming a signal $S_{in}(j\omega)$ is applied to the input of a predistorter, which affects only the linear amplifier output. To compensate for the linear distortion and crosstalk four parameters are introduced:

$$S_{\text{BB,Re}}(j\omega) = K_{II,1}(j\omega)K_{lin,I}(j\omega)S_{in,\text{Re}}(j\omega) + K_{QI,1}(j\omega)K_{lin,Q}(j\omega)S_{in,\text{Im}}(j\omega)$$
$$S_{\text{BB,Im}}(j\omega) = K_{IQ,1}(j\omega)K_{lin,I}(j\omega)S_{in,\text{Re}}(j\omega) + K_{QQ,1}(j\omega)K_{lin,Q}(j\omega)S_{in,\text{Im}}(j\omega)$$

(3.203)

The filters are set to $K_{lin,I}(j\omega) = 1$ and $K_{lin,Q}(j\omega) = 1$ for compensating the linear amplifier response. After inserting (3.203) into the linear part of (3.202) the expressions of the linear correction factors are

derived:

$$K_{II,1}(j\omega) = H_{QQ,1}(j\omega)/K_{\text{Denom}}(j\omega)$$
$$K_{IQ,1}(j\omega) = H_{QI,1}(j\omega)/K_{\text{Denom}}(j\omega)$$
$$K_{QQ,1}(j\omega) = H_{II,1}(j\omega)/K_{\text{Denom}}(j\omega) \tag{3.204}$$
$$K_{QI,1}(j\omega) = -H_{IQ,1}(j\omega)/K_{\text{Denom}}(j\omega)$$
$$K_{\text{Denom}}(j\omega) = H_{II,1}(j\omega)H_{QQ,1}(j\omega) + H_{IQ,1}(j\omega)H_{QI,1}(j\omega)$$

Passing these signals through the BB amplifier block results in the following linear response:

$$S_{\text{Amp},1}(j\omega) = K_{lin,I}(j\omega)S_{in,\text{Re}}(j\omega) + jK_{lin,Q}(j\omega)S_{in,Im}(j\omega) \tag{3.205}$$

If the filters $K_{lin,I}(j\omega)$, $K_{lin,Q}(j\omega)$ are set to

$$K_{lin,I}(j\omega) = 1/[K_{II,1}(j\omega) + K_{QI,1}(j\omega)]$$
$$K_{lin,Q}(j\omega) = 1/[K_{QI,1}(j\omega) + K_{QQ,1}(j\omega)] \tag{3.206}$$

no compensation of the linear amplifier response will be performed. This choice of the filters will be advantageously used for the construction of the complete transmitter predistorter in Section 3.9. The corresponding second-order part of the amplifier output is given in (3.207) to (3.210).

$$S_{\text{Amp},2}(j\omega) = S_{\text{Amp},II,\text{Re}}(j\omega) + S_{\text{Amp},QQ,\text{Re}}(j\omega) + S_{\text{Amp},IQ,\text{Re}}(j\omega)$$
$$+ j\big[S_{\text{Amp},II,\text{Im}}(j\omega) + S_{\text{Amp},QQ,\text{Im}}(j\omega) + S_{\text{Amp},IQ,\text{Im}}(j\omega)\big] \tag{3.207}$$

$$S_{\text{Amp},II,\text{Re}}(j\omega) = (H_{II,2}(j\omega)H_{QQ,1}(j\omega)S_{Pre,I,K}(j\omega)) * (H_{II,2}(j\omega)H_{QQ,1}(j\omega)S_{Pre,I,K}(j\omega))$$
$$- (H_{IQ,2}(j\omega)H_{QQ,1}(j\omega)S_{Pre,I,K}(j\omega)) * (H_{IQ,2}(j\omega)H_{QQ,1}(j\omega)S_{Pre,I,K}(j\omega))$$
$$- 2(H_{QI,2}(j\omega)H_{IQ,1}(j\omega)S_{Pre,I,K}(j\omega)) * (H_{QQ,2}(j\omega)H_{IQ,1}(j\omega)S_{Pre,I,K}(j\omega))$$
$$S_{\text{Amp},II,\text{Im}}(j\omega) = (H_{QQ,2}(j\omega)H_{IQ,1}(j\omega)S_{Pre,I,K}(j\omega)) * (H_{QQ,2}(j\omega)H_{IQ,1}(j\omega)S_{Pre,I,K}(j\omega))$$
$$- (H_{QI,2}(j\omega)H_{IQ,1}(j\omega)S_{Pre,I,K}(j\omega)) * (H_{QI,2}(j\omega)H_{IQ,1}(j\omega)S_{Pre,I,K}(j\omega))$$
$$+ 2(H_{IQ,2}(j\omega)H_{QQ,1}(j\omega)S_{Pre,I,K}(j\omega)) * (H_{II,2}(j\omega)H_{QQ,1}(j\omega)S_{Pre,I,K}(j\omega)) \tag{3.208}$$

$$S_{\text{Amp},QQ,\text{Re}}(j\omega) = (H_{II,2}(j\omega)H_{QI,1}(j\omega)S_{Pre,Q,K}(j\omega)) * (H_{II,2}(j\omega).*H_{QI,1}(j\omega).*S_{Pre,Q,K}(j\omega))$$
$$- (H_{IQ,2}(j\omega)H_{QI,1}(j\omega)S_{Pre,Q,K}(j\omega)) * (H_{IQ,2}(j\omega)H_{QI,1}(j\omega)S_{Pre,Q,K}(j\omega))$$
$$- 2(H_{QI,2}(j\omega)H_{II,1}(j\omega)S_{Pre,Q,K}(j\omega)) * (H_{QQ,2}(j\omega)H_{II,1}(j\omega)S_{Pre,Q,K}(j\omega))$$
$$S_{\text{Amp},QQ,\text{Im}}(j\omega) = (H_{QQ,2}(j\omega)H_{II,1}(j\omega)S_{Pre,Q,K}(j\omega)) * (H_{QQ,2}(j\omega)H_{II,1}(j\omega)S_{Pre,Q,K}(j\omega))$$
$$- (H_{QI,2}(j\omega)H_{II,1}(j\omega)S_{Pre,Q,K}(j\omega)) * (H_{QI,2}(j\omega)H_{II,1}(j\omega)S_{Pre,Q,K}(j\omega))$$
$$+ 2(H_{IQ,2}(j\omega)H_{QI,1}(j\omega)S_{Pre,Q,K}(j\omega)) * (H_{II,2}(j\omega)H_{QI,1}(j\omega)S_{Pre,Q,K}(j\omega)) \tag{3.209}$$

$$
\begin{aligned}
S_{\text{Amp},IQ,\text{Re}}(j\omega) =& 2\big[(H_{II,2}(j\omega)H_{QQ,1}(j\omega)S_{Pre,I,K}(j\omega)) * (H_{II,2}(j\omega)H_{QI,1}(j\omega)S_{Pre,Q,K}(j\omega)) \\
& - (H_{IQ,2}(j\omega)H_{QQ,1}(j\omega)S_{Pre,I,K}(j\omega)) * (H_{IQ,2}(j\omega)H_{QI,1}(j\omega)S_{Pre,Q,K}(j\omega)) \\
& + (H_{QQ,2}(j\omega)H_{IQ,1}(j\omega)S_{Pre,I,K}(j\omega)) * (H_{QI,2}(j\omega)H_{II,1}(j\omega)S_{Pre,Q,K}(j\omega)) \\
& + (H_{QI,2}(j\omega)H_{IQ,1}(j\omega)S_{Pre,I,K}(j\omega)) * (H_{QQ,2}(j\omega)H_{II,1}(j\omega)S_{Pre,Q,K}(j\omega))\big] \\
S_{\text{Amp},IQ,\text{Im}}(j\omega) =& 2\big[(H_{QI,2}(j\omega)H_{IQ,1}(j\omega)S_{Pre,I,K}(j\omega)) * (H_{QI,2}(j\omega)H_{II,1}(j\omega)S_{Pre,Q,K}(j\omega)) \\
& - (H_{QQ,2}(j\omega)H_{IQ,1}(j\omega)S_{Pre,I,K}(j\omega)) * (H_{QQ,2}(j\omega)H_{II,1}(j\omega)S_{Pre,Q,K}(j\omega)) \\
& + (H_{II,2}(j\omega)H_{QQ,1}(j\omega)S_{Pre,I,K}(j\omega)) * (H_{IQ,2}(j\omega)H_{QI,1}(j\omega)S_{Pre,Q,K}(j\omega)) \\
& + (H_{IQ,2}(j\omega)H_{QQ,1}(j\omega)S_{Pre,I,K}(j\omega)) * (H_{II,2}(j\omega)H_{QI,1}(j\omega)S_{Pre,Q,K}(j\omega))\big]
\end{aligned}
$$

(3.210)

where $S_{Pre,I,K}(j\omega)$ and $S_{Pre,I,K}(j\omega)$ are defined as:

$$
\begin{aligned}
S_{Pre,I,K}(j\omega) &= K_{lin,I}(j\omega)S_{in,\text{Re}}(j\omega)/K_{\text{Denom}}(j\omega) \\
S_{Pre,Q,K}(j\omega) &= K_{lin,Q}(j\omega)S_{in,\text{Im}}(j\omega)/K_{\text{Denom}}(j\omega)
\end{aligned}
$$

(3.211)

For compensating these distortion products they must be generated with opposite sign at the amplifier output. To do so the distortion signals derived above must be provided at the corresponding inputs of the linear predistorter (3.203):

$$
\begin{aligned}
S_{Pre,I,2}(j\omega) =& -\Big(K_{II,1}(j\omega)\big[S_{\text{Amp},II,\text{Re}}(j\omega) + S_{\text{Amp},QQ,\text{Re}}(j\omega) + S_{\text{Amp},IQ,\text{Re}}(j\omega)\big] \\
& + K_{QI,1}(j\omega)\big[S_{\text{Amp},II,\text{Im}}(j\omega) + S_{\text{Amp},QQ,\text{Im}}(j\omega) + S_{\text{Amp},IQ,\text{Im}}(j\omega)\big]\Big) \\
S_{Pre,Q,2}(j\omega) =& -\Big(K_{IQ,1}(j\omega)\big[S_{\text{Amp},II,\text{Re}}(j\omega) + S_{\text{Amp},QQ,\text{Re}}(j\omega) + S_{\text{Amp},IQ,\text{Re}}(j\omega)\big] \\
& + K_{QQ,1}(j\omega)\big[S_{\text{Amp},II,\text{Im}}(j\omega) + S_{\text{Amp},QQ,\text{Im}}(j\omega) + S_{\text{Amp},IQ,\text{Im}}(j\omega)\big]\Big)
\end{aligned}
$$

(3.212)

Proceeding in the same way, the third-order distortion components are identified and added to the input with opposite sign after being filtered by the linear compensator:

$$
\begin{aligned}
S_{\text{Amp},III,\text{Re}}(j\omega) =& 3(H_{QI,3}(j\omega)H_{IQ,1}(j\omega)S_{Pre,I,K}(j\omega)) * (H_{QQ,3}(j\omega)H_{IQ,1}(j\omega)S_{Pre,I,K}(j\omega)) \\
& * (H_{QQ,3}(j\omega)H_{IQ,1}(j\omega)S_{Pre,I,K}(j\omega)) \\
& + 3(H_{II,3}(j\omega)H_{QQ,1}(j\omega)S_{Pre,I,K}(j\omega)) * (H_{IQ,3}(j\omega)H_{QQ,1}(j\omega)S_{Pre,I,K}(j\omega)) \\
& * (H_{IQ,3}(j\omega)H_{QQ,1}(j\omega)S_{Pre,I,K}(j\omega)) \\
& - (H_{II,3}(j\omega)H_{QQ,1}(j\omega)S_{Pre,I,K}(j\omega)) * (H_{II,3}(j\omega)H_{QQ,1}(j\omega)S_{Pre,I,K}(j\omega)) \\
& * (H_{II,3}(j\omega)H_{QQ,1}(j\omega)S_{Pre,I,K}(j\omega)) \\
& - (H_{QI,3}(j\omega)H_{IQ,1}(j\omega)S_{Pre,I,K}(j\omega)) * (H_{QI,3}(j\omega)H_{IQ,1}(j\omega)S_{Pre,I,K}(j\omega)) \\
& * (H_{QI,3}(j\omega)H_{IQ,1}(j\omega)S_{Pre,I,K}(j\omega))
\end{aligned}
$$

(3.213)

$$
\begin{aligned}
S_{\text{Amp},III,\text{Im}}(j\omega) =& 3(H_{IQ,3}(j\omega)H_{QQ,1}(j\omega)S_{Pre,I,K}(j\omega)) * (H_{II,3}(j\omega)H_{QQ,1}(j\omega)S_{Pre,I,K}(j\omega)) \\
& * (H_{II,3}(j\omega)H_{QQ,1}(j\omega)S_{Pre,I,K}(j\omega)) \\
& + 3(H_{QQ,3}(j\omega)H_{IQ,1}(j\omega)S_{Pre,I,K}(j\omega)) * (H_{QI,3}(j\omega)H_{IQ,1}(j\omega)S_{Pre,I,K}(j\omega)) \\
& * (H_{QI,3}(j\omega)H_{IQ,1}(j\omega)S_{Pre,I,K}(j\omega)) \\
& - (H_{QQ,3}(j\omega)H_{IQ,1}(j\omega)S_{Pre,I,K}(j\omega)) * (H_{QQ,3}(j\omega)H_{IQ,1}(j\omega)S_{Pre,I,K}(j\omega)) \\
& * (H_{QQ,3}(j\omega)H_{IQ,1}(j\omega)S_{Pre,I,K}(j\omega)) \\
& - (H_{IQ,3}(j\omega)H_{QQ,1}(j\omega)S_{Pre,I,K}(j\omega)) * (H_{IQ,3}(j\omega)H_{QQ,1}(j\omega)S_{Pre,I,K}(j\omega)) \\
& * (H_{IQ,3}(j\omega)H_{QQ,1}(j\omega)S_{Pre,I,K}(j\omega))
\end{aligned}
\tag{3.214}
$$

$$
\begin{aligned}
S_{\text{Amp},QQQ,\text{Re}}(j\omega) =& 3(H_{QI,3}(j\omega)H_{IQ,1}(j\omega)S_{Pre,I,K}(j\omega)) * (H_{QQ,3}(j\omega)H_{IQ,1}(j\omega)S_{Pre,I,K}(j\omega)) \\
& * (H_{QQ,3}(j\omega)H_{IQ,1}(j\omega)S_{Pre,I,K}(j\omega)) \\
& + 3(H_{II,3}(j\omega)H_{QQ,1}(j\omega)S_{Pre,I,K}(j\omega)) * (H_{IQ,3}(j\omega)H_{QQ,1}(j\omega)S_{Pre,I,K}(j\omega)) \\
& * (H_{IQ,3}(j\omega)H_{QQ,1}(j\omega)S_{Pre,I,K}(j\omega)) \\
& - (H_{II,3}(j\omega)H_{QQ,1}(j\omega)S_{Pre,I,K}(j\omega)) * (H_{II,3}(j\omega)H_{QQ,1}(j\omega)S_{Pre,I,K}(j\omega)) \\
& * (H_{II,3}(j\omega)H_{QQ,1}(j\omega)S_{Pre,I,K}(j\omega)) \\
& - (H_{QI,3}(j\omega)H_{IQ,1}(j\omega)S_{Pre,I,K}(j\omega)) * (H_{QI,3}(j\omega)H_{IQ,1}(j\omega)S_{Pre,I,K}(j\omega)) \\
& * (H_{QI,3}(j\omega)H_{IQ,1}(j\omega)S_{Pre,I,K}(j\omega))
\end{aligned}
\tag{3.215}
$$

$$
\begin{aligned}
S_{\text{Amp},QQQ,\text{Im}}(j\omega) =& 3(H_{IQ,3}(j\omega)H_{QQ,1}(j\omega)S_{Pre,I,K}(j\omega)) * (H_{II,3}(j\omega)H_{QQ,1}(j\omega)S_{Pre,I,K}(j\omega)) \\
& * (H_{II,3}(j\omega)H_{QQ,1}(j\omega)S_{Pre,I,K}(j\omega)) \\
& + 3(H_{QQ,3}(j\omega)H_{IQ,1}(j\omega)S_{Pre,I,K}(j\omega)) * (H_{QI,3}(j\omega)H_{IQ,1}(j\omega)S_{Pre,I,K}(j\omega)) \\
& * (H_{QI,3}(j\omega)H_{IQ,1}(j\omega)S_{Pre,I,K}(j\omega)) \\
& - (H_{QQ,3}(j\omega)H_{IQ,1}(j\omega)S_{Pre,I,K}(j\omega)) * (H_{QQ,3}(j\omega)H_{IQ,1}(j\omega)S_{Pre,I,K}(j\omega)) \\
& * (H_{QQ,3}(j\omega)H_{IQ,1}(j\omega)S_{Pre,I,K}(j\omega)) \\
& - (H_{IQ,3}(j\omega)H_{QQ,1}(j\omega)S_{Pre,I,K}(j\omega)) * (H_{IQ,3}(j\omega)H_{QQ,1}(j\omega)S_{Pre,I,K}(j\omega)) \\
& * (H_{IQ,3}(j\omega)H_{QQ,1}(j\omega)S_{Pre,I,K}(j\omega)
\end{aligned}
\tag{3.216}
$$

$$
\begin{aligned}
S_{\text{Amp},IIQ,\text{Re}}(j\omega) =&\, 3(H_{II,3}(j\omega)H_{QQ,1}(j\omega)S_{Pre,I,K}(j\omega)) * (H_{II,3}(j\omega)H_{QQ,1}(j\omega)S_{Pre,I,K}(j\omega)) \\
&* (H_{II,3}(j\omega)H_{QI,1}(j\omega)S_{Pre,Q,K}(j\omega)) \\
&+ 3(H_{QI,3}(j\omega)H_{IQ,1}(j\omega)S_{Pre,I,K}(j\omega)) * (H_{QI,3}(j\omega)H_{IQ,1}(j\omega)S_{Pre,I,K}(j\omega)) \\
&;\!* (H_{QI,3}(j\omega)H_{II,1}(j\omega)S_{Pre,Q,K}(j\omega)) \\
&- 9(H_{QQ,3}(j\omega)H_{IQ,1}(j\omega)S_{Pre,I,K}(j\omega)) * (H_{QQ,3}(j\omega)H_{IQ,1}(j\omega)S_{Pre,I,K}(j\omega)) \\
&* (H_{QI,3}(j\omega)H_{II,1}(j\omega)S_{Pre,Q,K}(j\omega)) \\
&+ 9(H_{IQ,3}(j\omega)H_{QQ,1}(j\omega)S_{Pre,I,K}(j\omega)) * (H_{IQ,3}(j\omega)H_{QQ,1}(j\omega)S_{Pre,I,K}(j\omega)) \\
&* (H_{II,3}(j\omega)H_{QI,1}(j\omega)S_{Pre,Q,K}(j\omega))
\end{aligned}
$$

$$(3.217)$$

$$
\begin{aligned}
S_{\text{Amp},IIQ,\text{Im}}(j\omega) =&\, 3(H_{QQ,3}(j\omega)H_{IQ,1}(j\omega)S_{Pre,I,K}(j\omega)) * (H_{QQ,3}(j\omega)H_{IQ,1}(j\omega)S_{Pre,I,K}(j\omega)) \\
&* (H_{QQ,3}(j\omega)H_{II,1}(j\omega)S_{Pre,Q,K}(j\omega)) \\
&+ 9(H_{II,3}(j\omega)H_{QQ,1}(j\omega)S_{Pre,I,K}(j\omega)) * (H_{II,3}(j\omega)H_{QQ,1}(j\omega)S_{Pre,I,K}(j\omega)) \\
&* (H_{IQ,3}(j\omega)H_{QI,1}(j\omega)S_{Pre,Q,K}(j\omega)) \\
&- 3(H_{IQ,3}(j\omega)H_{QQ,1}(j\omega)S_{Pre,I,K}(j\omega)) * (H_{IQ,3}(j\omega)H_{QQ,1}(j\omega)S_{Pre,I,K}(j\omega)) \\
&* (H_{IQ,3}(j\omega)H_{QI,1}(j\omega)S_{Pre,Q,K}(j\omega)) \\
&- 9(H_{QI,3}(j\omega)H_{IQ,1}(j\omega)S_{Pre,I,K}(j\omega)) * (H_{QI,3}(j\omega)H_{IQ,1}(j\omega)S_{Pre,I,K}(j\omega)) \\
&* (H_{QQ,3}(j\omega)H_{II,1}(j\omega)S_{Pre,Q,K}(j\omega))
\end{aligned}
$$

$$(3.218)$$

$$
\begin{aligned}
S_{\text{Amp},IQQ,\text{Re}}(j\omega) =&\, 3(H_{II,3}(j\omega)H_{QI,1}(j\omega)S_{Pre,Q,K}(j\omega)) * (H_{II,3}(j\omega)H_{QI,1}(j\omega)S_{Pre,Q,K}(j\omega)) \\
&* (H_{II,3}(j\omega)H_{QQ,1}(j\omega)S_{Pre,I,K}(j\omega)) \\
&+ 3(H_{QI,3}(j\omega)H_{II,1}(j\omega)S_{Pre,Q,K}(j\omega)) * (H_{QI,3}(j\omega)H_{II,1}(j\omega)S_{Pre,Q,K}(j\omega)) \\
&* (H_{QI,3}(j\omega)H_{IQ,1}(j\omega)S_{Pre,I,K}(j\omega)) \\
&+ 9(H_{QQ,3}(j\omega)H_{II,1}(j\omega)S_{Pre,Q,K}(j\omega)) * (H_{QQ,3}(j\omega)H_{II,1}(j\omega)S_{Pre,Q,K}(j\omega)) \\
&* (H_{QI,3}(j\omega)H_{IQ,1}(j\omega)S_{Pre,I,K}(j\omega)) \\
&- 9(H_{IQ,3}(j\omega)H_{QI,1}(j\omega)S_{Pre,Q,K}(j\omega)) * (H_{IQ,3}(j\omega)H_{QI,1}(j\omega)S_{Pre,Q,K}(j\omega)) \\
&* (H_{II,3}(j\omega)H_{QQ,1}(j\omega)S_{Pre,I,K}(j\omega))
\end{aligned}
$$

$$(3.219)$$

$$
\begin{aligned}
S_{\text{Amp},IQQ,\text{Im}}(j\omega) =\ &9(H_{II,3}(j\omega)H_{QI,1}(j\omega)S_{Pre,Q,K}(j\omega)) * (H_{II,3}(j\omega)H_{QI,1}(j\omega)S_{Pre,Q,K}(j\omega)) \\
&* (H_{IQ,3}(j\omega)H_{QQ,1}(j\omega)S_{Pre,I,K}(j\omega)) \\
&+ 9(H_{QI,3}(j\omega)H_{II,1}(j\omega)S_{Pre,Q,K}(j\omega)) * (H_{QI,3}(j\omega)H_{II,1}(j\omega)S_{Pre,Q,K}(j\omega)) \\
&* (H_{QQ,3}(j\omega)H_{IQ,1}(j\omega)S_{Pre,I,K}(j\omega)) \\
&- 3(H_{QQ,3}(j\omega)H_{II,1}(j\omega)S_{Pre,Q,K}(j\omega)) * (H_{QQ,3}(j\omega)H_{II,1}(j\omega)S_{Pre,Q,K}(j\omega)) \\
&* (H_{QQ,3}(j\omega)H_{IQ,1}(j\omega)S_{Pre,I,K}(j\omega)) \\
&- 3(H_{IQ,3}(j\omega)H_{QI,1}(j\omega)S_{Pre,Q,K}(j\omega)) * (H_{IQ,3}(j\omega)H_{QI,1}(j\omega)S_{Pre,Q,K}(j\omega)) \\
&* (H_{IQ,3}(j\omega)H_{QQ,1}(j\omega)S_{Pre,I,K}(j\omega))
\end{aligned}
\tag{3.220}
$$

$$
\begin{aligned}
S_{Pre,I,3}(j\omega) =\ & \\
& -\Big(K_{II,1}(j\omega)\big[S_{\text{Amp},III,\text{Re}}(j\omega) + S_{\text{Amp},QQQ,\text{Re}}(j\omega) + S_{\text{Amp},IIQ,\text{Re}}(j\omega) + S_{\text{Amp},IQQ,\text{Re}}(j\omega) \big] \\
& +K_{QI,1}(j\omega)\big[S_{\text{Amp},III,\text{Im}}(j\omega) + S_{\text{Amp},QQQ,\text{Im}}(j\omega) + S_{\text{Amp},IIQ,\text{Im}}(j\omega) + S_{\text{Amp},IQQ,\text{Im}}(j\omega) \big] \Big) \\
S_{Pre,Q,3}(j\omega) =\ & \\
& c - \Big(K_{IQ,1}(j\omega)\big[S_{\text{Amp},III,\text{Re}}(j\omega) + S_{\text{Amp},QQQ,\text{Re}}(j\omega) + S_{\text{Amp},IIQ,\text{Re}}(j\omega) + S_{\text{Amp},IQQ,\text{Re}}(j\omega) \big] \\
& +K_{QQ,1}(j\omega)\big[S_{\text{Amp},III,\text{Im}}(j\omega) + S_{\text{Amp},QQQ,\text{Im}}(j\omega) + S_{\text{Amp},IIQ,\text{Im}}(j\omega) + S_{\text{Amp},IQQ,\text{Im}}(j\omega) \big] \Big)
\end{aligned}
\tag{3.221}
$$

Due to the complexity of the expressions (3.213) to (3.220) the contributions caused by the second order compensation signal were neglected.

3.8.11.2   RF nonlinearity predistorter

The compensator of the RF nonlinearity is located before the BB compensator. In this way the BB amplifier distortion is canceled out and interactions between the two predistorters are avoided. To compensate the impact of the odd-order polynomial RF nonlinearity an odd-order polynomial predistorter is selected. In [121] the applicability of using the composition of two polynomials to compensate the distortion at the output up to a chosen order was proven. The coefficients of the predistorter polynomial are evaluated using the same approach as in the last section. For this approach a transparent BB amplifier behavior is assumed. The polynomial predistorter is given by:

$$
s_{\text{BP}}(t) = \sum_{k=1}^{(N_{\text{Comp}}+1)/2} g_{\text{C},2k-1} s_{\text{in}}(t)|s_{\text{in}}(t)|^{2(k-1)}
\tag{3.222}
$$

As in the last section the input signal to the compensator is identified by $s_{\text{in}}(t)$. The parameter N_{Comp} specifies the order of the predistorter. The output of the compensator is directly applied to the RF NL input $s_{\text{BP}}(t)$:

$$
s_{\text{mod}}(t) = g_{\text{M},1} s_{\text{BP}}(t) + g_{\text{M},3} s_{\text{BP}}(t)|s_{\text{BP}}(t)|^2
\tag{3.223}
$$

As in Section 3.8.5 the RF polynomial was truncated at the third-order. The inclusion of higher-order coefficients is straight forward. The linear coefficient $g_{\text{C},1}$ is derived by inserting (3.222) into (3.223)

and evaluating the linear response:

$$g_{\mathrm{C},1} = \frac{1}{g_{\mathrm{M},1}} \qquad (3.224)$$

Applying this result to (3.222) and performing the same steps again also the other predistorter coefficients are derived. In (3.225) the corresponding expressions up to seventh order are specified.

$$g_{\mathrm{C},3} = \frac{-g_{\mathrm{M},3}}{g_{\mathrm{M},1}^2 |g_{\mathrm{M},1}|^2}$$

$$g_{\mathrm{C},5} = \frac{g_{\mathrm{M},3} \left(g_{\mathrm{M},3}^* g_{\mathrm{M},1} + 2g_{\mathrm{M},3} g_{\mathrm{M},1}^* \right)}{g_{\mathrm{M},1}^2 |g_{\mathrm{M},1}|^6}$$

$$g_{\mathrm{C},7} = \frac{-g_{\mathrm{M},3} \left(5|g_{\mathrm{M},3}|^2 |g_{\mathrm{M},1}|^2 + 5g_{\mathrm{M},3}^2 g_{\mathrm{M},1}^{*2} + 2g_{\mathrm{M},3}^{*2} g_{\mathrm{M},1}^2 \right)}{g_{\mathrm{M},1}^2 |g_{\mathrm{M},1}|^{10}} \qquad (3.225)$$

3.8.11.3 Predistorter performance

For visualizing the performance of the presented predistorter simulations have been performed using the parameters of the transmitter characterization in the high distortion configuration. In this way frequency dependent transmitter characteristics including the distortion crosstalk discussed in Section 3.8.10 were applied for the performance evaluation. This transmitter model showed an $\mathrm{IP}_{2,\mathrm{BB}}$ of about 59 dBm, an $\mathrm{IP}_{3,\mathrm{BB}}$ of about 32 dBm and an $\mathrm{IP}_{3,\mathrm{RF}}$ of approx. 37 dBm. The DC offset was neglected. A multi-tone signal composed of 100 tones covering a bandwidth of 20 MHz was selected for the simulation. This signal is shifted to a frequency offset of -10 MHz relative to the carrier to include also imbalance effects in the simulation.

The linearization performance of the suggested predistorter is highlighted by the improvement of the NMSE compared to the direct model output. Assuming that the signals are represented by time-discrete sequences the NMSE is given by (3.198). In this expression the reference sequence $y_{\mathrm{ref}}(n)$ identifies the input signal, the transmitter response is represented by $y_{\mathrm{Model}}(n)$. The summation over the index n includes all elements of the corresponding sequences. Using this metric the ability of the predistorter for linearizing the considered system is related to the reduction of the NMSE compared to the unlinearized case. A comparison of the NMSE with and without predistorter is depicted in Figure 3.18(a). The output signal spectra with and without predistortion at $\mathrm{P}_{\mathrm{in}} = 5$ dBm is presented in Figure 3.18(b). At the predistorted transmitter response a reduction of all distortion components can be recognized.

3.9 Model and compensator for the direct conversion transmitter

After characterizing the transmitter by separately evaluating several distortion mechanisms a model and a compensator are designed combining all these results.

The structure of the transmitter model is depicted in Figure 3.19. At the beginning the input signal is divided in its real and imaginary part and fed into the corresponding baseband nonlinearities. After combining the output of these blocks the DC-offset is added. The magnitude and phase imbalance of the cascade of lowpass filters and BB amplifiers and the I/Q mixer phase error can either be represented by

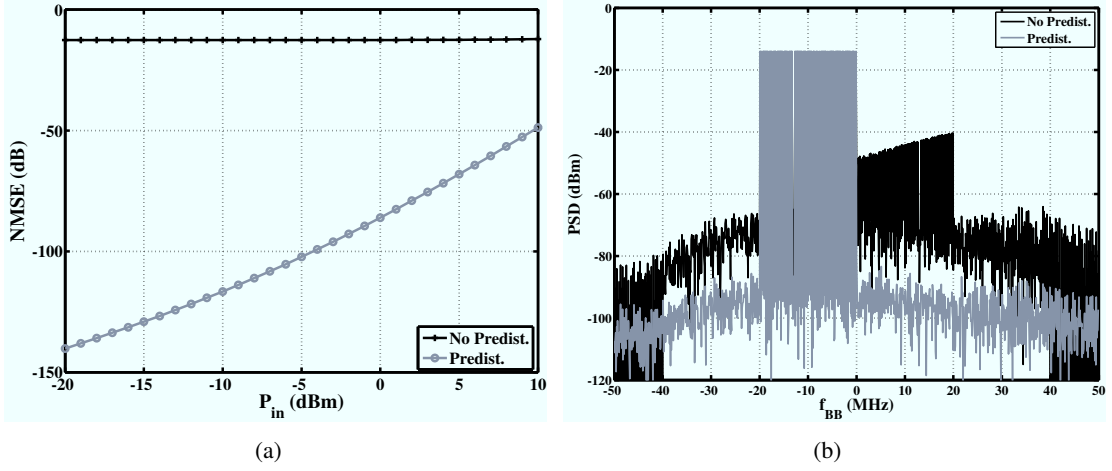(a)   (b)

Figure 3.18: Comparison of the original and the predistorted transmitter output. (a) NMSE between the actual and the undistorted transmitter response and (b) transmitter output spectrum comparison for a multi-tone input signal.

the PCWMs of the BB amplifiers or by a separate imbalance block. After the imbalance was introduced the spurious emissions are added. The spurs are evaluated directly from the transmitter input signal. The modeling of the RF nonlinearity finalizes the output signal calculation.
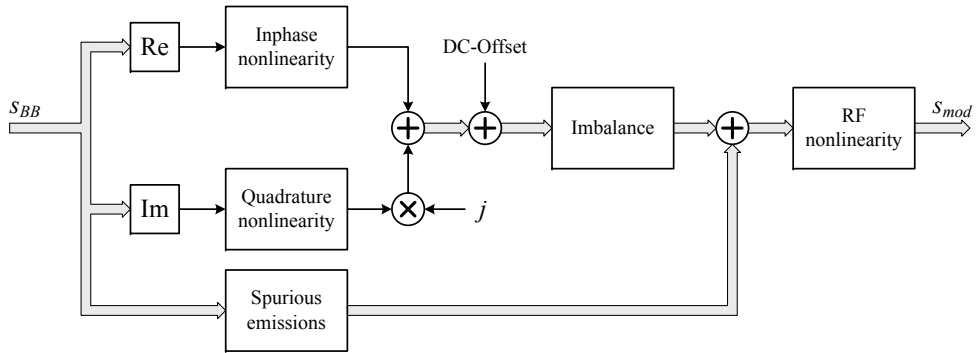

Figure 3.19: Structure of the model used for representing the complete transmitter.

The spurious emissions block is composed of N_{spur} parallel branches (compare (3.80)). Each branch models the distortion products for one frequency offset $\Delta\omega_k$. The structure of such a branch is depicted in Figure 3.20. The upper part of the structure generates the spurious emission associated with $+\Delta\omega_k$. Here, the input signal is filtered by the gain of the reference channel. After this, the imbalance of the desired signal is introduced. Finally, the signal is scaled and frequency shifted to the corresponding offset. The lower branch performs the same operations associated with the spectrally mirrored input signal.

The transmitter compensator structure is shown in Figure 3.21. In a first step the reference channel gain of the transmitter is compensated as indicated in Section 3.6. Then the RF nonlinearity impact is
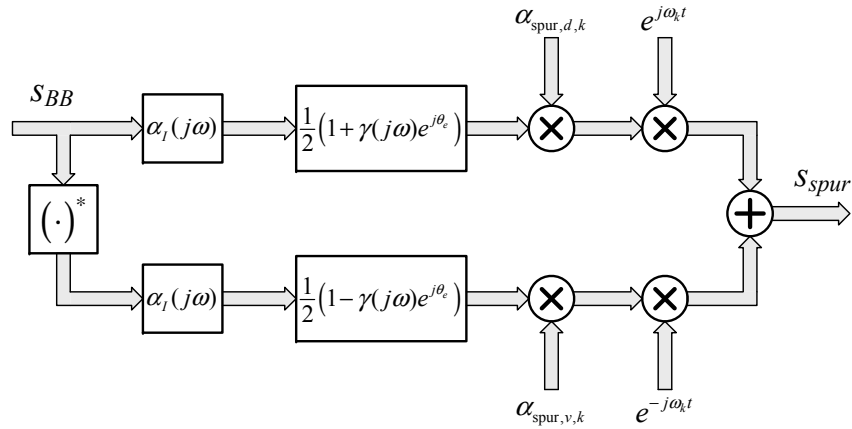
Figure 3.20: Model of a branch of the spurious emission block.

removed. Thereafter, the cancelation of the magnitude and phase imbalance is performed. For removing the transmitter imbalance the component based compensator derived in Section 3.6.3.1 was implemented. As both the gain and the magnitude imbalance are already considered, the predistorter may not linearize the linear frequency response. This can be achieved by setting the parameters $K_{lin,I}$ and $K_{lin,Q}$, introduced in (3.203), to one. Independent of this choice, the higher order distortion products are still removed by the predistorter. Finally, the DC-offset and the spurious emissions compensation signals are added to the predistorter output. The spurious emission compensator is implemented as described in Section 3.7.1.
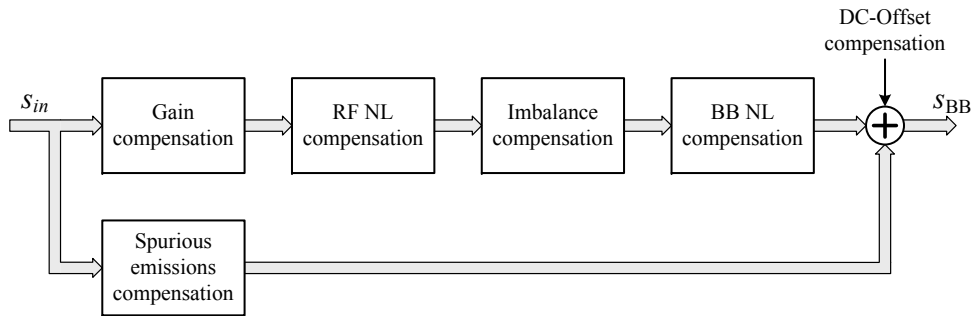

Figure 3.21: Structure of the transmitter compensator.

Chapter 4

Receiver modeling and compensation

The model of the imperfections of a direct conversion receiver is presented in Figure 4.1. The RF input signal is first filtered by an ideal bandpass filter for suppressing all out-of-band signal components. The filtered input signal $\tilde{r}_{\mathrm{RF}}$ is then scaled by the nonlinear amplifier $\tilde{g}_{\mathrm{M}}(\tilde{r}_{\mathrm{RF}})$ and then divided into two equal parts. After ideal bandpass filtering for suppressing all harmonics generated by $\tilde{g}_{\mathrm{M}}(\,\cdot\,)$ the signal $\tilde{r}_{\mathrm{BP}}$ is provided to the demodulator mixers. As for the modulator, the asymmetrical phase-error model is used for describing the phase imbalance of the I/Q demodulator. Next, the carrier signals are amplified, the DC-offsets are added and then fed into the corresponding mixer. The local oscillator provides the carrier signal which is degraded by phase noise and spurious emissions. The following amplifiers g_{CI} and g_{CQ} are modeled distortion free. The two output signals of the mixer are lowpass filtered and then amplified by the nonlinear amplifiers $g_I(r_{\mathrm{mod},I})$ and $g_Q(r_{\mathrm{mod},Q})$.
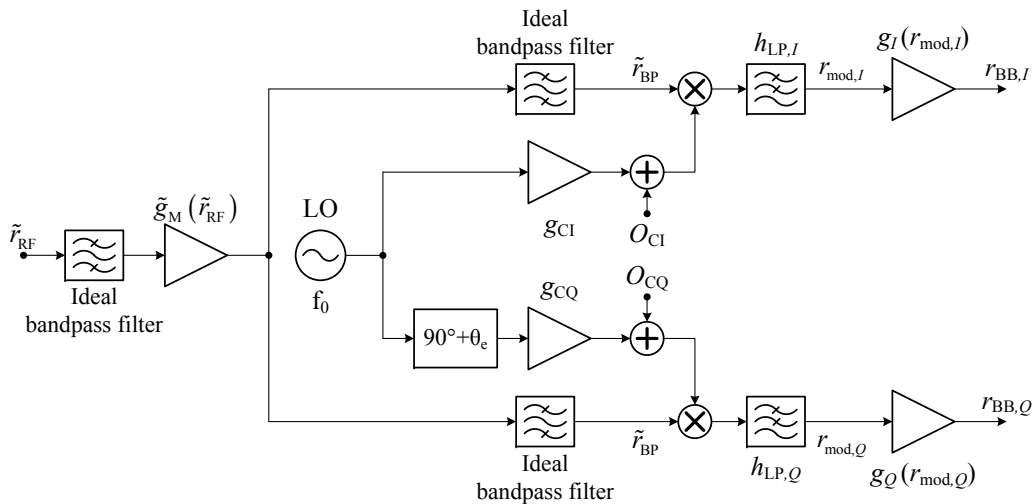

Figure 4.1: Model of the imperfections of a direct conversion receiver.

Using a similar way as in Chapter 3 the behavior of the receiver is analyzed. For this derivation it is assumed, that any frequency offset between the local oscillators of the transmitter and receiver branch of the communication system is compensated. The phase difference between the two local oscillators is

expressed by $\Delta\varphi_{\text{LO}}$. The bandpass filtered receiver input signal is given by:

$$\tilde{r}_{\text{RF}}(t) = s_{\text{BB},I}(t)\cos(\omega_0 t + \varphi_{\text{LO}}) - s_{\text{BB},Q}(t)\sin(\omega_0 t + \varphi_{\text{LO}}) \tag{4.1}$$

After passing this signal through the RF nonlinearity of the mixer and ideal bandpass filtering this signal is represented by:

$$\begin{aligned} \tilde{r}_{\text{BP}}(t) &= g_{\text{M}}(\tilde{r}_{\text{RF}}(t)) \\ &= r_{\text{BP},I}(t)\cos(\omega_0 t + \varphi_{\text{LO}}) - r_{\text{BP},Q}(t)\sin(\omega_0 t + \varphi_{\text{LO}}) \end{aligned} \tag{4.2}$$

The inphase and quadrature component of the signals after the mixers are given by:

$$\begin{aligned} \tilde{r}_{\text{BP}}(t) \cdot &\left[O_{\text{CI}} + 2\sum_{k=0}^{N_{\text{spur}}} g_{\text{CI},k}\cos([\omega_0 + \Delta\omega_k]t + \varphi_{\text{LO}} + \varphi_{\text{PH},k}(t) + \Delta\varphi_{\text{LO},k}) \right] = \\ O_{\text{CI}}&\tilde{r}_{\text{BP}}(t) + \sum_{k=0}^{N_{\text{spur}}} g_{\text{CI},k}\big[r_{\text{BP},I}(t)\cos(\Delta\omega_k t + \varphi_{\text{PH},k}(t) + \Delta\varphi_{\text{LO},k}) \\ &+ r_{\text{BP},Q}(t)\sin(\Delta\omega_k t + \varphi_{\text{PH},k}(t) + \Delta\varphi_{\text{LO},k})\big] \\ &+ \sum_{k=0}^{N_{\text{spur}}} g_{\text{CI},k}\big[r_{\text{BP},I}(t)\cos(2\omega_0 t + \Delta\omega_k t + 2\varphi_{\text{LO}} + \varphi_{\text{PH},k}(t) + \Delta\varphi_{\text{LO},k}) \\ &- r_{\text{BP},Q}(t)\sin(2\omega_0 t + \Delta\omega_k t + 2\varphi_{\text{LO}} + \varphi_{\text{PH},k}(t) + \Delta\varphi_{\text{LO},k})\big] \end{aligned} \tag{4.3}$$

At this equation N_{spur} spurious emissions are present at the output of the local oscillator. These emissions are at an offset $\Delta\omega_k$ from the center frequency. The carrier is identified by the index $k = 0$ (i.e., $\Delta\omega_0 = 0$). For simplifying the notation the magnitudes of the spurious emissions are represented by $g_{\text{CI},k}$. These amplitudes were chosen for keeping the magnitude of the complex envelope between the RF and the baseband at the same level. The time-varying phases $\varphi_{\text{PH},k}(t)$ describe the impact of the phase noise on the carrier and the spurious emissions. In contrast to the other parameters used for the model $\varphi_{\text{PH},k}(t)$ represent random processes of the jitter in the phase-locked oscillator. The corresponding quadrature channel expression becomes:

$$\begin{aligned} \tilde{r}_{\text{BP}}(t) \cdot &\left[O_{\text{CQ}} - 2\sum_{k=0}^{N_{\text{spur}}} g_{\text{CQ},k}\sin([\omega_0 + \Delta\omega_k]t + \varphi_{\text{LO}} + \varphi_{\text{PH},k}(t) + \Delta\varphi_{\text{LO},k} + \theta_e) \right] = \\ O_{\text{CQ}}&\tilde{r}_{\text{BP}}(t) + \sum_{k=0}^{N_{\text{spur}}} g_{\text{CQ},k}\big[-r_{\text{BP},I}(t)\sin(\Delta\omega_k t + \varphi_{\text{PH},k}(t) + \Delta\varphi_{\text{LO},k} + \theta_e) \\ &+ r_{\text{BP},Q}(t)\cos(\Delta\omega_k t + \varphi_{\text{PH},k}(t) + \Delta\varphi_{\text{LO},k} + \theta_e)\big] \\ &- \sum_{k=0}^{N_{\text{spur}}} g_{\text{CQ},k}\big[r_{\text{BP},I}(t)\sin(2\omega_0 t + \Delta\omega_k t + 2\varphi_{\text{LO}} + \varphi_{\text{PH},k}(t) + \Delta\varphi_{\text{LO},k} + \theta_e) \\ &+ r_{\text{BP},Q}(t)\cos(2\omega_0 t + \Delta\omega_k t + 2\varphi_{\text{LO}} + \varphi_{\text{PH},k}(t) + \Delta\varphi_{\text{LO},k} + \theta_e)\big] \end{aligned} \tag{4.4}$$

The RF signal feed-through can be clearly recognized in (4.3), (4.4). No carrier leakage is present as no DC-offset was added to $\tilde{r}_{\text{BP}}(t)$ signal before it was applied to the mixer inputs. After the lowpass filtering the components located at the fundamental and the second harmonic of the center frequency are

removed. This filtering process introduces also a frequency dependent scaling of the inphase and the quadrature baseband signals. The lowpass filtered mixer output signals are summarized by:

$$
\begin{aligned}
r_{\mathrm{mod},I}(t) = & \sum_{k=0}^{N_{\mathrm{spur}}} g_{\mathrm{CI},k} h_{\mathrm{LP},I}(t) * \big[r_{\mathrm{BP},I}(t) \cos(\Delta\omega_k t + \varphi_{\mathrm{PH},k}(t) + \Delta\varphi_{\mathrm{LO},k}) \\
& + r_{\mathrm{BP},Q}(t) \sin(\Delta\omega_k t + \varphi_{\mathrm{PH},k}(t) + \Delta\varphi_{\mathrm{LO},k}) \big] \\
r_{\mathrm{mod},Q}(t) = & \sum_{k=0}^{N_{\mathrm{spur}}} g_{\mathrm{CQ},k} h_{\mathrm{LP},Q}(t) * \big[- r_{\mathrm{BP},I}(t) \sin(\Delta\omega_k t + \varphi_{\mathrm{PH},k}(t) + \Delta\varphi_{\mathrm{LO},k} + \theta_e) \\
& + r_{\mathrm{BP},Q}(t) \cos(\Delta\omega_k t + \varphi_{\mathrm{PH},k}(t) + \Delta\varphi_{\mathrm{LO},k} + \theta_e) \big]
\end{aligned}
\tag{4.5}
$$

The corresponding complex baseband representation can be written as:

$$
\begin{aligned}
r_{\mathrm{mod}}(t) = & \frac{1}{2} \sum_{k=0}^{N_{\mathrm{spur}}} r_{\mathrm{BP}}(t) e^{-j(\Delta\omega_k t + \varphi_{\mathrm{PH},k}(t) + \Delta\varphi_{\mathrm{LO},k})} * \Big(g_{\mathrm{CI},k} h_{\mathrm{LP},I}(t) + g_{\mathrm{CQ},k} h_{\mathrm{LP},Q}(t) e^{-j\theta_e} \Big) \\
& + \frac{1}{2} \sum_{k=0}^{N_{\mathrm{spur}}} r_{\mathrm{BP}}^*(t) e^{j(\Delta\omega_k t + \varphi_{\mathrm{PH},k}(t) + \Delta\varphi_{\mathrm{LO},k})} * \Big(g_{\mathrm{CI},k} h_{\mathrm{LP},I}(t) - g_{\mathrm{CQ},k} h_{\mathrm{LP},Q}(t) e^{j\theta_e} \Big)
\end{aligned}
\tag{4.6}
$$

After boosting $r_{\mathrm{mod}}(t)$ by the two nonlinear baseband amplifiers the receiver output signal is found to be:

$$
\begin{aligned}
r_{\mathrm{BB},I}(t) &= g_I\big(r_{\mathrm{mod},I}(t)\big) \\
r_{\mathrm{BB},Q}(t) &= g_Q\big(r_{\mathrm{mod},Q}(t)\big) \\
|r_{\mathrm{BB}}(t)| &= \sqrt{r_{\mathrm{BB},I}^2(t) + r_{\mathrm{BB},Q}^2(t)} \\
\angle r_{\mathrm{BB}}(t) &= \arctan\left(\frac{r_{\mathrm{BB},Q}(t)}{r_{\mathrm{BB},I}(t)}\right)
\end{aligned}
\tag{4.7}
$$

4.1 Linear receiver model

Based on these derivations the linear receiver response can be evaluated. At the linear model the spurious emissions were neglected. The same naming convention as in Section 3.1 was applied. The frequency domain representation of the linear receiver output signal is given by [122, 123, 124]:

$$
\begin{aligned}
R_{\mathrm{BB}}(j\omega) = & 2\pi\delta(j\omega) O_{\alpha_d} + g_{\mathrm{M}} \alpha_d(j\omega) R_{\mathrm{RF}}(j\omega) * S_{\mathrm{PH},0}^*(-j\omega) e^{-j\Delta\varphi_{\mathrm{LO},0}} \\
& + g_{\mathrm{M}}^* \alpha_v(j\omega) R_{\mathrm{RF}}^*(-j\omega) * S_{\mathrm{PH},0}(j\omega) e^{j\Delta\varphi_{\mathrm{LO},0}}
\end{aligned}
\tag{4.8}
$$

where g_M represents the linear gain of the RF nonlinearity and $S_{\text{PH},0}(j\omega)$ the PSD of the carrier phase noise. The scaling coefficients in this expression are summarized in (4.9).

$$
\begin{aligned}
\alpha_I(j\omega) &= g_{\text{CI},0} g_I H_{\text{LP},I}(j\omega) \\
\alpha_Q(j\omega) &= g_{\text{CQ},0} g_Q H_{\text{LP},Q}(j\omega) \\
\alpha_d(j\omega) &= \tfrac{1}{2}\left[\alpha_I(j\omega) + \alpha_Q(j\omega)\, e^{-j\theta_e}\right] \\
\alpha_v(j\omega) &= \tfrac{1}{2}\left[\alpha_I(j\omega) - \alpha_Q(j\omega)\, e^{j\theta_e}\right] \\
O_{\alpha_d} &= g_{I,0} + j g_{Q,0}
\end{aligned}
\tag{4.9}
$$

Equations (4.6) and (4.8) show clearly, that the LO phase difference and phase noise can be properly modeled by introducing the corresponding phase rotation to the complex envelope of the I/Q-mixer input signal. In a similar way also the mixer input nonlinearity g_M performs a scaling and rotation of the RF input signal. It is therefore advantageous introducing the following abbreviation:

$$
r_{\text{RF},g_M}(t) = g_M r_{\text{RF}}(t) e^{-j(\varphi_{\text{PH},0}(t) + \Delta\varphi_{\text{LO},0})}
\tag{4.10}
$$

Based on this abbreviation the input signal of the linear model (4.8) can also be written as:

$$
\begin{aligned}
R_{\text{BB}}(j\omega) =& 2\pi\delta(j\omega)O_{\alpha_d} + \frac{1}{2}\alpha_I(j\omega)\Big[\left(1 + \gamma(j\omega)\, e^{-j\theta_e}\right) R_{\text{RF},g_M}(j\omega) \\
& + \left(1 - \gamma(j\omega)\, e^{j\theta_e}\right) R^*_{\text{RF},g_M}(-j\omega)\Big] \\
=& 2\pi\delta(j\omega)O_{\alpha_d} + \alpha_I(j\omega)\Big[R_{\text{RF},g_M,I}(j\omega)\big[1 - j\gamma(j\omega)\sin(\theta_e)\big] \\
& + j R_{\text{RF},g_M,Q}(j\omega)\gamma(j\omega)\cos(\theta_e)\Big]
\end{aligned}
\tag{4.11}
$$

where $\gamma(j\omega)$ was defined in (3.8) and $R_{\text{RF},g_M,I}(j\omega)$, $R_{\text{RF},g_M,Q}(j\omega)$ correspond to the Fourier transforms of the real and imaginary part of (4.10). A frequency dependent mixer phase error can be easily introduced to (4.11) by replacing θ_e by $\theta_e(j\omega)$.

If this result is compared to the imbalance at the transmitter branch (3.5) and (3.7) important differences can be recognized. In both the transmitter and the receiver case, the asymmetrical phase-error model was used. At the transmitter branch the impact of the phase imbalance due to the baseband filtering and the mixer phase error coincide with the model presented in (3.5). Both introduce a magnitude reduction of the quadrature signal and a cross-talk of the quadrature to the inphase branch. At the receiver side the imbalance caused by the baseband filtering results in the same distortion mechanisms if the I/Q-mixer shows no phase imbalance (e.g $\theta_e \approx 0$). The mixer phase error generates a scaling of the quadrature branch signal, and an additional impact of the baseband filtering on the inphase to quadrature crosstalk.

It is interesting to note the changes in (4.11) if the mixer phase imbalance is shifted from the quadra-

ture to the inphase branch of the mixer:

$$
\begin{aligned}
R_{\mathrm{BB}}(j\omega) =& 2\pi\delta(j\omega)O_{\alpha_d} + \frac{1}{2}\alpha_I(j\omega)\Big[\Big(e^{-j\theta_e} + \gamma(j\omega) \Big) R_{\mathrm{RF},g_{\mathrm{M}}}(j\omega) \\
&+ \Big(e^{j\theta_e} - \gamma(j\omega) \Big) R_{\mathrm{RF},g_{\mathrm{M}}}^{*}(-j\omega)\Big] \\
=& 2\pi\delta(j\omega)O_{\alpha_d} + \alpha_I(j\omega)\Big(R_{\mathrm{RF},g_{\mathrm{M}},I}(j\omega)\cos(\theta_e) \\
&+ jR_{\mathrm{RF},g_{\mathrm{M}},Q}(j\omega)\left[\gamma(j\omega) - j\sin(\theta_e)\right] \Big)
\end{aligned}
\tag{4.12}
$$

Throughout the shift of the mixer phase error the linear model based on $R_{\mathrm{RF},g_{\mathrm{M}},I}(j\omega)$, $R_{\mathrm{RF},g_{\mathrm{M}},Q}(j\omega)$ simplifies while the one based on $R_{\mathrm{RF},g_{\mathrm{M}}}(j\omega)$, $R_{\mathrm{RF},g_{\mathrm{M}}}^{*}(-j\omega)$ shows increased complexity.

4.2 Enhanced linear receiver model

An important difference in the behavior of the linear receiver compared to the transmitter was not discussed up to now. As mentioned in Section 3.1 and Section 3.6 $\gamma(j\omega)$ is derived from the ratio of the quadrature channel frequency response to the inphase channel one (3.8). The resulting real-valued characteristic of $\gamma(j\omega)$ may be violated by a non-negligible RF-transfer characteristic of the transmitter output network as this filter may alter both the desired signal and the imbalance distortion.

Applying a single-tone input signal to the receiver an arbitrary frequency response of the RF input network cannot introduce imbalance distortion. The following modeling of the imbalance generation is based on the response of the real-valued inphase and quadrature branch response. Even if assuming an arbitrary response of the RF network the overall imbalance distortion modeling shows a real-valued system behavior. To introduce a complex-valued imbalance generation characteristic without infringing the real-valued behavior of the two baseband branches an enhancement of the linear receiver model (4.11) must be derived.

As mentioned in the last section, if $\gamma(j\omega)$ shows a real-valued time domain characteristic, a cross-talk from the inphase to the quadrature channel and a scaling of the later one is introduced (compare (4.11)). A complex-valued $\gamma(t)$ would introduce an additional cross-talk of the quadrature to the inphase branch as well as an inphase channel scaling. Compared to the real-valued case the inphase branch would lose its significance as reference channel introduced by the asymmetrical phase error model. The scaling of the inphase branch would be performed by $\alpha_d(j\omega)$, $\gamma(j\omega)$ and it would be deteriorated by the quadrature channel crosstalk. To pretend a real-valued $\gamma(t)$ behavior while using a complex-valued characteristic an input signal depending mapping of the complex- to the corresponding real-valued gamma progress can be implemented. This mapping is realized by dividing $R_{\mathrm{RF},g_{\mathrm{M}}}(j\omega)$ and $\gamma(j\omega)$ in their contributions located above and below the carrier. The corresponding real-valued gamma is then derived using spectral averaging:

$$
\gamma_{\mathrm{map}}(j\omega) = \begin{cases} \dfrac{\gamma(j\omega)|R_{\mathrm{RF},g_{\mathrm{M}}}(j\omega)| + \gamma^{*}(-j\omega)|R_{\mathrm{RF},g_{\mathrm{M}}}(-j\omega)|}{R_{\mathrm{RF},g_{\mathrm{M},\mathrm{Denom}}}(j\omega)} & \omega >= 0 \\ \gamma_{\mathrm{map}}^{*}(-j\omega) & \omega < 0 \end{cases}
\tag{4.13}
$$

Clearly, by applying the complex conjugate relationship in the second line of (4.13), the real-valued time domain property of $\gamma_{\mathrm{map}}(j\omega)$ is enforced. Depending on the location of the spectral content of the input signal the corresponding gamma is selected. In case of an excitation, symmetric to the carrier, the

mean of $\gamma(j\omega)$ and $\gamma^*(-j\omega)$ is used. The function $R_{\mathrm{RF},g_{\mathrm{M}},\mathrm{Denom}}(j\omega)$ compensated the dependency on the absolute magnitude of $R_{\mathrm{RF},g_{\mathrm{M}}}(j\omega)$:

$$R_{\mathrm{RF},g_{\mathrm{M}},\mathrm{Denom}}(j\omega) = \varepsilon + |R_{\mathrm{RF},g_{\mathrm{M}}}(j\omega)| + |R_{\mathrm{RF},g_{\mathrm{M}}}(-j\omega)| \tag{4.14}$$

The parameter ε in this expression accounts for the noise which may be present at the input signal. A sufficiently large ε avoids undesired boosting of $\gamma_{\mathrm{map}}(j\omega)$. Therefore, ε should be below the considered input signal spectral content and above the noise level.

Different ways for implementing (4.13) and (4.14) are possible and will not be detailed here any further. After evaluating $\gamma_{\mathrm{map}}(j\omega)$ it can be inserted into (4.11) and the corresponding linear receiver response can be derived. In the following the notation $\gamma_{\mathrm{map}}(j\omega, R_{\mathrm{RF},g_{\mathrm{M}}})$ will be used in cases where it is not clear which signal will be used for the mapping.

4.3 Nonlinear direct conversion receiver model

After the general discussion and the presentation of the linear description of the receiver in the last section, a Volterra series approximation is developed now. As for the transmitter, the RF nonlinearity will be modeled by a first zone output of a third-order polynomial. The baseband nonlinearities are represented by 3rd-order PCWMs.

Having passed the receiver input signal through RF nonlinearity and the following bandpass filter it is given by:

$$r_{\mathrm{BP},k}(t) = g_{\mathrm{M},1}\breve{r}_{\mathrm{RF},k}(t) + g_{\mathrm{M},3}\breve{r}_{\mathrm{RF},k}(t)|\breve{r}_{\mathrm{RF},k}(t)|^2 \tag{4.15}$$

where $g_{\mathrm{M},1}$ and $g_{\mathrm{M},3}$ are the coefficients of the polynomial. The functions $\breve{r}_{\mathrm{RF},k}(t)$ represent the RF input signal including the frequency offset, phase rotation and phase noise caused by the carrier and the spurious emissions:

$$\breve{r}_{\mathrm{RF},k}(t) = r_{\mathrm{RF}}(t)e^{-j(\Delta\omega_k t + \varphi_{\mathrm{PH},k}(t) + \Delta\varphi_{\mathrm{LO},k})} \tag{4.16}$$

Feeding the frequency shifted input signal $\breve{r}_{\mathrm{RF},k}(t)$ into the RF nonlinearity $g_{\mathrm{M}}(\,\cdot\,)$ is equivalent to multiplying the output signal of $g_{\mathrm{M}}(r_{\mathrm{RF},k}(t))$ by $e^{-j(\Delta\omega_k + \varphi_{\mathrm{PH},k}(t) + \Delta\varphi_{\mathrm{LO},k})}$. For simplifying the notation the desired signal $\breve{r}_{\mathrm{RF},0}(t)$ is abbreviated by $\breve{r}_{\mathrm{RF}}(t)$. The signals $\breve{r}_{\mathrm{RF},k}(t)$ are now downconverted to the baseband by the I/Q-mixer:

$$
\begin{aligned}
r_{\mathrm{mod},k}(t) = \frac{1}{2}\Big[& g_{\mathrm{M},1}\left(g_{\mathrm{CI},k} + g_{\mathrm{CQ},k}e^{-j\theta_e}\right)\breve{r}_{\mathrm{RF},k}(t) + g_{\mathrm{M},1}^*\left(g_{\mathrm{CI},k} - g_{\mathrm{CQ},k}e^{j\theta_e}\right)\breve{r}_{\mathrm{RF},k}^*(t) \\
& + g_{\mathrm{M},3}\left(g_{\mathrm{CI},k} + g_{\mathrm{CQ},k}e^{-j\theta_e}\right)\breve{r}_{\mathrm{RF},k}(t)|\breve{r}_{\mathrm{RF},k}(t)|^2 \\
& + g_{\mathrm{M},3}^*\left(g_{\mathrm{CI},k} - g_{\mathrm{CQ},k}e^{j\theta_e}\right)\breve{r}_{\mathrm{RF},k}^*(t)|\breve{r}_{\mathrm{RF},k}(t)|^2 \Big]
\end{aligned}
\tag{4.17}
$$

The scaling functions in this expression are similar to (4.9). The difference to the linear model scaling is the absence of the baseband amplifier gain g_I and g_Q. By the magnitude and phase imbalance of the mixer and the lowpass filters the undesired spectrally mirrored counterpart $\breve{r}_{\mathrm{RF}}^*(t)$ of the desired input signal $\breve{r}_{\mathrm{RF}}(t)$ and the corresponding IMD is generated.

The BB amplifier response, represented by PCWMs, is given by (exemplified for the inphase branch):

$$g_I\big(r_{\mathrm{mod},I}(t)\big) = g_{I,0} + \sum_{p=1}^{P}\big(g_{I,p}(t) * r_{\mathrm{mod},I}(t)\big)^p \tag{4.18}$$

where $g_{I,0}$ specifies the DC-offset of the amplifier and $g_{I,p}(t)$ represents the p$^{\text{th}}$-order frequency dependent nonlinear "coefficient" of the BB nonlinearity. As each function $g_{I,p}(t)$ is convolved with the corresponding lowpass filter in the receiver setup, this series connection can be abbreviated as:

$$
\begin{aligned}
h_{I,p}(t) &= g_{\text{CI},0} h_{\text{LP},I}(t) * g_{I,p}(t) \\
h_{Q,p}(t) &= g_{\text{CQ},0} h_{\text{LP},Q}(t) * g_{Q,p}(t)
\end{aligned}
\tag{4.19}
$$

By feeding the filtered mixer output signal into the baseband amplifiers the desired signal is boosted and a large number of distortion products is created. For the extraction of the significant contributors to the receiver output signal it was assumed, that the linear part of $r_{\text{mod}}(t)$ dominates the BB amplifier's input (i.e., lines one and two in (4.17) for $k = 0$). The interactions of the RF nonlinearity IMD with the other signal components were neglected. Additionally, only the linear BB amplifier response caused by the spurious LO emissions was included.

The Volterra series describing the receiver behavior covers distortion products up to third-order:

$$
r_{\text{BB}}(t) \approx (g_{I,0} + j g_{Q,0}) + r_{\text{BB},1}(t) + r_{\text{BB},2}(t) + r_{\text{BB},3}(t)
\tag{4.20}
$$

The linear receiver response is given by:

$$
\begin{aligned}
r_{\text{BB},1}(t) = &\int_{-\infty}^{\infty} \frac{1}{2} g_{\text{M},1}[h_{I,1}(\tau) + h_{Q,1}(\tau)\, e^{-j\theta_e}] \breve{r}_{\text{RF}}(t - \tau) d\tau \\
&+ \int_{-\infty}^{\infty} \frac{1}{2} g_{\text{M},1}^*[h_{I,1}(\tau) - h_{Q,1}(\tau)\, e^{j\theta_e}] \breve{r}_{\text{RF}}^*(t - \tau) d\tau \\
&+ \sum_{k=1}^{N_{\text{spur}}} \int_{-\infty}^{\infty} \frac{1}{2} g_{\text{M},1}[\frac{g_{\text{CI},k}}{g_{\text{CI},0}} h_{I,1}(\tau) + \frac{g_{\text{CQ},k}}{g_{\text{CQ},0}} h_{Q,1}(\tau)\, e^{-j\theta_e}] \breve{r}_{\text{RF},k}(t - \tau) d\tau \\
&+ \sum_{k=1}^{N_{\text{spur}}} \int_{-\infty}^{\infty} \frac{1}{2} g_{\text{M},1}^*[\frac{g_{\text{CI},k}}{g_{\text{CI},0}} h_{I,1}(\tau) - \frac{g_{\text{CQ},k}}{g_{\text{CQ},0}} h_{Q,1}(\tau)\, e^{j\theta_e}] \breve{r}_{\text{RF},k}^*(t - \tau) d\tau
\end{aligned}
\tag{4.21}
$$

The first two lines of this expression present the linear Volterra kernels due to the desired receiver output signal. The second part of (4.21) summarizes the distortion generated by the spurious emissions of the LO. The ratios $g_{\text{CI},k}/g_{\text{CI},0}$, $g_{\text{CQ},k}/g_{\text{CQ},0}$ represent the magnitude of these products relative to the carrier.

For analyzing the second-order receiver output a comparison with the memoryless BB amplifier description summarized in (3.50) will be drawn. In this expression the terms $|r_{\text{mod}}(t)|^2$ and $\text{Re}\{r_{\text{mod}}(t)\}^2$ cause the second-order distortion. Each of the two distortion mechanisms can be allocated to the input signal functions $\breve{r}_{\text{RF}}(t)\breve{r}_{\text{RF}}^*(t)$, $\breve{r}_{\text{RF}}(t)^2$, $\breve{r}_{\text{RF}}^*(t)^2$. The corresponding Volterra series representation results to:

$$
\begin{aligned}
r_{\text{BB},2}(t) \approx &\int_{-\infty}^{\infty} \int_{-\infty}^{\infty} \frac{1}{4} g_{\text{M},1}^2 [h_{I,2}(\tau_1) h_{I,2}(\tau_2) - j h_{Q,2}(\tau_1) h_{Q,2}(\tau_2)\, e^{-2j\theta_e}] \breve{r}_{\text{RF}}(t - \tau_1) \breve{r}_{\text{RF}}(t - \tau_2) d\tau_1 d\tau_2 \\
&+ \int_{-\infty}^{\infty} \int_{-\infty}^{\infty} \frac{1}{2} |g_{\text{M},1}|^2 [h_{I,2}(\tau_1) h_{I,2}(\tau_2) + j h_{Q,2}(\tau_1) h_{Q,2}(\tau_2)] \breve{r}_{\text{RF}}(t - \tau_1) \breve{r}_{\text{RF}}^*(t - \tau_2) d\tau_1 d\tau_2 \\
&+ \int_{-\infty}^{\infty} \int_{-\infty}^{\infty} \frac{1}{4} g_{\text{M},1}^{*2} [h_{I,2}(\tau_1) h_{I,2}(\tau_2) - j h_{Q,2}(\tau_1) h_{Q,2}(\tau_2)\, e^{2j\theta_e}] \breve{r}_{\text{RF}}^*(t - \tau_1) \breve{r}_{\text{RF}}^*(t - \tau_2) d\tau_1 d\tau_2
\end{aligned}
\tag{4.22}
$$

At the 3rd-order distortion the contribution present in the imbalance free case is composed of $\breve{r}_{\text{RF}}^{*3}(t)$ and $\breve{r}_{\text{RF}}(t)|\breve{r}_{\text{RF}}(t)|^2$. The distortion components introduced by the imbalance of the BB branches consists of the complex conjugate of the two functions. Together with the linear scaled RF output nonlinearity IMD these six terms approximate the third-order nonlinear response of the receiver:

$$
\begin{aligned}
r_{\text{BB},3}(t) \approx & \\
& \int_{-\infty}^{\infty}\int_{-\infty}^{\infty}\int_{-\infty}^{\infty} \tfrac{1}{8}g_{\text{M},1}^{*3}\big[h_{I,3}(\tau_1)h_{I,3}(\tau_2)h_{I,3}(\tau_3) + h_{Q,3}(\tau_1)h_{Q,3}(\tau_2)h_{Q,3}(\tau_3)\,e^{3j\theta_e}\big] \\
& \cdot \breve{r}_{\text{RF}}^{*}(t-\tau_1)\breve{r}_{\text{RF}}^{*}(t-\tau_2)\breve{r}_{\text{RF}}^{*}(t-\tau_3)d\tau_1 d\tau_2 d\tau_3 \\
& + \int_{-\infty}^{\infty}\int_{-\infty}^{\infty}\int_{-\infty}^{\infty} \tfrac{1}{8}g_{\text{M},1}^{3}\big[h_{I,3}(\tau_1)h_{I,3}(\tau_2)h_{I,3}(\tau_3) - h_{Q,3}(\tau_1)h_{Q,3}(\tau_2)h_{Q,3}(\tau_3)\,e^{-3j\theta_e}\big] \\
& \cdot \breve{r}_{\text{RF}}(t-\tau_1)\breve{r}_{\text{RF}}(t-\tau_2)\breve{r}_{\text{RF}}(t-\tau_3)d\tau_1 d\tau_2 d\tau_3 \\
& + \int_{-\infty}^{\infty}\int_{-\infty}^{\infty}\int_{-\infty}^{\infty} \tfrac{1}{8}\bigg(3g_{\text{M},1}|g_{\text{M},1}|^2\big[h_{I,3}(\tau_1)h_{I,3}(\tau_2)h_{I,3}(\tau_3) + h_{Q,3}(\tau_1)h_{Q,3}(\tau_2)h_{Q,3}(\tau_3)\,e^{-j\theta_e}\big] \\
& \quad +4\int_{-\infty}^{\infty} g_{\text{M},3}\big[h_{I,1}(\tau_4) + h_{Q,1}(\tau_4)\,e^{-j\theta_e}\big]\delta(\tau_1-\tau_4)\delta(\tau_2-\tau_1)\delta(\tau_3-\tau_2)\,d\tau_4\bigg) \\
& \cdot \breve{r}_{\text{RF}}(t-\tau_1)\breve{r}_{\text{RF}}(t-\tau_2)\breve{r}_{\text{RF}}^{*}(t-\tau_3)d\tau_1 d\tau_2 d\tau_3 \\
& + \int_{-\infty}^{\infty}\int_{-\infty}^{\infty}\int_{-\infty}^{\infty} \tfrac{1}{8}\bigg(3g_{\text{M},1}^{*}|g_{\text{M},1}|^2\big[h_{I,3}(\tau_1)h_{I,3}(\tau_2)h_{I,3}(\tau_3) - h_{Q,3}(\tau_1)h_{Q,3}(\tau_2)h_{Q,3}(\tau_3)\,e^{j\theta_e}\big] \\
& \quad +4\int_{-\infty}^{\infty} g_{\text{M},3}^{*}\big[h_{I,1}(\tau_4) - h_{Q,1}(\tau_4)\,e^{j\theta_e}\big]\delta(\tau_1-\tau_4)\delta(\tau_2-\tau_1)\delta(\tau_3-\tau_2)\,d\tau_4\bigg) \\
& \cdot \breve{r}_{\text{RF}}(t-\tau_1)\breve{r}_{\text{RF}}^{*}(t-\tau_2)\breve{r}_{\text{RF}}^{*}(t-\tau_3)d\tau_1 d\tau_2 d\tau_3
\end{aligned}
$$

$$(4.23)$$

The first two integrals of this expression present the Volterra kernels of the third-order harmonics. The other two are the sum of the IMD of the BB amplifiers and the RF nonlinearity. The series connection of $g_{\text{M}}(\cdot)$ and the linear filters $h_{I,1}(t)$ and $h_{Q,1}(t)$ results in a Hammerstein structured nonlinear system. The linear filtering of the nonlinear distortion product is expressed by the convolution integral covered in the corresponding Volterra kernels.

Simulations were performed for evaluating the accuracy of the presented approximation. These simulations utilized the same parameters as used for the evaluation of the transmitter model: both lowpass-filters were frequency-independent. The gain imbalance was set to $\gamma = 0.95$. A phase error of $\theta_e = 3°$ was selected. These parameters introduce a ISR of $-28\,\text{dB}$. The BB amplifiers showed an $\text{IP}_{2,\text{output}}$ of $44\,\text{dBm}$ and an $\text{IP}_{3,\text{output}}$ of $24\,\text{dBm}$. The magnitude of the DC-offset causing $30\,\text{dB}$ below the magnitude of a full-scale carrier signal. The RF nonlinearity was set to the same gain and IP_3 as used for the BB amplifiers. The impact of the phase noise and the spurious emissions were neglected for these simulations.

The error of the model (4.20) - (4.23) for a two-tone power sweep is presented in Figure 4.2. The two-tone signal was simulated using incommensurable frequencies to avoid phase dependent gain changes as presented in Section 3.2. The error of this approximation for the sweep is presented in Figure 4.2(a). At this simulation all parameters were selected as described above, only the magnitude imbalance was varied between 0.78 and 0.94. In this plot the ISR is used to quantify the resulting imbalance. A similar

simulation was also performed for the phase imbalance. As only slight differences in the modeling error were recognizable for both effects only the magnitude imbalance dependent simulation is presented. Clearly, the presented receiver model provides a correct prediction of the imbalance effects independent of the input power. In Figure 4.2(b) the impact of odd and even order distortion is visualized. When operating the modulator in back-off both types of distortion contribute nearly equally to the resulting approximation error. At around $P_{BB} = 5$ dBm the odd order distortion has a dominant influence on the model accuracy.

(a)

(b)
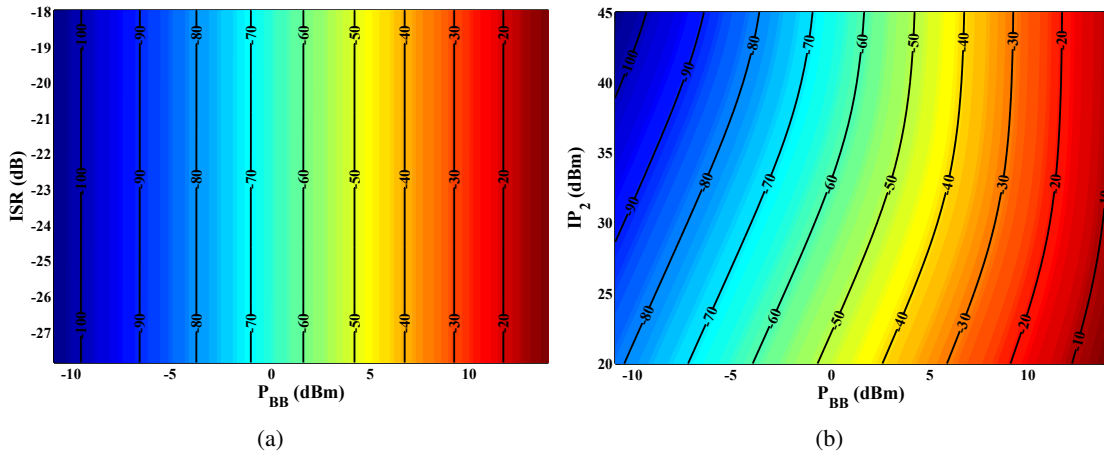
Figure 4.2: Mean square error between the full and the approximated receiver description (a) for a sweep of the input power and the magnitude imbalance. The impact of the this imbalance is quantified using the ISR. (b) Input power and IP_2 sweep.

4.4 Enhanced nonlinear receiver model

In Section 3.8.10 difficulties in the implementation of the extracted PCWM filtering function for the transmitter were discussed. A major issue was a phase of the filtering function which does not trend to zero or $-180°$ for $|f| \rightarrow 0$. This type of behavior results in an complex-valued output signal of the real-valued BB branches. Modeling this type of behavior was easy in the transmitter case as only the complex-valued output signal of the whole structure was observed, but not the real-valued outputs of the BB channels. Despite of the simple model, this behavior demanded for increased complexity in the predistorter design.

At the receiver case the output of the two baseband branches are captured. Using this information the overall receiver response is composed. Therefore, a complex-valued output of the models BB branches results in an increased modeling error. A nonvanishing filtering function phase behavior around DC cannot be implemented by complex-valued characteristic of these functions.

Additionally, at the receiver side the magnitude and phase of the harmonic distortion at each branch is known. This is a significant difference to the transmitter case, where the BB branch output signal are a result of the RF output NL deembedding process as described in Section 3.8.6. Hence, it makes sense to extract the magnitude and phases of all harmonic distortion components from the measured output

signals of both channels. Thereafter, the behavior of related distortion products, like the 3rd-order IMD and HD distortion, can be compared. Differences in the required filtering functions for the IMD and the HD components force the usage of an own "coefficient" for each type of distortion. Such differences can be ascribed to linear filtering of the BB amplifier output signal which is not represented in the model. In the following an improved structure for the nonlinear receiver model is derived, able of coping with nonvanishing filtering function phase behavior as well as different scaling of each distortion component.

The requirements for implementing the nonvanishing filtering function phase behavior are similar to the statement of the problem at Section 4.2. Therefore, the same approach of an input signal based mapping of the complex-valued PCWM filtering function to their real-valued correspondent will be used. In the following $h_{\text{map},I,p}(t), h_{\text{map},Q,p}(t)$ represent the real-valued implementation of the complex-valued functions $h_{I,p}(t), h_{Q,p}(t)$. The mapping is described in (4.13) after exchanging $\gamma(j\omega)$ and $R_{\text{RF},g_M}(j\omega)$ by the corresponding filtering function and input signal $r_{\text{mod}}(t)$, respectively.

To implement the independent treatment of the distortion components generated by the same polynomial order a separation of the different contributions must be derived. This goal is achieved by using the analytical representation of the real-valued input signal to the BB nonlinearity branch. In case of the second order distortion the relationship between the powers of an arbitrary real-valued signal $r_{\text{Re}}(t)$ and its analytical correspondent $r_{\text{Ana}}(t)$ are given by:

$$
\begin{aligned}
r_{\text{Ana}}(t) &= r_{\text{Re}}(t) + j\mathcal{H}\{r_{\text{Re}}(t)\} \\
r_{\text{Re}}^2(t) &= \left(\frac{1}{2}[r_{\text{Ana}}(t) + r_{\text{Ana}}^*(t)]\right)^2 = \frac{1}{2}\left[\text{Re}\left\{r_{\text{Ana}}^2(t)\right\} + |r_{\text{Ana}}(t)|^2\right]
\end{aligned}
\tag{4.24}
$$

In this expression $\mathcal{H}\{\cdot\}$ identifies the Hilbert transformation [118]. This equation proves that the HD_2 distortion components located at DC is given by $|r_{\text{Ana}}(t)|^2$. The contribution and twice the input frequency is selected by $\text{Re}\{r_{\text{Ana}}^2(t)\}$. It should be noted that, throughout the use of the PCWM all dynamics are represented by the filtering functions applied to the input signal before the NL operations. The static NL solution to the distortion components separation shown in (4.24) is therefore fully applicable without changing the dynamic behavior. The extension of this relationship for an arbitrary even order power is derived applying the binomial formula [114]:

$$
\left(\frac{1}{2}[r_{\text{Ana}}(t) + r_{\text{Ana}}^*(t)]\right)^{2n} = \sum_{p=0}^{n} \frac{2^{\text{sign}(n-p)}}{4^n}\binom{2n}{p}|r_{\text{Ana}}(t)|^{2p}\text{Re}\left\{r_{\text{Ana}}^{2(n-p)}(t)\right\}
\tag{4.25}
$$

If $r_{\text{Re}}(t)$ represents a narrowband modulated signal (4.25) identifies the contribution at the different harmonics of the carrier. In this way (4.25) is a special case to the response of memoryless nonlinearities derived by Blachman [125] using the Chebyshev transform. For an odd-order power the relationship results to:

$$
\left(\frac{1}{2}[r_{\text{Ana}}(t) + r_{\text{Ana}}^*(t)]\right)^{2n-1} = \sum_{p=0}^{n-1} \frac{1}{4^{n-1}}\binom{2n-1}{p}|r_{\text{Ana}}(t)|^{2p}\text{Re}\left\{r_{\text{Ana}}^{2(n-p)-1}(t)\right\}
\tag{4.26}
$$

Due to the complexity introduced by the distortion component separation the enhanced model will not be based on the receiver input signal. Instead, the modifications are only applied to the BB amplifier responses which are driven by the real and imaginary part of the modulator output signal $r_{\text{mod}}(t)$ (4.17).

Also the treatment of the spurious emissions was neglected. The BB amplifier behavior is shown, exemplified for the inphase channel, considering NL products up to third order. Based on these prerequisites the linear BB amplifier response is given by:

$$r_{\mathrm{BB},I,1}(t) = h_{\mathrm{map},I,1}(t) * r_{\mathrm{mod},I}(t) \tag{4.27}$$

It should be emphasized that despite of the real-valued input signal $r_{\mathrm{mod},I}(t) = \mathrm{Re}\{r_{\mathrm{mod}}(t)\}$ to the BB amplifier the spectral averaging process for the filtering function $h_{I,1}(t)$ uses the complex-valued correspondent. For discussing the second order NL response two new filtering functions $h_{\mathrm{map},I,2,\mathrm{DC}}(t)$, $h_{\mathrm{map},I,2,\mathrm{HD}}(t)$ are introduced allowing a different scaling of the distortion products mentioned in (4.24). As indicated, spectral averaging may be applied to these filtering functions if required. The corresponding second order BB amplifier response is shown in (4.28).

$$r_{\mathrm{BB},I,2}(t) = \frac{1}{2} \left| h_{\mathrm{map},I,2,\mathrm{DC}}(t) * r_{\mathrm{mod},\mathrm{Ana},I}(t) \right|^2 + \frac{1}{2} \mathrm{Re} \left\{ \left[h_{\mathrm{map},I,2,\mathrm{HD}}(t) * r_{\mathrm{mod},\mathrm{Ana},I}(t) \right]^2 \right\} \tag{4.28}$$

Here, $r_{\mathrm{mod},\mathrm{Ana},I}(t)$ is derived as shown in the first line of (4.24). In a similar way the third order distortion components result to:

$$\begin{aligned} r_{\mathrm{BB},I,3}(t) =& \frac{3}{4} \left| h_{\mathrm{map},I,3,\mathrm{IMD}}(t) * r_{\mathrm{mod},\mathrm{Ana},I}(t) \right|^2 \mathrm{Re} \left\{ h_{\mathrm{map},I,3,\mathrm{IMD}}(t) * r_{\mathrm{mod},\mathrm{Ana},I}(t) \right\} \\ &+ \frac{1}{4} \mathrm{Re} \left\{ \left[h_{\mathrm{map},I,3,\mathrm{HD}}(t) * r_{\mathrm{mod},\mathrm{Ana},I}(t) \right]^3 \right\} \end{aligned} \tag{4.29}$$

In this expression $h_{\mathrm{map},I,3,\mathrm{IMD}}(t)$ and $h_{\mathrm{map},I,3,\mathrm{HD}}(t)$ are the scaling function for the IMD and HD distortion.

4.5 Characterization and compensation of the receiver distortion

The nonlinear dynamic receiver model developed in the last sections is a direct result of the hardware implementation issues of the various direct conversion receiver structures [8, 50]. The impact of the corresponding receiver imperfections on the performance of a transmission system are similar to the transmitter case, as analyzed in [88].

Based on these receiver models measurement approaches are developed in this section for characterizing the distortion effects. Thereafter, compensators are presented for removing the impact of the receiver imperfections.

Several approaches can be found in the literature discussing the characterization and compensation of the linear direct conversion receiver distortion. One of the first approaches for the evaluation and compensation of the imbalance distortion using digital signal processing was presented in [126]. Based on the measurement of a single-tone test signal the I/Q mixer phase imbalance and magnitude imbalance and DC-offset of the analog signal processing were extracted at one frequency. In [127] the same approach was used for identifying these parameters over the input bandwidth of the receiver. The extracted set of coefficients was then used for designing two FIR filters performing the broadband compensation.

Further examples for the characterization and compensation of the I/Q mixer phase imbalance and the magnitude imbalance and DC-offset of the analog signal processing using adaptive signal processing can be found, for example, in [76, 122, 123, 128, 129]. The application of nonlinear least square (NLS)

for the parameter extraction was discussed in [130]. The evaluation of the imbalance parameters from the statistics of the measured baseband signals is an interesting approach if no information on the type and modulation of the input signal is available [131].

In contrast to the former approaches a wideband characterization of the magnitude and phase imbalance of the analog BB processing using a multi-tone input signal was discussed in [77, 78].

A similar linear receiver model as presented in (4.11) was derived by Mailand *et. al.* [132]. Unfortunately, in this publication neither the parameter identification nor a broadband compensator is presented. The combined extraction of the I/Q mixer phase imbalance, the frequency-dependent magnitude and phase imbalance of the analog signal processing and the LO frequency offset for an OFDM input signal can be achieved using NLS techniques [124].

In [133] the authors described the imbalance effects by a frequency-dependent I/Q mixer phase imbalance and a frequency-dependent magnitude imbalance of the analog signal processing. In this way the distinction between I/Q mixer and analog signal processing phase imbalance was avoided. The behavior of the receiver was characterized from single-tone measurements over the considered baseband bandwidth and the resulting parameters were used for compensating the receiver. This compensator provided the magnitude and the phase of the complex envelope instead of the usual inphase and quadrature components.

The time domain measurement system presented in [91] provided a full calibration of the linear effects of the transmitter and the receiver. The properties of this measurement setup were already discussed at the beginning of Section 3.4.

To the best of the author's knowledge the parameterization and compensation of the nonlinear receiver behavior was not discussed in the literature up to now. This may be ascribed to the missing of devices introducing strong nonlinearities (i.e., power amplifier) in the signal chain of a linear receiver.

The characterization and compensation of the phase noise impact faces the same problems that are presented in the transmitter case. Due to this reason, also for the receiver no characterization for compensation of the phase noise will be treated. However, the cancelation of the inband spurious emissions will be performed at the receiver compensator.

4.5.1 Receiver model partitioning

The development of the receiver characterization algorithm and composing the model from these results was performed applying the same prerequisites as in the transmitter case. Again, an important default was avoiding a superposition of the distortion generated by the transmitter with the ones created by the imperfections of the receiver (compare Section 3.4.1). Therefore, for the characterization of the receiver, the input signal should be provided from single-tone sources. By combining these sources using a resistive network, a low distortion imbalance-free input signal to the receiver can be generated.

The magnitude of the tones present at the receiver input can be verified by a combined measurement using a power meter and a spectrum analyzer. The quantification of the tone phases could be achieved by the use of a vector signal analyzer (VSA) or a wideband oscilloscope. In this sense the VSA / scope acts as a golden device providing the phase reference the DUT is compared to.

As in the transmitter case, we face the problem that the model developed in the last section shows ambiguities in the selected parameters. For example, the gain of the inphase branch is influenced by the coefficients: $g_{M,1}$, g_{CI}, $h_{LP,I}(t)$ and $g_{I,1}(t)$. Therefore, the receiver characterization is performed by dividing its behavior in groups, where each one is related to a single distortion mechanism.

Each distortion effect must be excitable by single- or two-tone test signals which can be generated using CW-sources. During the measurement of a distortion mechanism interactions with other distortion effects must be avoided (or at least, kept low). The partitioning of the receiver behavior is performed based on the following distinguishable distortion effects:

- DC-Offset

- Imbalance distortion for a single-tone input signal

- Mixing of a single-tone input by spurious emissions

- Intermodulation and harmonic distortion from single-tone and two-tone input signals

The DC-offset is related to the factor O_{α_d} (4.9). From the imbalance measurement results the magnitude and phase of $\gamma(j\omega)$ and the I/Q mixer phase imbalance θ_e are extracted. The nonlinear behavior of the I/Q mixer input nonlinearity and the two baseband amplifiers are evaluated from single-tone and two-tone measurements. Based on these measurements the magnitude and phase of $g_{\mathrm{M},p}$ is evaluated. Also the parameters $h_{I,p}(t)$ and $h_{Q,p}(t)$ are characterized from the nonlinear receiver response.

When composing a receiver model from the parameterized distortion mechanisms, care must be taken for avoiding undesired interactions. For example, the magnitude imbalance $|\gamma(j\omega)|$ is extracted by characterizing the imbalance between the two BB branches. In the same way a difference in the BB amplifier gain evaluated from the nonlinear receiver response causes also a magnitude imbalance.

It is important to note, that in difference to the transmitter case, the power levels at the input of the I/Q mixer and at the input of the BB amplifiers may vary due to the introduction of switchable attenuators or variable gain amplifier for maximizing the dynamic range for a given input signal (compare Section 2.1). This flexibility in the selection of the input powers at the nonlinear components leads to the requirement of different models for the different operation conditions. Each model is characterized by the (peak) I/Q mixer input power level which results in a full conduction of the receiver ADCs.

For characterizing the receiver behavior single- and two-tone measurements of the direct conversion receiver introduced in Section 2.1 are taken. The measurement setup applicable for this purpose is depicted in Figure 2.19.

4.6 Receiver DC-offset

Several different mechanisms are known for introducing DC-offset into the signal path of the direct conversion receiver [40, 10]:

- DC-offset caused by LO self-mixing and LO re-radiation

- DC-offset introduced by the BB amplifiers

- Even-order distortion of the BB amplifiers

The first mechanism is based on a leakage of the LO signal to the RF input which appears as a DC-offset in the baseband. For the receiver setup sketched in Figure 2.19 a coupling is caused by a limited LO/RF rejection of the I/Q mixer and a reflection of this signal at the mixer input port.

The BB amplifiers generate additional DC-offset due to two mechanisms. On the one hand an inherent DC-offset is inserted in the BB amplifier stages. This DC-offset shows a significant drift over temperature. On the other hand DC-offset is caused by even-order distortion. Clearly, the signal dependent DC-offset generated by this even-order distortion can only be removed by postprocessing of the sampled input signals in the digital domain. The other two mechanisms introduce a DC-offset even if no RF input signal is applied. Despite of the possibility performing the compensation of this DC-offset completely in the postprocessing stage, the shift of the analog signals at the ADC-inputs caused by the DC-offsets results in a loss of dynamic range. Therefore, they should be canceled in the analog domain before the ADCs.

After this analog DC-offset cancelation was performed the residual DC-offset can be removed by a subtraction of a constant during the postprocessing. In contrast to the transmitter case, the evaluation and compensation in the digital domain of the receiver is straight forward. By averaging the measured inputs without a RF signal applied to the receiver, the residual DC-offsets are quantified. These values will be subtracted during the recording of the measurement signals. Care must be taken to select a sufficiently long time constant for the integration to avoid interactions with the dynamic DC-offset introduced by the even order distortion.

4.7 Receiver imbalance

A prerequisite for the evaluation of the receiver imbalance coefficients is the independency from the transmitter branch of the measurement system as mentioned at the beginning of Section 4.5.1. This prerequisite forces the usage of a test signal generated by a frequency conversion method different from the one applied in the receiver. Single-tone input signals generated by a CW-source meet this requirement.

4.7.1 Imbalance characterization

The basis for the suggested imbalance characterization approach is the extraction of the parameters from the baseband measurement results of a single-tone input signal. By sweeping the single-tone over the whole receiver bandwidth the frequency dependency of the coefficients is recorded. In contrast to former publications on imbalance parameter extraction from single-tone measurements, mentioned at the beginning of Section 4.5, the imbalance description will be based on the three coefficients $|\gamma(j\omega)|$, $\phi_\gamma(j\omega)$ and θ_e. Based on the linear receiver model (i.e., (4.11)) it is not possible neglecting either the mixer phase imbalance or the I/Q mixer phase error as their impact on the resulting imbalance is caused by different mechanisms. This is also an important difference to the transmitter case (compare (3.5)) where the distortion mechanism for $\phi_\gamma(j\omega)$ and θ_e coincide. This indistinguishability in the distortion mechanism led to the combined treatment of the two parameters in Section 3.6.2.

Evaluating the imbalance coefficients, a single-tone signal is provided at the input of the receiver:

$$r_{\mathrm{RF}}(t) = A_{\mathrm{f}_m}\, e^{j\omega_m t} \tag{4.30}$$

where $A_{\mathrm{f}_m} = |A_{\mathrm{f}_m}| \exp(j\phi_{A_{\mathrm{f}_m}})$ is the complex amplitude of the input tone and $\omega_m = 2\pi\mathrm{f}_m$ is the frequency of the input tone relative to the center frequency of the receiver. By substituting the frequency transform of (4.30) into (4.11) and converting the resulting expression back into the time-domain the

response of the linear receiver onto this input signal results to (neglecting the DC-offset and the LO phase difference):

$$
\begin{aligned}
r_{\mathrm{BB,f}_m}(t) =\ & \tfrac{1}{2}\alpha_I(j\omega)\left(1+\gamma(j\omega_m)e^{-j\theta_e}\right)g_{\mathrm{M}}A_{\mathrm{f}_m}e^{j\omega_m t} \\
& +\tfrac{1}{2}\alpha_I(-j\omega)\left(1-\gamma(-j\omega_m)e^{j\theta_e}\right)g_{\mathrm{M}}^*A_{\mathrm{f}_m}^*e^{-j\omega_m t}
\end{aligned}
\tag{4.31}
$$

Assuming a real-valued $\alpha(t)$ and $\gamma(t)$ the corresponding inphase and quadrature branch output signals are given by:

$$
\begin{aligned}
r_{\mathrm{BB},I,\mathrm{f}_m}(t) =\ & \frac{1}{2}\alpha_I(j\omega)g_{\mathrm{M}}A_{\mathrm{f}_m}e^{j\omega_m t}+\frac{1}{2}\alpha_I^*(j\omega)g_{\mathrm{M}}^*A_{\mathrm{f}_m}^*e^{-j\omega_m t} \\
r_{\mathrm{BB},Q,\mathrm{f}_m}(t) =\ & \frac{j}{2}\alpha_I^*(j\omega)|\gamma(j\omega_m)|e^{j(-\phi_\gamma(j\omega_m)+\theta_e)}g_{\mathrm{M}}^*A_{\mathrm{f}_m}^*e^{-j\omega_m t} \\
& -\frac{j}{2}\alpha_I(j\omega)|\gamma(j\omega_m)|e^{j(\phi_\gamma(j\omega_m)-\theta_e)}g_{\mathrm{M}}A_{\mathrm{f}_m}e^{j\omega_m t}
\end{aligned}
\tag{4.32}
$$

Using only (4.32) it is not possible to separate $\phi_\gamma(j\omega_m)$ and θ_e as they occur only with opposite sign. For isolating the two phase coefficients the receiver response for an input tone located at $-\mathrm{f}_m$ has to be taken into account:

$$
\begin{aligned}
r_{\mathrm{BB},I,-\mathrm{f}_m}(t) =\ & \frac{1}{2}\alpha_I^*(j\omega)g_{\mathrm{M}}A_{-\mathrm{f}_m}e^{-j\omega_m t}+\frac{1}{2}\alpha_I(j\omega)g_{\mathrm{M}}^*A_{-\mathrm{f}_m}^*e^{j\omega_m t} \\
r_{\mathrm{BB},Q,-\mathrm{f}_m}(t) =\ & \frac{j}{2}\alpha_I(j\omega)|\gamma(j\omega_m)|e^{j(\phi_\gamma(j\omega_m)+\theta_e)}g_{\mathrm{M}}^*A_{-\mathrm{f}_m}^*e^{j\omega_m t} \\
& -\frac{j}{2}\alpha_I^*(j\omega)|\gamma(j\omega_m)|e^{-j(\phi_\gamma(j\omega_m)+\theta_e)}g_{\mathrm{M}}A_{-\mathrm{f}_m}e^{-j\omega_m t}
\end{aligned}
\tag{4.33}
$$

where $A_{-\mathrm{f}_m}$ represents the complex amplitude of the single-tone input located at $-\mathrm{f}_m$. Here, also the real-valued time-domain property of $\alpha(t)$, $\gamma(t)$ was used. In a next step the following amplitudes are extracted from the baseband output signals:

$$
\begin{aligned}
A_{\mathrm{BB},I,\mathrm{f}_m} =\ & \mathcal{F}\{r_{\mathrm{BB},I,\mathrm{f}_m}(t)e^{-j\omega_m t}\}|_{\omega=0} = \tfrac{1}{2}\alpha_I(j\omega)g_{\mathrm{M}}A_{\mathrm{f}_m} \\
A_{\mathrm{BB},Q,\mathrm{f}_m} =\ & \mathcal{F}\left\{\left(r_{\mathrm{BB},Q,\mathrm{f}_m}(t)e^{j\omega_m t}\right)^*\right\}|_{\omega=0} = -\tfrac{j}{2}\alpha_I(j\omega)|\gamma(j\omega_m)|e^{j(\phi_\gamma(j\omega_m)-\theta_e)}g_{\mathrm{M}}A_{\mathrm{f}_m} \\
A_{\mathrm{BB},I,-\mathrm{f}_m} =\ & \mathcal{F}\{r_{\mathrm{BB},I,-\mathrm{f}_m}(t)e^{j\omega_m t}\}|_{\omega=0} = \tfrac{1}{2}\alpha_I^*(j\omega)g_{\mathrm{M}}A_{-\mathrm{f}_m} \\
A_{\mathrm{BB},Q,-\mathrm{f}_m} =\ & \mathcal{F}\left\{\left(r_{\mathrm{BB},Q,-\mathrm{f}_m}(t)e^{-j\omega_m t}\right)^*\right\}|_{\omega=0} = -\tfrac{j}{2}\alpha_I^*(j\omega)|\gamma(j\omega_m)|e^{-j(\phi_\gamma(j\omega_m)+\theta_e)}g_{\mathrm{M}}A_{-\mathrm{f}_m}
\end{aligned}
\tag{4.34}
$$

For removing the dependency on the input signal amplitude, g_{M}, and $\alpha(j\omega)$ relative amplitudes are used instead of the absolute ones:

$$
\begin{aligned}
\Delta A_{\mathrm{f}_m} =\ & \frac{A_{\mathrm{BB},Q,\mathrm{f}_m}}{A_{\mathrm{BB},I,\mathrm{f}_m}} = -j|\gamma(j\omega_m)|e^{j(\phi_\gamma(j\omega_m)-\theta_e)} \\
\Delta A_{-\mathrm{f}_m} =\ & \frac{A_{\mathrm{BB},Q,-\mathrm{f}_m}}{A_{\mathrm{BB},I,-\mathrm{f}_m}} = -j|\gamma(j\omega_m)|e^{-j(\phi_\gamma(j\omega_m)+\theta_e)}
\end{aligned}
\tag{4.35}
$$

From these ratios it is easy extracting the desired imbalance parameters:

$$|\hat{\gamma}(j\omega_m)| = \frac{1}{2}(|\Delta A_{\text{f}_m}| + |\Delta A_{-\text{f}_m}|)$$

$$\hat{\phi}_\gamma(j\omega_m) = -\frac{1}{2}\angle\left\{\frac{\Delta A_{-\text{f}_m}}{\Delta A_{\text{f}_m}}\right\} \tag{4.36}$$

$$\hat{\theta}_e(j\omega_m) = -\frac{1}{2}\angle\{-\Delta A_{-\text{f}_m} \cdot \Delta A_{\text{f}_m}\}$$

where the "ˆ" is used for identifying the estimated coefficients. The sketched method for the coefficients extraction provides also the frequency dependency of $\hat{\theta}_e$. By averaging $\hat{\theta}_e(j\omega)$ over frequency range $\text{f}_m > 0$ the corresponding frequency-independent I/Q mixer phase error can be calculated. The imbalance parameter extraction is based on the linear receiver model (4.11) implementing a real-valued $\gamma(t)$. Hence, single-tone measurements at f_m and $-\text{f}_m$ were used for the evaluation of the imbalance coefficients at f_m. The response of $\hat{\gamma}(j\omega)$ at $\omega < 0$ is given by the symmetry $\hat{\gamma}(-j\omega) = \hat{\gamma}^*(j\omega)$ due to the mentioned assumptions.

4.7.2 Imbalance compensation based on real-valued $\gamma(t)$

In (4.11) the relationship between $r_{\text{RF},g_{\text{M}},I}(t)$, $r_{\text{RF},g_{\text{M}},Q}(t)$ and $r_{\text{BB}}(t) = r_{\text{BB},I}(t) + jr_{\text{BB},Q}(t)$ was established for using a real-valued $\gamma(t)$ (neglecting the DC-offset):

$$\begin{aligned}
R_{\text{BB}}(j\omega) &= \alpha_I(j\omega)\Big[R_{\text{RF},g_{\text{M}},I}(j\omega)\big[1 - j\gamma(j\omega)\sin(\theta_e)\big] \\
&\quad + jR_{\text{RF},g_{\text{M}},Q}(j\omega)\gamma(j\omega)\cos(\theta_e)\Big]
\end{aligned} \tag{4.37}$$

The part of this equation located within the outer squared brackets is responsible for the imbalance generation. The real and imaginary components of this expression are given by:

$$\begin{aligned}
R_{\text{BB},I}(j\omega) &= R_{\text{RF},g_{\text{M}},I}(j\omega) \\
R_{\text{BB},Q}(j\omega) &= -R_{\text{RF},g_{\text{M}},I}(j\omega)\gamma(j\omega)\sin(\theta_e) + R_{\text{RF},g_{\text{M}},Q}(j\omega)\gamma(j\omega)\cos(\theta_e)
\end{aligned} \tag{4.38}$$

The ideal output signal of the compensator corresponds to the complex envelope of the RF input signal. Therefore, for extracting the equations describing the imbalance compensation the RF input signal components $R_{\text{RF},g_{\text{M}},I}(j\omega)$ and $R_{\text{RF},g_{\text{M}},Q}(j\omega)$ in (4.38) are substituted by the output signals of the compensator $R_{\text{BB,Comp},I}(j\omega)$ and $R_{\text{BB,Comp},Q}(j\omega)$:

$$\begin{aligned}
R_{\text{BB},I}(j\omega) &= R_{\text{BB,Comp}}(j\omega) \\
R_{\text{BB},Q}(j\omega) &= -R_{\text{BB,Comp},I}(j\omega)\gamma(j\omega)\sin(\theta_e) + R_{\text{BB,Comp},Q}(j\omega)\gamma(j\omega)\cos(\theta_e)
\end{aligned} \tag{4.39}$$

By expressing $R_{\text{BB,Comp},I}(j\omega)$ and $R_{\text{BB,Comp},Q}(j\omega)$ as a function of the receiver baseband signals $R_{\text{BB},I}(j\omega)$, $R_{\text{BB},Q}(j\omega)$ the desired imbalance compensator is found:

$$R_{\text{BB,Comp}}(j\omega) = r_{\text{BB},I}(j\omega)\big[1 + j\tan(\theta_e)\big] + j\frac{r_{\text{BB},Q}(j\omega)}{\gamma(j\omega)\cos(\theta_e)} \tag{4.40}$$

4.7.3 Imbalance compensation based on complex-valued $\gamma(t)$

Using the imbalance compensator presented in the last section and the extracted imbalance coefficients derived by (4.36) the imbalance distortion generated by the single-tone input signal was reduced. In a next step an optimization of the imbalance compensation was investigated using a similar approach as in the transmitter case (compare Section 3.6.2). Both magnitude and phase of $\hat{\gamma}(j\omega)$ were altered until the residual imbalance distortion was close to the noise level. This process was performed over the complete input frequency range. At each frequency the optimization started from the real-valued $\hat{\gamma}(j\omega)$ coefficients derived in (4.36). The complex conjugate of the altered $\hat{\gamma}(j\omega_m)$ was applied to $\hat{\gamma}(-j\omega_m)$ to assure the applicability of (4.40). The resulting frequency characteristic of $\hat{\gamma}_{\mathrm{opt}}(j\omega)$ lost its even magnitude and odd phase symmetry. Therefore, an updated version of the imbalance compensator derived in the last section is required guaranteeing imbalance distortion reduction down to the noise floor.

In Section 4.2 a linear receiver model was derived able to cope with a complex-valued $\hat{\gamma}(t)$ response without sacrificing the real-valued characteristic for the BB branches. This goal was achieved by using input signal dependent mapping of the complex-valued $\hat{\gamma}(t)$ to its real-valued correspondent. The same approach can be directly applied to (4.40). In contrast to the model case the input signal to the receiver is not available to the compensator. Therefore, the receiver output signal $R_{\mathrm{BB}}(j\omega)$ is used as an estimation of the receiver input signal for the spectral averaging process (4.13). As long as the uncompensated imbalance product at the receiver output is more than $15\,\mathrm{dB}$ below the carrier a negligible impact of this distortion on the mapped imbalance response $\hat{\gamma}_{\mathrm{map,opt}}(j\omega)$ can be recognized. As discussion of the imbalance reduction performance of the real- and complex-valued compensator is given in Section 5.2 based on the measured receiver response.

Despite the fact that compensation of the observed receiver behavior proves the applicability of the presented imbalance compensation process, the question still remains, if there are no structurally simpler compensators achieving the same performance. Especially, if compared to the transmitter case, as presented in Section 3.6.3.1, a compensation of an arbitrary $\hat{\gamma}(j\omega)$ response was implemented in an one step approach. In that case techniques as spectral averaging were not required. The answer to this question is provided by the fundamental difference of pre- and postcompensation. In the predistortion case the desired transmitter output signal is provided at the input of the imbalance precompensator. This situation is visualized in Figure 4.3(a). Suppose a single-tone input signal located at the frequency $\mathrm{f_m}$ is applied to the input of the imbalance compensator. Based on the imbalance coefficients the distortion cancelation signal is evaluated and fed into the transmitter. In this way the imbalance distortion at the transmitter output is reduced. If the single-tone is shifted to $-\mathrm{f_m}$ the situation does not change as the imbalance compensator can select the desired coefficients in both cases.

The behavior of the receiver postcompensator is presented in Figure 4.3(b). The single-tone input signal to the receiver results in an distorted response fed into the imbalance postcompensator. The linear behavior of the imbalance compensator derived in (4.40) alters the tone at $\mathrm{f_m}$ using the coefficient $\hat{\gamma}(j\omega_m)$ and the distortion at $-\mathrm{f_m}$ using $\hat{\gamma}(-j\omega_m)$. In case the receiver input signal is shifted to $-\mathrm{f_m}$ again the same imbalance coefficients are applied. Hence, without any additional signal processing the linear imbalance postcompensator is not able to distinguish between the two input signals. Clearly, a real-valued $\hat{\gamma}(t)$ treats both input signals in the same way and provides the optimum performance under these constraints. By applying the input signal dependent mapping technique, information on the original location of the single-tone at the receiver input is provided which allows distinguishing between the two input signals. As a result of this approach the overall imbalance postcompensator lost its linear behavior.
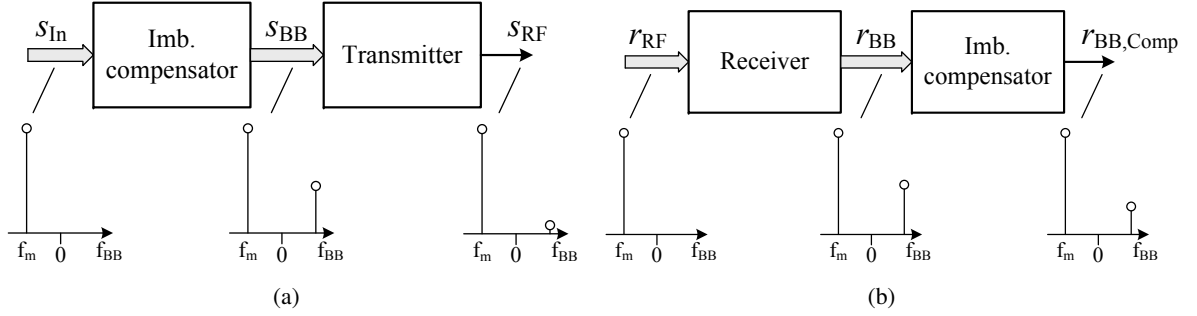
Figure 4.3: Imbalance compensation process in the (a) transmitter and (b) receiver case exemplified for a single-tone input signal at f_m.

The increased complexity of the distortion compensators in the receiver case is a direct consequence of the missing information on the undistorted input signal which is available to the transmitter predistorter.

4.8 Spurious emissions

The discussion of the spurious emissions characterization at the receiver follows the same approach as in the transmitter case. As mentioned before, nonlinear effects were not considered. Also the phase noise and DC-offset were not incorporated into the spurs model. Based on these assumptions the receiver output signal results to:

$$
\begin{aligned}
r_\mathrm{BB}(t) = \ & \tfrac{1}{2} g_\mathrm{M} \sum_{k=0}^{N_\mathrm{spur}} r_\mathrm{RF}(t) e^{-j(\Delta\omega_k + \Delta\varphi_{\mathrm{LO},k})} * \big(g_{\mathrm{CI},k} h_{\mathrm{LP},I}(t) + g_{\mathrm{CQ},k} h_{\mathrm{LP},Q}(t) e^{-j\theta_e} \big) \\
& + \tfrac{1}{2} g_\mathrm{M}^* \sum_{k=0}^{N_\mathrm{spur}} r_\mathrm{RF}^*(t) e^{j(\Delta\omega_k + \Delta\varphi_{\mathrm{LO},k})} * \big(g_{\mathrm{CI},k} h_{\mathrm{LP},I}(t) - g_{\mathrm{CQ},k} h_{\mathrm{LP},Q}(t) e^{j\theta_e} \big)
\end{aligned}
\tag{4.41}
$$

The frequency domain representation of this expression is given by:

$$
\begin{aligned}
R_\mathrm{BB}(j\omega) = \ & \tfrac{1}{2} \bigg[g_\mathrm{M} R_\mathrm{RF}(j\omega) e^{-j\Delta\varphi_{\mathrm{LO},0}} \big(\alpha_I(j\omega) + \alpha_Q(j\omega) e^{-j\theta} \big) \\
& + g_\mathrm{M}^* R_\mathrm{RF}^*(-j\omega) e^{j\Delta\varphi_{\mathrm{LO},0}} \big(\alpha_I(j\omega) - \alpha_Q(j\omega) e^{j\theta_e} \big) \\
& + g_\mathrm{M} \sum_{k=1}^{N_\mathrm{spur}} R_\mathrm{RF}(j\omega + j\Delta\omega_k) e^{-j\Delta\varphi_{\mathrm{LO},k}} \big(g_{\mathrm{CI},k} H_{\mathrm{LP},I}(j\omega) + g_{\mathrm{CQ},k} H_{\mathrm{LP},Q}(j\omega) e^{-j\theta_e} \big) \\
& + g_\mathrm{M}^* \sum_{k=1}^{N_\mathrm{spur}} R_\mathrm{RF}^*(-j\omega - j\Delta\omega_k) e^{j\Delta\varphi_{\mathrm{LO},k}} \big(g_{\mathrm{CI},k} H_{\mathrm{LP},I}(j\omega) - g_{\mathrm{CQ},k} H_{\mathrm{LP},Q}(j\omega) e^{j\theta_e} \big) \bigg]
\end{aligned}
\tag{4.42}
$$

where $\alpha_I(j\omega)$, $\alpha_Q(j\omega)$ was defined in (4.9). The first two lines of (4.42) present the spurious free receiver response similar to (4.8). In this expression the magnitude of the spurs is set by $g_{\mathrm{CI},k}$ and $g_{\mathrm{CQ},k}$. For presenting these magnitudes relative to the one of the carrier, the functions $g_{\mathrm{CI},k} H_{\mathrm{LP},I}(j\omega) \pm g_{\mathrm{CQ},k} H_{\mathrm{LP},Q}(j\omega) \exp(\mp j\theta_e)$ must be expressed in terms of $\alpha_d(j\omega)$ and $\alpha_v(j\omega)$. Based on this substitu-

tion and after rearranging the result (4.42) can be written as:

$$R_{\mathrm{BB}}(j\omega) =$$

$$g_{\mathrm{M}}e^{-j\Delta\varphi_{\mathrm{LO},0}}\left[R_{\mathrm{RF}}(j\omega)\alpha_d(j\omega) + \sum_{k=1}^{N_{\mathrm{spur}}} R_{\mathrm{RF}}(j\omega+j\Delta\omega_k)e^{-j\Delta\varphi_{0,k}}\frac{g_{\mathrm{CI},k}+g_{\mathrm{CQ},k}}{g_{\mathrm{CI},0}+g_{\mathrm{CQ},0}}\alpha_d(j\omega)\right]$$

$$+g_{\mathrm{M}}^*e^{j\Delta\varphi_{\mathrm{LO},0}}\left[R_{\mathrm{RF}}^*(-j\omega)\alpha_v(j\omega) + \sum_{k=1}^{N_{\mathrm{spur}}} R_{\mathrm{RF}}^*(-j\omega-j\Delta\omega_k)e^{j\Delta\varphi_{0,k}}\frac{g_{\mathrm{CI},k}-g_{\mathrm{CQ},k}}{g_{\mathrm{CI},0}-g_{\mathrm{CQ},0}}\alpha_v(j\omega)\right] \tag{4.43}$$

where the phase of the spurs was expressed relative to the carrier by introducing $\Delta\varphi_{0,k}$:

$$\Delta\varphi_{0,k} = \Delta\varphi_{\mathrm{LO},k} - \Delta\varphi_{\mathrm{LO},0} \tag{4.44}$$

It is interesting to note the similarities between (4.43) and the linear part of the nonlinear receiver model presented in (4.21). In the latter one the spurious emissions magnitude is normalized separately for the inphase and the quadrature branch. The result derived before normalizes the distortion products on the desired signal and its spectral mirrored counterpart basis. Equivalent to (4.43) the imbalance can also be expressed by $\alpha_I(j\omega)$, $\gamma(j\omega)$, and θ_e:

$$R_{\mathrm{BB}}(j\omega) = \frac{g_{\mathrm{M}}}{2}e^{-j\Delta\varphi_{\mathrm{LO},0}}\left[\alpha_I(j\omega)R_{\mathrm{RF}}(j\omega)\left(1+\gamma(j\omega)e^{-j\theta_e}\right)\right.$$

$$+ \sum_{k=1}^{N_{\mathrm{spur}}}\alpha_I(j\omega)R_{\mathrm{RF}}(j\omega+j\Delta\omega_k)\alpha_{\mathrm{spur},d,k}\left(1+\gamma(j\omega)e^{-j\theta_e}\right)\Bigg]$$

$$+\frac{g_{\mathrm{M}}^*}{2}e^{j\Delta\varphi_{\mathrm{LO},0}}\left[\alpha_I(j\omega)R_{\mathrm{RF}}^*(-j\omega)\left(1-\gamma(j\omega)e^{j\theta_e}\right)\right.$$

$$+ \sum_{k=1}^{N_{\mathrm{spur}}}\alpha_I(j\omega)R_{\mathrm{RF}}^*(-j\omega-j\Delta\omega_k)\alpha_{\mathrm{spur},v,k}\left(1-\gamma(j\omega)e^{j\theta_e}\right)\Bigg] \tag{4.45}$$

In this expression the complex-valued scaling factor $\alpha_{\mathrm{spur},d,k}$, $\alpha_{\mathrm{spur},v,k}$ were introduced for representing the relationship to the carrier signal:

$$\alpha_{\mathrm{spur},d,k} = \frac{g_{\mathrm{CI},k}+g_{\mathrm{CQ},k}}{g_{\mathrm{CI},0}+g_{\mathrm{CQ},0}}e^{-j\Delta\varphi_{0,k}}$$

$$\alpha_{\mathrm{spur},v,k} = \frac{g_{\mathrm{CI},k}-g_{\mathrm{CQ},k}}{g_{\mathrm{CI},0}-g_{\mathrm{CQ},0}}e^{j\Delta\varphi_{0,k}} \tag{4.46}$$

Equation (4.45) provides a linear model of the spurious emissions using the parameters as extracted during the imbalance characterization. In this result an important difference to the transmitter case, (3.80), can be recognized. At the transmitter the BB input signal is first passed through cascade composed by the BB amplifier and the LP-filter and is then shifted to the RF frequency range. From there, the desired signal at f_0 and the spurious emissions at $f_0 \pm \Delta f_k$ will show the same ISR. At the receiver the RF input signal is first downconverted to DC or to $\pm\Delta f_k$ and then fed into the analog BB processing. This results in different ISR levels at the desired signal and the spurious emissions, as the filters are evaluated at different frequencies.

It is important to note, that $\alpha_{\mathrm{spur},d,k}$, $\alpha_{\mathrm{spur},v,k}$ only represent complex-valued scaling factors if a deterministic relationship between the phases of the spurs and the carrier can be assumed. Otherwise, these two parameters were random variables and their characterization as discussed below would fail.

Similar to the transmitter case the inband spurious emissions are characterized using a single-tone input signal:

$$R_{\mathrm{RF,ST}}(j\omega) = 2\pi A_{ST}\delta(j\omega - j\omega_m) \tag{4.47}$$

By sweeping the single-tone over the receiver bandwidth and tracing the magnitude of the generated distortion products the spurs can be identified, as they are always at a constant frequency offset from the single-tone signal.

After the spurs are identified the coefficients $\alpha_{\mathrm{spur},d,k}$ and $\alpha_{\mathrm{spur},v,k}$ can be extracted. The receiver response onto the single-tone input results to:

$$
\begin{aligned}
R_{\mathrm{BB}}(j\omega) = \quad & \pi g_{\mathrm{M}} A_{\mathrm{ST}} e^{-j\Delta\varphi_{\mathrm{LO},0}} \left[\alpha_I(j\omega_m)\left(1 + \gamma(j\omega_m)e^{-j\theta_e}\right) \right. \\
& \left. + \sum_{k=1}^{N_{\mathrm{spur}}} \alpha_{\mathrm{spur},d,k}\alpha_I(j\omega_m - j\Delta\omega_k)\left(1 + \gamma(j\omega_m - j\Delta\omega_k)e^{-j\theta_e}\right) \right] \\
& + \pi g_{\mathrm{M}}^* A_{\mathrm{ST}}^* e^{j\Delta\varphi_{\mathrm{LO},0}} \left[\alpha_I(-j\omega_m)\left(1 - \gamma(-j\omega_m)e^{j\theta_e}\right) \right. \\
& \left. + \sum_{k=1}^{N_{\mathrm{spur}}} \alpha_{\mathrm{spur},v,k}\alpha_I(-j\omega_m + j\Delta\omega_k)\left(1 - \gamma(-j\omega_m + j\Delta\omega_k)e^{j\theta_e}\right) \right]
\end{aligned} \tag{4.48}
$$

Each line of this expression identifies the magnitude and phase of the corresponding output signal component. For evaluating the scaling factors of the spurious emissions the amplitude of the corresponding distortion product is normalized by the amplitude of the desired and the spectrally mirrored receiver response. In the following $A_{\mathrm{BB},\mathrm{f}_m}$ identifies the signal components' amplitudes at the frequency f_m. Using this notation the normalized spurious emission amplitudes are given by:

$$
\begin{aligned}
\frac{A_{\mathrm{BB},(\mathrm{f}_m - \Delta\mathrm{f}_k)}}{A_{\mathrm{BB},\mathrm{f}_m}} &= \frac{\alpha_{\mathrm{spur},d,k}\alpha_I(j\omega_m - j\Delta\omega_k)\left(1 + \gamma(j\omega_m - j\Delta\omega_k)e^{-j\theta_e}\right)}{\alpha_I(j\omega_m)\left(1 + \gamma(j\omega_m)e^{-j\theta_e}\right)} \\
\frac{A_{\mathrm{BB},(-\mathrm{f}_m + \Delta\mathrm{f}_k)}}{A_{\mathrm{BB},-\mathrm{f}_m}} &= \frac{\alpha_{\mathrm{spur},v,k}\alpha_I(-j\omega_m + j\Delta\omega_k)\left(1 - \gamma(-j\omega_m + j\Delta\omega_k)e^{j\theta_e}\right)}{\alpha_I(-j\omega_m)\left(1 - \gamma(-j\omega_m)e^{j\theta_e}\right)}
\end{aligned} \tag{4.49}
$$

By this normalization the dependency on the input signal magnitude and phase is removed. From these expressions the desired scaling functions $\alpha_{\mathrm{spur},d,k}$ and $\alpha_{\mathrm{spur},v,k}$ are derived by:

$$
\begin{aligned}
\hat{\alpha}_{\mathrm{spur},d,k}(j\omega_m) &= \frac{A_{\mathrm{BB},(\mathrm{f}_m - \Delta\mathrm{f}_k)}}{A_{\mathrm{BB},\mathrm{f}_m}} \frac{\alpha_I(j\omega_m)\left(1 + \gamma(j\omega_m)e^{-j\theta_e}\right)}{\alpha_I(j\omega_m - j\Delta\omega_k)\left(1 + \gamma(j\omega_m - j\Delta\omega_k)e^{-j\theta_e}\right)} \\
\hat{\alpha}_{\mathrm{spur},v,k}(-j\omega_m) &= \frac{A_{\mathrm{BB},(-\mathrm{f}_m + \Delta\mathrm{f}_k)}}{A_{\mathrm{BB},-\mathrm{f}_m}} \frac{\alpha_I(-j\omega_m)\left(1 - \gamma(-j\omega_m)e^{j\theta_e}\right)}{\alpha_I(-j\omega_m + j\Delta\omega_k)\left(1 - \gamma(-j\omega_m + j\Delta\omega_k)e^{j\theta_e}\right)}
\end{aligned} \tag{4.50}
$$

As in the transmitter case the dependency on the frequency offset of the input signal was highlighted by introducing $\hat{\alpha}_{\mathrm{spur},d,k}(j\omega_m)$ and $\hat{\alpha}_{\mathrm{spur},v,k}(j\omega_m)$. For calculating the scaling factors, the beforehand extracted imbalance parameters and the gain of the reference branch are required. The problem with this

result is, that $\alpha_I(j\omega)$ must be known in magnitude and phase to fully characterize the two parameters. If only the magnitude of the input tone is captured it is still sufficient for the compensation signal generation but not to fully model the receiver response. Additionally it should be noted, that for small magnitudes of $|1 - \gamma(j\omega_m)\exp(j\theta_e)|$ the extraction of $\hat{\alpha}_{\text{spur},v,k}(j\omega_m)$ can be deteriorated by noise amplification effects.

Assuming that only $|\alpha_I(j\omega)|$ is available for the extraction of $\hat{\alpha}_{\text{spur},d,k}(j\omega_m)$ and $\hat{\alpha}_{\text{spur},v,k}(j\omega_m)$, an evaluation of these two functions covering the BB frequency range is required. Due to the phase difference incorporated into these functions an approximately constant behavior cannot be expected. This is a significant difference to the transmitter case, where such a behavior could be expected.

4.8.1 Spurious emissions compensation

For canceling the spurious emissions an estimation of the RF input signal is required. In a first approach the linear equalized receiver output can be used for this task:

$$\hat{R}_{\text{RF}}(j\omega) = \frac{R_{\text{BB}}(j\omega)}{\alpha_I(j\omega)\left(1 + \gamma(j\omega)e^{-j\theta_e}\right)} \tag{4.51}$$

Assuming that the imbalance is the dominating linear distortion of the receiver, it is advantageous compensating this effect before calculating the estimated RF input signal:

$$\hat{R}_{\text{RF}}(j\omega) = \frac{\text{Comp}_{\text{Imb.}}\{R_{\text{BB}}(j\omega)\}}{\alpha_I(j\omega)} \tag{4.52}$$

where $\text{Comp}_{\text{Imb.}}\{\cdot\}$ represents the imbalance compensator. Based on this signal the spurious emission compensator results to:

$$
\begin{aligned}
R_{\text{BB,Comp,spur},k}(j\omega) = \quad & -\sum_{k=1}^{N_{\text{spur}}} \hat{\alpha}_{\text{spur},d,k}(j\omega)\alpha_I(j\omega)\left(1 + \gamma(j\omega)e^{-j\theta_e}\right)\left[\hat{R}_{\text{RF}}(j\omega) * \delta(j\omega + j\omega_k)\right] \\
& -\sum_{k=1}^{N_{\text{spur}}} \hat{\alpha}_{\text{spur},v,k}(j\omega)\alpha_I(j\omega)\left(1 - \gamma(j\omega)e^{j\theta_e}\right)\left[\hat{R}_{\text{RF}}^*(-j\omega) * \delta(j\omega - j\omega_k)\right]
\end{aligned}
\tag{4.53}
$$

4.9 Receiver nonlinear behavior

In this section the characterization of the nonlinear receiver behavior is discussed. This nonlinear behavior is a result of the cascade of the RF input and the two baseband nonlinearities. The basic idea for this process is finding a model of the nonlinear effects introduced by the RF input nonlinearity. Using this model the signals present at the input of the two BB amplifiers are calculated. Based on these signals and the measured receiver response the BB amplifiers are identified.

The extraction of the full RF input NL description would require the knowledge of the signal at the input and the output of this device. Especially the output signal can't be evaluated without the knowledge of the BB amplifier behavior. The separation of the NL RF and BB contribution is achieved using a similar approach as in the transmitter case. By investigating the behavior of the inband third

order harmonic distortion the contribution of the BB amplifier is estimated. This information is applied to characterize the RF input NL block. The disadvantage of this approach is that no indication of the distribution of the linear gain between the RF and the BB section is provided. Hence, the resulting RF input NL model is assumed to show a linear gain of 0 dB. The complete linear receiver response is represented by the BB amplifiers.

Obviously, the presence of a harmonic distortion in the BB amplifier behavior is a requirement for the applicability of the sketched parameter extraction process. As a harmonic distortion of reasonable magnitude needn't be present, the necessity for using this extraction approach should be verified in advance. Hence, a classification of the receiver nonlinearities should be performed before the extraction of the parameters is started. This classification is based on the receiver response on a FSTT signal:

$$
\begin{aligned}
\tilde{r}_{\mathrm{RF,FSTT}}(t) &= A_{\mathrm{FSTT}} \cos(2\pi \mathrm{f}_{sp} t + \phi_{sp}) \cos(2\pi \mathrm{f}_m t + \phi_m) \cos(2\pi \mathrm{f}_0 t) \\
&\quad - A_{\mathrm{FSTT}} \cos(2\pi \mathrm{f}_{sp} t + \phi_{sp}) \sin(2\pi \mathrm{f}_m t + \phi_m) \sin(2\pi \mathrm{f}_0 t) \\
&= \mathrm{Re}\left\{ A_{\mathrm{FSTT}} \cos(2\pi \mathrm{f}_{sp} t + \phi_{sp}) e^{j2\pi(\mathrm{f}_m + \mathrm{f}_0)t + j\phi_m} \right\}
\end{aligned}
\tag{4.54}
$$

In this equation f_{sp} and f_m are the tone spacing and the carrier frequency offset of the FSTT signal. The parameters A_{FSTT} and f_0 represent the magnitude of the input signal and the center frequency of the receiver. The phases of the upper and lower input tone are given by $\phi_{sp} + \phi_m$ and $-\phi_{sp} + \phi_m$.

In a first step, the receiver response to a FSTT input signal with narrow tone spacing (i.e., $0 < \mathrm{f}_{sp} \ll \mathrm{f}_m \ll \mathrm{f}_s/2$), is captured. Then, by comparing the magnitude of the IMD$_3$ and the HD$_3$ distortion, the receiver behavior can be classified as:

IMD$_3 \gg$ HD$_3$:   Dominant RF input nonlinearity: the impact of the baseband NL can be neglected.

IMD$_3 \simeq$ HD$_3 + 3$dB :   RF input and BB nonlinearities are of similar magnitude: use the approach sketched above for identifying all nonlinearities.

IMD$_3 \simeq$ HD$_3$:   Dominant BB nonlinearities: the impact of the RF input NL can be neglected.

Based on this classification, information is gained if a part of the receiver nonlinearities can be neglected. In such a case the residual nonlinearity can be directly extracted from the receiver measurement results. The order of this nonlinearity can be estimated from the intermodulation distortion excited by the FSTT.

If the impact of the nonlinearities is of similar size the fitting of the RF input NL from the harmonic distortion of the BB amplifier must be performed. In this case all nonlinearities are of the same order which can be estimated from the dominant IMD components at the receiver output. In Section 4.9.1 the analytical representation of the receiver response onto a FSTT input signal is derived. Based on these results the parameter extraction will be explained in Section 4.9.4 and Section 4.9.5.

For the validity of the suggested receiver identification the following assumptions must be fulfilled:

- The RF input NL is frequency independent.

- The IMD and HD of the baseband nonlinearities are not altered by linear filtering (i.e., the PCWM is applicable).

The fist assumption is required for describing the RF input NL by a memoryless system. In case of a frequency dependent RF input NL the separation of the dynamic receiver behavior in the BB and the RF part is not unique. This task would again require the availability of the RF input NL output signal.

The tone spacing f_{sp} of the FSTT input signal has to be set sufficiently small to guarantee that:

$$H_{I,p}(j\omega_m) \simeq H_{I,p}(j\omega_m \pm j(2p-1)\omega_{sp}) \tag{4.55}$$

This relationship has to be fulfilled for the desired tones (i.e., $p = 1$) and all IMD products generated by the RF input NL. In this case the convolution of the BB amplifier input signal with the lowpass filter impulse response $h_{I,p}(t)$ reduces to a multiplication with a constant factor. The magnitude of this factor is abbreviated by $|\bar{h}_{I,p}| = |H_{I,p}(j\omega_m)|$. The angle of the linear filtering function is expressed by $\bar{\phi}_I = \angle H_{I,1}(j\omega_m)$. A phase difference to $\bar{\phi}_I$ at the NL parameters will be expressed by complex-valued coefficients. Hence, real-valued NL coefficients indicate the absence of AM-PM conversion in the BB amplifier behavior. Note that these parameters are frequency-independent for the considered input signal but still show a dependency on f_m. An analog notation applies for the quadrature channel.

For the extraction of the nonlinear receiver behavior the carrier phase offset $\Delta\varphi_{\text{LO},0}$ is not considered for simplifying the notation. This phase shift performs a rotation of the I/Q mixer input signal as highlighted by the linear model (4.8).

4.9.1 Receiver response onto a FSTT input signal

The FSTT input signal to the receiver was defined in (4.54). This excitation is applied to the RF input NL:

$$r_{\text{BP}}(t) = \sum_{p=1}^{(N_{\text{RF}}+1)/2} g_{\text{M},2p-1} r_{\text{RF,FSTT}}(t) |r_{\text{RF,FSTT}}(t)|^{2(p-1)}$$

$$= \sum_{p=1}^{(N_{\text{RF}}+1)/2} \sum_{q=p}^{(N_{\text{RF}}+1)/2} \frac{1}{4^{q-1}} g_{\text{M},2q-1} A_{\text{FSTT}}^{2q-1} \binom{2q-1}{q-p} \cos([2p-1][2\pi f_{sp}t + \phi_{sp}]) e^{j(2\pi f_m t + \phi_m)}$$

$$\tag{4.56}$$

where N_{RF} represents the order of the RF input nonlinearity. In this expression the signal magnitude A_{FSTT} is a positive, real-valued constant. After the downconversion by the I/Q mixer the inphase and quadrature branch signals are given by:

$$r_{\text{mod}}(t) = \frac{1}{2} \left(g_{\text{CI}} + g_{\text{CQ}} e^{-j\theta_e} \right) r_{\text{BP}}(t) + \frac{1}{2} \left(g_{\text{CI}} - g_{\text{CQ}} e^{j\theta_e} \right) r_{\text{BP}}^*(t)$$

$$\text{Re}\{r_{\text{mod}}(t)\} = \sum_{p=1}^{(N_{\text{RF}}+1)/2} \sum_{q=p}^{(N_{\text{RF}}+1)/2} \frac{1}{4^{q-1}} g_{\text{CI}} |g_{\text{M},2q-1}| A_{\text{FSTT}}^{2q-1} \binom{2q-1}{q-p}$$

$$\cdot \cos([2p-1][2\pi f_{sp}t + \phi_{sp}]) \cos(2\pi f_m t + \phi_m + \phi_{g_{\text{M},2q-1}}) \tag{4.57}$$

$$\text{Im}\{r_{\text{mod}}(t)\} = \sum_{p=1}^{(N_{\text{RF}}+1)/2} \sum_{q=p}^{(N_{\text{RF}}+1)/2} \frac{1}{4^{q-1}} g_{\text{CQ}} |g_{\text{M},2q-1}| A_{\text{FSTT}}^{2q-1} \binom{2q-1}{q-p}$$

$$\cdot \cos([2p-1][2\pi f_{sp}t + \phi_{sp}]) \sin(2\pi f_m t + \phi_m + \phi_{g_{\text{M},2q-1}} - \theta_e)$$

In these expressions $\phi_{g_{M,2p-1}}$ represents the angle of $g_{M,2p-1}$. The magnitude $A_{\text{des.}}$ will be used for summarizing the impact of the RF input nonlinearity on the desired signal amplitude. The parameter

$\phi_{\text{des.}}$ identifies the phase shift introduced by this block. The parameters $A_{\text{des.}}$ and $\phi_{\text{des.}}$ are evaluated from the complex phasor representation of (4.57):

$$A_{\text{des.}} e^{j\phi_{\text{des.}}} = \sum_{p=1}^{(N_{\text{RF}}+1)/2} \frac{1}{4^{p-1}} g_{\text{M},2p-1} A_{\text{FSTT}}^{2p-1} \binom{2p-1}{p-1} \tag{4.58}$$

The squared magnitude of the resulting phasor is given by:

$$
\begin{aligned}
A_{\text{des.}}^2 =\ & \sum_{p=1}^{(N_{\text{RF}}+1)/2} \frac{1}{4^{p-1}} |g_{\text{M},2p-1}|^2 A_{\text{FSTT}}^{2(2p-1)} \binom{2p-1}{p-1} \\
& + 2 \sum_{p=1}^{[(N_{\text{RF}}+1)/2]-1} \sum_{q=p+1}^{(N_{\text{RF}}+1)/2} \frac{1}{4^{p+q-2}} |g_{\text{M},2p-1}||g_{\text{M},2q-1}| A_{\text{FSTT}}^{2(p+q-1)} \binom{2p-1}{p-1}\binom{2q-1}{q-1} \\
& \cdot \cos(\phi_{g_{\text{M},2p-1}} - \phi_{g_{\text{M},2q-1}})
\end{aligned}
\tag{4.59}
$$

The phase shift can be extracted from the ratio of the real and imaginary part of (4.58):

$$\tan(\phi_{\text{des.}}) = \frac{\displaystyle\sum_{p=1}^{(N_{\text{RF}}+1)/2} \frac{1}{4^{p-1}} |g_{\text{M},2p-1}| A_{\text{FSTT}}^{2p-1} \binom{2p-1}{p-1} \sin(\phi_{g_{\text{M},2p-1}})}{\displaystyle\sum_{p=1}^{(N_{\text{RF}}+1)/2} \frac{1}{4^{p-1}} |g_{\text{M},2p-1}| A_{\text{FSTT}}^{2p-1} \binom{2p-1}{p-1} \cos(\phi_{g_{\text{M},2p-1}})} \tag{4.60}$$

If real and imaginary signals defined in (4.57) are applied to the inputs of the corresponding lowpass filter, BB amplifier cascade, a large number of distortion products is created. Taking into account that most direct conversion receivers are optimized for linear operation the magnitude of the two desired tones is much higher than the ones of the IMD. Therefore, instead of calculating the BB amplifier response based on $\text{Re}\{r_{\text{mod}}(t)\}$ and $\text{Im}\{r_{\text{mod}}(t)\}$, it will be derived only from the two desired tones:

$$
\begin{aligned}
r_{\text{D},I}(t) &= g_{\text{CI}} A_{\text{des.}} \cos(2\pi f_{sp} t + \phi_{sp}) \cos(2\pi f_m + \phi_m + \phi_{\text{des.}}) = \text{Re}\{r_{\text{mod}}(t)\}\Big|_{p=1} \\
r_{\text{D},Q}(t) &= g_{\text{CQ}} A_{\text{des.}} \cos(2\pi f_{sp} t + \phi_{sp}) \sin(2\pi f_m + \phi_m + \phi_{\text{des.}} - \theta_e) = \text{Im}\{r_{\text{mod}}(t)\}\Big|_{p=1}
\end{aligned}
\tag{4.61}
$$

After the response of the BB NL on $r_{\text{D},I}(t)$ and $r_{\text{D},Q}(t)$ is evaluated, it will be combined with the scaled IMD of the RF input NL. In this way only the nonlinear interaction of the RF input NL distortion with the other signal components present at the BB amplifier inputs are neglected for the receiver response calculation.

Another simplification in the calculation of the receiver response was introduced by the selection of a sufficiently narrowband tone spacing as mentioned before. Using this assumption the response of the inphase lowpass filter, BB amplifier cascade onto the "desired" I/Q mixer output signal $r_{\text{D},I}(t)$ results

to:

$$r_{\text{BB},I,r_{\text{D},I}}(t) = \sum_{p=1}^{N_{\text{O,BB}}} \bar{h}_{I,2p-1}^{2p-1} A_{\text{des.}}^{2p-1} \cos^{2p-1}(2\pi\text{f}_{sp}t + \phi_{sp}) \cos^{2p-1}(2\pi\text{f}_m t + \phi_m + \phi_{\text{des.}} + \bar{\phi}_I)$$
$$+ \sum_{p=1}^{N_{\text{E,BB}}} \bar{h}_{I,2p}^{2p} A_{\text{des.}}^{2p} \cos^{2p}(2\pi\text{f}_{sp}t + \phi_{sp}) \cos^{2p}(2\pi\text{f}_m t + \phi_m + \phi_{\text{des.}} + \bar{\phi}_I) \tag{4.62}$$

It should be noted that the parameter g_{CI} has been incorporated into $\bar{h}_{I,p}$. In this expression the DC component was neglected as it is characterized independently from the nonlinear BB amplifier effects. The separate treatment of the even- and odd-order distortion components led to the introduction of the summation parameters $N_{\text{O,BB}}$ and $N_{\text{E,BB}}$ assuming a BB NL of order N_{BB}:

$$N_{\text{O,BB}} = \left\lfloor \frac{N_{\text{BB}} + 1}{2} \right\rfloor \qquad N_{\text{E,BB}} = \left\lfloor \frac{N_{\text{BB}}}{2} \right\rfloor \tag{4.63}$$

If this result is expanded using trigonometric identities [114] and rearranged based on the frequency of the signal components the receiver output signal can be written as:

$$\begin{aligned}
r_{\text{BB},I,r_{\text{D},I}}(t) = &\sum_{p=1}^{N_{\text{O,BB}}} \sum_{q=1}^{N_{\text{O,BB}}} \sum_{r=\max(p,q)}^{N_{\text{O,BB}}} \frac{1}{16^{r-1}} \bar{h}_{I,2r-1}^{2r-1} A_{\text{des.}}^{2r-1} \binom{2r-1}{r-p} \binom{2r-1}{r-q} \\
&\cdot \cos([2q-1][2\pi\text{f}_{sp}t + \phi_{sp}]) \cos([2p-1][2\pi\text{f}_m t + \phi_m + \phi_{\text{des.}} + \bar{\phi}_I]) \\
&+ \sum_{p=1}^{N_{\text{E,BB}}} \frac{1}{16^p} \bar{h}_{I,2p}^{2p} A_{\text{des.}}^{2p} \binom{2p}{p}^2 \\
&+ \sum_{p=1}^{N_{\text{E,BB}}} \sum_{q=p}^{N_{\text{E,BB}}} \frac{2}{16^q} \bar{h}_{I,2q}^{2q} A_{\text{des.}}^{2q} \binom{2q}{q} \binom{2q}{q-p} \\
&\cdot \left[\cos(2q[2\pi\text{f}_{sp}t + \phi_{sp}]) + \cos(2p[2\pi\text{f}_m t + \phi_m + \phi_{\text{des.}} + \bar{\phi}_I]) \right] \\
&+ \sum_{p=1}^{N_{\text{E,BB}}} \sum_{q=1}^{N_{\text{E,BB}}} \sum_{r=\max(p,q)}^{N_{\text{E,BB}}} \frac{4}{16^r} \bar{h}_{I,2r}^{2r} A_{\text{des.}}^{2r} \binom{2r}{r-p} \binom{2r}{r-q} \\
&\cdot \cos(2q[2\pi\text{f}_{sp}t + \phi_{sp}]) \cos(2p[2\pi\text{f}_m t + \phi_m + \phi_{\text{des.}} + \bar{\phi}_I])
\end{aligned} \tag{4.64}$$

The steps required for achieving this result are similar to (3.91) - (3.101) and, therefore, not repeated here. The contribution of the RF input NL distortion to the inphase channel output signal, scaled by the linear BB amplifier gain, is given by:

$$\begin{aligned}
r_{\text{BB},I,\text{RFNL}}(t) = &\sum_{p=2}^{(N_{\text{RF}}+1)/2} \sum_{q=p}^{(N_{\text{RF}}+1)/2} \frac{1}{4^{q-1}} \bar{h}_{I,1} |g_{\text{M},2q-1}| A_{\text{FSTT}}^{2q-1} \binom{2q-1}{q-p} \\
&\cdot \cos([2p-1][2\pi\text{f}_{sp}t + \phi_{sp}]) \cos(2\pi\text{f}_m t + \phi_m + \phi_{g_{\text{M},2q-1}} + \bar{\phi}_I)
\end{aligned} \tag{4.65}$$

By combining $r_{\text{BB},I,r_{\text{D},I}}(t)$ and $r_{\text{BB},I,\text{RFNL}}(t)$ the desired approximation for the inphase channel receiver response is achieved.

$$
\begin{aligned}
r_{\text{BB},I}(t) \approx\; & r_{\text{BB},I,r_{\text{D},I}}(t) + r_{\text{BB},I,\text{RFNL}}(t) \\
= & \sum_{p=1}^{N_{\text{O,BB}}} \sum_{q=1}^{N_{\text{O,BB}}} \sum_{r=\max(p,q)}^{N_{\text{O,BB}}} \frac{1}{16^{r-1}} \bar{h}_{I,2r-1}^{2r-1} A_{\text{des.}}^{2r-1} \binom{2r-1}{r-p}\binom{2r-1}{r-q} \\
& \cdot \cos([2q-1][2\pi\text{f}_{sp}t + \phi_{sp}]) \cos([2p-1][2\pi\text{f}_m t + \phi_m + \phi_{\text{des.}} + \bar{\phi}_I]) \\
+ & \sum_{p=2}^{(N_{\text{RF}}+1)/2} \sum_{q=p}^{(N_{\text{RF}}+1)/2} \frac{1}{4^{q-1}} \bar{h}_{I,1} |g_{\text{M},2q-1}| A_{\text{FSTT}}^{2q-1} \binom{2q-1}{q-p} \\
& \cdot \cos([2p-1][2\pi\text{f}_{sp}t + \phi_{sp}]) \cos(2\pi\text{f}_m t + \phi_m + \phi_{g_{\text{M},2q-1}} + \bar{\phi}_I) \\
+ & \sum_{p=1}^{N_{\text{E,BB}}} \frac{1}{16^p} \bar{h}_{I,2p}^{2p} A_{\text{des.}}^{2p} \binom{2p}{p}^2 \\
+ & \sum_{p=1}^{N_{\text{E,BB}}} \sum_{q=p}^{N_{\text{E,BB}}} \frac{2}{16^q} \bar{h}_{I,2q}^{2q} A_{\text{des.}}^{2q} \binom{2q}{q}\binom{2q}{q-p} \\
& \cdot \big[\cos(2q[2\pi\text{f}_{sp}t + \phi_{sp}]) + \cos(2p[2\pi\text{f}_m t + \phi_m + \phi_{\text{des.}} + \bar{\phi}_I])\big] \\
+ & \sum_{p=1}^{N_{\text{E,BB}}} \sum_{q=1}^{N_{\text{E,BB}}} \sum_{r=\max(p,q)}^{N_{\text{E,BB}}} \frac{4}{16^r} \bar{h}_{I,2r}^{2r} A_{\text{des.}}^{2r} \binom{2r}{r-p}\binom{2r}{r-q} \\
& \cdot \cos(2q[2\pi\text{f}_{sp}t + \phi_{sp}]) \cos(2p[2\pi\text{f}_m t + \phi_m + \phi_{\text{des.}} + \bar{\phi}_I])
\end{aligned}
\tag{4.66}
$$

The first summation of this expression identifies the odd-order BB amplifier response onto the two desired tones. This part includes the generated intermodulation and odd-order harmonic distortion. The next term represents the IMD caused by the RF input nonlinearity which adds up with the IMD from the baseband amplifier. The other three summations model the even-order distortion. The first summation of this group identifies the DC-offset added to the output signal. The second one describes the even-order distortion caused by interactions of the two desired tones with the DC-offset. The last summation represents the harmonic distortion located above the modulation frequency f_m. The corresponding quadrature channel output signal is also composed of the BB amplifier response onto the "desired" I/Q-mixer output signal $r_{\text{D},Q}(t)$ and the scaled RF input NL IMD:

$$r_{\text{BB},Q,r_{\text{D},Q}}(t) = \sum_{p=1}^{N_{\text{O,BB}}} \bar{h}_{Q,2p-1}^{2p-1} A_{\text{des.}}^{2p-1} \cos^{2p-1}(2\pi f_{sp}t + \phi_{sp})$$

$$\cdot \sin^{2p-1}(2\pi f_m t + \phi_m + \phi_{\text{des.}} + \bar{\phi}_Q - \theta_e)$$

$$+ \sum_{p=1}^{N_{\text{E,BB}}} \bar{h}_{Q,2p}^{2p} A_{\text{des.}}^{2p} \cos^{2p}(2\pi f_{sp}t + \phi_{sp}) \sin^{2p}(2\pi f_m t + \phi_m + \phi_{\text{des.}} + \bar{\phi}_Q - \theta_e)$$

$$r_{\text{BB},Q,\text{RFNL}}(t) = \sum_{p=2}^{(N_{\text{RF}}+1)/2} \sum_{q=p}^{(N_{\text{RF}}+1)/2} \frac{1}{4^{q-1}} \bar{h}_{Q,1} |g_{\text{M},2q-1}| A_{\text{FSTT}}^{2q-1} \binom{2q-1}{q-p}$$

$$\cdot \cos([2p-1][2\pi f_{sp}t + \phi_{sp}]) \sin(2\pi f_m t + \phi_m + \phi_{g_{\text{M},2q-1}} + \bar{\phi}_Q)$$

$$(4.67)$$

After expanding and rearranging of $r_{\text{BB},Q,r_{\text{D},Q}}(t)$ the approximate quadrature channel response is given by:

$$r_{\text{BB},Q}(t) \approx r_{\text{BB},Q,r_{\text{D},Q}}(t) + r_{\text{BB},Q,\text{RFNL}}(t)$$

$$= \sum_{p=1}^{N_{\text{O,BB}}} \sum_{q=1}^{N_{\text{O,BB}}} \sum_{r=\max(p,q)}^{N_{\text{O,BB}}} \frac{(-1)^{p+1}}{16^{r-1}} \bar{h}_{Q,2r-1}^{2r-1} A_{\text{des.}}^{2r-1} \binom{2r-1}{r-p}\binom{2r-1}{r-q}$$

$$\cdot \cos([2q-1][2\pi f_{sp}t + \phi_{sp}]) \sin([2p-1][2\pi f_m t + \phi_m + \phi_{\text{des.}} + \bar{\phi}_Q - \theta_e])$$

$$+ \sum_{p=2}^{(N_{\text{RF}}+1)/2} \sum_{q=p}^{(N_{\text{RF}}+1)/2} \frac{1}{4^{q-1}} \bar{h}_{Q,1} |g_{\text{M},2q-1}| A_{\text{FSTT}}^{2q-1} \binom{2q-1}{q-p}$$

$$\cdot \cos([2p-1][2\pi f_{sp}t + \phi_{sp}]) \sin(2\pi f_m t + \phi_m + \phi_{g_{\text{M},2q-1}} + \bar{\phi}_Q - \theta_e)$$

$$+ \sum_{p=1}^{N_{\text{E,BB}}} \frac{1}{16^p} \bar{h}_{Q,2p}^{2p} A_{\text{des.}}^{2p} \binom{2p}{p}^2$$

$$(4.68)$$

$$+ \sum_{p=1}^{N_{\text{E,BB}}} \sum_{q=p}^{N_{\text{E,BB}}} \frac{2}{16^q} \bar{h}_{Q,2q}^{2q} A_{\text{des.}}^{2q} \binom{2q}{q}\binom{2q}{q-p}$$

$$\cdot \left[\cos(2q[2\pi f_{sp}t + \phi_{sp}]) + (-1)^p \cos(2p[2\pi f_m t + \phi_m + \phi_{\text{des.}} + \bar{\phi}_Q - \theta_e]) \right]$$

$$+ \sum_{p=1}^{N_{\text{E,BB}}} \sum_{q=1}^{N_{\text{E,BB}}} \sum_{r=\max(p,q)}^{N_{\text{E,BB}}} \frac{4(-1)^p}{16^r} \bar{h}_{Q,2r}^{2r} A_{\text{des.}}^{2r} \binom{2r}{r-p}\binom{2r}{r-q}$$

$$\cdot \cos(2q[2\pi f_{sp}t + \phi_{sp}]) \cos(2p[2\pi f_m t + \phi_m + \phi_{\text{des.}} + \bar{\phi}_Q - \theta_e])$$

For validating the accuracy of this approximation the response of a receiver onto a FSTT input signal was simulated. For this simulation the same parameters were used as for the nonlinear model accuracy evaluation in Section 4.3 (i.e., $\gamma = 0.95$, $\theta_e = 3°$, $\text{IP}_{2,\text{output}} = 44\,\text{dBm}$ and an $\text{IP}_{3,\text{output}} = 24\,\text{dBm}$,

(a)   (b)
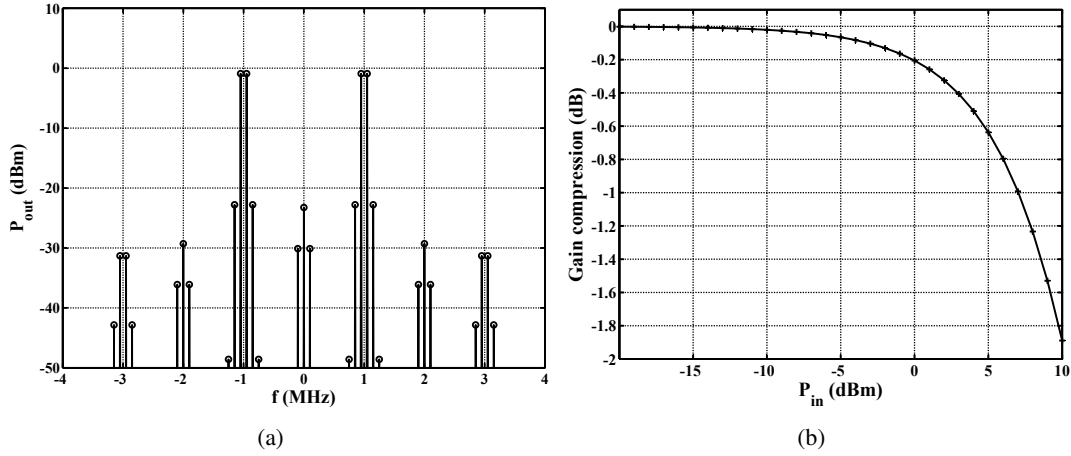
Figure 4.4: Simulation of a receiver response on a FSTT input signal. (a) Spectrum of the inphase channel output for an input signal at $P_{in} = 5$ dBm, (b) gain compression of the receiver.

$IP_{3,RF,output} = 24$ dBm). The inphase channel response for a 5 dBm input signal and the gain compression of the receiver for an input signal power sweep are depicted in Figure 4.4.

The simulated receiver response was then compared to the approximation presented in (4.66) and (4.68). The differences between the predicted and simulated magnitudes and phases of the output signal components are summarized in Figure 4.5. In these plots the receiver output signal components are identified using the same naming convention as introduced in Section 3.8. The magnitude of the FSTT signal component recorded at the inphase channel located at nf_{sp} and mf_m is identified by $A_{FSTT,I,n,m}$. The corresponding phase is represented by $\phi_{FSTT,I,n,m}$. Using this magnitude and phase the corresponding signal component is given by:

$$r_{BB,I,n,m}(t) = (A_{FSTT,I,n,m}/2)\mathrm{Re}\left\{e^{j(2\pi[nf_{sp}+mf_m]t+\phi_{FSTT,I,n,m})}\right\} \qquad (4.69)$$

The definition of the magnitude $A_{FSTT,I,n,m}$ as exemplified in this expression is equivalent to the magnitude A_{FSTT} in (4.54). Note that changing the sign of the parameter n can be used for selecting the upper or lower tone of a two-tone signal. For a static nonlinearity the magnitude of the upper and lower tones are equal, but their phases may change.

For the desired tones (i.e., $A_{FSTT,I,1,1}$, $\phi_{FSTT,I,1,1}$) the maximum magnitude and phase errors are 0.04 dB and 0.05°. The prediction of the 3rd-order IMD (i.e., $A_{FSTT,I,3,1}$, $\phi_{FSTT,I,3,1}$) results in an error of 1.2 dB and $-0.9°$ at maximum input power. These prediction errors correspond to a receiver gain compression of about 1.9 dB. As linear receivers are usually not operated at such high levels of gain compression, these results can be seen as a worst case for the prediction error of the expressions describing the analytical receiver response.

Clearly, neglecting the RF input NL distortion interactions is much more severe at the distortion components than at the desired output tones. Considering higher orders of distortion will result in a further increase of the approximation error. In Figure 4.5 only the results for the inphase channel are shown. The approximation accuracy for the quadrature channel is identical and, therefore, not printed.
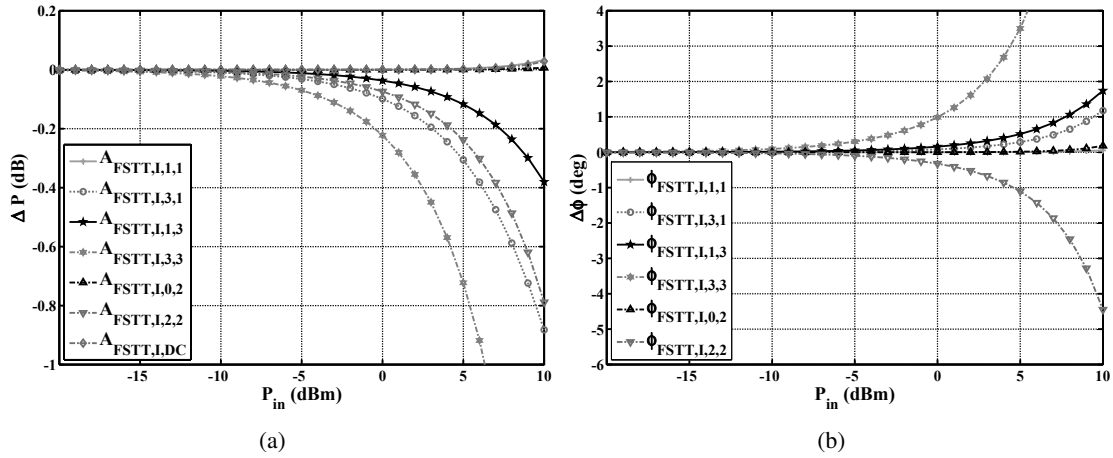
Figure 4.5: Accuracy of the receiver response calculation exemplified for the inphase channel. (a) Magnitude error, (b) phase error.

4.9.2 Power normalization

In the last section the two-tone receiver response was derived. The output signals are captured by the ADCs. Hence, the different signal components are known in magnitude and phase. As indicated in Section 4.5.1 the input signal magnitude may be measured by the use of a power meter and/or a SA. These power values must be converted to the corresponding magnitudes before they can be used for the receiver parameterization. In FSTT signal power results to:

$$
\begin{aligned}
r_{\mathrm{RF}}(t) &= A_{\mathrm{FSTT}} \cos(2\pi \mathrm{f}_{sp} t + \phi_{sp}) \, e^{j2\pi(f_m + f_0)t + j\phi_m} \\
\mathrm{P}_{\mathrm{FSTT}} &= \frac{A_{\mathrm{FSTT}}^2}{2 Z_0}
\end{aligned}
\tag{4.70}
$$

As in the transmitter case two different possibilities for the magnitude calculation are possible depending on the application of the resulting model. On the one hand, the extracted model may be used for predicting the receiver response. On the other hand the model parameters could be used for compensating the generated distortion. In this case the receiver should have a desired gain (usually 0 dB). Otherwise, the receiver postdistorter, additionally to the distortion reduction, introduces a scaling of the output signal. In the predistortion case the magnitudes are evaluated from a predefined maximum input signal magnitude (in the sense of the BB signal processing) scaled by the relative changes of the input power. These relative changes express the power sweep of the input signal. The maximum input signal magnitude relates the input magnitude $A_{\mathrm{FSTT,max}}$ to the maximum magnitude measured by the ADCs. In this way also the linear gain of the receiver is set.

4.9.3 FSTT delay and phase extraction

In 4.9.1 the analytical description of the receiver response onto a FSTT input signal was derived. Using this result the parameters representing the nonlinear receiver behavior will be extracted. For this purpose power and frequency sweep measurements covering the BB frequency range are required. After these

measurements are gathered the overall receiver delay must be derived and compensated. Then, the phase parameters ϕ_m and ϕ_{sp} are extracted for each frequency f_m at which a power sweep was performed. Both, the delay evaluation and the identification of ϕ_m, ϕ_{sp} was described in Section 3.8.4 for the transmitter case driven by a CBTT input signal. Therefore, only a brief summary of the process will be presented in this section.

Due to its notational compactness the measurement results of a power sweep are arranged in a vector. The vector $\mathbf{A}_{\mathrm{FSTT},n,m}$ summarizes the K normalized magnitudes and phases of the FSTT input signal components located at $n\mathrm{f}_{sp}$ and $m\mathrm{f}_m$:

$$\mathbf{A}_{\mathrm{FSTT},n,m} = \begin{pmatrix} A_{\mathrm{FSTT},n,m,\mathrm{P}_1} e^{j\phi_{\mathrm{FSTT},n,m,\mathrm{P}_1}} \\ A_{\mathrm{FSTT},n,m,\mathrm{P}_2} e^{j\phi_{\mathrm{FSTT},n,m,\mathrm{P}_2}} \\ \vdots \\ A_{\mathrm{FSTT},n,m,\mathrm{P}_K} e^{j\phi_{\mathrm{FSTT},n,m,\mathrm{P}_K}} \end{pmatrix} \tag{4.71}$$

The same notation will be used for characterizing the inphase and quadrature output signal components $\mathbf{A}_{\mathrm{FSTT},I,n,m}$, $\mathbf{A}_{\mathrm{FSTT},Q,n,m}$. Clearly, for the receiver input signal only $n = \pm 1$, $m = 1$ is valid.

As mentioned before, for the calculation of the receiver response the carrier phase offset $\Delta\varphi_{\mathrm{LO},0}$ was not considered. It is assumed that during the power and frequency sweep measurements $\Delta\varphi_{\mathrm{LO},0}$ stays constant. If this prerequisite is violated, relating the measurement results at two different BB frequencies $\mathrm{f}_{m,1}$, $\mathrm{f}_{m,2}$ is not possible. In that case the linear phase response of the receiver cannot be extracted.

As the FSTT input signal may be generated using single-tone sources the values of ϕ_m and ϕ_{sp} have to be calculated from the measured input tone phases. In case the excitation signal is generated by an arbitrary waveform generator (AWG) a fixed value of ϕ_{sp} is achieved but ϕ_m can still be changed by a phase shift. In both cases the actual values of these parameters have to be derived from the receiver input signal. In the following a constant ϕ_m, ϕ_{sp} was assumed during a power sweep. If this prerequisite is not fulfilled the corresponding equations must take care of the changing tone phases at each power level. This step was avoided due to the increased complexity of the resulting equations.

The parameter $\hat{\phi}_{sp}$ is estimated from the measured input tone phases $\boldsymbol{\phi}_{\mathrm{FSTT},\pm1,1} = \angle\mathbf{A}_{\mathrm{FSTT},\pm1,1}$ by:

$$\hat{\phi}_{sp} = \frac{1}{2K}\mathbf{1}^T \cdot \left(\boldsymbol{\phi}_{\mathrm{FSTT},+1,1} - \boldsymbol{\phi}_{\mathrm{FSTT},-1,1} \right) \tag{4.72}$$

This calculation requires $\mathrm{sign}(\boldsymbol{\phi}_{\mathrm{FSTT},+1,1}(k)) = \mathrm{sign}(\boldsymbol{\phi}_{\mathrm{FSTT},-1,1}(k))$ for a correct result. The corresponding phase manipulation, if the stated condition is not fulfilled, is shown in (3.122). In a similar way $\hat{\phi}_m$ is evaluated by:

$$\hat{\phi}_m = \frac{1}{2K}\mathbf{1}^T \cdot \left(\boldsymbol{\phi}_{\mathrm{FSTT},+1,1} + \boldsymbol{\phi}_{\mathrm{FSTT},-1,1} \right) \tag{4.73}$$

Due to the π periodicity of the results (4.72) and (4.73) a crosscheck must be performed if $\hat{\phi}_{sp}$ and $\hat{\phi}_m$ represent the tone phases $\boldsymbol{\phi}_{\mathrm{FSTT},\pm1,1}$ correctly. Otherwise, $\hat{\phi}_m$ is shifted by π.

In a next step a frequency sweep is performed at a constant input power level. From the measured receiver output signal $r_{\mathrm{BB}}(t) = r_{\mathrm{BB},I}(t) + jr_{\mathrm{BB},Q}(t)$ the phases of the desired tones are extracted. The slope of these phases is used for extracting the overall receiver delay. A discussion on important issues for identifying the delay in this way is presented in Section 3.8.4. After this delay is evaluated its impact is compensated from all measured tone phases.

From the delay compensated power sweep measurements the phase factors $\phi_{\mathrm{FSTT},I,n,m,\mathrm{P}_k}$, $\phi_{\mathrm{FSTT},Q,n,m,\mathrm{P}_k}$ combine all phase shifts of the corresponding output signal component at the kth power level as presented in (4.68) (exemplified for the quadrature channel, m, n odd):

$$\phi_{\mathrm{FSTT},Q,n,m,\mathrm{P}_k} = -(\pi/2) + \pi^{([m-1]/2)_2} + n\phi_{sp} + m(\phi_m + \phi_{\mathrm{des.}} + \bar{\phi}_Q + \Delta\varphi_{\mathrm{LO},0} - \theta_e) \quad (4.74)$$

In the transmitter case the four desired tone phases derived from the CBTT measurements, selected by choosing $m = \pm 1$ and $n = \pm 1$, were considered for the identification of the phase parameters. At the receiver case using a FSTT input signal only the tone phases at $m = 1$, $n = \pm 1$ are of interest, as the ones located at the negative BB frequency $m = -1$ are linear dependent due to the real-valued signal $r_{\mathrm{BB},Q}(t)$. Hence, in the receiver case it is not possible distinguishing between the RF and the BB contribution appearing in connection with ϕ_m.

The phase factors $\phi_{sp,Q}$ and $\phi_{m,Q}$ are extracted from the measured quadrature branch output signal:

$$\phi_{\mathrm{FSTT},Q,n,m,\mathrm{P}_k} = -(\pi/2) + \pi^{([m-1]/2)_2} + n\hat{\phi}_{sp} + m\phi_{m,Q} + m\hat{\phi}_m$$
$$\phi_{m,Q} = \phi_{\mathrm{des.}} + \bar{\phi}_Q - \theta_e \quad (4.75)$$

The parameter $\hat{\phi}_{sp,Q}$ is derived from the receiver output signal as $\hat{\phi}_{sp}$ from the input one:

$$\hat{\phi}_{sp,Q} = \frac{1}{2K}\mathbf{1}^T \cdot \left(\boldsymbol{\phi}_{\mathrm{FSTT},Q,+1,1} - \boldsymbol{\phi}_{\mathrm{FSTT},Q,-1,1}\right) \quad (4.76)$$

A difference between these two phase factors indicates incomplete delay compensation. In a similar way $\hat{\phi}_{m,Q}$ is evaluated by:

$$\hat{\phi}_{m,Q} = \frac{\pi}{2} + \left(\frac{1}{2}\boldsymbol{\phi}_{\mathrm{FSBTT},Q,+1,1}(1) + \frac{1}{2}\boldsymbol{\phi}_{\mathrm{FSTT},Q,-1,1}(1)\right)_{2\pi} + \hat{\theta}_e \quad (4.77)$$

In this equation the factor $\pi/2$ compensates for the rotation of the quadrature compared to the inphase branch (4.68). By using only the measured tone phases at low input power levels a deterioration by AM-PM conversion effects, represented by $\phi_{\mathrm{des.}}$, is circumvented. Due to the π periodicity of the results (4.76) and (4.77) a crosscheck must be performed if $\pm\hat{\phi}_{sp,Q}$ and $\hat{\phi}_{m,Q} - \hat{\theta}_e$ represent the tone phases $\phi_{\mathrm{FSTT},Q,\pm 1,1}$ correctly.

Thereafter, the same identification process is performed for the inphase branch. It should be noted that the difference $\hat{\phi}_{m,Q} - \hat{\phi}_{m,I}$ should agree with $\hat{\gamma}_{\mathrm{opt}}(j\omega_m)$ presented in Section 4.7.1. If a significant difference between these results exists, either the imbalance characterization or nonlinear parameter extraction is faulty. By neglecting any RF phase rotation (for example $\Delta\varphi_{\mathrm{LO},0}$) $\hat{\phi}_{m,I} - \hat{\phi}_m$ equals to $\bar{\phi}_I$ and $\hat{\phi}_{m,Q} - \hat{\phi}_m$ to $\bar{\phi}_Q$ at low input power levels (compare (4.68)). Hence, without a loss of generality all phase rotations introduced by the different receiver components are represented by the lowpass filter phase shifts.

4.9.4 RF input nonlinearity parameterization

The RF input nonlinearity extraction in the receiver case follows a similar approach as at the transmitter. Using the odd-order harmonic distortion generated by the BB amplifiers their NL behavior is estimated. The evaluated coefficients of the BB nonlinearity are then applied to postdistort the measured receiver

output signal. In this way the BB amplifier impact is minimized and an estimation for the signal present at the output of the RF NL block is derived. This information allows the identification of the corresponding polynomial coefficients.

Initially the NL BB amplifier parameters are evaluated. For the RF input NL parameterization the linear BB response is irrelevant as the gain of this block is set to $0\,\text{dB}$. Additionally, problems due to a highly linear system behavior as described in Section 3.8.5.1 are avoided if the linear response is excluded from the corresponding model. In the following the BB NL response estimation is exemplified for the quadrature channel. The HD_3 components up to $N_{\text{ID,HD}}$ order are considered for this task. The $(2K(N_{\text{ID,HD}} + 1)/2) \times 1$ vector, representing the measured receiver odd-order harmonics, is defined as:

$$\mathbf{Y} = \begin{pmatrix} \mathbf{A}_{\text{FSTT},Q,(-N_{\text{ID,HD}}),-3} \\ \mathbf{A}_{\text{FSTT},Q,(-N_{\text{ID,HD}}+2),-3} \\ \vdots \\ \mathbf{A}_{\text{FSTT},Q,-1,-3} \\ \mathbf{A}_{\text{FSTT},Q,1,-3} \\ \vdots \\ \mathbf{A}_{\text{FSTT},Q,(N_{\text{ID,HD}}),-3} \end{pmatrix} \tag{4.78}$$

The BB amplifier HD response is modeled by (compare (4.68)):

$$\mathbf{H}_{\text{BB,HD},k,q,p}^{(+)} = \frac{-j\,\text{sign}(k)(-1)^{(|k|+3)/2}}{16^{r-1}} \begin{pmatrix} 2r-1 \\ r-(|k|+1)/2 \end{pmatrix} \begin{pmatrix} 2r-1 \\ r-q \end{pmatrix} \mathbf{A}_{\text{FSTT}}^{2r-1} e^{j(k(\hat{\phi}_m-\hat{\theta}_e)+(2q-1)\hat{\phi}_{sp})}$$

$$\mathbf{H}_{\text{BB,HD},k,q,p}^{(-)} = \frac{-j\,\text{sign}(k)(-1)^{(|k|+3)/2}}{16^{r-1}} \begin{pmatrix} 2r-1 \\ r-(|k|+1)/2 \end{pmatrix} \begin{pmatrix} 2r-1 \\ r-q \end{pmatrix} \mathbf{A}_{\text{FSTT}}^{2r-1} e^{j(k(\hat{\phi}_m-\hat{\theta}_e)-(2q-1)\hat{\phi}_{sp})}$$

$$r = \max(q, p, (|k|+1)/2)$$

$$\tag{4.79}$$

These equations describe the odd-order harmonic distortion located at $k\text{f}_m$. The factor $-j$ accounts for the quadrature branch phase rotation. The following expression $\text{sign}(k)(-1)^{(|k|+3)/2}$ represents the changing sign at the different odd-order harmonics. The index r used to guarantee that the distortion products at the kth harmonic are generated by the NL response equal or higher to k. Assuming that the same number of NL coefficients is extracted as HD_3 components are considered for the identification, the BB amplifier response is composed in a $(2KN_{\text{O,ID,HD}}) \times N_{\text{O,ID,HD}}$ matrix:

$$\mathbf{H}_{\text{BB,HD}} = \begin{pmatrix} & & & & \mathbf{H}_{\text{BB,HD},-3,N_{\text{O,ID,HD}},N_{\text{O,ID,HD}}}^{(-)} \\ & & & \iddots & \vdots \\ & & \mathbf{H}_{\text{BB,HD},-3,2,3}^{(-)} & \cdots & \mathbf{H}_{\text{BB,HD},-3,2,N_{\text{O,ID,HD}}}^{(-)} \\ & \mathbf{H}_{\text{BB,HD},-3,1,2}^{(-)} & \mathbf{H}_{\text{BB,HD},-3,1,3}^{(-)} & \cdots & \mathbf{H}_{\text{BB,HD},-3,1,N_{\text{O,ID,HD}}}^{(-)} \\ & \mathbf{H}_{\text{BB,HD},-3,1,2}^{(+)} & \mathbf{H}_{\text{BB,HD},-3,1,3}^{(+)} & \cdots & \mathbf{H}_{\text{BB,HD},-3,1,N_{\text{O,ID,HD}}}^{(+)} \\ & & \mathbf{H}_{\text{BB,HD},-3,2,3}^{(+)} & \cdots & \mathbf{H}_{\text{BB,HD},-3,2,N_{\text{O,ID,HD}}}^{(+)} \\ & & & \ddots & \vdots \\ & & & & \mathbf{H}_{\text{BB,HD},-3,N_{\text{O,ID,HD}},N_{\text{O,ID,HD}}}^{(+)} \end{pmatrix} \tag{4.80}$$

where $N_{\mathrm{O,ID,HD}} = \lfloor (N_{\mathrm{ID,HD}} + 1)/2 \rfloor$ identifies the number of considered coefficients. These BB amplifier coefficients are arranged in the vector $\hat{\boldsymbol{\lambda}}_{\mathrm{BB,HD,}Q} = (\hat{g}_{\mathrm{BB,HD,}Q,3} \cdots \hat{g}_{\mathrm{BB,HD,}Q,N_{\mathrm{ID,HD}}})^T$ and evaluated by solving the equation:

$$\mathbf{H}_{\mathrm{BB,HD}}^{H}\mathbf{H}_{\mathrm{BB,HD}}\hat{\boldsymbol{\lambda}}_{\mathrm{BB,HD,}Q} = \mathbf{H}_{\mathrm{BB,HD}}^{H}\mathbf{Y} \tag{4.81}$$

Finally the predefined unity linear gain is added to the identification result $\hat{\boldsymbol{\lambda}}_{\mathrm{BB,HD,}Q} = (1\ \hat{\boldsymbol{\lambda}}_{\mathrm{BB,HD,}Q}^{T})^T$. It is important to note that the suggested BB amplifier modeling approach neglects also the even-order distortion. The impact of this distortion mechanism on the odd-order IMD at the receiver output is qualified as second order effect. Due to the odd-order distortion characterization using the measured HD$_3$ response any linear filtering of these signal components may introduce a higher modeling error compared to neglecting the even-order response. Furthermore it should be mentioned, that the memoryless NL model derived by using (4.81) is only valid for the FSTT excitation at the corresponding frequency f$_m$. Any dynamics are excluded from the actual BB amplifier model as they are not required for a proper parameterization of the RF input NL.

Accomplishing the parameter extraction for the inphase branch the same process is applied. After changing at (4.78) to (4.81) the indices for Q to I and updating the BB amplifier response modeling as shown in (4.82) the coefficients are derived equivalently.

$$\begin{aligned}
\mathbf{H}_{\mathrm{BB,HD,}k,q,p}^{(+)} &= \frac{1}{16^{r-1}}\binom{2r-1}{r-(|k|+1)/2}\binom{2r-1}{r-q}\mathbf{A}_{\mathrm{FSTT}}^{2r-1}e^{j(k\hat{\phi}_m + (2q-1)\hat{\phi}_{sp})} \\
\mathbf{H}_{\mathrm{BB,HD,}k,q,p}^{(-)} &= \frac{1}{16^{r-1}}\binom{2r-1}{r-(|k|+1)/2}\binom{2r-1}{r-q}\mathbf{A}_{\mathrm{FSTT}}^{2r-1}e^{j(k\hat{\phi}_m - (2q-1)\hat{\phi}_{sp})} \\
r &= \max(q, p, (|k|+1)/2)
\end{aligned} \tag{4.82}$$

The inphase and quadrature channel parameters are required for configuring the polynomial postdistorter. Using a similar approach as in Section 3.8.11.2 and Section 4.9.8.2 the odd-order polynomial BB amplifier response is compensated using an odd-order polynomial postdistorter. The validity of this approach was proven in [121]. For the evaluation of the postdistorter parameters the BB amplifier response is modeled by (exemplified for the quadrature channel):

$$r_{\mathrm{BB,}Q}(t) = \sum_{r=1}^{N_{\mathrm{O,ID,HD}}} \hat{g}_{\mathrm{BB,HD,}Q,2r-1} r_{\mathrm{mod,Im}}(t)|r_{\mathrm{mod,Im}}(t)|^{2(r-1)} \tag{4.83}$$

The output of the BB amplifier is directly applied to the postdistorter input $r_{\mathrm{post,Q}}(t)$:

$$r_{\mathrm{post,Q}}(t) = \sum_{r=1}^{(N_{\mathrm{Comp}}+1)/2} g_{\mathrm{C,}2r-1} r_{\mathrm{BB,}Q}(t)|r_{\mathrm{BB,}Q}(t)|^{2(r-1)} \tag{4.84}$$

The order of the postdistorter is specified by N_{Comp}. A 5$^{\mathrm{th}}$-order BB polynomial was selected for the calculation of the correction coefficients. As in the RF predistorter case a unity gain of the BB amplifier postdistorter cascade was selected. The linear response of this composition is given by:

$$r_{\mathrm{post,Q,1}}(t) = g_{\mathrm{C,1}}\hat{g}_{\mathrm{BB,HD,}Q,1} r_{\mathrm{mod,Im}}(t) \tag{4.85}$$

From this equation a unity gain of the composition (4.83) and (4.84) is achieved by selecting:

$$g_{C,1} = \frac{1}{\hat{g}_{BB,HD,Q,1}} \tag{4.86}$$

This parameter is then applied to (4.84) and the resulting response of the composition of the two polynomials is used for identifying the third-order NL contribution. The coefficient $g_{C,3}$ is then selected canceling this output signal component. Proceeding in this way the postdistorter coefficients result to:

$$g_{C,3} = -\frac{\hat{g}_{BB,HD,Q,3}}{\hat{g}_{BB,HD,Q,1}^3 \hat{g}_{BB,HD,Q,1}^*}$$

$$g_{C,5} = -\frac{-2\hat{g}_{BB,HD,Q,3}^2 \hat{g}_{BB,HD,Q,1}^* + \hat{g}_{BB,HD,Q,5}|\hat{g}_{BB,HD,Q,1}|^2 - |\hat{g}_{BB,HD,Q,3}|^2 \hat{g}_{BB,HD,Q,1}}{\hat{g}_{BB,HD,Q,1}^5 \hat{g}_{BB,HD,Q,1}^{*3}}$$

$$g_{C,7} = \Big(2\hat{g}_{BB,HD,Q,5}\hat{g}_{BB,HD,Q,3}^* \hat{g}_{BB,HD,Q,1}|\hat{g}_{BB,HD,Q,1}|^2 - 5\hat{g}_{BB,HD,Q,3}|\hat{g}_{BB,HD,Q,3}|^2|\hat{g}_{BB,HD,Q,1}|^2$$

$$- 5\hat{g}_{BB,HD,Q,3}^3 \hat{g}_{BB,HD,Q,1}^{*2} + 5\hat{g}_{BB,HD,Q,3}\hat{g}_{BB,HD,Q,5}|\hat{g}_{BB,HD,Q,1}|^2 \hat{g}_{BB,HD,Q,1}^*$$

$$+ \hat{g}_{BB,HD,Q,3}\hat{g}_{BB,HD,Q,5}^* \hat{g}_{BB,HD,Q,1}|\hat{g}_{BB,HD,Q,1}|^2 - 2|\hat{g}_{BB,HD,Q,3}|^2\hat{g}_{BB,HD,Q,3}\hat{g}_{BB,HD,Q,1}^2 \Big)$$

$$\cdot \frac{1}{\hat{g}_{BB,HD,Q,1}^7 \hat{g}_{BB,HD,Q,1}^{*5}} \tag{4.87}$$

The evaluation of ninth and higher order postdistorter coefficients is straight forward and not shown here due to the lengthy expressions.

After the coefficients are calculated using (4.86) and (4.87) the baseband amplifier output signal can be fed into the postdistorter. During the actual receiver parameterization it turned out that an "artificial" BB amplifier output signal consisted only of the desired tones and the IMD resulted in a higher modeling accuracy than the measured one. This effect may be ascribed to neglecting the even-order distortion in the BB amplifier model. Additionally, any spurious emissions are also suppressed for this identification step. After this "artificial" BB amplifier signal was processed by the postdistorter the magnitudes and phases of the output tones are calculated. For a complete power sweep these tone amplitudes are represented by the vector $\mathbf{A}_{FSTT,post,Q,q,1}$.

After evaluating the postdistorted tone amplitudes for the inphase and the quadrature branch the magnitudes and phases corresponding to the mixer output signal are derived by:

$$\mathbf{A}_{FSTT,mod,q,1} = \frac{1}{2}(\mathbf{A}_{FSTT,I,q,1} + j\mathbf{A}_{FSTT,Q,q,1}) \tag{4.88}$$

From the postdistortion process the IMD components up to $N_{ID,HD}$ are provided. Using these signal components $N_{ID,RF}$ polynomial coefficients are identified. For this task the postdistorted signal amplitudes are arranged in the vector:

$$\mathbf{Y} = \begin{pmatrix} \mathbf{A}_{\text{FSTT,mod},(-N_{\text{ID,HD}}),1} \\ \mathbf{A}_{\text{FSTT,mod},(-N_{\text{ID,HD}}+2),1} \\ \vdots \\ \mathbf{A}_{\text{FSTT,mod},-1,1} \\ \mathbf{A}_{\text{FSTT,mod},1,1} \\ \vdots \\ \mathbf{A}_{\text{FSTT,mod},(N_{\text{ID,HD}}),1} \end{pmatrix} \tag{4.89}$$

The corresponding system response matrix describing the RF input NL behavior is composed as presented in (4.90) and (4.91).

$$\mathbf{H}_{\text{RF},q,p}^{(+)} = \frac{1}{4^{p-1}} \binom{2p-1}{p-q} |\mathbf{A}_{\text{FSTT,mod},q,1}|^{2p-1} \circ e^{j(\hat{\phi}_m + \angle \mathbf{A}_{\text{FSTT,mod},q,1} + (2q-1)\hat{\phi}_{sp})}$$
$$\mathbf{H}_{\text{RF},q,p}^{(-)} = \frac{1}{4^{p-1}} \binom{2p-1}{p-q} |\mathbf{A}_{\text{FSTT,mod},q,1}|^{2p-1} \circ e^{j(\hat{\phi}_m + \angle \mathbf{A}_{\text{FSTT,mod},q,1} - (2q-1)\hat{\phi}_{sp})} \tag{4.90}$$

$$\mathbf{H}_{\text{RF}} = \begin{pmatrix} & & & & \mathbf{H}_{\text{RF},N_{\text{O,ID,HD}},N_{\text{O,ID,RF}}}^{(-)} \\ & & \iddots & & \vdots \\ & & \mathbf{H}_{\text{RF},2,2}^{(-)} & \cdots & \mathbf{H}_{\text{RF},2,N_{\text{O,ID,RF}}}^{(-)} \\ \mathbf{H}_{\text{RF},1,1}^{(-)} & \mathbf{H}_{\text{RF},1,2}^{(-)} & \cdots & \mathbf{H}_{\text{RF},1,N_{\text{O,ID,RF}}}^{(-)} \\ \mathbf{H}_{\text{RF},1,1}^{(+)} & \mathbf{H}_{\text{RF},1,2}^{(+)} & \cdots & \mathbf{H}_{\text{RF},1,N_{\text{O,ID,RF}}}^{(+)} \\ & \mathbf{H}_{\text{RF},2,2}^{(+)} & \cdots & \mathbf{H}_{\text{RF},2,N_{\text{O,ID,RF}}}^{(+)} \\ & & \ddots & & \vdots \\ & & & & \mathbf{H}_{\text{RF},N_{\text{O,ID,HD}},N_{\text{O,ID,RF}}}^{(+)} \end{pmatrix} \tag{4.91}$$

where $N_{\text{O,ID,RF}} = \lfloor (N_{\text{ID,RF}} + 1)/2 \rfloor$. The RF input NL polynomial coefficients $\hat{\boldsymbol{\lambda}}_{\text{RF}} = (\hat{g}_{\text{M},1} \, \hat{g}_{\text{M},3} \, \ldots \, \hat{g}_{\text{M},N_{\text{ID,RF}}})^T$ are extracted by:

$$\hat{\boldsymbol{\lambda}}_{\text{RF}} = \text{LS}_{\text{opt}}(\mathbf{H}_{\text{RF}}, \mathbf{Y}) \tag{4.92}$$

For this identification process the optimized LS approach may be required to cope with the measurement errors of the desired tones. To force a unity linear gain of the RF input block the extracted coefficients must be normalized:

$$\hat{\boldsymbol{\lambda}}_{\text{RF}} = \hat{\boldsymbol{\lambda}}_{\text{RF}}/\hat{g}_{\text{M},1} \tag{4.93}$$

4.9.5 Baseband amplifier parameter extraction

After the coefficients of the RF input NL are extracted, the PCWMs describing the behavior of the baseband amplifiers can be extracted. For this task the delay compensated FSTT power sweep measurements are required. Additionally, the impact of the RF input NL gain compression onto the two desired tones, expressed by $A_{\text{des.}}$ and $\phi_{\text{des.}}$ has to be calculated (compare Section 4.9.1). As in the transmitter case,

polynomial coefficients will be extracted from each power sweep. To investigate the frequency response of the different distortion components an own set of polynomial coefficients is derived for each distortion product. At the second-order distortion case, this approach includes the extraction of separate polynomial coefficients for the distortion located around DC and at $\pm 2\mathrm{f}_m$. In case of the third-order response parameters will be evaluated for the IMD$_3$ and the HD$_3$ response.

The extracted polynomial coefficients are represented by $\hat{g}_{\mathrm{BB},I,p,\mathrm{f}_m} = \hat{h}^p_{I,p,\mathrm{f}_m}$, $\hat{g}_{\mathrm{BB},Q,p,\mathrm{f}_m} = \hat{h}^p_{Q,p,\mathrm{f}_m}$. These coefficients are indexed by f_m indicating the dependency on the different center frequencies of the two-tone signal. After performing these tasks for all power sweeps the input related "Wiener" coefficients $\hat{h}_{I,p,\mathrm{f}_m}$, $\hat{h}_{Q,p,\mathrm{f}_m}$ are derived from the polynomial ones. Based on these parameters the PCWM filtering functions $\hat{h}_{I,p}(t)$, $\hat{h}_{Q,p}(t)$ are generated. Each coefficient $\hat{h}_{I,p,\mathrm{f}_m}$, $\hat{h}_{Q,p,\mathrm{f}_m}$ is interpreted as a sampling point for the corresponding p^{th}-order filtering function. From these frequency domain sampling points the associated time-domain function is derived.

The tone spacing selected for the FSTT power sweeps must be sufficiently small to guarantee the validity of the approximation introduced in Section 4.9.1. Again, the power sweep should start from a sufficiently small input power level at which a negligible AM-AM and AM-PM conversion occur. The FSTT input signal to the receiver was introduced in (4.54). The phases $\hat{\phi}_m$ and $\hat{\phi}_{sp}$ were extracted using (4.72) and (4.73). Additionally, the AM-AM and AM-PM conversion introduced by the RF input NL is required for the BB amplifier model identification. This gain compression was expressed in Section 4.9.1 by the $A_{\mathrm{des.}}$ and $\phi_{\mathrm{des.}}$. Based on the beforehand evaluated RF input NL coefficients, these quantities can be calculated for each input power level of the power sweep. These results are combined in the vector $\mathbf{A}_{\mathrm{des.}}$ (4.58):

$$\mathbf{A}_{\mathrm{des.}}(k) = \sum_{r=1}^{N_{\mathrm{O,ID,RF}}} \frac{1}{4^{r-1}} \hat{g}_{\mathrm{M},2r-1} \mathbf{A}^{2r-1}_{\mathrm{FSTT}}(k) \binom{2r-1}{r-q} \tag{4.94}$$

Here, the vector $\mathbf{A}_{\mathrm{FSTT}}$ provides the magnitudes of the input signal applied during the power sweep.

In the following the extraction of the models of the BB amplifiers will be explained exemplified for the quadrature channel. In a first step the odd-order coefficients for the desired tones and the IMD generated by the BB amplifiers are extracted. The $(2KN_{\mathrm{O,BB}}) \times 1$ vector, representing the measured receiver response, is defined as follows:

$$\mathbf{Y}_{Q,O} = \begin{pmatrix} \mathbf{A}_{\mathrm{FSTT},Q,(-2N_{\mathrm{O,BB}}+1),1} \\ \mathbf{A}_{\mathrm{FSTT},Q,(-2N_{\mathrm{O,BB}}+3),1} \\ \vdots \\ \mathbf{A}_{\mathrm{FSTT},Q,-1,1} \\ \mathbf{A}_{\mathrm{FSTT},Q,1,1} \\ \vdots \\ \mathbf{A}_{\mathrm{FSTT},Q,(2N_{\mathrm{O,BB}}-1),1} \end{pmatrix} \tag{4.95}$$

The powers of the gain compressed input signal are summarized by the vectors:

$$\mathbf{H}^{(+)}_{Q,q,r}(k) = -j\frac{1}{16^{r-1}}\mathbf{A}_{\mathrm{des.}}(k)|\mathbf{A}_{\mathrm{des.}}(k)|^{2(r-1)}\binom{2r-1}{r-1}\binom{2r-1}{r-q}e^{j(\hat{\phi}_m-\hat{\theta}_e+(2q-1)\hat{\phi}_{sp})}$$

$$\mathbf{H}^{(-)}_{Q,q,r}(k) = -j\frac{1}{16^{r-1}}\mathbf{A}_{\mathrm{des.}}(k)|\mathbf{A}_{\mathrm{des.}}(k)|^{2(r-1)}\binom{2r-1}{r-1}\binom{2r-1}{r-q}e^{j(\hat{\phi}_m-\hat{\theta}_e-(2q-1)\hat{\phi}_{sp})} \tag{4.96}$$

The vectors provide the contributions of the $(2r-1)^{\text{th}}$-order nonlinear polynomial to the $\text{IMD}_{(2q-1)}$. These indices are the same as used for the receiver response calculation in (4.68). The distortion generated by the RF input NL contributing to the $\text{IMD}_{(2q-1)}$ is represented by:

$$\mathbf{H}_{\text{BP},Q,q}^{(+)}(k) = -j \sum_{r=q}^{N_{\text{O,ID,RF}}} \frac{1}{4^{r-1}} \hat{g}_{\text{M},2r-1} \mathbf{A}_{\text{FSTT}}^{2r-1}(k) \binom{2r-1}{r-q} e^{j(\hat{\phi}_m - \hat{\theta}_e + (2q-1)\hat{\phi}_{sp})}$$

$$(4.97)$$

$$\mathbf{H}_{\text{BP},Q,q}^{(-)}(k) = -j \sum_{r=q}^{(N_{\text{O,ID,RF}})} \frac{1}{4^{r-1}} \hat{g}_{\text{M},2r-1} \mathbf{A}_{\text{FSTT}}^{2r-1}(k) \binom{2r-1}{r-q} e^{j(\hat{\phi}_m - \hat{\theta}_e - (2q-1)\hat{\phi}_{sp})}$$

The vectors defined in (4.96) and (4.97) are now used for composing the $(2KN_{\text{O,BB}}) \times N_{\text{O,BB}}$ matrix $\mathbf{H}_{\text{BB,IMD},Q}$:

$$\mathbf{H}_{\text{BB,IMD},Q} = \begin{pmatrix} \mathbf{H}_{\text{BP},Q,N_{\text{O,BB}}}^{(-)} & & & \mathbf{H}_{Q,N_{\text{O,BB}},N_{\text{O,BB}}}^{(-)} \\ \vdots & & \iddots & \vdots \\ \mathbf{H}_{\text{BP},Q,3}^{(-)} & & \mathbf{H}_{Q,3,3}^{(-)} & \cdots & \mathbf{H}_{Q,3,N_{\text{O,BB}}}^{(-)} \\ \mathbf{H}_{\text{BP},Q,2}^{(-)} & \mathbf{H}_{I,2,2}^{(-)} & \mathbf{H}_{Q,2,3}^{(-)} & \cdots & \mathbf{H}_{Q,2,N_{\text{O,BB}}}^{(-)} \\ \mathbf{H}_{Q,1,1}^{(-)} & \mathbf{H}_{Q,1,2}^{(-)} & \mathbf{H}_{I,1,3}^{(-)} & \cdots & \mathbf{H}_{Q,1,N_{\text{O,BB}}}^{(-)} \\ \mathbf{H}_{Q,1,1}^{(+)} & \mathbf{H}_{Q,1,2}^{(+)} & \mathbf{H}_{I,1,3}^{(+)} & \cdots & \mathbf{H}_{Q,1,N_{\text{O,BB}}}^{(+)} \\ \mathbf{H}_{\text{BP},Q,2}^{(+)} & \mathbf{H}_{I,2,2}^{(+)} & \mathbf{H}_{Q,2,3}^{(+)} & \cdots & \mathbf{H}_{Q,2,N_{\text{O,BB}}}^{(+)} \\ \mathbf{H}_{\text{BP},Q,3}^{(+)} & & \mathbf{H}_{Q,3,3}^{(+)} & \cdots & \mathbf{H}_{Q,3,N_{\text{O,BB}}}^{(+)} \\ \vdots & & & \ddots & \vdots \\ \mathbf{H}_{\text{BP},Q,N_{\text{O,BB}}}^{(+)} & & & \cdots & \mathbf{H}_{Q,N_{\text{O,BB}},N_{\text{O,BB}}}^{(+)} \end{pmatrix}$$

$$(4.98)$$

For identifying the odd-order polynomial coefficients they are combined in the $N_{\text{O,BB}} \times 1$ parameter vector $\boldsymbol{\lambda}_{\text{IMD,O},Q}$:

$$\boldsymbol{\lambda}_{\text{IMD,O},Q} = \left(\hat{g}_{\text{BB},Q,1} \, \hat{g}_{\text{BB},Q,3} \, \cdots \, \hat{g}_{\text{BB},Q,(2N_{\text{O,BB}}-1)} \right)^T \tag{4.99}$$

In case of known coefficients the magnitude and phase of the BB amplifier output signal components can be calculated by:

$$\mathbf{Y}_{Q,O} = \mathbf{H}_{\text{BB,IMD},Q} \boldsymbol{\lambda}_{\text{IMD,O},Q} \tag{4.100}$$

As for the RF input NL extraction the NL coefficients are evaluated using the optimized LS approach if the characterized receiver shows a high linearity system behavior:

$$\boldsymbol{\lambda}_{\text{IMD,O},Q} = \text{LS}_{\text{opt}}(\mathbf{H}_{\text{BB,IMD},Q}, \mathbf{Y}_{Q,O}) \tag{4.101}$$

Identifying the corresponding inphase branch parameters the same extraction procedure is applied. Only at (4.95) to (4.101) the indices Q are replaced by I. Additionally, the modeled amplifier output components have to be updated:

$$\mathbf{H}_{I,q,r}^{(\pm)} = j\mathbf{H}_{Q,q,r}^{(\pm)} e^{j\hat{\theta}_e}$$

$$\mathbf{H}_{\text{BP},I,q}^{(\pm)} = j\mathbf{H}_{\text{BP},Q,q}^{(\pm)} e^{j\hat{\theta}_e}$$

$$(4.102)$$

Evaluating an own polynomial model for the harmonic distortion components is very similar to the BB amplifier modeling approach used to extract the RF input NL. Again the HD_3 signal components are applied. Similar to the IMD identification $N_{O,BB}$ odd order polynomial coefficients will be extracted. The $(2KN_{O,BB}) \times 1$ vector summarizing the measured tone amplitudes was presented in (4.78). The equations describing the BB amplifier HD response (4.79) must be updated by using the gain compressed input signal:

$$
\begin{aligned}
\mathbf{H}^{(+)}_{BB,HD,k,q,p} =& \frac{-j\,\text{sign}(k)(-1)^{(|k|+3)/2}}{16^{r-1}} \binom{2r-1}{r-(|k|+1)/2} \binom{2r-1}{r-q} \\
& \cdot |\mathbf{A}_{\text{des.}}|^{2r-1} \circ e^{j(k(\hat{\phi}_m - \hat{\theta}_e + \phi_{\text{des.}}) + (2q-1)\hat{\phi}_{sp})} \\
\mathbf{H}^{(-)}_{BB,HD,k,q,p} =& \frac{-j\,\text{sign}(k)(-1)^{(|k|+3)/2}}{16^{r-1}} \binom{2r-1}{r-(|k|+1)/2} \binom{2r-1}{r-q} \\
& \cdot |\mathbf{A}_{\text{des.}}|^{2r-1} \circ e^{j(k(\hat{\phi}_m - \hat{\theta}_e + \phi_{\text{des.}}) - (2q-1)\hat{\phi}_{sp})} \\
r =& \max(q, p, (|k|+1)/2)
\end{aligned}
\tag{4.103}
$$

After composing the system response matrix (4.80) using the updated amplifier response the corresponding coefficients $\hat{\boldsymbol{\lambda}}_{HD,O,Q}$ are evaluated by solving (4.81). The modifications required for the corresponding inphase branch identification process are presented in Section 4.9.4.

The extraction of the even-order polynomial coefficients is very similar to the HD_3 one. In the following the identification process is discussed using the HD products located at nf_m and the ones at $nf_m \pm 2f_{sp}$. Thereafter, the same steps are repeated for the even-order distortion located around DC. These signal components may show a different response due to interactions by an adaptive DC removal unit present in many direct conversion receivers (c.f., [8, 53]).

Based on the selected measurements the vector containing the receiver response is composed as:

$$
\mathbf{Y}_{Q,E} = \begin{pmatrix}
\mathbf{A}_{FSTT,Q,0,2} \\
\mathbf{A}_{FSTT,Q,0,4} \\
\vdots \\
\mathbf{A}_{FSTT,Q,0,2N_{E,BB}} \\
\mathbf{A}_{FSTT,Q,+2,2} \\
\vdots \\
\mathbf{A}_{FSTT,Q,+2,2N_{E,BB}} \\
\mathbf{A}_{FSTT,Q,-2,2} \\
\vdots \\
\mathbf{A}_{FSTT,Q,-2,2N_{E,BB}}
\end{pmatrix}
\tag{4.104}
$$

The calculation of the even-order polynomial response on the gain compressed two-tone signal is similar

to the odd-order case. These results are combined by the vectors:

$$\mathbf{H}_{C,Q,q,r}(k) = (-1)^q \frac{2}{16^r} |\mathbf{A}_{\text{des.}}(k)|^{2r} \binom{2r}{r} \binom{2r}{r-q} e^{2qj(\hat{\phi}_m - \hat{\theta}_e + \phi_{\text{des.}}(k))}$$

$$\mathbf{H}_{S,Q,q,p,r}^{(+)}(k) = (-1)^q \frac{4}{16^r} |\mathbf{A}_{\text{des.}}(k)|^{2r} \binom{2r}{r-p} \binom{2r}{r-q} e^{2pj(\hat{\phi}_m - \hat{\theta}_e + \phi_{\text{des.}}(k))} e^{2qj\hat{\phi}_{sp}} \quad (4.105)$$

$$\mathbf{H}_{S,Q,q,p,r}^{(-)}(k) = (-1)^q \frac{4}{16^r} |\mathbf{A}_{\text{des.}}(k)|^{2r} \binom{2r}{r-p} \binom{2r}{r-q} e^{2pj(\hat{\phi}_m - \hat{\theta}_e + \phi_{\text{des.}}(k))} e^{-2qj\hat{\phi}_{sp}}$$

The vectors representing the $2r^{\text{th}}$ contribution to the harmonic distortion at $2qf_m$ is identified by $\mathbf{H}_{C,Q,q,r}$. The ones for the distortion at $2pf_m \pm 2qf_{sp}$ are $\mathbf{H}_{S,Q,q,p,r}^{(+)}$ and $\mathbf{H}_{S,Q,q,p,r}^{(-)}$. Based on the placement of the distortion products in the $\mathbf{Y}_{Q,E}$ vector the associated matrix $\mathbf{H}_{\text{HD},Q}$ is composed as follows:

$$\mathbf{H}_{\text{BB,HD},Q} = \begin{pmatrix} \mathbf{H}_{C,Q,1,1} & \mathbf{H}_{C,Q,1,2} & \cdots & \mathbf{H}_{C,Q,1,N_{\text{E,BB}}} \\ & \mathbf{H}_{C,Q,2,2} & \cdots & \mathbf{H}_{C,Q,2,N_{\text{E,BB}}} \\ & & \ddots & \vdots \\ & & & \mathbf{H}_{C,Q,N_{\text{E,BB}},N_{\text{E,BB}}} \\ \mathbf{H}_{S,Q,1,1,1}^{(+)} & \mathbf{H}_{S,Q,1,1,2}^{(+)} & \cdots & \mathbf{H}_{S,Q,1,1,N_{\text{E,BB}}}^{(+)} \\ & \mathbf{H}_{S,Q,2,1,2}^{(+)} & \cdots & \mathbf{H}_{S,Q,2,1,N_{\text{E,BB}}}^{(+)} \\ & & \ddots & \vdots \\ & & & \mathbf{H}_{S,Q,N_{\text{E,BB}},1,N_{\text{E,BB}}}^{(+)} \\ \mathbf{H}_{S,Q,1,1,1}^{(-)} & \mathbf{H}_{S,Q,1,1,2}^{(-)} & \cdots & \mathbf{H}_{S,Q,1,1,N_{\text{E,BB}}}^{(-)} \\ & \mathbf{H}_{S,Q,2,1,2}^{(-)} & \cdots & \mathbf{H}_{S,Q,2,1,N_{\text{E,BB}}}^{(-)} \\ & & \ddots & \vdots \\ & & & \mathbf{H}_{S,Q,N_{\text{E,BB}},1,N_{\text{E,BB}}}^{(-)} \end{pmatrix} \quad (4.106)$$

The dimension of the vector $\mathbf{Y}_{Q,E}$ and the matrix $\mathbf{H}_{\text{BB,HD},Q}$ depend on the considered HD products. For the presented case $\mathbf{Y}_{Q,E}$ and $\mathbf{H}_{\text{BB,HD},Q}$ have the dimensions $(3KN_{\text{E,BB}}) \times 1$ and $(3KN_{\text{E,BB}}) \times N_{\text{E,BB}}$. The corresponding $N_{\text{E,BB}} \times 1$ parameter vector $\boldsymbol{\lambda}_{\text{HD,E},Q}$ is given by:

$$\boldsymbol{\lambda}_{\text{HD,E},Q} = \left(\hat{g}_{\text{BB},Q,2} \, \hat{g}_{\text{BB},Q,4} \, \cdots \, \hat{g}_{\text{BB},Q,(2N_{\text{E,BB}})} \right)^T \quad (4.107)$$

These parameters are identified by solving the equation:

$$\mathbf{H}_{\text{BB,HD},Q}^H \mathbf{H}_{\text{BB,HD},Q} \boldsymbol{\lambda}_{\text{HD,E},Q} = \mathbf{H}_{\text{BB,HD},Q}^H \mathbf{Y}_{Q,E} \quad (4.108)$$

Using the presented even-order extraction process for the inphase branch modifications to the BB amplifier response modeling as shown in (4.109) must be applied.

$$\mathbf{H}_{C,I,q,r} = (-1)^q \mathbf{H}_{C,Q,q,r} e^{2qj\hat{\theta}_e}$$

$$\mathbf{H}_{S,I,q,p,r}^{(\pm)} = (-1)^p \mathbf{H}_{S,Q,q,p,r}^{(\pm)} e^{2pj\hat{\theta}_e} \quad (4.109)$$

Evaluating an own coefficient set for the even-order distortion located around DC is very similar to the former case. The vector providing the corresponding output signal components is given by:

$$\mathbf{Y}_{Q,E} = \begin{pmatrix} \mathbf{A}_{\text{FSTT},Q,2,0} \\ \mathbf{A}_{\text{FSTT},Q,4,0} \\ \vdots \\ \mathbf{A}_{\text{FSTT},Q,2N_{\text{E,BB}},0} \end{pmatrix} \tag{4.110}$$

Here, the DC contribution $\mathbf{A}_{\text{FSTT},Q,0,0}$ is neglected as it is usually deteriorated by additional distortion mechanisms or even completely suppressed. The modeled amplifier output signal components are shown in (4.111). It should be noted, that the index Q was dropped as the relationship is the same for the inphase and the quadrature branch.

$$\mathbf{H}_{\text{DC},q,r}(k) = \frac{2}{16^r} |\mathbf{A}_{\text{des.}}(k)|^{2r} \binom{2r}{r} \binom{2r}{r-q} e^{2qj\hat{\phi}_{sp}} \tag{4.111}$$

The matrix $\mathbf{H}_{\text{BB,DC}}$ arranging the amplifier response equivalently to (4.110) is the same as the first part of $\mathbf{H}_{\text{HD},Q}$ (4.106) after exchanging $\mathbf{H}_{\text{C},Q,q,r}$ by $\mathbf{H}_{\text{DC},q,r}$. The parameters $\boldsymbol{\lambda}_{\text{DC,E},Q}$ are extracted by solving (4.108) using $\mathbf{H}_{\text{BB,DC}}$ and the corresponding $\mathbf{Y}_{Q,E}$. The inphase branch coefficients are derived equivalently as no update on the BB amplifier response modeling is required.

In summary the following coefficient vectors were extracted from the quadrature and the inphase channel for the selected power sweeps covering the BB bandwidth (exemplified for the quadrature branch):

$$\begin{matrix} \hat{\boldsymbol{\lambda}}_{\text{IMD,O},Q,\text{f}_m}, & \hat{\boldsymbol{\lambda}}_{\text{HD,O},Q,\text{f}_m} \\ \hat{\boldsymbol{\lambda}}_{\text{HD,E},Q,\text{f}_m}, & \hat{\boldsymbol{\lambda}}_{\text{DC,E},Q,\text{f}_m} \end{matrix} \tag{4.112}$$

These vectors were extracted while considering $\hat{\phi}_{m,\text{f}_m}$ at the amplifier response model. In case only the magnitude of the receiver input signal measured $\hat{\phi}_{m,\text{f}_m}$ cannot be extracted. In this case $\hat{\phi}_{m,I,\text{f}_m}$ and $\hat{\phi}_{m,Q,\text{f}_m}$ can be used instead. By this approach the possibility to model and compensate the linear phase response is lost. But still the NL receiver behavior is captured and can be compensated!

Up to now the argumentation for considering an own coefficient vector for the odd-order harmonic distortion and the even-order distortion around DC was comparing their frequency response to $\hat{\boldsymbol{\lambda}}_{\text{IMD,O},Q,\text{f}_m}$ and $\hat{\boldsymbol{\lambda}}_{\text{HD,E},Q,\text{f}_m}$, respectively. In contrast to the transmitter case such a comparison makes sense for the receiver as the BB amplifier output signals are accessible. These issues are discussed in Section 4.9.7.

After identifying the polynomial coefficients for the inphase and quadrature channel the corresponding input related "Wiener" parameters can be calculated by taking the pth-root of the parameter vectors (4.112). Despite of a real-valued time domain progress of these Wiener filtering functions their frequency domain sampling points are, in general, complex-valued. A proper evaluation of these roots takes care, for example, that the pth-root of -1 for an odd p is still -1 and not $\exp(j\pi/p)$. Hence, for the odd-order parameter vectors it must be decided if the angle of the coefficient is closer to 0 or π. Depending on this decision the odd-order "Wiener" parameters are derived by (exemplified for $\hat{\boldsymbol{\lambda}}_{\text{IMD,O},Q,\text{f}_m}$):

$$\hat{h}_{Q,2p-1,\text{f}_m} = \left| \hat{\boldsymbol{\lambda}}_{\text{IMD,O},Q,\text{f}_m}(p) \right|^{\frac{1}{2p-1}} \cdot \begin{cases} e^{\frac{j}{2p-1} \angle \hat{\boldsymbol{\lambda}}_{\text{IMD,O},Q,\text{f}_m}(p)} & |\angle \hat{\boldsymbol{\lambda}}_{\text{IMD,O},Q,\text{f}_m}(p)| \leq \pi/2 \\ e^{j\pi + \frac{j}{2p-1} \angle \{-\hat{\boldsymbol{\lambda}}_{\text{IMD,O},Q,\text{f}_m}(p)\}} & |\angle \hat{\boldsymbol{\lambda}}_{\text{IMD,O},Q,\text{f}_m}(p)| > \pi/2 \end{cases} \tag{4.113}$$

For the even-order parameter vectors no advantage is gained by considering the phase of the coefficient. In case of $\hat{\boldsymbol{\lambda}}_{\mathrm{HD,E},Q,\mathrm{f}_m}$ the "Wiener" parameters are derived by:

$$\hat{h}_{Q,2p,\mathrm{f}_m} = \left(\hat{\boldsymbol{\lambda}}_{\mathrm{HD,E},Q,\mathrm{f}_m}(p) \right)^{\frac{1}{2p}} \tag{4.114}$$

After the roots were evaluated for all inphase and quadrature coefficient vectors the connection to the imbalance extraction must be established. In Section 4.7 the parameters $|\hat{\gamma}_{\mathrm{opt}}(j\omega_m)|$, $\hat{\phi}_{\gamma_{\mathrm{opt}}}(j\omega_m)$ and $\hat{\theta}_e$ were extracted from single-tone measurement results. As mentioned before the angle $\hat{\phi}_{m,Q,\mathrm{f}_m} + \hat{\theta}_e - \hat{\phi}_{m,I,\mathrm{f}_m}$ should agree with $\hat{\phi}_\gamma(j\omega_m)$. In a similar way $|\hat{h}_{Q,1,\mathrm{f}_m}/\hat{h}_{I,1,\mathrm{f}_m}|$ should agree with up to an error due to measurement noise. For a complete model of the receiver, as discussed in Section 4.10, the impact of $\hat{\gamma}_{\mathrm{opt}}(j\omega_m)$ can be represented by the BB amplifier models or by an additional imbalance block. This decision influences the conversion of the parameters $\hat{h}_{I,2p-1,\mathrm{f}_m}$, $\hat{h}_{Q,2p-1,\mathrm{f}_m}$ to the corresponding PCWM filtering functions. In case of an imbalance block usage no additional magnitude or phase imbalance may be introduced by the BB amplifier models. This restriction applies only to the linear model response. The ratio between linear output and predicted nonlinear distortion may not be changed. As the inphase branch is taken as reference, these coefficients stay the same. Therefore, the other parameters convert to:

$$\begin{aligned} \hat{h}_{I,p,\mathrm{f}_m,\mathrm{fin.}} &= \hat{h}_{I,p,\mathrm{f}_m} \\ \hat{h}_{Q,1,\mathrm{f}_m,\mathrm{fin.}} &= \hat{h}_{I,1,\mathrm{f}_m} \\ \hat{h}_{Q,p,\mathrm{f}_m,\mathrm{fin.}} &= \frac{\hat{h}_{Q,p,\mathrm{f}_m}}{\hat{\gamma}_{\mathrm{opt}}(j2\pi\mathrm{f}_m)} \quad p > 1 \end{aligned} \tag{4.115}$$

In case the imbalance block models only the I/Q mixer phase error, the magnitude of the extracted nonlinear coefficient stays unchanged.

These input related parameters can now be arranged in N_{BB} filters each one representing the frequency response of the corresponding nonlinear order. Depending on the implementation of the receiver model / receiver compensator the filters can be realized in the time or in the frequency domain. An approach for implementing the filters in the time domain, using linear phase FIR filter synthesis, can be found in the literature (for example [118]). As in the transmitter case the frequency domain implementation of the filters was used here.

This filter synthesis step provides the transition of the set of memoryless polynomial coefficients $\hat{h}_{I,p,\mathrm{f}_m}$, $\hat{h}_{Q,p,\mathrm{f}_m}$ to their PCWM dynamic correspondent $\hat{H}_{I,p}(j\omega)$, $\hat{H}_{Q,p}(j\omega)$. The PCWM filters together with the RF input nonlinearity coefficients and the receiver imbalance compose a model of the nonlinear dynamic receiver behavior.

4.9.6 Nonlinear parameter extraction algorithm performance

The accuracy of the polynomial coefficients extraction depends on the validity of the receiver response approximation for a FSTT input signal as well as the proper identification of the phase parameters (i.e., $\hat{\phi}_m$, $\hat{\phi}_{sp}$). Simulations using a frequency independent receiver model have been performed for visualizing the accuracy of the extracted model as well as the sensitivity to noise.

The simulation is based on the same parameters as used for the validation of the FSTT receiver response approximation in Section 4.9.1 (i.e., $\gamma = 0.95$, $\theta_e = 3°$, $\mathrm{IP}_{2,\mathrm{output}} = 44\,\mathrm{dBm}$ and an $\mathrm{IP}_{3,\mathrm{output}} = 24\,\mathrm{dBm}$, $\mathrm{IP}_{3,\mathrm{RF,output}} = 24\,\mathrm{dBm}$). Additionally, a linear phase shift of the RF input

NL $\angle g_{\mathrm{M},1} = 10°$ and lowpass filter phase shifts $\bar{\phi}_I = 10°$, $\bar{\phi}_Q = -10°$ were considered. For extracting the receiver parameters, FSTT power sweeps between $\mathrm{P_{in}} = -30\ldots0\,\mathrm{dBm}$ were used. The RF input NL and the BB amplifiers were described by 3rd-order polynomials. The identified coefficients were incorporated into a receiver model. The response of the model onto a FSTT power sweep was evaluated. Then the NMSE between the measured and modeled inphase and quadrature channel response was calculated for each power level of the sweep. The mean over all power levels and both branches was used as modeling error. This error was named $\mathrm{NMSE_{Model}}$. Also the identification error of $\hat{g}_{\mathrm{M},3}$ was evaluated by calculating $\Delta g_{\mathrm{M},3}/g_{\mathrm{M},3,\mathrm{Ref}} = (\hat{g}_{\mathrm{M},3} - g_{\mathrm{M},3,\mathrm{Ref}})/g_{\mathrm{M},3,\mathrm{Ref}}$. The parameter $g_{\mathrm{M},3,\mathrm{Ref}}$ represents the scaled 3rd-order RF input NL coefficient $g_{\mathrm{M},3}/g_{\mathrm{M},1}$. No additional parameter sets were used describing the HD_3 distortion and the HD_2 components located around DC.

The extraction of the RF input NL coefficients depends on the correct evaluation of the BB amplifier behavior from the measured HD_3 response and on the applicability of the postdistortion process to calculate the output signal of the RF NL block. Clearly, noise will deteriorate the modeling performance. The impact of this distortion effect on the accuracy of $\hat{g}_{\mathrm{M},3}$ and the resulting modeling is presented in Figure 4.6. Here, the noise power level was evaluated relative to the highest input power level during the power sweep (i.e., $\mathrm{P_{in,max}} = 0\,\mathrm{dBm}$). This noise level was used for the corresponding power sweep. In this way, the measurements at low input signal power are more affected by the measurement noise. To cope with this problem five times averaging of the measurement results was used.
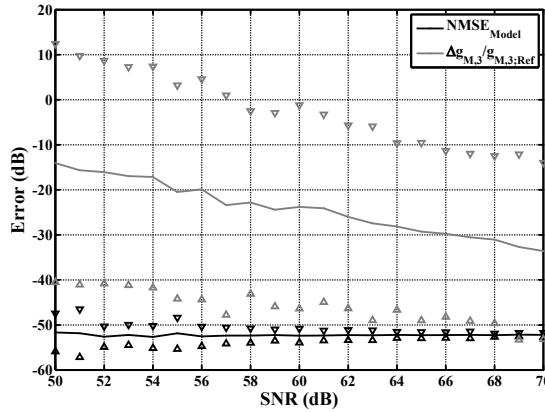
Figure 4.6: Simulation of the $g_{\mathrm{M},3}$ evaluation accuracy and the modeling error at the presence of measurement noise

For each SNR level the model coefficient extraction was repeated 30 times. The continuous lines in Figure 4.6 represent the mean over all realizations. The upper and lower triangles identify the 3σ variation range of the corresponding error function. It is interesting to note, that the $\mathrm{NMSE_{Model}}$ is nearly independent of the SNR level. This may be explained by the fact that the BB amplifier PCWM compensate for most of the mismatch caused by the RF input NL modeling error. The resulting model correctly predicts the IMD of the receiver but will show deviations in the magnitude of the HD components. This compensation mechanism explains the almost independent behavior of the mean modeling error from the SNR level, even if the $\hat{g}_{\mathrm{M},3}$ coefficient identification error is continuously increasing.

The impact of the FSTT response approximation on the modeling accuracy is evaluated in Figure 4.7(a). At this simulation a model composed of third-order RF and BB nonlinearities was used for generating

the noise-free measurement results. From these data a model of the same order was extracted. Increasing the $IP_{3,RF}$ at a constant $IP_{3,BB}$ results in a continuous increase of the $NMSE_{Model}$. This behavior is due to the decrease of the distortion magnitude at the input of the BB amplifiers which were neglected at (4.64) and (4.66). Increasing $IP_{3,BB}$ at a constant $IP_{3,RF}$ also decreases the $NMSE_{Model}$ up to the point where the error due to the neglected IMD at the BB amplifier inputs is dominating. For the actual simulation parameters this point is at $IP_{3,BB} \approx 31\,\mathrm{dBm}$ independent of $IP_{3,RF}$.

(a)   (b)
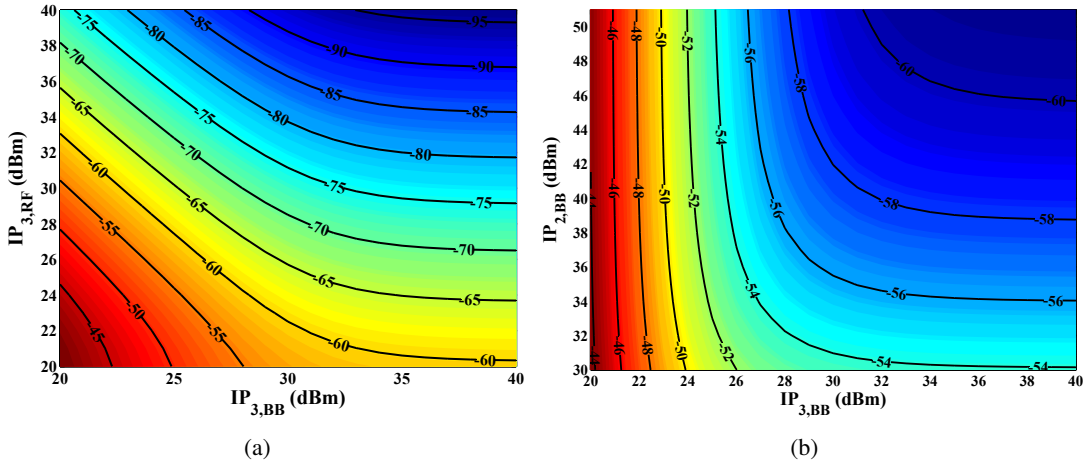
Figure 4.7: Simulation of the modeling error $NMSE_{Model}$ as a function of (a) the $IP_{3,RF}$, $IP_{3,BB}$ and (b) the $IP_{2,BB}$, $IP_{3,BB}$.

A comparison of the second- and third-order BB amplifier distortion impact on the modeling error is shown in Figure 4.7(b). This simulation result highlights that the even-order distortion prediction is almost independent of the parameters $IP_{3,BB}$ and $IP_{3,RF}$. Clearly, by lowering the $IP_{3,BB}$ the achievable $NMSE_{Model}$ improvement is reduced, but no threshold effect can be recognized. As the neglected IMD at the BB amplifier input generates only minor contributions to the even-order distortion, explains this insignificant interrelationship.

4.9.7 Model implementation issues

Starting from the polynomial coefficient vectors the PCWM filtering functions are derived for modeling or compensating the considered receiver. The principle process for this task was presented in the last section. Any additional steps for calculating the filtering functions based on the direct conversion receiver introduced in Chapter 2 are now discussed. All filtering function presented in this section describe the receiver behavior at 6 dB attenuation of the step-attenuator. A comprehensive presentation of the receiver performance is given in Chapter 5.

The magnitude and phase of the linear BB amplifier response is shown in Figure 4.8. At both channels the frequency progress does not correspond to a real-valued time-domain system. But, despite of an offset between the traces of the two channels, a similar behavior in the frequency domain can be recognized. Therefore, the inphase branch progress was implemented as a prefilter located before the input to the BB amplifiers. Using this prefilter for both channels allows shifting this block to the RF input

NL output. Avoiding undesired interaction with the imbalance calculation it must be located before the imbalance filtering. In this way the residual inphase channel response corresponds to a unity gain in the frequency domain. At the quadrature channel the linear progress describes the magnitude and phase imbalance. Implementing this imbalance by an own block circumvents any problems associated by a complex-valued response of the real-valued BB amplifiers.
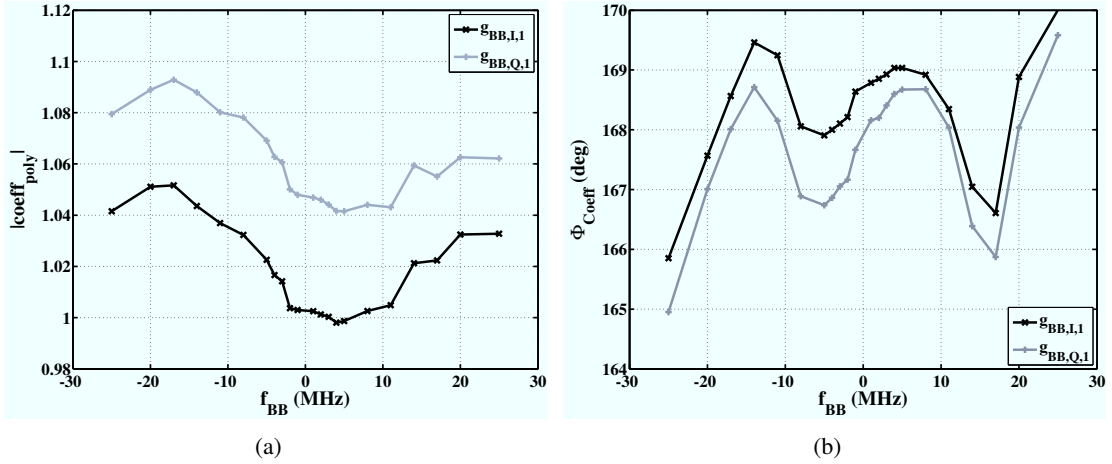
Figure 4.8: Evaluated linear (a) Magnitude and (b) phase response for the BB amplifiers of the direct conversion receiver introduced in Chapter 2 at 6 dB attenuation of the step-attenuator.

Assuring the same NL behavior of the BB section the other parameter vectors must be divided by the prefilter (exemplified for the quadrature branch):

$$
\begin{aligned}
\hat{\boldsymbol{\lambda}}_{\mathrm{IMD,O},Q,\mathrm{f}_m}(p) &= \hat{\boldsymbol{\lambda}}_{\mathrm{IMD,O},Q,\mathrm{f}_m}(p)/\hat{g}_{\mathrm{BB},I,1,\mathrm{f}_m}^{\frac{1}{2p-1}} \\
\hat{\boldsymbol{\lambda}}_{\mathrm{HD,O},Q,\mathrm{f}_m}(p) &= \hat{\boldsymbol{\lambda}}_{\mathrm{HD,O},Q,\mathrm{f}_m}(p)/\hat{g}_{\mathrm{BB},I,1,\mathrm{f}_m}^{\frac{1}{2p+1}} \\
\hat{\boldsymbol{\lambda}}_{\mathrm{HD,E},Q,\mathrm{f}_m}(p) &= \hat{\boldsymbol{\lambda}}_{\mathrm{HD,E},Q,\mathrm{f}_m}(p)/\hat{g}_{\mathrm{BB},I,1,\mathrm{f}_m}^{\frac{1}{2p}} \\
\hat{\boldsymbol{\lambda}}_{\mathrm{DC,E},Q,\mathrm{f}_m}(p) &= \hat{\boldsymbol{\lambda}}_{\mathrm{DC,E},Q,\mathrm{f}_m}(p)/\hat{g}_{\mathrm{BB},I,1,\mathrm{f}_m}^{\frac{1}{2p}}
\end{aligned}
\tag{4.116}
$$

For the calculation of the odd-order roots the same approach as presented in (4.113) must be applied. Especially for the inphase branch the prefilter usage results in a normalization of the polynomial coefficients. The frequency response of the corresponding third-order coefficients extracted from the IMD measurements is depicted in Figure 4.9. As in the linear case a complex-valued time-domain behavior is generated by both filtering functions. Using some imagination the inphase branch magnitude progress can be substituted by a constant and the phase one by $180°$. In this way the real-valued system response would be enforced. In case of the quadrature branch such an approach would be highly questionable as the mean coefficients' phase is around $140°$ (compared to $168°$ at the inphase branch).

At a first guess an approach similar to the transmitter case was applied. There, a reasonable solution was found by accepting the complex-valued response of the two BB amplifier models. This solution may also be argued, as a real-valued linear response is already ensured, and the NL output signal components
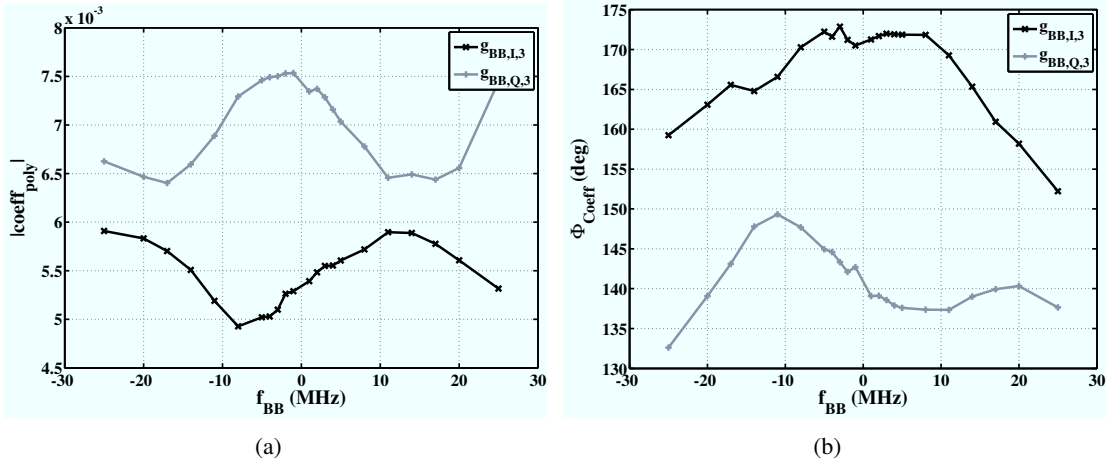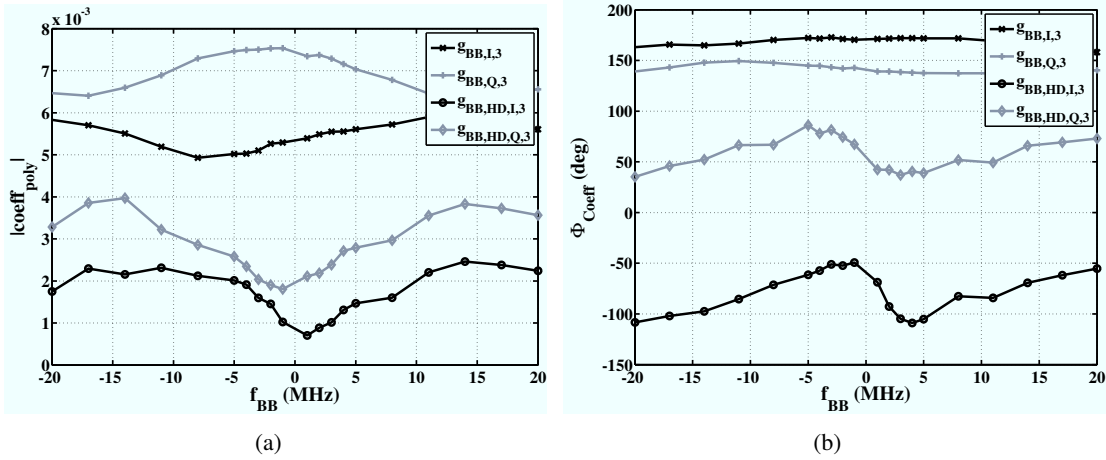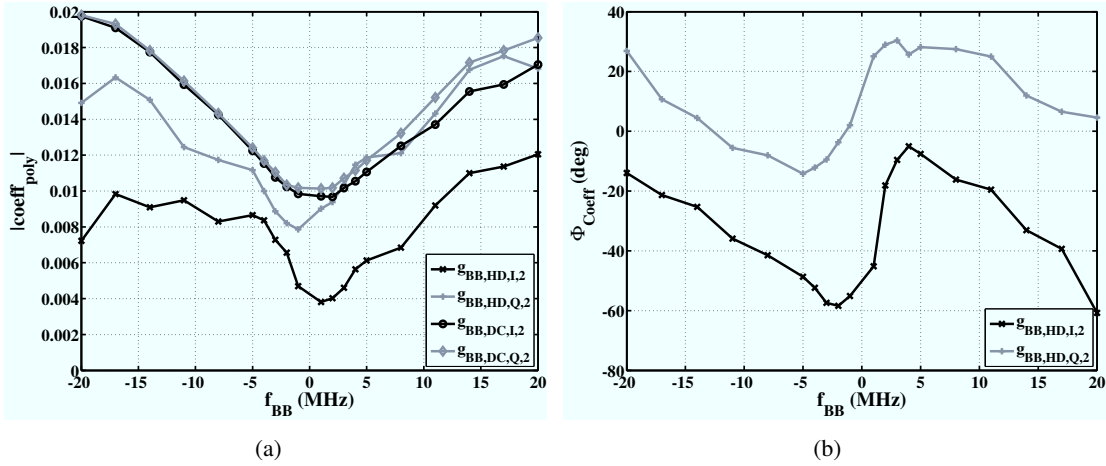
Figure 4.9: (a) Magnitude and (b) phase response of the third-order polynomial coefficients extracted from the measured IMD response. The prefilter impact was removed from these parameters.

are of much lower magnitude. Comparing the resulting model response to the measurements a significant degradation in the distortion prediction was observed in relation to the ones evaluated by (4.66) and (4.68). This result showed that it is mandatory to find a modeling approach which uses the complex-valued NL coefficients but generates a real-valued output signal from it.

A solution for this problem was already introduced in Section 4.4 by the input signal dependent mapping of the complex-valued filtering function to their real-valued correspondent. This technique was exemplified for a complex-valued $\gamma(t)$ progress in (4.13). The same solution was already applied in Section 4.7 handling $\gamma_{\mathrm{opt}}(j\omega)$ at the imbalance model and compensator. In this way the extracted PCWM filtering function can be evaluated by the model and the compensator without applying any further restrictions.

At this point of the extraction process a comparison of the coefficients describing the IMD and the HD_3 signal components can be performed. This comparison is presented in Figure 4.10. The magnitude of the HD_3 coefficients is about 3.5 times (inphase branch) and 2.5 times (quadrature branch) lower than the ones extracted from the IMD measurements. Also the shape of the magnitude traces for both distortion types is different. A similar situation is found at the phase response. The difference between the IMD and the HD_3 may be ascribed by linear filtering between the devices generating the distortion and the ADC's output signals. Such filtering is not described by the receiver model. Another explanation for the discrepancy between the IMD and the HD_3 polynomials is based on the parameter extraction process. At Section 4.9.4 the HD_3 response is used for estimating the BB amplifier IMD behavior and deembed its impact. The deembedding task provides the RF input NL output signal which is used for the characterization of this block. Any error introduced in this process results in a change of the ratio between the IMD and the HD_3 polynomial coefficients. Hence, thinking the other way around, after evaluating the two parameter vectors the ratio $\boldsymbol{\lambda}_{\mathrm{IMD},O,Q,\mathrm{f}_m}(p)/\hat{\boldsymbol{\lambda}}_{\mathrm{HD},O,Q,\mathrm{f}_m}(p+1), p > 1$ describes the magnitude and phase difference between the polynomial coefficients of the same order at the quadrature branch. This information, derived from both channels, can be used during a reevaluation of the RF input NL extraction process to update the parameters extracted by (4.81). In this way the mean difference between

Figure 4.10: (a) Magnitude and (b) phase response of the third-order polynomial coefficients extracted from the measured IMD and HD$_3$ response.

the IMD and the HD$_3$ polynomials is compensated. As the RF input NL is modeled memoryless it is not possible to equalize the shape of the frequency response of these traces.

Using this update iteration in the receiver model extraction the difference between the IMD and the HD$_3$ polynomial coefficients can be reduced. If the remaining discrepancy between the filtering functions inhibit a proper modeling of both distortion mechanisms a separate treatment must be implemented. The approach for this task was also presented in Section 4.4

If the remaining discrepancy between the filtering functions of the two distortion mechanisms is too large a separate treatment must be implemented. The approach for this task was also presented in Section 4.4. Using the analytical correspondent to the real-valued input signal both mechanisms can be generated independently. Together with the input signal dependent mapping technique an accurate description of each distortion mechanism can be realized.

Finally, the progress of the even-order polynomials describing the generation of harmonics and the distortion located around DC are compared. At Figure 4.11(a) the magnitude response of these parameters are plotted. Compared to the odd-order distortion case a much better alignment of the traces can be recognized. The ratio between the coefficient magnitudes resulted to about 0.6 for the inphase and 0.9 for the quadrature channel. At the phase response, shown in Figure 4.11(b), only the traces of the HD$_2$ polynomials are shown. Clearly, any phase information of the PCWM filtering function describing the distortion generation around DC will be suppressed by the required squared magnitude calculation. Hence, an arbitrary phase progress can be used in this context. Due to the acceptable alignment between the coefficients of the two even-order distortion mechanisms no need for a separate treatment is given. Still the application of the input signal dependent mapping of the corresponding filtering functions is required.

Figure 4.11: (a) Magnitude and (b) phase response of the second-order polynomial coefficients extracted from the measured HD_2 response and the distortion located around DC.

4.9.8 Postdistorter design

After a nonlinear model of the receiver was parameterized it should be used for compensating the generated distortion. The basis of the postdistorter will be a receiver model composed of a 3rd-order polynomial followed by a 3rd-order PCWM. It is assumed that the DC-offset was already canceled. The receiver output signal is first fed into the BB postdistorter block. Then the imbalance compensation is performed. Thereafter, the distortion of the RF input NL is reduced.

4.9.8.1 BB amplifier postdistorter

In the following the BB amplifier postdistorter will be derived exemplified for the inphase channel. The expressions for the quadrature channel are identical. As the PCWM filtering function was implemented in the frequency domain also the BB amplifier postdistorter will be developed using the frequency domain representation. Initially the postdistorter equations will be derived assuming real-valued time-domain PCWM filtering functions. One set of filtering functions is used to describe the IMD and HD_3 distortion generation. The same assumption is applied for the even-order case as well. At the end of this section the extension of the derived postdistorter to cope with the input signal dependent mapping technique as well as the separate treatment of the different distortion mechanisms is provided.

The impact of the cascade of lowpass filter and BB amplifier was introduced in Section 4.3 (4.20) - (4.23) as:

$$r_{\text{BB},I}(t) = h_{I,1}(t) * r_{\text{mod},I}(t) + [h_{I,2}(t) * r_{\text{mod},I}(t)]^2 + [h_{I,3}(t) * r_{\text{mod},I}(t)]^3 \qquad (4.117)$$

where $r_{\text{mod},I}(t) = \text{Re}\{r_{\text{mod}}(t)\}$ was defined in (4.17). The corresponding frequency domain represen-

tation is given by:

$$
\begin{aligned}
R_{\mathrm{BB},I}(j\omega) = {} & H_{I,1}(j\omega)R_{\mathrm{mod},I}(j\omega) + H_{I,2}(j\omega)R_{\mathrm{mod},I}(j\omega) * H_{I,2}(j\omega)R_{\mathrm{mod},I}(j\omega) \\
& + H_{I,3}(j\omega)R_{\mathrm{mod},I}(j\omega) * H_{I,3}(j\omega)R_{\mathrm{mod},I}(j\omega) * H_{I,3}(j\omega)R_{\mathrm{mod},I}(j\omega) \qquad (4.118) \\
= {} & R_{I,1}(j\omega) + R_{I,2}(j\omega) + R_{I,3}(j\omega)
\end{aligned}
$$

The derivation of the postdistorter was based on the approach suggested in [87]. This linearization strategy successively compensates the different orders of the nonlinear products starting from the linear one. Assuming a linear BB amplifier model, the output first-order post compensator has to satisfy:

$$
\begin{aligned}
R_{\mathrm{mod},I}(j\omega) &= K_{I,1}(j\omega)R_{\mathrm{BB},I}(j\omega) \\
K_{I,1}(j\omega) &= H_{I,1}^{-1}(j\omega)
\end{aligned} \qquad (4.119)
$$

where $K_{I,1}(j\omega)$ has to represent the causal linear inverse of the linear BB amplifier response $H_{I,1}(j\omega)$. For satisfying these requirements and guaranteeing the stability of $k_{I,1}(t) = \mathscr{F}^{-1}\{K_{I,1}(j\omega)\}$ all zeros of the Laplace transform $H_{I,1}(s)$ must be in the left half of the s-plane [87]. In case the linear inphase channel response is implemented as a prefilter, as described in the last section, also this filter must be inverted. The same prerequisites apply also for this inversion operation.

It should be noted that, by selecting $K_{I,1}(j\omega) = 1$, no compensation of the linear transmitter response is performed. This selection is advantageous if the linear response equalization is performed by another block in the postdistorter chain but still the BB amplifier nonlinearities should be canceled. Also in this case the stable causal linear inverse of $h_{I,1}(t) = \mathscr{F}^{-1}\{H_{I,1}(j\omega)\}$ is required.

Passing the complete BB amplifier output signal through the linear postdistorter results to:

$$
\begin{aligned}
R_{\mathrm{BB,post},I,1}(j\omega) &= K_{I,1}(j\omega)R_{\mathrm{BB},I}(j\omega) \\
&= K_{I,1}(j\omega)H_{I,1}(j\omega)R_{\mathrm{mod},I} + K_{I,1}(j\omega)R_{I,2}(j\omega) + K_{I,1}(j\omega)R_{I,3}(j\omega)
\end{aligned} \qquad (4.120)
$$

In the following the linear compensated BB amplifier output is abbreviated by:

$$
\begin{aligned}
\hat{R}_{\mathrm{mod},I}(j\omega) &= H_{I,1}^{-1}R_{\mathrm{BB},I}(j\omega) \\
&= R_{\mathrm{mod},I} + H_{I,1}^{-1}(j\omega)R_{I,2}(j\omega) + H_{I,1}^{-1}(j\omega)R_{I,3}(j\omega)
\end{aligned} \qquad (4.121)
$$

This signal is also an estimation for the BB amplifier input signal. Using $\hat{R}_{\mathrm{mod},I}(j\omega)$ the nonlinear BB amplifier response is approximated by:

$$
\begin{aligned}
\hat{R}_{I,2}(j\omega) &= H_{I,2}(j\omega)\hat{R}_{\mathrm{mod},I}(j\omega) * H_{I,2}(j\omega)\hat{R}_{\mathrm{mod},I}(j\omega) \\
\hat{R}_{I,3}(j\omega) &= H_{I,3}(j\omega)\hat{R}_{\mathrm{mod},I}(j\omega) * H_{I,3}(j\omega)\hat{R}_{\mathrm{mod},I}(j\omega) * H_{I,3}(j\omega)\hat{R}_{\mathrm{mod},I}(j\omega)
\end{aligned} \qquad (4.122)
$$

Based on these results the second-order distortion at the $R_{\mathrm{BB,post},I,1}(j\omega)$ is compensated by:

$$
\begin{aligned}
R_{\mathrm{BB,post},I,2}(j\omega) = {} & R_{\mathrm{BB,post},I,1}(j\omega) - K_{I,1}(j\omega)\hat{R}_{I,2}(j\omega) \\
= {} & K_{I,1}(j\omega)H_{I,1}(j\omega)R_{\mathrm{mod},I} + K_{I,1}(j\omega)R_{I,3}(j\omega) - K_{I,1}(j\omega)\Big[\\
& 2H_{I,2}(j\omega)R_{\mathrm{mod},I}(j\omega) * H_{I,1}^{-1}(j\omega)H_{I,2}(j\omega)R_{I,2}(j\omega) \\
& + 2H_{I,2}(j\omega)R_{\mathrm{mod},I}(j\omega) * H_{I,1}^{-1}(j\omega)H_{I,2}(j\omega)R_{I,3}(j\omega) \\
& + H_{I,1}^{-1}(j\omega)H_{I,2}(j\omega)R_{I,2}(j\omega) * H_{I,1}^{-1}(j\omega)H_{I,2}(j\omega)R_{I,2}(j\omega) \\
& + 2H_{I,1}^{-1}(j\omega)H_{I,2}(j\omega)R_{I,2}(j\omega) * H_{I,1}^{-1}(j\omega)H_{I,2}(j\omega)R_{I,3}(j\omega) \\
& + H_{I,1}^{-1}(j\omega)H_{I,2}(j\omega)R_{I,3}(j\omega) * H_{I,1}^{-1}(j\omega)H_{I,2}(j\omega)R_{I,3}(j\omega)\Big]
\end{aligned} \qquad (4.123)
$$

The second part of this equation presents the linearized output together with the additional distortion products generated by using $\hat{R}_{I,2}(j\omega)$ instead of the unknown $R_{I,2}(j\omega)$ for the second-order distortion cancelation. Signal components up to the 6th-order are generated by $\hat{R}_{I,2}(j\omega)$. Clearly, higher order compensators are required for lowering the impact of the undesired products. By extracting the third-order signal components from (4.123) and subtracting them from $R_{\text{BB,post},I,2}(j\omega)$ using estimated BB amplifier response (4.122) the third-order postdistorter equation results to:

$$
\begin{aligned}
R_{\text{BB,post},I,3}(j\omega) = R_{\text{BB,post},I,2}(j\omega) + K_{I,1}(j\omega)\big[& -\hat{R}_{I,3}(j\omega) \\
& +2H_{I,2}(j\omega)\hat{R}_{\text{mod},I}(j\omega) * H_{I,1}^{-1}(j\omega)H_{I,2}(j\omega)\hat{R}_{I,2}(j\omega)\big]
\end{aligned}
$$
(4.124)

For achieving a reasonable performance of the postdistorter, also the fourth and fifth-order compensation expressions were evaluated. These compensators are presented in (4.125) and (4.126). In these two expressions not all distortion components were included. Based on simulations, using the same parameters as for the performance evaluation of the algorithm for the receiver parameterization, the negligible distortion components were identified.

$$
\begin{aligned}
R_{\text{BB,post},I,4}(j\omega) = R_{\text{BB,post},I,3}(j\omega) + K_{I,1}(j\omega)\Big[& \\
+3H_{I,3}(j\omega)\hat{R}_{\text{mod},I}(j\omega) * H_{I,3}(j\omega)\hat{R}_{\text{mod},I}(j\omega) * & H_{I,1}^{-1}(j\omega)H_{I,3}(j\omega)\hat{R}_{I,2}(j\omega) \\
+2H_{I,2}(j\omega)\hat{R}_{\text{mod},I}(j\omega) * & H_{I,1}^{-1}(j\omega)H_{I,3}(j\omega)\hat{R}_{I,3}(j\omega) \\
-5H_{I,1}^{-1}(j\omega)H_{I,2}(j\omega)\hat{R}_{I,2}(j\omega) * & H_{I,1}^{-1}(j\omega)H_{I,2}(j\omega)\hat{R}_{I,2}(j\omega)\Big]
\end{aligned}
$$
(4.125)

$$
\begin{aligned}
R_{\text{BB,post},I,5}(j\omega) = R_{\text{BB,post},I,4}(j\omega) + K_{I,1}(j\omega)\Big(& \\
+3H_{I,3}(j\omega)\hat{R}_{\text{mod},I}(j\omega) * H_{I,3}(j\omega)\hat{R}_{\text{mod},I}(j\omega) * & H_{I,1}^{-1}(j\omega)H_{I,3}(j\omega)\hat{R}_{I,3}(j\omega) \\
-3H_{I,3}(j\omega)\hat{R}_{\text{mod},I}(j\omega) * H_{I,1}^{-1}(j\omega)H_{I,3}(j\omega)\hat{R}_{I,2}(j\omega) * & H_{I,1}^{-1}(j\omega)H_{I,3}(j\omega)\hat{R}_{I,2}(j\omega) \\
-18H_{I,1}^{-1}(j\omega)H_{I,2}(j\omega)\hat{R}_{I,2}(j\omega) * & H_{I,1}^{-1}(j\omega)H_{I,2}(j\omega)\hat{R}_{I,3}(j\omega) \\
+14H_{I,1}^{-1}(j\omega)H_{I,2}(j\omega)\hat{R}_{\text{mod},I}(j\omega) * H_{I,2}(j\omega)\big[& H_{I,1}^{-1}(j\omega)H_{2,3}(j\omega)\hat{R}_{\text{mod},I}(j\omega) \\
*H_{I,1}^{-1}(j\omega)H_{2,3}(j\omega)\hat{R}_{\text{mod},I}(j\omega)\big]\Big) &
\end{aligned}
$$
(4.126)

The postdistorter equations (4.119) to (4.126) are designed for compensating the BB amplifier model introduced in Section 4.3. At the enhanced receiver model two additional techniques were introduced required for fully representing the evaluated receiver behavior. Hence, extensions to the presented postdistorter equations are required to meet this demand. Of major importance is the correct evaluation of the input signal depending mapping of the complex-valued PCWM filtering functions onto their real-valued correspondent. It is assumed that this technique is only applied for the NL distortion products. In Section 4.9.7 an approach for handling a complex-valued linear response by introducing a prefilter was explained.

Using the notation introduced in Section 4.2 the second-order postdistorter response applying the

mapping technique is given by:

$$R_{\text{BB,post},I,2}(j\omega) = R_{\text{BB,post},I,1}(j\omega) - K_{I,1}(j\omega)R_{\text{BB,post},I,2,\text{P1}}(j\omega)$$
$$R_{\text{BB,post},I,2,\text{P1}}(j\omega) = H_{I,2,\text{map}}(j\omega, \hat{R}_{\text{mod}})\hat{R}_{\text{mod},I}(j\omega) * H_{I,2,\text{map}}(j\omega, \hat{R}_{\text{mod}})\hat{R}_{\text{mod},I}(j\omega) \quad (4.127)$$
$$\hat{R}_{\text{mod}}(j\omega) = H_{I,1}^{-1}R_{\text{BB,I}}(j\omega) + jH_{Q,1}^{-1}R_{\text{BB,Q}}(j\omega)$$

It should be noted, that the input signal to the BB amplifier section would be required for the correct mapping of $H_{I,2}$. This signal is estimated by $\hat{R}_{\text{mod}}(j\omega)$, the receiver output signal scaled by the inverse linear response of the two BB amplifiers. The third-order postdistorter output signal is shown in (4.128).

$$R_{\text{BB,post},I,3}(j\omega) = R_{\text{BB,post},I,2}(j\omega) + K_{I,1}(j\omega)\big[- R_{\text{BB,post},I,3,\text{P1}}(j\omega)$$
$$+ R_{\text{BB,post},I,3,\text{P2}}(j\omega)\big]$$
$$R_{\text{BB,post},I,3,\text{P1}}(j\omega) = H_{I,3,\text{map}}(j\omega, \hat{R}_{\text{mod}})\hat{R}_{\text{mod},I}(j\omega) * H_{I,3,\text{map}}(j\omega, \hat{R}_{\text{mod}})\hat{R}_{\text{mod},I}(j\omega)$$
$$* H_{I,3,\text{map}}(j\omega, \hat{R}_{\text{mod}})\hat{R}_{\text{mod},I}(j\omega) \quad (4.128)$$
$$R_{\text{BB,post},I,3,\text{P2}}(j\omega) = 2H_{I,2,\text{map}}(j\omega, \hat{R}_{\text{mod}})\hat{R}_{\text{mod},I}(j\omega)$$
$$* H_{I,2,\text{map}}(j\omega, H_{I,1}^{-1}R_{\text{BB,post},I,2,\text{P1}})H_{I,1}^{-1}(j\omega)R_{\text{BB,post},I,2,\text{P1}}(j\omega)$$

The contribution $R_{\text{BB,post},I,3,\text{P1}}(j\omega)$ is calculated analogous to $R_{\text{BB,post},I,2,\text{P1}}(j\omega)$. The second signal component $R_{\text{BB,post},I,3,\text{P2}}(j\omega)$ suppressed an undesired contribution of the second-order distortion compensation. Due to the two different input signals to the frequency domain convolution also two differently mapped filtering functions are used. In the same way also the fourth and fifth order contribution are adapted for the input signal dependent mapping technique.

Introducing an independent treatment of the two second- and third-order distortion generation mechanisms the equations (4.123) - (4.126) or (4.127) - (4.128), respectively, must be arranged into groups of associated squared and cubic operations. These operations are then replaced by their underlying distortion generation mechanisms. In case of the second-order postdistorter response including the mapping technique (4.127) has to be extended by:

$$R_{\text{BB,post},I,2}(j\omega) = R_{\text{BB,post},I,1}(j\omega) - K_{I,1}(j\omega)R_{\text{BB,post},I,2,\text{P1}}(j\omega)$$
$$R_{\text{BB,post},I,2,\text{P1}}(j\omega) = \frac{1}{2}\big[R_{\text{BB,post},I,2,\text{P2}}(j\omega) + R_{\text{BB,post},I,2,\text{P2}}^*(-j\omega)\big]$$
$$R_{\text{BB,post},I,2,\text{P2}}(j\omega) = H_{I,2,\text{HD,map}}(j\omega, \hat{R}_{\text{mod}})\hat{R}_{\text{mod},I,\text{Ana}}(j\omega) * H_{I,2,\text{HD,map}}(j\omega, \hat{R}_{\text{mod}})\hat{R}_{\text{mod},I,\text{Ana}}(j\omega)$$
$$+ H_{I,2,\text{DC,map}}(j\omega, \hat{R}_{\text{mod}})\hat{R}_{\text{mod},I,\text{Ana}}(j\omega)$$
$$* H_{I,2,\text{DC,map}}^*(-j\omega, \hat{R}_{\text{mod}})\hat{R}_{\text{mod},I,\text{Ana}}^*(-j\omega)$$
$$\hat{R}_{\text{mod},I,\text{Ana}}(j\omega) = \mathcal{F}\Big\{\hat{r}_{\text{mod},I}(t) + j\mathcal{H}\{\hat{r}_{\text{mod},I}(t)\}\Big\}$$
$$(4.129)$$

At these expressions $R_{\text{BB,post},I,2,\text{P2}}(j\omega)$ introduces the separate treatment of the HD$_2$ distortion and the distortion located around DC using the analytical correspondent $\hat{R}_{\text{mod},I,\text{Ana}}(j\omega)$ of the real-valued input signal $\hat{R}_{\text{mod},I}(j\omega)$. To get the desired compensation signal the imaginary part of $R_{\text{BB,post},I,2,\text{P2}}(j\omega)$ in the time-domain must be suppressed. If $H_{I,2,\text{DC,map}}(j\omega, \hat{R}_{\text{mod}})$ is replaced by $H_{I,2,\text{HD,map}}(j\omega, \hat{R}_{\text{mod}})$

the same output is provided by (4.127) and (4.129). The adopted version of the third-order postdistorter response (4.128) is presented at (4.130) to (4.132). The signals $R_{\mathrm{BB,post},I,3,\mathrm{P3}}(j\omega)$ and $R_{\mathrm{BB,post},I,3,\mathrm{P4}}(j\omega)$ represent the two postdistorter signal components before the real-value operation is applied. The signal $R_{\mathrm{BB,post},I,3,\mathrm{P3}}(j\omega)$ implements the separate treatment of the IMD and the $\mathrm{HD_3}$ response calculation in a similar way to (4.129). Equation (4.132) highlights the accomplishment of the squared operation using different contributing signal components. In an analogous way also the fourth- and fifth-order postdistorter response can be updated. Due to the extent for the resulting equations these expressions are not presented.

$$
\begin{aligned}
R_{\mathrm{BB,post},I,3}(j\omega) =&\, R_{\mathrm{BB,post},I,2}(j\omega) + K_{I,1}(j\omega)\big[- R_{\mathrm{BB,post},I,3,\mathrm{P1}}(j\omega) \\
&+ R_{\mathrm{BB,post},I,3,\mathrm{P2}}(j\omega)\big] \\
R_{\mathrm{BB,post},I,3,\mathrm{P1}}(j\omega) =&\, \frac{1}{2}\big[R_{\mathrm{BB,post},I,3,\mathrm{P3}}(j\omega) + R^*_{\mathrm{BB,post},I,3,\mathrm{P3}}(-j\omega)\big] \\
R_{\mathrm{BB,post},I,3,\mathrm{P2}}(j\omega) =&\, \frac{1}{2}\big[R_{\mathrm{BB,post},I,3,\mathrm{P4}}(j\omega) + R^*_{\mathrm{BB,post},I,3,\mathrm{P4}}(-j\omega)\big]
\end{aligned}
\tag{4.130}
$$

$$
\begin{aligned}
R_{\mathrm{BB,post},I,3,\mathrm{P3}}(j\omega) =&\, H_{I,3,\mathrm{IMD,map}}(j\omega,\hat{R}_{\mathrm{mod}})\hat{R}_{\mathrm{mod},I}(j\omega) * H_{I,3,\mathrm{IMD,map}}(j\omega,\hat{R}_{\mathrm{mod}})\hat{R}_{\mathrm{mod},I}(j\omega) \\
&* H^*_{I,3,\mathrm{IMD,map}}(-j\omega,\hat{R}_{\mathrm{mod}})\hat{R}^*_{\mathrm{mod},I}(-j\omega) \\
&+ H_{I,3,\mathrm{HD,map}}(j\omega,\hat{R}_{\mathrm{mod}})\hat{R}_{\mathrm{mod},I}(j\omega) * H_{I,3,\mathrm{HD,map}}(j\omega,\hat{R}_{\mathrm{mod}})\hat{R}_{\mathrm{mod},I}(j\omega) \\
&* H_{I,3,\mathrm{HD,map}}(j\omega,\hat{R}_{\mathrm{mod}})\hat{R}_{\mathrm{mod},I}(j\omega)
\end{aligned}
\tag{4.131}
$$

$$
\begin{aligned}
R_{\mathrm{BB,post},I,3,\mathrm{P4}}(j\omega) =&\, 2\Big[H_{I,2,\mathrm{HD,map}}(j\omega,\hat{R}_{\mathrm{mod}})\hat{R}_{\mathrm{mod},I,\mathrm{Ana}}(j\omega) \\
&* H_{I,2,\mathrm{HD,map}}(j\omega, H_{I,1}^{-1}R_{\mathrm{BB,post},I,2,\mathrm{P1}})H_{I,1}^{-1}(j\omega)R_{\mathrm{BB,post},I,2,\mathrm{P1,Ana}}(j\omega) \\
&+ H_{I,2,\mathrm{DC,map}}(j\omega,\hat{R}_{\mathrm{mod}})\hat{R}_{\mathrm{mod},I,\mathrm{Ana}}(j\omega) \\
&* H^*_{I,2,\mathrm{DC,map}}(-j\omega, H_{I,1}^{-1}R_{\mathrm{BB,post},I,2,\mathrm{P1}})H_{I,1}^{-*}(-j\omega)R^*_{\mathrm{BB,post},I,2,\mathrm{P1,Ana}}(-j\omega)\Big]
\end{aligned}
\tag{4.132}
$$

4.9.8.2   RF input NL postdistorter

After the compensation of the BB amplifiers and the I/Q mixer non-ideal behavior an estimation for the RF input NL output signal is available. As introduced in (4.15) this signal is generated by a third-order polynomial. For compensating the impact of the RF input NL $\hat{r}_{\mathrm{BP}}(t)$ is fed into another polynomial. As shown in [121] it is possible calculating the composition of two polynomials and select the coefficient in order to cancel the impact of the first one. Neglecting the impact of the LO phase difference, the RF input NL output signal is given by:

$$
r_{\mathrm{BP}}(t) = g_{\mathrm{M},1}r_{\mathrm{RF}}(t) + g_{\mathrm{M},3}r_{\mathrm{RF}}(t)|r_{\mathrm{RF}}(t)|^2
\tag{4.133}
$$

The postdistortion polynomial can be written as:

$$\hat{r}_{\text{RF}}(t) = \sum_{k=1}^{(N_{\text{RF,Comp}}+1)/2} g_{MC,2k-1} r_{\text{BP}}(t) |r_{\text{BP}}(t)|^{2(k-1)} \tag{4.134}$$

where $N_{\text{RF,Comp}}$ specifies the order of the compensation polynomial. Similar to the BB case the coefficients $g_{MC,k}$ are iteratively calculated starting from the first order. The linear coefficient is defined as:

$$g_{MC,1} = \frac{\mu}{g_{\text{M},1}} \tag{4.135}$$

The gain of the RF input NL, postdistorter cascade is set by the parameter μ. By evaluating (4.134) up to the first order using (4.135) and selecting the inverse of the third-order coefficient provides $g_{MC,3}$:

$$g_{MC,3} = -\frac{\mu g_{\text{M},3}}{g_{\text{M},1}^2 |g_{\text{M},1}|^2} \tag{4.136}$$

The other coefficients of the postdistorter polynomial are extracted in the same way. Equation (4.137) presents these parameters up to 9$^{\text{th}}$ order.

$$\begin{aligned} g_{MC,5} &= \mu \frac{g_{\text{M},1}^2 \left| g_{\text{M},3}^2 / g_{\text{M},1}^2 \right| + 2g_{\text{M},3}^2}{g_{\text{M},1}^3 |g_{\text{M},1}|^4} \\[2mm] g_{MC,7} &= -\mu \frac{5g_{\text{M},3}^4 + 5g_{\text{M},1}^2 g_{\text{M},3}^2 \left| g_{\text{M},3}^2 / g_{\text{M},1}^2 \right| + 2g_{\text{M},1}^4 \left| g_{\text{M},3}^4 / g_{\text{M},1}^4 \right|}{g_{\text{M},1}^4 |g_{\text{M},1}|^6 g_{\text{M},3}} \\[2mm] g_{MC,9} &= \mu \frac{14g_{\text{M},3}^6 + 5g_{\text{M},1}^6 \left| g_{\text{M},3}^6 / g_{\text{M},1}^6 \right| + 15g_{\text{M},3}^2 g_{\text{M},1}^4 \left| g_{\text{M},3}^4 / g_{\text{M},1}^4 \right| + 21g_{\text{M},3}^4 g_{\text{M},1}^2 \left| g_{\text{M},3}^2 / g_{\text{M},1}^2 \right|}{g_{\text{M},1}^5 |g_{\text{M},1}|^8 g_{\text{M},3}^2} \end{aligned} \tag{4.137}$$

4.9.8.3 Postdistorter performance evaluation

For verifying the performance of the presented postdistorter, simulations were accomplished. Similar to the transmitter case a multi-tone signal composed of 100 tones covering a bandwidth of 12.5 MHz was selected for the simulation. This signal was shifted 12.5 MHz away from the center frequency for including also imbalance effects in the simulation. The tone phases were chosen to minimize the crest-factor, which resulted in a PAPR of 2.4 dB. The performance of the postdistorter was analyzed in two different configurations. On the one hand the real-valued PCWM filtering functions were applied. These BB amplifier model allows the usage of the postistorter equations (4.120) to (4.126) for the compensation. On the other hand the BB amplifier model extracted from the characterized receiver was provided. By this way both the mapping technique and using both distortion mechanisms at the even- and odd-order response were introduced. In this way all extensions introduced by the enhanced receiver model must be compensated. To assure comparability between the two cases the NL receiver parameters of the standard model are the real-valued time-domain correspondent of the enhanced model coefficients.

For both scenarios the postdistorter was composed of a 5th-order BB amplifier and a 9th-order RF input NL compensator. The performance of this linearizer was evaluated for a power sweep of the multi-tone signal between -10 and $10\,\text{dBm}$. In Figure 4.12 the NMSE (3.198) between the input signal, the output of the receiver, and the compensator is depicted. In both configurations the uncompensated receiver shows a NMSE of about $-25\,\text{dB}$ even at low input power levels due to the imbalance effects. At the enhanced model scenario a significantly reduced compensator performance can be observed. This behavior is caused by the AM-PM conversion in the BB amplifier behavior as shown in the phase response of the corresponding polynomial coefficients Figure 4.10(b) and Figure 4.11(b). As a result the error vector between the desired signal and the distorted one is significantly increased. Additionally, the mapping technique used at the enhanced model causes some deviations between PCWM filtering functions applied at the model and the one applied at the postcompensator. A comparison of the receiver
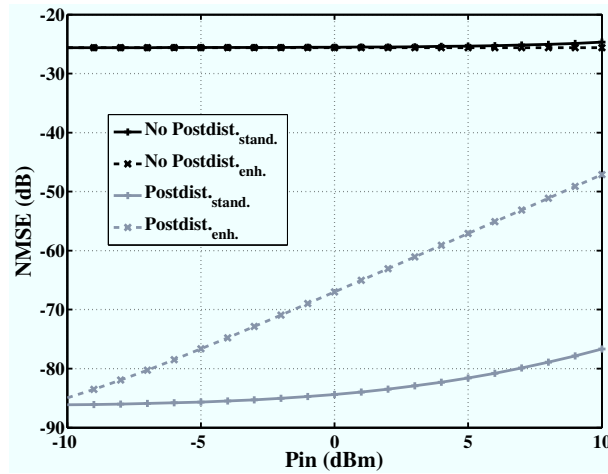
Figure 4.12: NMSE of the receiver and the postdistorter output signal for the standard and the enhanced model.

output spectra with and without postdistortion at $P_{\text{in}} = 5\,\text{dBm}$ is presented in Figure 4.13. Here it can be recognized that a residual IMD distortion at the enhanced postcompensator output is responsible for the reduced performance highlighted in Figure 4.12.

4.10 Model and compensator for the direct conversion receiver

Based on the different parameterization algorithms discussed in Section 4.5 a model and a compensator are designed combining all these results.

The structure of the receiver model is presented in Figure 4.14. At the beginning the input signal is passed through the RF input NL. The output of this nonlinear block is provided to the prefilter and to the spurious emissions modeling. As mentioned in Section 4.9.4 and Section 4.9.5 the magnitude and phase imbalance of the cascade of lowpass filters and BB amplifiers can either be represented by the PCWMs or by the imbalance block. In the following the complex-valued signal is divided in its real and imaginary part and fed into the corresponding baseband nonlinearities. After combining the output of these blocks

(a)   (b)
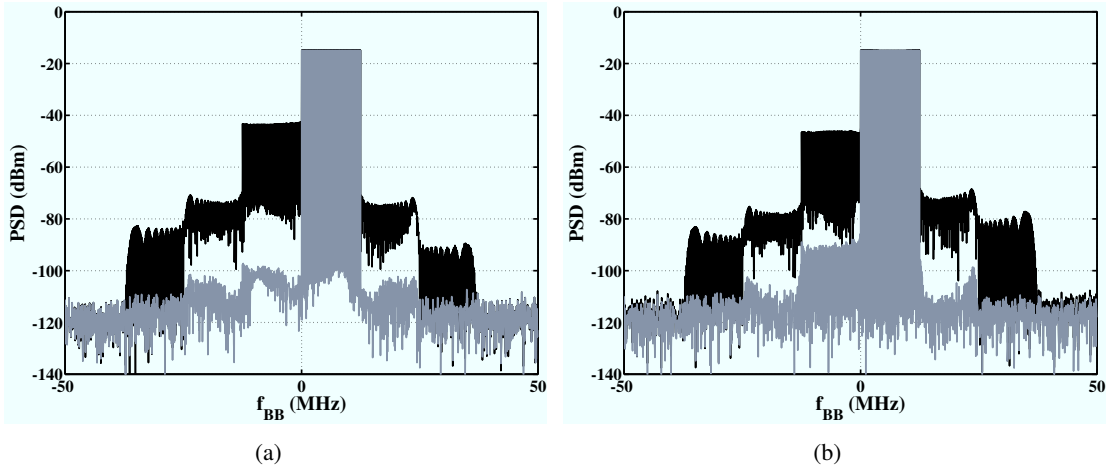
Figure 4.13: Simulated receiver output spectra for a multi-tone input signal with and without postdistortion using (a) the standard and (b) the enhanced receiver model. At both plots the black traces show the receiver output signal while the gray ones display the postdistorter response.

the DC-offset and the spurious emissions are added. This signal represents the receiver model output signal.
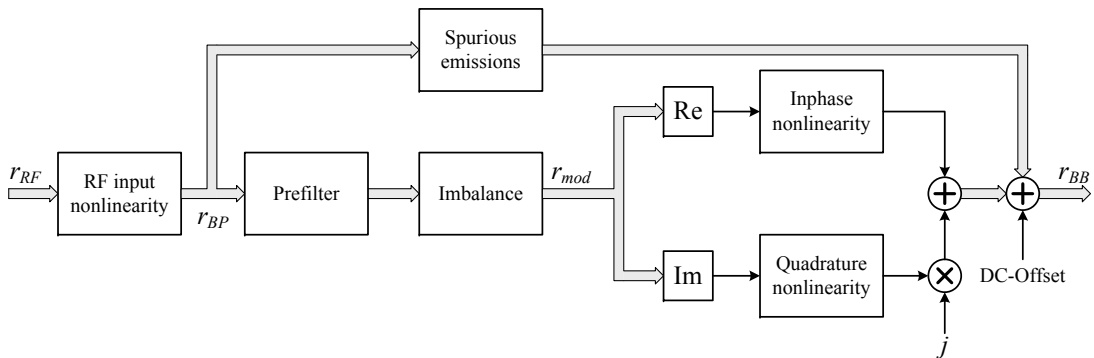
Figure 4.14: Structure of the model used for representing the complete receiver.

The spurious emissions block is composed of N_{spur} parallel branches (compare (4.45)). Each branch models the distortion products for one frequency offset $\Delta\omega_k$. The structure of such a branch is depicted in Figure 4.15. The upper part of the structure generates the spurious emission associated with the input signal, while the lower part generates the one of the spectrally mirrored input. In both branches the signal is first frequency shifted, then the response of the reference channel is introduced. After these steps the imbalance is modeled. Finally, the scaling of the spurious emissions by the functions $\alpha_{\mathrm{spur},d,k}(j\omega_m)$ and $\alpha_{\mathrm{spur},v,k}(j\omega_m)$ is performed.

The receiver compensator structure is shown in Figure 4.16. In a first step the DC-offset is removed. Then the impacts of the BB amplifiers are compensated. As in the receiver model case the usage of the imbalance compensation block depends on the information represented by the PCWMs. If the magnitude
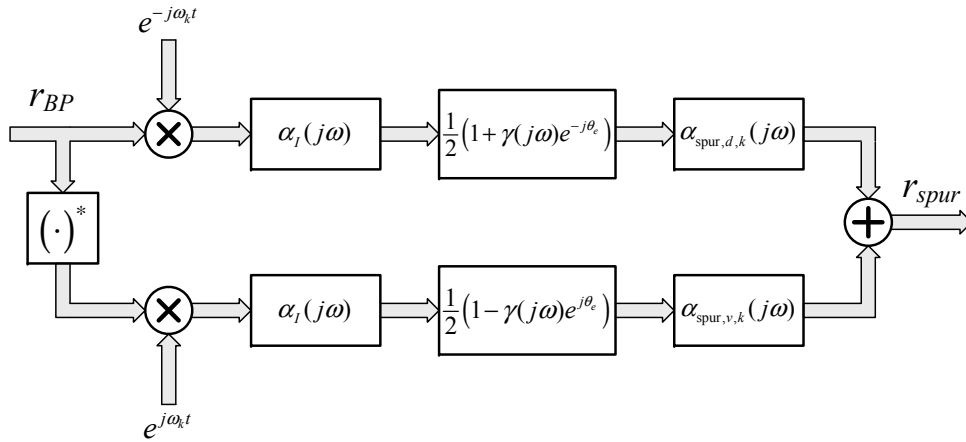
Figure 4.15: Model of a branch of the spurious emission block.

and phase response of the two branches is incorporated into the BB amplifier models the magnitude and phase imbalance compensation is accomplished at the BB section. The imbalance compensation must only compensate the impact of the I/Q mixer phase error. In this case the parameter $K_1(j\omega)$ equals $H_1^{-1}(j\omega)$ (compare (4.119)) for both branches.

If the magnitude and phase response should not be treated by the BB amplifier compensators the parameter $K_1(j\omega)$ is set to unity. If so, the gain compensation equalizes the frequency response of the lowpass filters, BB amplifiers cascade. The imbalance block corrects the impact of $|\gamma(j\omega)|$, $\phi_\gamma(j\omega)$ and θ_e.

After the imbalance compensation is accomplished the equalization of the receiver gain is performed. Then the signal for the spurious emission suppression is added. This signal is evaluated as described in Section 4.8.1. Thereafter, the RF input NL impact is removed by the next block before the compensated output signal is available.
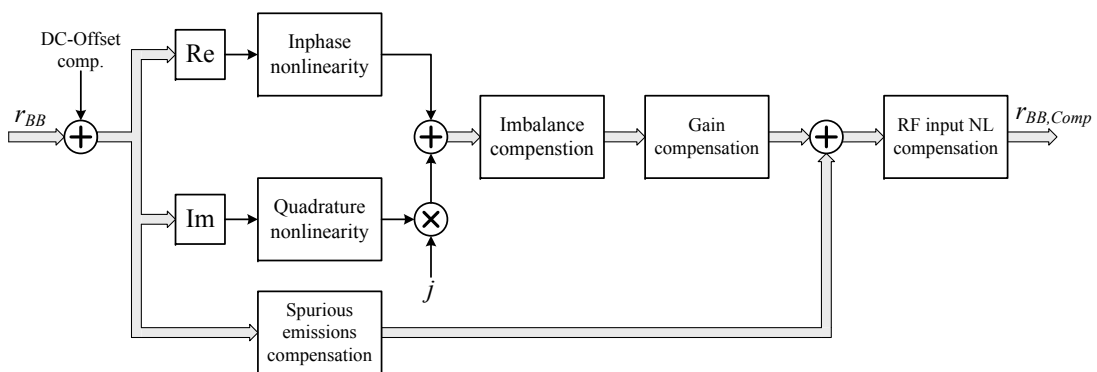
Figure 4.16: Structure of the receiver compensator.

It should be noted that this model / compensator is valid up to a peak input power level specified by the maximum input power during the NL coefficients extraction. If the receiver has variable attenuators

at the input of the I/Q mixer or in front of the BB amplifiers, this model is only valid for the setting of these attenuators used during the characterization. The NL parameter extraction has to be repeated for all other combinations of these attenuators if a generally valid receiver model / compensator should be generated.

Chapter 5

Transmitter and receiver measurements and parameterization

After discussing the custom built direct conversion transmitter and receiver setups in Chapter 2 the techniques for characterizing and compensating their behavior can be applied. In this chapter the different distortion mechanisms of the transmitter and the receiver are investigated and the parameterization processes derived in Chapters 3 and 4 are utilized. Instead of a separate treatment, each distortion mechanism is simultaneously explored for both, transmitter and receiver. This approach will be used for the linear response as well as for the imbalance and the NL distortion. The spurious emissions are evaluated at the transmitter case only as the receiver setup didn't show this effect. Finally the performance of the compensated transmitter and receiver are highlighted. For these measurements the transmitter provided the broadband input signal for the receiver. In this way their ability operating as transparent frequency translating devices will be discussed.

As mentioned at the beginning of Chapter 2 all measurement and characterization tasks will be performed at a center frequency of 3.5 GHz. The baseband sampler board is operated at 100 Msps clock rate. A change of these settings, albeit supported by the measurement setups, was omitted for keeping the extent of the measurements manageable. At both concepts a low and a high distortion operation mode will be investigated (compare Section 2.1).

5.1 Linear response and delay characterization

The characterization of the linear transmitter and receiver response was performed using a real-valued multi-tone signal composed of 80 tones covering the BB frequency range $-39.5\,\text{MHz} \leq \text{f}_{\text{BB}} \leq 39.5\,\text{MHz}$. By this selection the passband bandwidth is sampled using 1 MHz tone spacing. To keep the NL distortion low, the peak-to-average power ratio (PAPR) was minimized using the tone phases as suggested by Newman [134]. By this approach a PAPR of 2.5 dB was achieved. In the transmitter case the real-valued input signal was applied to the inphase and quadrature channel separately. The magnitude response of both channels for the low and high distortion case are presented in Figure 5.1. To show the frequency dependency at the two operation conditions more clearly the mean output power at both channels were subtracted from the displayed traces. In the low and high distortion operation mode the mean output power resulted to -1.8 and $9.6\,\text{dBm}$. The differences between the frequency dependency of the mea-

Figure 5.1: Relative output power of the inphase and the quadrature channel at the two operation modes.
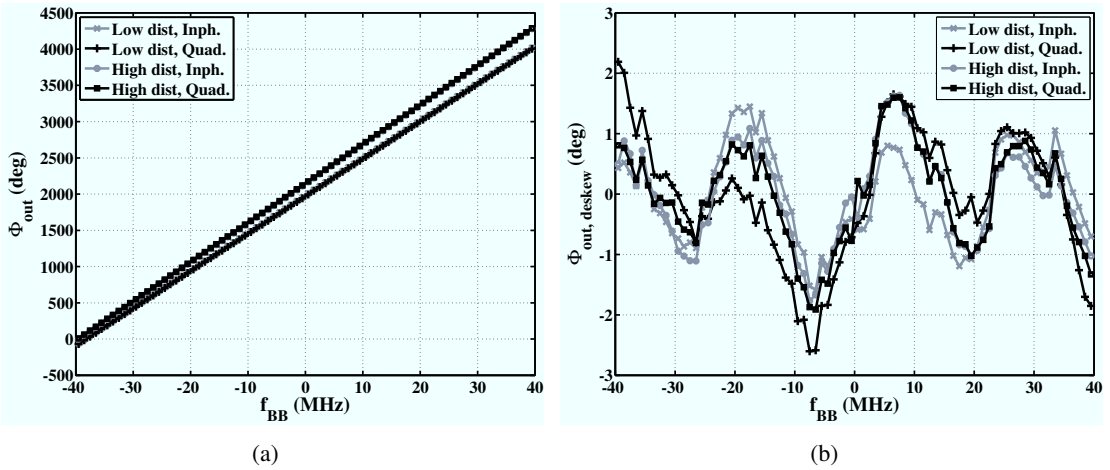
Figure 5.2: (a) Unwrapped and (b) delay compensated version of the phase response of the two BB channels presented for both operation conditions.

surement results at the two cases can be mainly ascribed to the different AD-branch gains of the interface board depicted in Figure 2.8.

The corresponding phase response is visualized in Figure 5.2. In Figure 5.2(a) the unwrapped phase is characterized by a positive slope corresponding to a negative time delay. As described in Section 3.8.4 the long delay introduced by the transmitter setup causes nearly 360° phase rotation at the 1 MHz tone spacing. Hence, the unconstrained unwrapping of the phase response resulted in this non-physical behavior. By forcing a negative slope a time delay of 849.5 and 856.5 ns for the low and high distortion case was evaluated. After compensating these delays from the measured phases the progress shown in Figure 5.2(b) is observed. The difference between the quadrature and inphase channel response corresponds to the phase imbalance. Hence, this approach would be much faster for characterizing the
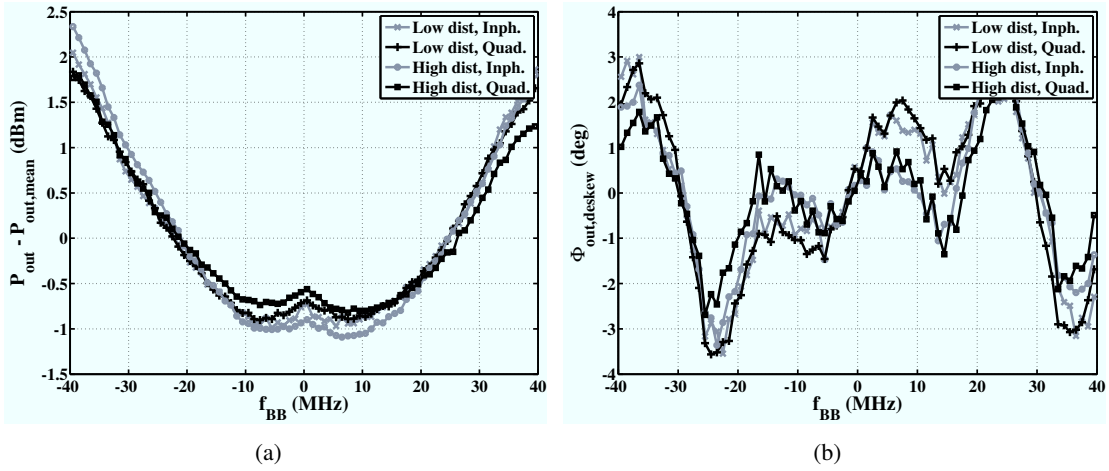
Figure 5.3: (a) Magnitude and (b) delay compensated phase response of the receiver BB channels presented for both operation conditions.

imbalance compared to the iterative one suggested in Section 3.6. The disadvantage of this imbalance identification approach is that the measurement errors of the setup will degrade the achievable imbalance suppression. Additionally, if the delay estimation is only slightly erroneous it has a significant impact on the deskewed phases due to the large magnitudes of the delays.

The RF output signal generated by the transmitter BB branches is phase rotated by the LO. During the downconversion by the receiver it is again phase shifted before being applied to the BB channels. Hence, the real-valued transmitter input signal is observable at both receiver channels. The magnitudes of the corresponding receiver BB signals is set by the overall phase shift introduced by the up- and downconversion. For the linear characterization of the receiver the RF signal generated by the inphase channel excitation of the transmitter was used. In the low and high distortion case the mean power levels of the two BB branches differed by approx. 2 dB and 4 dB, respectively. The magnitude and phase response measured at the receiver outputs are summarized in Figure 5.3. The larger changes in the power levels of the two receiver channels compared to the transmitter ones is caused by the $\sin(x)/x$ compensation of the anti-aliasing filters (compare Section 2.1.2). The variation recognized at the delay compensated phase response are in the same range as observed at the transmitter. A delay of 550.3 and 567.6 ns was extracted for the low and high distortion operation mode. The significantly lower value compared to the transmitter case is explained by the missing RF driver amplifier at the receiver setup.

For both the transmitter and the receiver linear response compensators were derived. The performance of these compensators is discussed together with the NL behavior equalization.

5.2 Imbalance distortion characterization and compensation

In the transmitter case the imbalance distortion generated by using the direct conversion principle is measured and iteratively compensated. The process for finding the corresponding imbalance parameters was discussed in Section 3.6.2. For this purpose single-tone measurement covering the BB bandwidth $-40\,\text{MHz} \leq f_{\text{BB}} \leq 40\,\text{MHz}$ in steps of 1 MHz were performed. The magnitude of the input tone to
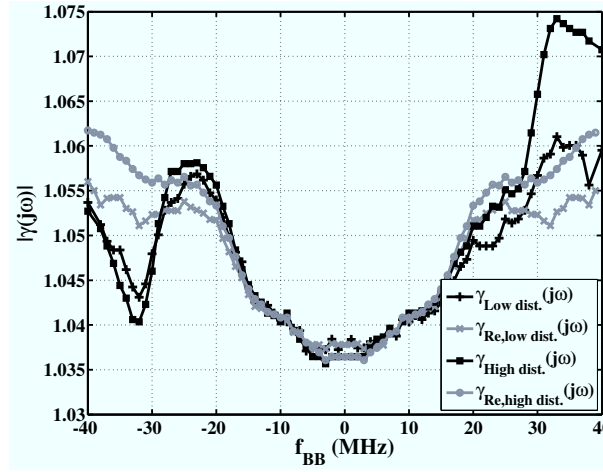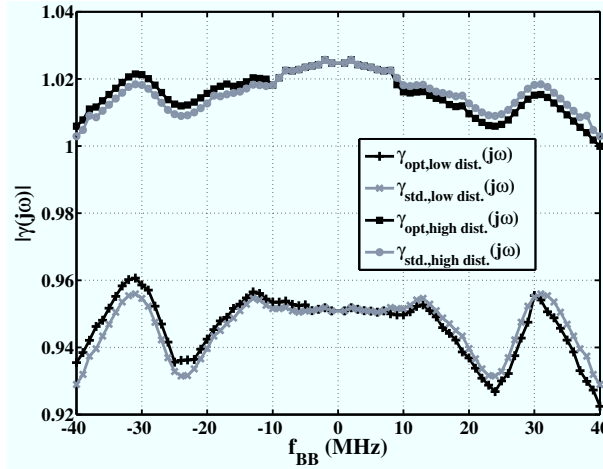
Figure 5.4: Magnitude imbalance evaluated for both operation conditions. $\hat{\gamma}_{\mathrm{Re}}(j\omega)$ identifies the magnitude response resulting in a real-valued time domain characteristic of this parameter.
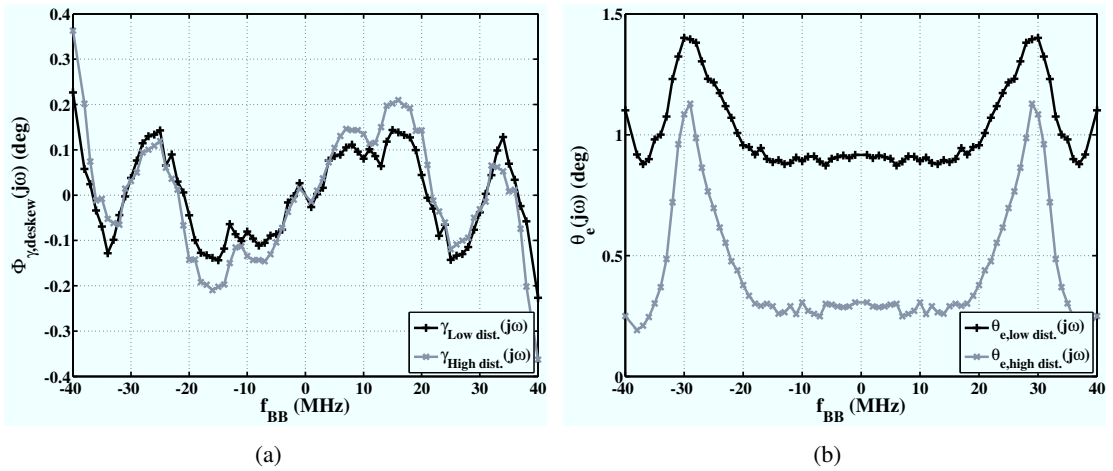
Figure 5.5: (a) Delay compensated phase imbalance and (b) mixer phase error presented for both operation modes.

the transmitter was 1 dB below the full-scale excitation of the DACs. At each of these frequencies the imbalance distortion cancelation was accomplished. The resulting imbalance coefficients are presented in Figure 5.4 and 5.5. The parameter $\hat{\gamma}(j\omega)$ introduced in (3.8) is larger than one over the whole frequency range indicating a higher gain at the quadrature compared to the inphase channel. In Figure 5.4 the progress of $\hat{\gamma}_{\mathrm{Re}}(j\omega)$ is added. This behavior would be recognized if the imbalance is generated by the BB channel mismatch only. For both operation modes a significant deviation between $\hat{\gamma}(j\omega)$ and $\hat{\gamma}_{\mathrm{Re}}(j\omega)$ is observed at frequencies above 20 MHz distance to the carrier corresponding to a transmitter RF network contribution.

The phase response of $\hat{\gamma}(j\omega)$ was divided in its even and odd frequency component. The even re-
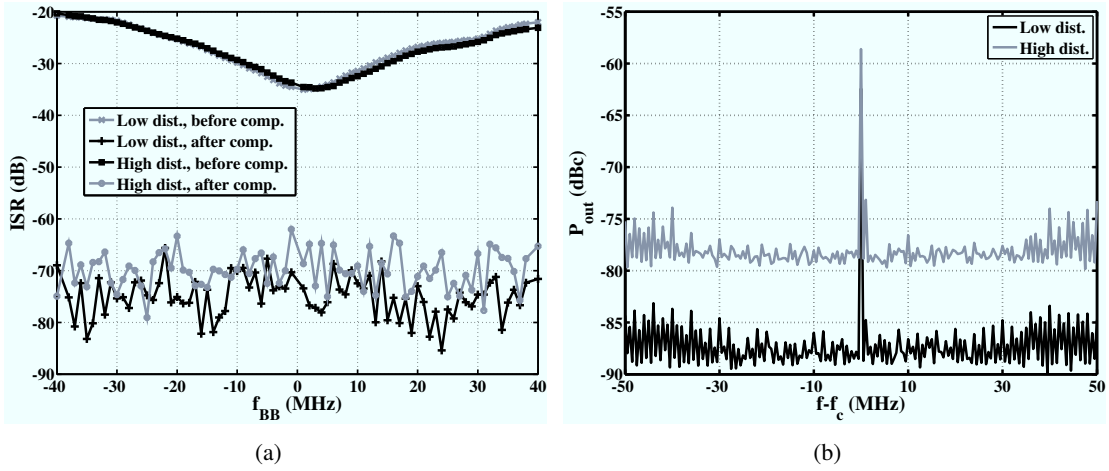
Figure 5.6: (a) ISR of the uncompensated and compensated transmitter and (b) noise floor present during the measurements shown for both operation modes.

sponse was ascribed to $\hat{\theta}_e(j\omega)$ plotted in Figure 5.5(b). By this separation an odd frequency characteristic of $\hat{\phi}_\gamma(j\omega)$ is enforced circumventing the need to distinguish between $\hat{\gamma}(j\omega)$ and $\hat{\gamma}_{\text{Re}}(j\omega)$ as in case of $|\hat{\gamma}(j\omega)|$. The dominant contribution of $\hat{\phi}_\gamma(j\omega)$ is a delay mismatch between the two BB channels. In Figure 5.5(a) only the delay compensated phase response is shown. For the low and high distortion case delays of 6.6 and 6.4 ns, respectively, were determined. These time delay mismatches result in about $9°$ phase difference at the edges of the band.

The ISR of the transmitter with and without imbalance compensation is shown in Figure 5.6(a). In the uncompensated case the imbalance distortion varies between -20 and -35 dB below the carrier. The higher ISR levels at the band edges are due to the delay mismatch of the BB branches. Using the imbalance compensator derived in Section 3.6.3.1 the distortion magnitude can be lowered down to the quantization noise of the DA-converters. The 5 dB reduced ISR performance at the high distortion operation condition can be explained by NL effects interacting with the linear compensator.

To justify the arguments stated above the mean noise floor level during the single-tone measurements is depicted in Figure 5.6(b) relative to the mean single-tone output power. These traces were evaluated by averaging the noise power density over all measurements after canceling the desired tone, the imbalance distortion and the HD$_2$ components. The underlying broadband measurements were performed by the scope in the setup presented in Figure 2.15. In the low distortion case a noise power of -129 dBm/Hz was evaluated. The mean desired signal output power resulted to 6.6 dBm. A SFDR of better 80 dB was evaluated after removing the HD$_2$ distortion. In the high distortion case the noise floor and the mean desired signal power level were calculated to -109 dBm/Hz and 15.3 dBm, respectively. A rise in the noise floor of about 10 dB was observed between the low and high distortion operation mode.

In the receiver case the response onto a single-tone input signal was measured using the setup shown in Figure 2.19. The imbalance parameterization approach discussed in Section 4.7.1 was then applied for deriving the coefficients. The corresponding parameters are presented in Figure 5.7 and 5.8. An even and odd frequency dependency is recognizable at the magnitude and phase of $\hat{\gamma}_{\text{Std.}}(j\omega)$. In contrast to the transmitter case the different levels of $|\hat{\gamma}_{\text{Std.}}(j\omega)|$ at the two operation conditions are remarkable.

Figure 5.7: Magnitude imbalance evaluated for both operation conditions. $\hat{\gamma}_{\text{Std.}}(j\omega)$ identifies the magnitude response evaluated using the analytical approach given by (4.30) to (4.36).

The characterization was also performed at other attenuation settings at the interface board, each one characterized by a different mean value of $|\hat{\gamma}_{\text{Std.}}(j\omega)|$. This behavior is explainable by the analytical coefficient derivation instead of a purely optimization based solution. At the transmitter a magnitude imbalance of one and zero phase imbalance provided the starting point for the minimum search. It is therefore expectable that the corresponding optimum parameters are in the vicinity of the starting points. Such starting conditions are not required at the receiver case using (4.36) for the evaluation.

At the traces representing the phase imbalance in the receiver case no delay correction was applied. The overall phase variation of $\pm 1°$ is still lower as the one of the deskewed transmitter phase response. These lower changes in the phase imbalance are not compensated by larger variations of the mixer phase errors. The magnitude of $\hat{\theta}_e(j\omega)$ is similar for the transmitter and the receiver setup.

The imbalance generated by the uncompensated receiver is highlighted in Figure 5.9(a). The distortion magnitude is approximately constant agreeing to the frequency dependency of the imbalance coefficients. Using the real-valued imbalance compensator derived in Section 4.7.2 the distortion reduction shown by the gray traces with cross- and circular-shaped markers was achieved. As discussed in Section 4.7.3 the real-valued compensation approach cannot distinguish between single-tone input signals provided at $f_{\text{BB}} - f_c$ and $f_{\text{BB}} + f_c$. Treating both cases in the same way forces a real-valued characteristic of $\hat{\gamma}_{\text{Std.}}(t)$. This compensation technique shows similar performance as in the transmitter case in a frequency range close to the carrier only. At $|f_{\text{BB}}| > 10\,\text{MHz}$ significant deviations from the real-valued imbalance characteristic result in a drop of the achievable ISR. A procedure handling also complex-valued $\gamma(t)$ behavior was proposed in Section 4.2 and 4.7.3 by the input signal dependent mapping $\gamma_{\text{map}}(j\omega, R_{\text{RF},g_M})$. Using a minimum search as in the transmitter case $\hat{\gamma}_{\text{Std.}}(j\omega)$ was optimized for maximum distortion reduction over the whole BB bandwidth. This search process initially varied the magnitude and the phase of $\hat{\gamma}(j\omega)$. Finally a combined sweep of both parameters is performed. The optimization result is identified by $\hat{\gamma}_{\text{opt}}(j\omega)$ and represented by the black traces in Figure 5.7 and 5.8(a). For this optimization $\theta_e(j\omega)$ was kept constant. It is interesting to note, that only marginal changes at the phase imbalance were observed. Most of the adaptation was required for the magnitude of gamma.
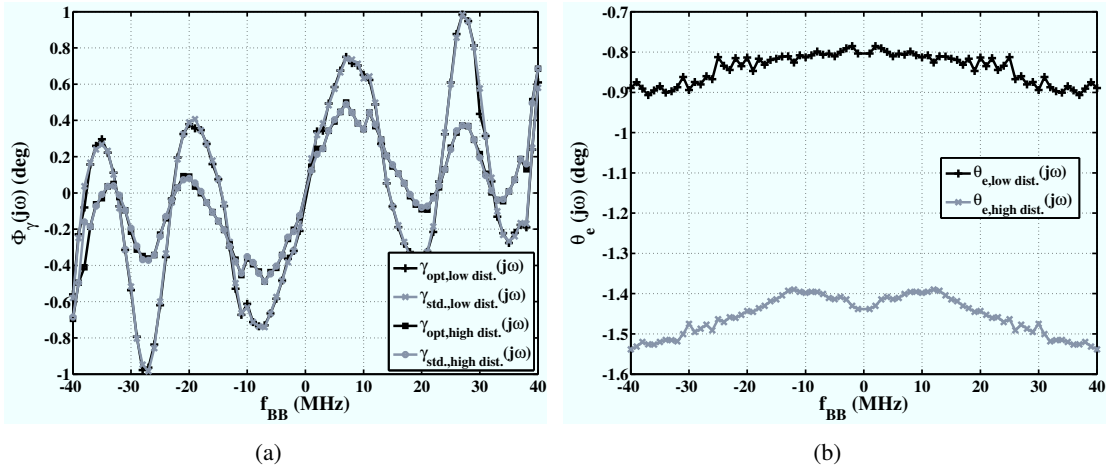
Figure 5.8: (a) Phase imbalance and (b) mixer phase error presented for both operation modes.

Applying $\hat{\gamma}_{\text{opt}}(j\omega)$ together with the enhanced imbalance compensator showed constant magnitude of the residual imbalance distortion over the full BB bandwidth. A mean ISR of -76 dB was evaluated at both operation modes which is again close to the noise floor of the receiver.

This noise floor is analyzed in Figure 5.9(b). In the low distortion configuration a mean noise level of -123 dBm/Hz was recognized. The mean desired tone power at the receiver output was 5.2 dBm indicating an operation approx. 6 dB below the full-scale excitation of the ADC. At the high distortion configuration the mean single-tone output power was 9.8 dBm which corresponds to a full-scale drive of the ADCs. A mean noise floor of -121 dBm/Hz was present at the receiver output. The evaluation of the noise floor was accomplished in the same way as in the transmitter case. At the high distortion receiver response represented by the gray trace in Figure 5.9(b) fluctuations in the noise power level can be recognized. This frequency dependency indicates the presence of additional distortion sources to the imbalance and the HD_2 one which were canceled out. Compared to the transmitter the receiver shows a higher noise floor indicating that the noise figure of the amplifier located after the IQ-mixer output is too high to achieve equal performance at both setups (compare Figure 2.3).

5.3 Characterization and cancelation of spurious emissions

During the characterization of the transmitter shown in Figure 2.21, spurious emissions at $f_m \pm 25$ MHz were recognized. The absolute output power of the spurs compared to the one of the imbalance distortion is shown in Figure 5.10(a). The two traces with the squared- and the star-shaped markers identify the power of the spurs. The power of the imbalance distortion generated by the same input signal is depicted by the dashed line. The level of the spurs is about 10 dB - 20 dB below the one of the imbalance distortion of this transmitter. Due to the characterization of the spurs based on cancelation, the distortion product located at $f_{\text{BB}} - 25$ MHz can be compensated within a frequency range -25 MHz $< f_{\text{BB}} < 50$ MHz. The correction frequency range for the $f_{\text{BB}} + 25$ MHz distortion product is -50 MHz $< f_{\text{BB}} < 25$ MHz. After characterizing and compensating the spurious emissions the power of the distortion is significantly reduced. The frequency responses of the distortion products in these cases are visualized by the traces
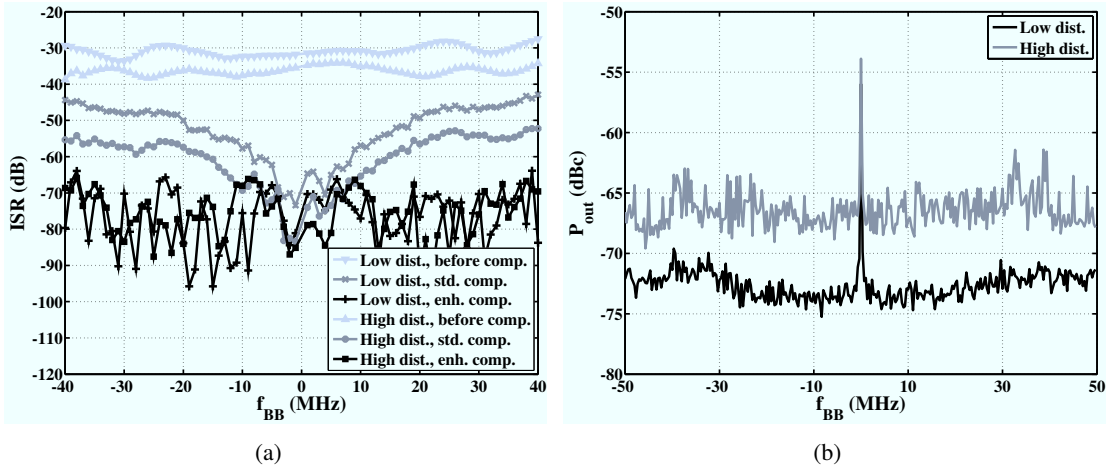
Figure 5.9: (a) ISR of the uncompensated and compensated receiver and (b) noise floor present during the measurements shown for both operation modes.

with the circular and the diamond-shaped markers.

Clearly, the frequency response of the spurious emission magnitude is similar to the power of the image product. For this reason these spurs were treated separately. In both cases the frequency response of $\hat{\alpha}_{\mathrm{spur},v,k}(j\omega_m)$ varies by about ± 3 dB and by $\pm 10°$ over the BB bandwidth. The magnitude variations are quite low compared to the changes in the power of the spurious emissions, which proves the validity of the selected model. Nevertheless, the functions $\hat{\alpha}_{\mathrm{spur},v,k}(j\omega_m)$ were used for describing the behavior of the spurs due to the higher modeling accuracy.
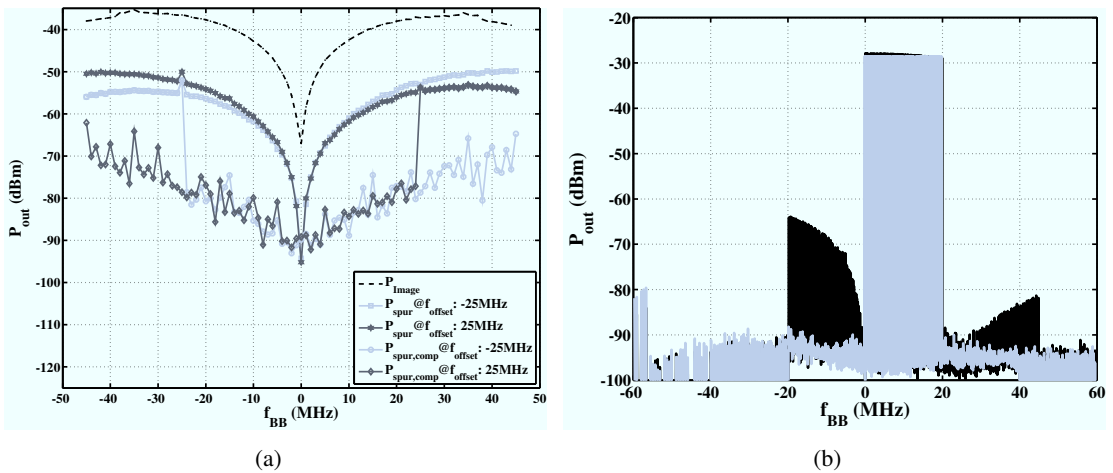
Figure 5.10: (a) Impact of the spurious emissions and (b) original and compensated response of the transmitter presented in Figure 2.21.

Evaluating the performance of the suggested compensator the same transmitter was driven by multi-

tone input signals. Ten different realizations of an odd random phase multi-sine signal [135] were generated, where each realization used a different set of random phases. These signals were composed of 80 tones which covered a bandwidth of 20 MHz. To excite also imbalance distortion the multi-tone signal was frequency-shifted by 10 MHz. The signals showed a PAPR of approx. 7.5 dB. The transmitter response onto each multi-sine signal was measured using the SA. The average over all measured realizations composed the wanted transmitter output signal depicted in Figure 5.10(b). For the uncompensated transmitter the distortion components located between $f_{BB} = -20$ MHz and 0 MHz are caused by the transmitter imbalance. The signal components found between $f_{BB} = 25$ MHz and 45 MHz are mainly due to the spurious emissions. By using the imbalance and the spurs compensator, presented in (3.70) and (3.86), the corresponding distortion effects are removed.

5.4 Nonlinear behavior identification

In this section the results gathered during the NL transmitter and receiver parameterization are summarized. For both configurations different types of two-tone signals are used to excite NL system response. Common to all these measurements is the need for a proper delay and phase extraction to assure a valid parameter identification. The phase extraction results exemplified for the transmitter CBTT measurement are presented in the following section. All other types of two-tone signals can be treated in a similar way but do not require the same effort. Thereafter the parameterization of the static NL model of the RF section is derived for both setups. The polynomial coefficients of the RF NL together with the corresponding two-tone measurements provide the basis for the identification of the BB section. This process is discussed for the transmitter and the receiver separately. In this context also the evaluation of the PCWM filtering functions and the composition of the full model is investigated.

5.4.1 Two-tone phase extraction

As emphasized in Section 3.8.4 and 4.9.3 the delay estimation is performed as first task during the phase extraction. In Figure 5.11 the transmitter delay is derived from a f_m-sweep at several f_{sp} values and vice versa. During the f_m-sweep the frequency range between 2 MHz and 10 MHz was covered in steps of 1 MHz. As shown in Figure 5.11(a) the estimated delay is nearly independent of f_{sp}. Due to the 1 MHz frequency spacing the delay is underestimated significantly based on the same effect as highlighted in connection with Figure 5.2(a). At the f_{sp}-sweep tone spacings between 200 kHz and 1 MHz were measured in steps of 200 kHz. The significantly larger delay identified in this case verifies the suitability of sweeping the tone spacing for the characterization of long time delays.

For the delay evaluation of the FSTT and the CBTT measurements initially a f_{sp}-sweep was performed to derive the transmitter delay. Thereafter, the impact of the delay was compensated from the corresponding measurements. The successful deskewing of the measurement results is proven by evaluating $\hat{\phi}_{sp}$. A deviation of $\pm 0.05°$ from the ϕ_{sp} used for the signal generation was achieved.

In the following the different phase shifts introduced by the transmitter in the high distortion configuration are presented. The dependency of $\hat{\phi}_{BB,I}$ and $\hat{\phi}_{RF}$ on the two-tone center frequency f_m and the mean input power level is visualized in Figure 5.12. At these measurements a tone spacing of 200 kHz was used. The CBTT center frequency was swept in steps of 1 MHz from 1 MHz to 15 MHz and then in steps of 5 MHz up to 40 MHz. At each center frequency a power sweep was performed covering the
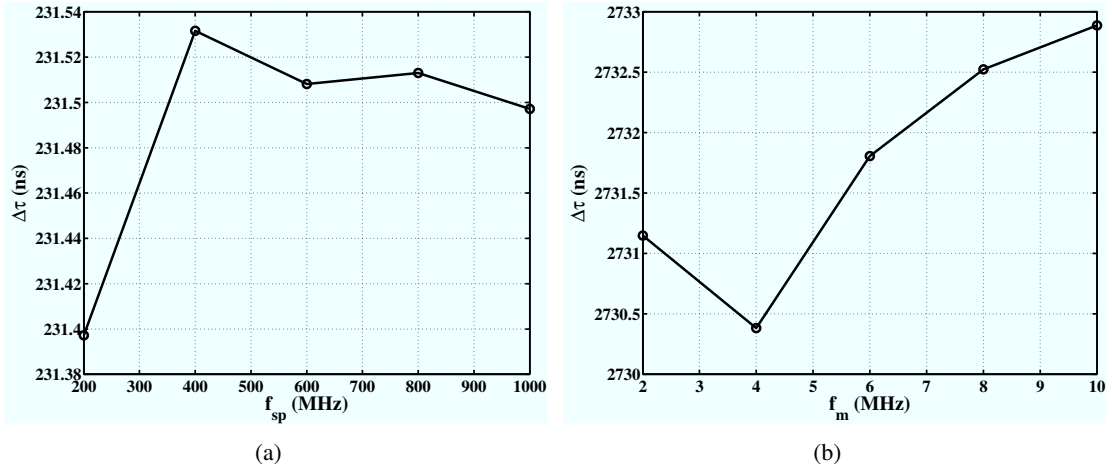
Figure 5.11: Transmitter delay extracted from a two-tone (a) f_m- and (b) f_{sp}-sweep.

input power range between $-12\,\mathrm{dB}$ and $0\,\mathrm{dB}$. The $0\,\mathrm{dB}$ input signal corresponds to a full-scale excitation of the DA-converters. At $-12\,\mathrm{dB}$ back-off from the full-scale input level no NL distortion products were recognizable. The reduced density of the CBTT measurements at higher BB frequencies resulted in a significant drop of the overall measurement duration. At all CBTT measurements ϕ_{sp} was set to zero and ϕ_m to 0 and $180°$. In this way systematic errors in the phase extraction process are detectable. The BB and RF phase shifts were extracted using (3.119) to (3.129).
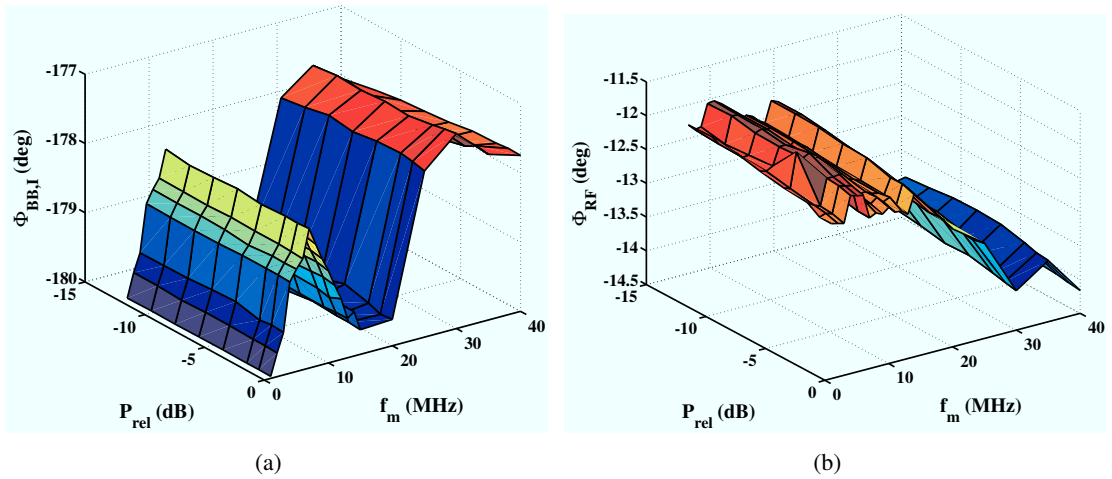
Figure 5.12: (a) $\phi_{\mathrm{BB,I}}$ and (b) ϕ_{RF} extracted from the CBTT power sweep measurements in the high distortion operation mode.

At both phase factors the input power dependent phase variation was in the range of the system measurement errors. At $\hat{\phi}_{\mathrm{BB,I}}$ a $3°$ deviation from $180°$ is observed over the BB bandwidth. At the transmitter model presented in Figure 3.19 $\phi_{\mathrm{BB,I}}$ will be represented by the corresponding BB block.
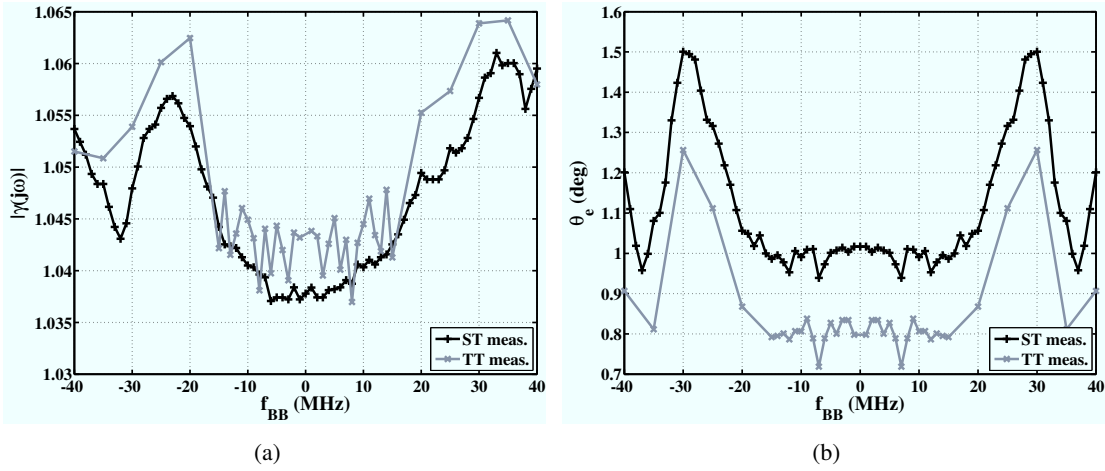
Figure 5.13: Comparison of imbalance parameters (a) $|\hat{\gamma}(j\omega)|$ and (b) $\hat{\theta}_e(j\omega)$ extracted for the single-tone and the CBTT measurements.

The behavior of the RF network is implemented in the memoryless nonlinearity at the transmitter output. This approach results in neglecting the $2°$ phase variation of $\hat{\phi}_{RF}$ over the BB bandwidth. It should be emphasized that only the CBTT measurements are able to provide this information.

Both the BB and the RF phase shift were extracted from the inphase and the quadrature channel measurements. The difference between the linear response of the two BB channels is expressed by $\gamma(j\omega)$. A comparison of the magnitude of $\hat{\gamma}(j\omega)$ derived from the single-tone measurements as shown in Figure 5.4 and the CBTT ones is shown in Figure 5.13(a). A mean deviation of 1.0032 between the two traces is observed. As the CBTT measurements performed power sweeps at each f_m consecutively for both channels slight drifts in the measurement setup may be responsible for the variation of the CBTT $|\hat{\gamma}(j\omega)|$ in the frequency range below 15 MHz. At higher frequencies the 5 MHz distance between the measurement frequencies masks this behavior. Comparing the phase imbalance no offset between the two measurement results was present. The standard deviation of the different $\hat{\phi}_\gamma$ over the considered bandwidth is at $0.03°$.

The mixer phase error derived from the single-tone and the CBTT measurements is compared in Figure 5.13(b). Here, an offset of $-0.2°$ is observed. Despite of this offset the shape of the two traces is very similar. During the transmitter imbalance characterization using the single-tone excitation the presence of NL distortion effects was neglected. At the CBTT imbalance parameter extraction the coefficients were derived from the desired signals only. Hence, NL effects are less critical as during the image distortion cancelation process.

After combining NL and imbalance compensation (discussed in Section 5.5) a tuning of the imbalance coefficients was required to regain the full imbalance compensation performance. For this tuning it was sufficient shifting the imbalance parameters by an offset indicated by the differences between the single-tone and the CBTT identification results.
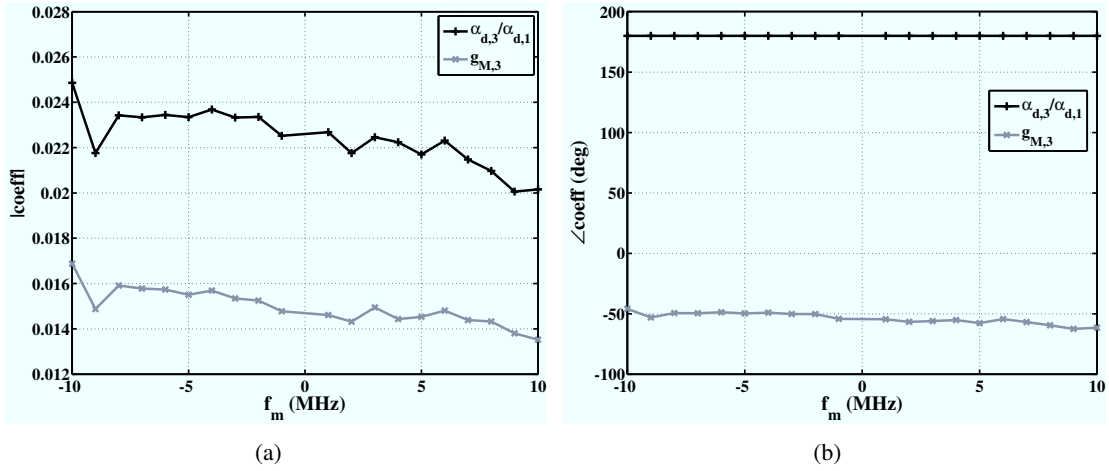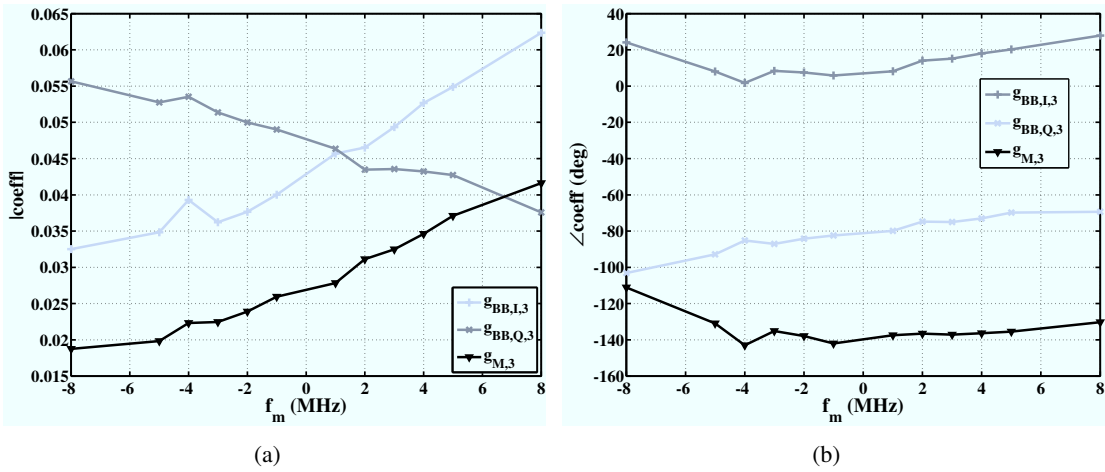
Figure 5.14: (a) Magnitude and (b) phase of the transmitter output NL coefficient $\hat{g}_{M,3}$ and the corresponding normalized BB parameter $\hat{\alpha}_{d,3}/\hat{\alpha}_{d,1}$ evaluated at the high distortion operation mode.

5.4.2 RF nonlinearity behavior parameterization

In the transmitter case FSTT power sweep measurements performed close to the carrier are used for the RF nonlinearity extraction. In principle only one power sweep would be sufficient for the parameter identification. Allowing to analyze the frequency dependency of the derived coefficients the FSTT power sweeps were accomplished between $-10\,\text{MHz}$ and $10\,\text{MHz}$ in steps of $1\,\text{MHz}$. The same values for ϕ_{sp} and ϕ_m as mentioned in the last section were used. Also the same input levels for the power sweep were applied.

Based on these measurements the linear and NL baseband amplifier response is estimated up to the third-order based on the desired tones and the HD$_3$ distortion as described in Section 3.8.5. The frequency dependency of the normalized third-order parameter $\hat{\alpha}_{d,3}/\hat{\alpha}_{d,1}$ implementing the BB amplifier behavior is shown in Figure 5.14 exemplified for the high distortion operation condition. An approximately constant magnitude of this parameter is observed over the selected frequency range. At this identification task the BB amplifier behavior is assumed to be AM-PM free. The resulting NL coefficient phase is only allowed to be zero or $180°$ selected by minimizing the error function (3.143).

Based of $\hat{\alpha}_{d,1}, \hat{\alpha}_{d,3}$ the gain and IMD of the BB section is calculated and incorporated into the RF nonlinearity characterization. The linear gain of this third-order memoryless polynomial is set to unity. The frequency progress of the corresponding $\hat{g}_{M,3}$ coefficient is also depicted in Figure 5.14. The shape of its frequency dependent behavior is similar to the normalized NL BB parameter. The mean over the considered frequency range was used as outcome of the extraction process. Based on the normalized input signal magnitude an IP$_{3,\text{output}}$ of 45 dBm and 34 dBm was evaluated for the low and high distortion operation mode. The corresponding intercept points for the measured output power levels are 40 dBm and 39 dBm. Both values are in close agreement to the IP$_3$ of the transmitter driver amplifier (40 dBm) specified in Section 2.1.

Using the extracted BB and the mean RF coefficients the complex-valued output tone amplitudes can be calculated and compared to the measured transmitter response. In this way a NMSE of $-52\,\text{dB}$

and $-39\,\text{dB}$ was achieved for the low and high distortion operation conditions. Considering only the distortion products the corresponding $\text{NMSE}_{\text{dist.}}$ resulted to $-9\,\text{dB}$ and $-13\,\text{dB}$. The low $\text{NMSE}_{\text{dist.}}$ in the low distortion operation mode visualized the difficulty of accurate distortion modeling in highly linear systems.

The drawback of the mixer output NL characterization, the AM-PM free modeling of the BB amplifier behavior is compensated by the postidentification process. After the BB amplifier models have been extracted the correct input signal to the mixer output NL can be calculated and the corresponding coefficient can be extracted. This information is used to get an improved RF NL identification.

In the receiver case FSTT power sweeps provide the basis for the complete NL extraction. The input signal generation using two synchronized single-tone sources was described in Section 2.3. The scope in the measurement setup shown in Figure 2.19 enables the measurement of the phases of the input tones. From this information $\hat{\phi}_{sp,\text{P}_K}$ and $\hat{\phi}_{m,\text{P}_K}$ are calculated. The frequency range $-40\,\text{MHz} \leq f_m \leq 40\,\text{MHz}$ was covered by the FSTT measurements. For $|f_m| \geq 20\,\text{MHz}$ and $5\,\text{MHz} < |f_m| < 20\,\text{MHz}$ steps of $5\,\text{MHz}$ and $3\,\text{MHz}$ were performed, respectively. Below $5\,\text{MHz}$ the power sweep was accomplished in steps of $1\,\text{MHz}$. Again a $200\,\text{kHz}$ tone spacing was selected for the measurements.

For each configuration the input power level corresponding to a full-scale excitation of the ADCs was evaluated at a frequency close to the carrier. The power sweep covers a range of $12\,\text{dB}$ back-off from this level. The sweep was accomplished in steps of $2\,\text{dB}$.

(a)   (b)

Figure 5.15: (a) Magnitude and (b) phase of the receiver input NL coefficient $\hat{g}_{M,3}$ and the corresponding BB parameters $\hat{g}_{\text{BB,I}}, \hat{g}_{\text{BB,Q}}$ evaluated at the high distortion operation mode.

Based on these prerequisites the measurements were performed. For the RF input NL extraction the power sweeps located within $|f_m| \leq 8\,\text{MHz}$ were selected. As described in Section 4.9.4 the NL behavior of the two BB sections are evaluated based on the HD_3 response. A unity linear gain is set for the corresponding polynomials. The magnitude and phase of $\hat{g}_{\text{BB,I,3}}$ and $\hat{g}_{\text{BB,Q,3}}$ are presented in Figure 5.15. Compared to the transmitter case no restrictions on the BB amplifier phase were imposed at this identification step. A larger frequency dependency in both magnitude and phase is observed at the receiver parameters $\hat{g}_{\text{BB,I,3}}$ and $\hat{g}_{\text{BB,Q,3}}$. These parameters provide the basis for the postdistortion and the parameterization tasks. A normalized third-order polynomial describes the RF input NL behavior. The

corresponding parameter $\hat{g}_{M,3}$ is also depicted in Figure 5.15. By averaging over the covered frequency range the memoryless RF input NL coefficients are extracted.

Based on the normalized input signal magnitude an $IP_{3,\text{output}}$ of 45 dBm and 32 dBm was evaluated for the low and high distortion case, respectively. The corresponding input intercept points based on the measured input power levels are 15 dBm and 22 dBm. Compared to the transmitter case a significant deviation of the two values is recognized. Taking a closer look at the postdistorted tone magnitudes large variation of the IMD distortion products is found in the low distortion configuration. Due to these uncertainties an underestimation of the linearity performance of the RF input NL occurred. In the high distortion case the derived IP_3 is larger than the one evaluated by two-tone measurements of the mixers. This independent two-tone characterization evaluates the behavior of the full mixer. It may not be compared to the one derived now which covers only RF section performance.

For evaluating the modeling accuracy the calculated response based on the evaluated RF coefficients and the postdistorted tone amplitudes are compared. In this way a NMSE of -33 dB and -29 dB was achieved. The distortion NMSE resulted to -3 dB and -12 dB for the low and the high distortion operation mode. The small value of $\text{NMSE}_{\text{dist.}}$ in the low distortion case is another result of the uncertainties in the magnitude of the distortion products applied for the parameter extraction. The overall lower performance compared to the transmitter case can be ascribed to the increased frequency dependent behavior of the parameters observed at the receiver.

5.4.3 Transmitter baseband nonlinearity characterization

The mixer output NL coefficients and the CBTT measurements are required to proceed with the BB parameterization. The mixer parameters configure the postdistorter which calculates the tone amplitudes present at the output of the inphase and quadrature channel as discussed in Section 3.8.6. A comparison of the IMD_3 measured at the transmitter output together with the deembedded results is presented in Figure 5.16. This IMD performance was evaluated in the high distortion operation mode at the maximum input power level. The NL behavior excited by the CBTT signal shows a slightly higher distortion level at the quadrature than at the inphase channel. After the mixer output NL deembedding an increased IMD_3 level is recognized for both BB channels. Hence, some part of the distortion generated in the RF section counteracts the one of the two BB channels. After the postdistortion process the distance between the IMD levels observed at the two BB channels is reduced.

The deembedding tone amplitudes up to third-order are thereafter used for identifying the polynomial coefficients describing the BB amplifier behavior. This task is performed for each of the measured power sweeps separately. The magnitudes of the resulting parameters are summarized in Figure 5.17. The difference between the two linear responses shown in Figure 5.17(a) corresponds to the magnitude imbalance introduced by the BB section as well as by the filtering of the transmitter RF network. Only the real-valued system representation of the complex-valued RF section imbalance can be expressed here. Due to this reason it is advisable compensating the imbalance expressed by the linear BB response and model it independently. As discussed in Section 3.8.7 the compensation of the imbalance modeling in the BB section is accomplished during the calculation of the corresponding PCWM parameters. The same approach was also suggested for the receiver as discussed in Section 4.9.7.

The frequency response of the even- and odd-order NL parameters are depicted in Figure 5.17(b). In both cases a higher distortion magnitude is observed at the quadrature channel. These coefficient values correspond to an IP_2 and IP_3 of 59 dBm and 33 dBm at the inphase and of 59 dBm and 32 dBm at the
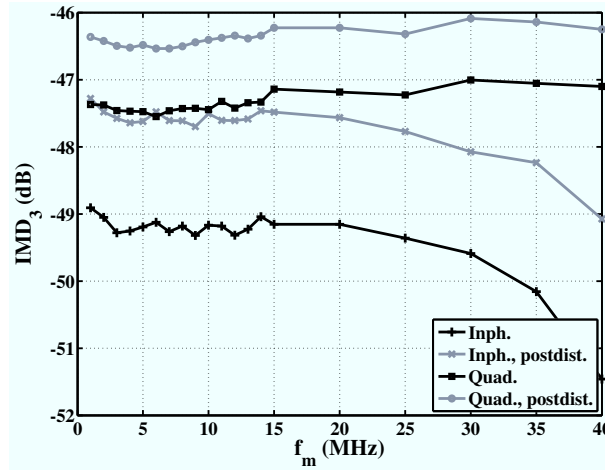
Figure 5.16: Comparison of the IMD before and after the postdistortion process of the inphase and quadrature channel at full-scale excitation.
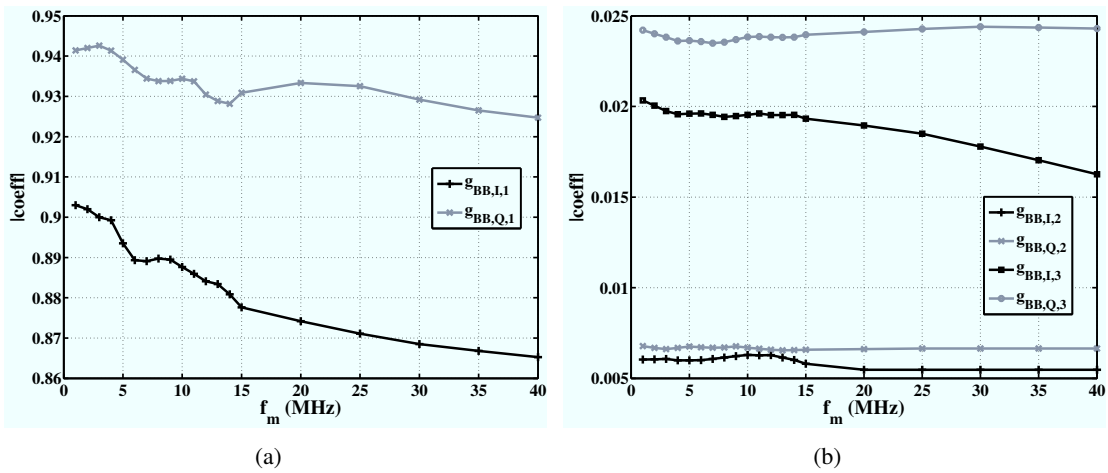

Figure 5.17: Magnitude of the (a) linear and (b) NL polynomial coefficients of the BB section evaluated at the high distortion operation mode.
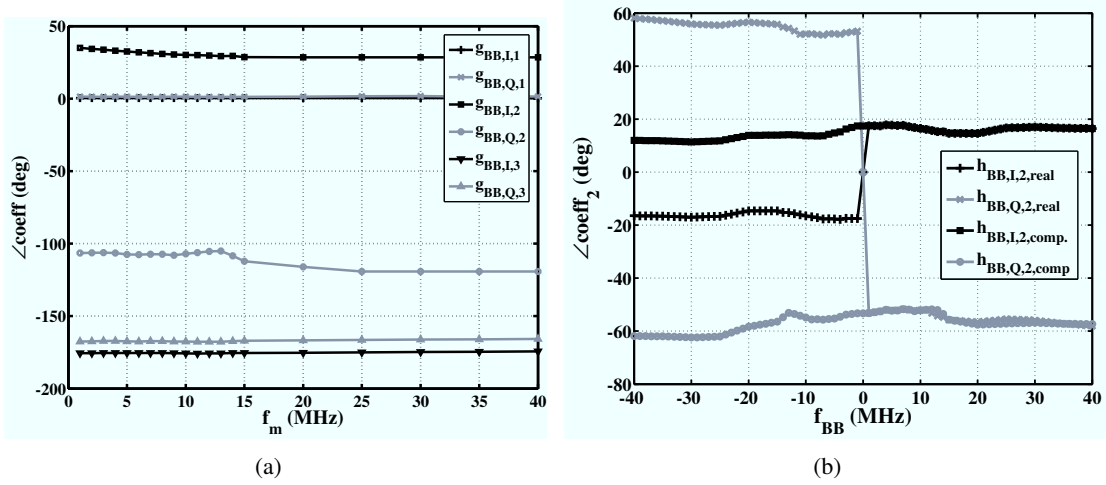
Figure 5.18: (a) Phases of the polynomial BB coefficients. (b) Real- and complex-valued implementation of the 2nd-order PCWM parameters. Both results were extracted for the high distortion operation mode.

quadrature channel for the normalized input amplitude. The 3rd-order input intercept point derived for the corresponding mixer input power level results to $19\,\text{dBm}$ agreeing roughly to the specified mixer performance. As mentioned in the last section a slightly higher IP_3 value of the model was anticipated accounting for the NL distortion generated in the RF section.

In the low distortion case the IP_2 and IP_3 derived using the normalized input signal result in $70\,\text{dBm}$ and $42\,\text{dBm}$ at the inphase and in $69\,\text{dBm}$ and $41\,\text{dBm}$ in the quadrature channel case. The corresponding $IP_{3,\text{input}}$ based on the actual power levels in the setup are at $10\,\text{dBm}$. Here, the deviation of the linearity performance of the actual amplifier mixer cascade is even larger.

The phases of the identified BB coefficients in the high distortion case are presented in Figure 5.18(a). The second and third-order quadrature channel parameter response agree to the progress exemplified in Figure 3.17(a) while discussing the PCWM implementation issues at the transmitter. The phase of the linear coefficients are below $2°$ for both channels. These values implement the difference between the phases of the deembedded tones and the parameter $\hat{\phi}_m(j\omega)$ evaluated from the CBTT measurements.

The progress of the third-order coefficients $\hat{g}_{\text{BB,I,3}}, \hat{g}_{\text{BB,Q,3}}$ are close to $180°$ for $\text{f}_m \rightarrow 0$. They can be forced to show exactly $180°$ at DC with only a little loss of modeling accuracy. As stated in Section 3.8.10 this condition is required for a real-valued implementation of the corresponding PCWM parameters. A different situation is found at the second-order coefficients. Their real- and complex-valued implementation is presented in Figure 5.18(b). As shown in Figure 3.17(b) the real-valued implementation of the corresponding PCWM parameters did not agree to the frequency response of the HD_2 distortion generated by the FSTT input signal.

To highlight the modeling performance the difference between the response predicted by the BB coefficients and the deembedded tone amplitudes is calculated. A NMSE of the BB section derived by the polynomial model of $-28\,\text{dB}$ and $-29\,\text{dB}$ for the I- and the Q-channel was evaluated in the high distortion operation mode. For the even- and odd-order NL response a $\text{NMSE}_{\text{dist.}}$ of better $-22\,\text{dB}$ and $-17\,\text{dB}$ is observed for both channels. In the low distortion case the polynomial model showed a NMSE

of -51 dB and -49 dB for the inphase and quadrature channel. A NMSE$_{\text{dist.}}$ of better -14 dBm and -5 dB was calculated for the even- and odd-order NL behavior prediction.

For the transition of the polynomial model to the PCWM filtering functions a real-valued implementation of the odd-order response was used. The imbalance was described by an extra block in the complete model. Based on these prerequisites the ability of the full transmitter model in representing the measured CBTT and FSTT response was evaluated. A NMSE of -33 dB and -35 dB was achieved for the low and high distortion operation mode. After the mixer output NL postidentification these values improved to -44 dB and -37 dB.

5.4.4 Receiver baseband nonlinearity characterization

The evaluation of the BB coefficients for the receiver case requires the RF input NL parameters as well as the FSTT measurements. A discussion of this identification process and a presentation of the frequency response of the extracted coefficients for the receiver working in high distortion operation mode is given in Section 4.9.7. The second-order coefficients are depicted in Figure 4.11. The ones extracted from the HD$_2$ measurements showed an IP$_2$ of better 58 dBm and 55 dBm in the low and high distortion operation mode, respectively. These results were achieved based on the normalized input signal power level. Interestingly, the IP$_2$ corresponding to the second order response located around DC showed a value of better than 54 dBm in the high distortion case, slightly below the HD$_2$ based one. In the low distortion case an IP$_{2,\text{DC}}$ of better than 62 dBm is observed indicating an opposite behavior compared with the high distortion case.

The IP$_3$ calculated from the IMD and the HD$_3$ distortion based on the normalized input signal was at least 36 dBm and 39 dBm in the high distortion case. The corresponding coefficients are exemplified in Figure 4.10. In the low distortion configuration an IP$_{3,\text{IMD}}$ and IP$_{3,\text{HD}}$ of better than 44 dBm and 34 dBm was evaluated. At the two operation conditions the normalized receiver output signal is roughly equal. Hence, it is interesting to note, that an IP$_{2,\text{HD}}$ and an IP$_{3,\text{HD}}$ of similar magnitude was observed, while the IP$_{2,\text{DC}}$ and the IP$_{3,\text{IMD}}$ diverge significantly.

Calculating the IP$_{3,\text{IMD}}$ corresponding to the measured receiver output signal magnitude at the ADC inputs results to 24 dBm in the high distortion case. This value is significantly below the one anticipated from the link budget presented in Table 2.3. The measured signal based IP$_{3,\text{HD}}$ is 4 dB higher but still too low. The IP$_{3,\text{IMD}}$ derived for the measured ADC magnitude in the low distortion case of about 33 dBm agrees to the ones used for the link budget calculation. At this operation mode the IP$_{3,\text{HD}}$ of 24 dBm indicates a higher distortion level than expected.

The different values of the IMD$_3$ and HD$_3$ distortion magnitudes don't follow the behavior observed at weakly nonlinear systems. Despite of the input signal level the only difference between the low and high distortion configuration is the step-attenuator setting at the interface board. Assuming that the IMD generated in the RF is partly compensated by the one introduced in the BB section may explain this behavior. To validate this assumption, measurements at the preamplifier output and at the interface board input would be required. By analyzing the IMD$_3$ and the HD$_3$ at the different stages of the receiver structure any cancelation of the different signal components could be identified. Due to a lack of time this task was not accomplished.

As a result of the observed odd-order distortion behavior an alignment of the IMD$_3$ and HD$_3$ by a RF input NL reevaluation, as described in Section 4.9.7, was not accomplished. Instead, an own set of polynomial coefficients was used for each of them. The same approach was also used at the second-order

distortion mechanism.

Comparing the coefficients representing the NL transmitter and receiver response, depicted in Figure 5.17, 4.10, and 4.11, a significantly larger frequency dependency of the receiver parameters is observed. The complex-valued PCWM implementation of the 2nd-order transmitter response can be interpreted as analogy to the receiver case. Here, due to the missing information on the receiver input signal at the BB section, the signal dependent mapping of the corresponding filtering functions was introduced. This technique guaranteed a real-valued output signal of the BB amplifier models despite of the complex-valued characteristic of the applied PCWM parameters. At the transmitter the chosen solution is more relaxed. The complex-valued output signal of the two BB amplifier models doesn't matter much, as long as the output signal of the transmitter is correctly predicted. Interestingly, a similar approach failed to work at the receiver, was mentioned in Section 4.9.7.

The modeling accuracy of the receiver BB coefficients is evaluated similar to the transmitter case. A NMSE of better than $-34\,$dB and $-33\,$dB was achieved for the low and high distortion operation mode. The even- and odd-order distortion modeling in the high distortion configuration was better than $-15\,$dB and $-16\,$dB. The corresponding $\text{NMSE}_{\text{dist.}}$ in the low distortion operation mode resulted to $-11\,$dB and $-4\,$dB. As for the RF NL extraction the BB section distortion modeling accuracy in the receiver case is below the one of the transmitter. Only a better representation of the linear response was derived at the receiver.

After extracting the BB coefficients and the prefilter representing the linear response, the PCWM filtering functions are derived and the full receiver model is composed. Again, an own block in the model will be used for modeling the imbalance effects. The full model is then used to predict the receiver response for the FSTT input signal. A NMSE of better than $-32\,$dB and $-31\,$dB was achieved. Some loss of accuracy is recognized at the transition from the polynomial coefficients to the corresponding PCWM filtering functions. Simulations showed that the application of the input signal dependent mapping technique is not responsible for this decrease.

5.5 Transmitter and receiver compensation

To validate the performance of the presented parameter extraction approach the transmitter was driven by different multi-tone signals. Using the derived model the undesired behavior should be compensated. Similar to Section 5.1 the phases of the multi-tone signals were selected using the Newman algorithm [134] minimizing the resulting PAPR. In this way the average output power is increased and a better excitation of the NL behavior is provided.

In Figure 5.19(a) two measurements of the uncompensated transmitter operating in the high distortion configuration mode are presented. Both input signals are composed of 40 tones covering 40 MHz bandwidth. These signals are characterized by a PAPR of 2.5 dB. To excite imbalance distortion the signals are shifted by $\pm20\,$MHz occupying either the frequency range above or below the carrier. A transmitter output power of 12.5 dBm was measured for both excitations. The observed imbalance distortion agrees with the performance evaluated by the single-tone measurements shown in Figure 5.6(a). After applying the imbalance compensator the ISR is lowered down to $-51\,$dB. This result is approximately 13 dB above the ISR level observed during the single-tone measurements.

To evaluate this limited imbalance compensation performance when operating with multi-tone signals, measurements with different compensator configurations were performed. The ISR achieved by
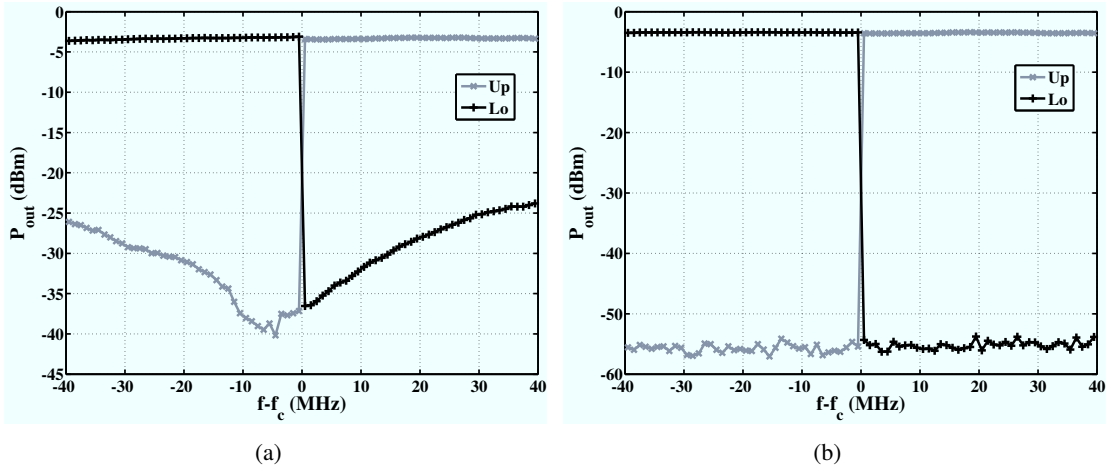
Figure 5.19: (a) Uncompensated and (b) imbalance compensated transmitter response onto two multi-tone input signals. The measurements were performed in the high distortion operation mode.
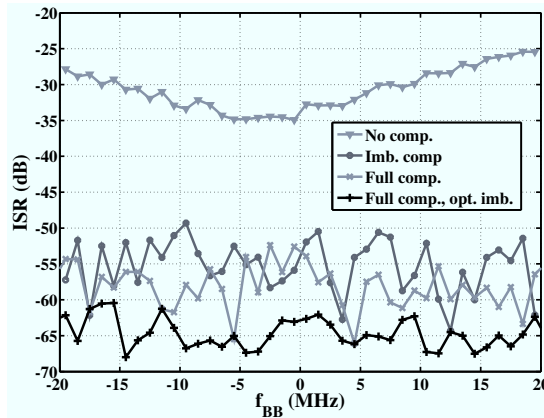

Figure 5.20: Comparison of the transmitter imbalance for different compensator configurations excited by multi-tone excitation signals.

these measurements is summarized in Figure 5.20. Allowing a better NL distortion compensation the input signal bandwidth was reduced to 20 MHz while keeping the tone spacing. Using only the imbalance compensator an ISR of about -54 dB was achieved. A combined operation of imbalance and NL distortion compensation improves this result to -57 dB. After a scaling of $|\hat{\gamma}(j\omega)|$ by a constant factor and introducing a constant offset to $\hat{\theta}_e(j\omega)$ the full compensator lowered the imbalance suppression to a similar level as observed during the single-tone measurements. The selected approach for the imbalance parameter tuning was indicated during the phase extraction of the CBTT measurements (compare Figure 5.13). The requirement for this manipulation is explained by the single-tone imbalance characterization process, which cancels the imbalance component without taking care of the NL transmitter behavior.

A comparison of the transmitter operating in the high and low distortion configuration is shown in

(a)   (b)
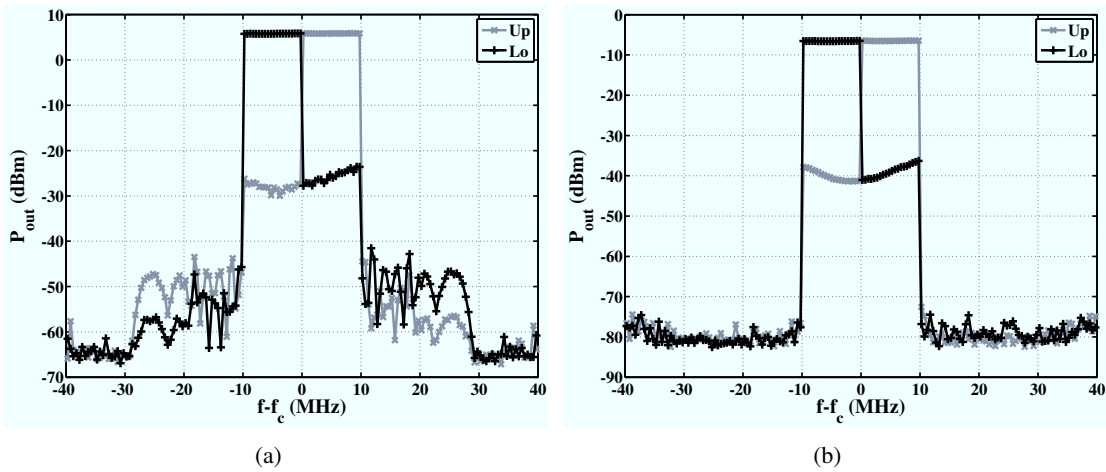
Figure 5.21: (a) High and (b) low distortion operation mode of the uncompensated transmitter driven by a narrowband multi-tone signal.

Figure 5.21. An output power of $18.9\,\mathrm{dBm}$ and $6.1\,\mathrm{dBm}$ at the corresponding operation condition was measured. By reducing the bandwidth to $10\,\mathrm{MHz}$ the areas for the second- and third-order harmonics are distinguishable. The input signals were composed of 20 tones. Again a PAPR of $2.5\,\mathrm{dB}$ was selected. At the high distortion mode the NL distortion products are about $53\,\mathrm{dB}$ below the level of the desired tones. As predicted by (3.50) the HD_3 located at the spectrally mirrored frequencies is higher than the one located at three times the input frequency. Interestingly, the same response is recognized for the HD_2 signal components. This behavior is not directly derivable from the static NL BB amplifier description. At the low distortion measurements only some slight indications of NL products above the noise floor can be observed.

The impact of the imbalance compensation under this excitation is visualized in Figure 5.22. In the high distortion configuration the imbalance distortion is reduced down to the level of the NL signal components. The imbalance parameters used in this case were not optimized for a combined operation with the NL predistorter. In the low distortion operation mode a mean ISR level of $-62\,\mathrm{dB}$ is recognized indicating a similar performance as for the single-tone measurements. Thereafter the measurements were repeated applying both the linear and NL compensation. These results are summarized in Figure 5.23. At both operation modes a drop of the transmitter output power by $0.7\,\mathrm{dB}$ was measured. For the high distortion case the mean ISR was lowered to $-64\,\mathrm{dB}$. A reduction of the dominant HD_2 and HD_3 signal components located at the spectrally mirrored frequencies by $10\,\mathrm{dB}$ is observed. The NL distortion located at twice or three times the input tone frequencies, respectively, were not lowered by the same amount. These distortion products set the limit for the achieved SFDR of $60\,\mathrm{dB}$. In the low distortion case the usage of the full compensator did not result in any significant improvements. The mean ISR is now at $-63\,\mathrm{dB}$. The SFDR of $62\,\mathrm{dB}$ stayed the same as compared to the usage of the imbalance compensation alone.

In summary the presented transmitter compensator comprehensively reduced all types of distortion generated by the custom built direct conversion transmitter setup. Using the transmitter in the high distortion operation mode together with the full compensator shows the same SFDR as the imbalance
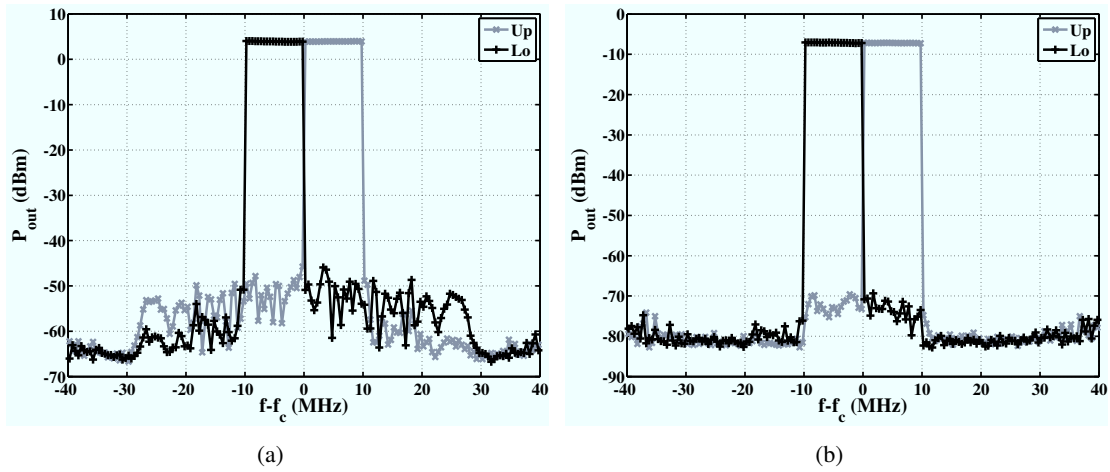
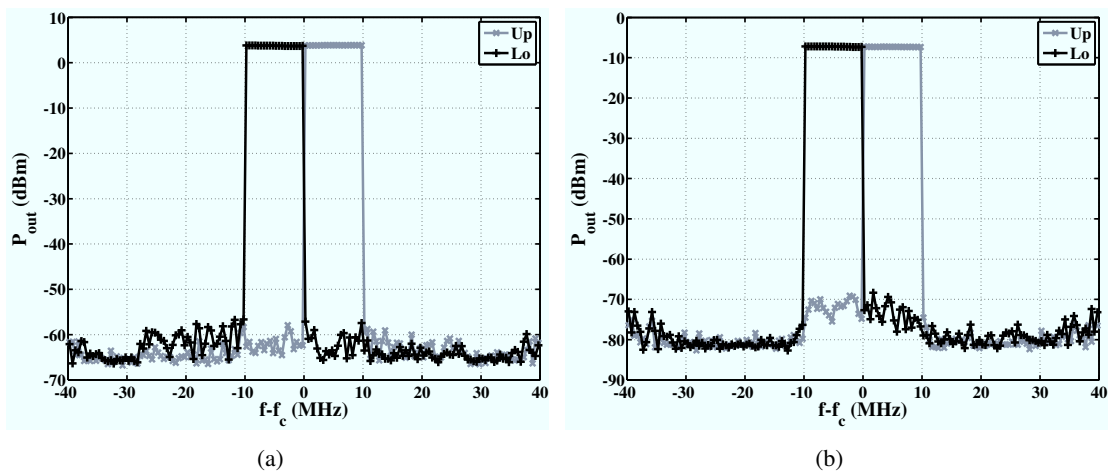Figure 5.22: (a) High and (b) low distortion operation mode of the imbalance compensated transmitter.

Figure 5.23: (a) High and (b) low distortion operation mode of the fully compensated transmitter.

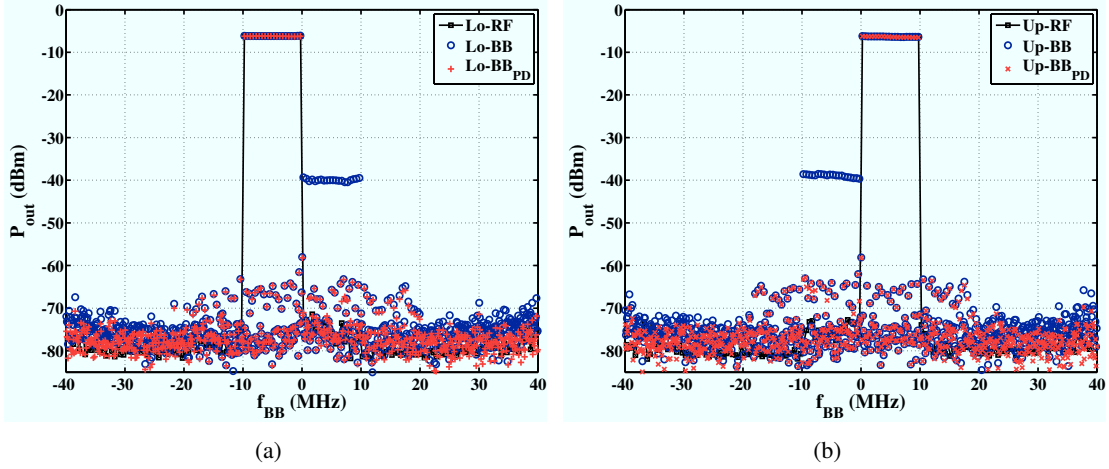(a)   (b)

Figure 5.24: Receiver response on a narrowband multi-tone input signal shifted (a) below and (b) above the carrier. In these plots the black traces in the background show the measured transmitter output signal. The traces with the blue circular and red cross-shaped markers represent the receiver output signal before and after the imbalance postcompensation.

compensated low distortion transmitter. The equivalent performance was achieved at a $13\,\mathrm{dB}$ higher output power level.

The compensated transmitter output signal was also applied to the direct conversion receiver. In this way the behavior of the receiver and of the postdistorter was analyzed. The response of the receiver in the low distortion operation mode onto the narrowband transmitter output signals is summarized in Figure 5.24. Here, the desired tone magnitudes of all measured signals was aligned to the one generated by the imbalance postcompensator. The uncompensated receiver output signal is represented by the circular markers. Using the imbalance postcompensator the ISR is reduced from $-33\,\mathrm{dB}$ to $-63\,\mathrm{dB}$. Compared to the transmitter case a recognizable NL content is observed at the receiver output signal.

The availability of the complex-valued BB signals at the receiver output allows the quantification of the transmitter and receiver performance using the NMSE. For this task also the transmitter output signal was measured using the SA and the scope at the measurement setup. The RF signal was captured covering the $80\,\mathrm{MHz}$ bandwidth around the carrier using a tone spacing of $500\,\mathrm{kHz}$. Each of these tones was compared in magnitude and phase to the corresponding FFT bins of the BB input signal. For this task the delay observed in the RF was evaluated and compensated. Additionally, using a complex-valued constant, the mean gain deviation and phase shift was removed. The modified NMSE used for the performance evaluation in this case is given by:

$$\mathrm{NMSE}_{\mathrm{RF}} = \frac{\sum\limits_{\mathrm{f}} \left(V_{\mathrm{meas.}}(\mathrm{f}) - V_{\mathrm{BB}}(\mathrm{f})\right)^2}{\sum\limits_{\mathrm{f}} V_{\mathrm{BB}}^2(\mathrm{f})} \tag{5.1}$$

In this expression the summation over f includes all considered signal components. The function $V_{\mathrm{meas.}}(\mathrm{f})$ represents the spectral components derived from the SA and scope measurements. Using (5.1) a $\mathrm{NMSE}_{\mathrm{RF}}$ of $-42\,\mathrm{dB}$ was evaluated for the transmitter in low distortion operation. Applying the same approach a
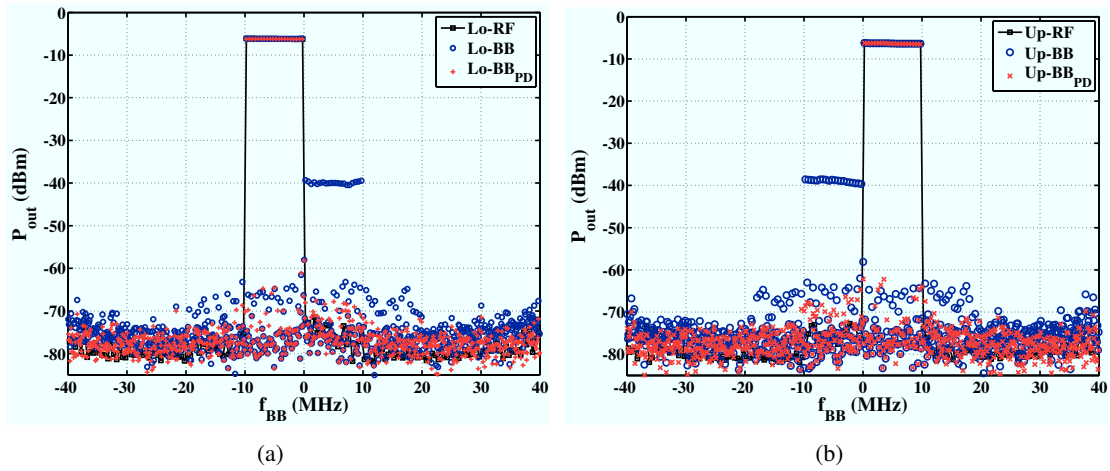
Figure 5.25: Receiver response on a narrowband multi-tone input signal shifted (a) below and (b) above the carrier. The blue and red traces represent the receiver output signal before and after the full postdistorter.

NMSE$_{\mathrm{RF}}$ of $-32\,$dB was derived for the uncompensated receiver response in the low distortion mode. A comparison of the transmitter input signal with the uncompensated receiver output resulted in a drop of the NMSE of 1 dB. Also for this evaluation the delay mismatch as well as a constant gain and phase offset between the two signals was compensated.

After performing the imbalance postcompensation the NMSE$_{\mathrm{RF}}$ and the deviation from the transmitter input signal were derived. In this case a NMSE$_{\mathrm{RF}}$ of better than $-40\,$dB was calculated. Again the NMSE accomplished from the BB signals was 1 dB lower.

The same receiver output signals were also filtered by the full postdistortion algorithm. The corresponding response is presented in Figure 5.25. By the combined usage of imbalance and NL distortion compensators the mean ISR improved by -3 dB. By the same amount the HD$_2$ signal components were lowered. In this way a SFDR of 58 dB is observed at the receiver output. Due to the low magnitude of the compensated distortion the NMSE compared to the transmitter input signal did only improve by 0.1 dB.

The same receiver was also used to measure the response of the transmitter operating in the high distortion mode. As expressed by the SFDR the NMSE$_{\mathrm{RF}}$ is equal in both operation modes.

Finally, measurements of the low distortion transmitter driving the receiver in high distortion configuration were performed. The response of the receiver onto the multi-tone signal located above the carrier is depicted in Figure 5.26. At these measurements a wrong configuration ruined the results for the multi-tone signal located below the carrier. Due to a lack of time these measurements could not be repeated.

For the actually presented measurement the switching between the low and high distortion transmitter configuration resulted in a rise of the generated imbalance distortion by mistake. To gain some information from this measurement the imbalance parameters at the receiver were adopted to compensate for the imbalance effects of the transmitter receiver cascade. In this way the mean ISR observed at the postdistorter output was at $-66\,$dB. Using the NL compensator the HD$_2$ and IMD components were lowered by $8\,$dB and $12\,$dB, respectively. Overall a SFDR of 59 dB was accomplished. Comparing the
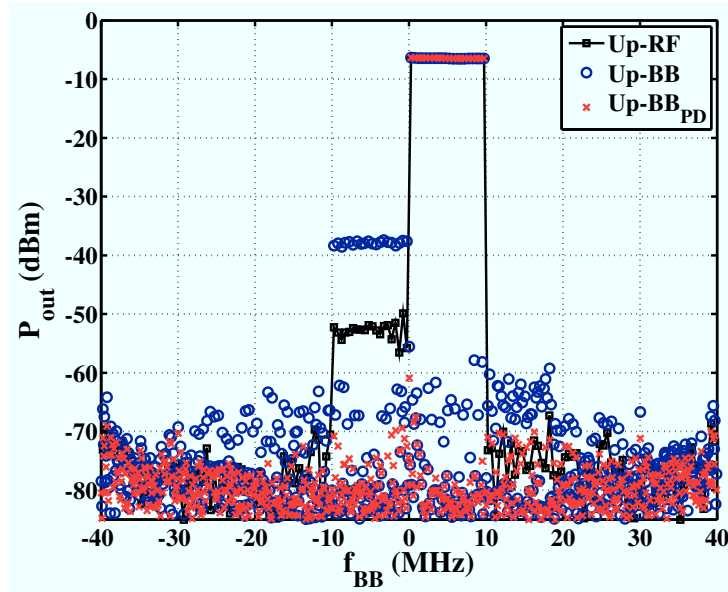
Figure 5.26: Receiver response operating in the high distortion mode with and without full postcompensation.

transmitter input and the postdistorter output signal a NMSE of -44 dB was achieved.

A summary of the different NMSE values derived from the transmitter and receiver measurements is given in Table 5.1. These results correspond to the fully compensated response for each operation mode. At highly linear systems only slight deviations in the linear response may cause an error which completely covers the NL effects. Therefore, the NMSE was reevaluated while aligning the desired tones to the ones of the reference signal. The corresponding $\text{NMSE}_{\text{Gain equalized}}$ is also summarized in Table 5.1. For both approaches a higher NMSE of the receiver operating in the high distortion mode in relation to the low distortion one is observed when comparing the two BB signals. This result may be ascribed to the low NL modeling accuracy observed in the low distortion configuration. Hence, an error is introduced during the NL compensation which degrades the NMSE. This relationship is not revealed when using the RF measurements for the NMSE calculation. Due to the significantly lower number of tones in relation to the samples of the BB signals the NL behavior is less accurately represented.

	NMSE (dB)			$\text{NMSE}_{\text{Gain equalized}}$ (dB)		
	$BB \rightarrow RF$	$RF \rightarrow BB$	$BB \rightarrow BB$	$BB \rightarrow RF$	$RF \rightarrow BB$	$BB \rightarrow BB$
Tr_{LD} & Re_{LD}	-42	-40	-39	-60	-56	-50
Tr_{HD} & Re_{LD}	-42	-41	-44	-58	-56	-47
Tr_{LD} & Re_{HD}			-44			-52

Table 5.1: NMSE and $\text{NMSE}_{\text{Gain equalized}}$ calculated from the different input and output signals of the transmitter and receiver.

Chapter 6

Summary

Direct conversion transmitter and receiver concepts are important for realizing modern mobile communication systems. Their major advantage is the structural simplicity making them attractive for high level integration while allowing a flexible RF frequency selection. These benefits are confronted by limitations imposed by the non-ideal characteristics of the analog components implementing the concepts. Within this work algorithms were developed to characterize and compensate the behavior of direct conversion transmitters and receivers enabling a high performance operation of the corresponding structures.

In the transmitter case the development of the algorithms was started by analyzing the behavior of the underlying structure theoretically. The outcome of this task was a Volterra model representing the different distortion mechanisms introduced by the direct conversion configuration. Additionally, an analysis of the variations of the mean gain introduced by changes of the phase of single- or two-tone signals was performed. It was proven that imbalance as well as odd-order NL distortion introduce these PM-AM and PM-PM conversion effects if a DC-symmetrical two-tone signal is applied. Perfectly equalizing the two branches of a direct conversion transmitter will cancel the input phase dependency introduced by the imbalance distortion mechanism. However, the phase dependent gain variations caused by the odd-order harmonic distortion will still be present.

For the characterization and parameterization of the transmitter its behavior was partitioned in distinguishable distortion mechanisms. For each mechanism an approach was derived to characterize its response. Care was taken to keep the interactions with other distortion effects low. A LS minimization was found as optimum solution for canceling the DC-offset. In case of the imbalance distortion and the LO spurious emissions the response onto a single-tone input signal was measured. The desired parameters were found by minimizing the amplitude of the distortion component at the output signal. For this purpose the magnitude and phase of the coefficients parameterizing the corresponding compensator are swept consecutively until the desired distortion suppression ratio is accomplished.

The characterization approach for the NL transmitter behavior uses measurements of the response onto FSTT and CBTT power sweeps. The FSTT input signal excites IMD generation at the BB and the mixer output NL. The odd-order harmonic distortion is only caused in the BB part of the transmitter. The different magnitudes of these two distortion products allow deriving the characteristic of the mixer output NL. Thereafter, the corresponding coefficients are applied to postdistort the measured CBTT response and evaluate the signal present at the input of the mixer output NL. By accomplishing this step all information required for the identification of the frequency dependent NL behavior of the BB section

are available. To successfully apply this methodology for the parameter extraction of the NL transmitter behavior a careful preprocessing of the measurement results is required. This preprocessing includes the power normalization, the delay estimation and the extraction of the phase shifts introduced in the BB and the RF part of the transmitter. For the parameterization of the nonlinearities the transmitter response onto a FSTT and a CBTT signal was derived analytically. Combining the modeled and measured signal magnitudes and phases the coefficients describing the considered NL behavior can be evaluated using the LS technique. For measurement results acquired at a highly linear operation mode of the transmitter a modification of the classical LS approach was required. Despite its low magnitude the errors introduced during the measurement of the desired tones resulted in larger NL coefficient magnitudes as required by the NL distortion effects. Hence, a separated treatment of the linear and NL coefficients is required to overcome this behavior. This procedure was named "optimized LS". The transition of the polynomial parameters of the BB nonlinearities identified for each frequency point independently to the corresponding PCWM filtering function finalizes the NL transmitter extraction. Based on the design of the parameter identification process the linear response of the BB section can always be represented by PCWM filtering functions showing a real-valued time domain progression. At the NL distortion coefficients such "real-valued" PCWM filtering functions may result in an improper modeling of the transmitter behavior. Hence, a complex-valued time domain progression of the corresponding filtering functions may be required. This fact resulted in a significant rise of the complexity of the predistorter for the BB section. To verify the correctness of the implemented parameter extraction algorithm extensive simulations of the transmitter response were performed under varying operation conditions. Using these results the parameters were identified and compared to the ones used for the simulations. In this way the influence of the different NL parameters and the measurement noise on the resulting model accuracy was identified.

The availability of the coefficients derived from the different distortion mechanism allows composing the model and the compensator of the full transmitter. As the different distortion effects were characterized independently only the ones providing a significant contribution to the transmitter behavior will be included. The same set of coefficient is used to parameterize the model and the compensator of the transmitter.

As at the transmitter case the algorithm development at the receiver was started by analyzing the behavior of the underlying structure. This structure is composed of a memoryless RF input NL, ideal mixers and the BB section showing a frequency dependent NL behavior. One of the most important findings of this work is that, despite of the complexity of the underlying structure, it was not possible representing all aspects of the behavior derived from the measurement results. If an input signal is applied with a frequency offset below or above the carrier the impact of the BB section should be the same in both cases. This behavior is caused by processing only real-valued signals at the BB. Measurements showed that the output signal of the BB branches were scaled differently for both cases. Hence, the purely real-valued characteristic of the receiver BB section had to be extended to represent this behavior. For this task a dependency on the original complex-valued input signal to the receiver was introduced while assuring the real-valued characteristic of the output signal of the BB section. Using an input signal dependent mapping of the complex-valued filtering function to its real-valued correspondent meets these demands. This behavior had to be introduced for the imbalance calculation as well as for deriving the NL BB response. The corresponding modifications to the underlying structure were summarized by the term "enhanced" linear and nonlinear model.

To characterize the receiver behavior the partitioning in distinguishable distortion mechanisms was performed analogous to the transmitter case. The extraction process of the imbalance coefficient applied

an analytical solution for deriving the parameters showing a real-valued progression in the time domain. Their complex-valued correspondent was found using an optimization approach. For the suppression of the imbalance distortion a postcompensator was developed able to handle coefficients showing a real-valued progression. To handle also the complex-valued ones the input signal dependent mapping technique was applied. For the evaluation and cancelation of the LO spurious emissions the same approach as in the transmitter case was used.

The evaluation of the NL receiver behavior is derived from power sweep measurements of the FSTT signal only. In a first step the power normalization, delay extraction and phase shift identification was performed. Analyzing the magnitude of the intermodulation and the odd-order harmonic distortion from these measurements an initial description of the BB nonlinearities was derived. Using the preliminary models the signal present at the output of the RF NL was calculated. Combining the input and output signal of this NL its parameters were extracted. These coefficients allow calculating the input signals at the two BB nonlinearities and deriving the parameters of the BB section. Based on the frequency dependence of the BB coefficients the decision is drawn if the extended NL model must be applied. This decision influences the transition of the polynomial parameters of the BB nonlinearities to the corresponding PCWM filtering functions. At that time the need for a separate modeling of the intermodulation and harmonic distortion is also investigated. The postcompensator for the BB section must be able to operate with coefficients corresponding to the normal as well as the extended NL model. The NL interaction required for the distortion suppression are the same in both cases. The usage of the extended NL description results in an increased complexity for the calculation of the corresponding NL responses.

After all required distortion mechanisms are parameterized the model and the compensator of the full receiver is composed. The same considerations as in the transmitter case apply also here.

For testing the performance of the presented algorithms a custom hardware platform was developed. A flexible configurability was mandatory for its design. In this way a linear and nonlinear operation of the transmitter and receiver is supported. The central device of the setups was the sampler card providing the AD and DA converters and the control circuitry for the external amplifiers and DC-offset sources. The sampler card is remotely accessed by the host-PC. The driver amplifier for the ADCs and DACs were designed for 40 MHz bandwidth. Within this range the passband ripple was below 0.3 dB. The magnitude imbalance between the two BB channels was below 0.2 dB. A SFDR of at least 70 dB was achieved for the driver amplifier at the receiver when operating the ADCs 2 dB in back-off. The BB section at the transmitter branch is able to generate two-tone signals up to 5 dBm output power. At this power level the 70 dB SFDR is accomplished over the full bandwidth.

At the receiver a low noise wideband preamplifier is required. This 25 dB amplifier is characterized by a 0.1 dB bandwidth of 50 MHz. At 50 Ω input impedance the generated DC-offset is below 300 μV. An $IP_{3,output}$ of better than 32 dBm is achieved over the BB bandwidth at both channels.

The output of the transmitter and the receiver input signal were characterized in magnitude and phase. For this task measurement results of a random sampling scope, a spectrum analyzer, and a power meter were combined. A concept was developed assuring a proper phase alignment of the traces recorded by the random sampling scope to the signals generated and measured by the sampler board, respectively. Using this concept the phase drift stayed below $10°$ over a time period of 25 minutes. The short time phase variation was below $0.2°$. These results were derived for a two-tone signal at a center frequency of 3.5 GHz showing 200 kHz tone spacing.

Using the measurement setup the behavior of the transmitter and receiver was characterized and the parameters were extracted. For both configurations a high and a low distortion mode were considered.

Focusing on the imbalance distortion only the transmitter and receiver were driven by single-tone input signals. In the transmitter case the ISR performance was improved by at least 28 dB by the imbalance compensator. The residual imbalance distortion was more than 62 dB below the desired tone being close to the magnitude of the output noise. The imbalance postcompensation in the receiver case resulted in a reduction of the distortion of at least 32 dB. The residual distortion magnitude was more than 66 dB below the desired output signal.

To highlight the performance of the full transmitter and receiver compensators multi-tone signals covering 10 MHz bandwidth were used. These signals were shifted by ± 5 MHz occupying the frequency range above or below the carrier. The phases of the multi-tone signal were optimized showing a PAPR of 2.5 dB. At the linearized high distortion operation mode of the transmitter an output power of 18.2 dBm was measured. In this configuration a SFDR of better than 60 dB was observed. In the low distortion configuration the transmitter delivered an output power of 5.4 dBm. In this case the compensator accomplished a SFDR of more than 62 dB.

The linearized transmitter output signals were also applied to the receiver. A SFDR of 58 dB and 59 dB was accomplished in the low and high distortion configuration using the full postcompensator.

For a combined operation of the direct conversion transmitter and receiver a $\text{NMSE}_{\text{Gain equalized}}$ of at least -47 dB was evaluated. These results are among the best known by the author for a hardware with equivalent specification. This performance was accomplished without any averaging as usually required.

6.1 Outlook

Despite trying to provide comprehensive algorithms for the parameterization and compensation of direct conversion transmitters and receivers several tasks could not be carried out in the framework of this thesis:

Algorithm development using an updated transmitter and receiver structure:
The models and compensators were developed based on the structure of the direct conversion transmitter and receiver. It must be admitted, that despite of the efforts put into a proper modeling of both setups further improvements of the model structure are required. Especially at the receiver case the input signal dependent mapping technique was implemented allowing an accurate prediction of the measured receiver response. An improved model structure should be able to achieve a similar performance level while avoiding the usage of such enhanced signal processing techniques. The experiences gathered by developing an updated receiver model may also be applied at the transmitter avoiding a complex-valued output signal from the real-valued BB section.

Extraction of parameters characterizing the transmitter imbalance:
The extraction of the imbalance parameters in the transmitter case uses an iterative approach. It was proven that this process provides the parameters required for an imbalance distortion reduction down to the noise level. The simplicity and robustness of the suggested parameter extraction comes at the cost of a time consuming search process. Using a measurement of the transmitter response in magnitude and phase a one step derivation of the imbalance parameters should be possible. Using such an approach it would be interesting to investigate if an analytical coefficients calculation results in different combinations of the parameters $\gamma(j\omega)$ and $\theta_e(j\omega)$ as compared with those derived by the search process.

Receiver imbalance compensator:

The actual version of the receiver imbalance compensator uses an input signal based mapping of the complex-valued $\gamma(t)$ to its real-valued correspondent for a reduction of the imbalance distortion down to the noise level. An iterative imbalance compensation approach similar to Section 3.6.3.2 should be able to achieve a similar performance without the usage of spectral averaging. Additionally, the evaluation of the imbalance coefficients could be derived without the real-valued $\gamma(t)$ assumption. Such a solution would avoid the optimization procedure used to acquire the magnitude and phase imbalance $\gamma_{\mathrm{opt}}(j\omega)$.

The mixer output NL extraction process at the transmitter case:

The presented mixer output NL extraction approach assumes an AM-PM free BB amplifier behavior. The BB section characterization showed that this assumption may be violated. Of course it can be argued, that the RF NL postidentification overcomes this limitation. Yet an update of the identification procedure dropping this prerequisite may result in a better identification performance.

Predistortion linearization of power amplifiers:

The usage of a compensated transmitter and receiver should enhance the performance of PA linearization based on the predistortion technique. Due to a lack of time such measurements could not be performed. It would be interesting to evaluate the performance improvements with and without transmitter and receiver compensation. In the literature several discussions on the direct conversion transmitter imbalance of PA predistortion can be found. An evaluation of the receiver distortion impact on the predistortion linearization behavior should be performed.

Appendix A

Amplifier boards schematics

The schematics of the interface board are presented in Figure A.3 to A.9. The ones of the preamplifier circuitry are shown in Figure A.10 to A.12. Pictures of the interface and the preamplifier board are shown in Figure A.1 and A.2.
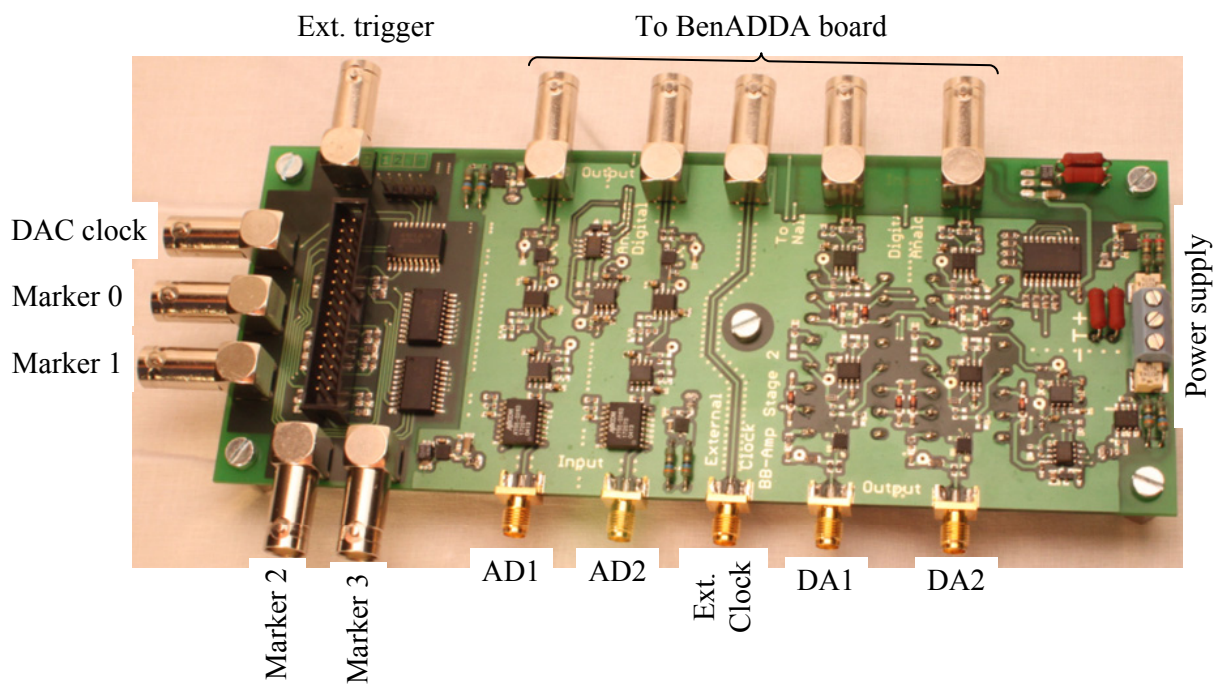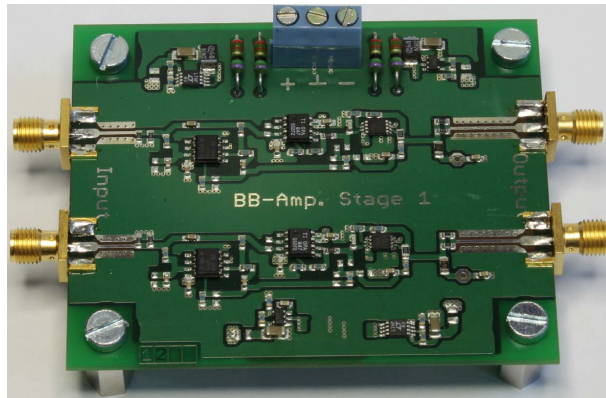

Figure A.1: Picture of the interface board.

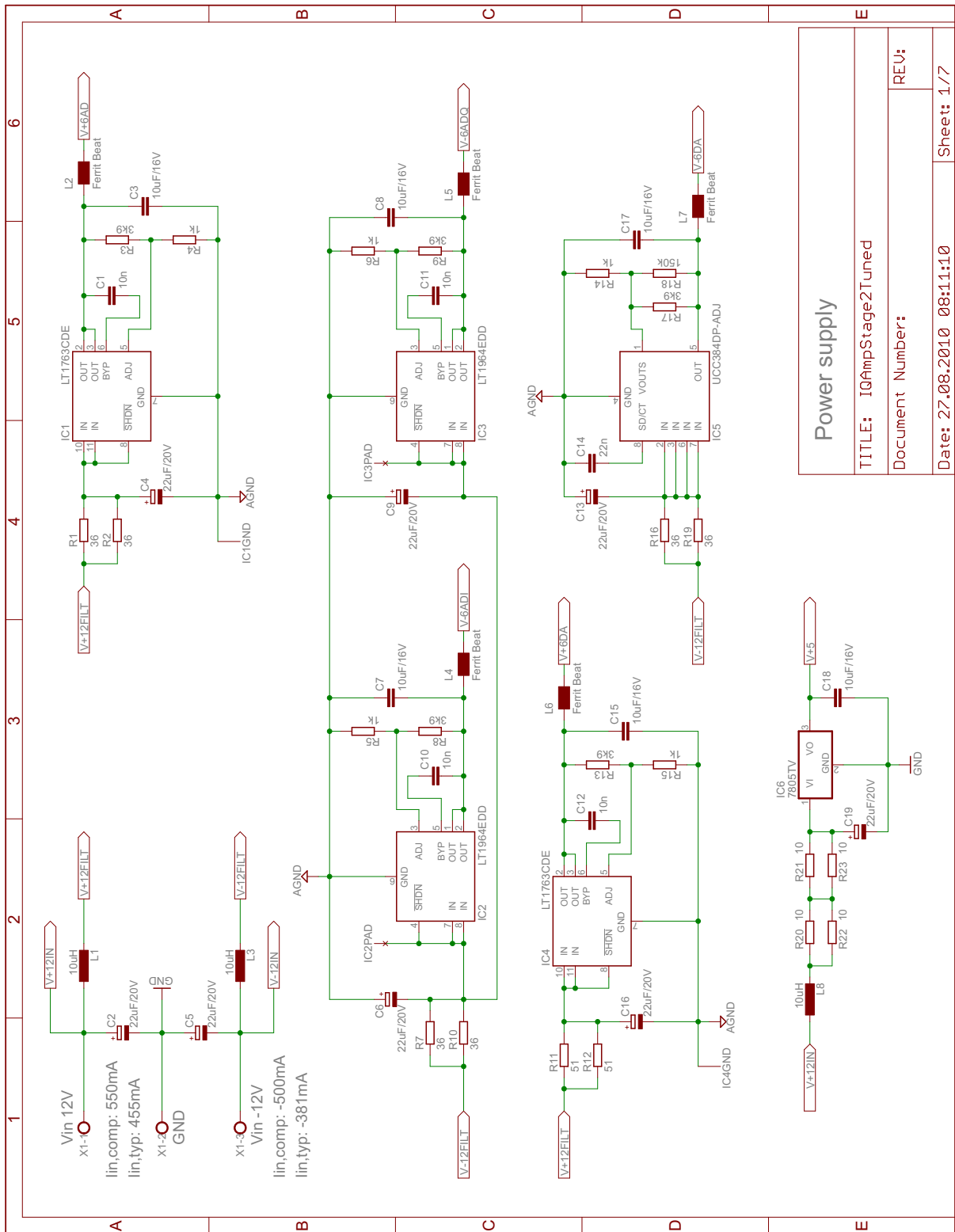Figure A.2: Picture of the preamplifier board.

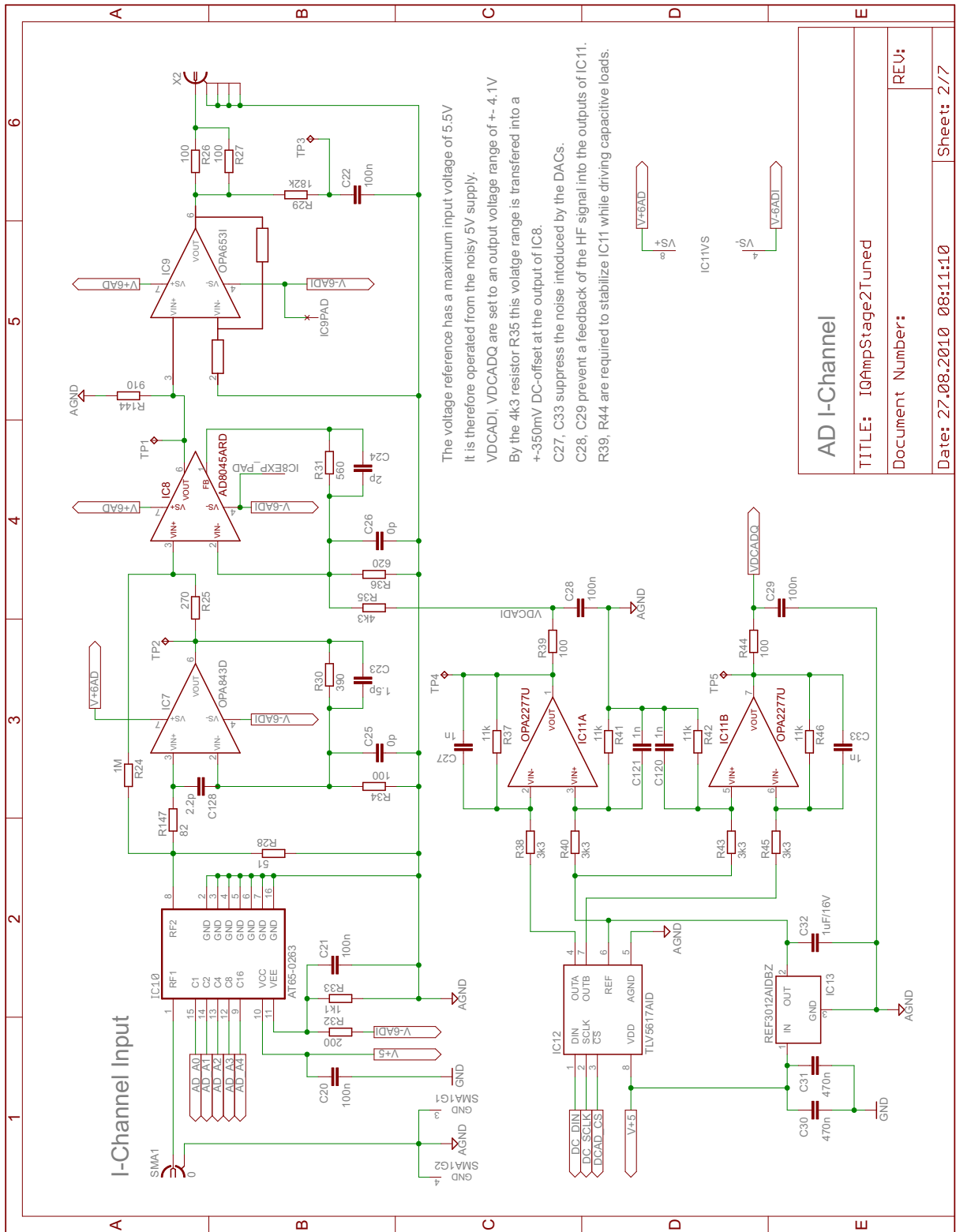Figure A.3: Schematic of the interface board, power supply unit.

Figure A.4: Schematic of the interface board, AD conversion, inphase channel including DC-offset generation.
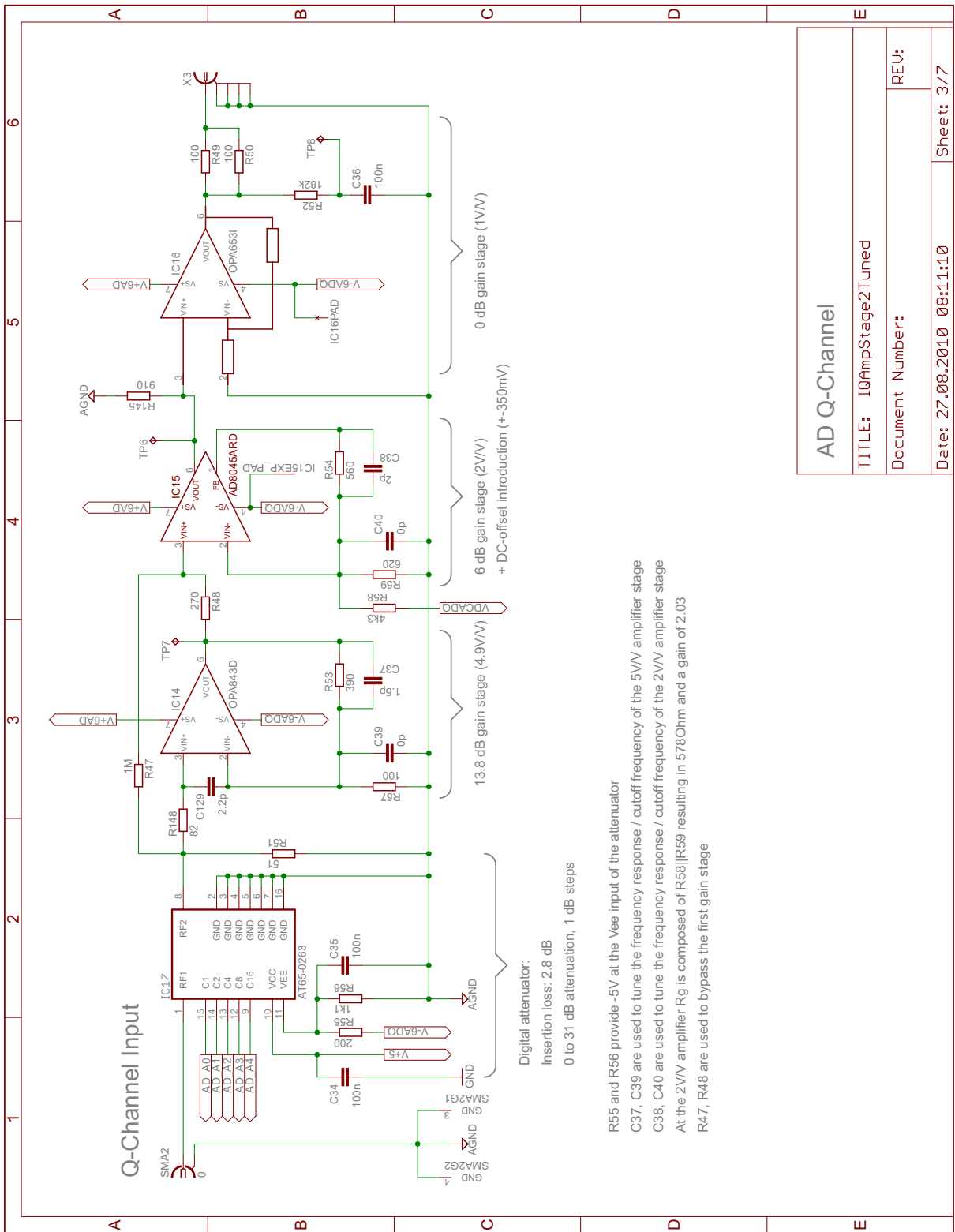
Figure A.5: Schematic of the interface board, AD conversion, quadrature channel.
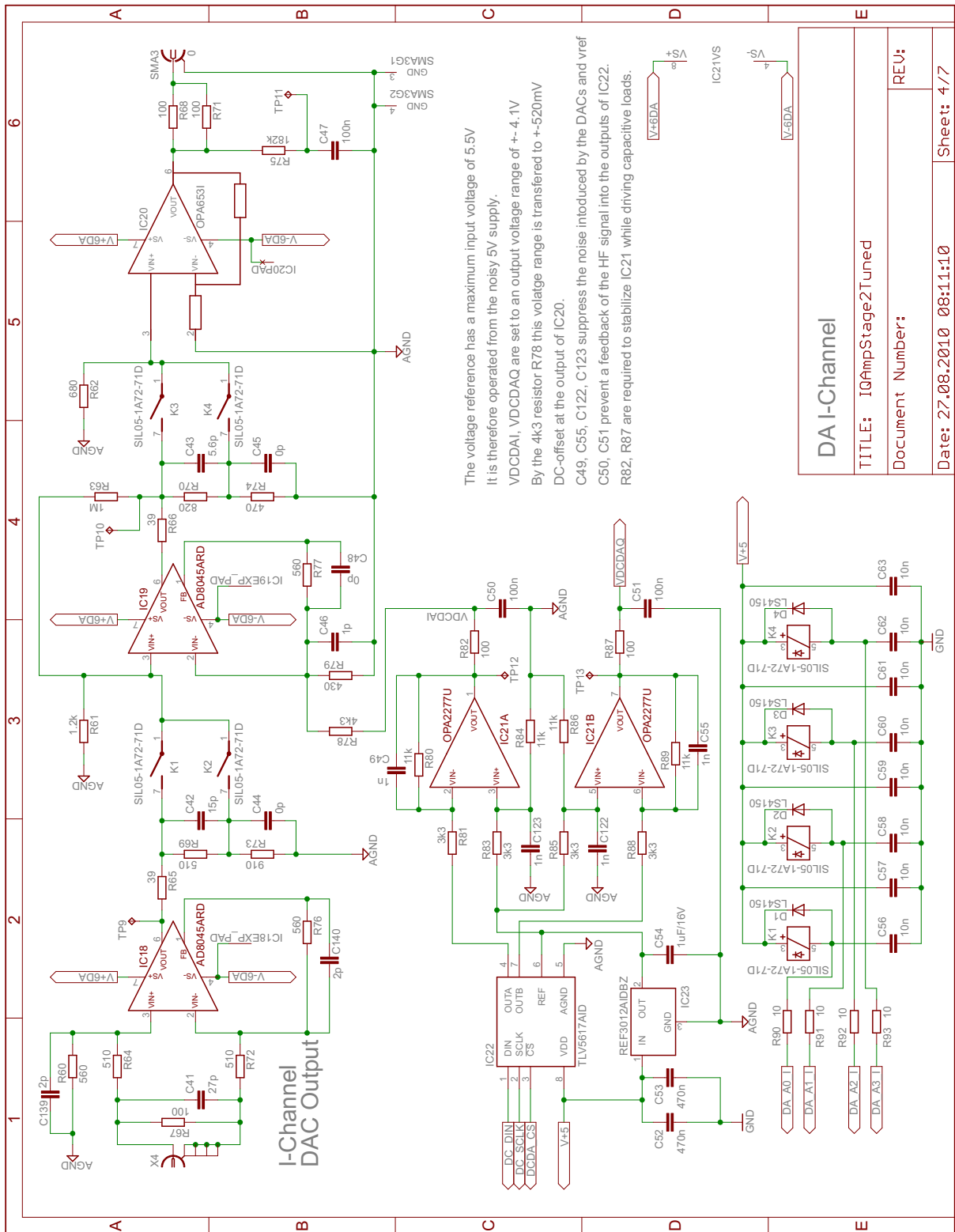
Figure A.6: Schematic of the interface board, DA conversion, inphase channel including DC-offset generation and reed contact control.
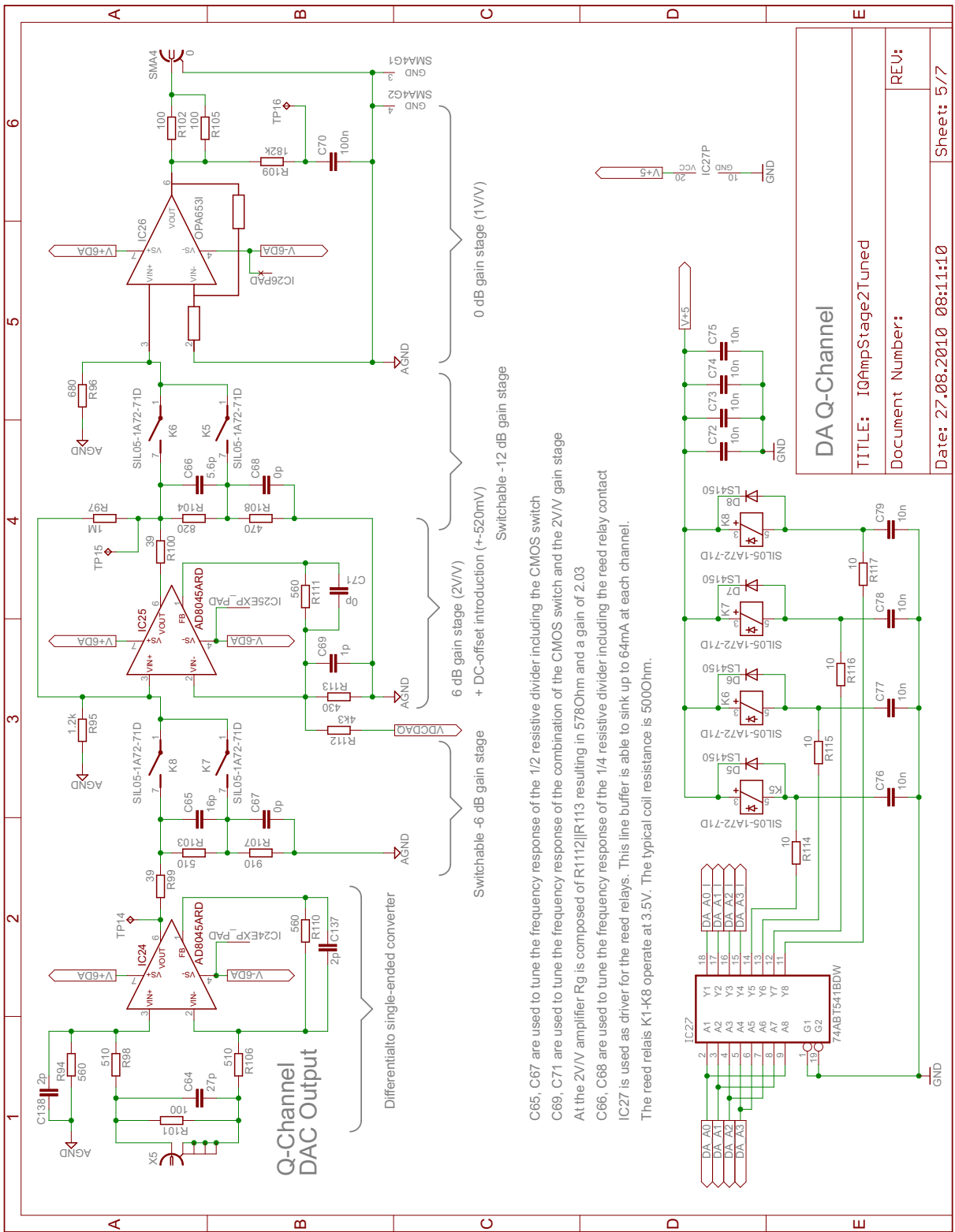
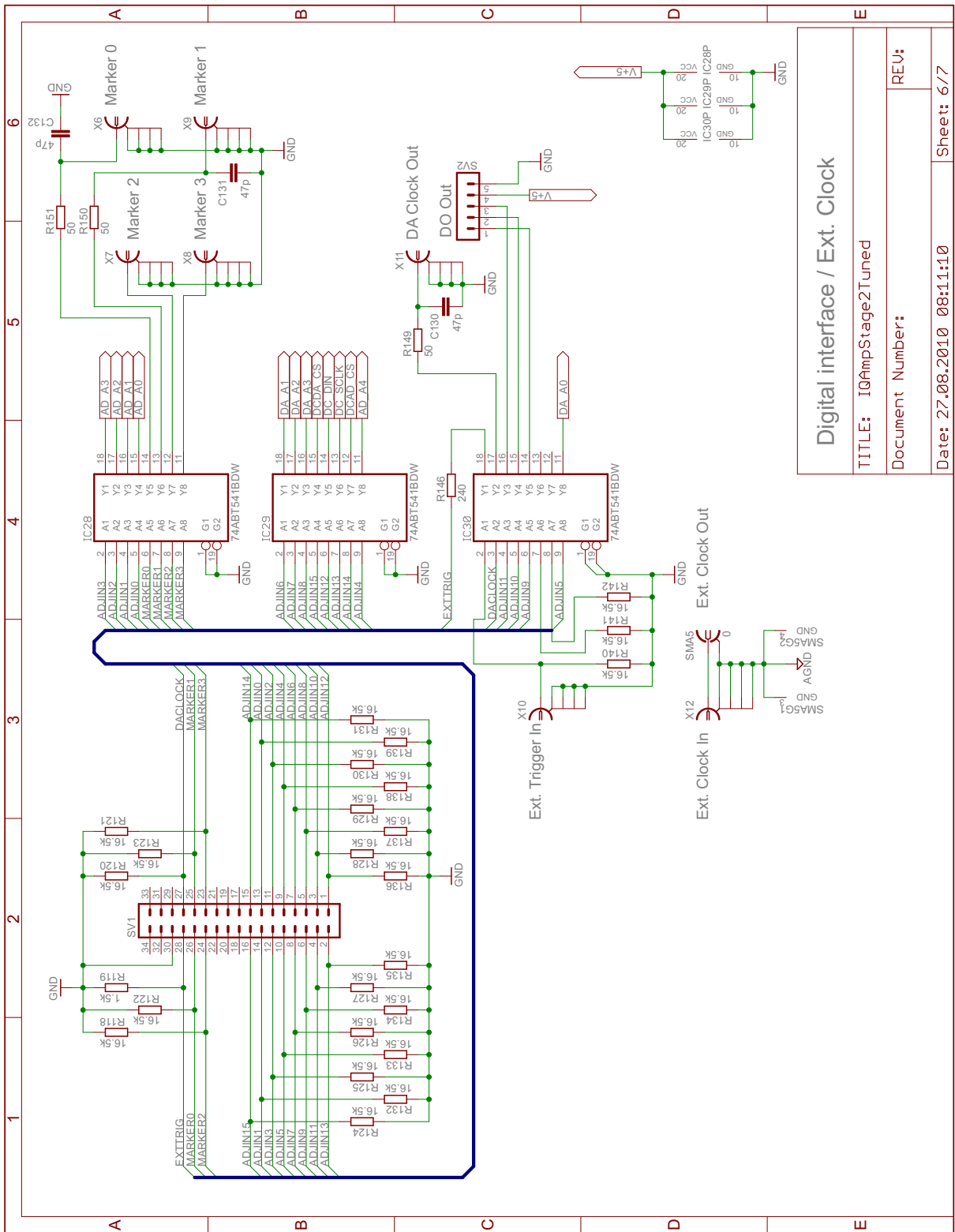Figure A.7: Schematic of the interface board, DA conversion, quadrature channel and reed contact control.

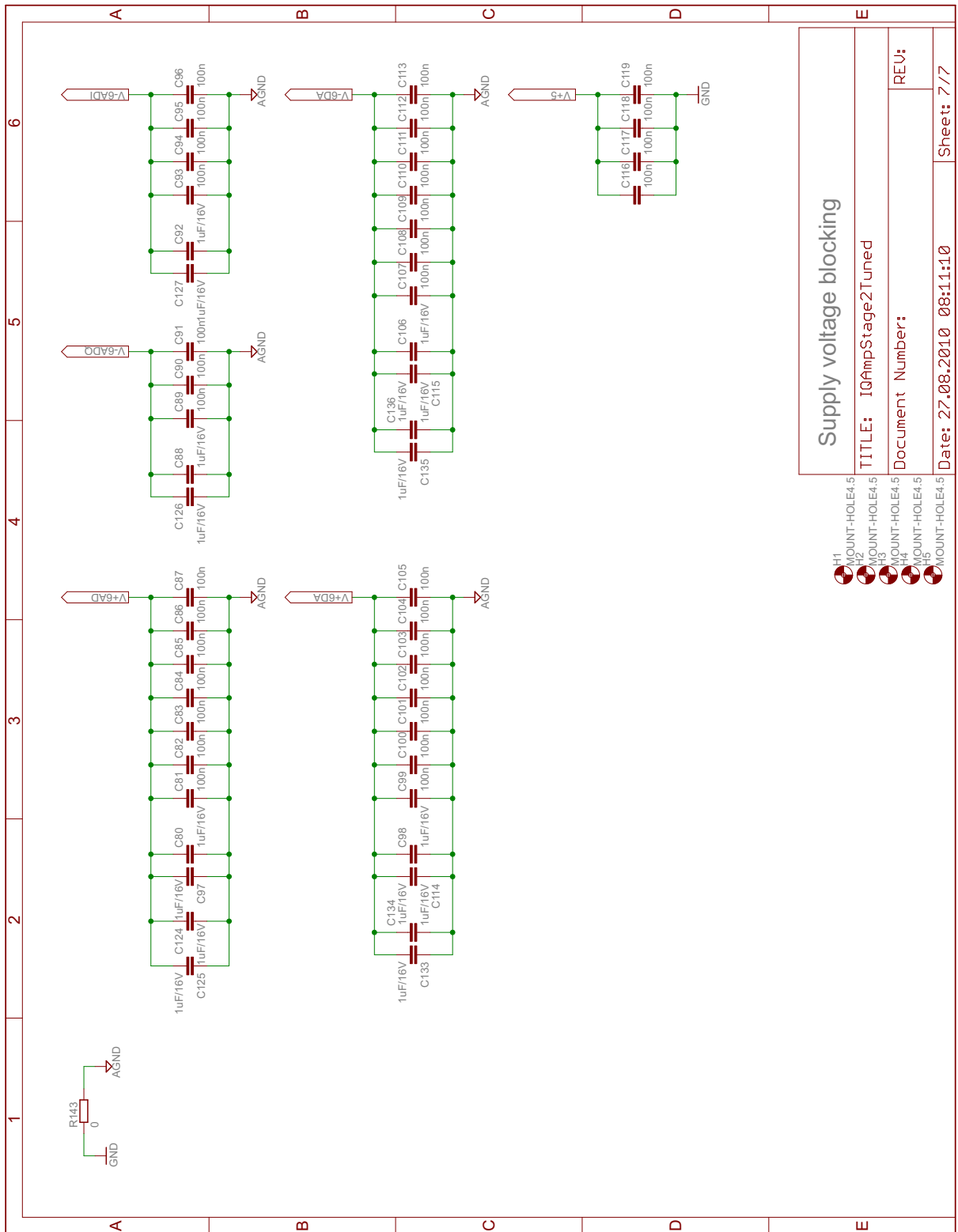Figure A.8: Schematic of the interface board, digital interface.
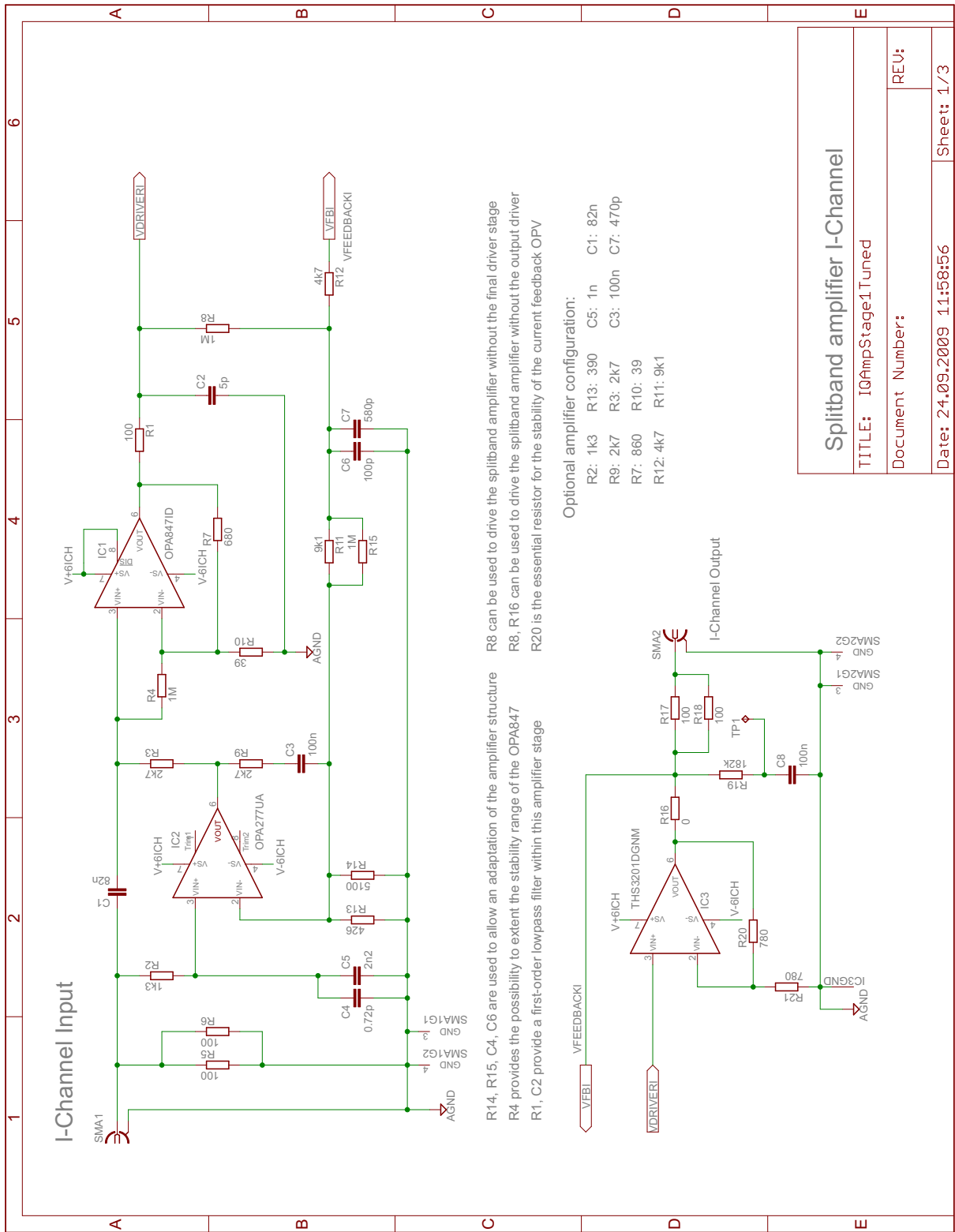
Figure A.9: Schematic of the interface board, blocking capacitors.

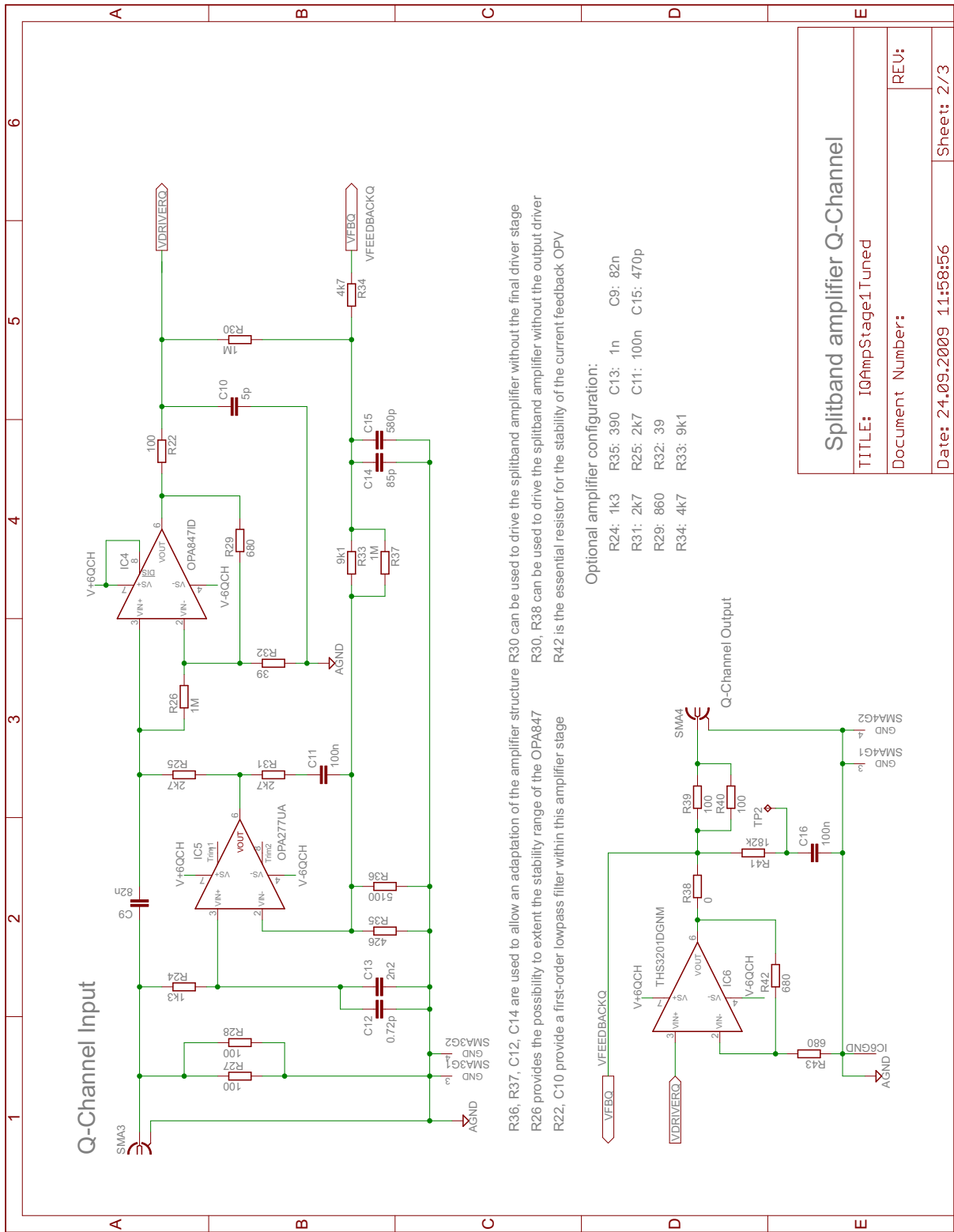Figure A.10: Schematic of the preamplifier board, inphase channel.

Figure A.11: Schematic of the preamplifier board, quadrature channel.
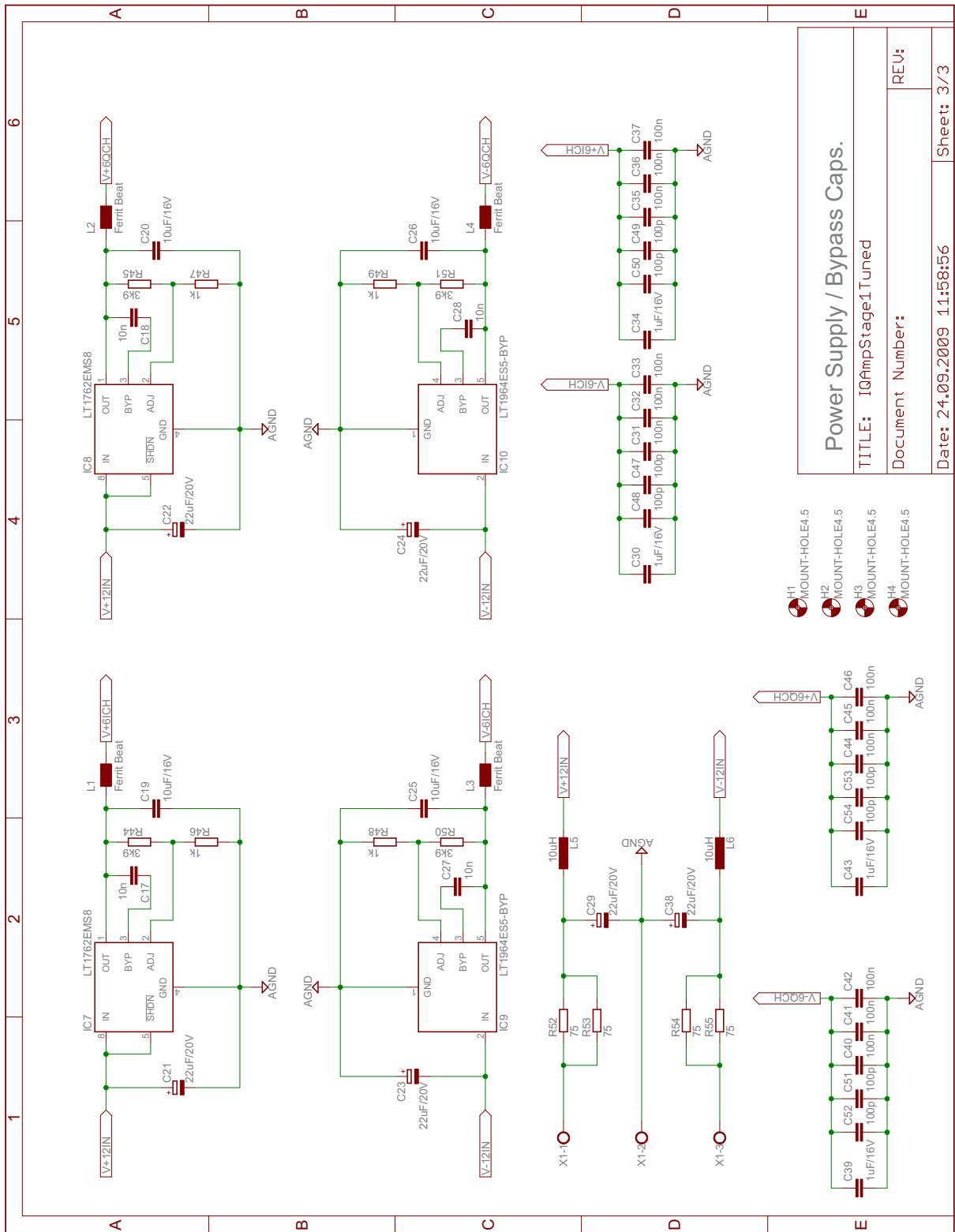
Figure A.12: Schematic of the preamplifier board, power supply unit and blocking capacitors.

Appendix B

5th-order postdistorter equations

The equations to deembed the impact of the mixer output nonlinearity for a third-order power series and polynomial based predistorter were presented in Subsection 3.8.6. In the following the corresponding results for a fifth-order postdistorter are presented. These equation were truncated after the 7th-order.

The equation for the case of real-valued mixer output nonlinearity coefficients are given by (polynomial postdistorter):

$$
\begin{aligned}
A_{\text{comp},1,1} \;=\; & -\frac{k_{lin}g_{M,3}}{g_{M,1}^4}\left(\frac{9}{16}A_{1,1}^3 + \frac{9}{8}A_{1,1}^2 A_{3,1} + 6A_{1,1}A_{0,2}A_{0,0} + 3A_{0,0}^2 A_{1,1} + \frac{3}{4}A_{1,1}A_{2,2}^2\right. \\
& + \frac{3}{2}A_{1,1}A_{2,2}A_{0,0} + \frac{3}{16}A_{1,1}^2 A_{3,3} + 3A_{1,1}A_{0,2}A_{2,2} + \frac{9}{2}A_{0,2}^2 A_{1,1} + \frac{21}{8}A_{3,1}^2 A_{1,1} \\
& + \frac{3}{2}A_{0,2}A_{3,3}A_{2,2} + \frac{3}{2}A_{2,2}A_{3,3}A_{0,0} + 6A_{0,2}A_{3,1}A_{0,0} + \frac{9}{2}A_{3,1}A_{2,2}A_{0,2} \\
& + 3A_{3,1}A_{2,2}A_{0,0} + \frac{3}{2}A_{3,1}A_{3,3}A_{1,1} + \frac{3}{2}A_{2,2}A_{1,1}A_{4,2} + 3A_{0,4}A_{0,2}A_{1,1} \\
& + \frac{3}{2}A_{0,4}A_{1,1}A_{2,2} + \frac{3}{2}A_{0,2}A_{1,1}A_{4,2} + \frac{3}{8}A_{1,1}A_{4,4}A_{2,2} + \frac{3}{2}A_{0,2}^2 A_{3,3} + \frac{3}{4}A_{3,3}^2 A_{1,1} \\
& \left. + \frac{3}{4}A_{3,1}A_{2,2}^2 + \frac{9}{2}A_{0,2}^2 A_{3,1} + \frac{3}{16}A_{2,2}^2 A_{3,3}\right) \\
& + \frac{k_{lin}g_{M,3}^2}{g_{M,1}^7}\left(\frac{75}{64}A_{1,1}^5 + 15A_{0,0}A_{1,1}^3 A_{2,2} + \frac{105}{4}A_{1,1}^3 A_{0,2}A_{2,2} + \frac{375}{64}A_{1,1}^4 A_{3,1}\right. \\
& \left. + \frac{735}{128}A_{1,1}^3 A_{2,2}^2 + \frac{135}{8}A_{0,0}^2 A_{1,1}^3 + \frac{375}{256}A_{1,1}^4 A_{3,3} + 45A_{0,0}A_{1,1}^3 A_{0,2} + \frac{555}{16}A_{1,1}^3 A_{0,2}^2\right)
\end{aligned}
$$
$$\text{(B.1)}$$

$$
\begin{aligned}
A_{\text{comp},3,1} \;=\; & -\frac{k_{lin}g_{M,3}}{g_{M,1}^4}\left(\frac{3}{16}A_{1,1}^3 + \frac{3}{2}A_{1,1}A_{2,2}A_{0,0} + \frac{9}{4}A_{0,2}^2A_{1,1} + \frac{21}{6}A_{1,1}^2A_{3,1} + \frac{3}{8}A_{1,1}^2A_{3,3}\right.\\
& +\frac{9}{4}A_{1,1}A_{0,2}A_{2,2} + \frac{3}{8}A_{1,1}A_{2,2}^2 + 3A_{1,1}A_{0,2}A_{0,0} + \frac{9}{8}A_{3,1}^2A_{1,1} + 3A_{0,0}^2A_{3,1}\\
& +\frac{3}{16}A_{1,1}^2A_{5,3} + \frac{9}{16}A_{1,1}^2A_{5,1} + 3A_{0,2}A_{3,3}A_{0,0} + \frac{3}{2}A_{1,1}A_{4,2}A_{0,0} + 3A_{0,4}A_{1,1}A_{0,0}\\
& +\frac{3}{2}A_{0,2}A_{3,3}A_{2,2} + 3A_{0,2}A_{3,1}A_{0,0} + 3A_{3,1}A_{2,2}A_{0,2} + \frac{3}{2}A_{3,1}A_{2,2}A_{0,0} + \frac{3}{2}A_{3,1}A_{3,3}A_{1,1}\\
& +\frac{9}{8}A_{2,2}A_{1,1}A_{4,2} + 3A_{0,4}A_{0,2}A_{1,1} + \frac{3}{2}A_{0,4}A_{1,1}A_{2,2} + 3A_{0,2}A_{1,1}A_{4,2} + \frac{3}{8}A_{1,1}A_{4,4}A_{2,2}\\
& \left.+\frac{3}{4}A_{0,2}^2A_{3,3} + \frac{15}{16}A_{3,1}A_{2,2}^2 + \frac{9}{2}A_{0,2}^2A_{3,1} + \frac{3}{8}A_{2,2}^2A_{3,3} + \frac{3}{4}A_{1,1}A_{4,4}A_{0,2}\right)\\
& +\frac{k_{lin}g_{M,3}^2}{g_{M,1}^7}\left(\frac{75}{128}A_{1,1}^5 + \frac{225}{128}A_{1,1}^4A_{3,3} + \frac{525}{128}A_{1,1}^3A_{2,2}^2 + \frac{195}{8}A_{0,0}A_{1,1}^3A_{0,2}\right.\\
& \left.+\frac{45}{8}A_{0,0}^2A_{1,1}^3 + \frac{45}{4}A_{0,0}A_{1,1}^3A_{2,2} + \frac{615}{32}A_{1,1}^3A_{0,2}A_{2,2} + \frac{1275}{256}A_{1,1}^4A_{3,1} + \frac{345}{16}A_{1,1}^3A_{0,2}^2\right)
\end{aligned}
\tag{B.2}
$$

$$
\begin{aligned}
A_{\text{comp},0,2} \;=\; & -\frac{k_{lin}g_{M,3}}{g_{M,1}^4}\left(\frac{3}{4}A_{1,1}^2A_{0,0} + \frac{9}{8}A_{1,1}^2A_{0,2} + \frac{3}{8}A_{1,1}^2A_{2,2} + \frac{9}{4}A_{0,2}A_{3,1}A_{1,1}\right.\\
& +\frac{3}{2}A_{0,0}A_{3,1}A_{1,1} + \frac{3}{8}A_{2,2}A_{1,1}A_{3,3} + 3A_{0,0}A_{0,2}A_{2,2} + \frac{3}{8}A_{1,1}^2A_{0,4} + \frac{9}{4}A_{0,2}^3\\
& \left.+\frac{9}{8}A_{2,2}^2A_{0,2} + \frac{3}{16}A_{1,1}^2A_{4,2} + \frac{9}{8}A_{2,2}A_{3,1}A_{1,1} + \frac{3}{4}A_{1,1}A_{0,2}A_{3,3} + 3A_{0,0}^2A_{0,2}\right)\\
& +\frac{k_{lin}g_{M,3}^2}{g_{M,1}^7}\left(\frac{555}{128}A_{1,1}^4A_{0,2} + \frac{105}{64}A_{1,1}^4A_{2,2} + \frac{45}{16}A_{0,0}A_{1,1}^4\right)
\end{aligned}
\tag{B.3}
$$

$$
\begin{aligned}
A_{\text{comp},2,2} \;=\; & -\frac{k_{lin}g_{M,3}}{g_{M,1}^4}\left(\frac{3}{2}A_{1,1}^2A_{0,2} + \frac{3}{4}A_{1,1}^2A_{0,0} + \frac{3}{4}A_{1,1}^2A_{2,2} + 3A_{0,0}A_{3,1}A_{1,1}\right.\\
& +\frac{3}{2}A_{1,1}A_{0,2}A_{3,3} + 3A_{2,2}A_{0,0}^2 + \frac{3}{2}A_{1,1}A_{0,0}A_{3,3} + \frac{3}{4}A_{1,1}^2A_{0,4} + \frac{3}{16}A_{1,1}^2A_{4,4}\\
& +\frac{3}{8}A_{2,2}A_{1,1}A_{3,3} + 6A_{0,2}^2A_{0,0} + \frac{3}{2}A_{2,2}A_{3,1}A_{1,1} + \frac{3}{4}A_{1,1}^2A_{4,2}\\
& \left.+\frac{9}{2}A_{0,2}A_{3,1}A_{1,1} + \frac{9}{16}A_{2,2}^3 + \frac{9}{2}A_{0,2}^2A_{2,2})\right)\\
& +\frac{k_{lin}g_{M,3}^2}{g_{M,1}^7}\left(\frac{735}{256}A_{1,1}^4A_{2,2} + \frac{15}{4}A_{0,0}A_{1,1}^4 + \frac{105}{16}A_{1,1}^4A_{0,2}\right)
\end{aligned}
\tag{B.4}
$$

Bibliography

[1] M. Kosunen, "Digital signal processing and digital-to-analog converters for wide-band transmitters," Ph.D. dissertation, Electronic Circuit Design Laboratory, Helsinki University of Technology, 2006.

[2] National Instruments, "Sources of error in IQ based RF signal," White paper, Tech. Rep., Jan. 2007.

[3] M. Valkama, A. Springer, and G. Hueber, "Digital signal processing for reducing the effects of rf imperfections in radio devices — an overview," in *Proc. IEEE Int Circuits and Systems (ISCAS) Symp*, Jun. 2010, pp. 813–816.

[4] A. Zolfaghari, *Low-Power CMOS Design for Wireless Transceivers*. Springer, Oct. 2002.

[5] F. Ellinger, *Radio Frequency Integrated Circuits and Technologies*, 2nd ed. Springer, Nov. 2010.

[6] A. Luzzatto and G. Shirazi, *Wireless Transceiver Design: Mastering the Design of Modern Wireless Equipment and Systems*. Wiley, Mar. 2007.

[7] R. Xu, Y. Jin, and C. Nguyen, "Power-efficient switching-based CMOS UWB transmitters for UWB communications and radar systems," *IEEE Trans. Microwave Theory Tech.*, vol. 54, no. 8, pp. 3271–3277, Aug. 2006.

[8] A. Abidi, "Direct-conversion radio transceivers for digital communications," *IEEE J. Solid-State Circuits*, vol. 30, no. 12, pp. 1399–1410, Dec. 1995.

[9] B. Razavi, "RF transmitter architectures and circuits," in *Proc. Custom Integrated Circuits*, May 1999, pp. 197–204.

[10] A. Loke and F. Ali, "Direct conversion radio for digital mobile phones-design issues, status, and trends," *IEEE Trans. Microwave Theory Tech.*, vol. 50, no. 11, pp. 2422–2435, Nov. 2002.

[11] F. H. Raab, P. Asbeck, S. Cripps, P. B. Kenington, Z. B. Popovic, N. Pothecary, J. F. Sevic, and N. O. Sokal, "Power amplifiers and transmitters for RF and microwave," *IEEE Trans. Microwave Theory Tech.*, vol. 50, no. 3, pp. 814–826, Mar. 2002.

[12] A. Bateman and D. M. Haines, "Direct conversion transceiver design for compact low-cost portable mobile radio terminals," in *Proc. IEEE 39th Vehicular Technology Conf.*, May 1989, pp. 57–62.

[13] C. Masse, "A direct-conversion transmitter for WiMAX and WiBro applications," *RF design*, pp. 42 – 46, Jan. 2006.

[14] H. Jeong, B.-J. Yoo, C. Han, S.-Y. Lee, K.-Y. Lee, S. Kim, D.-K. Jeong, and W. Kim, "A 0.25-μm CMOS 1.9-GHz PHS RF transceiver with a 150-kHz low-IF architecture," *IEEE J. Solid-State Circuits*, vol. 42, no. 6, pp. 1318–1327, Jun. 2007.

[15] M. Cassia, A. Hadjichristos, H. S. Kim, J.-S. Ko, J. Yang, S.-O. Lee, and G. Sahota, "A low-power CMOS SAW-less quad band WCDMA/HSPA/HSPA+/1X/EGPRS transmitter," *IEEE J. Solid-State Circuits*, vol. 44, no. 7, pp. 1897–1906, Jul. 2009.

[16] B. Tenbroek, J. Strange, D. Nalbantis, C. Jones, P. Fowers, S. Brett, C. Beghein, and F. Beffa, "Single-chip tri-band WCDMA/HSDPA transceiver without external SAW filters and with integrated TX power control," in *IEEE Int. Solid-State Circuits Conf. ISSCC 2008*, Feb. 2008, pp. 202–607.

[17] J. Choi, D. Kang, D. Kim, J. Park, B. Jin, and B. Kim, "Power amplifiers and transmitters for next generation mobile handsets," *Jour. of Semicon. Tech. and Sci.*, vol. 9, no. 4, pp. 249 – 256, Dec. 2009.

[18] J. Vankka, M. Kosunen, I. Sanchis, and K. A. I. Halonen, "A multicarrier QAM modulator," *IEEE Trans. Circuits Syst. II, Analog Digit. Signal Process.*, vol. 47, no. 1, pp. 1–10, Jan. 2000.

[19] K.-H. Cho and H. Samueli, "A frequency-agile single-chip QAM modulator with beamforming diversity," *IEEE J. Solid-State Circuits*, vol. 36, no. 3, pp. 398–407, Mar. 2001.

[20] M. Helaoui, S. Boumaiza, A. Ghazel, and F. M. Ghannouchi, "Low-IF 5 GHz WLAN linearized transmitter using baseband digital predistorter," in *Proc. 10th IEEE Int. Conf. Electronics, Circuits and Systems ICECS 2003*, Dec. 2003, pp. 260–263.

[21] D. Miyashita, H. Ishikuro, T. Shimada, T. Tanzawa, S. Kousai, H. Kobayashi, H. Majima, K. Agawa, M. Hamada, and F. Hatori, "A low-IF CMOS single-chip bluetooth EDR transmitter with digital I/Q mismatch trimming circuit," in *Proc. Digest of Technical Papers VLSI Circuits 2005 Symp*, Jun. 2005, pp. 298–301.

[22] Y. Kim and C.-S. Lee, "A novel method to remove the mismatch of the up-conversion mixer for a low IF transmitter," in *Proc. 47th Midwest Symp. Circuits and Systems MWSCAS '04*, Nov. 2004.

[23] V. Petrovic and W. Gosling, "Polar-loop transmitter," *Electronics Letters*, vol. 15, no. 10, pp. 286–288, Nov. 1979.

[24] P. B. Kenington, *High-Linearity RF Amplifier Design*. Artech House, 2000.

[25] M. R. Elliott, T. Montalvo, B. P. Jeffries, F. Murden, J. Strange, A. Hill, S. Nandipaku, and J. Harrebek, "A polar modulator transmitter for GSM/EDGE," *IEEE J. Solid-State Circuits*, vol. 39, no. 12, pp. 2190–2199, Dec. 2004.

[26] J. Choi, D. Kim, D. Kang, and B. Kim, "A polar transmitter with cmos programmable hysteretic-controlled hybrid switching supply modulator for multistandard applications," *IEEE Trans. Microwave Theory Tech.*, vol. 57, no. 7, pp. 1675–1686, Jul. 2009.

[27] T.-W. Kwak, M.-C. Lee, and G.-H. Cho, "A 2W CMOS hybrid switching amplitude modulator for EDGE polar transmitters," *IEEE J. Solid-State Circuits*, vol. 42, no. 12, pp. 2666–2676, Dec. 2007.

[28] J. N. Kitchen, C. Chu, S. Kiaei, and B. Bakkaloglu, "Combined linear and Δ-modulated switch-mode PA supply modulator for polar transmitters," *IEEE J. Solid-State Circuits*, vol. 44, no. 2, pp. 404–413, Feb. 2009.

[29] P. M. Cabral, J. C. Pedro, J. A. Garcia, and L. Cabria, "A linearized polar transmitter for wireless applications," in *Proc. IEEE MTT-S Int. Microwave Symp. Digest*, Jun. 2008, pp. 935–938.

[30] P. B. Kenington, *RF and Baseband Techniques for Software Defined Radio.* Artech House Publishers, Jun. 2005.

[31] P. Cruise, C.-M. Hung, R. B. Staszewski, O. Eliezer, S. Rezeq, K. Maggio, and D. Leipold, "A digital-to-RF-amplitude converter for GSM/GPRS/EDGE in 90-nm digital CMOS," in *Proc. Digest of Papers Radio Frequency integrated Circuits (RFIC) Symp. 2005 IEEE*, Jun. 2005, pp. 21–24.

[32] P. T. M. van Zeijl and M. Collados, "A digital envelope modulator for a WLAN OFDM polar transmitter in 90 nm CMOS," *IEEE J. Solid-State Circuits*, vol. 42, no. 10, pp. 2204–2211, Oct. 2007.

[33] P. Eloranta, P. Seppinen, S. Kallioinen, T. Saarela, and A. Parssinen, "A multimode transmitter in 0.13 μm CMOS using direct-digital RF modulator," *IEEE J. Solid-State Circuits*, vol. 42, no. 12, pp. 2774–2784, Dec. 2007.

[34] S. Kousai and A. Hajimiri, "An octave-range, watt-level, fully-integrated CMOS switching power mixer array for linearization and back-off-efficiency improvement," *IEEE J. Solid-State Circuits*, vol. 44, no. 12, pp. 3376–3392, Dec. 2009.

[35] C.-L. Ti and T.-H. Lin, "A 2.4-GHz 18mW two-point delta-sigma modulation transmitter for IEEE 802.15.4," in *International Symposium on VLSI Design, Automation and Test, 2007*, Apr. 2007, pp. 1–4, vLSI Design, Automation and Test, 2007. VLSI-DAT 2007. International Symposium on.

[36] C. Schuberth, P. Singerl, M. E. Gadringer, H. Arthaber, A. Wiesbauer, and G. Magerl, "Highly efficient switched-mode transmitter using a current mode class-D RF amplifier," *Int J RF and Microwave Comp Aid Eng*, vol. 20, no. 4, pp. 446–457, Jul. 2010.

[37] N. Demirel, E. Kerherve, R. Negra, and F. M. Ghannouchi, "A study of high-frequency bandpass delta-sigma transmitter architectures," in *Proc. 13th IEEE Int. Conf. Electronics, Circuits and Systems ICECS '06*, Dec. 2006, pp. 1117–1120.

[38] S.-R. Yoon and S.-C. Park, "All-digital transmitter architecture based on bandpass delta-sigma modulator," in *Proc. 9th Int. Symp. Communications and Information Technology ISCIT 2009*, Sept. 2009, pp. 703–706.

[39] T. Blocher and P. Singerl, "Coding efficiency for different switched-mode RF transmitter architectures," in *Proc. 52nd IEEE Int. Midwest Symp. Circuits and Systems MWSCAS '09*, Aug. 2009, pp. 276–279.

[40] S. Mirabbasi and K. Martin, "Classical and modern receiver architectures," *IEEE Commun. Mag.*, vol. 38, no. 11, pp. 132–139, Nov. 2000.

[41] F. Chastellain, C. Botteron, and P. Farine, "Looking inside modern receivers," *IEEE Microw. Mag.*, vol. 12, no. 2, pp. 87–98, Apr. 2011.

[42] J. Crols and M. S. J. Steyaert, "Low-IF topologies for high-performance analog front ends of fully integrated receivers," *IEEE Trans. Circuits Syst. II, Exp. Briefs*, vol. 45, no. 3, pp. 269–282, Mar. 1998.

[43] G. Girlando, S. A. Smerzi, T. Copani, and G. Palmisano, "A monolithic 12-GHz heterodyne receiver for DVB-S applications in silicon bipolar technology," *IEEE Trans. Microwave Theory Tech.*, vol. 53, no. 3, pp. 952–959, Mar. 2005.

[44] B. Razavi, "A millimeter-wave CMOS heterodyne receiver with on-chip LO and divider," *IEEE J. Solid-State Circuits*, vol. 43, no. 2, pp. 477–485, Feb. 2008.

[45] A. Parsa and B. Razavi, "A new transceiver architecture for the 60-GHz band," *IEEE J. Solid-State Circuits*, vol. 44, no. 3, pp. 751–762, Mar. 2009.

[46] B. Razavi, "Design considerations for direct-conversion receivers," *IEEE Trans. Circuits Syst. II, Analog Digit. Signal Process.*, vol. 44, no. 6, pp. 428–435, Jun. 1997.

[47] M. Kitsunezuka, T. Tokairin, T. Maeda, and M. Fukaishi, "A low-IF/zero-IF reconfigurable analog baseband IC with an I/Q imbalance cancellation scheme," *IEEE J. Solid-State Circuits*, vol. 46, no. 3, pp. 572–582, Mar. 2011.

[48] F. Beffa, T. Y. Sin, A. Tanzil, D. Ivory, B. Tenbroek, J. Strange, and W. Ali-Ahmad, "A receiver for WCDMA/EDGE mobile phones with inductorless front-end in 65nm CMOS," in *Proc. IEEE Int. Solid-State Circuits Conf.*, Feb. 2011, pp. 370–372.

[49] D. Kaczman, C. Dozier, N. Godambe, M. Shah, H. Guimaraes, M. Rachedine, M. Alam, L. Han, W. Shepherd, D. Cashen, J. Ganger, K. Couglar, B. Getka, E. Brotkowski, D. Wong, and D. Hayes, "A tri-band (2100/1900/800 MHz) single-chip cellular transceiver for WCDMA/HSDPA," in *Proc. Digest of Papers Radio Frequency integrated Circuits (RFIC) Symp. 2005 IEEE*, Jun. 2005, pp. 281–284.

[50] D. Stuetzle, "IP2 & IP3 design considerations with direct conversion I/Q demodulator receiver," *Microwave Engineering Europe*, no. 6, pp. 32–37, Jun. 2008.

[51] A. Taparia, S. A. Nakvi, and B. Banerjee, "A low-IF WiMAX RF transceiver in 0.18μm CMOS technology," in *Proc. IEEE Dallas Circuits and Systems Workshop: System-on-Chip - Design, Applications, Integration, and Software*, Oct. 2008, pp. 1–4.

[52] A. Hietala, S. Humphreys, R. Arkiszewski, B. Hunt, and S. Morris, "Self-shielded quad-band EGPRS transceiver with spur avoidance," *IEEE Trans. Microwave Theory Tech.*, vol. 57, no. 4, pp. 910–918, April 2009.

[53] J. Rudell, J.-J. Ou, T. Cho, G. Chien, F. Brianti, J. Weldon, and P. Gray, "A 1.9-GHz wide-band IF double conversion CMOS receiver for cordless telephone applications," *IEEE J. Solid-State Circuits*, vol. 32, no. 12, pp. 2071–2088, Dec. 1997.

[54] L. Xu, Q. Wang, J. Gao, Y. Wang, and P. Zhang, "A novel low-IF topology for high performance integrated receivers," in *International Conference on Intelligent Information Hiding and Multimedia Signal Processing, 2006.*, Dec. 2006, pp. 559–562.

[55] J.-S. Syu, C.-C. Meng, Y.-H. Teng, and H.-Y. Liao, "Large improvement in image rejection of double-quadrature dual-conversion low-IF architectures," *IEEE Trans. Microwave Theory Tech.*, vol. 58, no. 7, pp. 1703–1712, Jul. 2010.

[56] J. Li, R. G. Bosisio, and K. Wu, "Computer and measurement simulation of a new digital receiver operating directly at millimeter-wave frequencies," *IEEE Transactions on Microwave Theory and Techniques*, vol. 43, no. 12, pp. 2766–2772, Dec. 1995.

[57] P. Hakansson and S. Gong, "Ultra-wideband six-port transmitter and receiver pair 3.1–4.8 GHz," in *Proc. Asia-Pacific Microwave Conf.*, Dec. 2008, pp. 1–4.

[58] N. K. Mallat and S. O. Tatu, "Six-port receiver in millimeter-wave systems," in *Proc. ISIC Systems, Man and Cybernetics*, Oct. 2007, pp. 2693–2697.

[59] S. M. Winter, A. Koelpin, and R. Weigel, "Six-port receiver analog front-end: Multilayer design and system simulation," *IEEE Trans. Circuits Syst. II, Exp. Briefs*, vol. 55, no. 3, pp. 254–258, Mar. 2008.

[60] P. Perez-Lara, J. A. Medina-Rodriguez, I. Molina-Fernandez, J. G. Wanguemert-Perez, and A. Gonzalez-Salguero, "Wideband homodyne six-port receiver with high LO-RF isolation," *IET Microwaves, Antennas & Propagation*, vol. 3, no. 5, pp. 882–888, Aug. 2009.

[61] F. M. Ghannouchi and A. Mohammadi, *The Six-Port Technique with Microwave and Wireless Applications*. Artech House Publishers, Sep. 2009.

[62] H. Pekau and J. Haslett, "A comparison of analog front end architectures for digital receivers," in *Proceedings of the 2005 Canadian Conference on Electrical and Computer Engineeering (CCECE '05)*. IEEE, May. 2005, pp. 1073–1077.

[63] M. Streifinger, T. Muller, J.-F. Luy, and E. Biebl, "A software-radio front-end for microwave applications," in *Silicon Monolithic Integrated Circuits in RF Systems, 2003. Digest of Papers. 2003 Topical Meeting on*, Apr. 2003, pp. 53–56.

[64] S. A. Bassam, M. Helaoui, and F. M. Ghannouchi, "De-interleaved direct down-conversion receiver for SDR applications," in *Proc. IEEE MTT-S Int. Microwave Symp. Digest MTT '09*, Jun. 2009, pp. 1661–1664.

[65] A. Geis, J. Ryckaert, L. Bos, G. Vandersteen, Y. Rolain, and J. Craninckx, "A 0.5mm^2 power scalable 0.5-3.8GHz CMOS DT-SDR receiver with 2nd order RF band-pass sampler," *IEEE J. Solid-State Circuits*, vol. 45, no. 11, pp. 2375–2387, Nov. 2010.

[66] D. Hilborn, S. Stapleton, and J. Cavers, "An adaptive direct conversion transmitter," *IEEE Trans. Veh. Technol.*, vol. 43, no. 2, pp. 223–233, May 1994.

[67] V. Reding, "COMMISSION DECISION of 21 May 2008 on the harmonisation of the 3400-3800 MHz frequency band for terrestrial systems capable of providing electronic communications services in the community," EC Document number C(2008) 1873, Tech. Rep., Jun. 2008.

[68] H. Nachtnebel, "BenADDA system: High performance AD/DA converter system," Institute of Computer Technology, Vienna University of Technology, Tech. Rep., Nov. 2009.

[69] I. E. Burovoi, "Fast measurement of group delay in long electric networks," *Measurement Techniques*, vol. 32, no. 5, pp. 457–459, May 1989.

[70] M. E. Gadringer, T. Faseth, C. Schuberth, H. Arthaber, and G. Magerl, "Broadband baseband amplifier for a direct conversion measurement receiver," in *Mikroelektroniktagung*, Apr. 2010, pp. 203 – 207.

[71] R. Pazelt and H. Schweinzer, *Elektrische Messtechnik*, 2nd ed.   Springer Verlag, 1996.

[72] P. Wambacq and W. Sansen, *Distortion Analysis of Analog Integrated Circuits*.   Kluwer Academic Publishers, 1998.

[73] Agilent Technonogies, "Optimizing dynamic range for distortion measurements," Application Note, PN 5980-3079EN, Jun. 2002.

[74] E. McCune, "Taming the quadrature modulator," Tropian Inc., Jan. 2000, Whitepaper. [Online]. Available: http://www.tropian.com/tech/tech_docs/wse00.pdf

[75] A. Baier, "Quadrature mixer imbalances in digital TDMA mobile radio receivers," in *Proc. Seminar on Digital Communications 'Electronic Circuits and Systems for Communications'*, Mar. 1990, pp. 147–162.

[76] J. K. Cavers and M. W. Liao, "Adaptive compensation for imbalance and offset losses in direct conversion transceivers," *IEEE Trans. Veh. Technol.*, vol. 42, no. 4, pp. 581–588, Nov. 1993.

[77] R. A. Green, R. Anderson-Sprecher, and J. W. Pierre, "Quadrature receiver mismatch calibration," *IEEE Trans. Signal Process.*, vol. 47, no. 11, pp. 3130–3133, Nov. 1999.

[78] R. A. Green, "An optimized multi-tone calibration signal for quadrature receiver communication systems," in *IEEE Workshop on Statistical Signal and Array Processing*, Aug. 2000, pp. 664–667.

[79] M. E. Gadringer, T. Faseth, and G. Magerl, "Comparison of the imbalance effects in direct conversion transmitters and receivers," in *2011 Workshop on Integrated Nonlinear Microwave and Millimetre-wave Circuits Conference Proceedings*, Apr. 2011, pp. 89–92.

[80] J. K. Cavers, "The effect of quadrature modulator and demodulator errors on adaptive digital predistorters for amplifier linearization," *IEEE Trans. Veh. Technol.*, vol. 46, no. 2, pp. 456–466, May 1997.

[81] P. Kiss and V. Prodanov, "One-tap wideband I/Q compensation for zero-IF filters," *IEEE Trans. Circuits Syst. I, Reg. Papers*, vol. 51, no. 6, pp. 1062–1074, Jun. 2004.

[82] A. Ushida and L. O. Chua, "Frequency-domain analysis of nonlinear circuits driven by multi-tone signals," *IEEE Trans. Circuits Syst.*, vol. CAS-31, no. 9, pp. 766–779, Sept. 1984.

[83] D. Zill and P. Shanahan, *A First Course in Complex Analysis With Applications*, 2nd ed. Jones & Bartlett Publishers, 2008.

[84] V. Mathews and G. Sicuranza, *Polynomial Signal Processing*. John Wiley & Sons, 2000.

[85] H. Ku, M. D. McKinley, and J. S. Kenney, "Quantifying memory effects in RF power amplifiers," *IEEE Trans. Microwave Theory Tech.*, vol. 50, no. 12, pp. 2843–2849, Dec. 2002.

[86] M. C. Jeruchim, P. Balaban, and S. K. Shanmugan, *Simulation of Communication Systems*, 2nd ed., J. K. Wolf, Ed. Kluwer Academic / Plenum Publisher, 2001.

[87] M. Schetzen, *The Volterra and Wiener Theories of Nonlinear Systems*. Krieger Pub., 1989.

[88] J. Tubbax, B. Come, L. Van der Perre, L. Deneire, S. Donnay, and M. Engels, "OFDM versus single carrier with cyclic prefix: a system-based comparison," in *IEEE Vehicular Technology Conf. Dig.*, 2001, pp. 1115–1119.

[89] M. Faulkner, T. Mattsson, and W. Yates, "Automatic adjustment of quadrature modulators," *Electronics Letters*, vol. 27, no. 3, pp. 214–216, Jan. 1991.

[90] L. Ding, Z. Ma, D. R. Morgan, M. Zierdt, and G. Zhou, "Compensation of frequency-dependent gain/phase imbalance in predistortion linearization systems," *IEEE Trans. Circuits Syst. I, Reg. Papers*, vol. 55, no. 2, pp. 378–385, Feb. 2008.

[91] C. J. Clark, M. S. Muha, C. P. Silva, and A. A. Moulthrop, "Baseband time-domain waveform measurement method," U.S. Patent 6,211,663, Apr. 2001.

[92] F. Macraigne, T. Reveyrand, G. Neveux, D. Barataud, J.-M. Nébus, A. Soury, and E. NGoya, "Time-domain envelope measurements for characterization and behavioral modeling of nonlinear devices with memory," *IEEE Trans. Microwave Theory Tech.*, vol. 54, no. 8, pp. 3219–3226, Aug. 2006.

[93] D. Wisell and T. Öberg, "Analysis and identification of transmitter non-linearities," in *Symp. on communication systems, networks and digital signal processing*, Jul. 2000, pp. 418–421.

[94] D. Wisell, "Identification and measurement of transmitter non-linearities," in *Proc. th ARFTG Conference Digest-Fall*, Nov. 2000, pp. 1–6.

[95] H. Cao, A. Soltani Tehrani, C. Fager, T. Eriksson, and H. Zirath, "I/Q imbalance compensation using a nonlinear modeling approach," *IEEE Trans. Microwave Theory Tech.*, vol. 57, no. 3, pp. 513–518, Mar. 2009.

[96] D. Rabijns, W. van Moer, and G. Vandersteen, "Spectrally pure excitation signals: Only a dream?" in *Automatic RF Techniques Group Conf. Proc.*, Jun. 2003, pp. 53–63.

[97] N. B. Carvalho, J. C. Pedro, and J. P. Martins, "A corrected microwave multisine waveform generator," *IEEE Trans. Microwave Theory Tech.*, vol. 54, no. 6, pp. 2659–2664, Jun. 2006.

[98] L. Anttila, P. Handel, and M. Valkama, "Joint mitigation of power amplifier and I/Q modulator impairments in broadband direct-conversion transmitters," *IEEE Trans. Microwave Theory Tech.*, vol. 58, no. 4, pp. 730–739, Apr. 2010.

[99] A. Weinberg, "The effects of transponder imperfections on the error probability performance of a satellite communication system," *IEEE Trans. Commun.*, vol. 28, no. 6, pp. 858–872, Jun. 1980.

[100] C. Olgaard, "Using advanced signal analysis to identify sources of WLAN transmitter degradations," *RF design*, no. 10, pp. 28–36, Oct. 2004.

[101] D. Korn, "The effect of phase noise and spurs on coherent communications performance," in *IEEE Military Communications Conf. Proc.*, Nov. 1995, pp. 383–387.

[102] T. Lee and A. Hajimiri, "Oscillator phase noise: a tutorial," *IEEE J. Solid-State Circuits*, vol. 35, no. 3, pp. 326–336, Mar. 2000.

[103] H. Hedayati, B. Bakkaloglu, and W. Khalil, "Closed-loop nonlinear modeling of wideband $\Sigma\Delta$ fractional-N frequency synthesizers," *IEEE Trans. Microwave Theory Tech.*, vol. 54, no. 10, pp. 3654–3663, Oct. 2006.

[104] C. F. Lee and S. T. Peng, "Systematic analysis of the offset-PLL output spur spectrum," *IEEE Trans. Microwave Theory Tech.*, vol. 53, no. 9, pp. 3024–3034, Sep. 2005.

[105] C. Wicpalek, T. Mayer, L. Maurer, U. Vollenbruch, T. Pittorino, and A. Springer, "Analysis of spurious emission and in-band phase noise of an all digital phase locked loop for RF synthesis using a frequency discriminator," in *Int. Symp. on Circuits and Systems*, May 2007, pp. 3518–3521.

[106] L. Zhao and W. Namgoong, "A novel phase-noise compensation scheme for communication receivers," *IEEE Trans. Commun.*, vol. 54, no. 3, pp. 532–542, Mar. 2006.

[107] A. Tarighat, R. Hsu, A. Sayed, and B. Jalali, "Digital adaptive phase noise reduction in coherent optical links," *J. Lightw. Technol.*, vol. 24, no. 3, pp. 1269–1276, Mar. 2006.

[108] H.-G. Ryu, Y. Li, and J.-S. Park, "An improved ICI reduction method in OFDM communication system," *IEEE Trans. Broadcast.*, vol. 51, no. 3, pp. 395–400, Sep. 2005.

[109] N. Koster, B. Koster, D. Erni, and A. Beyer, "Oscillator design for suppressing spurious signals," *IEEE Microw. Mag.*, vol. 8, no. 3, pp. 67–80, Jun. 2007.

[110] V. Kratyuk, P. Hanumolu, U.-K. Moon, and K. Mayaram, "A low spur fractional-N frequency synthesizer architecture," in *Int. Symp. on Circuits and Systems*, May 2005, pp. 2807–2810.

[111] J. Kenney and P. Fedorenko, "Identification of RF power amplifier memory effect origins using third-order intermodulation distortion amplitude and phase asymmetry," in *IEEE MTT-S Int. Microwave Symposium Dig.*, June 2006, pp. 1121–1124.

[112] A. Walker, M. Steer, and K. Gard, "A vector intermodulation analyzer applied to behavioral modeling of nonlinear amplifiers with memory," *IEEE Trans. Microwave Theory Tech.*, vol. 54, no. 5, pp. 1991–1999, May 2006.

[113] D. Carl, *A Practical Guide to Splines*.　Springer, 2001.

[114] M. R. Siegel and J. Liu, *Schaum's Mathematical Handbook of Formulas and Tables*, 2nd ed.　McGraw-Hill, Feb. 1999.

[115] A. D. Poularikas, *Handbook of Formulas and Tables for Signal Processing*.　CRC Press, Sep. 1998.

[116] O. Hammi, S. Boumaiza, and F. Ghannouchi, "On the robustness of digital predistortion function synthesis and average power tracking for highly nonlinear power amplifiers," *IEEE Trans. Microwave Theory Tech.*, vol. 55, no. 6, pp. 1382–1389, June 2007.

[117] S.-J. Yi, S. Nam, S.-H. Oh, and J.-H. Han, "Prediction of a CDMA output spectrum based on intermodulation products of two-tone test," *IEEE Trans. Microwave Theory Tech.*, vol. 49, no. 5, pp. 938–946, May 2001.

[118] H. Baher, *Analog and Digital Signal Processing*, 2nd ed.　John Wiley & Sons, 2001.

[119] D. M. M.-P. Schreurs, M. O'Droma, A. A. Goacher, and M. E. Gadringer, *RF Power Amplifier Behavioral Modeling*.　Cambridge University Press, 2009.

[120] X. Y. Gao and W. M. Snelgrove, "Adaptive linearization schemes for weakly nonlinear systems using adaptive linear and nonlinear FIR filters," in *Proc. Midwest Symposium on Circuits and Systems*, Aug. 1990, pp. 9–12.

[121] J. Tsimbinos and K. Lever, "Measurement, composition and inversion of orthogonal representations of memoryless nonlinearities," in *Int. Symp. on Circuits and Systems*, May 1993, pp. 2494–2497.

[122] M. Valkama, M. Renfors, and V. Koivunen, "Advanced methods for I/Q imbalance compensation in communication receivers," *IEEE Trans. Signal Process.*, vol. 49, no. 10, pp. 2335–2344, Oct. 2001.

[123] ——, "Compensation of frequency-selective I/Q imbalances in wideband receivers: models and algorithms," in *IEEE Workshop on Signal Processing Advances in Wireless Communications*, Mar. 2001, pp. 42–45.

[124] G. Xing, M. Shen, and H. Liu, "Frequency offset and I/Q imbalance compensation for OFDM direct-conversion receivers," in *IEEE Conf. on Acoustics, Speech, and Signal Processing*, Apr. 2003, pp. 708–711.

[125] N. Blachman, "Detectors, bandpass nonlinearities, and their optimization: Inversion of the Chebyshev transform," *IEEE Trans. Inf. Theory*, vol. 17, no. 4, pp. 398–404, Jul. 1971.

[126] F. Churchill, G. Ogar, and B. Thompson, "The correction of I and Q errors in a coherent processor," *IEEE Trans. Aerosp. Electron. Syst.*, vol. AES-17, no. 1, pp. 131–137, Jan. 1981.

[127] K.-P. Pun, J. Franca, and C. Azeredo-Leme, "Wideband digital correction of I and Q mismatch in quadrature radio receivers," in *Int. Symp. on Circuits and Systems*, May 2000, pp. 661–664.

[128] A. Lohtia, P. Goud, and C. Englefield, "An adaptive digital technique for compensating for analog quadrature modulator/demodulator impairments," in *Proc. IEEE Pacific Rim Conf. on Communications, Computers and Signal Processing*, May 1993, pp. 447–450.

[129] M. Valkama, M. Renfors, and V. Koivunen, "Blind I/Q signal separation-based solutions for receiver signal processing," *EURASIP Jour. on Advances in Signal Processing*, vol. 2005, no. 1, pp. 2708–2718, Jan. 2005.

[130] F. Harris, "Digital filter equalization of analog gain and phase mismatch in I-Q receivers," in *Universal Personal Communication Conf.*, Oct. 1996, pp. 793–796.

[131] M. D. Kulkarni and A. B. Kostinski, "A simple formula for monitoring quadrature phase error with arbitrary signals," *IEEE Trans. Geosci. Remote Sens.*, vol. 33, no. 3, pp. 799–802, 1995.

[132] M. Mailand, R. Richter, and H.-J. Jentschel, "IQ-imbalance and its compensation for non-ideal analog receivers comprising frequency-selective components," *Adv. Radio Sci.*, no. 4, pp. 189–195, 2006.

[133] J. Lee, "Wideband I/Q demodulators: measurement technique and matching characteristics," *IEE Proceedings -Radar, Sonar and Navigation*, vol. 143, no. 5, pp. 300–306, Oct. 1996.

[134] S. Boyd, "Multitone signals with low crest factor," *IEEE Trans. Circuits Syst.*, vol. CAS-33, no. 10, pp. 1018–1022, Oct. 1986.

[135] Y. Rolain, W. Van Moer, R. Pintelon, and J. Schoukens, "Experimental characterization of the nonlinear behavior of RF amplifiers," *IEEE Trans. Microwave Theory Tech.*, vol. 54, no. 8, pp. 3209–3218, Aug. 2006.

Curriculum Vitae

Personal

Name:	Michael Ernst Gadringer
Date of birth:	8 December 1972
Place of birth:	Ried im Innkreis, Austria

Education

Period:	since January 2003
Institution:	Vienna University of Technology,
	Institute of Electrodynamics, Microwave and Circuit Engineering
Position:	PHD student

Duration:	March 1997 — Nov. 2002
Institution:	Vienna University of Technology
Degree:	Dipl.-Ing
Diploma Thesis:	Feedforward amplifier for GSM2+

Duration:	1987 — 1992
Institution:	HTBLA Braunau, Austria
	Training program: Electronic / Informatics
Degree:	General qualification for university entrance

Employment History

Period:	since July 2010
Function:	University Assistant
Institution:	Graz University of Technology,
	Institute of microwave and photonic engineering

Period:	January 2003 — June 2010
Institution:	Vienna University of Technology,
	Institute of Electrodynamics, Microwave and Circuit Engineering
Position:	Research Assistant

Period:	June 1993 — Feb. 1997
Function:	PLC development
Company:	Thyssen Aqua Engineering; Salzburg, Austria

Awards

Student Paper	IEEE Radio and Wireless Conference 2007
Competition:	Third place

Field of Interest

Topics:	Nonlinear behavioral modeling of microwave devices and systems
	Linearization of microwave devices and systems using digital
	pre- and postdistortion as well as feedforward techniques
	Microwave and mm-wave device characterization

Publications

Books :	D. Schreurs, M. O'Droma, A. A. Goacher, and M. Gadringer, "RF Power Amplifier Behavioral Modeling," Cambridge University Press, ISBN-13: 9780521881739, Oct. 2008.
Journal articles :	M. E. Gadringer, W. Bösch, and G. Magerl, "Phase Dependent Distortion in Direct Conversion Transmitters," IEEE Trans. Microwave Theory Tech., *accepted*.

C. Schuberth, P. Singerl, M. E. Gadringer, H. Arthaber, A. Wiesbauer, and G. Magerl,
"Highly Efficient Switched-Mode Transmitter Using a Current Mode Class-D RF Amplifier," Int. Jour. of RF and Microwave CAE, vol. 20, no 4, pp. 446 – 457, Jul. 2010.

M. E. Gadringer, C. Schuberth, and G. Magerl,
"Behavioral Modeling of the Frequency Translation Process in Direct Conversion Transmitters," Int. Jour. of RF and Microwave CAE, vol 20, no. 3, pp. 347 – 359, May 2010.

D. D. Silveira, P. L. Gilabert, P. M. Lavrador, J. C. Pedro, M. E. Gadringer, G. Montoro, E. Bertran, and G. Magerl,
"Improvements and Analysis of Nonlinear Parallel Behavioral Models," Int. Jour. of RF and Microwave CAE, vol. 19, no. 5, pp. 615 – 626, Sept. 2009.

P. L. Gilabert, M. E. Gadringer, G. Montoro, M. L. Mayer, D. D. Silveira, E. Bertran, and G. Magerl,
"An efficient combination of digital predistortion and OFDM clipping for power amplifiers," Int. Jour. of RF and Microwave CAE, vol. 19, no. 5, pp. 583 – 591, Sept. 2009.

P. L. Gilabert, D. D. Silveira, G. Montoro, M. E. Gadringer, and E. Bertran,
"Heuristic algorithms for power amplifier behavioral modeling," IEEE Microw. Wireless Compon. Lett., vol. 17, no. 10, pp. 715 – 717, Oct. 2007.

H. Arthaber, M. L. Mayer, A. Gafni, M. E. Gadringer, and G. Magerl,
"A time domain large signal measurement setup," Int. Jour. of RF and Microwave CAE, vol. 15, no. 1, pp. 3 – 12, Jan. 2005.

Conference paper :   M. E. Gadringer, T. Faseth, C. Schuberth, H. Arthaber, and G. Magerl,
"Broadband Baseband Amplifier for a Direct Conversion Measurement Receiver," Mikroelektroniktagung, pp. 203 – 207, Apr. 2010.

C. Schuberth, P. Singerl, H. Arthaber, M. Gadringer, and G. Magerl
"Design of a Current Mode Class-D RF Amplifier Using Load Pull Techniques," IEEE MTT-S Int. Microwave Symposium Dig., pp. 1521 – 1524, Jun. 2009.

M. E. Gadringer, C. Schuberth, and G. Magerl,
"Characterization and Modeling of Direct Conversion Transmitters," European Microwave Conf. Proc., pp. 745 – 748, Oct. 2008.

M. E. Gadringer, P. L. Gilabert, D. D. Silveira, G. Montoro, M. Mayer, E. Bertran, and G. Magerl,
"Hardware demonstrator for WiMax power amplifier linearisation using DPD algorithms," Proceedings of TARGET Days, pp. 37 – 40, Dec. 2007.

M. E. Gadringer, D. Silveira, and G. Magerl,
"Efficient power amplifier identification using modified parallel cascade Hammerstein models," IEEE Radio and Wireless Conf. Dig., pp. 305 – 308, Jan. 2007.

M. O'Droma; A.A. Goacher, E. Aschbacher, E. Bertran, P. Colantonio, S. Donati Guerrieri, F. Filicori, M. E. Gadringer, J. Luger, A. Meazza, M. Olavsbråten, J. Portilla, R. Quay, A. Zhu, K. Aamo, J. Berenguer, V. Camarchia, N. Carpenzano, F. J. Casas, A. Cesare, J. M. Collantes, C. Devlin, G. Ghione, P. L. Gilabert, J. Jugo, Y. Lei, T. Mathiesen, N. Mgebrishvili, G. Montoro, T. Parra, M. Pirola, M. Rossi, J. Santiago, T. J. Brazil, and G. Magerl,
"RF power amplifier linearisation — an overview," Proceedings of TARGET Days, pp. 9 – 12, Oct. 2006.

D. Silveira, M. E. Gadringer, P. L. Gilabert, G. Montoro, Y. Lei, E. R. Srinidhi, E. G. Lima, V. Camarchia, M. Pirola, G. Magerl, E. Bertran, A. A. Goacher, M. O'Droma, G. Kompa, and S. Donati,
"Comparison of RF power amplifier behavioural models estimated from shared measurement data," Proceedings of TARGET Days, pp. 129 – 132, Oct. 2006.

231

M. E. Gadringer, D. Silveira, and G. Magerl,
"Dynamic nonlinear model of a cancelation loop with application to the feedforward linearization technique," European Microwave Conf. Proc., pp. 1173 – 1176, Sept. 2006.

D. Silveira, M. E. Gadringer, M. Mayer, and G. Magerl,
"Analysis of RF-power amplifier modeling performance using a 16-QAM modulation over AWGN channels," International Workshop on Integrated Nonlinear Microwave and Millimeter-Wave Circuits, pp. 164 – 167, Jan. 2006.

D. Silveira, M. E. Gadringer, H. Arthaber, and G. Magerl,
"RF-power amplifier characteristics determination using parallel cascade Wiener models and pseudo-inverse techniques," Asia Pacific Microwave Conf. Dig., pp. 204 – 207, Dec. 2005.

D. Silveira, M. E. Gadringer, H. Arthaber, M. Mayer, and G. Magerl,
"Modeling, analysis and classificaton of a PA based on identified Volterra kernels," Gallium Arsenide and other Compound Semiconductors Application Symp., pp. 405 – 408, Oct. 2005.

M. O'Droma, E. Bertran, M. E. Gadringer, S. Donati, A. Zhu, P. Gilabert, and J. Portilla,
"Developments in predistortion and feedforward adaptive power amplifier linearisers," Gallium Arsenide and other Compound Semiconductors Application Symp., pp. 337 – 340, Oct. 2005.

M. E. Gadringer, C. Schuberth, and G. Magerl,
"Approximation of digital modulated carriers by multi-tone signal for device measurements," Integrated Nonlinear Microwave and Millimetre-wave Circuits Workshop, pp. 57 – 60, Nov. 2004.

M. E. Gadringer, H. Arthaber, and G. Magerl,
"Feedforward amplifier using power sensors for the loop balancing," European Microwave Conf. Proc., pp. 1223 – 1226, Oct. 2003.

M. E. Gadringer, H. Arthaber, and G. Magerl,
"Loop controller for a feedforward amplifier minimizing the measured power signal," IEEE Radio and Wireless Conf. Dig., pp. 281 – 284, Aug. 2003.